

NASA Conference Publication 3152
Part 1

International Symposium on Magnetic Suspension Technology

*Proceedings of an international symposium held at
Langley Research Center
Hampton, Virginia
August 19-23, 1991*

The NASA logo, consisting of the word "NASA" in a bold, sans-serif font, followed by a stylized "meatball" symbol. The logo is positioned at the bottom right of the page, below a horizontal line.

NASA Conference Publication 3152
Part 1

International Symposium on Magnetic Suspension Technology

Edited by
Nelson J. Groom
NASA Langley Research Center
Hampton, Virginia

Colin P. Britcher
Old Dominion University
Norfolk, Virginia

Proceedings of an international symposium sponsored by the
National Aeronautics and Space Administration,
Washington, D.C., and held at
Langley Research Center
Hampton, Virginia
August 19–23, 1991



National Aeronautics and
Space Administration
Office of Management
Scientific and Technical
Information Program

1992

INTRODUCTION

An International Symposium on Magnetic Suspension Technology was held at the Langley Research Center in Hampton, Virginia, on August 19–23, 1991. The symposium was sponsored by the Langley Research Center in coordination with the office of Aeronautics, Exploration, and Technology (OAET) in NASA Headquarters and was hosted by the Spacecraft Controls Branch at Langley Research Center. The symposium was chaired by the following people:

Nelson J. Groom, Co-Chairman
NASA
Langley Research Center
Hampton, VA 23665-5225

Dr. Robert A. Kilgore, Co-Chairman
NASA
Langley Research Center
Hampton, VA 23665-5225

Dr. Colin P. Britcher, Technical Program Co-Chairman
Dept. of Mechanical Engineering and Mechanics
Old Dominion University
Norfolk, VA 23529-0247

Dr. James R. Downer, Technical Program Co-Chairman
SatCon Technology Corporation
12 Emily Street
Cambridge, MA 02139-4507

Emily E. Kornegay, Administrative Chairman
NASA
Langley Research Center
Hampton, VA 23665-5225

The goal of the symposium was to examine the state of technology of all areas of magnetic suspension and to review related recent developments in sensors and controls approaches, superconducting magnet technology, and design/implementation practices. The symposium included 17 technical sessions in which 55 papers were presented. The technical sessions covered the areas of bearings, sensors and controls, microgravity and vibration isolation, superconductivity, manufacturing applications, wind tunnel magnetic suspension systems, magnetically levitated trains (MAGLEV), space applications, and large gap magnetic suspension systems. A list of attendees appears at the end of the document.

Certain materials and processes are identified in this publication in order to adequately specify procedures. In no case does such identification imply recommendation or endorsement by the government, nor does it imply that the materials or processes are the only or best ones available for the purpose.

Session 4 - Microgravity and Vibration Isolation 1

Chairman - Mike Scott, NASA Langley Research Center

- A Six Degree-of-Freedom Magnetic Bearing for Microgravity Vibration Isolation** 209 ✓
A. Peter Allan, Carl R. Knospe
- A Six Degree-of-Freedom Lorentz Force Vibration Isolator with Nonlinear Controls** 219 ✓
Ralph C. Fenn, Michael Gerver, and Bruce Johnson

Session 5 - Superconductivity 1

Chairman - Jim Downer, SatCon Technology Corporation

- Recent Progress Towards Developing a High Field, High- T_c Superconducting Magnet for Magnetic Suspension and Balance Systems** 247 ✓
L. Pierre de Rochemont, Carlton E. Oakes, Michael R. Squillante, Hong-Min Duan,
Allen M. Hermann, Robert J. Andrews, Roger B. Poeppel, Victor A. Maroni,
Ingrid A. Carlberg, and Warren C. Kelliher
- Levitation of $YBa_2Cu_3O_{7-x}$ Superconductor in a Variable Magnetic Field** 267 ✓
Alexander N. Terentiev and Anatoliy A. Kuznetsov
- Hybrid Superconducting Magnetic Bearing (HSMB) for High Load Devices** 279 ✓
C. K. McMichael, K. B. Ma, M. A. Lamb, M. W. Lin, L. Chow, R. L. Meng
P. H. Hor, and W.-K. Chu
- Characterization of Superconducting Magnetic Bearings (Dynamic stiffness and damping coefficients in axial direction)** 289 ✓
Ryoichi Takahata, Hirochika Ueyama, and Tsutom Yotsuya

Session 6 - Bearings 2

Chairman - Claude Keckler, NASA Langley Research Center

- Feasibility of Magnetic Bearings for Advanced Gas Turbine Engines** 299 ✓
David Hibner and Lewis Rosado
- Low Power Magnetic Bearing Design for High Speed Rotating Machinery** 317 ✓
P. E. Allaire, E. H. Maslen, R. R. Humphris, C. K. Sortore, and P. A. Studer
- Progress of Magnetic Suspension Systems and Magnetic Bearings in the USSR** 331 ✓
A. V. Kuzin

Session 7 - Sensors and Controls 2

Chairman - Monique Gaffney, SatCon Technology Corporation

- Extended H_2 Synthesis for Multiple Degree-of-Freedom Controllers** 363 ✓
R. David Hampton and Carl R. Knospe - University of Virginia

CONTENTS

| | |
|------------------------|-----|
| Introduction | iii |
|------------------------|-----|

Part 1

Session 1 - Introductions and Review Papers

Chairman - Robert A. Kilgore, NASA Langley Research Center

| | |
|--|------|
| Overview of Magnetic Suspension Research at NASA Langley Research Center | 3 ✓ |
| Nelson J. Groom | |
| Professor Jesse W. Beams and the First Practical Magnetic Suspension | 25 ✓ |
| Paul E. Allaire, Robert R. Humphris, and David W. Lewis | |
| Large-Gap Magnetic Suspension Systems | 33 ✓ |
| Colin P. Britcher | |

Session 2 - Bearings 1

Chairman - Paul E. Allaire, University of Virginia

| | |
|--|-------|
| Magnetic Bearings: A Key Technology for Advanced Rocket Engines? | 53 ✓ |
| J. Ph. Girault | |
| Active Magnetic Bearings—As Applied to Centrifugal Pumps | 73 ✓ |
| Lev Nelik, Paul Cooper, Graham Jones, Dennis Galecki, Frank Pinckney, and Gordon Kirk | |
| Precision Magnetic Suspension Linear Bearing | 89 ✓ |
| David L. Trumper and Michael A. Queen | |
| Modelling and Design for PM/EM Magnetic Bearings | 105 ✓ |
| D. Pang, J. A. Kirk, D. K. Anand, R. G. Johnson, and R. B. Zmood | |

Session 3 - Sensors and Controls 1

Chairman - Mark Motter, NASA Langley Research Center

| | |
|--|-------|
| Application of Narrow Band Control to Reduce Vibrations in Magnetic Bearing Systems | 123 ✓ |
| Monique S. Gaffney and Bruce G. Johnson | |
| Dynamics and Control of High Precision Magnetically Levitated Vibration Isolation Systems | 149 ✓ |
| K. Youcef-Toumi and T-J Yeh | |
| Stability and Performance of Notch Filter Controllers for Unbalanced Response | 181 ✓ |
| Carl R. Knospe | |

| | |
|--|-------|
| Experimental Results in Nonlinear Compensation of a One Degree-of-Freedom Magnetic Suspension | 385 ✓ |
| David L. Trumper, James C. Sanders, Tiep H. Nguyen, and Michael A. Queen | |
| Control Concepts for Active Magnetic Bearings | 401 ✓ |
| R. Siegwart, D. Vischer, R. Larssonneur, R. Herzog, A. Traxler, H. Bleuler, and G. Schweitzer | |
| Computer Aided Design of a Digital Controller for Radial Active Magnetic Bearings | 423 ✓ |
| Zhong Cai, Zupei Shen, Zuming Zhang, and Hongbin Zhao | |

Session 8 - Microgravity and Vibration Isolation 2

Chairman - Ralph Fenn, SatCon Technology Corporation

| | |
|--|-------|
| A Microgravity Vibration Isolation Rig | 435 ✓ |
| Bibhuti B. Banerjee, Carl R. Knospe, and Paul E. Allaire | |
| Vibration Damping of Elastic Waves in Electrically Conducting Media Subjected to High Magnetic Fields | 457 ✓ |
| T. G. Horwath | |
| Coarse-Fine Residual Gravity Cancellation System with Magnetic Levitation | 473 ✓ |
| S. E. Salcudean, H. Davis, C. T. Chen, D. E. Goertz, and B. V. Tryggvason | |
| Attendees | 493 ✓ |

Part 2*

Session 9 - Superconductivity 2

Chairman - Warren C. Kelliher, NASA Langley Research Center

| | |
|--|-----|
| Magnetic Suspension Using High Temperature Superconducting Cores | 507 |
| R. G. Scurlock | |
| Effect of Flux Penetration on the Load Capacity of Passive Superconducting Bearings | 519 |
| Dantam K. Rao | |
| Application of Ceramic Superconductors in High Speed Turbines | 535 |
| C. K. McMichael, M. A. Lamb, M. W. Lin, K. B. Ma, and W. K. Chu | |
| Cryogenic Test Rig with an Aerodynamic Magnetically Levitated Carriage | 547 |
| Sergey Yu. Borisov, Anton L. Iskra, and Anatoly P. Philatov | |

Session 10 - Bearings 3

Chairman - Jim Downer, SatCon Technology Corporation

| | |
|---|-----|
| The Bearingless Electrical Machine | 561 |
| J. Bichsel | |

*Part 2 is presented under separate cover.

| | |
|--|-----|
| Wide Gap, Permanent Magnet Biased Magnetic Bearing System | 575 |
| Karl Boden | |

| | |
|---|-----|
| Force Analysis of Magnetic Bearings with Power-Saving Controls | 595 |
| Dexter Johnson, Gerald V. Brown, and Daniel J. Inman | |

Session 11 - Manufacturing Applications

Chairman - Nelson J. Groom, NASA Langley Research Center

| | |
|--|-----|
| Manipulation and Identification of Objects by Magnetic Forces | 617 |
| Benjamin Joffe | |

| | |
|---|-----|
| Precise Positioning and Compliance Synthesis for Automatic Assembly Using Lorentz Levitation | 639 |
| R. L. Hollis and S. Salcudean | |

Session 12 - Bearings 4

Chairman - Timothy Hawkey, SatCon Technology Corporation

| | |
|---|-----|
| Development of a Differentially Balanced Magnetic Bearing and Control System for use with a Flywheel Energy Storage System | 657 |
| Mark A. Higgins, David P. Plant, Douglas M. Ries, James A. Kirk, and Davinder K. Anand | |

| | |
|--|-----|
| Design of Bearings for Rotor Systems Based on Stability | 673 |
| D. Dhar, L. E. Barrett, and C. R. Knospe | |

| | |
|--|-----|
| An Evaluation of Some Strategies for Vibration Control of Flexible Rotors | 691 |
| C. R. Burrows | |

Session 13 - Wind Tunnel Magnetic Suspension Systems

Chairman - Robert A. Kilgore, NASA Langley Research Center

| | |
|---|-----|
| Propulsion Simulator for Magnetically Suspended Wind Tunnel Models | 709 |
| P. B. Joshi, M. R. Malonson, G. P. Sacco, C. L. Goldey, K. Garbutt, M. Goodyer, and P. Lawing | |

| | |
|---|-----|
| Present Status of the MIT/NASA Langley 6 inch MSBS | 741 |
| Timothy Schott, Thomas Jordan, and Taumi Daniels | |

| | |
|---|-----|
| Progress of Magnetic Suspension and Balance Systems for Wind Tunnels in the USSR | 765 |
| A. V. Kuzin, Y. D. Vyshkov, and G. K. Shapovalov | |

| | |
|--|-----|
| Wind Tunnel Magnetic Suspension Systems at the University of Southampton, England | 775 |
| Michael J. Goodyer | |

Session 14 - Magnetically Levitated Trains (MAGLEV) 1

Chairman - Colin P. Britcher, Old Dominion University

| | |
|--|------------|
| Attractive and Repulsive Magnetic Suspension Systems Overview | 791 |
| David B. Cope and Richard R. Fontana | |
| Change in the Coil Distribution of Electrodynamic Suspension System | 813 |
| Hisashi Tanaka | |
| The Concept of the Mechanically Active Guideway as a Novel Approach to Maglev | 827 |
| T. G. Horwath | |

Session 15 - Space Applications

Chairman - Nelson J. Groom, NASA Langley Research Center

| | |
|---|------------|
| Space Applications of Diamagnetic Suspensions | 847 |
| Ronald E. Pelrine | |
| Magnetic Bearing Wheels for Very High Pointing Accuracy Satellite Missions | 857 |
| J. P. Roland | |
| An Electrostatically Suspended, Micro-Mechanical Rate Gyroscope | 873 |
| Timothy Hawkey and Richard Torti | |

Session 16 - Magnetically Levitated Trains (MAGLEV) 2

Chairman - Colin P. Britcher, Old Dominion University

| | |
|---|------------|
| Battery Cars on Superconducting Magnetically Levitated Carriers—One Commuting Solution | 895 |
| B. Mike Briggs and Henry Oman | |
| Knolle Magnetrams, A Magnetically Levitated Train System | 907 |
| Ernst G. Knolle | |
| Computation of Magnetic Suspension of Maglev Systems Using Dynamic Circuit Theory | 919 |
| J. L. He, D. M. Rote, and H. T. Coffey | |

Session 17 - Large-Gap Magnetic Suspension Systems

Chairman - Nelson J. Groom, NASA Langley Research Center

| | |
|--|------------|
| Large-Gap Magnetic Positioning System Having Advantageous Configuration | 941 |
| Paul Chong, Colin Commandeur, Harold Davis, and Lorne Whitehead | |
| Performance of a Superconducting Large-Angle Magnetic Suspension | 955 |
| James R. Downer, Dariusz A. Bushko, Vijay Gondhalekar, and Richard P. Torti | |

| | |
|--|------------|
| The Large-Angle Magnetic Suspension Test Fixture | 971 |
| Colin P. Britcher, Mehran Ghofrani, Thomas C. Britton, and Nelson J. Groom | |
| Attendees | 987 |

Part 1

Session 1

INTRODUCTIONS AND REVIEW PAPERS

Chairman - Robert A. Kilgore
NASA Langley Research Center

N 9 2 - 2 7 7 2 2

**OVERVIEW OF MAGNETIC SUSPENSION RESEARCH
AT LANGLEY RESEARCH CENTER**

Nelson J. Groom

SUMMARY

An overview of research in small- and large-gap magnetic suspension systems at Langley Research Center (LaRC) is presented. The overview is limited to systems which have been built as laboratory models or engineering models. Small-gap systems applications include the Annular Momentum Control Device (AMCD), which is a momentum storage device for the stabilization and control of spacecraft, and the Annular Suspension and Pointing System (ASPS), which is a general purpose pointing mount designed to provide orientation, mechanical isolation, and fine pointing of space experiments. These devices are described and control and linearization approaches for the magnetic suspension systems for these devices are discussed. Large-gap systems applications at LaRC have been almost exclusively wind tunnel magnetic suspension systems. A brief description of these efforts is also presented.

INTRODUCTION

Research in small-gap magnetic suspension systems at Langley Research Center (LaRC) began in the early 1970's with the development of the Annular Momentum Control Device (AMCD) concept. The AMCD is a momentum storage device with applications to the stabilization and control of spacecraft (ref. 1). This research was continued with the development of the Annular Suspension and Pointing System (ASPS) concept. The ASPS is a derivative of the AMCD and is a general purpose pointing mount designed to provide orientation, mechanical isolation, and fine pointing of space experiments (refs. 2 and 3). These devices will be described, and control and linearization approaches for the magnetic suspension systems for these devices will be discussed.

Research in large-gap magnetic suspension systems at LaRC began in the early 1960's and has been focused almost entirely on wind tunnel systems. The research began with the development of a single degree-of-freedom demonstration system (ref. 4) and has continued to the present with design studies of large-scale systems with superconducting magnets (ref. 5). A brief description of the wind tunnel magnetic suspension system efforts at LaRC will be presented.

SMALL-GAP SUSPENSION SYSTEMS

Annular Momentum Control Device (AMCD)

Magnetic suspension has historically been viewed as a promising solution to several problems encountered in the long-term utilization of momentum storage devices for spacecraft control. However, earlier efforts toward the application of magnetic suspension technology were focused on developing a direct physical replacement for the mechanical bearings of conventional shaft-driven and suspended-steel flywheels. The conventional approach, using a central hub with a shaft to provide support for both translational forces and rotational moments, was motivated in part by the need to keep the bearings self-contained and as small as possible so that bearing surface speed and drag effects could be kept to acceptable levels. With magnetic suspension there are no contacting surfaces and, with proper design,

drag losses can be made relatively small. Therefore, bearing surface speed ceases to be a constraint. A reexamination of conventional approaches to the design of momentum storage devices on both a device and system level, without the bearing surface speed constraint, led to the concept of the AMCD (ref. 6). The basic concept of the AMCD consists of a spinning annular rim suspended by a minimum of three noncontacting magnetic suspension stations and is driven by a noncontacting electromagnetic spin motor. The use of a thin annular rim provides the maximum momentum-to-mass ratio for any material since the spinning mass is concentrated at the largest mean radius. Significant improvements in this ratio can be obtained by using lightweight, high strength, composite materials since, for a rim, the stresses due to rotation are predominantly circumferential. The utilization of noncontacting suspension and driving elements eliminates mechanical wear and lubrication subsystem failures and results in system reliability characteristics equal to those of the magnetic suspension and rim drive motor electronics. A further advantage of the magnetic suspension system is that it can be tuned to provide for effective isolation of vibrations, generated by the rotating rim, from the vehicle and its scientific payloads. In addition, the magnetic suspension can produce smooth forces without threshold type nonlinearities (i.e., no mechanical breakout forces). The advantage of this characteristic is that small, precision, precessional torques can be generated by "gimbaling" the rim in the magnetic gaps.

In order to investigate technology requirements and evaluate certain design approaches, the AMCD was implemented as a laboratory test model. The laboratory model, shown in figure 1, consists of a graphite/epoxy composite rim, three magnetic suspension stations, three spin motor stator element pairs (one pair per suspension station), and six pneumatic backup bearings (required for laboratory use only). The suspension assemblies are attached to an aluminum base plate. A vacuum cover fits over the suspension-motor-rim-backup bearing assembly and bolts to the base plate for high-speed spin tests. The rim is 1.7m (5.5 ft) in diameter, weighs 22.68 kg (50 lb), and is designed to rotate at 2,741 rpm. The rim momentum at this speed is 4,068 N-m-s (3,000 ft-lb-sec). A detailed description of the AMCD laboratory test model, as delivered, is given in reference 7, and preliminary test results are presented in reference 8. Additional information related to the laboratory model is available in references 9-16. Potential applications of the AMCD concept are presented in references 17-22.

Annular Suspension and Pointing System (ASPS)

The ASPS was developed to meet the need for a multipurpose experiment pointing platform which was established during NASA Earth-orbital systems technology guidance and control planning activities in the early 1970's. The ASPS is a derivative of the AMCD and uses a similar magnetic bearing design and suspension technique. However, the two are very different in purpose and operation (refs. 23-24). The ASPS (fig. 2) consists of a vernier assembly, which uses magnetic suspension, and a mechanical gimbal assembly, which uses conventional *dc* motor technology. The magnetic suspension of the vernier assembly provides high accuracy pointing (0.01 arcsec) and isolation from carrier motion disturbances. The mechanical gimbal assembly allows for system deployment, target acquisition and tracking, retargeting, and can serve as a backup, at reduced performance levels, in case of vernier assembly failure. A typical payload-ASPS-carrier vehicle configuration is shown in figure 3.

In order to demonstrate the very high accuracy pointing and control capability of the ASPS concept, a decision was made to fabricate and test an engineering model of the ASPS. The ASPS vernier assembly engineering model, with payload plate removed, is shown in figure 4. The payload plate bolts to the annular rotor which is suspended by five magnetic bearing actuators (MBA's) that provide control over three translational axes and rotations about the two transverse axes. Control about the roll axis is provided by a segmented *ac* induction motor. Power and data to and from the payload are provided by a rotary transformer and an optical coupler, respectively. Therefore, the only connection between payload and carrier vehicle is through the stiffness of the MBA servo loops which, because of the decoupling scheme used (ref. 2), acts through the payload's center of mass.

Additional information on the ASPS design and development and related analyses and simulations are presented in references 25-31.

SMALL-GAP ACTUATOR LINEARIZATION AND CONTROL APPROACHES

In order to define the basic type of small-gap magnetic bearing actuator which will be discussed in this paper, the simplified schematic of figure 5 is introduced. Shown are upper and lower electromagnets with currents I_U and I_L , producing forces F_U and F_L on a suspended element positioned in the center between the electromagnets at a gap distance G_o from the top electromagnet pole face. Since an electromagnet of the type being discussed produces an attractive force only, two are required to produce a bidirectional force capability. A position sensor is shown which measures the displacement G_s of the suspended element with respect to the centered position G_o . Position information is required for active control of the suspended element and is also required for some of the linearization approaches to be discussed. Under ideal assumptions, the force produced by a given electromagnet is directly proportional to the square of the coil current and inversely proportional to the square of the electromagnet gap (ref. 10) and can be written as

$$F = K(I^2/G^2) \quad (1)$$

Two approaches have been investigated for controlling this type of actuator. One approach involves controlling the upper and lower electromagnets differentially about a bias flux. The bias flux can either be supplied by permanent magnets in the magnetic circuit or by bias currents. In the other approach, either the upper electromagnet or the lower electromagnet is controlled depending on the direction of the force required.

Bias Flux Linearization and Control Approaches

Permanent Magnet.- The original control approach used for the laboratory model AMCD magnetic actuators was permanent magnet flux biasing. The operation of a permanent magnet flux-biased magnetic actuator can be described by referring to figure 6. This figure is a simplified schematic which shows a single actuator, for control along a single axis, which consists of a pair of magnetic bearing elements with permanent magnets mounted in the cores. The bearing elements are shown connected in a differential configuration. That is, for

a given input, the amplifier driver shown in the figure produces current in a direction to aid the permanent-magnet-produced flux in one element and, at the same time, produces equal current in a direction to subtract from the permanent-magnet-produced flux in the other element. This change in flux results in a net force produced on the suspended mass in a direction dependent on the polarity of the input to the amplifier driver. The force produced by this type actuator as a function of current, I , and gap, G , can be written as (from ref. 10)

$$F = \frac{K_1}{4} \left(\frac{[I_o + I]^2}{[x_o - G]^2} - \frac{[I_o - I]^2}{[x_o + G]^2} \right) \quad (2)$$

where K_1 , \bar{x}_o , and I_o are constants (defined in ref. 10). I_o can be thought of as an equivalent constant bias current provided by the permanent magnets. Figure 7 shows the composite force-current characteristic of this type actuator with the suspended mass centered in the gaps. This figure illustrates a linear electromagnet gain of the actuator at a given gap position. By performing a first order linearization of equation 2 about a fixed operating point, the actuator force as a function of differential coil current and displacement can be written as

$$F = K_B I + K_M G \quad (3)$$

where K_B is an equivalent electromagnet gain and K_M is an equivalent bias flux stiffness (for more detail see ref. 10). These gains would be different for different operating points.

Variable Bias Current.- A variation of the permanent-magnet flux bias approach was developed for the ASPS in order to provide a linear actuator characteristic over a wide gap range. This approach uses variable bias currents to provide the bias flux. Figure 8 is a simplified block diagram of the variable bias current approach that was implemented for the ASPS. As can be seen by working through the block diagram, the bias current and control currents of the upper and lower electromagnets are adjusted so that the bias force produced by each and the net force produced by a given command force are equal regardless of the suspended mass's location in the gap. The unbalanced bias-flux stiffness is thus eliminated and the electromagnet gain is constant. A detailed description of this implementation is given in reference 25.

Flux Feedback.- When considering simplicity, efficiency, and controllability of force around zero, the permanent magnet flux bias approach trades off better than the other magnetic bearing control and linearization approaches that were discussed in the previous sections. Disadvantages of this approach include a minimum bandwidth requirement for stability (ref. 8) and linear operation over a restricted gap range about a fixed operating point. The variable bias current approach used in the ASPS suspension system was developed to overcome these disadvantages. However, since current is the controlled variable, the implementation of this approach is relatively complicated and requires actuator core material and rotor material with very low hysteresis in order to provide a sufficiently accurate force-output to force-command transfer characteristic (ref. 25). By using flux feedback (fig. 9), the complex current calculation, with the attendant requirement for gap compensation, is no longer required. In addition, the nonlinear transfer characteristic between electromagnet coil current and flux is included in the forward loop of a feedback system with very high open loop gain. This reduces the sensitivity of the force-output to force-input transfer characteristic to a negligible level as long as the actuator is operated below the saturation flux density of

the electromagnet core material and rotor material. Bias flux can be supplied by either fixed bias currents or permanent magnets in the flux feedback approach. In most applications, permanent magnet flux bias is the preferred approach because of power consumption and actuator heating issues.

The force produced by a given electromagnet, as a function of current and gap, is given by equation 1. Under the same assumptions, the force produced by a given electromagnet, as a function of flux in the electromagnet gap, can be written as (ref. 16)

$$F = K\phi^2 \quad (4)$$

where ϕ is flux and K is defined in reference 16. Using figure 5 and the associated nomenclature again, the force produced by the upper and lower elements becomes

$$F_U = K\phi_U^2, F_L = K\phi_L^2 \quad (5)$$

For a bearing element pair with differential control of flux, the total force becomes

$$F_T = K(\phi_U^2 - \phi_L^2) \quad (6)$$

With differential control about a bias flux, ϕ_o , the flux in the upper and lower gaps becomes

$$\phi_U = \phi_o + \phi_c, \phi_L = \phi_o - \phi_c \quad (7)$$

where ϕ_c is flux command. Substituting equation 7 into equation 6 results in

$$F_T = K([\phi_o^2 + 2\phi_o\phi_c + \phi_c^2] - [\phi_o^2 - 2\phi_o\phi_c + \phi_c^2]) \quad (8)$$

which simplifies to

$$F_T = 4K\phi_o\phi_c \quad (9)$$

By defining $\phi_c = F_c$ and $K_F = 4K\phi_o$, the total actuator force output, F_T , as a function of command force input, F_c , can be written as

$$F_T = K_F F_c \quad (10)$$

Single Element Linearization and Control Approaches

As mentioned above, single element control involves controlling either the upper or lower electromagnet (shown in fig. 5), depending on the direction of the force required. Controlling the electromagnets in this way results in a highly nonlinear force-current characteristic. This is illustrated by figure 10 which shows the composite force-current characteristic of a magnetic actuator with individual element control and with the suspended mass centered in the actuator gaps. It should be noted that this curve is based on ideal assumptions, and that in practice, because of hardware considerations, the smooth crossover at zero is difficult to achieve.

Two linearization approaches have been investigated for individual element control. One approach, which has been implemented for the laboratory model AMCD, utilizes the analog solution of the force equation for a given element. Figure 11 is a simplified block diagram of this implementation which uses analog multipliers and square root modules. The equations for upper and lower elements are included in the figure. A detailed description of this implementation is given in reference 12. This approach proved to be very sensitive to bearing element calibration and alignment accuracy.

The other linearization approach investigated for individual element control is microprocessor based and uses a table lookup to generate control signals. This approach was bench tested but has not been used in the AMCD laboratory model suspension system. Figure 12 is a block diagram representation of the laboratory implementation. In this approach, actual calibration data for a given bearing element pair are used to build a lookup table which is stored in the memory of a microprocessor system. Using the force command and gap position as input data, the correct value of current input to the coil, for the suspended element centered in the actuator gaps, is obtained by using a table lookup routine. This current is compensated for displacement from center by multiplying by the calculated gap. This approach is described in more detail and test results are presented in reference 15.

LARGE-GAP SYSTEMS

Interest in large-gap magnetic suspension systems at NASA Langley began in the early 1960's. The principal goal was the elimination of aerodynamic support interference in wind tunnel testing, which can cause significant corruption of wind tunnel results, as illustrated in figure 13. A single degree-of-freedom demonstration suspension system was operational in 1964 (ref. 4) and is shown in figure 14. The suspension coil was 16 inches in overall diameter, water cooled and split into two independent windings, and fed from a *dc* "bias" supply and a unipolar SCR power amplifier. Figure 15 is a schematic of the major circuit components.

For almost a decade, the principal LaRC MSBS activity was through grants and contracts with the Massachusetts Institute of Technology (MIT) and the University of Virginia (UVA). Information on these efforts is presented in references 32 and 33. An extensive list of related publications can be found in reference 34. MIT constructed two small-scale MSBSs and used them for a variety of testing at subsonic and supersonic speeds. The MIT 6-inch system was a relatively sophisticated and successful design and was eventually moved to LaRC in 1980. The system is now operated by the Instrument Research Division, principally to aid in the development of more accurate position sensors and force calibration techniques. A schematic diagram of the system is shown in figure 16. UVA also constructed two systems; the superconducting system is believed to be the first superconducting suspension system of any type. The system was decommissioned in the late 1970's and the electromagnet array is now kept at LaRC for historical interest.

LaRC also supported research at the University of Southampton from the late 1970's until recently (refs. 34-35). Notable achievements were the development of a digital control system, demonstration of roll control techniques (providing control of the sixth degree-of-freedom), and the construction of a superconducting model core (ref. 36) which is the small model shown in figure 17.

The LaRC 13-inch MSBS was originally constructed at AEDC, Tullahoma, TN and was transferred to LaRC in 1979. Since then, almost all the original hardware has been replaced, including the control system (now digital), position sensors, and main electromagnets. The system is installed in a low-speed wind tunnel, illustrated in figure 18, and has been used for extensive aerodynamic testing (refs. 37-38). For many years, this system was the largest air-gap suspension system known, but it has recently been surpassed by other wind tunnel systems in the U.S.S.R. and Japan.

Under various contracts with General Electric Company and Madison Magnetics Incorporated (MMI), a series of design studies of large-scale MSBSs were completed (ref. 5). MMI also designed and constructed a second-generation superconducting solenoid model core, which is the large model shown in figure 17.

CONCLUDING REMARKS

An overview of research in small- and large-gap magnetic suspension systems at Langley Research Center has been presented. The overview was limited to systems which have been built as laboratory models or engineering models. Small-gap systems applications have been focused on space applications and include advanced spacecraft control actuators and experiment isolation and pointing mounts. Large-gap systems applications have been almost exclusively wind tunnel magnetic suspension systems. A comprehensive list of references which provides more details on the systems discussed in the overview was also presented.

REFERENCES

1. Anderson, Willard W.; and Groom, Nelson J.: The Annular Momentum Control Device (AMCD) and Potential Applications. NASA TN D-7866, March 1975.
2. Anderson, Willard W.; and Joshi, Suresh M.: The Annular Suspension and Pointing (ASP) System for Space Experiments and Predicted Pointing Accuracies. NASA TR R-448, December 1975.
3. Anderson, Willard W.; Groom, Nelson J.; and Woolley, Charles T.: The Annular Suspension and Pointing System. *Journal of Guidance and Control*, Vol. 2, No. 5, September-October 1979, pp. 367-373.
4. Hamlet, Irving L.; and Kilgore, Robert A.: Some Aspects of an Air-Core Single-Coil Magnetic Suspension System. Presented at the ARL Symposium on Magnetic Wind Tunnel Suspension and Balance Systems. April 1966.
5. Boom, Roger W.; Abdelsalam, Mustafa K.; Eyssa, Y. M.; and McIntosh, G. E.: Magnetic Suspension and Balance System Advanced Study-Phase II. NASA CR-4327, November 1990.
6. Anderson, Willard W.; and Groom, Nelson J.: Annular Momentum Control Device. U.S. Letters Patent No. 3,915,416; October 28 1975.
7. Ball Brothers Research Corporation: Annular Momentum Control Device (AMCD). Volume I: Laboratory Model Development. NASA CR-144917, 1976.

8. Groom, Nelson J.; and Terray, David E.: Evaluation of a Laboratory Test Model Annular Momentum Control Device. NASA TP-1142, March 1978.
9. Groom, Nelson J.: Fixed-Base and Two-Body Equations of Motion for an Annular Momentum Control Device (AMCD). NASA TM-78644, March 1978.
10. Groom, Nelson J.: Analytical Model of An Annular Momentum Control Device (AMCD) Laboratory Test Model Magnetic Bearing Actuator. NASA TM-80099, August 1979.
11. Groom, Nelson J.; and Waldeck, Gary C.: Magnetic Suspension System for a Laboratory Model Annular Momentum Control Device. Presented at the AIAA Guidance and Control Conference, Boulder, Colorado, August 1979. (Available as AIAA Paper 79-1755).
12. Sperry Flight Systems: Magnetic Suspension System for an Annular Momentum Control Device (AMCD). NASA CR-159255, December 1979.
13. Woolley, Charles T.; and Groom, Nelson J.: Description of a Digital Computer Simulation of an Annular Momentum Control Device (AMCD) Laboratory Test Model. NASA TM-81797, 1981.
14. Groom, Nelson J.; Woolley, Charles T.; and Joshi, Suresh M.: Analysis and Simulation of a Magnetic Bearing Suspension System for a Laboratory Model Annular Momentum Control Device. NASA TP-1799, March 1981.
15. Groom, Nelson J.; and Miller, James B.: A Microprocessor—Based Table Lookup Approach for Magnetic Bearing Linearization. NASA TP-1838, 1981.
16. Groom, Nelson J.: A Magnetic Bearing Control Approach Using Flux Feedback. NASA TM-100672, March 1989.
17. Ball Brothers Research Corporation: Annular Momentum Control Device (AMCD). Volume II: Application To A Large Space Telescope. NASA CR-144917, 1976.
18. Nadkarni, Arun A.; and Joshi, Suresh M.: Optimal Maneuvering and Fine-Pointing Control of a Large Space Telescope with a New Magnetically Suspended, Single Gimbale, Momentum Storage Device. Proceedings of the 15th IEEE Conference on Decision and Control, Clearwater Beach, FL, December 1-3, 1976.
19. Nadkarni, Arun A.; Groom, Nelson J.; and Joshi, Suresh M.: Optimal Fine Pointing of a Large Space Telescope using an Annular Momentum Control Device. Proceedings of the IEEE Southeastcon 77, Williamsburg, VA, April 4-6, 1978.
20. Joshi, Suresh M.; and Groom, Nelson J.: A Two-Level Controller Design Approach for Large Space Structures. Proceedings of the 1980 Joint Automatic Control Conference, San Francisco, CA, August 13-15, 1980.
21. Joshi, Suresh M.; and Groom, Nelson J.: Modal Damping Enhancement in Large Space Structures Using AMCD's. Journal of Guidance and Control, Vol. 3, No. 5, September-October 1980, pp. 477-479.
22. Joshi, Suresh M.: Damping Enhancement and Attitude Control of Large Space Structures. Proceedings of the 19th IEEE Conference on Decision and Control, Albuquerque, NM, December 10-12, 1980.
23. Anderson, Willard W.; and Groom, Nelson J.: Magnetic Suspension and Pointing System. U.S. Letters Patent No. 4,088,018, May 9, 1978.

24. Anderson, Willard W.; and Groom, Nelson J.: Magnetic Suspension and Pointing System. U.S. Letters Patent No. 4,156,548, May 29, 1979.
25. Cunningham, D. C.; Gismondi, T. P.; and Wilson, G. W.: System Design of the Annular Suspension and Pointing System (ASPS). Presented at the AIAA Guidance and Control Conference, Palo Alto, California, August 1978. (Available as AIAA Paper 78-1311).
26. Cunningham, David C.; et. al.: Design of the Annular Suspension and Pointing System (ASPS). NASA CR-3343, October, 1980.
27. Keckler, Claude R.; Kibler, Kemper S.; and Rowell, Larry F.: Determination of ASPS Performance for Large Payloads in the Shuttle Orbiter Disturbance Environment. NASA TM-80136, October, 1979.
28. Keckler, Claude R.: ASPS Performance with Large Payloads Onboard the Shuttle Orbiter. AIAA Journal of Guidance, Control, and Dynamics, Vol. 5, No. 1, pp. 32-36, January-February 1982.
29. Hamilton, Brian J.: Vibration Attenuation Using Magnetic Suspension Isolation. Presented at the Joint Automatic Control Conference, Charlottesville, VA, June 17-19, 1981.
30. Hamilton, Brian J.: Laboratory Evaluation of the Pointing Stability of the ASPS Vernier System. NASA CR-159307, June, 1980
31. Sperry Flight Systems: The Development of the ASPS Vernier System. Final Report under Contract No. NAS1-15008, June, 1983.
32. Covert, E. E.; Finston, M.; Vlajinac, M.; and Stephens, T.: Magnetic Balance and Suspension Systems for Use with Wind Tunnels. Progress in Aerospace Sciences, Volume 14, 1973.
33. Zapata, R. N.: Development of a Superconducting Electromagnetic Suspension and Balance System for Dynamic Stability Studies. NASA CR-132255, February 1973.
34. Tuttle, M. H.; Moore, D. L.; and Kilgore, R. A.: Magnetic Suspension and Balance Systems—A comprehensive, annotated, bibliography. NASA TM-4318, August 1991.
35. Britcher, C. P.: Progress toward Magnetic Suspension and Balance Systems for Large Wind Tunnels. AIAA Journal of Aircraft, Volume 22, April 1985.
36. Britcher, C. P.; Goodyer, M. J.; Scurlock, R. G.; and Wu, Y. Y.: A Flying Superconducting Model and Cryostat for Magnetic Suspension of Wind Tunnel Models. Cryogenics, April, 1984.
37. Dress, D. A.: Drag Measurements on a Laminar-Flow Body of Revolution in the 13-inch Magnetic Suspension and Balance System. NASA TP-2895, April, 1989.
38. Britcher, C. P.; and Alcorn, C. W.: Interference-Free Measurements of the Subsonic Aerodynamics of Slanted-Base Ogive Cylinders. AIAA Journal, April, 1991.

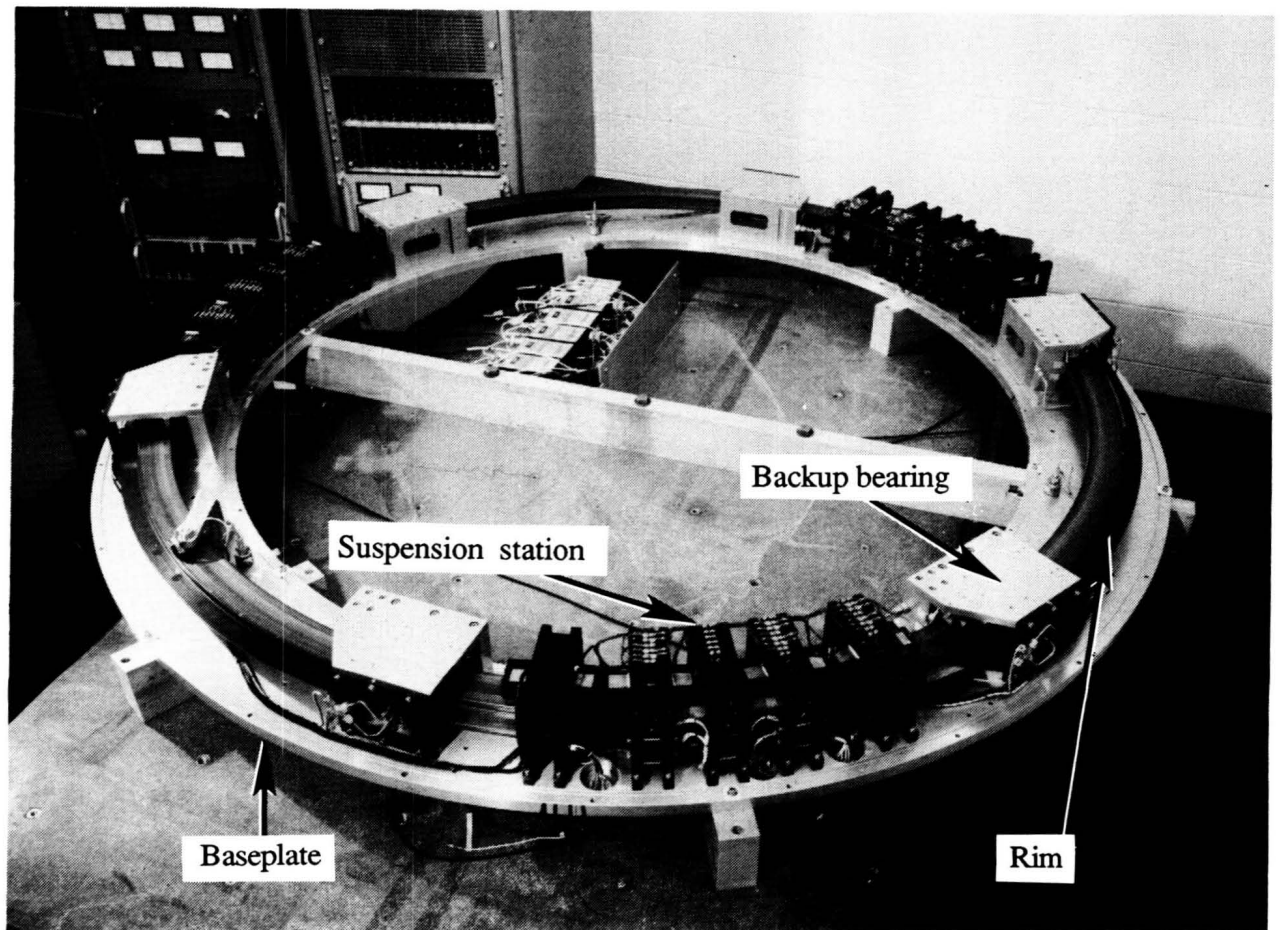
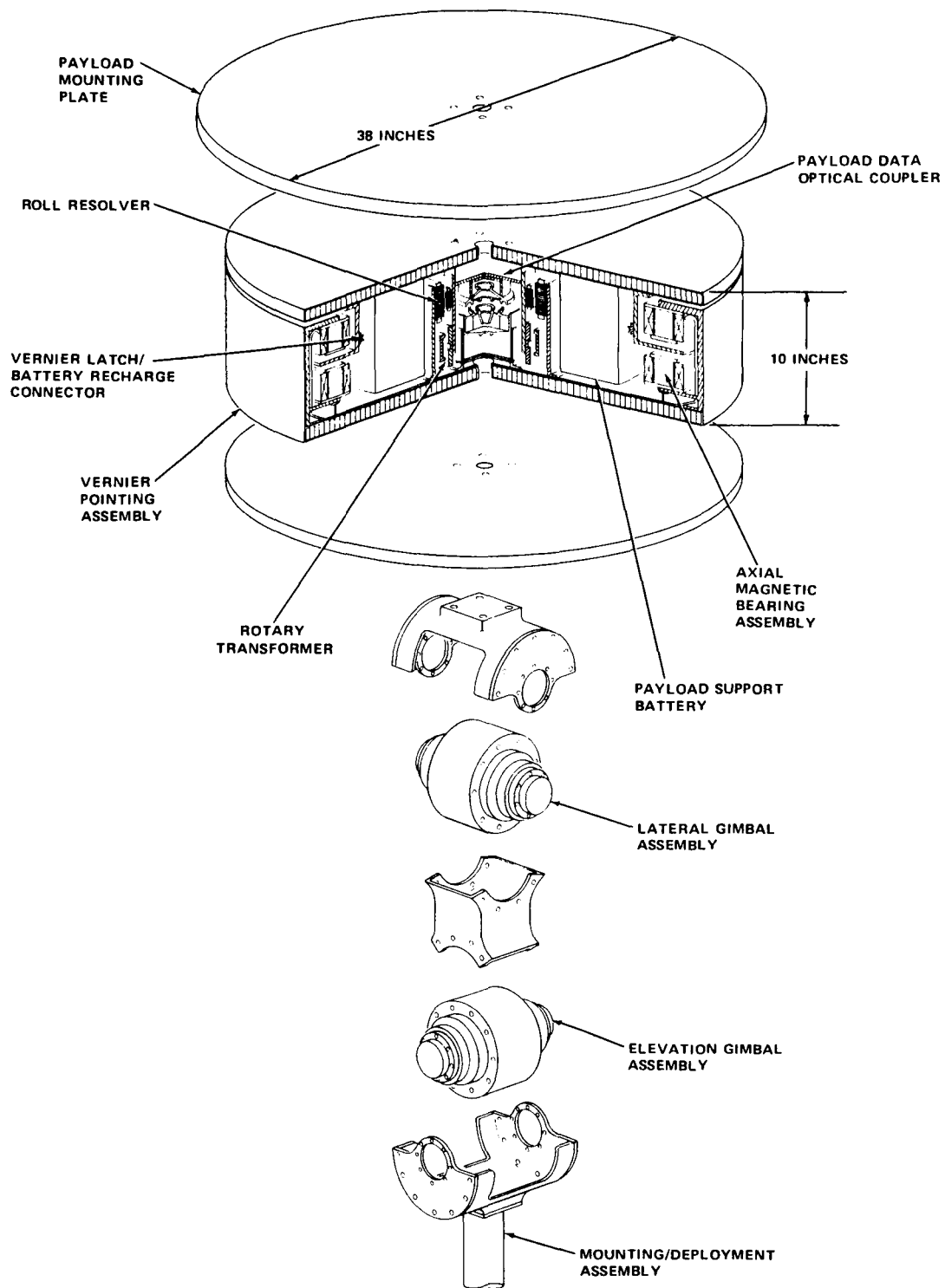


Figure 1. AMCD laboratory model.



ANNULAR SUSPENSION AND POINTING SYSTEM
(ASPS)—EXPLODED VIEW

Figure 2. ASPS configuration.

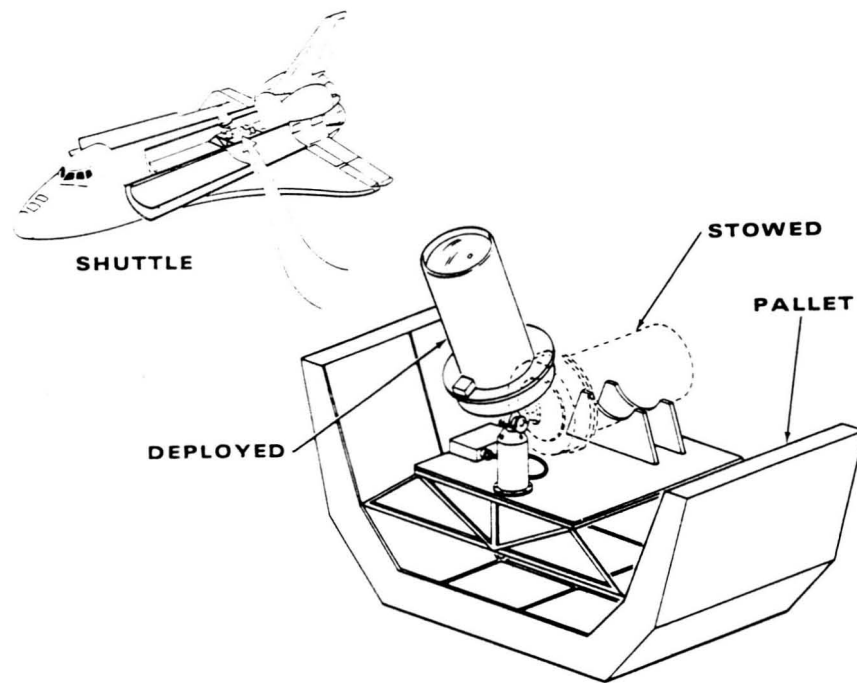


Figure 3. Typical payload ASPS carrier vehicle configuration.

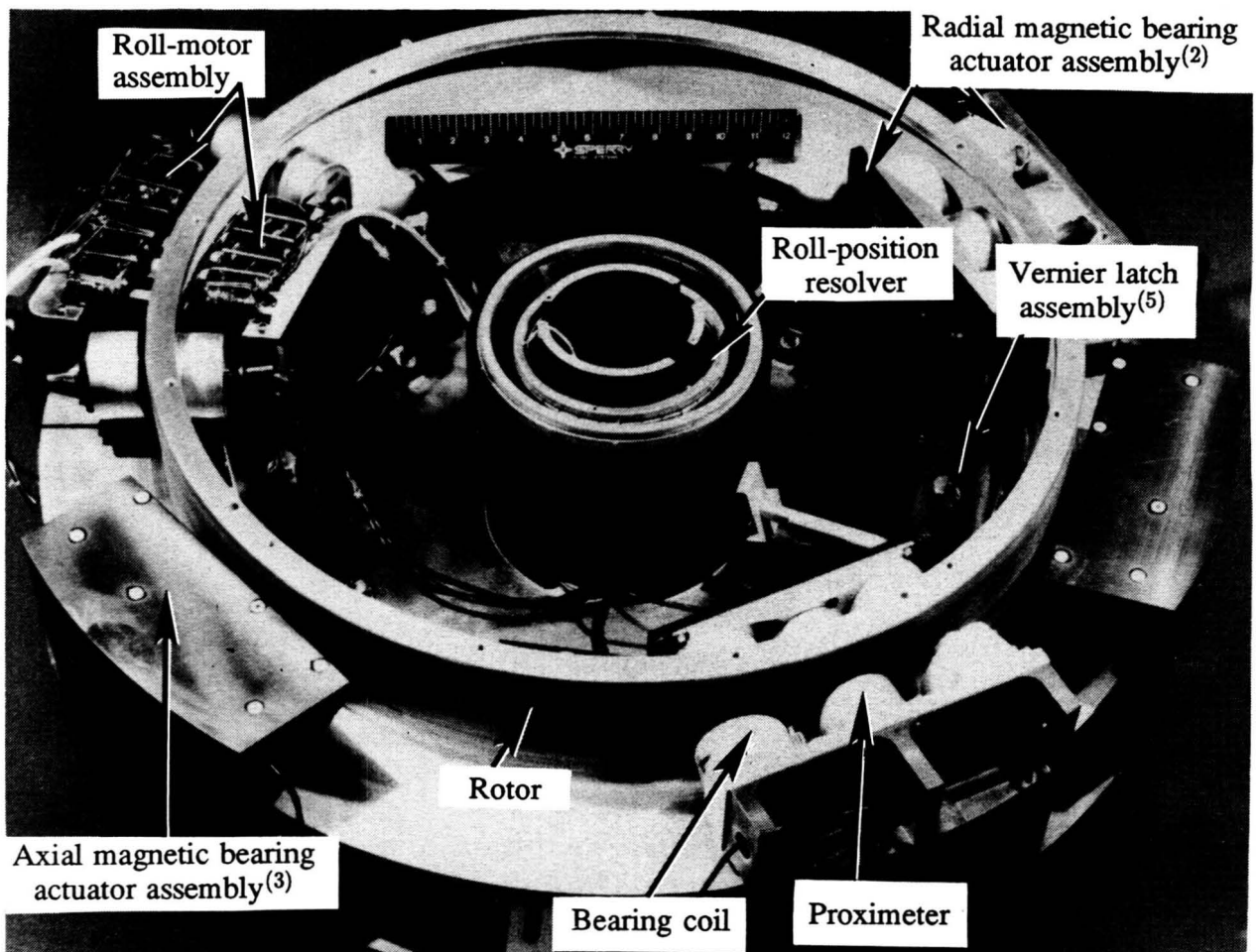


Figure 4. ASPS vernier assembly engineering model.

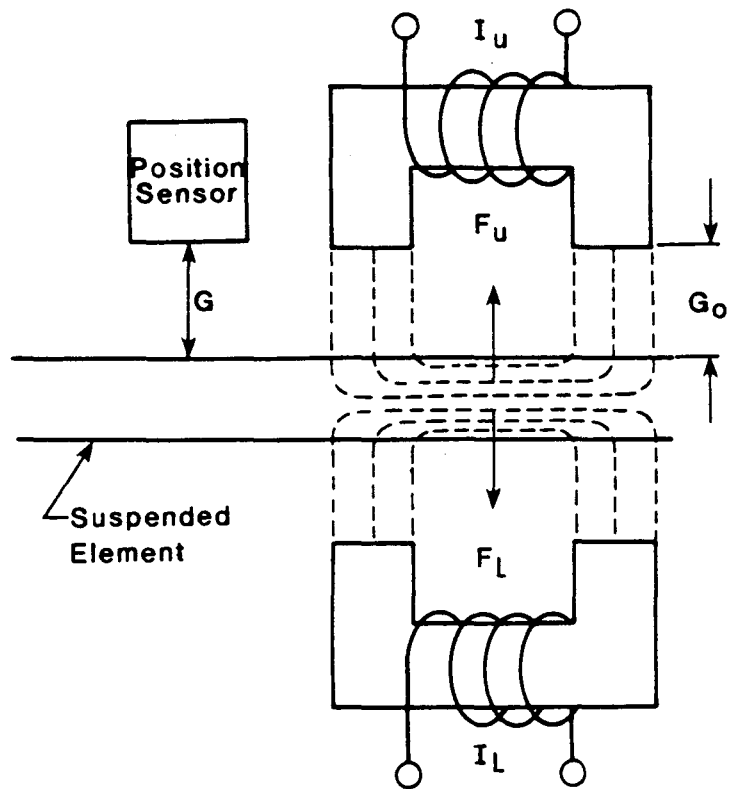


Figure 5. Magnetic bearing actuator.

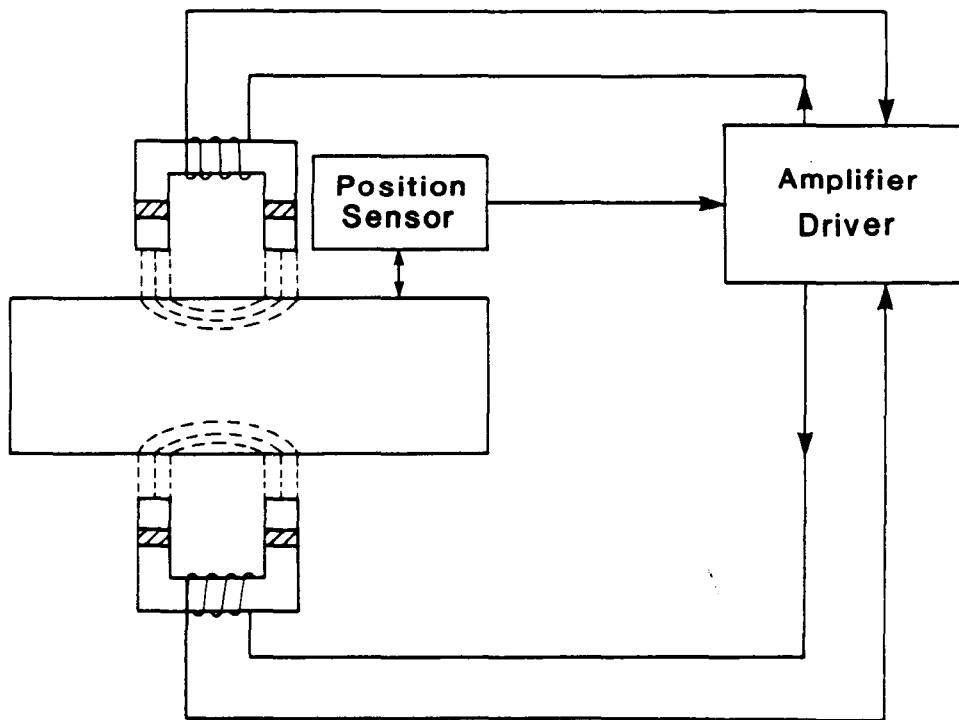


Figure 6. Permanent magnet flux-biased magnetic actuator.

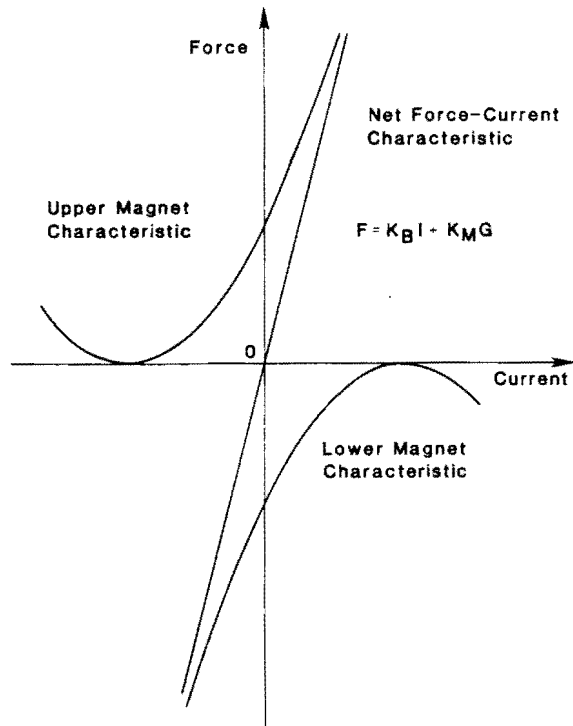


Figure 7. Force-current characteristic of a permanent magnet flux-biased magnetic actuator.

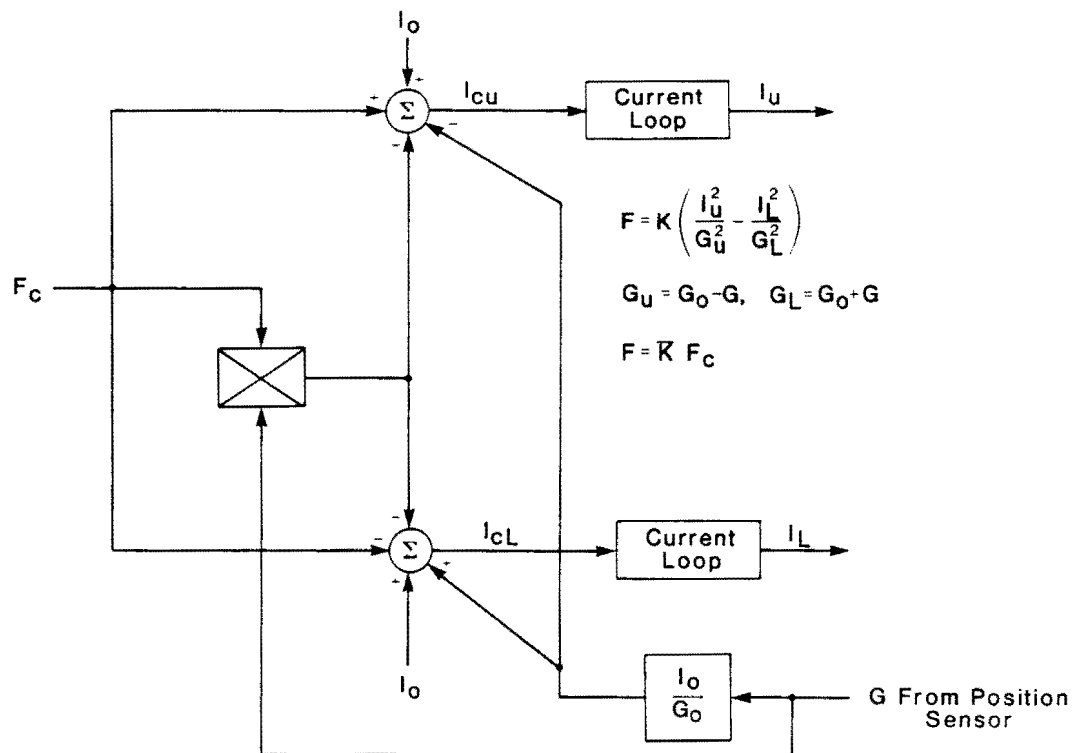


Figure 8. Variable biased current approach for magnetic actuator control.

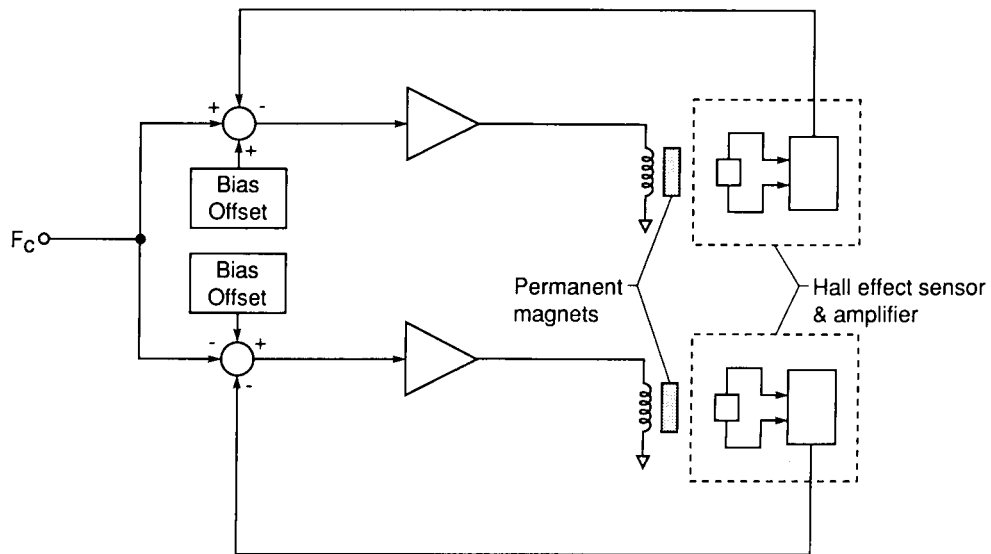


Figure 9. Flux feedback approach.

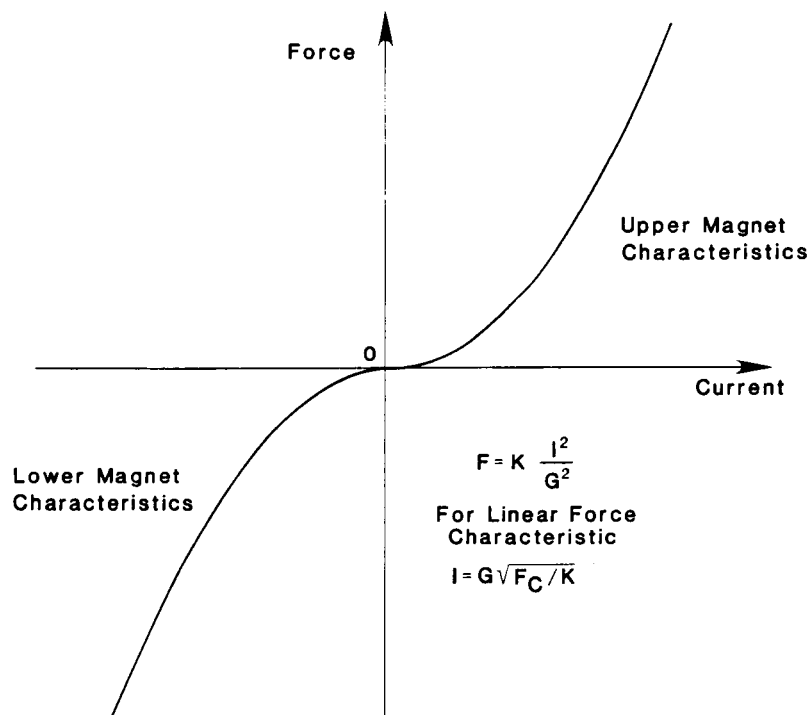


Figure 10. Force current characteristic of a magnetic actuator with individual element control.

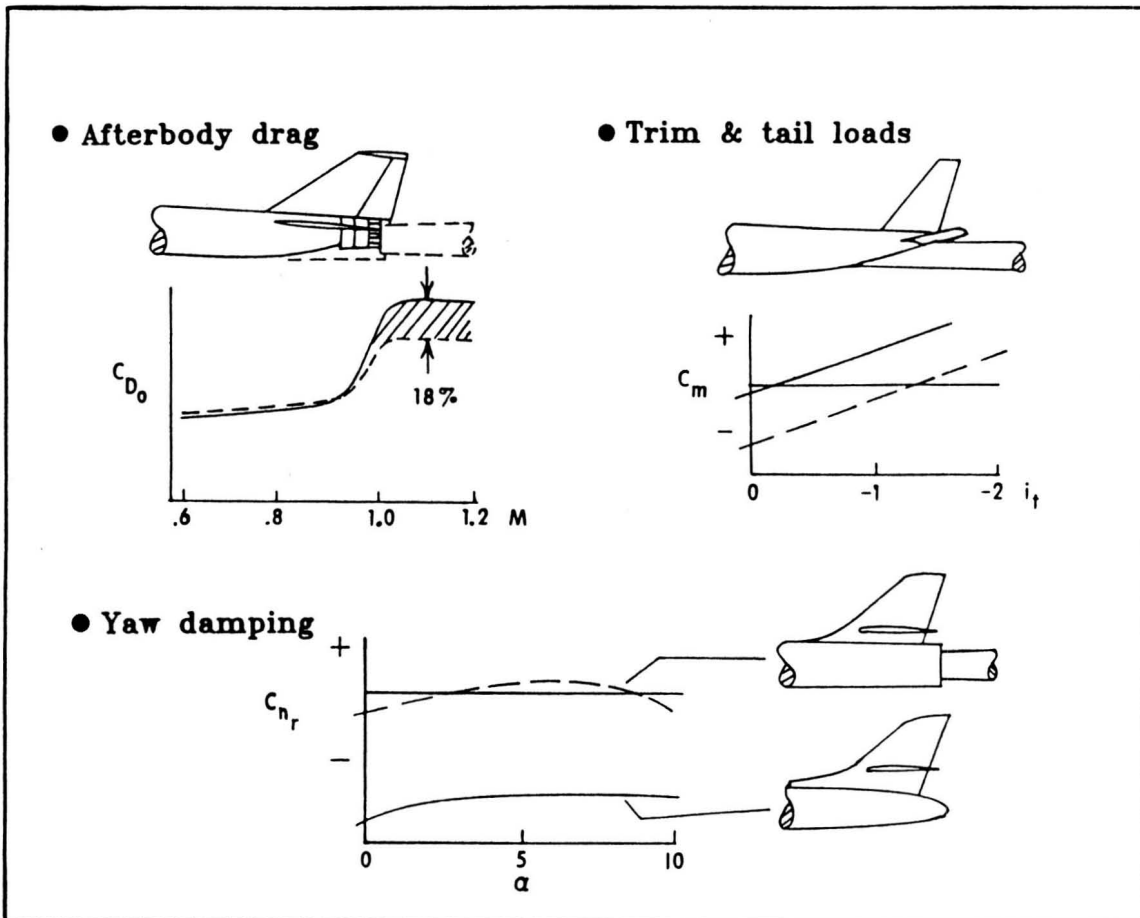


Figure 13. Examples of model support problems.

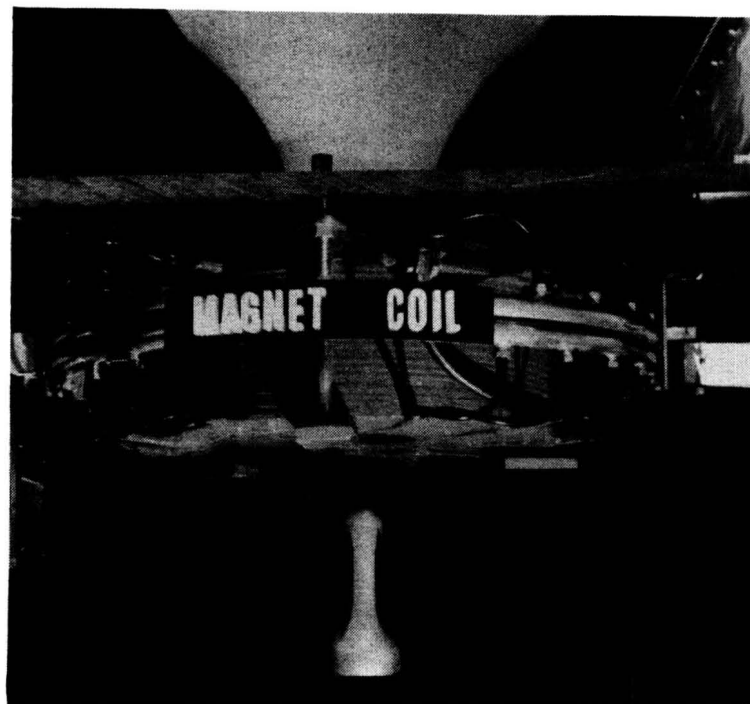


Figure 14. Photograph showing model supported in Langley magnetic suspension system.

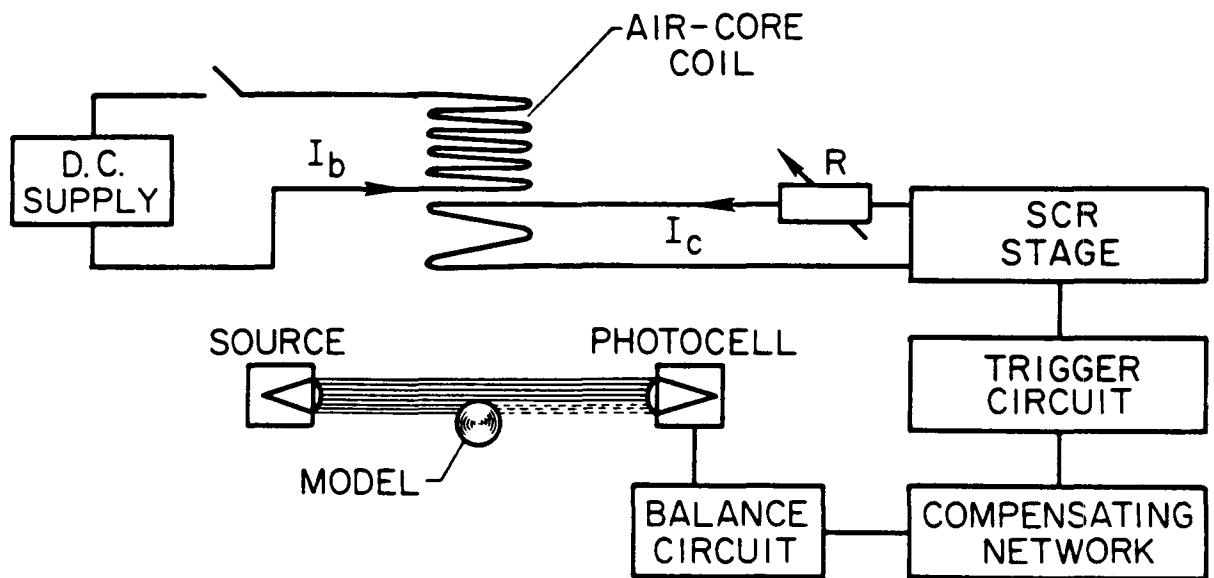


Figure 15. Schematic of major circuit components.

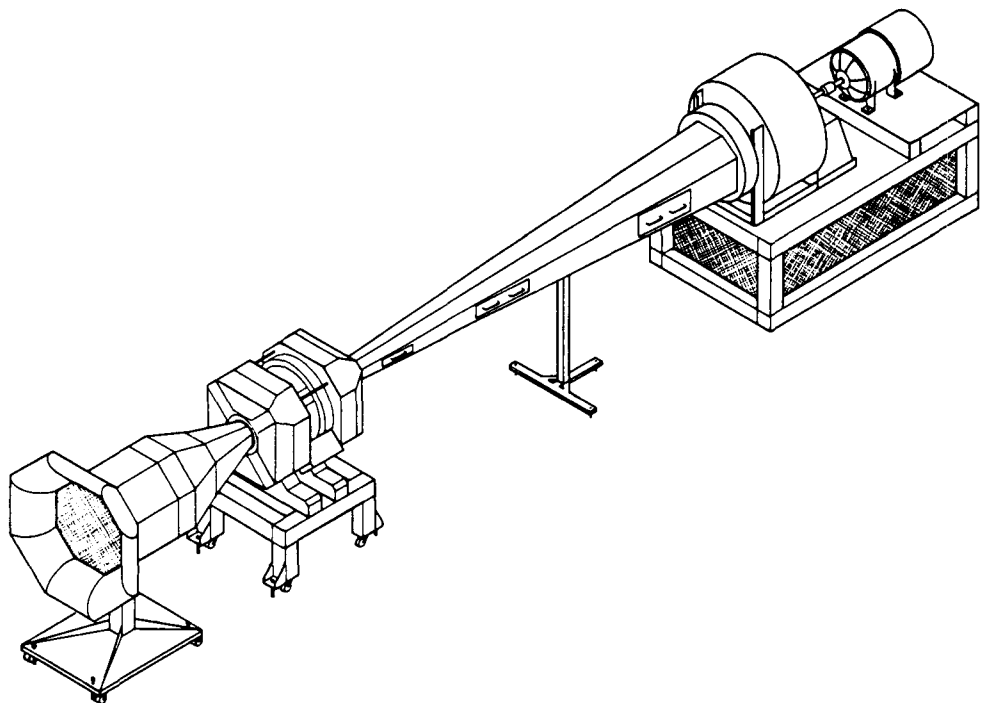


Figure 16. NASA LaRC/MIT 6-inch magnetic suspension and balance system.



Figure 17. Superconducting solenoid.

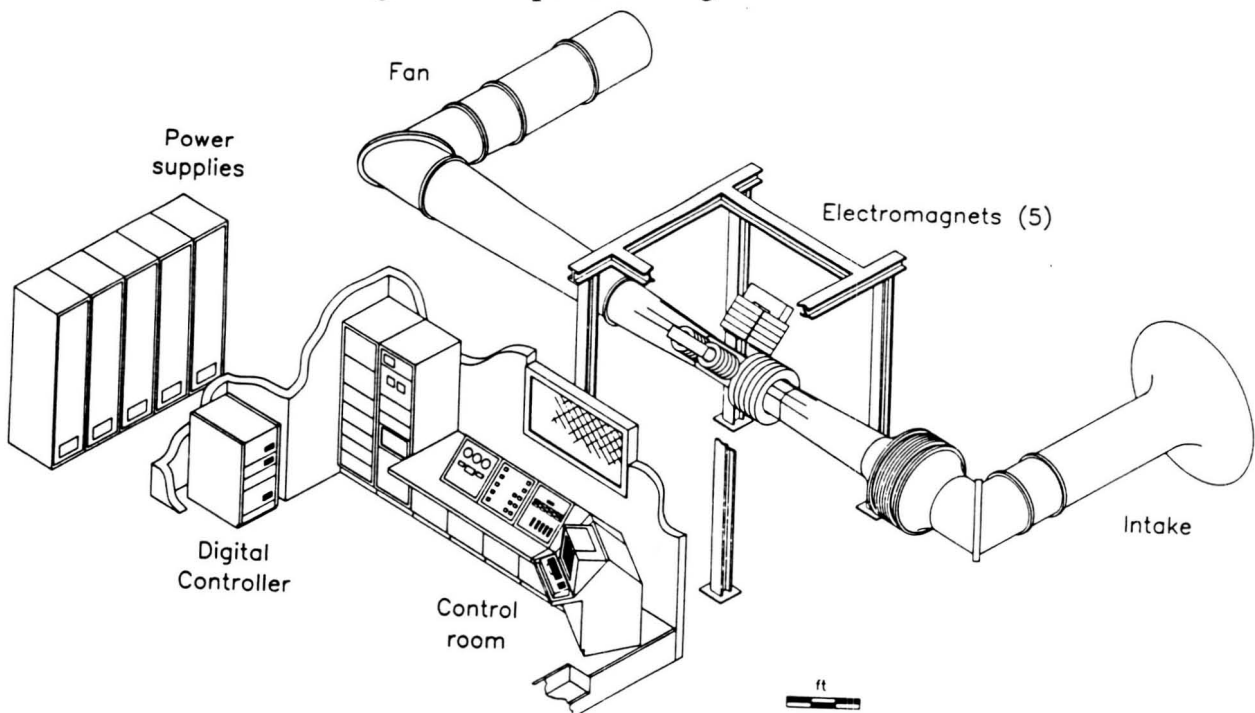


Figure 18. Thirteen inch magnetic suspension laboratory.

N 9 2 - 2 7 7 2 3

PROFESSOR JESSE W. BEAMS AND THE FIRST PRACTICAL MAGNETIC SUSPENSION

P. E. Allaire

R. R. Humphris

D. W. Lewis

Mechanical and Aerospace Engr. Dept., University of Virginia, Charlottesville, VA 22901

INTRODUCTION

Dr. Jesse W. Beams developed the first practical magnetic suspension for high speed rotating devices [1-2]. These devices included high speed rotating mirrors, ultracentrifuges and high speed centrifugal field rotors. Figure 1 shows a photograph of Dr. Beams in his laboratory.

Dr. Beams employed magnetic suspension as a means to carry out extensive experiments on physical properties in areas of isotope separation, biophysics, materials science, and gravitational physics. Typically, he thought of ways to modify and improve experiment equipment. The improved equipment then gave much better experimental results. Building on this advance, he then thought of some new type of experiment that could be performed with the technological advance in equipment and capabilities.

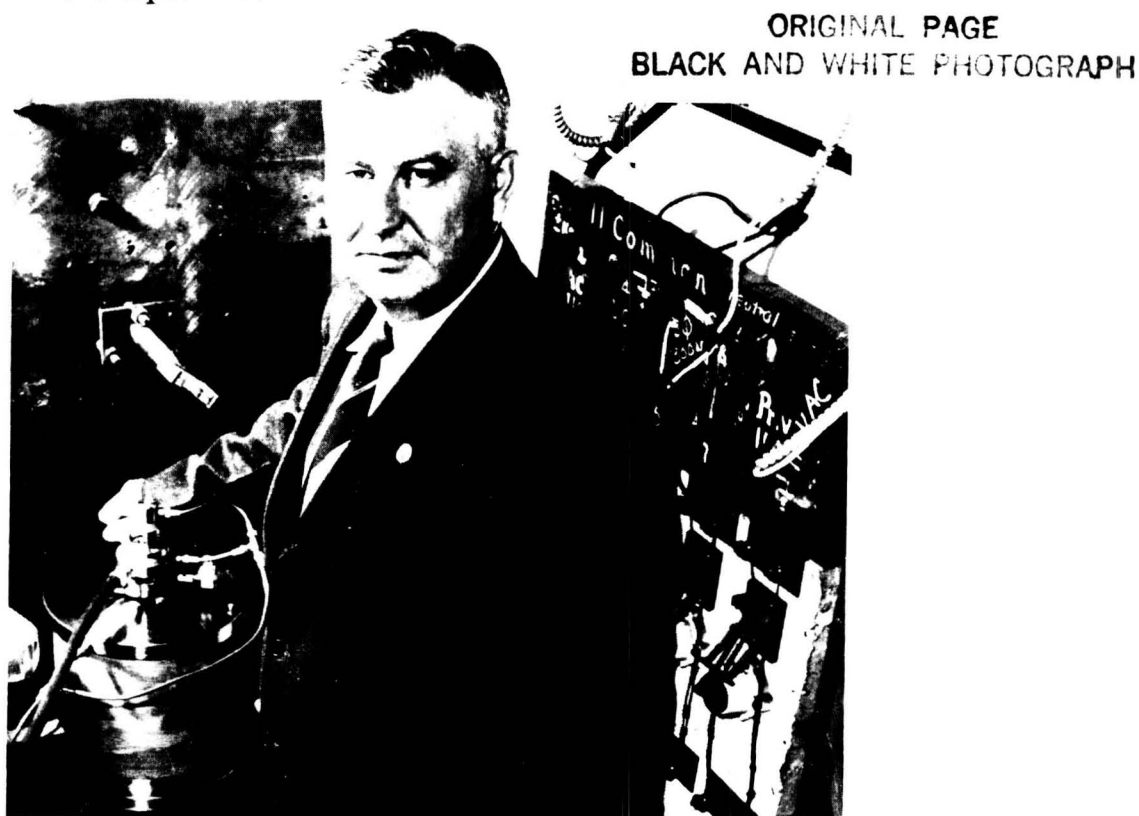


Fig. 1 Professor Jesse W. Beams, 1898-1977

EARLY AXIAL MAGNETIC SUSPENSION FOR ULTRACENTRIFUGES

The interest in high speed rotating devices extended to centrifuges. Around 1924, practical centrifuges were being developed in Sweden. Heavy particles in suspension will settle out more rapidly than light particles. This process can be speeded up by putting the suspension in a high speed centrifuge. However, convection currents caused by friction heating of the rotor surface due to the air outside caused problems. Beams removed this difficulty by placing the rotor in a vacuum.

Originally, the rotor was supported axially by compressed air. This was replaced by a magnetic suspension system. A vertical shaft in the centrifuge rotor was attracted upward by a

magnetic solenoid coaxial with it. The centrifuge was then radially stable, but axially unstable. Beams and two colleagues, Sheppard Black and Fred Holmes [3–6], devised a system of sensing the vertical position of the centrifuge rotor with a photoelectric cell. The position of the rotor was maintained by changing the current in the solenoid as needed. This type of system is now called automatic feedback control.

The principle was reported in [3]. Figure 2 illustrates the approach employed. “Solenoid 1 carries a steady direct current producing a magnetic field sufficiently strong to support a large fraction of the weight of the needle, N, and the attached cylindrical vane V. A source of light, S, is roughly focused on the upper edge of V so that some of the light passes over V and strikes a photo—cell P. The current from P operates a two-stage d.c. amplifier whose output is fed into a solenoid 2. Thus if N drops too low, the amount of light striking P is increased and the magnetic field is increased: if N rises too high, the field is decreased. In this way, if adequate damping is supplied, N may be automatically maintained at its equilibrium position.” Figure 3 gives the circuit diagram for controlling solenoid 2.

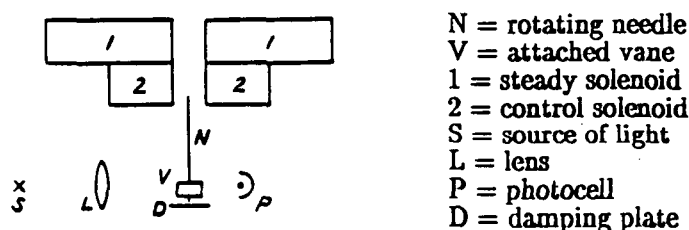


Fig. 2. Schematic of Vertical Magnetic Suspension System Employed by Beams, et. al. [3] in 1937.

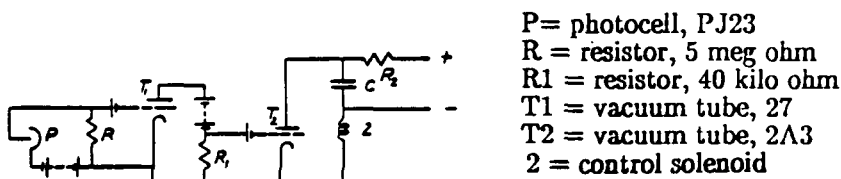


Fig. 3. Control Circuit [3] Feeding Solenoid 2 in Figure 1.

In a short period of time, the magnetic suspension was employed in an ultracentrifuge and a paper [5] published in 1939 showed the schematic diagram of Figure 4. “... The rotating parts consist of the centrifuge C, an armature D of the electric motor, a small iron rod S, and a flexible shaft A which connects them together. The shaft A passes through vacuum tight oil glands G1, which seals the vacuum chamber, and G2, which serves to center D in the field F.”

“... The rotating members are supported by an electromagnet consisting of an iron core M and windings L. The current through L is so adjusted that the magnetic attraction between M and the small iron rod S, rigidly attached to and coaxial with A, is just greater than necessary to lift S, A, D, and C.”

The new magnetic suspension system had several advantages. First, the vertical rotor position was controlled to such an extent that no vertical motion could be detected by a 100 power

microscope. Second, the power losses were so low that very high rotating speeds could be produced. Figure 5 shows a photograph of the magnetically supported centrifuge. In 1940, Skarstrom and Beams reported on an improved ultracentrifuge [6] as shown in Fig. 6. A viscous damper was added at the bottom to reduce lateral shaft vibrations. Figure 7 shows machinist P. Sommer in Dr. Beams' laboratory standing next to an ultracentrifuge.

As early as 1937, Beams and colleagues showed that the isotopes of elements could be purified by centrifuges. Further work was reported in [6]. During World War II, the Department of Physics conducted work on a long cylindrical centrifuge for the separation of uranium isotopes. A pilot plant was operated at Bayway, NJ starting early in the war for separating uranium 235 from uranium 238. However, this method was not employed for production of uranium 235 during the war. After the war, Dr. Beams continued to work with a classified project at the University to develop the centrifuge for eventual use in the production of uranium supplied to electric power reactors. The project continued until 1988.

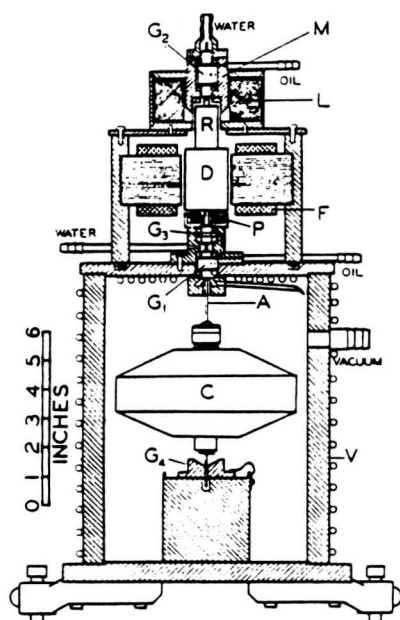


Figure 4. Drawing of Vacuum-Type Self-Balancing and Magnetically Supported Ultracentrifuge (1939).

C = centrifuge rotor
D = motor armature
S = iron rod
M = electromagnet iron core
L = electromagnet windings
A = flexible shaft
G1 = oil gland
G2 = oil bearing
F = field for rotation
N = clutch

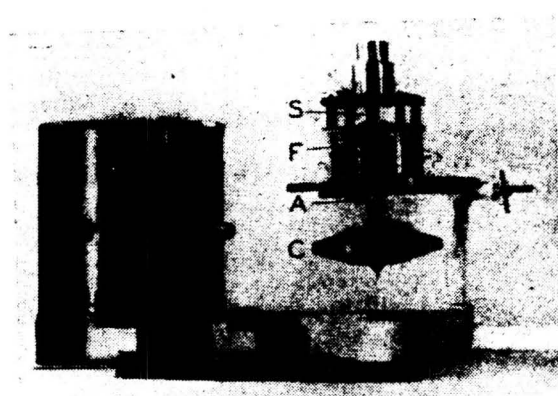
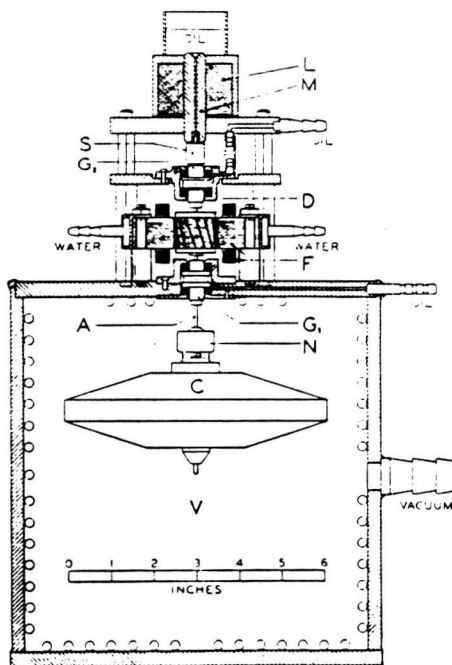


Figure 5. Photograph of Early Ultracentrifuge.



D = motor armature
R = mag. support core
M = cm iron core
L = support solenoid
C = rotor
A = shaft
G1 = oil bearing
G2 = oil bearing
G3 = oil bearing
G4 = viscous damper
P = pick up coil
F = motor stator
V = vacuum chamber

Fig. 6. Drawing of Assembled Electric Ultracentrifuge in 1940.

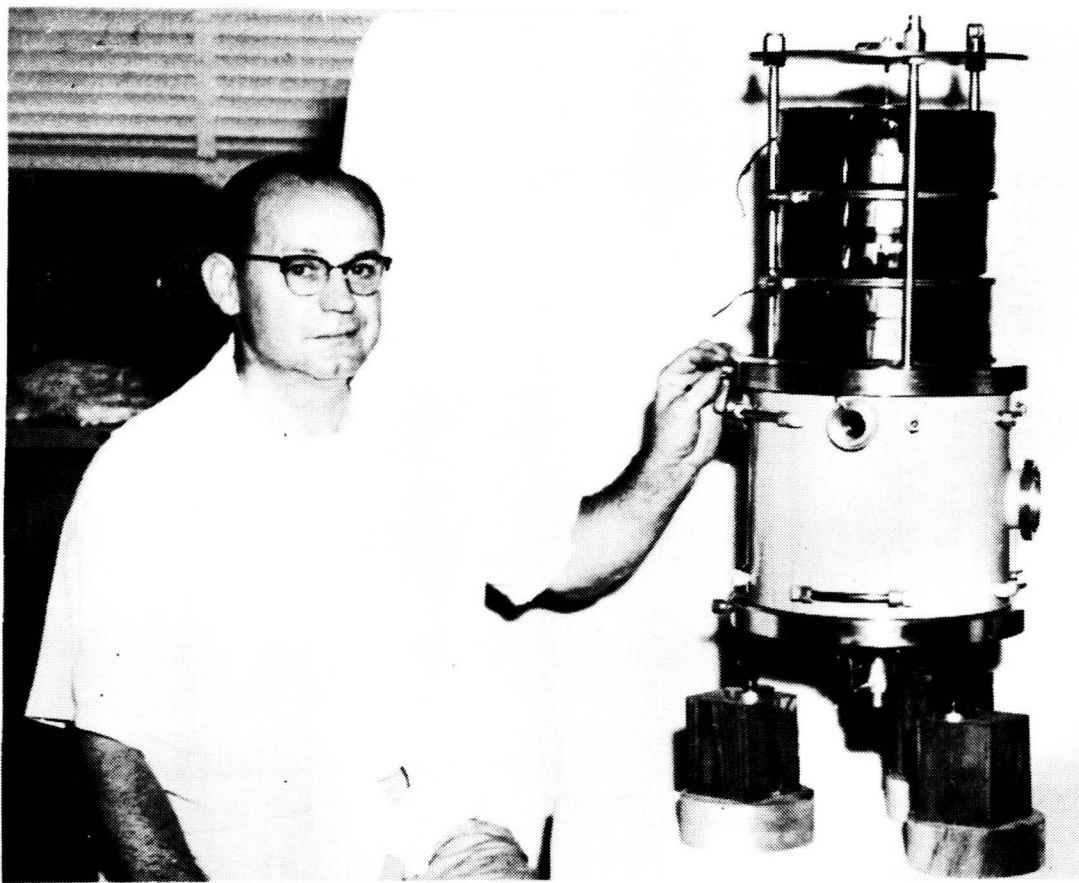


Fig. 7. Beams' Machinist, P. Sommer, with Early Version of Magnetically Supported Ultracentrifuge

In 1968, the National Medal of Science was presented to Dr. Beams by President Lyndon Johnson for his gas centrifuge work. Also, the Atomic Energy Commission in 1972 cited Dr. Beams for his outstanding contributions to the U. S. atomic energy program.

MAGNETIC SUSPENSION FOR HIGH CENTRIFUGAL FIELDS

Dr. Beams' interest in centrifugal effects continued after World War II. Small steel balls, in this case $1/32$ of an inch, were spun up to 386,000 revolutions per second [7]. In other works [8,9,10,11], he reported small balls rotating at speeds up to 800,000 revolutions per second. He and his co-workers filed for a patent on this device [12]. The electronic circuitry was constructed of vacuum tubes. He later received another patent with a rotational speed of 4,000,000 revolutions per second.

It may be noted that this work was not without risk of personal injury. During one experiment, the metal ball came out of support while spinning at an extremely high speed. The ball went through a railroad tie that was employed as the stationary barrier and through Dr. Beams' neck, just missing the carotid artery. He might easily have been killed. However, he was treated at the local hospital and was back at work in a few days.

CONCLUSIONS

While many others had speculated on the development of magnetic suspension of rotating devices, Dr. Beams was the first researcher to develop a practical magnetic suspension system. Work in his laboratory on magnetic bearings went on for many years. The later works of Dr. Beams and the laboratory that he founded in the Physics Department at the University of Virginia are not discussed in this brief paper.

On the morning of July 23, 1977, Dr. Beams had an idea and described to his wife, in great detail, how to construct what he felt would be the best gyroscope in the world. After dinner, he discussed current research with colleagues. At eight o'clock, he died. He lived a very full life.

Currently, magnetic suspension research continues at the University of Virginia in the Physics Department under Beams' colleague, Rogers Ritter. In the Nuclear Engineering and Engineering Physics Department, there is a strong program on magnetically supported medical devices, conducted by former student George Gilles. Also, the Mechanical and Aerospace Engineering Department has continued the work on magnetic bearings for rotating machines. This research program has become the Center for Magnetic Bearings.

For his pioneering work in the field, Dr. Jesse W. Beams deserves to be called the "Father of Magnetic Bearings."

BIOGRAPHY

In [REDACTED], Jesse Beams was born in [REDACTED]. He obtained a Ph. D. from the Department of Physics at the University of Virginia in 1925. After three years at Yale University, he returned to the University of Virginia as an Associate Professor of Physics. He became a Professor in 1930, Chairman of the Physics Department in 1948, and Smith Professor of Physics in 1953. He retired as Professor Emeritus in 1969 and continued to work in his laboratory at the University until his death on July 23, 1977.

Professor Beams was a kind and gentle man, always willing to discuss technical questions with anyone. Many of his experiments required intricate machining. He listened to his machinists' suggestions and often listed them as co-authors. He authored or co-authored 246 articles. The bibliographical records on Dr. Beams in the University library indicate 2.75 meters of information, including 14 patents.

Beams first worked on the timing of the emission of light by atoms excited by electric discharge in a device called a Kerr cell. He made improvements on a rapidly rotating mirror employed to detect the light. His first paper on this subject appeared in 1930.

REFERENCES

1. "Jesse Wakefield Beams," Obituary, 1977.
2. Leyh, C. H., "A Brief History for the Precision Measurement Group at the University of Virginia," Proceedings of 1983 Symposium on Precision Measurement and Gravity Experiment, Taipei, China, 1983.
3. Holmes, F. T., "Axial Magnetic Suspensions," Review of Scientific Instruments, Vol. 8, Nov. 1937, pp. 444-447.
4. Holmes, F. T. and Beams, J. W., "Frictional Torque of an Axial Magnetic Suspension," Nature, Vol. 140, July 3, 1937, pp. 30-31.
5. Beams, J. W., and Black, S. A., "Electrically-Driven Magnetically-Supported Vacuum-Type Ultracentrifuge," Vol. 10, Feb. 1939, pp. 59-63.

6. Skarstrom, C. and Beams, J. W., "The Electrically-Driven Magnetically Supported Vacuum Type Ultracentrifuge," *Review of Scientific Instruments*, Vol. 11, Dec. 1940, pp. 398-403.
7. Beams, J. W., Young, J. L., and Moore, J. W., "The Production of High Centrifugal Fields," *Journal of Applied Physics*, Vol. 17, Nov. 1946, pp. 886-890.
8. Beams, J. W., "Experiments With High Speed Rotors," *Science*, Vol. 107, 1948, p. 646.
9. Dillon, J. F., and Beams, J. W., "An Improved Axial Magnetic Suspension," *Physics Review*, Vol. 74, 1948, p. 117.
10. Beams, J. W., "Magnetic Suspension Balance," *Physics Review*, No. 78, 1950, p. 471.
11. Beams, J. W., "Magnetic Suspension for Small Rotors," *Review of Scientific Instruments*, Vol. 21, No. 2, 1950, pp. 182-184.
12. Beams, J. W., Kinsey, E. E., and Snoddy, L. E., "Magnetically Supported Rotating Bodies," U.S. Patent No. 2,691,306, 1951.

N92-27724

LARGE-GAP MAGNETIC SUSPENSION SYSTEMS

Colin P. Britcher

Department of Mechanical Engineering and Mechanics, Old Dominion University

SUMMARY

This paper will address the classification of magnetic suspension devices into small-gap and large-gap categories. The relative problems of position sensing, control systems, power supplies, electromagnets and magnetic field or force analysis will be discussed. The similarity of all systems from a controls standpoint will be qualified. Some applications where "large-gap" technology is being applied to systems with a physically small air-gap will be mentioned. Finally, the applicability of some other suspension approaches, such as electrodynamic or superconducting, will be addressed briefly.

INTRODUCTION

The majority of research concerning magnetic suspension devices has concentrated on systems and applications where the air-gap between suspended object and suspension elements has been relatively small. This has been especially true in recent years, with the strong growth of interest in, and application of, magnetic bearings. In turn, the predominant technical approach used to date for bearings has been the feedback-controlled electromagnet/ferromagnetic suspended element type. There are applications, however, where large air-gaps are essential; perhaps the longest-standing of these being Magnetic Suspension and Balance Systems for wind-tunnel models (MSBS) and magnetically-levitated trains (Maglev), both illustrated in Figure 1. Other applications are now emerging where large-gap systems are of interest or where the design approaches used in large-gap systems are applicable. Some examples of these applications are multi-degree-of-freedom microgravity vibration isolation and large-angle space-based gimbaling and pointing systems, illustrated in Figure 2. From a controls standpoint, the large- and small-gap systems prove to be quite similar, but in most other respects can be dramatically different.

FIELDS AND FORCES

This section will start with some simple analysis of small-gap systems, leading to consideration of larger-gaps, highlighting some of the important trends involved. Small-gap systems are frequently designed, at least in the preliminary stages, using magnetic circuit theory. A sketch of a representative two-pole suspension system is shown in Figure 3. The important features are the uniform air-gap, and the presence of iron yokes and/or back-iron. Examining the magnetic circuit, it is clear that the reluctance of the circuit is dominated by the air-gap, which is,

in turn, the parameter being controlled. Using standard formulations, chiefly :

$$\frac{F}{A} = \frac{B^2}{2 \mu_0} \quad - (1)$$

- it is easily shown that:

$$F = \frac{\mu_0 A (NI)^2}{4 h^2} \quad - (2)$$

A fringing factor is usually introduced to account for flux non-uniformity but is not necessary here. The total flux linking the coil is :

$$\phi = \frac{\mu_0 (NI) A}{2 h} \propto \frac{1}{h} \quad - (3)$$

The stored energy in the system can be calculated from :

$$E = \frac{B^2}{2 \mu_0} * Vol \quad - (4)$$

- where this expression is appropriate for linear material characteristics and is only large in the air region for this problem. The energy/force ratio is important and is found to be (see also Figure 4) :

$$\frac{E}{F} = h \quad - (5)$$

It is now argued that this is a crucial factor distinguishing small-gap and large-gap systems. Large-gap systems involve considerable stored energy, tending to lead to large, highly stressed electromagnets and large, expensive power supplies. Typically, the natural frequencies of the suspension system will tend to be reduced, principally due to the associated high inductance of the electromagnets, since :

$$E = \frac{1}{2} L I^2 \quad - (6)$$

Continuing with classical analysis and following established magnetic bearing terminology, the position and current stiffnesses can be found by differentiation of equation (2) :

$$K_x = - \left(\frac{\partial F}{\partial x} \right)_o = - \frac{\mu_0 A (NI)^2}{2 h^3} \quad - (7)$$

$$K_I = \left(\frac{\partial F}{\partial I} \right)_o = \frac{\mu_0 A N^2 I}{2 h^2} \quad - (8)$$

It is seen that the position stiffness is completely determined by the geometric configuration and is independent of the coil design. The current stiffness of course depends on the choice of the number of turns in the coil. Additional practical details include the effective magnetic "pressure" in the air-gap, found to be approximately 1 atmosphere

for $B=0.5T$, using (1). It is clear from (1-4) that the efficient transmission of large forces requires a small air-gap and large pole face area. It is also clear that this simple suspension configuration exhibits severe non-linearities with respect to gap and current.

In large-gap systems it is a practical impossibility to generate uniform flux penetrating the suspended object. The simple formulae shown above are therefore not applicable, though several options are available. First, it is recognized that (1) is merely the normal component of Maxwell stress. For large-gap systems, the Maxwell stresses on arbitrary surfaces completely enclosing the suspended object can be integrated to yield the total force (and moment) on the object [1], but normal and shear stresses must both be considered:

$$\vec{F} = \frac{1}{\mu_0} \int_S T_{ij} \cdot d\vec{S} \quad \text{where } T_{ij} = \begin{bmatrix} (B_x^2 - \frac{1}{2}|B|^2) & B_x B_y & B_x B_z \\ B_x B_y & (B_y^2 - \frac{1}{2}|B|^2) & B_y B_z \\ B_x B_z & B_y B_z & (B_z^2 - \frac{1}{2}|B|^2) \end{bmatrix} \quad - (8)$$

The terms on the leading diagonal of the stress tensor, T_{ij} are recognized as constituting the $\frac{B^2}{2\mu_0}$ term which in turn leads to the form of (1). Alternatively one may use :

$$\vec{F} = \int_V (\vec{M} \cdot \nabla) \vec{B} dV \quad \text{and} \quad \vec{T} = \int_V (\vec{M} \times \vec{B}) dV \quad - (9)$$

The latter forms may be quite convenient for permanent magnet suspended elements and are usable, though inconvenient, for soft-iron elements. In this application, \vec{B} in equation 9 may be taken as the “external” or applied field; the field that would exist if the magnetization of the suspended element were removed from the problem. This is easily calculated in the case of permanent magnet suspended elements, slightly more difficult for soft-iron, provided that there is negligible magnetization of suspension electromagnet cores by the suspended element. This is only likely to be the case with large-gap systems.

It should be clear that field gradients are the key factors in the production of forces, either directly through the $\nabla \vec{B}$ term in (9) or indirectly via integration over the closed surface in (8). It can be noted that a gradient exists in Figure 1, due to the reversal in sign of flux relative to the suspended object. That is, entering on one side and leaving on the other, although the magnitude of the flux is relatively uniform in the region of each pole face.

No simple formula exists for “position stiffness”, due to the presence of numerous field and field gradient terms. Previous work [2,3] has resulted in linearized models for suspended permanent magnet elements under certain restrictive conditions, from which current and position stiffnesses can be found. As a point of interest, if the suspended object has a permanent magnet core then the current stiffness can be deduced directly:

$$K_i = \frac{F_o}{I_o}$$

SOME ASPECTS of the TECHNICAL DEVELOPMENT of WIND TUNNEL MSBSs

With the local air-gap as the controlled variable in small-gap systems, each suspension station becomes a quasi-one-degree-of-freedom subsystem. With a rotor, for example, a minimum of five bearings would be needed for full control, typically a vertical and horizontal bearing at each end of the shaft, plus a single axial "thrust" bearing. This arrangement facilitates relatively straightforward decoupling between degrees-of-freedom. Extra complications do arise due to geometrical or mass asymmetries and due to structural flexibility, and are the subject of considerable research. Many microgravity or vibration isolation systems have been designed with this "built-in" decoupling.

The earliest, widespread application of large-gap suspension was to wind tunnel MSBSs. There is evidence that the early thinking with MSBSs was consistent with the point actuator viewpoint. For instance see Figure 5 [4,5], where the suspension systems are seen to resemble a bearing supported shaft. Further, many early MSBS control systems were configured so that the current in each electromagnet was controlled on the basis of the distance of the model from that electromagnet, i.e. the local airgap, just as in the magnetic bearing case. As the complexity of systems increased, and as the geometry of the suspended object became less like that of a slender shaft, this approach failed. MSBSs developed in the early to mid-1960s were generally based on "coupled" control systems, that is sensors were placed wherever convenient, signals were mixed to sensible degrees-of-freedom (usually the principal axes of the suspended element) with a distribution network to allocate control demand among suitable electromagnets. An alternative interpretation is a double coordinate transformation, from sensor axes to object axes, then from suspended object axes to electromagnet axes. This inevitably leads to the development of an entirely different set of governing equations, based directly on field and field gradient components in space, rather than point forces, as discussed earlier.

The next phase of development of design approaches is represented by the MIT 6-inch system, illustrated in Figure 6, where considerable efforts were made to ensure that separate field and field gradient components were generated independently, and also with good spatial uniformity, by separate sets of electromagnets [6]. Each of these sets was then wired in series and fed from an individual power supply. This again provides for controller decoupling, albeit in suspended object axes rather than MSBS axes, and considerably simplifies the force calibration, but has some disadvantages. Notably the maximum force capability of the electromagnet assembly cannot be realised, since individual electromagnets cannot be run up to their respective current limits independently, as shown in Figure 7.

Contemporary thinking is therefore to distribute an array of general-purpose electromagnets around the wind tunnel test section and operate each independently. This will provide the maximum possible force and moment capability at all attitudes, but can lead to complex calibration procedures; still a subject of considerable research [7].

SCALING of MAGNETIC SUSPENSION SYSTEMS

The subject of scaling laws has been addressed previously [8,9]. It is found that in many systems, where a limit to the maximum field intensity exists and is important (such as a superconductor critical field, permanent magnet coercive field and so on), scale such that the magnetic force varies as length squared, rather than as the volume of magnetic material as is often assumed. Relevant to previous discussions, the system stored energy will then scale as length cubed, leading to the expected result -

$$\frac{\text{Stored energy}}{\text{Force}} \Big|_{\text{Max. field limited}} \propto \frac{L^3}{L^2} \propto L \propto \text{Air-gap}$$

CONTROL and RELATED PROBLEMS

In large-gap systems the number of “actuators” (controlled currents) frequently exceeds the number of degrees-of-freedom to be controlled. This results in the equilibrium point (and the control problem in general) being underdetermined, i.e. an infinite set of solutions for suspension currents, more particularly current distribution, exist. This poses two problems, determination of a suitable current distribution to generate the required forces and torques, and the determination of the maximum force and moment capability, such as where hard electromagnet current limits exist.

The first problem can be overcome by physical argument, as used in Reference 7, where a systematic scheme was developed for “allocating” demand in a hierarchical manner, such that the most effective electromagnets took the largest load. Alternatively, matrix theory may be brought to bear in the following manner. If the forces and moments generated by the electromagnet array can be written in the linear form shown :

$$\begin{bmatrix} T_y \\ T_z \\ F_x \\ F_y \\ F_z \end{bmatrix} = \begin{bmatrix} K_{z1} & K_{z2} & K_{z3} & K_{z4} & K_{z5} \\ K_{y1} & \ddots & & & \\ K_{xx1} & & \ddots & & \\ K_{xy1} & & & \ddots & \\ K_{xz1} & & & & \ddots \end{bmatrix} \begin{bmatrix} I_1 \\ I_5 \end{bmatrix} \quad - (3)$$

- otherwise written as :

$$A I = F$$

- then the problem is to find a pseudoinverse A^{-1} that satisfies sensible physical constraints. The classical pseudoinverse (Moore-Penrose) yields a solution such that the 2-Norm of the solution current vector is minimized.

This corresponds to the minimum sum of squares of electromagnet currents, in other words the minimum power solution for conventionally conducting electromagnets, also the minimum stored energy solution in all cases, though perhaps requiring some scaling in the case of different sized electromagnets. An alternative inverse will give the minimum ∞ -Norm, corresponding to the maximum value of an individual current being a minimum, and by inference to the maximum force and moment capability. This is more appropriate in the case of superconducting electromagnets, or where hard current limits are important. A residual problem is that this latter solution has been shown to exhibit discontinuities as a function of some variable, such as suspended object orientation [9].

POSITION (or RATE) SENSING

A wide variety of sensing systems have been used for both small-gap and large-gap systems. Some, chiefly optical systems, are usable at all air-gaps, some are relatively specific to one size gap or the other. For example, commercial capacitive or inductive sensors are only suitable for small gaps. Rather than attempt a comprehensive survey of all techniques, a few technical observations relevant to large-gap systems will be made.

The most common approach used has been the analog optical obscuration approach. The X-ray system used in the AEDC MSBS was conceptually similar [5]. Although this approach is capable of picking off a single motion from one point of a suspended object, multi-degree-of-freedom systems become quite complex (Figure 8), extremely sensitive to detail geometry of the suspended object and prone to couplings between degrees-of-freedom. Nevertheless, the fact that high sensitivity can be achieved easily is a strong positive factor, and the approach remains the first choice for many experimental systems.

A significant refinement is the use of linear scanning photo-diode arrays as the light sensors. This greatly improves system linearity, repeatability and environmental tolerance, but does not overcome other objections mentioned above [10]. The way forward appears to be camera-based sensing, where some form of target is monitored by an array of cameras (presumably solid-state), illustrated in Figure 9. Existing camera technology is already adequate for low-to-medium frame rates, though the image processing requirements are formidable. Processing hardware capable of useful data rates is only just becoming available [11].

OTHER SUSPENSION APPROACHES

This paper has concentrated on the feedback-controlled electromagnet/ferromagnetic suspended element type of system. Numerous alternatives exist, including A.C. or eddy current methods, many variations incorporating diamagnetic material, or permanent magnets in repulsion. More comprehensive treatment and discussion can be found in Reference 12. Many of the alternative approaches could be applied to large-gap systems. However, in the context of the anticipated applications, all alternatives appear to have serious shortcomings.

Notably, in applications involving pointing and manipulation, set-point control is needed, which open-loop suspensions cannot easily provide. In many other applications, such as wind tunnel MSBSs or certain types of vibration isolation, heavy damping of suspended element motion is required. With the stored energy of all types of suspension system rising with increasing air-gap, it is not clear how good motion damping, implying dissipation of large quantities of energy, can be arranged. Further research and development will improve matters, as is clearly the case with the ElectroDynamic Suspension system (EDS), for Maglev trains. This system [13] is, by all reasonable measures, a large-gap suspension. That is, air-gap size is not small with respect to system scale.

A FEW FINAL THOUGHTS

The fringing fields generated by large-gap suspension systems are sometimes cited as a serious obstacle to their use in certain applications, perhaps particularly spaced-based applications. The production of powerful fields (possibly time-varying) in the region surrounding the suspension system is certainly a problem, but can be overstated.

It is noted here that since the field sources are essentially dipoles (current-loops or permanent magnets), the magnetic field strength in the far-field will decay at least as the cube of distance. Further, since the net strength of suspension system dipoles is often zero, the decay can be even faster, and the resultant force and torque in uniform external field (such as the earth's field) will be zero.

ACKNOWLEDGEMENTS

This work was partially supported by NASA Grant NAG-1-1056, Technical Monitor Nelson J. Groom.

REFERENCES

1. Lowther, D.A.; Silvester, P.P.: Computer-Aided Design in Magnetism. Springer-Verlag.
2. Groom, N.J.: Analytical Model of a Five Degree-of-Freedom Magnetic Suspension and Positioning System. NASA TM-100671, March 1989.
3. Groom, N.J.; Britcher, C.P.: Stability Considerations for Magnetic Suspension Systems Using Electromagnets Mounted in a Planar Array. NASA CP-10066, March 1991.
4. Moreau, R.: Use of Magnetic Suspension in O.N.E.R.A. Wind Tunnel. In ARL Symposium on Magnetic Wind Tunnel Model Suspension and Balance Systems. Dayton, OH, 1966. ARL-66-0135, July 1966.

5. Crain, C.D.; Brown, M.D.; Cortner, A.H.: Design and Initial Calibration of a Magnetic Suspension System for Wind Tunnel Models. AEDC-TR-65-187, September 1965. (In abbreviated form in ARL Symposium on Magnetic Wind Tunnel Model Suspension and Balance Systems. Dayton, OH, 1966. ARL-66-0135, July 1966)
6. Stephens, T.: Design, Construction and Evaluation of a Magnetic Suspension and Balance System for Wind Tunnels. MIT-TR-136, NASA CR-66903, November 1969.
7. Parker, D.H.: Techniques for Extreme Attitude Suspension of a Wind Tunnel Model in a Magnetic Suspension and Balance System. NASA CR-181895, October 1989.
8. Zapata, R.N.: Magnetic Suspension for Large-Scale Aerodynamic Testing. In Wind Tunnel Design and Testing Techniques, AGARD CP-174, March 1976.
9. Britcher, C.P.: Some Aspects of Wind Tunnel Magnetic Suspension Systems with Special Application at Large Physical Scales. NASA CR-172154, September 1983.
10. Schott, T.D.; Tchong, P.: The New Electro-Optical Displacement Measuring System for the 13-inch MSBS. In NASA Workshop on Aerospace Applications of Magnetic Suspension Technology, NASA CP-10066, March 1991.
11. Welch, S.S.; Clemmons, J.I.: The Optical Position Measurement System for a Large-Gap Suspension System. In NASA Workshop on Aerospace Applications of Magnetic Suspension Technology, NASA CP-10066, March 1991.
12. Jayawant, B.V.: Electromagnetic Levitation and Suspension Techniques. Edward Arnold, 1981.
13. Society of Automotive Engineers. Magnetic Levitation Technology and Transportation Strategies. SAE SP-834, August 1991.

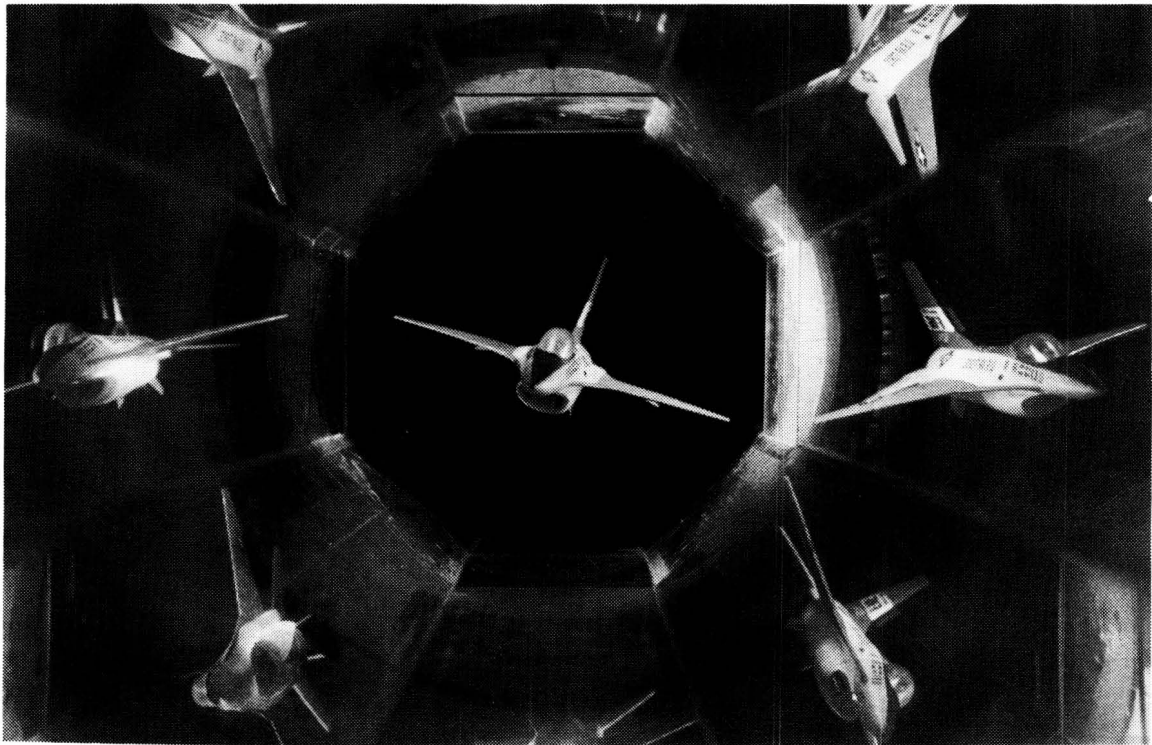
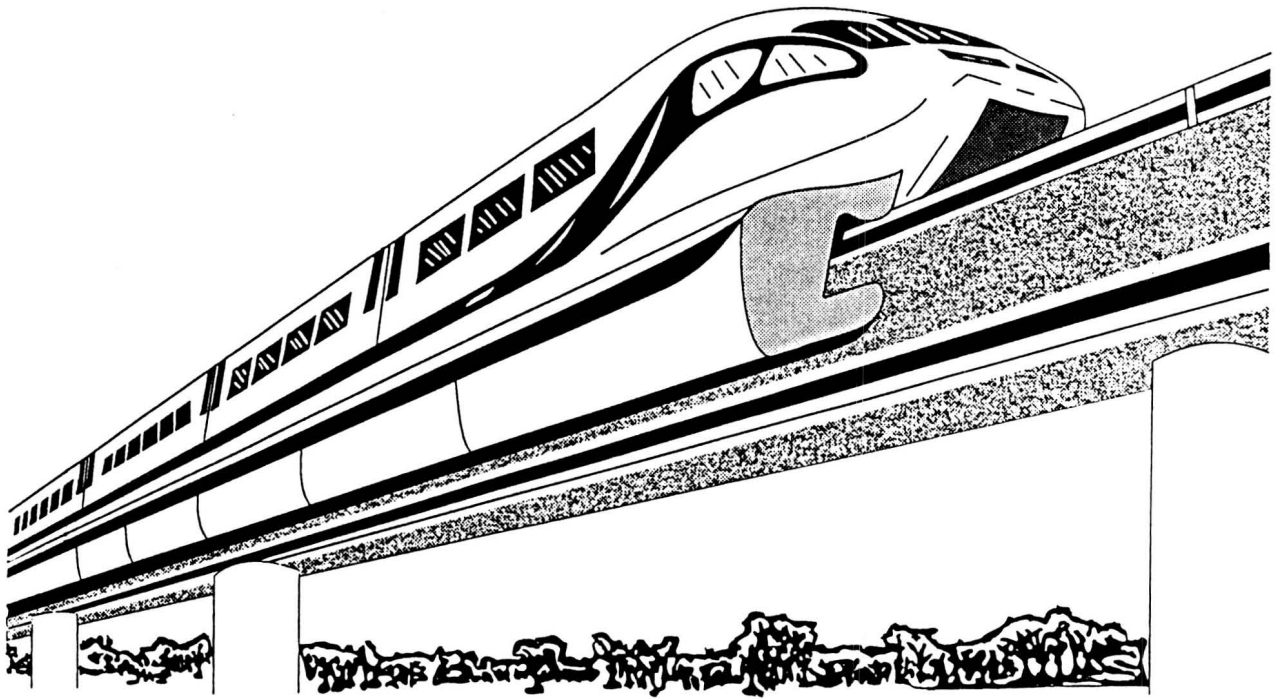


Figure 1 - Established Applications for Large-Gap Magnetic Suspensions
- Maglev and wind tunnel MSBSs

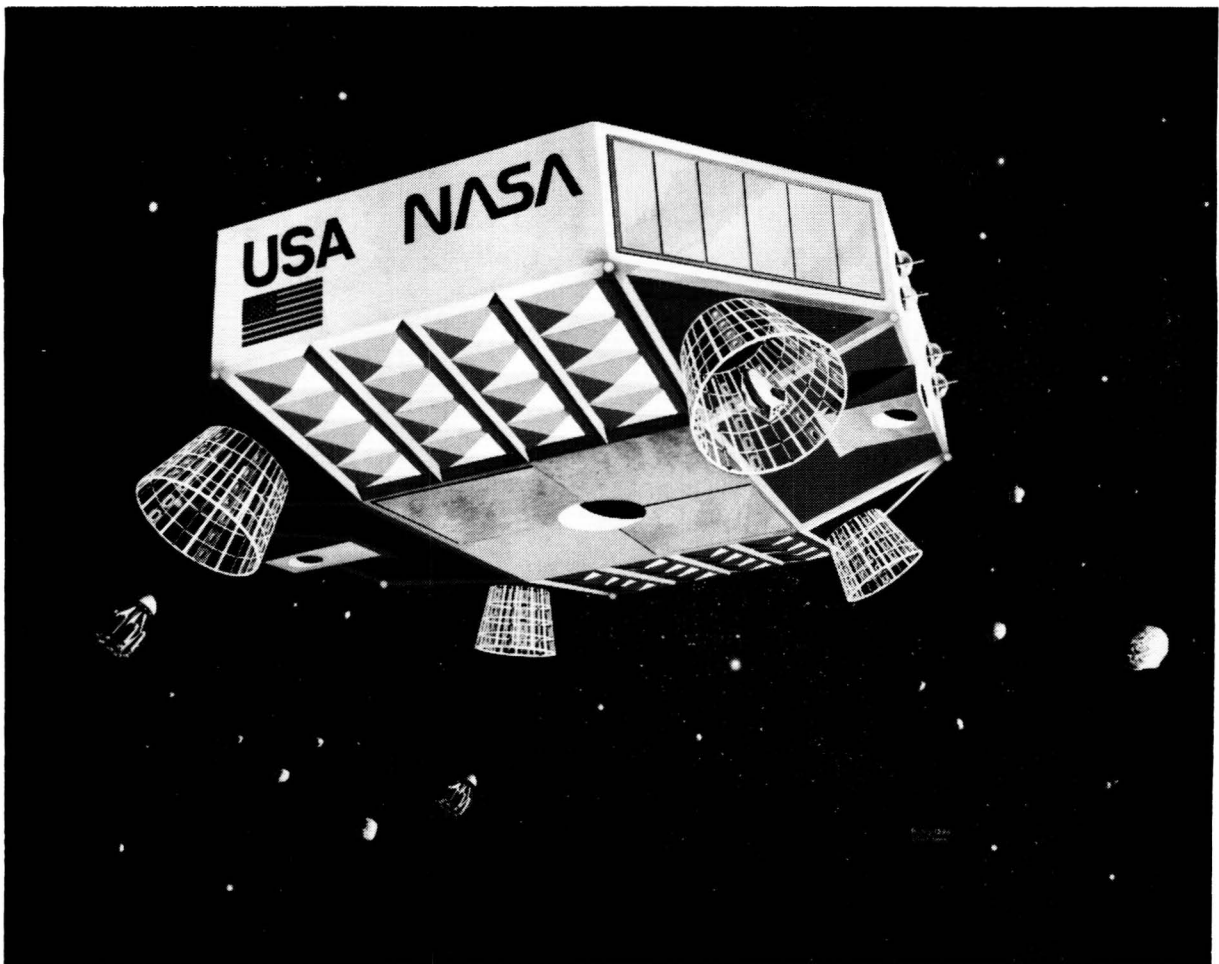
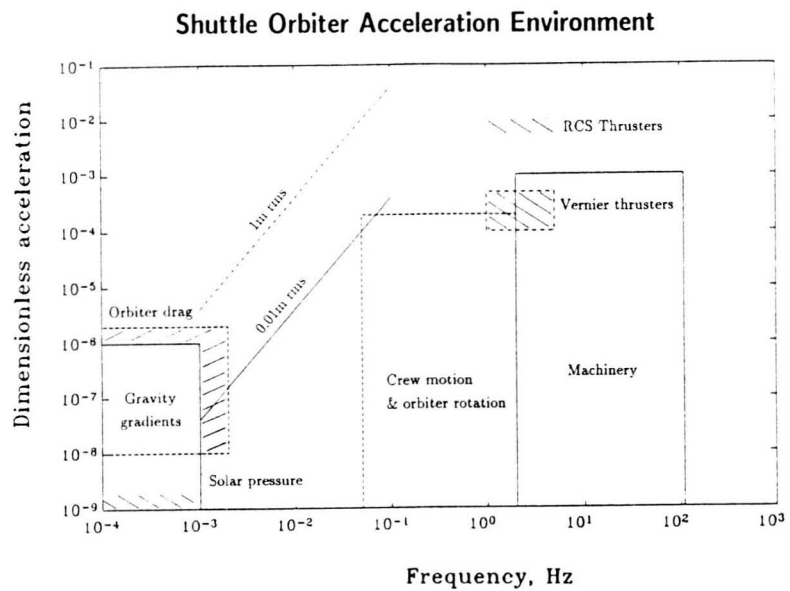


Figure 2 - Potential Applications for Large-Gap Magnetic Suspensions

- low frequency microgravity isolation, space-based pointing or payload manipulation

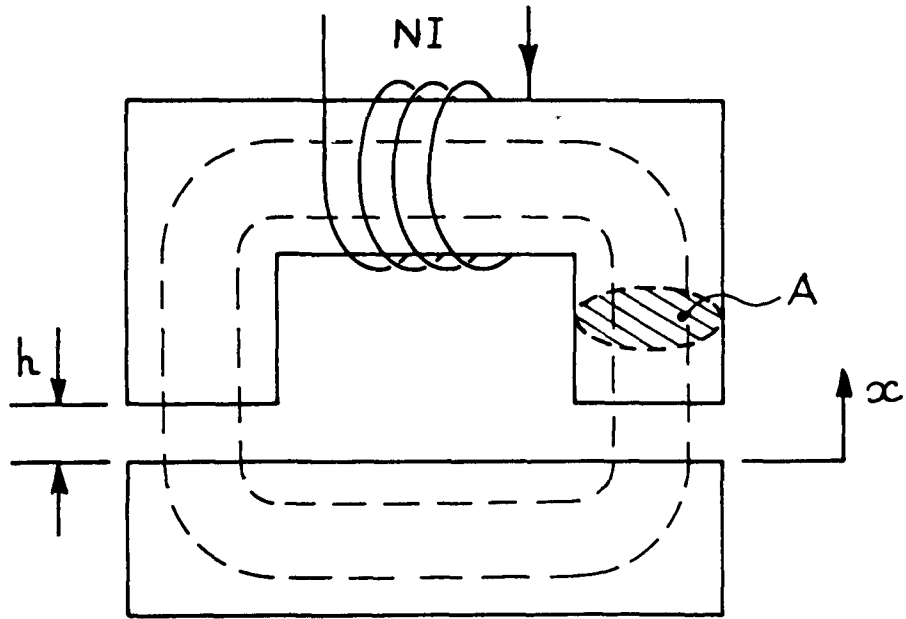


Figure 3 - Schematic Diagram of a 2-Pole Small-Gap Suspension

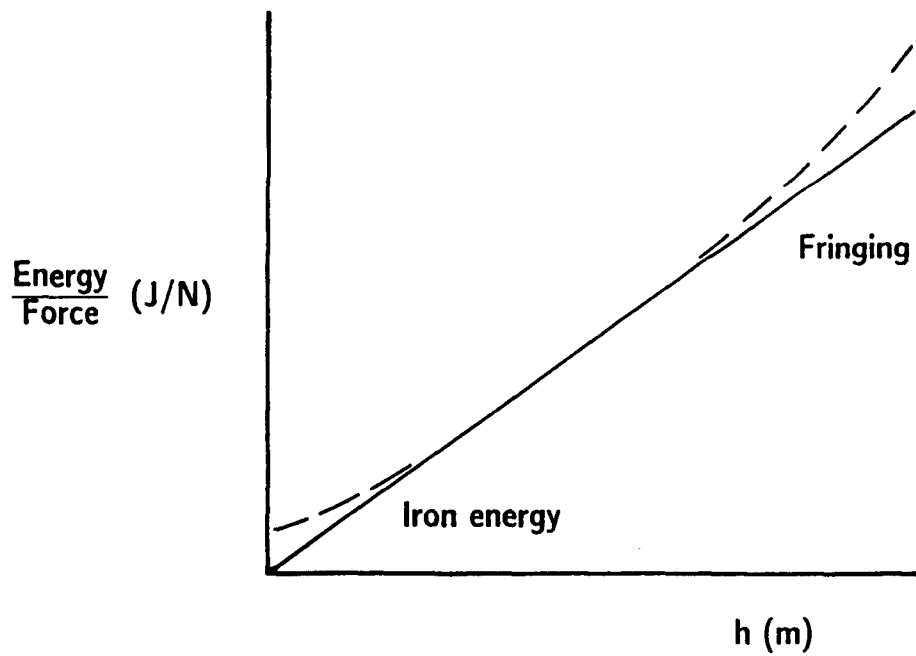


Figure 4 - Energy/Force Relation for a 2-Pole Small-Gap Suspension

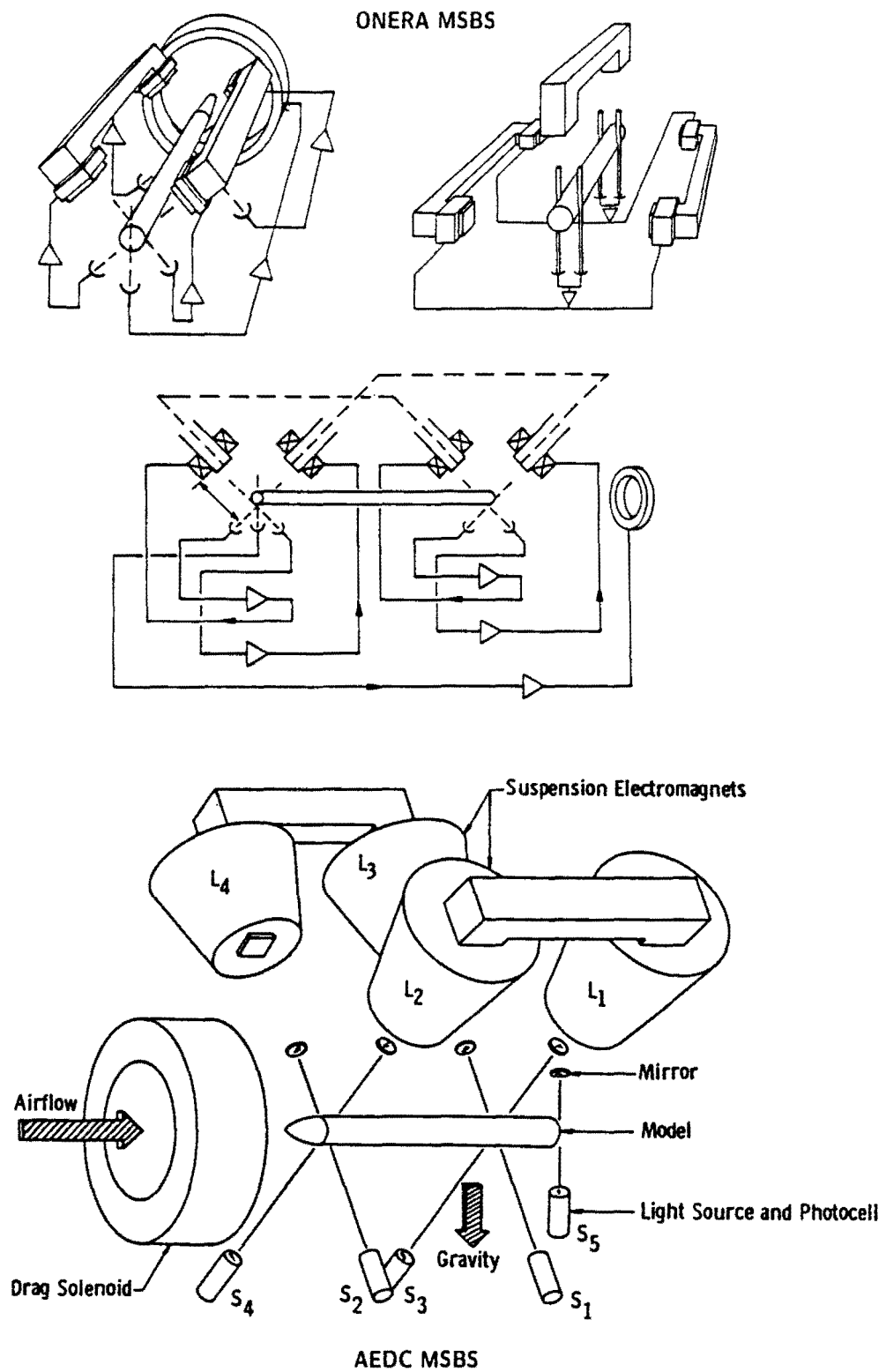


Figure 5 - Design Details of Early MSBSs
- ONERA and AEDC

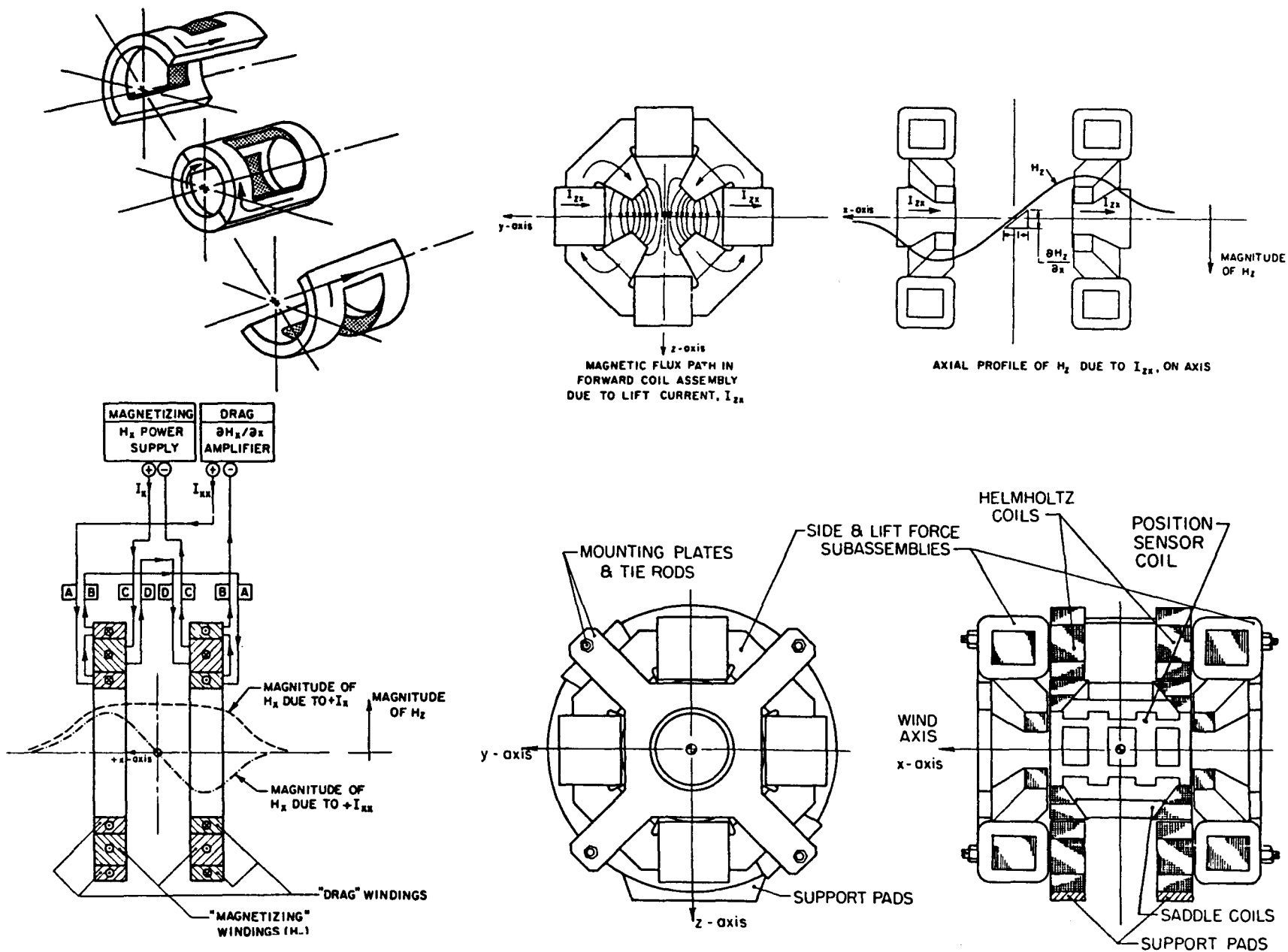


Figure 6 - Magnetic Configuration of the MIT 6-inch MSBS

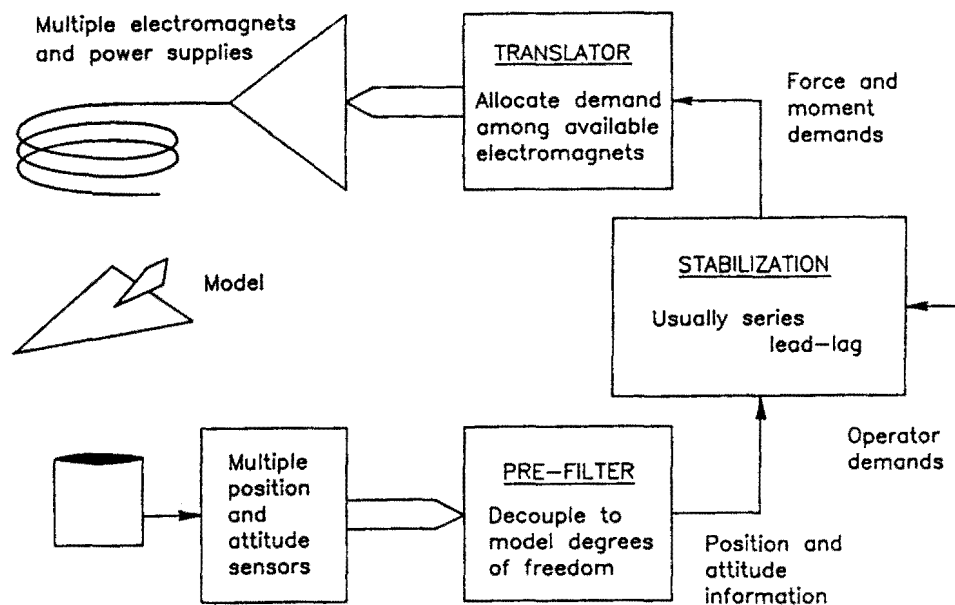
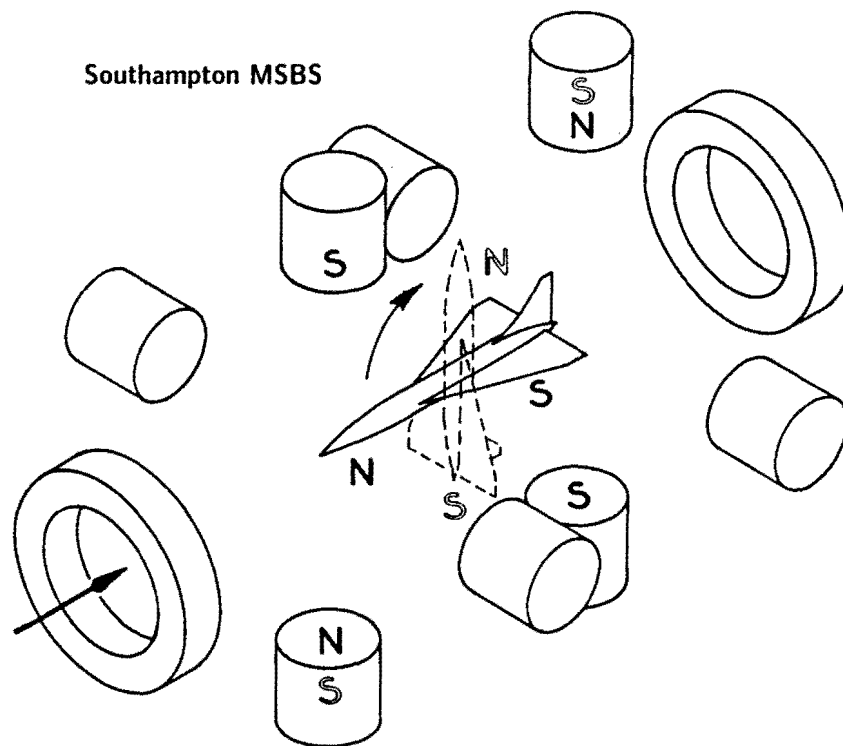


Figure 7 - Example of Contemporary Thinking Regarding MSBS Configuration

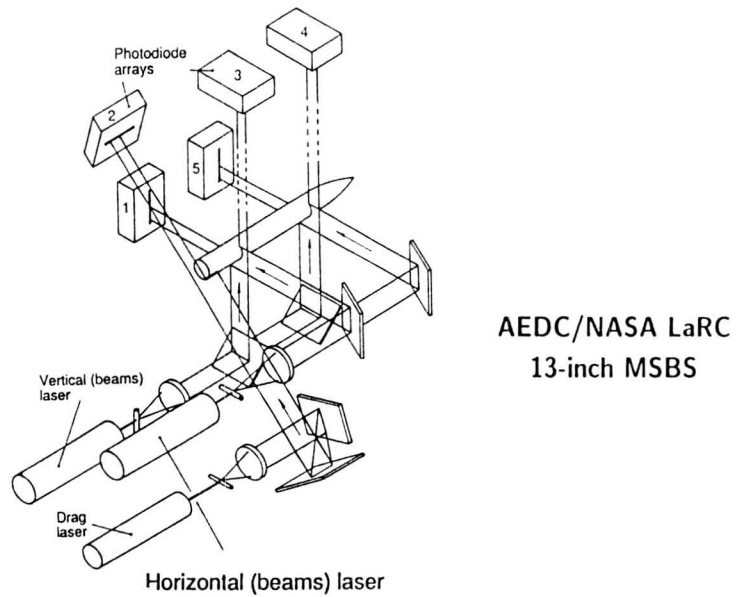


Figure 8 - Layout of Optical Position Sensing System for NASA 13-inch MSBS

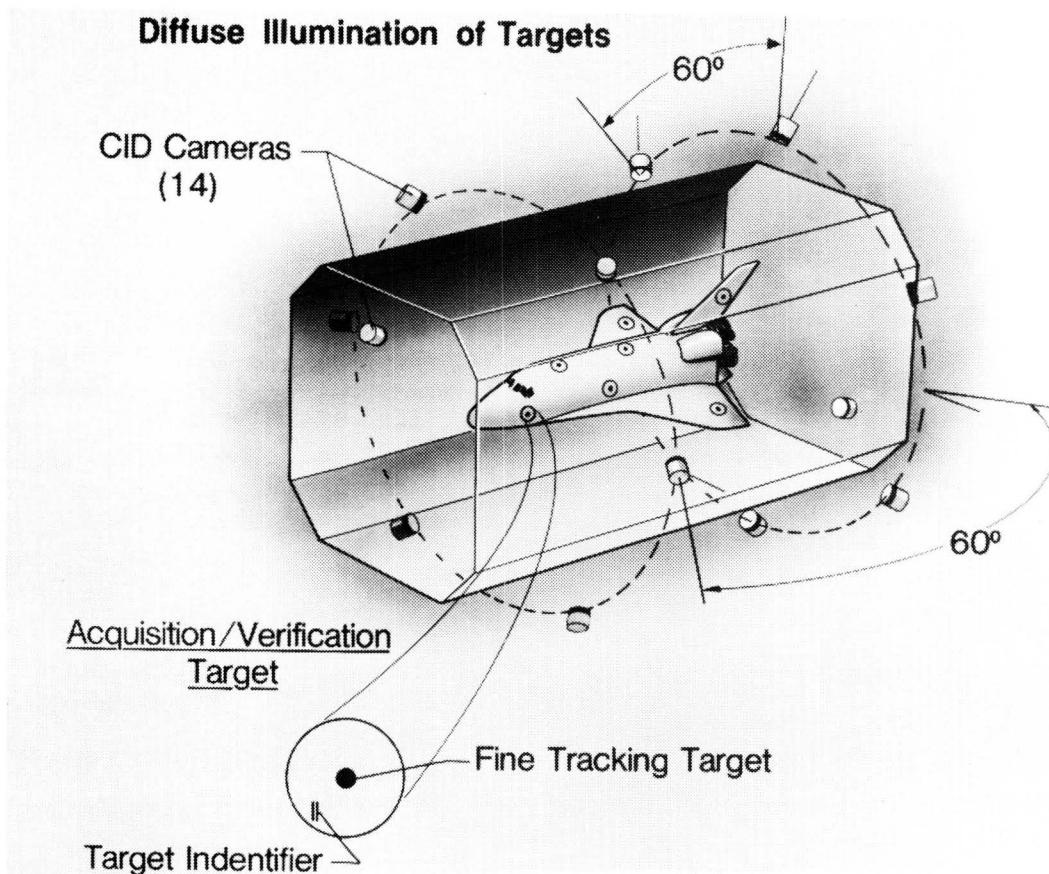


Figure 9 - Conceptual Layout of Advanced Optical Position Sensing System

Session 2

BEARINGS 1

Chairman - Paul E. Allaire
University of Virginia

N 9 2 - 2 7 7 2 5

**MAGNETIC BEARINGS : A KEY TECHNOLOGY
FOR ADVANCED ROCKET ENGINES ?**

**J.Ph. Girault
Société Européenne de Propulsion
Vernon - France**

SUMMARY

For several years, Active Magnetic Bearings (AMB) have demonstrated their capabilities in many fields, from industrial compressors to control wheel suspension for spacecrafts. Despite this broad area, no significant advance has been observed in rocket propulsion turbomachinery, where size, efficiency and cost are crucial design criteria.

To this respect, Société Européenne de Propulsion (SEP) has funded for several years significant efforts to delineate the advantages and drawbacks of AMB applied to rocket propulsion systems. Objectives of this work, relative technological basis and improvements are described in this paper, illustrated by advanced turbopump layouts.

Profiting from the advantages of compact design in cryogenic environment, the designs show considerable improvements in engine life, performances and reliability. However, these conclusions should still be tempered by high recurrent costs, mainly due to the space-rated electronics. Development work focused on this point and evolution of electronics show the possibility to decrease production costs by an order of magnitude.

INTRODUCTION

Every designer in Rotating Turbomachinery has already encountered difficulties in obtaining proper compromise between the machine specifications and the actual bearing capabilities. This is particularly true for Rocket Engine Turbopump (T/P) designs, where size, efficiency and costs are crucial design aspects, resulting in complex turbomachines with very high specific power (about 100 kW/kg for high efficiency engines) and rotational speed (up to 120,000 rpm), with a life limited to a few hours.

Thus the bearings appear to be key components in successful design, as well as imposing major limitations to further improvements in engine performance and life.

The figure 1 illustrates part of this assertion, reporting current and foreseen values for the bearing D.N. product, where D is the shaft diameter (in mm), and N the rotational speed (in rpm). It is clear that significant increase in one of these parameters, as dictated by advanced designs to improve T/P efficiencies and/or dynamic behaviour, exceed the rolling element bearing capabilities and call for innovative solutions.

Among other aspects, it is well-known that the use of on-board cryogenic propellants for cooling these bearings does not offer sufficient viscosity for lubrication, and consequently limits strongly the service life.

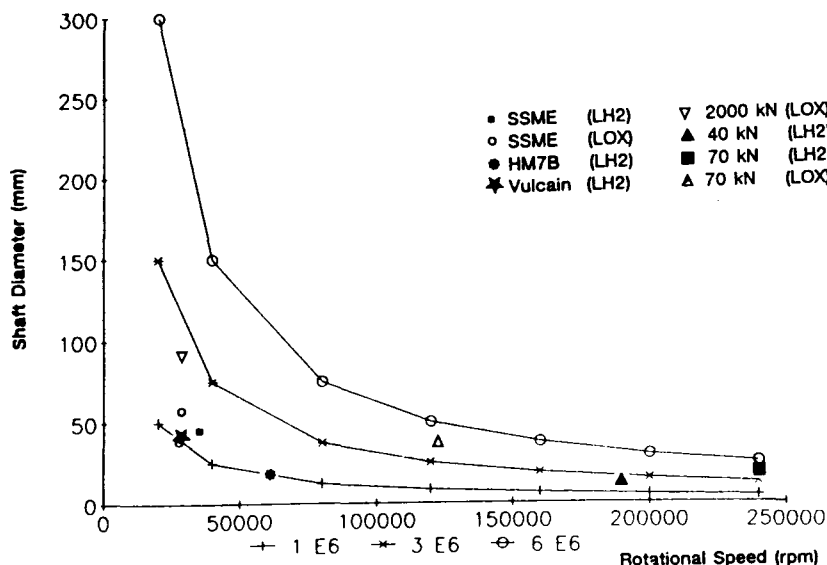


Figure 1 : Bearing D.N. Values for various T/P Designs

Consequently, the bearings, highly stressed by large static and dynamic loads, require careful analysis during the project, contribute predominantly to the failure mode allocations for the T/P, as illustrated figure 2 for a typical liquid hydrogen (LH2) turbopump, and involve expensive development tests and maintenance programs.

Following from this, rocket engine manufacturers have been studying for about two decades the capabilities and drawbacks of alternative bearings without any surface contact, i.e. fluid film bearing and magnetic bearings.

The former technique (fluid bearing) has been studied extensively for its noticeable advantages, with various practical concepts (hydrodynamic, hydrostatic and hybrid bearings) to minimize inherent drawbacks, such as rubbing in transients, complex dynamic behaviour and tight clearances. Actual turbopump tests have been performed (refs. 1, 2, 3) with positive results, but the few applications to space propulsion are biased toward storable propellants and low thrust engines (ref. 4).

Space applications of the second technique (mag bearing) have mainly concerned spacecraft attitude control (ref. 5, 6), with at least one degree of freedom (DOF) actively controlled. Despite numerous applications in industrial compressors and a growing interest in aerospace propulsion (refs. 7, 8), no practical work has been observed, although studies in jet engines are emerging.

In this field, this paper presents the objectives one can expect to meet by implementing such technology in aerospace propulsion together with the required analysis tools and technological basis for successful design, as the results of studies funded by Societe Europeenne de Propulsion (SEP) since 1986, and team work with Rocketdyne, Division of Rockwell International Corporation (RD) (Ref 9).

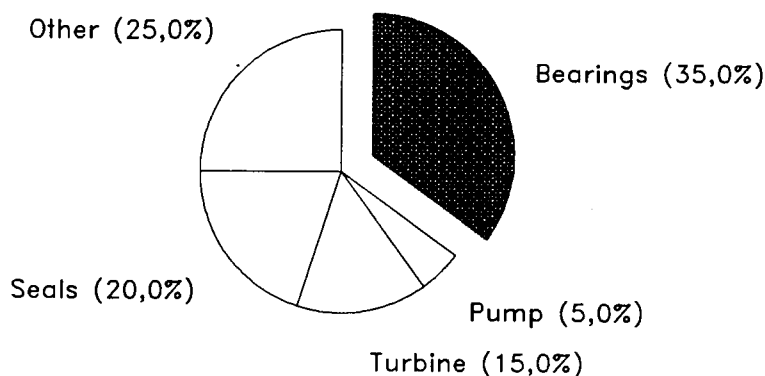


Figure 2 : Failure Mode Allocation for the VULCAIN LH2 Turbopump

T/P DESIGN & FUNCTIONAL FEATURES

Key features and corresponding T/P limitations can be pointed out on the figure 3, showing the strong interaction between the T/P design and the bearings specifications, as well as the inherent iterative process to finalize the T/P architecture.

This is particularly true by using Active Magnetic Bearings (AMB), where the link between the shaft (i.e. the bearings rotors) and the T/P housing (i.e. the bearings stator) is represented by the transfer functions, themselves function of the bearing specifications (speed, loads). The resulting bearing and associated controller change in turn the shaft assembly, stiffnesses and dampings, which leads to some modifications to the T/P design, thus changing the bearing specifications, until obtention of the final compromise.

Such T/P designs are illustrated in figure 4, reporting LH2 T/P layouts for a 40 kN thrust LOX/LH2 expander cycle rocket engine, and LOX T/P layouts for a 2000 kN thrust gas generator cycle engine. Main features of these designs and associated magnetic bearings are reported in table 1.

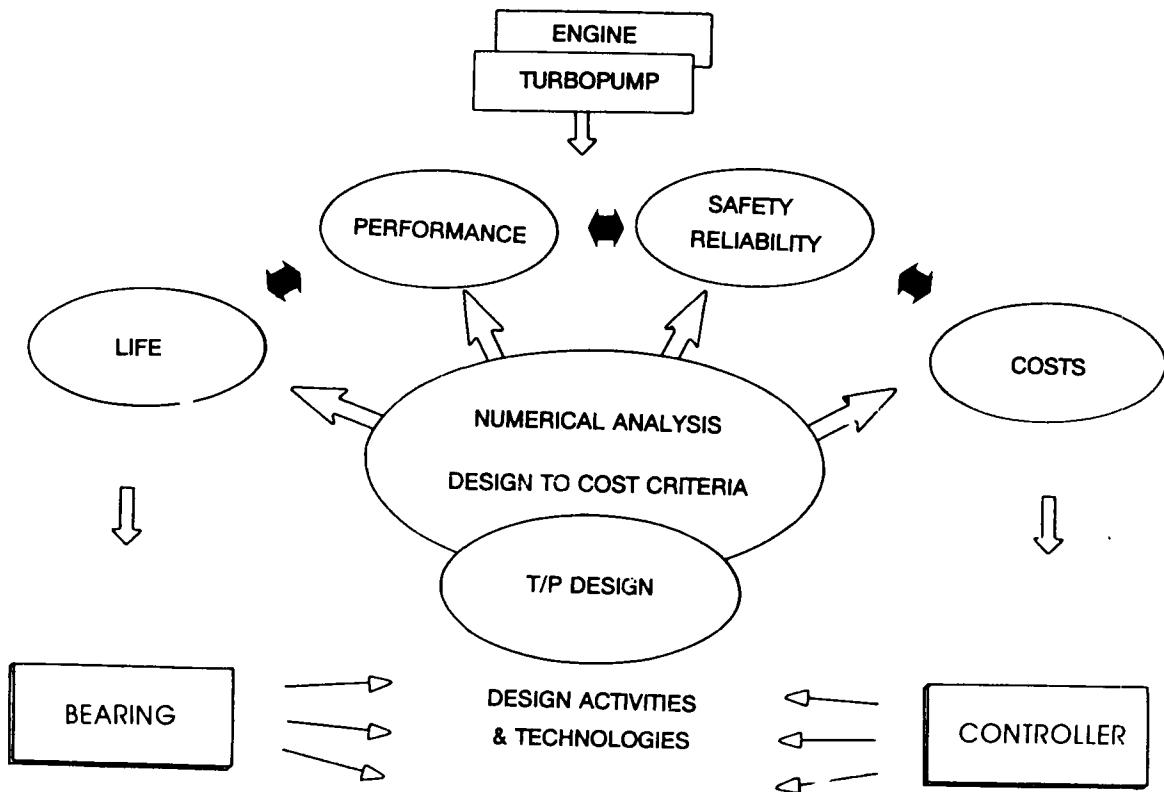


Figure 3 : T/P Design Methodology

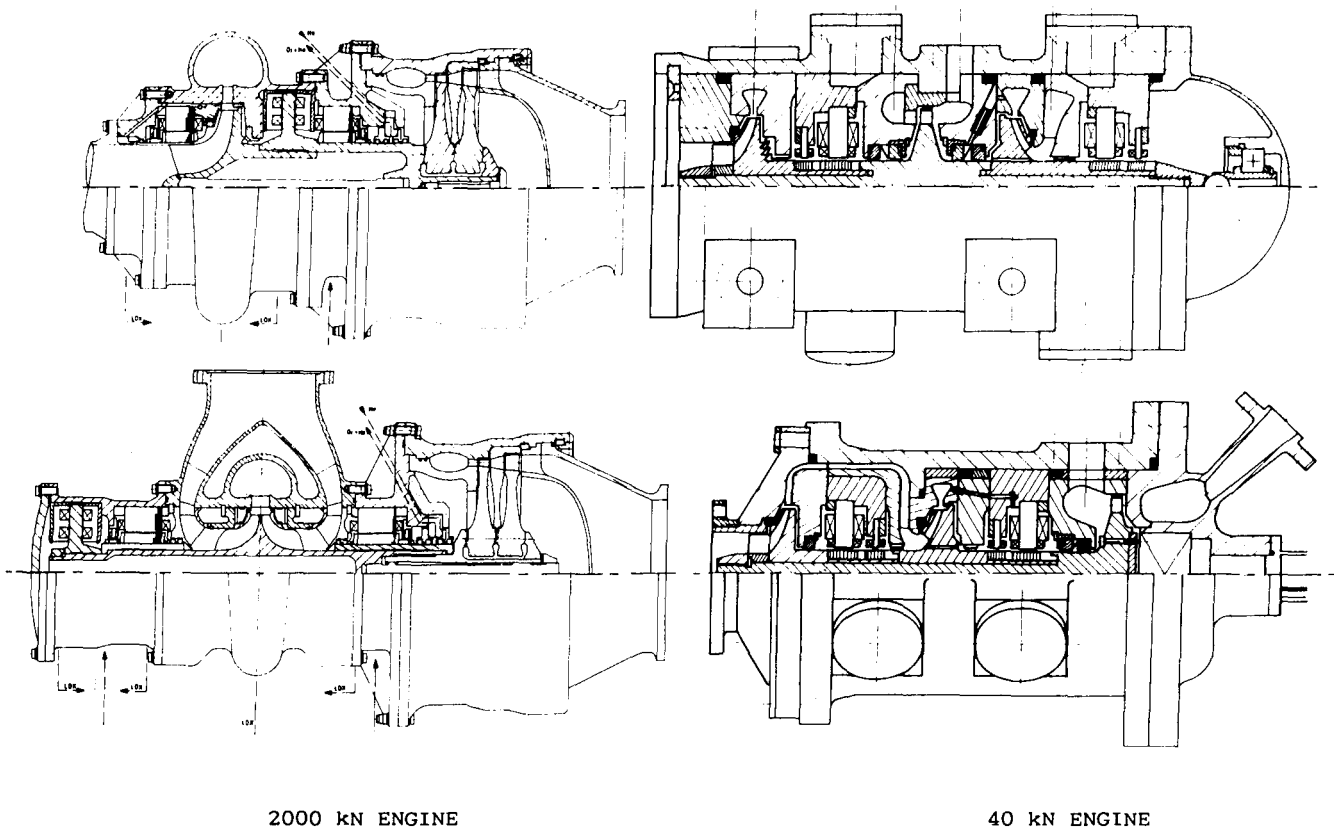


Figure 4. Advanced T/P Designs with AMB

**TABLE 1 : MAIN FEATURES OF ADVANCED ROCKET ENGINE T/P
AND ASSOCIATED MAGNETIC BEARINGS (AMB)**

| ENGINE THRUST - T/P | 40 kN/LH2 | 60 kN/LH2 | 2000 kN/LOX |
|----------------------------|-------------------|-------------------|-------------|
| <u>T/P CHARACTERISTICS</u> | | | |
| . Pressure rise (MPa) | 24 | 11 | 28 |
| . Shaft Power (kW) | 670 | 610 | 17,000 |
| . Rotor Speed (rpm) | 190,000 | 60,000 | 30,000 |
| . Overall Length (m) | 0.25 | 0.35 | 1,0 |
| . Weight (kg) | 4.8 | 28 | 260 |
| <u>AMB CHARACTERISTICS</u> | | | |
| . Load (N) (max) | 65 | 475 | 4,600 |
| . Stator O.D. (mm) | 60 | 75 | 210 |
| . Shaft O.D. (mm) | 12 | 25 | 91 |
| . Airgap (mm) | 0.2 | 0.2 | 0.4 |
| . Materials (rotor) | Fe-Si or Fe-Co | Fe-Si or Fe-Co | Fe-Si |
| . Materials (stator) | Fe-Co | Fe-Co | Fe-Co |
| . Weight (kg) | 0.6 | - | 30(w/axial) |
| . Power consumption (W) | 500 | 400 | 5,000 |

The use of AMB in these Advanced T/P designs results in high rotational speed for optimal pump efficiencies and reduced T/P size and weight. Thrust modulation and dynamic control is also facilitated by high damping over a large operating speed range, including the first two or three critical speeds. Unbalance requirements can be also relaxed to some extent to simplify assembly procedures and minimize production costs. Finally, the AMB Control System means the existence of Health and Control Monitoring (HCM) integrated in the T/P at the earliest steps of the design, making the development easier, safer and less expensive.

The results have been substantiated by comparison with alternative T/P designs fitted with fluid film bearings and/or rolling element bearings. This has shown important simplification of the fuel (LH2) T/P originally designed with ball bearings (e.g. 2 stages pump instead of 4 stages with ball bearings, and inboard bearing with overhanging turbine disc) but minor or no significant advantage for the oxidiser (LOX) T/P. For this latter, the viscous losses at the bearings increase drastically, as illustrated in figure 4. The high fluid density (about 16 times more for the LOX than for the LH2) leads also to moderate pump tip speeds, thus reducing interest in high peripheral speed at the AMB airgap, compared to LH2 cases.

Thanks to the cryogenic environment (between 40 and 100 K) in both cases, the bearing stator size can be reduced by more than 2, compared to ambient temperature applications, thus improving bearing integration.

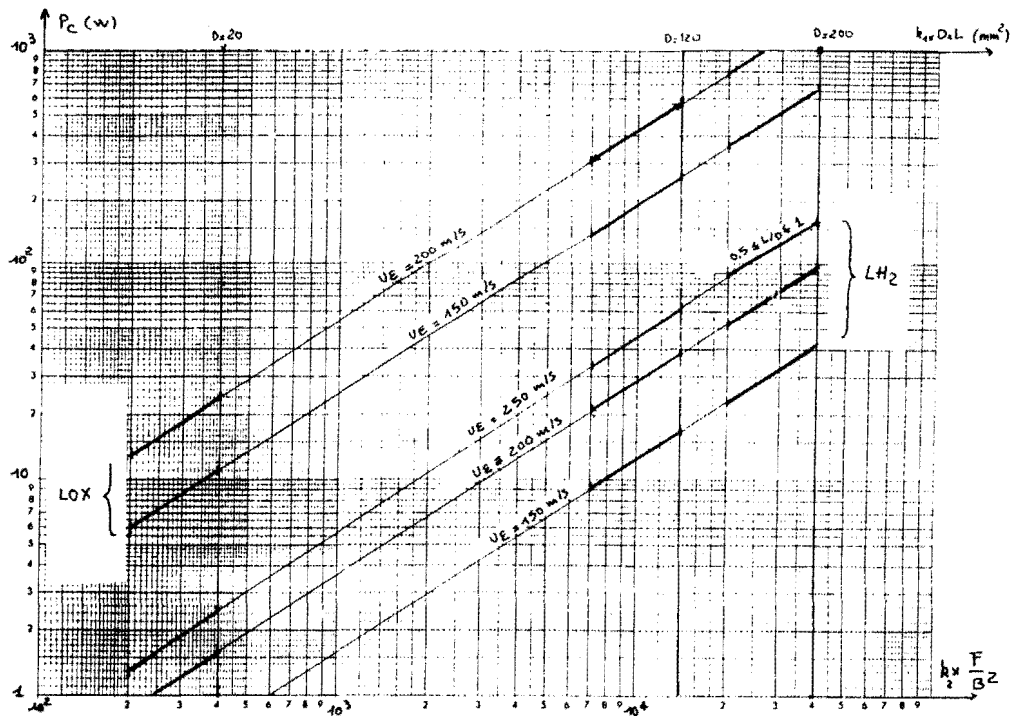


Figure 4 : Normalizes viscous losses as a function of speed at the airgap, fluid and bearing size

Trade-off between the AMB features and the clearances required along the shaft (with provision for misalignment and unbalance responses) generally results in a 0.2 mm (200 μ m) airgap for engine thrust up to about 100 kN. This is 5 to 10 times more than the clearance required for fluid film bearings, thus facilitating inactive long-term storage in space and misalignment tolerance.

On the other hand, the small LH2 flowrate required to chill down the bearing and maintain cryogenic temperatures improves the pump efficiency and reduces shaft power losses, leading to LH2 saving. Numerical values as reported (table 2) illustrate this point. For cumulated duty cycles in space, long-term storage and/or long duration propelled missions, this allows considerable LH2 tank size and mass reduction. For a gas generator (GG) cycle engine, in this thrust range, this will save between 30 and 50 kg of LH2 per hour. For expander cycle engine, this allows slight increase of the chamber pressure, increasing the engine specific impulse.

TECHNOLOGICAL BASIS

In parallel with design studies, technological effort was aimed at validating the bearing design and improving the current state-of-the-art.

This effort has been oriented along two axis : the bearing materials and the controller size reduction.

Bearing materials

Earlier work has been reported in 1988 (ref. 8), and the results are here completed. They are mainly driven by cryogenic aspects, compatibility with liquid and gaseous oxygen and hydrogen, and improvements of mechanical and magnetic characteristics.

Silicon-iron rotor laminations have been the traditional choice for industrial bearings. This cheaper material offers good mechanical properties in cryogenic conditions : a yield stress higher than 500 MPa, high fatigue limit (better than 120 MPa at 10^7 cycles), together with reasonable flux density (up to 1.5 Tesla).

Moreover, a GH2 brittleness experimental study, performed with disc burst tests as depicted, figure 5, have shown classical behaviour, with disappearance of GH2 brittleness in cryogenic conditions (fig. 6).

Standard tests to check compatibility with LOX or GOX (bomb test, adiabatic compressions) confirm suitability for use in T/P environment.

Accordingly, most of the T/P designs briefly presented here have used iron/silicon alloys for the rotor laminations and conventional iron/cobalt alloys for the stator laminations.

Nevertheless, to further improve future designs, new iron-cobalt alloys have been carefully studied. This kind of alloy traditionally exhibits very high flux density (up to 2.2 Tesla) together with poor mechanical properties (low yield stress, limited to 200 MPa and excessive brittleness). However, metallurgical progress has renewed interest in such alloys, exhibiting

**TABLE 2 : COMPARISON BETWEEN MAGNETIC AND HYDROSTATIC
BEARINGS FOR A 40 kN THRUST ENGINE LH2 T/P**

| | MAGNETIC | HYDROSTATIC |
|--------------------------------------|--------------|--|
| Flow rate (g/s) | 5 | 30 |
| Decrease in pump efficiency | 1 % | 5 % |
| Viscous losses (W) at the bearing | 450 | 800 (shaft centered, $\epsilon = 0$) 2500 ($\epsilon = 0,5$) |
| Load capacity (N) | 65 | 800 (at $\epsilon = 0,5$) |
| LH2 saving | + 30 kg/hour | |

GH2 EMBRITTLEMENT ON FeSi SAMPLES

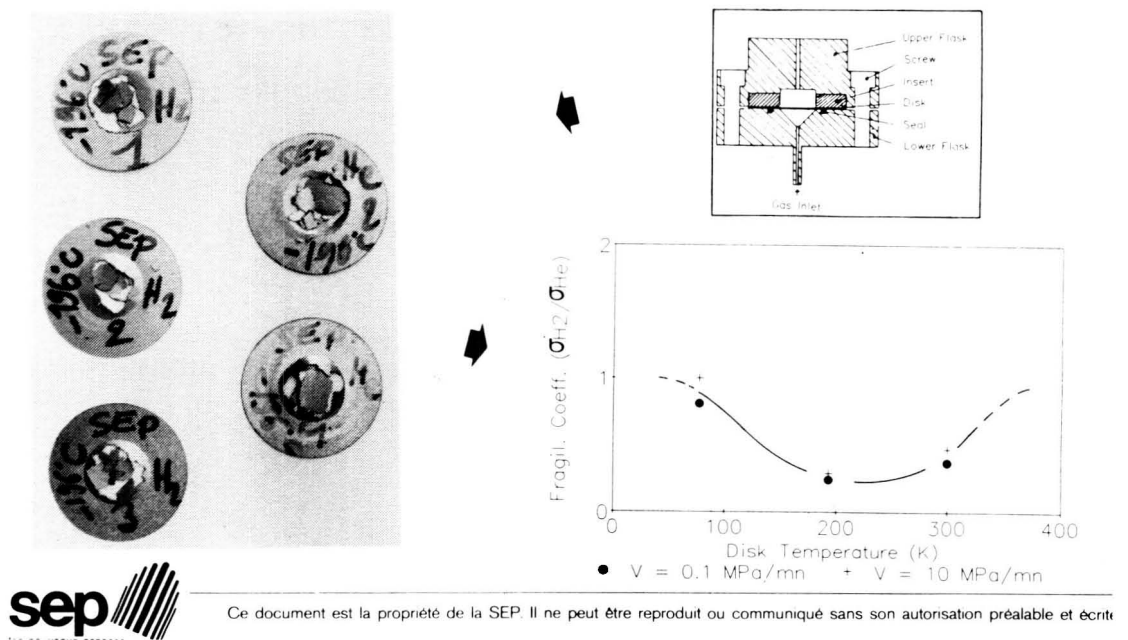


Figure 5 : Disc burst test for GH2 brittleness study

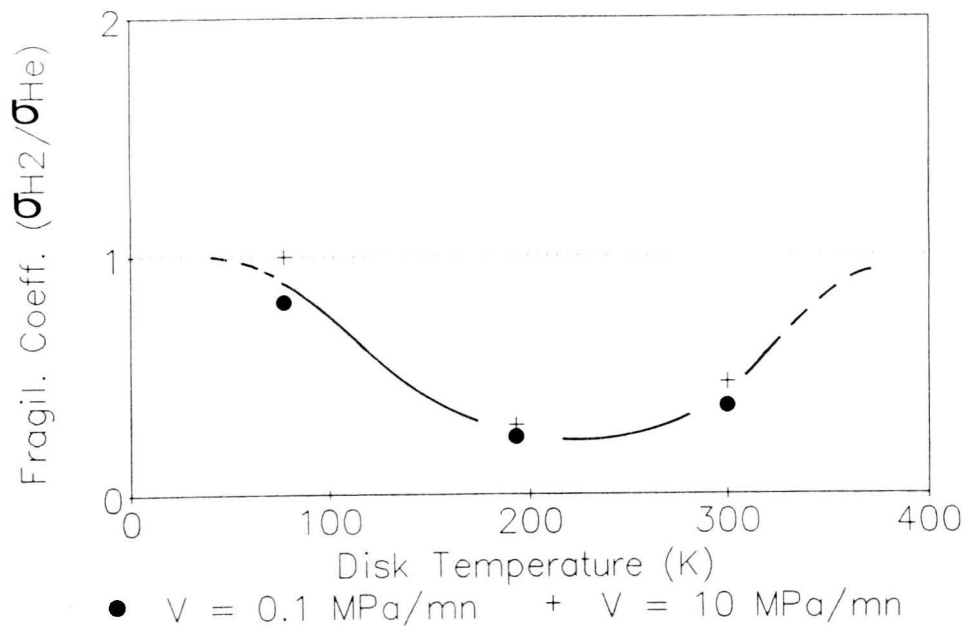


Figure 6 : Results of GH2 brittleness studies on Fe-Si laminations

more than 900 MPa for the yield stress in cryogenic conditions, together with high flux density (up to 2 Tesla). Hysteresis losses are higher than iron/silicon alloys at low frequencies and/or low magnetic field, but similar for higher values.

This alloy can then reduce by 30 % to 50 % the bearing length, or increase in the same proportions the load capacity, providing the AMB with a higher load factor (up to 190 N/cm²).

Regarding coil wire materials and insulations, tests performed with copper and copper-beryllium alloys, as well as fluorine polymers, has allowed final material selection, wire diameters decrease with thin insulation (less than 50 μ m) and production optimisation.

Controller

A significant step toward a flightweight controller (including power amplifiers and control PC boards) has been made by producing a space-rated power amplifier, whose electrical characteristics meet Upper Stage Engine LH2 Turbopump requirements.

This program has been focused on the power amplifier size reduction, due to the fact that they represent about 80 % of the controller size and weight, and almost 100 % of the power consumption of the board. Accordingly, joint effort between S2M, subsidiary of SEP and SEP personnel involved in space mechanism electronics has been funded to design, fabricate and test space-rated Pulse Width Modulation (PWM) power amplifiers. Trade-off studies have shown a significant gain in slightly decreasing the output voltage (from 120V to 100V) and increasing the current (from 6A to 7A) in order to meet component rating for space qualification. On the other side, design of PC board including two power amplifiers on the same card has been preferred for size reduction, thermal control and EMI requirements.

This concept is illustrated figure 7, with controller characteristics reported table 3.

Those power amplifiers can be driven by analogic or digital control PC boards, the latter solution being preferred for easier T/P development and integration of health and control monitoring (including Expert System). The former solution offers cheaper development and production costs, as well as full availability of space qualified components.

This prototype has highlighted the high recurrent costs resulting for the electronics, mainly due to the space-rated components and necessary quality management, with an order of magnitude of 100 k \$/kg.

This result is similar to existing electronics onboard rocket engines (e.g. the SSME flight controller), but progress in this field indicates that decrease by a factor of 10, consistent with reliability and life specifications, could be achieved (e.g. keeping the existing MTBF of 10.000 hours for life requirements limited to launch and transfer missions, and increasing up to 40.000 hours for long duration propelled mission).

TABLE 3 : 700 W AMB controller characteristics

| Industrial 120 V / 6A | | Space-rated 100 V / 7A | |
|--------------------------|----|---------------------------|--------|
| Volume (l) | 78 | 15 (+) | 10 (*) |
| Mass (kg) | 35 | 9 (+) | 6 (*) |
| Power cons. (W) | - | 30 | - |

+ current
* project

ORIGINAL PAGE
BLACK AND WHITE PHOTOGRAPH

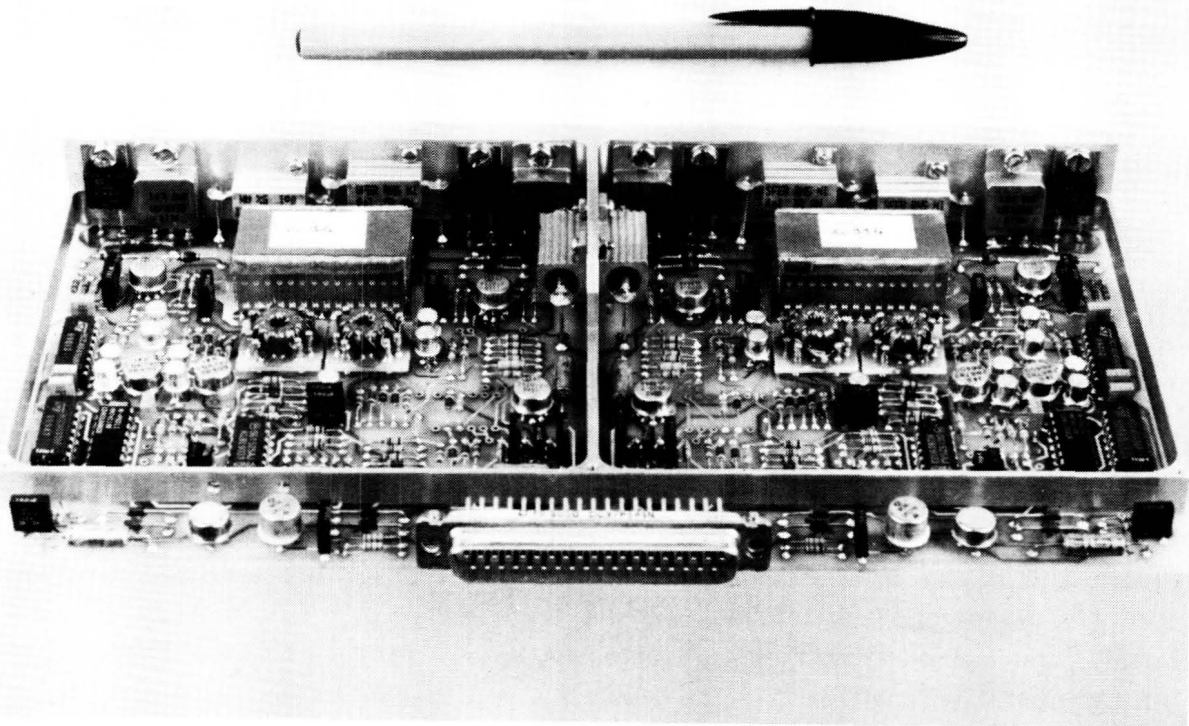


Figure 7. PC Board Prototype for Space-rated Power Amplifiers

A TYPICAL EXAMPLE

To further illustrate the magnetic bearing abilities, detailed design and studies of a demonstrative turbopump has been performed.

This machine (in battleship configuration) is illustrated, figure 8, showing a concept similar to LH2 T/P for Upper Stage Engine with two radial AMB. A retractable ball bearing is used to absorb axial loads during the transients.

Detailed rotordynamic analyses have been done during the design stage, both to optimise the design as explained previously, and to check consistency of the bearing specifications and machine behaviour.

During the iterative design process, modifications have been applied to bearing dimensions, as well as to the bearing impedances (modulus and phase), as reported, fig. 9. Explanations of the method and analysis tool can be found in ref. 10.

The nominal point has been placed slightly before the seventh mode (2nd shaft bending mode) at a speed of 200,000 rpm. Associated critical speed map and damping coefficient evolutions are reported figures 10 and 11. Reliability improvement is illustrated by the figure 12, where the bearing failure mode allocation becomes negligible compared to other potential failure sources (not improved here).

Different control modes have been simulated (axis by axis or plane by plane) as well as special features, such as notch filters or Automatic Balancing Control (ABC). Effect of such a feature is illustrated figure 13, showing drastic decrease in bearing synchronous load.

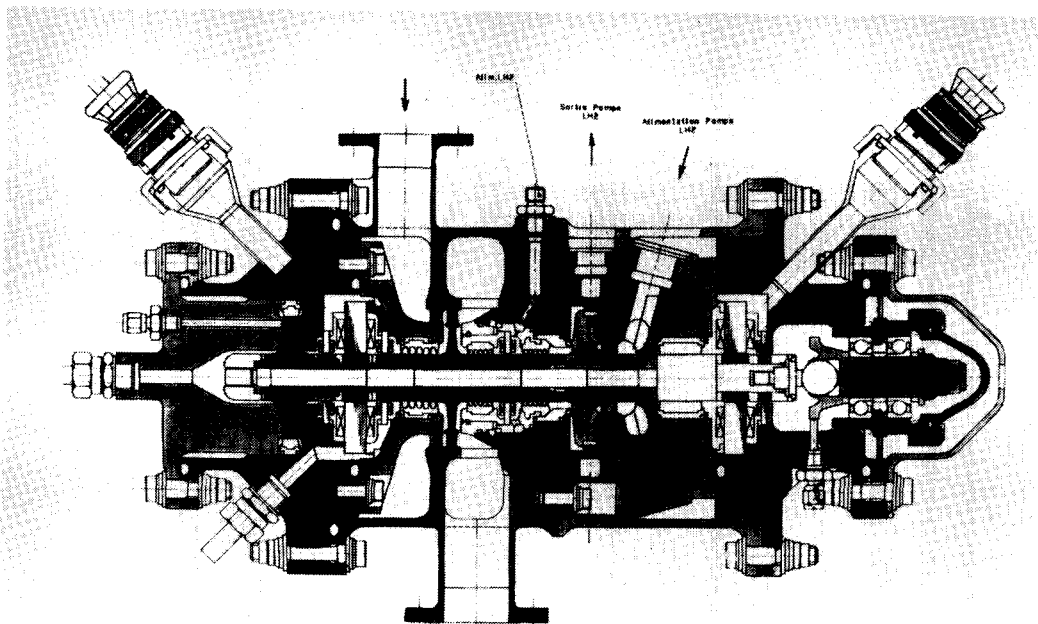


Figure 8. Turbomachine Design for AMB Qualification

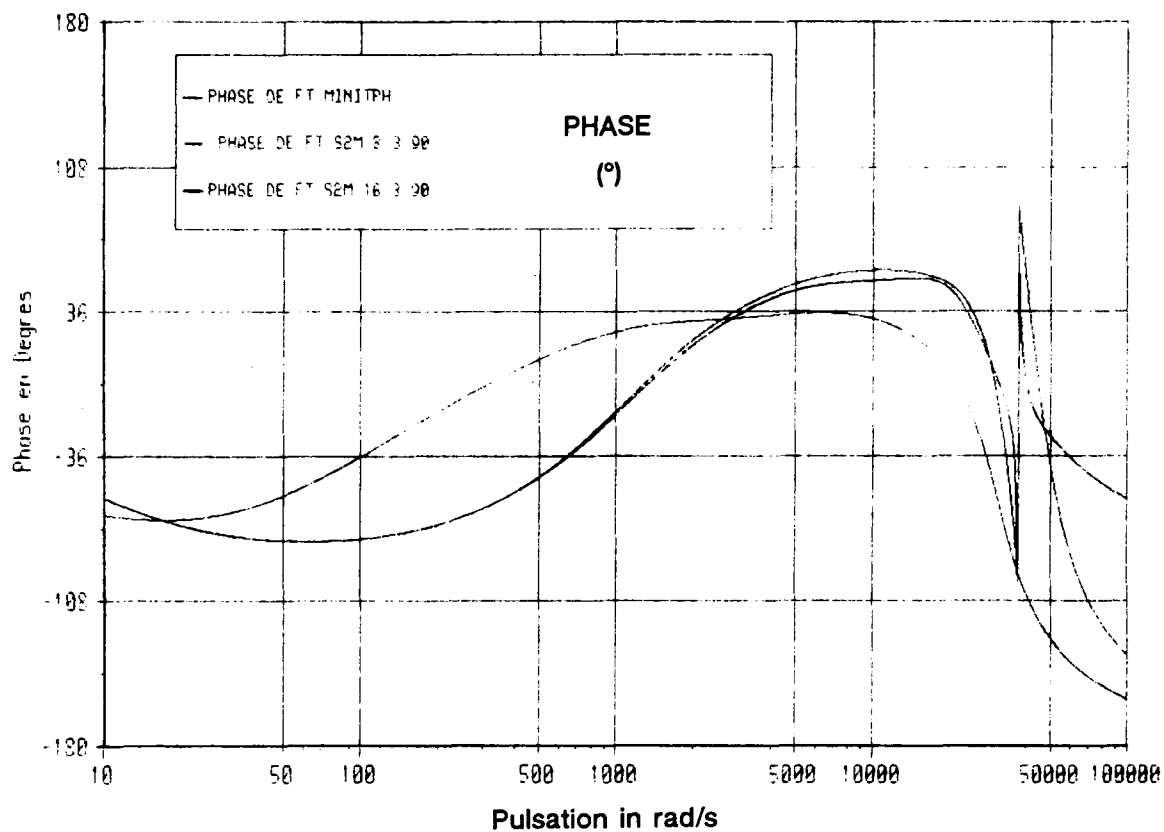
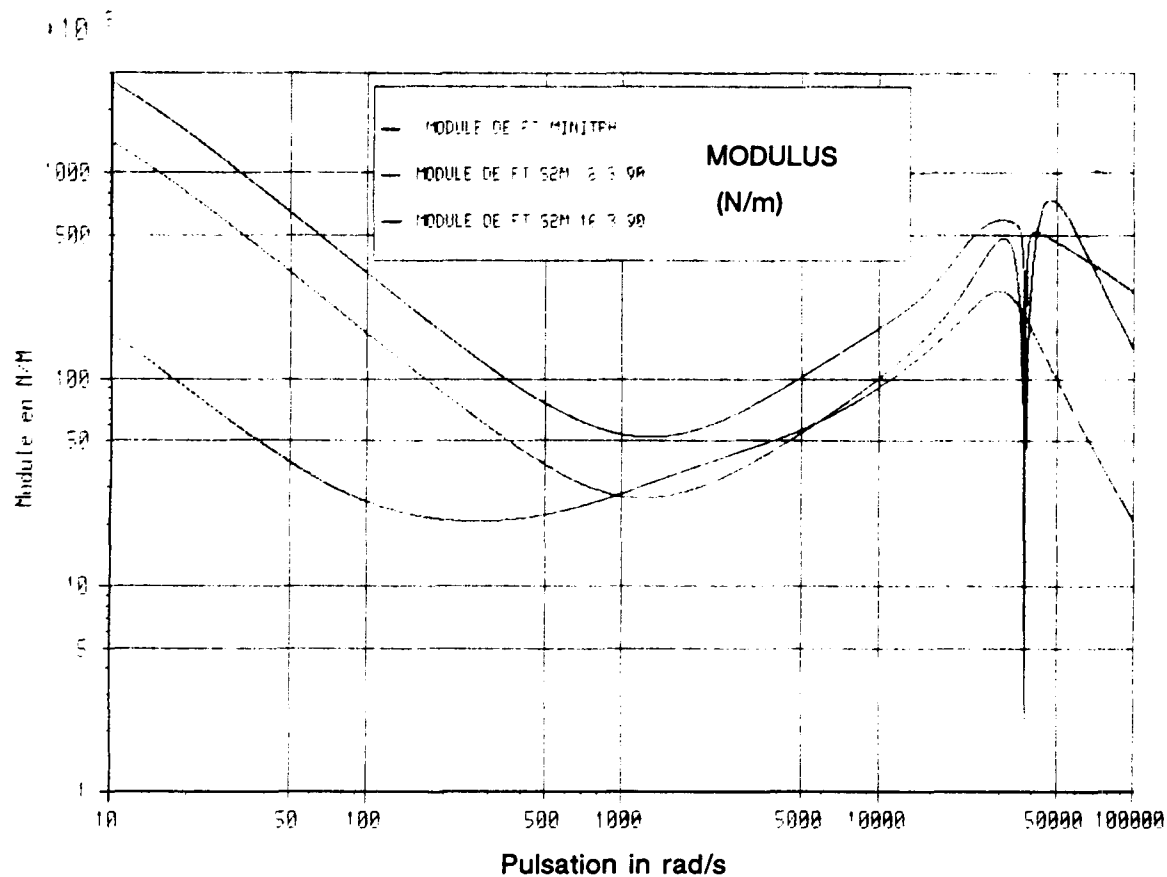


Figure 9. AMB Transfer Function

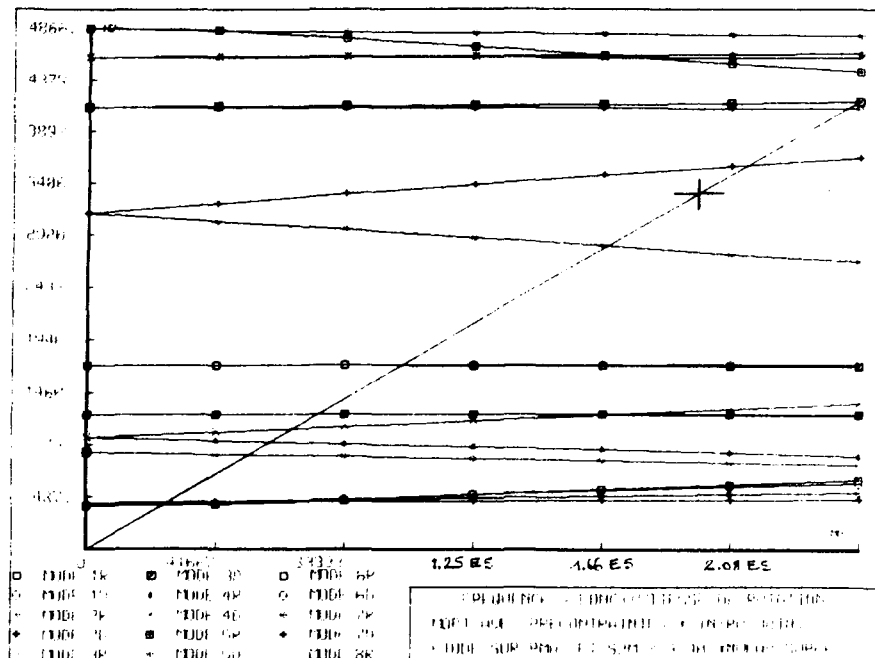


Figure 10. Critical Speed Map

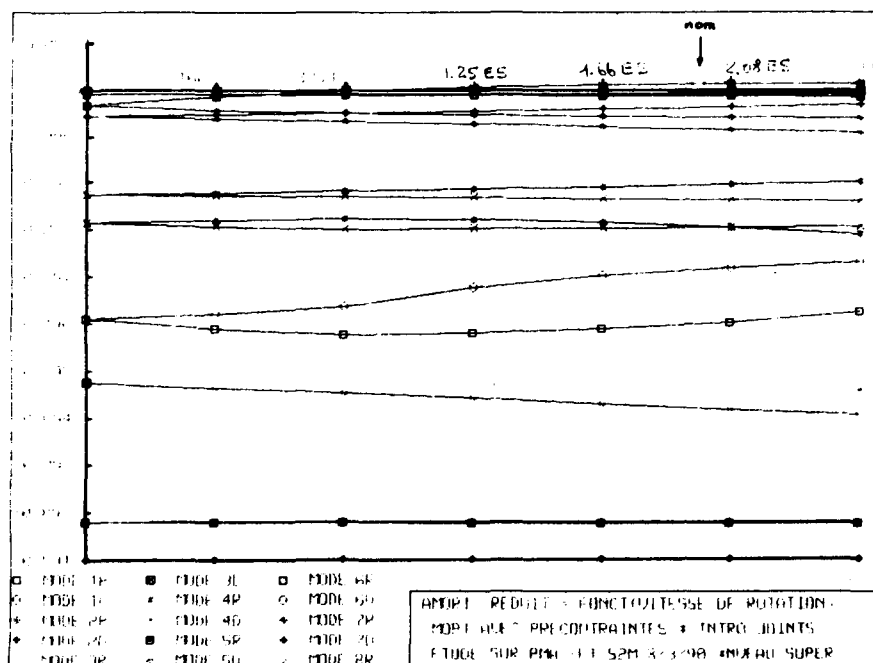


Figure 11. Damping Coefficients vs Rotational Speed

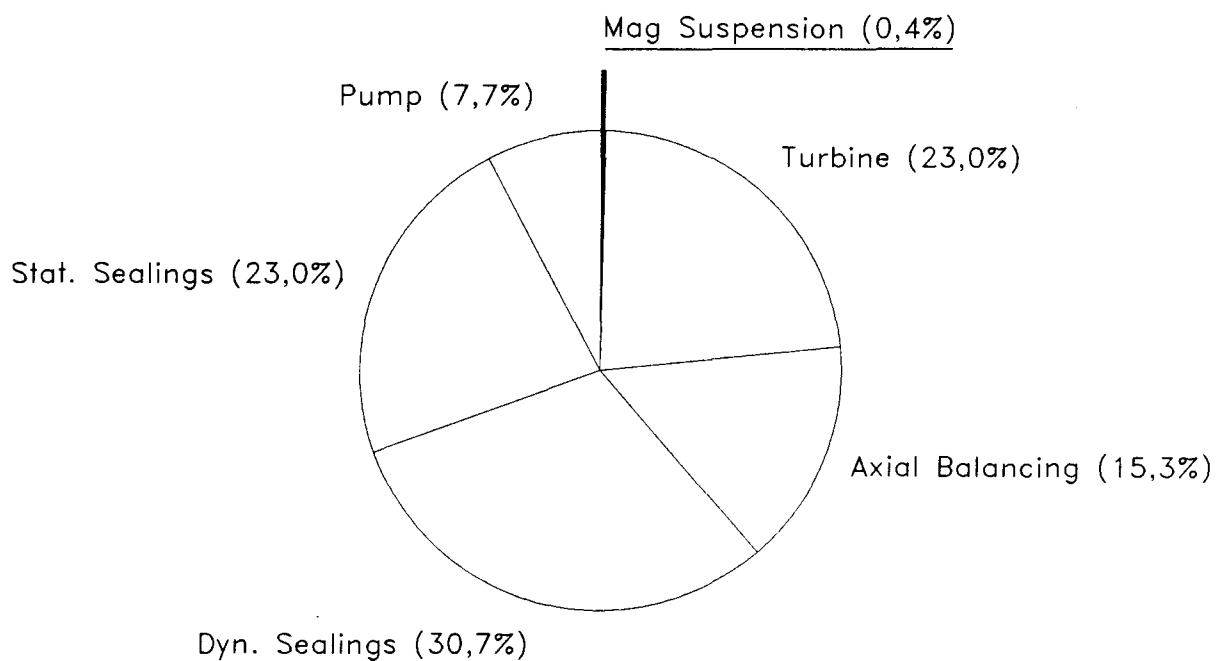


Figure 12. Typical Failure Mode Allocations with AMB
(for a duty cycle of 600 s)

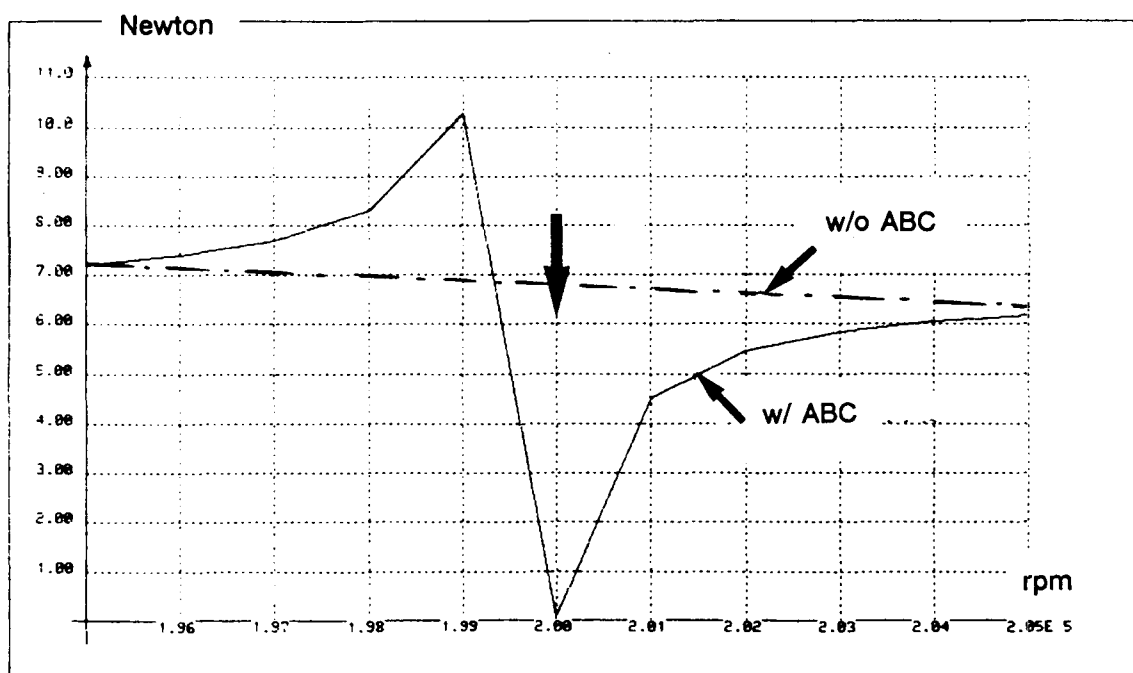


Figure 13. Effect of Automatic Balancing Control on
the Bearing Dynamic Load

CONCLUSIONS

Advanced Turbopump (T/P) Designs implementing Active Magnetic Bearings (AMB) have been presented in this paper, together with associated technological basis and rotordynamic analysis. Objectives of such integration have been emphasized, as well as the availability of the required hardware and sophisticated numerical tools.

As a result, it is clear that AMB Technology offers important improvements in turbomachine performances, life and reliability. This is particularly true for Liquid Hydrogen T/P, where the low fluid density does not limit the AMB capabilities.

Integrated Health Monitoring and throttleability are offered, as well as long-term and/or repetitive space storage or propulsion.

The production cost, estimated according to fabrication of space-rated power amplifiers, appears high today. Nevertheless, this feature can be favourably balanced in space or flight applications, especially with the expected evolutions in electronic components and avionics.

References :

- [1] J.M. Reddecliff, J.H. Vohr, *Hydrostatic Bearing for Cryogenic Rocket Engine Turbopumps*, Pratt & Whitney A., Journal of Lubrication Technology, July 1969, pp. 557-575
- [2] C.E. Nielson, *Hybrid Hydrostatic/Ball Bearings in High-Speed Turbomachinery*, Rocketdyne Division, NASA-CR-168124, January 1983
- [3] P.S. Buckmann, N.R. Shimp, and F. Viteri, M. Proctor, *Design and Test of an Oxygen Turbopump For a Dual Expander Cycle Rocket Engine*, Aerojet TechSystems & NASA Lewis R.C., AIAA Paper 89-2305, July 1989
- [4] R.L. McMillion, T.J. Treinen, S.L. Stohler, *Component Evaluations for the XLR-132 Advanced Storable Spacecraft Engine*, Rocketdyne Division, AIAA Paper 85-1228, July 1985
- [5] A. Nakajima, *Research and Development of Magnetic Bearing Flywheels for Attitude Control of Spacecraft*, Japanese National Aerospace Laboratory, Proceedings of the 1st International Symposium on Magnetic Bearings, Zürich, June 1988, pp.3-12
- [6] J.P. Roland, *Magnetic Bearing Wheels for Very High Pointing Accuracy Satellite Missions*, Aérospatiale, Proceedings of the Int. Symposium on Magnetic Suspension Technology, NASA Langley R.C., August 1991

- [7] J.P. Girault, *Implementation of Active Magnetic Bearings in Advanced Rocket Engine Turbopumps*, Société Européenne de Propulsion, Proceedings of the 1st International Symposium on Magnetic Bearings, Zürich, June 1988, pp.199-210
- [8] D. Hibner and L. Rosado, *Feasibility of Magnetic Bearings for Advanced Gas Turbine Engines*, Pratt & Whitney and Wright laboratory, Proceedings of the Int. Symposium on Magnetic Suspension Technology, NASA Langley R.C., August 1991
- [9] J.P. Girault and K.W. Lang, *Long Life and Reliability : Expectations for Advanced Turbomachinery in Space*, Société Européenne de Propulsion and Rocketdyne Division, AIAA Paper 91-2416, 27th Joint Propulsion Conference, Sacramento, June 1991
- [10] C. Brune, *Rotordynamics and Active Magnetic Bearings*, Société Européenne de Propulsion, 8th annual ROMAC Industrial Research Conference, June 1988

ACTIVE MAGNETIC BEARINGS - AS APPLIED TO CENTRIFUGAL PUMPS

Lev Nelik
Paul Cooper
Ingersoll-Rand Company (IR)

Graham Jones
Gas-Cooled Reactor Associates (GCRA)

Dennis Galecki, Frank Pinckney
Magnetic Bearings, Inc. (MBI)

Gordon Kirk
Virginia Polytechnic Institute & State University (VPI&SU)

ABSTRACT

Application of magnetic bearings to boiler feed pumps presents various attractive features, such as longer bearing life, lower maintenance costs, and improved operability through control of the rotordynamics.

Magnetic bearings have been fitted to an eight-stage, 600 hp boiler feed pump, which generates 2600 ft of head at 680 gpm and 3560 rpm. In addition to the varied and severe operating environment in steady state operation of this pump in a power plant, it is also subjected to transient loads during frequent starts and stops. These loads can now be measured by the in-built instrumentation of the magnetic bearings. The pump was factory tested, including the adjustment (tuning) of magnetic bearings. Following site installation, a follow-up bearing tune-up was performed, and pump transient response testing was conducted. The bearing response was completely satisfactory, ensuring trouble-free pump operation even in the range of reduced load. The experience gained so far through design and testing proves feasibility of magnetic bearings for boiler feed pumps, which sets the stage for application of even higher energy centrifugal pumps equipped with magnetic bearings.

INTRODUCTION

Utilization of magnetic bearings in pumps is a natural development considering the successes of these bearings in large (35,000 Hp) centrifugal compressors. Some notable capabilities of magnetic bearings, namely (1),

- o Theoretically infinite bearing life potential,
- o Control of rotordynamical behavior,
- o Rapid response to load variations so as to maintain shaft position,
- o Elimination of oil system,
- o Measurement of bearing static and dynamic loads as a diagnostic monitoring tool

are becoming more sought after for various types of heavy machinery. In particular, for pumps of significant power levels, the elimination of lubrication systems that would otherwise be needed for conventional bearings and the attendant reduction of maintenance are benefits that arise from claiming these capabilities.

It is the purpose of this paper to show how these benefits of magnetic bearings were obtained for a 600 HP boiler feed pump. Such pumps often operate with close internal clearances and flexible shafts, and the ability to adjust the stiffness and damping of magnetic bearings can improve rotordynamics. Increased availability and reduction in operating and maintenance costs were projected, leading to a favorable evaluation (2).

The design of a multistage boiler feed pump allows sufficient clearance for shaft flexure and thermal distortion and minimizes clearances to increase the efficiency of the impeller rings and the shaft sealing system.

Ideally the bearings would be mounted closer together than current practice dictates, allowing a smaller tolerance on shaft movement. If submerged magnetic bearings were used, this could be accomplished by eliminating the outboard (nondrive end) seal and putting the inboard bearing between the first-stage impeller and the inboard seals. The shaft could be held within 0.003 in (0.076 mm) at all times by the magnetic bearings (3).

There are phenomena unique to pumps that could affect magnetic bearing performance. These include stall effects caused by nonuniform flow interruptions or reversals that occur in a pump impeller and diffuser when operating at reduced flow rates (4,5). These effects introduce unsteady, random, radial and axial loads that are often accompanied and exacerbated by cavitating flow; wear of the impeller neck rings (or adjacent casing rings) which leads to loss of stabilization and, therefore, to adverse changes in rotordynamical behavior. The above phenomena and the corresponding mechanical responses become more evident and critical in pumps of high energy level; i.e., those of more concentrated and higher power. It was therefore important to gain further insight into magnetic bearing behavior in such pumps in general, to assess their ability to handle these otherwise detrimental situations, and to measure the actual instantaneous loads that might be encountered.

Since the current in a magnetic bearing is related to the load, readings of current vs time, speed and pump flow rate provided the needed insight into the stall effects. Scaling of the loads involved is fairly reliable and enables one to make a more informed estimate of the loads for a still-higher-power submerged-magnetic-bearing (canned) pump. Also, the ability of the magnetic bearings to cope with the rotordynamic uncertainties mentioned above has been revealed and could be analyzed for the future submerged-bearing application.

MAGNETIC BEARINGS

Figure 1 shows both active magnetic bearing assemblies and their relation to the boiler feed pump. The magnetic bearings for the boiler feed pump require a radial load capacity of 280 lbs (127 kg) steady state and an additional 280 lbs (127 kg) for transient conditions. For the magnetic thrust bearings, the required load capacities are 1000 lbs (454 kg) steady state and an additional 1000 lbs (454 kg) for transient conditions. In the design of active magnetic bearing systems, it is prudent to include load capacity margins to accommodate process-induced surge loads, abnormal imbalance or hydrodynamic loads.

Through the use of standardized magnetic bearing designs, which provided further margins over conventional practice, the resulting magnetic radial bearings provide a maximum steady state load capacity of 800 lbs (364 kg) and will modulate a force of 400 lbs (181 kg) at a frequency of 60 Hz (boiler feed pump running speed). The magnetic thrust bearing provides a maximum steady state load capacity of 4000 lbs (1814 kg) and will modulate a force of 1000 lbs (454 kg) at a frequency of 60 Hz.

The magnetic bearing assembly for the nondrive end of the boiler feed pump is shown on Figure 2. The completed stator assembly consists of two magnetic thrust bearing stators and an axial position sensor, a magnetic radial bearing stator (consisting of four electromagnets) and radial position sensor, a speed pick-up, and an auxiliary (emergency back-up) bearing. Additionally, the bearing windings are equipped with resistive temperature devices (RTDs) which can be used to monitor operating temperatures. The entire assembly provides the radial/thrust forces for the nondrive end of the pump. The drive end radial bearing is similar to that of the non-drive end.

The radial forces are transferred from the bearing assembly to the shaft via two 2.5 in (63.5 mm) by 6 in. (152.4 mm) diameter laminated silicon-steel rotors fitted as sleeves at each end of the shaft. The thrust forces are transmitted to the shaft through an interference-fitted 1 in (25.4 mm) by 11.25 in (285.8 mm) diameter disc. The shaft position is controlled by the magnetic bearing system which uses two inductive radial position sensors and one inductive axial position sensor. The radial position sensors (referred to as collocated sensors) are adjacent to the radial bearing lamination stacks and the axial position sensor is at the end of the machine. The radial sensors are designed to minimize rotor runout or other imperfections that would cause position sensor signal noise.

The control cabinet is self-contained with power conversion, signal processing, operation logic and alarm/trip monitoring of critical functions necessary for the active magnetic system. The air-cooled cabinet measures 52 in. (1321 mm) high, 21 in (533 mm) wide, and 20 in 508 mm) deep. The cabinet power supply requires 208 VAC, 3 phase (1.4 KVA) as input and is equipped with a battery backup which will power the system for ten minutes.

After ten minutes, the system will maintain operation, but the bearing load capacity may be diminished. The magnetic radial bearings are powered with eight 120V/15A power amplifiers and the magnetic thrust bearing is powered with two 120V/30A power amplifiers. Should the power to the magnetic bearings be lost, the reserve power is provided by the battery backup system. The auxiliary bearing at the nondrive end of the machine is a duplexed pair of angular-contact ball bearings. The bearing provides radial and axial load capability if the pump were required to coast to a stop because of a loss of both primary and backup power to the magnetic bearings. The auxiliary bearing at the drive end of the machine is a Conrad-type single radial bearing. The magnetic air gap for the radial bearings is 0.020 in (0.51mm), and the thrust bearing magnetic air gap is 0.028 in (0.71 mm). The auxiliary bearings are designed to prevent the shaft from moving past half the magnetic air gap clearance, hence the auxiliary bearing air gap for the radial and axial bearings is 0.010 in (0.25 mm) and 0.014 (0.36 mm) respectively.

With the use of auxiliary bearings, protection is assured against sustained loss of magnetic levitation as well as against any upset condition that might occur as a consequence of pump operation in the power plant environment. In addition, rotor bushings and impeller rings provide additional rotor damping, and further enhance the overall system reliability.

ROTOR DYNAMICS

The pump response to unbalance excitation was investigated using the recently developed AMB forced response computer program (6). This new computer code can include the influence of sensor axial location in addition to impeller and seal ring cross-coupling and direct stiffness and damping. The response of the pump rotor for a 0.5 oz-in unbalance placed at midspan is given in Table 1 for normal design conditions considering both dry and wet conditions. This level of unbalance corresponds to the API 4W/N balance specification. The results for dry running conditions indicate little influence of sensor position when operating at or near design speed. A greater influence of sensor position is indicated when operation is near the critical speed. The largest midspan response is for outboard sensor, smallest for inboard sensor. The predicted vibration levels at design speed are insensitive to sensor position for the normal wet conditions. The midspan response is indicated to be approximately 3-4 times the sensor location vibration. The forced response analysis predicts that the pump rotor could withstand just over 150 times this unbalance force and still have a response amplitude of less than 1.2 mil at the sensors and only 3.3 mils at midspan. For reference, the 0.5 oz-in unbalance corresponds to a force of 11.5 lbf for a rotor speed of 3560 rpm.

The dry first critical speed was predicted to be 1605 rpm, with the second critical at a speed of 5798 rpm. When the wet condition is considered, the forced response versus speed indicates that the first critical speed (5900) is critically damped as shown in Figure (3).

The stability of the pump was calculated considering various conditions of pre-swirl at the entrance to the front rings, center and outer bushings. A summary of the results are given in Table 2. For a zero preswirl, the pump 1st critical speed was predicted to be stable with a log decrement of 9.13. For 50% preswirl, the rotor first critical was also predicted to be stable with a log decrement of 15.5. If the impeller coefficients are not considered the 50% preswirl case log decrement reduces to 14.2. Actual test stand operation gave no indication of instability. The calculation of the actual seal inlet pre-swirl and the eccentric dynamic seal coefficients is not a proven capability for actual pump operating conditions. The results for this pump are not very sensitive to this influence.

The conclusions of the rotor dynamics analysis indicate that the pump design is acceptable for forced response excitation. The pump design, as built, can resist strong unbalance caused by hydraulic excitation forces which is much more important in pump design than the possibility of small self-excited vibration. The pump is predicted to have very good stability margins and may only respond to non-synchronous hydraulic excitation during off-design operation. The pump will not experience self-excited subsynchronous vibration during operation.

FACTORY AND ON-SITE TESTING

Prior to factory testing, the magnetic bearing controls had to be tuned to the characteristics of the shaft, with the pump in the wet condition. This took significantly less time than had been experienced on other projects, and was completed in under a week, by a team of two.

The factory tests, with the exception of an unplanned shutdown onto the battery backup as a result of a thunderstorm, were uneventful. It was noticed, however, that one of the motor-end journal bearing poles was showing a fairly high load. This was attributed to misalignment due to the temporary nature of the baseplate alignment for the test, and it was agreed to monitor this further on-site.

Figure 4 shows the pump installed in the power plant. The site start-up was uneventful, with the exception that the high bearing load noted above reappeared on the same motor-end bearing, but on a different pole. This seemed to confirm that it was an alignment load. By adjusting the coupling to be a little more flexible, the load was significantly reduced.

High loads were noted during the run up to full speed which took only about 2 seconds. These levels needed to be understood better, and a second retuning with test was performed, monitoring bearing loads over all representative running conditions. This second tuning took place 4 months later together with testing of the pump through start-up, shutdown and part load operations. During this testing, no indications of hydraulic and/or rotordynamic instability were observed. Bearing currents and shaft displacements were stored on a high speed "Adre" recorder for detailed analysis. The key results of this operation were that after some tuning adjustments, the pump rotor was held both axially and radially within about 1 mil during all transient and steady state operations.

Figures 5 (before tuning) and 6 (after tuning) show two traces of the shaft radial displacement as a function of time during the run up to full speed. Figure 5 shows displacements of the order of 5 mil, where the bearing did not fully control the shaft displacement. Figure 6 shows that the shaft is held geometrically to within 1 mil during the whole transient. Provided that the operating transients are all covered in the specification, this approach should ensure satisfactory lifetime operation.

Conventional bearings can often absorb higher than design loads, accompanied with increased wear rate, but not necessary leading to immediate failure. However, a magnetic bearing that reaches its design point where the electromagnet is saturated, will not resist any additional load and the shaft will make contact with whatever backup bearing device is provided. Any additional load will now be transferred to this auxiliary support system, and the shaft will be about 10 mil out of alignment on one or more axes.

For the reasons stated above it is absolutely essential for any prototype equipment running on magnetic bearings that this procedure of running the machine through all its operation transients and documenting the shaft response is carried out before putting the equipment into service.

Checking of the power consumption of the magnetic bearing feed pump against a conventional bearing machine purchased at the same time, and with the same rotor design showed a slight reduction in power consumption for the same feedwater flow. This was fairly consistent over a long time period.

Operator Acceptance - After an initial period of enthusiastic but cautious use of the pump, the operators' confidence has increased to the point where it is being operated as confidently as any other similar equipment.

Availability Experience - From studies referenced above, expectations for availability have been developed. To date, there have been no events on site that would indicate that these targets cannot be met even with the prototype unit. However, a longer time frame of several years will be needed to fully justify such high availability claims.

CONCLUSIONS

Boiler feed pumps in an electric utility may benefit from the expected life and low maintenance advantages of magnetic bearings. These pumps can provide a comprehensive platform for evaluating the feasibility of magnet bearing technology under a variety of severe operating conditions that can impose strong and random loads on the rotating elements.

Successful in-plant and on-site demonstrations of a 600 hp, magnetic-bearing-equipped, eight-stage volute-type boiler feed pump were conducted. No effects on pump operation were experienced that could be attributed to hydraulic and/or rotordynamic instability. From the standpoint of the user, experience gained so far has demonstrated that a pump equipped with magnetic bearings can be characterized as follows:

1. The bearings operate satisfactorily.
2. Equipment is reliable.
3. The pump is operable.
4. Provides new data, not available in the past: bearing loads and positions.
5. Requires less attention.
6. Requires less maintenance.

By monitoring the operation of the 600 hp pump, which has the magnetic bearings mounted external to the pump casing and running in air, it should be possible to gain the rotordynamical insights needed to design improved, higher-power machines with these bearings submerged in fluid within the interior of the casing. An order of magnitude more power, e.g. 10,000 hp, should be the next step.

A one-year test, monitoring and benefits evaluation program on two side-by-side new pumps - one with magnetic bearings; the other, with conventional bearings - is continuing through the remainder of 1991. To date the pump is fulfilling all the expectations that accompanied the initiation of the project, and provides a sound basis for future developments.

Specifically, we expect to develop availability estimates, spares requirements, running costs, and design specification requirements for future utility applications. We expect to have all but the availability estimates completed at the end of the first year of operation, that is by November 1991. The availability data will need to be acquired over several years of operation to be statistically significant, and until we have that data the experience in other industries is the only yardstick that we have. But that experience appears to be very encouraging and could provide an alternate technology to the utility industry resulting in lower forced outages, higher availability and more efficient operations.

REFERENCES

1. Hendrickson, T.A.; Leonard, J.S.; and Weise, D.A.: "Application of Magnetic Bearing Technology to Vibration Free Rotating Machinery." Naval Engineers Journal, May 1987, pp. 107-111.
2. Olson, E.A.J.; et al: "Applications for Magnetic Bearings on Electrical Generating Plant Equipment." Final report on EPRI Research Project 2079-22, prepared for EPRI, ESEERCO, GCRA and Public Service of Colorado by the S.M. Stoller Corp. and Novacorp International Consulting Ltd., EPRI Report RP 2079-21 & -22, December 1988.
3. Baxter, B.Z.; Burger, J.M.; and Jones, G.: "Magnetic Bearing Development for the Utility Industry." Proceedings of the American Power Conference, April 1990.
4. Cooper, P.; Wotring, T.L.; Makay, E.; and Corsi, L.: "Minimum Continuous Stable Flow in Feed Pumps." Symposium Proceedings: Power Plant Pumps, EPRI CS-5857, June 1988, pp. 2-97 to 2-132.
5. Cooper, P.: "Hydraulics and Cavitation." Symposium Proceedings: Power Plant Pumps, EPRI CS-5857, June 1988, pp. 4-109 to 4-149
6. Rawal, D., J. Keesee, and R. G. Kirk, "Critical Speed and Forced Response Solution for Active Magnetic Bearing Turbomachinery", Part 1 and 11, NASA Workshop on Aerospace Applications of Magnetic Suspension Technology, Langley Research Center, September 25-27, 1990.

TABLE 1 RESPONSE TO 0.5 oz-in at MIDSPAN (at design speed of 3560 RPM)

| <u>Condition</u> | <u>Thrust end</u> (mil-pp) | <u>Midspan</u> (mil-pp) | <u>Coupling End</u> (mil-pp) |
|---|-------------------------------|----------------------------|---------------------------------|
| a. <u>dry</u> | | | |
| collocated sensor | .010 | .384 (21.0 at N-cr) | .056 |
| outboard sensor | .062 | .380 (42.0 at N-cr) | .056 |
| inboard sensor | .064 | .392 (14.4 at N-cr) | .038 |
| b. <u>wet</u> (c = 0.010 in.- wear rings and bushings) | | | |
| collocated sensor | .006 | .022 | .008 |
| outboard sensor | .006 | .022 | .008 |

TABLE 2 STABILITY RESULTS SUMMARY for PUMP ROTOR DAMPED CRITICAL SPEEDS

| <u>Condition</u> | <u>real part</u> (sec ⁻¹) | <u>Eigenvalue</u> <u>damped critical</u> (cpm) | <u>log decrement</u> |
|---|--|--|----------------------|
| a. <u>dry</u> | | | |
| No influence of liquid seals | -0.76 -145. -19.5 | 1830 3807 6462 | 0.03 1.49 0.18 |
| b. <u>wet</u> (zero preswirl) | -323.5 -118.7 -198.7 | 2126 5549 6276 | 9.13 1.28 1.89 |
| c. <u>wet</u> (50% preswirl) | -349.1 -118.2 -197.2 | 1350 5552 6256 | 15.5 1.28 1.89 |
| d. <u>wet</u> (50% preswirl, no impeller characteristics) | -677.3 -120.2 -197.3 | 2882 5541 6323 | 14.2 1.30 1.88 |

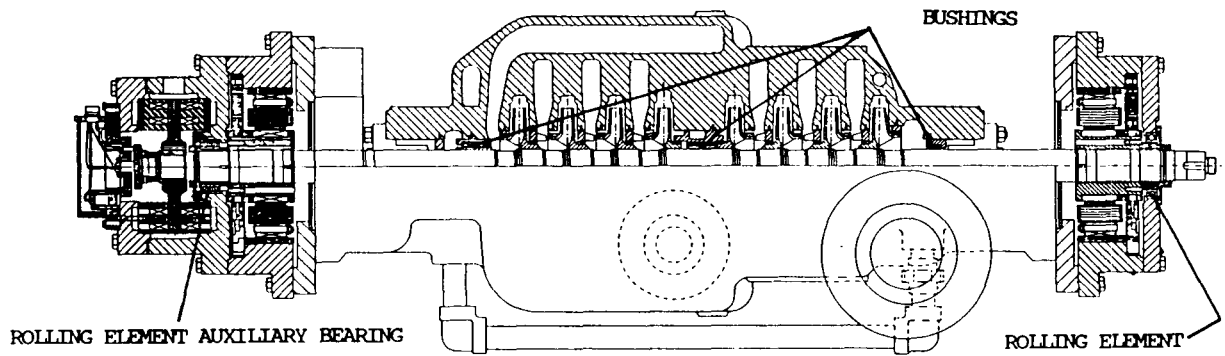


FIGURE 1 MULTISTAGE VOLUTE PUMP FITTED WITH MAGNETIC BEARINGS. I-R PUMP MODEL 4X10DA-8 WITH RADIAL BEARING ON DRIVE END AND RADIAL AND AXIAL BEARINGS ON NONDRIVE END.

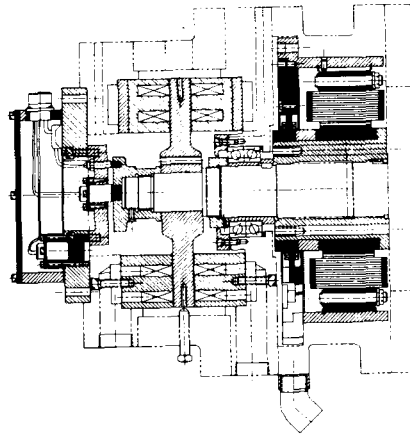


FIGURE 2 RADIAL AND AXIAL MAGNETIC BEARING ON NONDRIVE END OF PUMP.

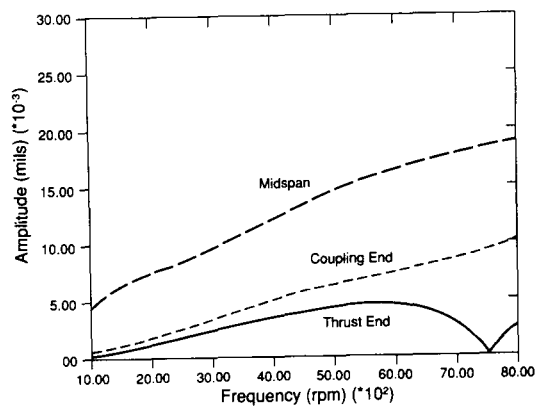


FIGURE 3 RESPONSE FOR 0.5 OZ-IN AT MIDSPAN INCLUDING WEAR RINGS, BUSHINGS, AND NON-COLLOCATED AMB SENSORS.

ORIGINAL PAGE
BLACK AND WHITE PHOTOGRAPH

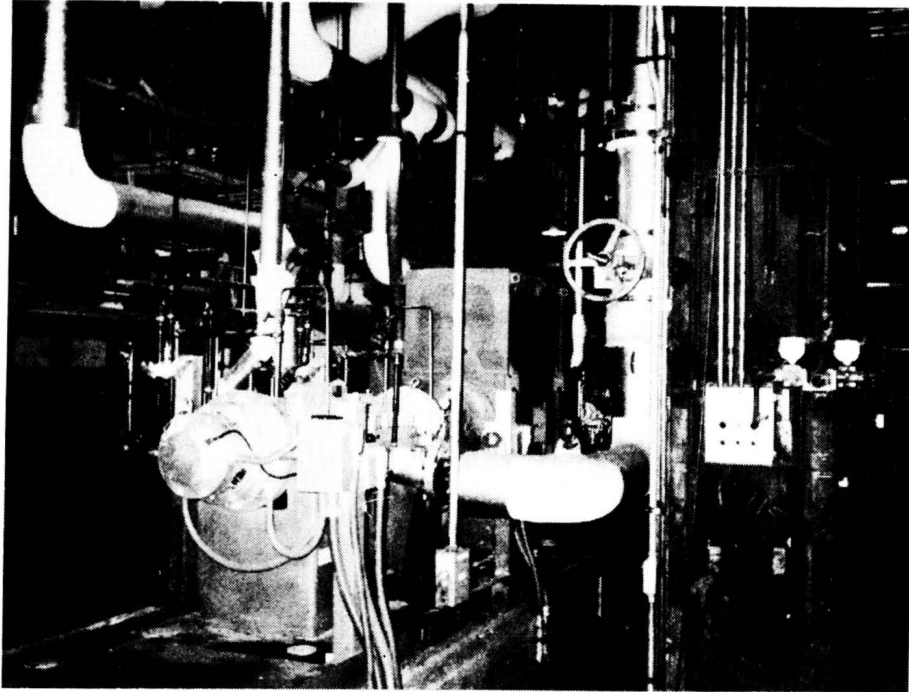


FIGURE 4 MULTI-STAGE BOILER FEED PUMP WITH MAGNETIC BEARINGS INSTALLED AT NEW YORK STATE ELECTRIC AND GAS POWER PLANT

Unacceptable Transient Bearing Response

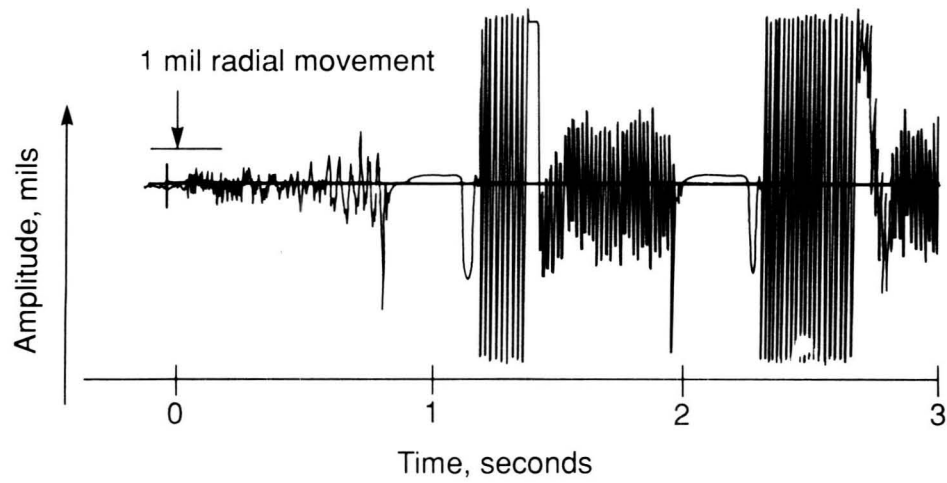


FIGURE 5 UNACCEPTABLE TRANSIENT BEARING RESPONSE

Acceptable Transient Bearing Response

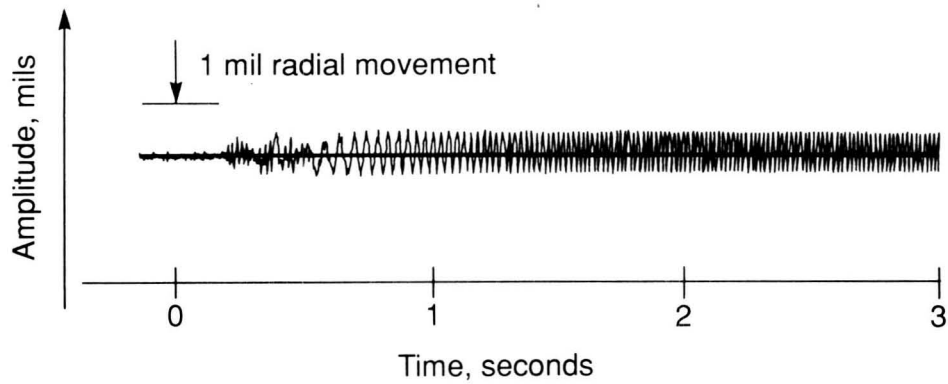


FIGURE 6 ACCEPTABLE TRANSIENT BEARING RESPONSE

N 9 2 - 2 7 7 2 7

Precision Magnetic Suspension Linear Bearing

**David L. Trumper, Michael A. Queen
Dept. of Electrical Engineering
Univ. of N. Carolina at Charlotte
Charlotte, NC 28223**

1 Introduction

Magnetic bearings represent a promising approach for achieving positioning with nanometer resolution. The first author has constructed a high-precision linear bearing which demonstrates 5 nm short-term position stability. This system represents the experimental implementation of an idea presented in [1] and has been investigated as part of the first author's Ph.D. thesis [2].

This study was initiated with support from the Molecular Measuring Machine (M^3) project at the National Institute of Standards and Technology [3]. The form-factor of the bearing was thus chosen such that it was compatible with the M^3 crossed-slide design. The bearing technology is also highly suitable for other precision applications, such as in stages for photolithography and diamond turning machines; these application areas provide the focus for our current research.

As shown in Figures 1–4, a 10.7 kg platen measuring 125 mm by 125 mm by 350 mm is suspended and controlled in five degrees of freedom by seven electromagnets, labelled as $B1$ through $B7$. Five capacitive probes located in the bearing centers measure position with nanometer resolution. The seven points at which the bearing forces act on the platen are shown as arrows and the five points at which the position measurements are taken are indicated as dots in Figure 1. The scale of Figures 2, 3, and 4 is indicated by the 100 mm reference shown in Figure 2.

The suspension acts as a linear bearing, allowing linear travel of 50 mm in the long axis of the platen. In previous work [2,4], the long-travel degree of freedom is not actively controlled. Efforts are currently directed at achieving control of this degree of freedom with 50 mm travel through a novel magnetic suspension linear motor. This motor consists of an array of permanent magnets attached to the moving platen and a stator array of coils attached to the fixed machine frame as shown in Figs. 2–4. Prototypes of this linear motor are currently under construction. Position in this degree of freedom is transduced by a laser interferometer. For simplicity, optics for this interferometer are not shown in the figures.

The key feature of the linear motor is that it affords control of forces in two degrees of freedom, one parallel to the air gap and lying on the axis of the magnet array and one perpendicular to the air gap. Thus it is possible to simultaneously control translation and suspension with a single motor structure. The motor design and control are the focus of this

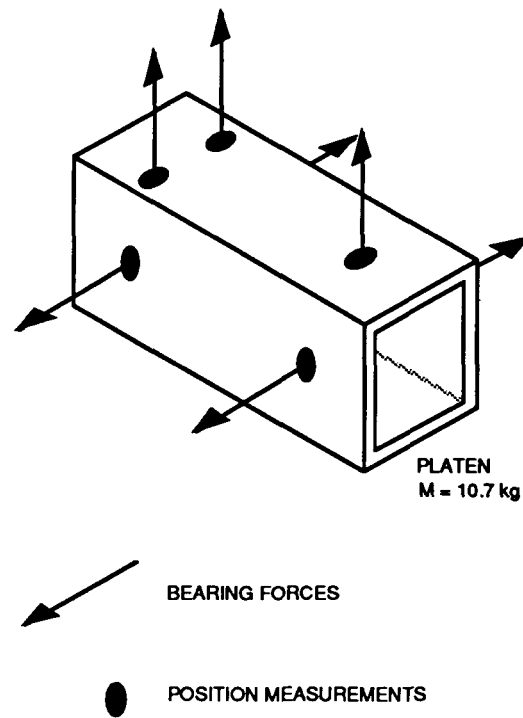


Figure 1: Points at which bearing forces are applied to platen, and points at which platen position is measured.

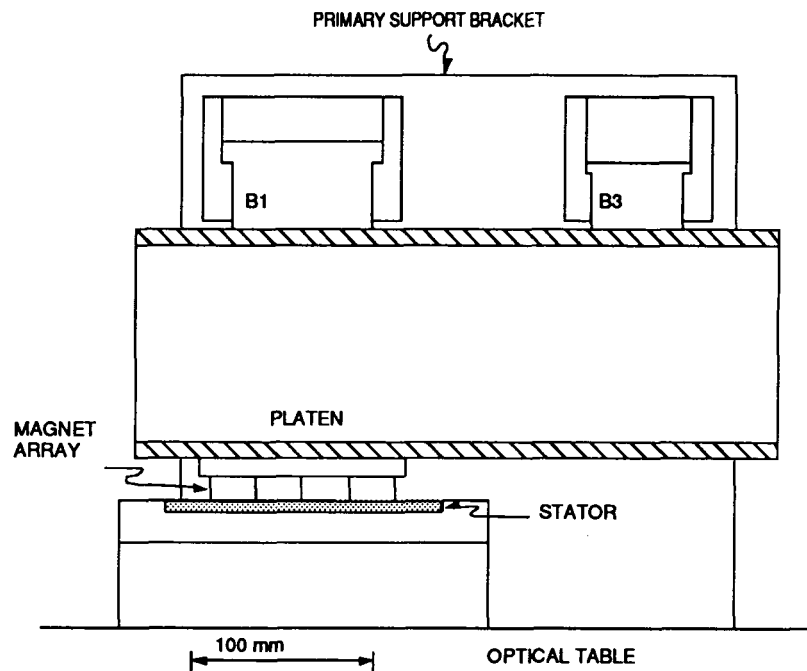


Figure 2: Side view of bearing and linear motor assembly.

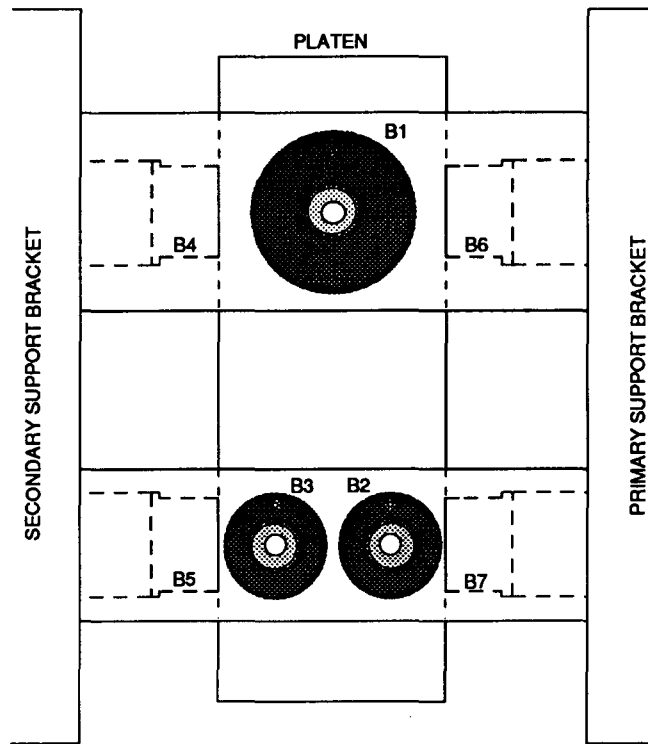


Figure 3: Top view of bearing and linear motor assembly.

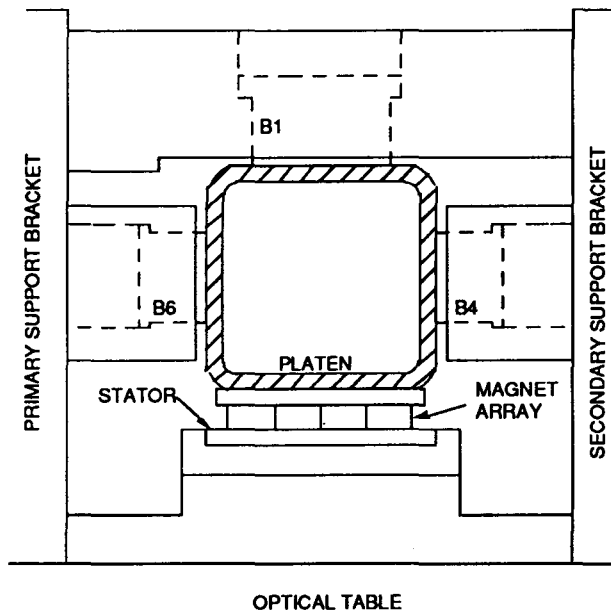


Figure 4: End view of bearing and linear motor assembly.

paper.

The paper is organized as follows. In the next section, the electromechanical characteristics of the linear motor are developed, and an example design is presented. With these results in hand, it is then shown how two degrees of freedom can be controlled using this linear motor. Following this, the conceptual design for a precision X-Y stage driven by four such motors is described. It is anticipated that this stage can achieve nanometer motion control, with travel in X and Y of several hundred millimeters. Finally, suggestions for further work are presented.

2 Motor fields and forces

To calculate the electromagnetic forces, the motor is idealized as a two dimensional structure as shown in Figure 5. Here, the motor is assumed to have a depth of w into the paper and to extend indefinitely in the $\pm z$ -direction. The stator is fixed in the laboratory frame x, y, z . The primed coordinate frame x', y', z' is fixed in the layer of magnetization, and is displaced from the unprimed frame by $(x_0 + \Delta)\bar{i}_x + z_0\bar{i}_z$.

The magnet array is modeled by a half-infinite region of sinusoidally distributed, x -directed magnetization $M_x = \text{Re}M_0e^{-jkz'}$. The magnetization layer is referred back to the unprimed frame by substituting $z' = z - z_0$ into M_x which gives $M_x = \text{Re}\tilde{M}e^{-jkz}$, with complex amplitude $\tilde{M} = M_0e^{jkz_0}$.

The stator is modeled by a sinusoidally distributed, y -directed current density $J_y = \text{Re}\tilde{J}e^{-jkz}$, in a layer from $x = 0$ to $x = \Delta$. The complex amplitude \tilde{J} is a function of the winding density η_0 , and the two phase currents, I_1 and I_2 . Specifically, $\text{Re}\tilde{J} = I_1\eta_0$ and $\text{Im}\tilde{J} = I_2\eta_0$. Throughout this discussion, the complex amplitudes indicated by a tilde represent the temporal variations in both amplitude and spatial phase.

The model is idealized in several ways. First, while the stator current in the real motor is distributed down the axis of the motor in a spatial square-wave, in the model the current density is sinusoidally distributed at the spatial fundamental of the actual stator current distribution. Further, although the real magnets are of finite thickness and distributed in a spatial square-wave of magnetization, we model the magnetized region as of half-infinite extent and with the magnetization distributed sinusoidally in space at the spatial fundamental of the actual magnetization distribution. It is reasonable to model only the fundamental components of magnetization and current, as these are responsible for the bulk of the motor force production. The additional harmonics present in the actual motor can readily be added as Fourier series components built upon the solution we develop herein.

The fields and forces for the finite-thickness stator in Figure 5 are obtained by first studying a simpler model as shown in Figure 6, in which the excitation consists of a current sheet (spatial impulse). Then, with the finite-thickness stator current distribution written as an integral of spatially-distributed current sheets, the linearity of the solution is exploited to write the forces on the finite thickness stator in the form of a convolution integral. This integral is readily solved, yielding the forces on the finite thickness stator.

The analysis follows the techniques and notation from [5], chapters 2, 3, and 4. The

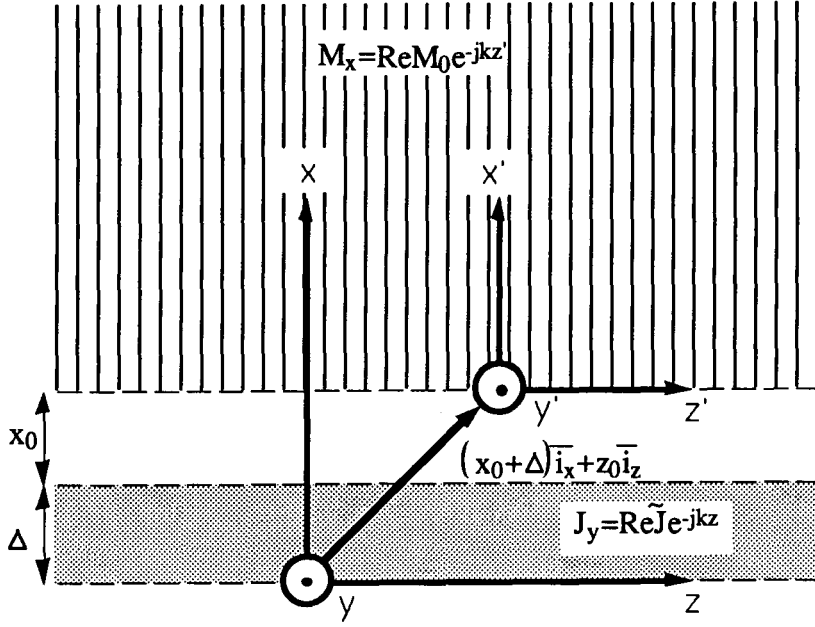


Figure 5: Geometry which represents the current density model of linear motor.

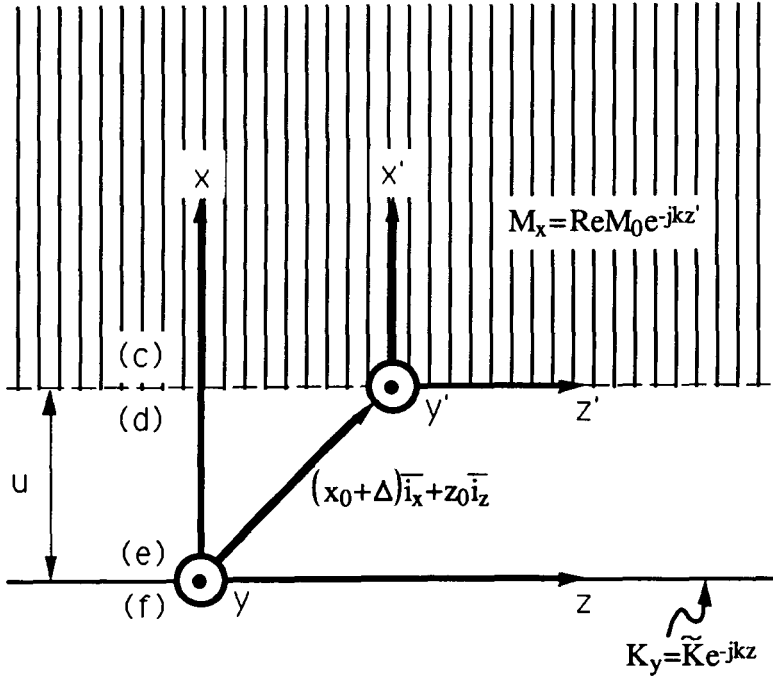


Figure 6: Geometry which represents current sheet model of linear motor.

magnetic field is given as the gradient of the magnetic scalar potential $\mathbf{H} = -\nabla\psi$. Fields and potentials are represented as the real part of a complex amplitude multiplied by a complex exponential in z . Superscripted letters denote a quantity evaluated at the corresponding boundary.

At the magnetization boundary the potential is continuous, $\tilde{\psi}^c = \tilde{\psi}^d$, and the normal field is discontinuous by the magnetization, $\tilde{H}_x^c - \tilde{H}_x^d = -\tilde{M}$. At the current sheet, normal H is continuous, $\tilde{H}_x^e = \tilde{H}_x^f$, and the tangential field is discontinuous by the value of the surface current, $\tilde{H}_z^e - \tilde{H}_z^f = -\tilde{K}$, or alternatively $\tilde{\psi}^e - \tilde{\psi}^f = j\frac{\tilde{K}}{k}$. These boundary conditions are summarized below

$$\tilde{\psi}^c = \tilde{\psi}^d \quad (1)$$

$$\tilde{H}_x^e = \tilde{H}_x^f \quad (2)$$

$$\tilde{\psi}^e - \tilde{\psi}^f = j\frac{\tilde{K}}{k} \quad (3)$$

$$\tilde{H}_x^c - \tilde{H}_x^d = -\tilde{M} \quad (4)$$

Applying the transfer relations from Section 2.16 of [5] yields the following four equations among the field and potential complex amplitudes at the boundaries.

$$\tilde{H}_x^c = k\tilde{\psi}^c \quad (5)$$

$$\tilde{H}_x^d = -k \coth(ku) \tilde{\psi}^d + \frac{k}{\sinh(ku)} \tilde{\psi}^e \quad (6)$$

$$\tilde{H}_x^e = \frac{-k}{\sinh(ku)} \tilde{\psi}^d + k \coth(ku) \tilde{\psi}^e \quad (7)$$

$$\tilde{H}_x^f = -k\tilde{\psi}^f \quad (8)$$

where $u = x_0 + \Delta$.

Together, equations (1)–(8) form a set of eight equations in eight unknowns, which are driven by the sources M_x and K_y .

In order to calculate the normal and tangential forces exerted on the platen, the potential and normal field at boundary (d) are calculated from equations (1)–(8) as:

$$\tilde{\psi}^d = \frac{1}{2k}(j\tilde{K}e^{-ku} - \tilde{M}) \quad (9)$$

and

$$\tilde{H}_x^d = \frac{1}{2}(j\tilde{K}e^{-ku} + \tilde{M}). \quad (10)$$

The tangential field \tilde{H}_z^d is related to the potential $\tilde{\psi}^d$ by the negative of the gradient with respect to z . Thus

$$\tilde{H}_z^d = -\frac{1}{2}(\tilde{K}e^{-ku} + j\tilde{M}). \quad (11)$$

The force acting on a volume of the magnet array is given by the integral of the Maxwell stress tensor over the surface enclosing this volume. For a spatially-periodic structure, the

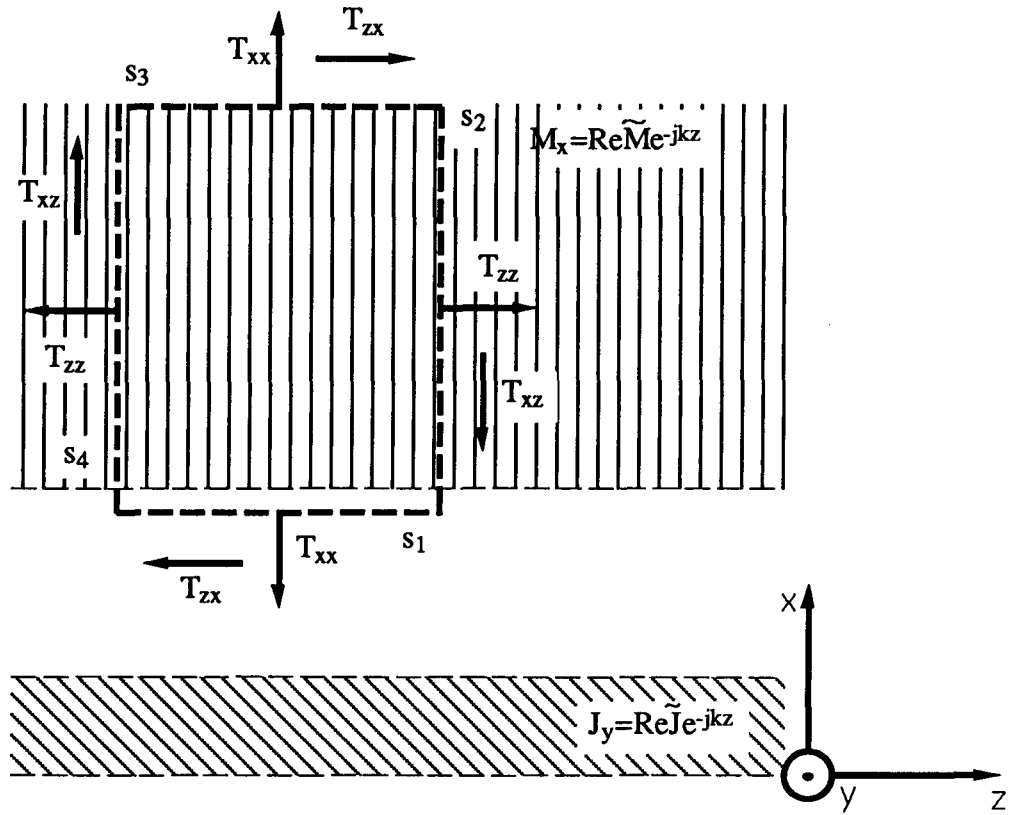


Figure 7: Showing the components of the Maxwell stress tensor acting on a surface which is used to find the forces acting on the magnet array.

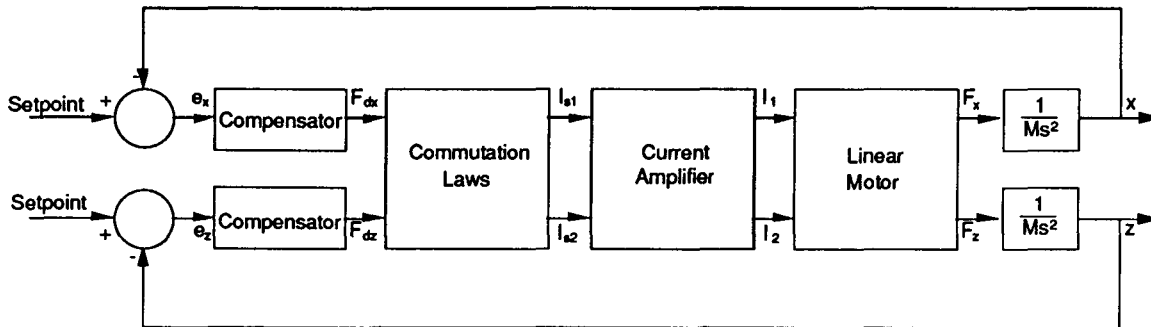


Figure 8: Two degree of freedom control loop block diagram.

integration is simplified if the volume encloses a single spatial period. The components of the stress tensor acting on such a volume are shown in Figure 7. The integrals of T_{xx} and T_{zz} on surface s_3 are found to equal zero. Also, the T_{xz} and T_{zx} components on s_2 and s_4 cancel, since these surfaces are one spatial wavelength apart. The only non-zero contribution is on s_1 . Over an integer number of spatial periods, this force can be written as the spatial average on z multiplied by the area of the surface. Specifically, the normal force acting on one spatial period of the magnet array is given by

$$F_x = -A_m \langle T_{xx} \rangle_z \quad (12)$$

where the expression $\langle \cdot \rangle_z$ stands for the spatial average with respect to z and $A_m = w2\pi/k$ is the area of one spatial period of the motor. Similarly, the tangential force is given by

$$F_z = -A_m \langle T_{zx} \rangle_z. \quad (13)$$

The minus signs in these expressions are accounted for by the direction of the stress tensor components acting on s_1 which is the *bottom* surface.

The stress tensor for magnetically-linear materials derived from the Korteweg-Helmholtz force density ([5], section 3.10) is

$$T_{ij} = \mu H_i H_j - \frac{\mu}{2} \delta_{ij} H_k H_k \quad (14)$$

using the Einstein summation convention where since the k 's appear twice in the same term they are to be summed from one to three. A final useful identity is the averaging theorem ([5], section 2.15).

$$\langle \text{Re} \tilde{A} e^{-jkz} \text{Re} \tilde{B} e^{-jkz} \rangle_z = \frac{1}{2} \text{Re} \tilde{A} \tilde{B}^*. \quad (15)$$

Applying equations (12)–(15) with the results (10) and (11), the forces are found to be

$$F_x = \frac{A_m \mu_0}{4} e^{-ku} \left(\text{Im}(\tilde{K}) \text{Re}(\tilde{M}) - \text{Re}(\tilde{K}) \text{Im}(\tilde{M}) \right) \quad (16)$$

and

$$F_z = \frac{A_m \mu_0}{4} e^{-ku} \left(\text{Re}(\tilde{K}) \text{Re}(\tilde{M}) + \text{Im}(\tilde{K}) \text{Im}(\tilde{M}) \right). \quad (17)$$

Thus we have derived the forces acting on the magnet array due to a sinusoidally distributed current sheet separated from the magnet array by a distance u .

Returning to the finite thickness of sinusoidally distributed current density shown in Figure 5 the forces acting on the magnet array in this case can be determined by summing the forces due to multiple current sheets of the form shown in Figure 6. That is, we integrate from $x = 0$ to $x = \Delta$ the force on the magnet array resulting from a current sheet at location x with intensity $\tilde{K} = \tilde{J} dx$. Specifically,

$$F_x = \frac{A_m \mu_0}{4} \int_0^\Delta \left(\text{Im}(\tilde{J}) \text{Re}(\tilde{M}) - \text{Re}(\tilde{J}) \text{Im}(\tilde{M}) \right) e^{-k(\Delta+x_0-x)} dx \quad (18)$$

and

$$F_z = \frac{A_m \mu_0}{4} \int_0^\Delta \left(\text{Re}(\tilde{J})\text{Re}(\tilde{M}) + \text{Im}(\tilde{J})\text{Im}(\tilde{M}) \right) e^{-k(\Delta+x_0-x)} dx. \quad (19)$$

In writing these integrals, the separation distance $\Delta + x_0 - x$ between the differential current element and the magnet array lower surface has been used to replace u in (16) and (17). Since within the stator J is independent of x , evaluating these integrals gives

$$F_x = \frac{A_m \mu_0}{4k} \left(\text{Im}(\tilde{J})\text{Re}(\tilde{M}) - \text{Re}(\tilde{J})\text{Im}(\tilde{M}) \right) e^{-kx_0} (1 - e^{-k\Delta}) \quad (20)$$

and

$$F_z = \frac{A_m \mu_0}{4k} \left(\text{Re}(\tilde{J})\text{Re}(\tilde{M}) + \text{Im}(\tilde{J})\text{Im}(\tilde{M}) \right) e^{-kx_0} (1 - e^{-k\Delta}). \quad (21)$$

As stated earlier, the current density J is driven by two phase currents $\text{Re}\tilde{J} = I_1\eta_0$ and $\text{Im}\tilde{J} = I_2\eta_0$. The forces in terms of these phase currents are found by using these relations and substituting the earlier derived result $\tilde{M} = M_0 e^{jkz_0}$ into (20) and (21). In matrix notation, the resulting equations are

$$\begin{bmatrix} F_x \\ F_z \end{bmatrix} = \eta_0 M_0 G e^{-kx_0} \begin{bmatrix} -\sin(kz_0) & \cos(kz_0) \\ \cos(kz_0) & \sin(kz_0) \end{bmatrix} \begin{bmatrix} I_1 \\ I_2 \end{bmatrix} \quad (22)$$

where several constants have been collected into $G = \frac{A_m \mu_0}{4k} (1 - e^{-k\Delta})$. The x_0 and z_0 dependencies are explicitly retained since these variables represent motion of the magnet array relative to the stator. This completes the derivation of the motor force equations.

3 Commutation and control

In operation, the motor will be used under closed-loop control. A loop controlling two degrees of freedom with a single linear motor is shown in block diagram form in Figure 8. Here we assume that a single linear motor is attached to a mass M which is allowed to move in only two degrees of freedom x and z . This is the same as assuming that the motor drives through the center of mass. If this assumption is not met, then the model will be more densely interconnected, but the control issues remain essentially unchanged. The linear motor currents I_1 and I_2 are assumed to be driven by a current amplifier. The current setpoints I_{s1} and I_{s2} are generated by the block labelled Commutation Laws. The function of this block is to determine these setpoints such that the motor applies forces F_x and F_z which are equal to the desired forces F_{dx} and F_{dz} . If this is properly accomplished, then the system appears linear and decoupled from inputs F_{dx} and F_{dz} to outputs x and z , and can be controlled by two independent linear compensators which act on errors e_x and e_z .

The commutation laws which achieve this decoupling are derived by inverting (22) to yield

$$\begin{bmatrix} I_{s1} \\ I_{s2} \end{bmatrix} = \frac{e^{kx_0}}{\eta_0 M_0 G} \begin{bmatrix} -\sin(kz_0) & \cos(kz_0) \\ \cos(kz_0) & \sin(kz_0) \end{bmatrix} \begin{bmatrix} F_x \\ F_z \end{bmatrix}. \quad (23)$$

This system of equations takes the desired normal and tangential forces and maps them to the currents needed to produce these forces. To the extent that the commutation laws are accurate, this decouples the two degrees of freedom.

4 Power dissipation

In a specific implementation, the maximum available force is limited by power dissipation in the stator windings. To develop the thermal limits imposed on the motor design, the power dissipation for a single sinusoidally distributed phase is calculated as follows. The power density in a region of conductivity σ carrying current density J is

$$P = \frac{J^2}{\sigma}. \quad (24)$$

In general, the current density is

$$J = \text{Re} \tilde{J} e^{-jkz} = \text{Re}(\tilde{J}) \cos(kz) + \text{Im}(\tilde{J}) \sin(kz). \quad (25)$$

With only a single phase excited, J becomes

$$J = I_1 \eta_0 \cos(kz). \quad (26)$$

The differential power element is

$$dP = \frac{I_1^2 \eta_0^2 w \Delta}{\sigma} \cos^2(kz) dz \quad (27)$$

The power dissipation P_λ per spatial wavelength $\lambda = \frac{2\pi}{k}$ is determined by integrating equation (27) over this wavelength. Thus

$$P_\lambda = \int_0^{\frac{2\pi}{k}} \frac{I_1^2 \eta_0^2 w \Delta}{\sigma} \cos^2(kz) dz. \quad (28)$$

Evaluating this integral gives

$$P_\lambda = \frac{I_1^2 \eta_0^2 w \Delta \lambda}{2\sigma}. \quad (29)$$

A prototype linear motor stator of length $l = 50.8 \times 10^{-3}$ m, width $w = 0.102$ m, depth $\Delta = 7.62 \times 10^{-3}$ m, spatial wavelength $\lambda = 50.8 \times 10^{-3}$ m, and winding density $\eta_0 = 4.4 \times 10^6$ turns/m² was constructed using number 26 copper wire. When supplied with approximately 10 W, this stator experiences a temperature rise of 50°C. This experiment provides an estimate of 5°C/W for the stator temperature coefficient in this geometry.

For a two-phase motor of these dimensions, with a phase current $I_1 = 1$ A, equation (22) yields a force level of 33.8 N. This force is sufficient to accelerate a 10 kg platen at more than 0.3 times the acceleration of gravity. At this current, equation (29) yields a power dissipation of 6.8 W. Using the temperature coefficient developed above, this results in a temperature rise of 34°C.

This temperature rise is well within the thermal limits of the motor materials, but is still a large power dissipation in the context of a precision machine, as the resulting thermal expansion can destroy machine accuracy. This problem can be addressed by taking advantage of the force/power scaling laws. Specifically, since power increases as the square of current, and force increases linearly with current, if the motor area is increased by a factor of n , then the current required to achieve a given force is reduced by this factor. However, with this reduced current, the power density is reduced by n^2 , and thus the total power is reduced by n . Thus it is likely that a larger motor will be used in the final design.

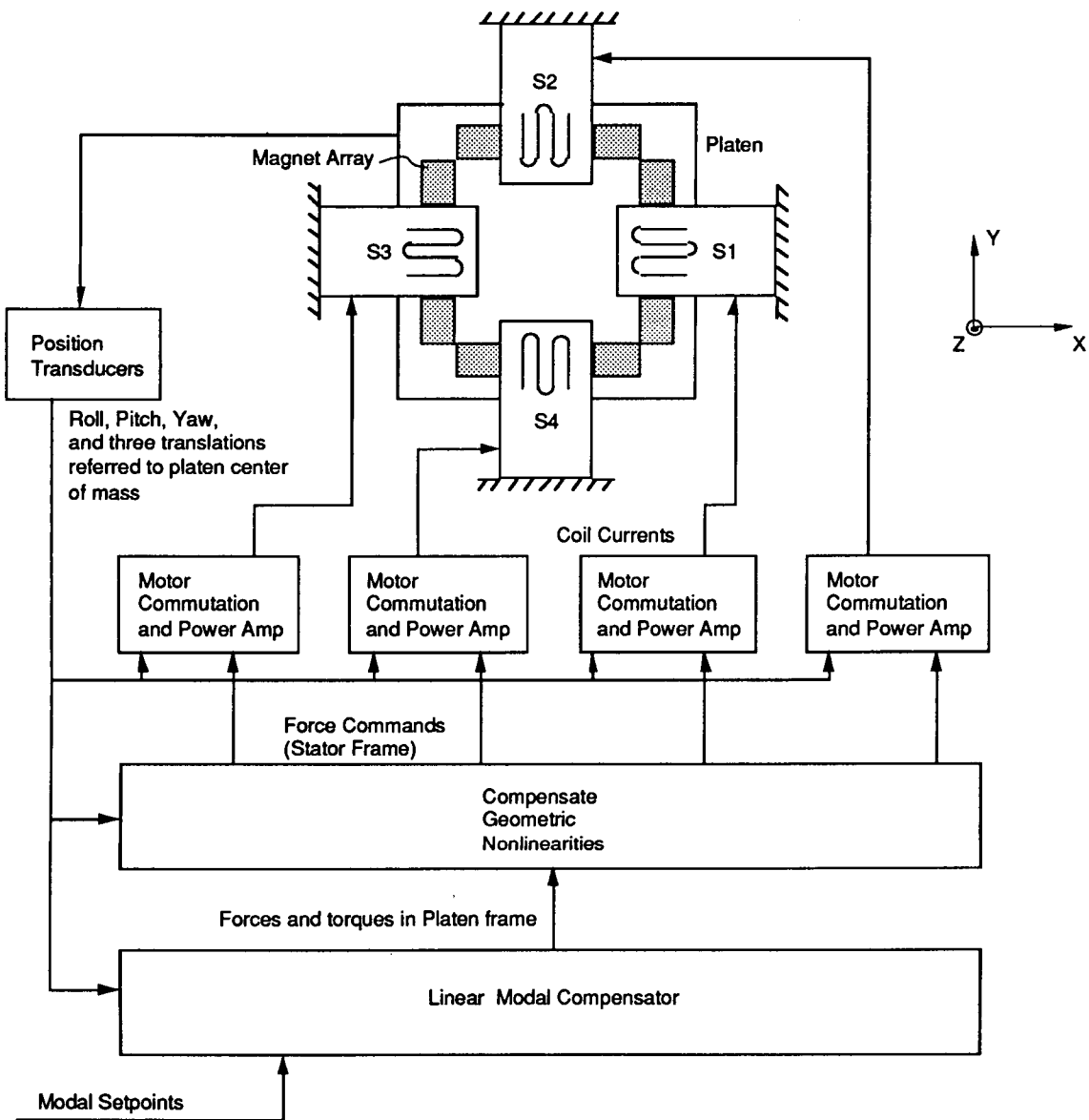


Figure 9: X-Y stage block diagram.

5 Magnetic bearing X-Y stage

Given a magnetic suspension linear motor as developed above, various stage geometries are possible. One such geometry is shown in Figure 9. Here, four linear suspension motors are combined to act on the top surface of a platen to implement an X-Y stage suitable for photolithography. The stators are labelled $S1$ through $S4$ and drive against four magnet arrays which are shown as grey rectangles. Stators $S1$ and $S3$ drive the platen in the Y-direction and stators $S2$ and $S4$ drive the platen in the X-direction. The four stators are driven appropriately to control the remaining four platen degrees of freedom.

The Linear Modal Compensator block consists of separate lead/lag compensators for each of the six degrees of freedom. The Compensate Geometric Nonlinearities block inverts the kinematic relations to translate forces and torques specified in the platen frame (where the system appears as linear) into forces specified in the stator frame (where they are actually applied to the platen). The Motor Commutation and Power Amp blocks each implement (23) for their respective stator assembly and contain power amplifiers for each of the stator phases.

This X-Y stage represents the long-term focus of our design efforts. In order to gain experience with the construction and control of the linear motor, the linear bearing system of Figs. 2-4 will be used as a test-bed for a single linear suspension motor. The design will be refined here before advancing to the X-Y system shown in Fig. 6.

6 Conclusions and suggestions for further work

We have shown the design and analyzed the electromechanics of a linear motor suitable for independently controlling two suspension degrees of freedom. This motor, at least on paper, meets the requirements for driving an X-Y stage of 10 kg mass with about 4 m/sec^2 acceleration, with travel of several hundred millimeters in X and Y, and with reasonable power dissipation. A conceptual design for such a stage has been presented.

However, this design has not yet been verified experimentally. A prototype of the linear motor is in construction and will be tested shortly. Initial testing is expected to take the form of operating the linear motor on a multi-axis load-cell in order to determine the extent to which the actual motor operation matches the theory developed herein. The commutation laws can then be modified based upon experimental data. Once the motor operation is verified experimentally, a single linear motor will be attached to the linear bearing as shown in Figures 2-4, in order to gain experience with control issues. After satisfactory testing on the linear bearing, the system shown in Figure 9 will be constructed in order to achieve the end goal of control of planar motion with 200 mm travel.

The systems described above can be improved in several ways. Currently, the linear bearing operates with purely linear control of the seven support electromagnets. The large-signal closed-loop performance of the bearing could be improved by including nonlinear compensation of the electromagnet force characteristic, as described in [6]. Additionally, the background noise of the five capacitive sensors currently limits the position stability. Thus it would be fruitful to investigate improved sensor techniques. Also, further work is needed in

developing sufficiently accurate and robust control techniques for the multivariable bearing system. Here, mechanical and electrical noise sources, uncertainties in the plant parameters, quantization of signals in the discrete-time controllers, saturation of power amplifiers and other non-idealities need to be considered as they impact the overall system performance. Finally, the magnet array technology developed by Halbach for linear accelerators [7,8] appears to be highly applicable to the linear motor magnet array. These magnet arrays use rotated blocks of magnets to provide a highly sinusoidal magnetic field concentrated on only a single side of the magnet array and thus a stronger fundamental component to interact with the stator winding. A magnet array using Halbach's topology is currently in design.

In conclusion, this paper has demonstrated the theoretical feasibility of linear and planar bearings using single or multiple magnetic suspension linear motors. It remains to demonstrate this feasibility experimentally, and we are proceeding in this direction.

References

- [1] Slocum, A.H., and Eisenhaure, D.B., "Design Considerations for Ultra-Precision Magnetic Bearing Supported Slides," NASA Magnetic Suspension Technology Conference, Hampton, Va. Feb. 2-4, 1988.
- [2] Trumper, D.L., "Magnetic Suspension Techniques for Precision Motion Control," Ph.D. Thesis, Dept. of Elec. Eng. and Comp. Sci., M.I.T., Camb., Mass., Sept., 1990.
- [3] Teague, E.C., "The National Institute of Standards and Technology molecular measuring machine project: Metrology and precision engineering design," *Journal of Vacuum Science Technology*, B7 (6), Nov/Dec, 1989, pp. 1898-1902.
- [4] Trumper, D.L., and Slocum, A. H., "Five-Degree-of-Freedom Control of an Ultra-Precision Magnetically-Suspended Linear Bearing," NASA Workshop on Aerospace Applications of Magnetic Suspension Technology, NASA Langley Research Center, Hampton, VA, Sept. 25-27, 1990.
- [5] Melcher, J.R., *Continuum Electromechanics*, MIT Press, Camb., Mass., 1981.
- [6] Trumper, D.L., "Nonlinear Compensation Techniques for Magnetic Suspension Systems," NASA Workshop on Aerospace Applications of Magnetic Suspension Technology, Hampton, VA, Sept. 25-27, 1990.
- [7] Halbach, K., "Design of Permanent Multipole Magnets with Oriented Rare Earth Cobalt Material," *Nuclear Instruments and Methods*, 169, 1980, pp. 1-10, North-Holland Publishing Co.
- [8] Halbach, K., "Physical and Optical Properties of Rare Earth Cobalt Magnets," *Nuclear Instruments and Methods*, 187, 1981, pp. 109-117, North-Holland Publishing Co.

MODELLING AND DESIGN FOR PM/EM MAGNETIC BEARINGS

D. Pang, J. A. Kirk, D. K. Anand, R. G. Johnson

**Department of Mechanical Engineering
University of Maryland, College Park, MD 20742, U. S. A.**

R. B. Zmood

**Department of Communication and Electrical Engineering
Royal Melbourne Institute of Technology, Melbourne, Victoria 3000, Australia**

SUMMARY

This paper presents a mathematical model of a permanent magnet/electromagnet [PM/EM] radially active bearing. The bearing is represented by both a reluctance model and a stiffness model. The reluctance model analyzes the magnetic circuit of the PM/EM bearing. The stiffness model uses force equilibrium equations to present the behavior of the bearing. By combining the two models the performance of the bearing can be predicted given geometric dimensions, permanent magnet strength, and the parameters of the EM coils.

The overall bearing design including the PM and EM design is subject to the performance requirement and physical constraints. A study of these requirements and constraints is discussed. The PM design is based on the required magnetic flux for proper geometric dimensions and magnet strength. The EM design is based on the stability and force slew rate consideration, and dictates the number of turns for the EM coils and the voltage and current of the power amplifier. An overall PM/EM bearing design methodology is proposed and a case study is also demonstrated.

INTRODUCTION

A magnetic bearing design combining permanent magnets and electromagnetic coils has the advantages of compact size, high efficiency and low heat generation. Permanent magnets containing mainly rare earth material have a high energy density and contribute the major magnetic flux in the bearing. The electromagnetic coils offer the additional magnetic flux to enhance the desired performance of the bearing. This design can decrease the size of the bearing, reduce the power consumption, and generate less heat in the bearing. There are various PM/EM bearing designs; this paper will discuss the PM/EM bearing developed in the University of Maryland for a flywheel energy storage system [1].

The PM/EM magnetic bearing shown Figure 1 is a passive axial support and radial active control design. The permanent magnets generate a bias flux across the air gap and support the axial load but create a destabilized force in the radial direction if the flywheel is not centered. A feedback control system senses the position of the flywheel and sends the appropriate control current into the EM coils. This generates the necessary corrective force to stabilize the system. The bearing's function is to magnetically suspend and center a rotating flywheel that can store kinetic energy.

The mathematical model of the PM/EM bearing can be represented by both a reluctance model and a stiffness model. The former applies the magnetic circuit theory and geometric dimensions of the bearing to analyze the magnetic flux in the air gap. The latter evaluates stiffness equations and force equilibrium equations to present the behavior of the bearing. By combining both models the bearing performance can be predicted and designed. There are some physical restrictions for the

mathematical model such as magnetic saturation, size limitation and electrical constraints that will be discussed later.

RELUCTANCE MODEL

In Figure 2 there is a typical hysteresis loop for the permanent magnetic material [2]. The permanent magnet inherits a flux density B_r , remanence, at zero magnetizing force. If a negative magnetizing force is applied to the magnet until the flux density reduces to zero, that magnetizing force is called the coercive force H_c . For most applications the permanent magnet operates in the second quadrant of the B-H curve between B_r and H_c . The slope of the B-H curve (the ratio of B to H) is denoted the permeability. The most commonly used permeability is the recoil permeability μ_r , which is the slope of the minor hysteresis loop. It is approximately equal to the slope of the B-H curve at zero magnetizing force and is usually presented as a relative value to the permeability of the air.

For an ideal permanent magnet having a strong intrinsic coercive force the B-H curve is a straight line between B_r and H_c shown in Figure 3. The minor hysteresis loop will follow the B-H curve and the recoil permeability is the ratio of B_r and H_c . The equation for the B-H curve is

$$B_m = \mu_0 \mu_r H_m + B_r \quad (1)$$

In a static magnetic field condition, magnetic circuit theory is used to analyze the magnetic flux by solving an equivalent electrical circuit. The reluctance of a magnetic flux path, which is analogous to an electrical resistance, is a function of its length L , cross section area A and permeability μ ,

$$R = L/(\mu A) \quad (2)$$

The permanent magnet can be simulated as a battery of voltage $B_r A_m R_m$ with an internal resistance R_m or a current source $H_m L_m$ with a shunt reluctance R_m [3]. The EM coils can be treated as voltage sources of quantity NI .

Figure 4(a) shows a magnetic circuit containing a permanent magnet, a core material of high (assumed infinite) permeability and an electromagnetic coil. There is a magnetic flux generated by the permanent magnet and the EM coil. When the magnetic flux passes through the air gap, it is separated into two paths: one is the air gap flux path directly across the pole faces and the other is a leakage flux path around the air gap flux path. The reluctance of the air gap and the leakage path are R_g and R_L . The total reluctance R_T is the combination of both reluctances. The equivalent electrical circuit can be plotted as Figure 4(b).

By applying the Ampere's circuital law, the magnetic flux equation and the reluctance equations, the magnetic circuit can be presented as the following:

$$H_m L_m + B_g A_g R_g = NI \quad (3)$$

$$B_m A_m = B_g A_g (R_g / R_T) \quad (4)$$

$$R_g = g_0 / (\mu_0 A_g) \quad (5)$$

$$R_m = L_m / (\mu_0 \mu_r A_m) \quad (6)$$

From equation (1), (3), (4) and (6), the operating flux density of the magnet can be written as

$$B_m = (B_r R_m + NI / A_m) / (R_m + R_T) \quad (7)$$

The operating flux density has been changed due to the magnetizing force from the EM coils. Figure 3 illustrates the load line of the magnet shifted parallel from its original load line. For the PM/EM bearing, the magnet will mainly operate at near zero magnetizing force so the operating flux density can be treated as a constant value of B_m with a variation ΔB_m . Furthermore, the permanent magnet design and the EM coil design can be studied independently as long as the

operating point of the magnet is along the straight line of the B-H curve. Equation (7) can be rewritten as the following:

$$B_m = B_r R_m / (R_m + R_T) \quad (8)$$

$$\Delta B_m = (NI/A_m)/(R_m + R_T) \quad (9)$$

In the PM/EM bearing the magnetic flux from one permanent magnet passes the one air gap to the return ring of the flywheel and return through the other air gap. The equation for the reluctance of the air gap is doubled,

$$R_g = 2g_o/\mu_o A_g \quad (10)$$

The bias flux generated by the permanent magnet is

$$B_u = (B_m A_m / A_g)(R_T / R_g) \quad (11)$$

The permanent magnet design is statically undetermined because there are five equations: (1), (6), (8), (10) and (11) with 12 variables: B_m , B_r , B_u , H_m , μ_r , L_m , g_o , A_m , A_g , R_T , R_m and R_g .

In the magnetic bearing design there are four EM coils of the same axis connected in parallel to the power amplifier. The magnetomotive force of the EM coils in each axis is NI_{max} . The flux density generated by the EM coils across the air gap is

$$B_{EM} = \mu_o NI_{max} / (4g_o) \quad (12)$$

STIFFNESS MODEL

The stiffness model for the magnetic bearing assumes the properties of the bearing to be linear over the operating range except the control current to the EM coils in the control system. The control current is linear until saturation of the power amplifier, after which it is held constant. The reason for the limitation of the control current is to avoid a magnetic saturation of the materials.

The static behavior of the bearing can be represented by force equilibrium equations. In the axial direction, the bearing passively supports the axial load of the flywheel.

$$F_A = K_z d_p \quad (13)$$

In the radial direction, the flywheel is affected by two forces: the destabilizing force from permanent magnets and the corrective force from electromagnetic coils. The combined restoring force of the bearing is

$$F_{rad} = K_i I - K_x X \quad (14)$$

Figure 5(a) represents the radial forces of the bearing including the destabilizing force, the corrective force, and the restoring force. Figure 5(b) shows the control current output from the power amplifier. The corrective force reaches its peak when the power amplifier becomes saturated and cannot supply more current. Simultaneously the restoring force also reaches the peak and begins to decline as the destabilizing force continues to increase and the corrective force stays constant. When the net restoring force is zero, the corrective force equals the destabilizing force. The maximum displacement of flywheel is defined as the maximum stable range and given by

$$X_{stb} = K_i I_{max} / K_x \quad (15)$$

There is a maximum displacement range the flywheel can travel without current saturation. The maximum range X_{lin} is called the linear range of the bearing, which is dependent on the current/displacement ratio C of the control system.

$$X_{lin} = I_{max} / C. \quad (16)$$

In the linear range, the force equilibrium equation (14) can also be written as

$$F_{rad} = K_a X = K_i I - K_x X \quad (17)$$

This active stiffness of bearing can be represented by

$$K_a = C K_i - K_x \quad (18)$$

The linear range, the maximum restoring force and the active stiffness are determined not only by the maximum control current to the EM coils but by the current/displacement ratio C of the control system. A lower current/displacement ratio means a larger linear range, lower active stiffness and smaller maximum restoring force. A higher current/displacement ratio has the opposite effects. For a magnetic bearing, a larger linear range, higher active stiffness and greater maximum restoring force are desired so there is a conflicting interest for the choice of the C . The bearing must balance all these performance requirements.

The geometric dimensions of the bearing such as the length and the cross section area of the air gap have major effects on the magnetic flux and the magnetic force because the flux directly across the air gap of two pole faces helps to support the weight as well as center the flywheel. The bias flux from the permanent magnet contributes the axial stiffness K_z and the passive radial stiffness K_x . The flux from both the permanent magnet and EM coils influences the force/current sensitivity K_i . The K_z , K_x and K_i values can be obtained from experimental or a theoretical analysis.

The axial stiffness of the magnetic bearing derived by Sabnis [4] using the Schwartz-Christoffel transformation shows that

$$K_z = 4B\mu^2 R_{mean}/\mu_0 \quad (19)$$

The passive radial stiffness and the force/current sensitivity can be derived as the following [1]:

$$K_x = 2pB\mu^2 R_{meantpf}/(\mu_0 g_0) \quad (20)$$

$$K_i = 2B\mu R_{meantpf}N/g_0 \quad (21)$$

PERMANENT MAGNET DESIGN

Permanent magnetic materials have greatly progressed in last decade due to the development of rare earth magnets [5]. Rare earth magnets such as samarium-cobalt and neodymium-iron-boron magnets have very high coercive forces combining with high remanence. Figure 6 shows the B-H curves of the rare-earth magnets compared to some older magnet types such as Alnico and ceramic magnets. The B-H curves for the rare-earth magnets are nearly straight lines in most of the second quadrant. The energy products of the rare earth magnet are four or five times values of older magnet types. It means smaller magnets can now generate same magnetic flux. A straight B-H curve also means the recoil lines of minor hysteresis loops will closely follow the B-H curve. The magnets can handle the external magnetizing force and any variation of the air gap in the magnetic circuit without degrading the performance. Thus, the rare earth magnets induce an easier magnetic circuit design with more dynamic applications.

Although there are many rare earth magnets, the commercially available magnets are generally separated into three groups: SmCo_5 , $\text{Sm}_2\text{Co}_{17}$, and NdFeB . SmCo_5 magnets are the first type of rare earth magnets and produce an energy product of 16 to 23 MGOe with very high intrinsic coercive force, which can resist strong adverse magnetizing fields. They have a high curie temperature at 750°C but the intrinsic coercive force drops off as the temperature increases. SmCo_5 magnets can only be used to about 250°C . $\text{Sm}_2\text{Co}_{17}$ magnets have a higher energy product of 20 to 30 MGOe and a higher remanence of 9.5 to 12 KG. Some types of $\text{Sm}_2\text{Co}_{17}$ have a lower intrinsic coercive force that results in a knee in the B-H curve. $\text{Sm}_2\text{Co}_{17}$ magnets have slightly better temperature performance than SmCo_5 and are useful to about 350°C . NdFeB magnets have the highest energy product of 25 to 40 MGOe and a remanence of 11 to 12.8 KG. NdFeB

magnets only have a curie temperature of 300°C and are useful only below 150°C. NdFeB is the cheapest rare earth component due to the vast amounts of the material resources currently available. NdFeB has a corrosion problem, however, and Sm_xCo_x magnets should not be used at the radiation environments. All three magnets are very hard and brittle and should be protected from large mechanical stresses.

The PM design has 5 equations with 12 variables as suggested from the reluctance model. Three dependent variables H_m , R_m and R_g can be eliminated using equations (1), (6) and (10). Three variable B_u , A_g and g_o are determined by the axial drop, axial load and radial load requirements. If the fundamental geometry of the magnetic circuit is known, the useful flux ratio (R_T/R_g) is approximated. For the current PM/EM bearing design, the useful flux ratio is in the range of 30% to 40%. The relative recoil permeability μ_r for the rare earth magnets is around 1.05. The PM design problem has been simplified into 2 equations, (8) and (11), with 4 variables: B_m , B_r , L_m and A_m .

For a maximum energy output from the permanent magnet, the operating flux density should be half its remanence. This design can also minimize the volume of the magnet and its material cost, and equates to

$$B_m = B_r/2 \text{ or } R_m = R_T \quad (22)$$

This may not be feasible due to other geometric constraints on the length and cross section area of the magnet. To avoid underestimation of the reluctance in the magnetic circuit or increase of the air gap, the operating flux density B_m is always designed above its calculated value (half the remanence). However, the B_m/B_r ratio is a good efficiency index for the magnet design. This B_m/B_r ratio can be used to choose an appropriate permanent magnet strength from the manufacturer catalog at a preliminary design.

Any two of the five variables: B_m , B_r , L_m , A_m and B_m/B_r can be chosen to solve the following equations derived from Equation (8) and (11),

$$B_r = (B_u A_g / A_m) (R_g / R_T) (B_r / B_m) \quad (23)$$

$$L_m / A_m = (\mu_r g_o / A_g) (R_T / R_g) / ((B_r / B_m) - 1) \quad (24)$$

$$A_m = B_g A_g L_m (R_g / R_T) / (B_r L_m - \mu_r B_g g_o) \quad (25)$$

PM design is one of the most difficult in the magnetic bearing because all the magnetic flux paths should be carefully calculated. The rare earth magnets are expensive and usually made to order for a specific configuration. If there is error in the design, the magnets most likely will be wasted.

ELECTROMAGNETIC COIL DESIGN

The EM coil design is based on the stability and the force slew rate considerations to choose the number of turns for the coil, and the voltage and current for the power amplifier. The stability consideration is derived from the nonlinear control system analysis used to remove the limit cycle oscillation and to improve the robustness of the bearing. The force slew rate consideration is derived from the dynamics requirements of the magnetic bearing for the external force or mass unbalance conditions. From both the experimental results and theoretical analysis the power amplifier voltage and the number of turns (inductance) of the EM coils have greater roles in stabilizing the bearing and responding to any disturbance.

Zmood et al [6] found, when the power was connected, the flywheel not only failed to self-suspend but often broke into self-sustaining oscillation unless the mechanical touchdown gap was well adjusted. Also, the magnetic bearing flywheel system broke into limit cycle oscillation due to a

large disturbance. The source of the oscillations is due to the combined effects of the power amplifier saturation, bearing radial stiffness K_x , the touchdown gap X_{td} and the inductance of the EM coil. A simplified nonlinear control system model shown in Figure 7 has been built to study the self-suspension and limit cycle oscillation phenomenon observed in the experiment. The model makes the following assumptions:

- (1) The back e.m.f. induced in the EM coils can be neglected;
- (2) The EM coil resistance can be neglected;
- (3) When the flywheel collides with the touchdown bearing the velocity and acceleration drop to zero;
- (4) There is no external disturbance force so the equation (14) can be applied;
- (5) There are only the current and displacement feedback loops;
- (6) The bearing actuator can be approximately modelled by a first order differential equation.

The equation for the stability condition of the bearing can be written as the following

$$1 < \frac{K_i}{K_x} \frac{C_x}{C_i} < \frac{1}{2} + \sqrt{\frac{1}{4} + \frac{K_i \alpha'}{K_x X_{td}}} \quad (26)$$

where $\alpha' = V_{cc}/(W_m' L_{ind})$ and $W_m' = (K_x/M)^{1/2}$.

For a stable system the parameters of the control system, C_x and C_i , should be chosen to satisfy the inequality equation (26). To increase the robustness of the control system and to relax the restriction on these parameters the right hand part of the inequality equation should be as large as possible. This part can also be viewed as the relative stability ratio δ of the control system. For our magnetic bearing there are four EM coils connected parallel together to the power amplifier at one axis. The magnetic flux from the EM coils will pass four air gap so the inductance becomes

$$L_{ind} = \mu_0 A_g N^2 / (4g_0) \quad (27)$$

From equation (26) and (27) the number of turns for the EM coil can be written as an inequality form.

$$N < \frac{4\sqrt{2}g_0}{\pi^2 B_u R_{meantpf}} \frac{V_{cc}}{W_m' X_{td} \delta^2 - \delta} \quad (28)$$

Maslen et al [7] studied the effects of the force slew rate on the dynamic performance of the bearing. If the bearing operates about its center, $X = 0$, the force slew rate can be derived from the radial force equation (14) as

$$dF/dt = K_i(dI/dt) \quad (29)$$

The force slew rate can also be written as the function of the applied voltage and the inductance of the EM coils.

$$dF/dt = K_i V_{cc} / L_{ind} \quad (30)$$

For a step force input F_R or a mass unbalance at a rotational speed of w rad/s with a distance X from the center, the force slew rate is proven to be

$$dF/dt > (2F_R^3 / 3MX)^{1/2} \quad (31)$$

$$dF/dt > Mw^3 X \quad (32)$$

The number of turns for the EM coils presented as the function of the force slew rate becomes

$$N < \frac{8\sqrt{2}B_u V_{cc}}{\pi \mu_0 \frac{dF}{dt}} \quad (33)$$

The maximum supply current for the EM coils can be calculated using equation (12),

$$I_{\max} = 4B_{\text{EM}g_0}/\mu_0 N \quad (34)$$

The power amplifier of the control system can be chosen based on the its voltage and current requirements.

PM/EM MAGNETIC BEARING DESIGN

The flowchart for the design methodology of the PM/EM bearing is shown in Figure 8. The design procedures start with design requirements for the magnetic bearing including the mass of the flywheel, the axial force, the radial force and the linear operating range. There are some initial inputs such as the saturation flux density of the magnetic material, the recoil permeability of the PM material, the operating point of the permanent magnet, the useful flux ratio, and power amplifier voltage. These values can be updated or changed with the choice of the specific materials and designs.

The bearing design is an iterative processes so the number of steps just shows a possible sequence. These procedures are used for the magnetic bearing flywheel energy storage system and designer can revise the procedures for other applications.

(1) Flux density consideration

The flux densities in any section of the magnetic bearing are limited by the saturation value of the magnetic material so the combined flux densities from the PM and EM are less than the saturation value. If there are equal flux densities from the PM and EM, the bearing can generate a maximum force. In most applications the flux density from the PM is greater than that from the EM.

(2) Geometric relationship consideration

Our PM/EM bearing is a small gap suspension design so the linear range is less than 15% of the air gap. To avoid large leakage flux and cross-talk between the pole faces of the magnet plates and return ring, the pole face thickness is at least 3 times of the air gap. Also, there is a minimum thickness for the PM to prevent too much leakage between the two magnet plates.

(3) Axial drop, axial load, and radial force consideration

The magnetic bearing is designed to satisfy the force requirements by choosing the flux densities and the geometric dimensions. Because of our radial active bearing design the load capability in the axial direction is weaker than the radial direction. If the bearing is used to handle the same force in both directions, the axial force requirement becomes dominate. To avoid the possibility that a larger axial drop may worsen the magnetic properties of the bearing the ratio of the axial drop and the pole face thickness is limited to 20%.

(4) Selection of a feasible design

After satisfying the performance requirement and physical constraints a feasible design is chosen including the flux densities from the PM and EM, the mean radius, the air gap, the pole face thickness, and other dimensions.

(5) Permanent magnet design

Using the information from the previous step the parameters of the permanent magnet design such as the magnet strength, thickness and cross section area can be decided by applying the equation (23), (24) and (25).

(6) Electromagnetic coil design

Based on the stability and force slew rate considerations the number of turns for the EM coils as well as the voltage and current for the power amplifier can be decided.

(7) Characteristics of the PM/EM bearing

The performance parameters such as X_{stb} , X_{lin} , K_a , C , K_z , K_x and K_i for the bearing can be calculated using the equation (15), (16), (17), (18), (19), (20) and (21).

(8) Optimization design

A optimization method for the PM/EM bearing design has been developed at the University of Maryland [8]. The designer can define an objective function with all equality and inequality constraints to find an optimum design.

After finishing the preliminary design the bearing needs a detailed study such as a finite element model for magnetic circuit agreement and dynamic simulation. Also, the control system and overall bearing flywheel system need further investigation but these are beyond the scope of this paper.

EXAMPLE

An example for the pancake magnetic bearing design is presented to demonstrate the proposed design methodology. Assume a pancake magnetic bearing for the energy storage system having a flywheel weight of 8 lbs. The bearing is designed to handle at least 16 lbs force at both axial and radial direction with an axial drop of no more than 20% of its pole face thickness. The magnetic bearing should allow at least 0.006 inch for the radial displacement before being limited by the mechanical touchdown bearing. The magnetic material for the bearing is nickel iron which has a saturation flux density of 1 Tesla. The maximum radius for the bearing is limited to 2 inch and the minimum height of the permanent magnet is 0.3 inch. The power amplifier of the control system has a voltage 24 volts and a maximum supply current 1.5 Ampere. The useful flux ratio is assumed to be 40% for this design.

(1) Design Requirements & Physical Constraints

The performance requirement and physical constraints of the magnetic bearing are rewritten as the following:

$$M = 8 \text{ lbs}$$

$$F_A \geq 16 \text{ lbs}$$

$$F_R \geq 16 \text{ lbs}$$

$$B_{sat} = 1 \text{ Tesla}$$

$$R_{mean} \leq 2 \text{ in}$$

$$X_{td} = 0.006 \text{ inch}$$

$$dp/tpf \leq 0.2$$

$$L_m \geq 0.3 \text{ inch}$$

$$V_{cc} = 24 \text{ V}$$

$$I_{max} \leq 1.5 \text{ Amp}$$

$$R_T/R_g = 0.4$$

(2) Flux Density Consideration

The flux density generated by the permanent magnet across the air gap is assumed to be 50% of the saturation value of magnetic material. The flux density from the EM coils is 40% of the saturation value.

$$B_u = 0.5 B_{sat} = 0.5 \text{ Tesla}$$

$$B_{EM} = 0.4 B_{sat} = 0.4 \text{ Tesla}$$

(3) Geometric Relationship

The touchdown gap is designed to be 15% of the air gap and the pole face thickness is three time of the air gap.

$$g_o = X_{td}/0.15 = 0.04 \text{ in}$$

$$tpf = 3 g_o = 0.12 \text{ in}$$

(4) Axial Drop, Axial Load and Radial Force Requirement

The axial stiffness equation is used to find the mean radius for the magnetic bearing.

$$dp = W_A/K_z = 0.2 tpf = 0.024 \text{ in}$$

$$R_{mean} = 2.89 \text{ in} > 2 \text{ in (Failure!)}$$

Because the calculated radius is larger than the allowable size the above design must be changed. One way is to choose the bearing radius as the maximum allowable value and to find the required flux density at the air gap which can satisfy the requirement.

$$R_{mean} = 2 \text{ in}$$

$$B_u = 0.6 \text{ Tesla}$$

$$B_{EM} = 0.3 \text{ Tesla}$$

$$F_A = 20.9 \text{ lbs} > 16 \text{ lbs (OK!)}$$

$$F_R = 25.1 \text{ lb} > 16 \text{ lbs (OK!)}$$

(5) Permanent Magnet Design

The permanent magnet is chosen to use the rare earth Recoma 20 material which has a remanence of 0.85 Tesla and a recoil permeability of 1.05. The length of the permanent magnet is assumed to be 0.3 in. The cross section area for the air gap is calculated to be 0.377 in². The radius and the operating flux density of the magnet can be calculated as the below

$$A_m = 0.829 \text{ in}^2$$

$$R_m = 0.94 \text{ in}$$

$$B_m = 0.68 \text{ Tesla}$$

(6) Electromagnetic Coil Design

The radial passive stiffness of the bearing is calculated to be 1567 lb/in. If the relative stability ratio is assumed to be 2, the number of turns for the EM coil can be calculated using the stability criteria

$$N < 1790 \text{ turns}$$

If the bearing is assumed to handle a step input force of 16 lbs at the touchdown gap. The force slew rate and the number of turns for the coil are:

$$dF/dt = 31254 \text{ N/s}$$

$$N < 1320 \text{ turns}$$

Finally the number of turns for the EM coil is chosen to be 1000 turns so the maximum supply current is 0.97 ampere which satisfies the constraint of the power amplifier.

(7) Characteristics of Pancake Magnetic Bearing

The performance parameters for the bearing are listed as the following:

$$K_x = 1567 \text{ lb/in}$$

$$K_i = 29.1 \text{ lb/Amp}$$

$$K_a = 2667 \text{ lb/in}$$

$$K_z = 332 \text{ lb/in}$$

$$C = 146 \text{ Amp/in}$$

$$X_{stb} = 0.018 \text{ in}$$

$$X_{lin} = 0.0066 \text{ in}$$

DISCUSSION AND CONCLUSION

In light of the demands of modern technology for more efficient and economic energy conversion, magnetic bearings certainly fit the requirements. The various magnetic bearings differ in function and form but a major commonality between them should be the theory that governs all physical and magnetic behavior. Although the specific numbers of these mathematical models for a flywheel

magnetic bearing are unique, the design methodology and magnetic developments encompass all such devices. As always, one must be careful to study the physical constraints and boundary conditions placed on the problem. University of Maryland has been successful in developing two different sizes of bearings and an operational combination of two bearings in a stack configuration. The success has come from proposing, modifying, and verifying the mathematical models presented here. A few grey areas remain, such as the crosstalk between magnetic flux paths and harmonic disturbances, which were beyond the scope of this paper. Future methodology will include dynamic effects, digital rather than analog control, and finite element analysis of the magnetic circuitry. As the system becomes more complex, so do the questions that are raised about its optimization.

SYMBOLS AND ABBREVIATIONS

| | |
|-----------|---|
| Ag: | Cross Section Area of Air Gap; for PM/EM Bearing = $\pi R_{mean} t_p / 2$ |
| Am: | Cross Section Area of Permanent Magnet = $\pi D_m^2 / 4$ |
| BEM: | Flux Density by Electromagnet at Pole Face |
| Bm: | Operating Flux Density of Permanent Magnet |
| Br: | Remanence of Permanent Magnet |
| Bsat: | Saturation Value of Magnetic Material |
| Bu: | Useful Flux Density by Permanent Magnet at Pole Face |
| Bg: | Flux Density Across Air Gap |
| C: | Current/Displacement Ratio of Control System |
| Cx: | Displacement Feedback Gain in Control System |
| Ci: | Current Feedback Gain in Control System |
| Dm: | Diameter of Permanent Magnet |
| dp: | Axial Drop of Flywheel |
| FA: | Maximum Axial Force |
| FR: | Maximum Radial Force at $X = X_{td}$ |
| Frad: | Restoring Radial Force = $K_i I - K_x X$ |
| go: | Air Gap |
| Hc: | Coercive Force of Permanent Magnet |
| Hm: | Magnetizing Force of Permanent Magnet |
| Imax: | Maximum Control Current to Electromagnetic Coils |
| Ka: | Active Stiffness of Magnetic Bearing = $CK_i - K_x$ |
| Ki: | Force/Current Sensitivity of Electromagnetic Coils |
| Kx: | Passive Radial Stiffness of Magnetic Bearing |
| Kz: | Passive Axial Stiffness of Magnetic Bearing |
| Lind: | Inductance of Electromagnetic Coils |
| Lm: | Length of Permanent Magnet |
| M: | Mass of Flywheel |
| N: | Number of Turns of One Electromagnetic Coils |
| Rg: | Reluctance of Air Gap at Pole Face |
| RL: | Reluctance of Leakage Flux |
| Rm: | Reluctance of Permanent Magnet |
| RT: | Total Reluctance = $R_g R_L / (R_g + R_L)$ |
| Rmean: | Mean Radius of Middle Point of Air Gap |
| tpf: | Pole Face Thickness |
| Xlin: | Linear Range of Magnetic Bearing |
| Xstb: | Stable Range of Magnetic Bearing = $X_{lin} (1 + K_a / K_x)$ |
| Xtd: | Touchdown Gap |
| Vcc: | Amplifier Supply Voltage |
| μ_o : | Permeability of Free Space = $4\pi \times 10^{-7}$ H/m |
| μ_r : | Recoil Permeability of Permanent Magnet |

$\frac{dF}{dt}$: Force Slew Rate
 ΔB_m : Varying Flux Density of Permanent Magnet

REFERENCE

1. Iwaskiw, A. P., "Design of a 500WH Magnetically Suspended Flywheel Energy Storage System", Master Thesis, University of Maryland, College Park, 1987.
2. McCaig, M., Clegg A. G., "Permanent Magnets in Theory and Practice", John Wiley & Sons, Inc., New York, 1987.
3. Parker, R. J., "Advances in Permanent Magnetism", John Wiley & Sons, Inc., New York, 1990.
4. Sabnis, A. V., "Analytical Techniques for Magnetic Bearings" PhD Dissertation, Univ. of California, Berkeley, 1974.
5. Strnat, K. J., "Modern Permanent Magnets for Applications in Electro-Technology", Proceedings of International Workshops on Rare-Earth Permanent Magnets and Applications, Pittsburgh, Penn., 1990.
6. Zmood, R. B., Pang D., Anand D. K., Kirk, J. A., "Improved Operation of Magnetic Bearings for Flywheel Energy Storage System", Proceedings of 25th Intersociety Energy Conversion Engineering Conference, Reno, Nevada, 1990.
7. Maslen, E., Hermann, P., Scott, M., Humphris, R. R., "Practical Limits to the Performance of Magnetic Bearings: Peak Force, Slew Rate, and Displacement Sensitivity", Proceedings of NASA Workshop on Magnetic Bearings, Langley, Virginia, 1988.
8. Pang, D., Kirk, J. A., Anand, D. K., Huang, C., "Design Optimization for Magnetic Bearing", Proceedings of 26th Intersociety Energy Conversion Engineering Conference, Boston, Mass., 1991.

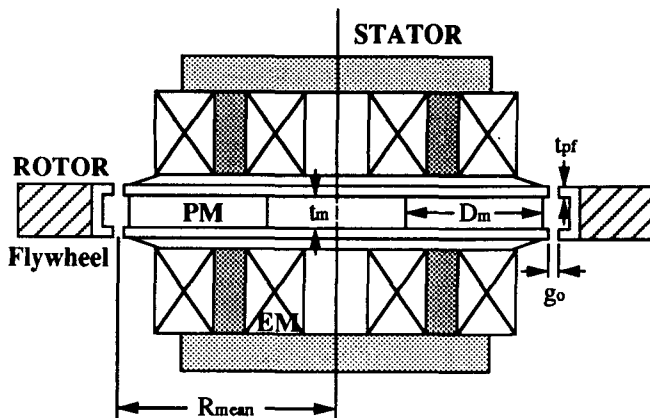


Fig. 1 PM/EM Magnetic Bearing

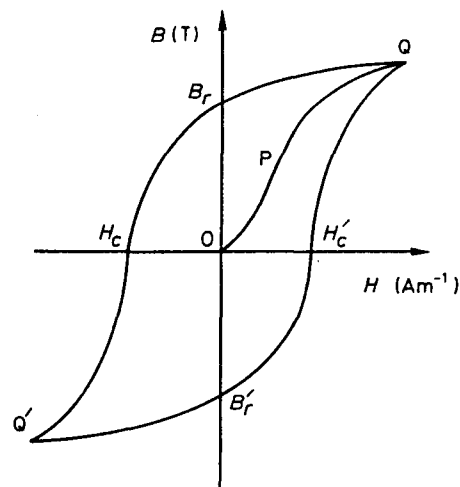


Fig. 2 PM Hysteresis Loop

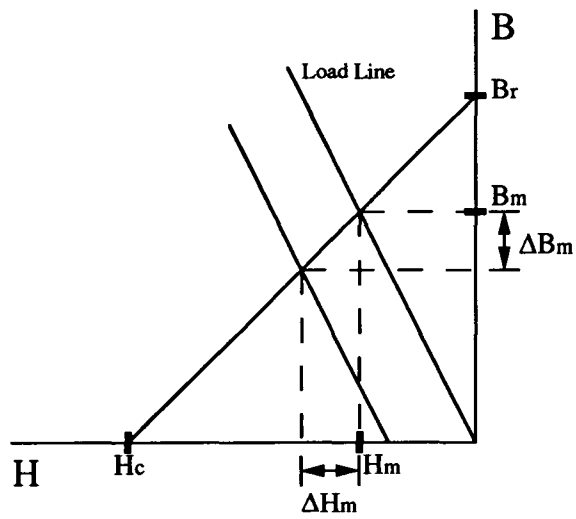


Fig. 3 Ideal PM B-H Curve

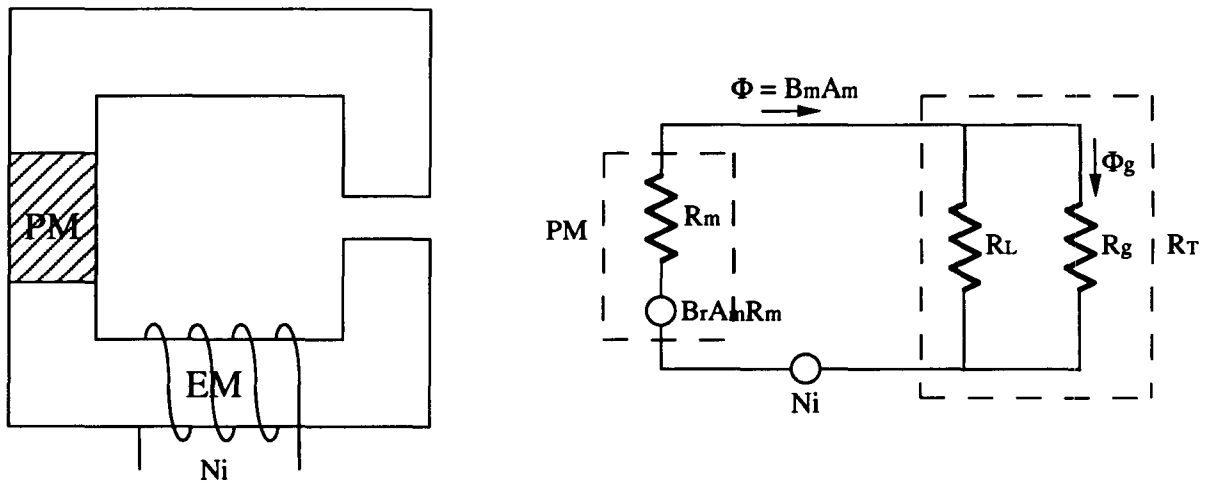


Fig. 4 PM/EM Magnetic Circuit

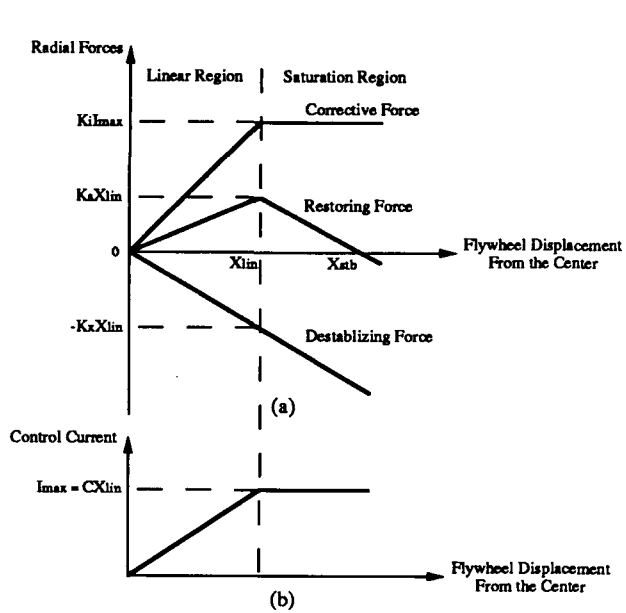


Fig. 5 Magnetic Bearing Radial Forces

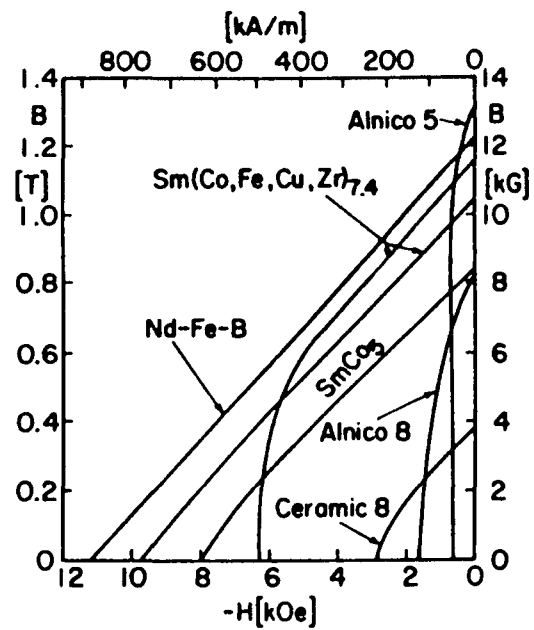


Fig. 6 Various PM B-H Curves

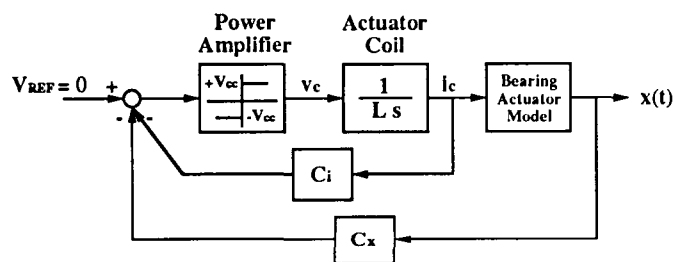


Fig. 7 Simplified Bearing Control System

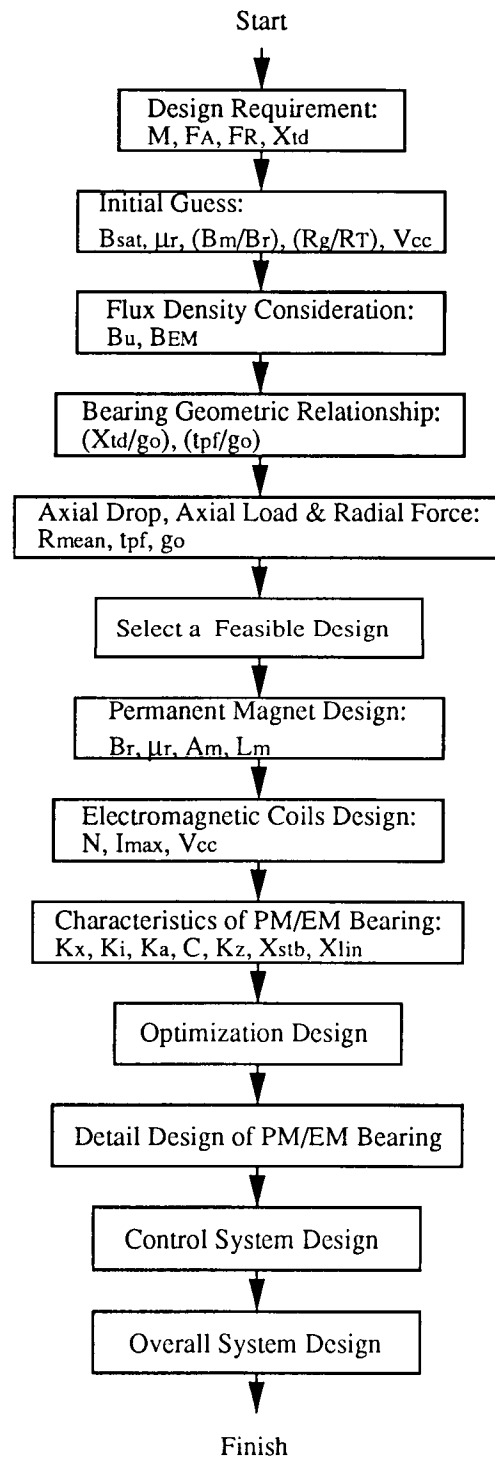


Fig. 8 PM/EM Bearing Design Flowchart

Session 3

SENSORS AND CONTROLS 1

Chairman - Mark Motter
NASA Langley Research Center

N 9 2 - 2 7 7 2 9

Application of Narrow Band Control to Reduce Vibrations in Magnetic Bearing Systems

**Monique S. Gaffney
Bruce G. Johnson
SatCon Technology Corporation
12 Emily Street
Cambridge, MA 02139**

The goal of this paper is to illustrate the benefits of narrowband control theory for simple, open-loop stable systems, then discuss how the control approach changes for magnetic bearing systems, which are open-loop unstable. Magnetic bearing systems are good applications for narrowband control theory. This paper discusses two sources of synchronous forces, the measurement error and the magnetic unbalance. Both the measurement error and the magnetic unbalance manifest themselves as synchronous disturbances (ref. 1). As will be shown, narrowband control theory for simple, open-loop stable systems provides excellent performance and good stability robustness. Because magnetic bearing systems are open-loop unstable, the narrowband control approach becomes more complex. Disturbance accommodating control (DAC) theory is introduced herein as an effective approach to reduce vibrations in magnetic bearing systems. It is used to develop a control/estimation scheme that enables the rotor to spin about its center of mass, in the presence of the measurement error disturbances.

OVERVIEW

- o Magnetic bearing systems are narrowband control applications**
- o Narrowband control theory for open-loop stable plants**
- o Narrowband control theory for magnetic bearing systems**
- o Satcon magnetic bearing system background**
- o Results from a disturbance accommodating controller**

Active control enables magnetic bearings to reduce vibrations in rotating machinery. One method of reducing the synchronous vibrations of a rotating system is to enable the rotor to spin about its true inertial axis. No synchronous forces are generated when the rotor spins about its center of mass because the acceleration of the center of mass of the rotor is zero. The figure below is a simplified free body diagram showing the forces acting between the rotor and stator in a magnetic bearing system. The figure presents an axial cross-section of the gap in a magnetic bearing system. For simplicity, the effects of gravity are neglected; nevertheless with gravity the conclusions are the same. Similarly, the angular motion is neglected, therefore the distance between the forces on the free body diagram is immaterial. The translational equation of motion for the rotor in one radial direction is,

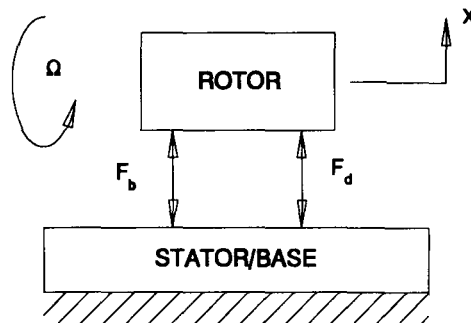
$$m\ddot{x} = F_b + F_d$$

The system will produce no net force on the rotor when,

$$F_b + F_d = 0$$

From the first equation, the acceleration of the center of mass of the rotor, \ddot{x} , must be zero for the second equation to be true. If the rotor spins at a constant speed about an axis other than its inertial axis, the center of mass is accelerated due to the changing direction of its velocity vector. This implies that when the axis of rotation is the inertial axis, such that $x = 0$, then there is no net force generated by the bearing system because the acceleration of the center of mass is zero, namely $\ddot{x} = 0$. In summary, spinning the rotor about its inertial axis eliminates the vibratory forces generated by the bearing system. However, the bearing control force F_b is not necessarily zero because it acts to "cancel" any other force F_d .

SPIN ABOUT THE CENTER OF MASS



Rotor/Stator Force Interaction

F_b is the bearing force

F_d is any force acting directly between the rotor and base
ie. magnetic unbalance force

Equations of Motion

$$m\ddot{x} = F_b + F_d$$

$$\text{want } F_b + F_d = 0$$

Bearing force "cancels" disturbance force for no vibrations

The figure below consists of a radial cross-section of a magnetic bearing system. The center of mass (M) is situated on the inertial axis of the rotor. Although its position is unknown, the inertial axis is the desired axis of rotation in order to minimize system vibrations as discussed previously. The measurement center (S) is defined by the position measurement sensors. The position sensors are mounted on the bearing housing and measure the distance to the rotor surface, or in other words, the gap. To give a physical perception of this center, the measurement center is the geometric center of the rotor, assuming an ideal surface measurement, (ie. the rotor surface is perfectly smooth and the material is perfectly homogenous). The line segment (ϵ_s) in the figure below is the unknown distance between the position the sensors measure and the position of the center of mass of the rotor. In conventional bearing systems, this distance is the mass imbalance. Consequently, (ϵ_s) is termed the measurement error because it is the amount of synchronous corruption of the center of mass position signal by the measurement system. Also from the figure, the kinematic relationship relating the center of mass to the measurement center, using complex coordinates, is

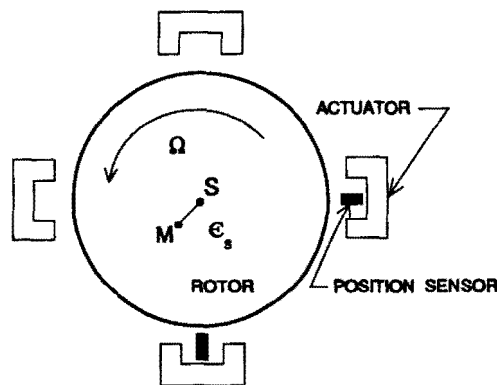
$$z_s = z + \epsilon_s e^{j\Omega t}$$

The effect of the measurement error or "mass imbalance" is to produce an additive disturbance at the output of the plant. The output disturbance is also a function of the synchronous frequency.

MEASUREMENT ERROR MODELLING

Goal - vibration reduction ==> spin about the center of mass

Problem - cannot measure the center of mass



M - rotor center of mass

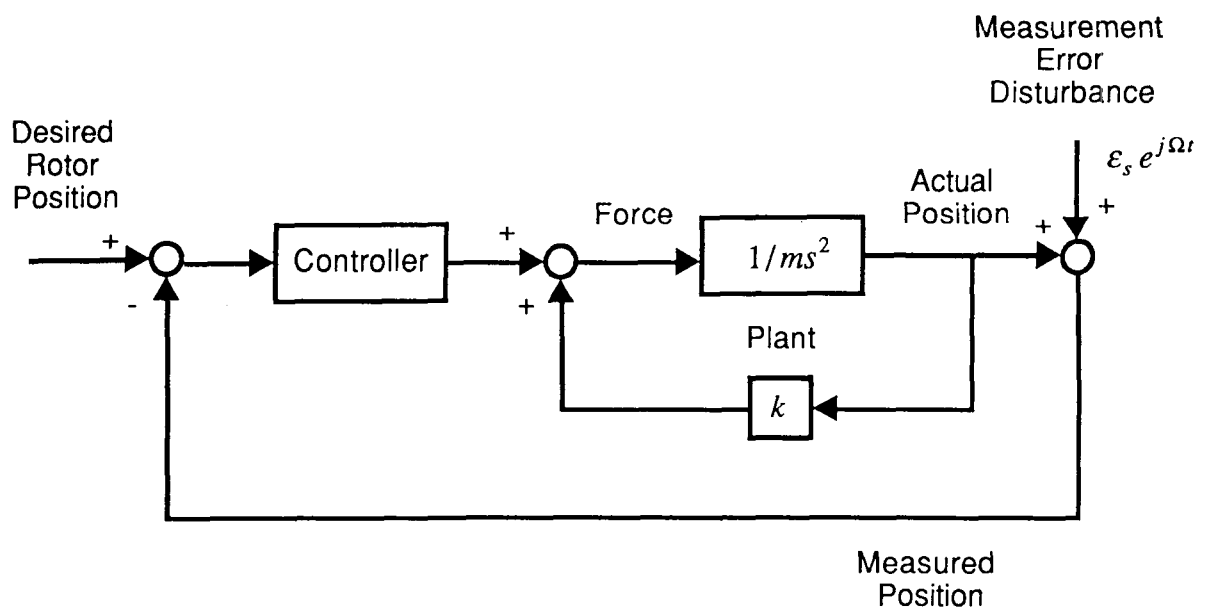
S - rotor measurement center ~ rotor geometric center

Kinematic relationship (complex notation) $z_s = z + \epsilon_s e^{j\Omega t}$

Additive output disturbance

The following figure is a simple block diagram of a magnetic bearing system, illustrating how the measurement error is an additive plant output disturbance that corrupts the center of mass position. Because the feedback signal, the measured position, is a combination of the inertial position and the measurement error disturbance, the controller drives the rotor to spin about its measurement center. As a result, the rotating system generates vibratory forces.

BLOCK DIAGRAM WITH MEASUREMENT ERROR

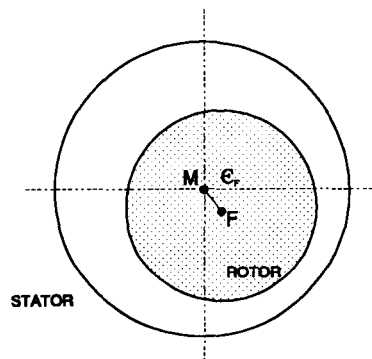


Another synchronous disturbance source is the magnetic unbalance. A magnetic center (F) is located axially along the rotor at each rotor/stator set, for example at the bearings and motor. All the rotor/stator sets on the shaft contribute to a resultant magnetic center. This center is the point of equilibrium for the resultant unstable spring force. In other words, if the rotor spins about its magnetic center, the change in magnetic gap (δG) would be zero. This center depends mainly upon the geometry of the rotor. Given a system with the bearings as the only source of side-loading forces, the magnetic center is the measurement center (or geometric center), assuming an ideal rotor surface measurement, with a smooth rotor surface and homogenous material properties. Consequently, the position of the magnetic center at each bearing is known from the position sensors. However, if the rotor has other electric components on it, such as an induction motor, the position of the magnetic center at these components cannot be extracted simply from information via sensors at the bearings. Therefore, the resultant magnetic center is unknown and is different than the measurement center. The point (F) in the figure below represents the magnetic center of the rotor at one rotor/stator set. As the rotor spins about its center of mass (M), the distance (ϵ_F) rotates with angular velocity (Ω). The kinematic relationship between the center of mass and the magnetic center, in complex coordinates, is given by

$$z_F = z + \epsilon_F e^{j\Omega t}$$

MAGNETIC UNBALANCE MODELLING

Electric machine interaction ==> radial attractive force ==> function of gap



M - rotor center of mass

F - magnetic (field) center ~ rotor geometric center

Linearized constitutive relation

$$F = K \Delta Z_G$$

$$F = K Z_F$$

K < 0, negative stiffness

assuming no base motion

Kinematic relationship (complex notation)

$$z_F = z + \epsilon_F e^{j\Omega t}$$

$$F = K z_F = K z + K \epsilon_F e^{j\Omega t} \implies \text{additive input disturbance}$$

The linearized constitutive relation for the side-loading forces from either the bearings or the motor is

$$F = -K \delta z_g$$

Assuming the rotor/stator set in question is located axially at the center of mass initially to avoid the angular terms, and also assuming no baseplate motion,

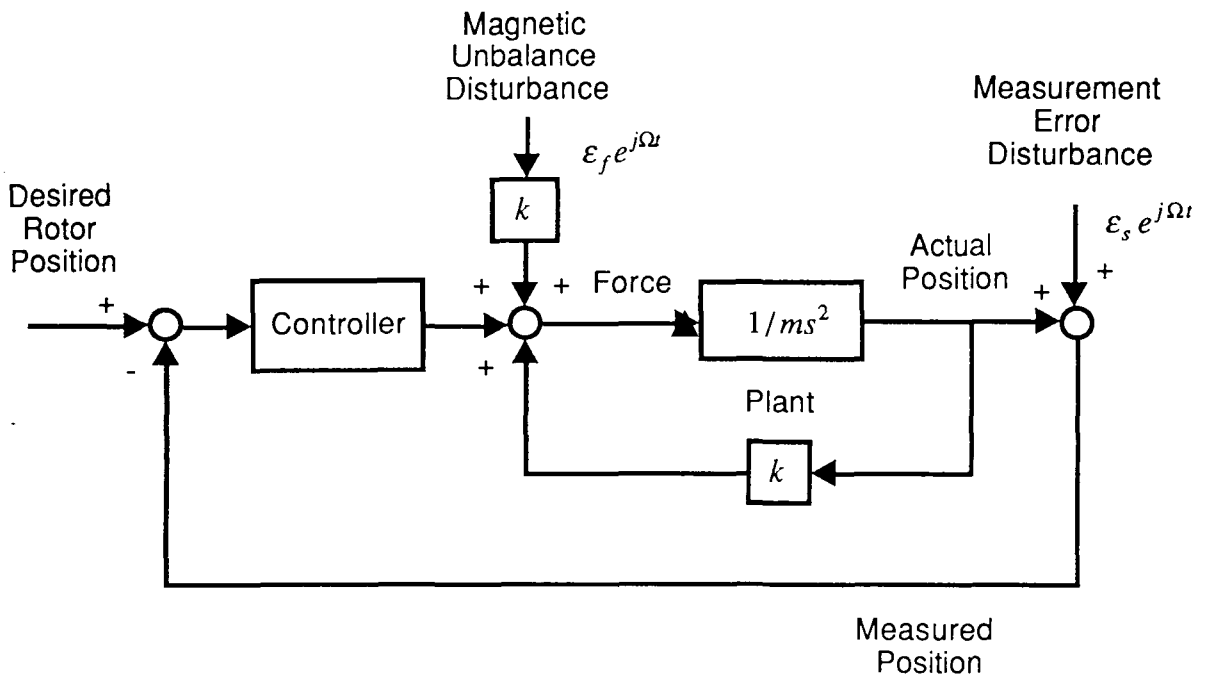
$$F = K z_F$$

because the change in magnetic gap is represented by a change in position of the magnetic center, where $(\delta z_F) = -(\delta z_g)$. Thus, combining this equation with the kinematic relation, the expression for the unstable spring force becomes

$$F = K z + K \epsilon_F e^{j\Omega t}$$

As shown in the block diagram below, the synchronous magnetic unbalance disturbances manifests itself as an additive input disturbance.

BLOCK DIAGRAM WITH BOTH DISTURBANCE INPUTS



Narrowband control theory for open-loop stable plants can provide excellent performance with good stability robustness for systems with periodic disturbances. As will be shown, the system is phase stable at the disturbance frequency and gain stable everywhere else. High levels of disturbance attenuation can be obtained. For simple cases, (SISO, linear, open-loop stable, and a constant disturbance frequency) the compensator design parameters consist of the plant gain and phase at the disturbance frequency. The resulting low-order filter is easy to implement.

NARROWBAND CONTROL ATTRIBUTES (open-loop stable)

Stability robustness

- o phase stable at disturbance frequency
- o gain stable everywhere else

Excellent performance

- o high levels of attenuation

Simple design and implementation

- o model consists of plant gain and phase at disturbance frequency
- o low order filter for coding

Numerous approaches exist to the narrowband disturbance control problem, including classical feedback and adaptive feedforward. An excellent survey of the different types of narrowband control approaches is found in (ref. 2). The performance of these algorithms, however, can be made similar, at least for the relatively simple problem of controlling a SISO, linear, open-loop stable plant that has a constant disturbance frequency. The implementation of these control algorithms, however, can differ significantly.

NARROWBAND CONTROL APPROACHES

Feedback

- o **classical control, bandpass filtering**
- o **modern control, frequency-shaped cost functionals**
- o **disturbance accommodating control**

Feedforward

- o **knob turning**
- o **adaptive feedforward filtering**
- o **higher harmonic control**

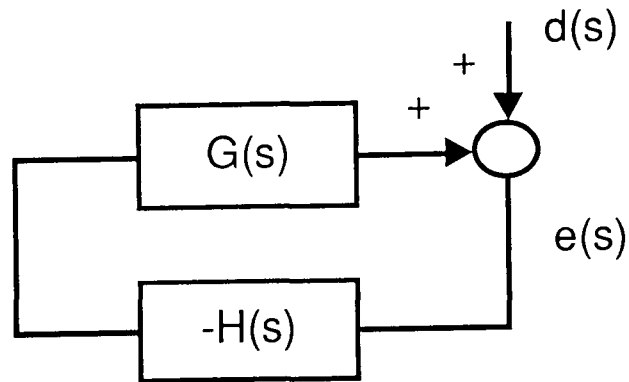
Others

- o **good survey in Sievers, L.A., vonFlotow, A.H., "Comparison and Extensions of Control Methods for Narrowband Disturbance Rejection". NCA-Vol.8, A.S.M.E. Winter Annual Meeting, Dallas, Texas, November 1990**

In the classical feedback approach, shown in the block diagram below, the compensator gain $H(s)$ is made infinite at the disturbance frequency ω_d and small elsewhere. Typically this is implemented with a second-order filter, an undamped oscillator. The transfer function is shown below, where k is the compensator gain and ω_d is the disturbance frequency. Because the feedback gain is infinite, the net error will be driven to zero, if the system is stable.

The stability of this narrow-band controller is easily analyzed with the use of a Bode plot of loop gain. On the following page is a loop transfer function that assumes a constant gain plant ($G(s) = g$). This plot can be roughly divided into two frequency ranges, frequencies near the disturbance frequency and frequencies not near the disturbance frequency. At the disturbance frequency, the loop gain becomes infinite and changes phase by 180 degrees, because of the undamped oscillator poles in the compensator. At frequencies not close to the disturbance frequency, the loop gain is small, well below 0 db. As a result of these small gains elsewhere, the system stability is determined only by the loop gain near the disturbance frequency. The loop phase changes from +90 degrees to -90 degrees at the disturbance frequency because of the zero in the compensator transfer function. Thus the phase margin, which is the amount the plant phase can change before the system becomes unstable, is seen to be ± 90 degrees. The gain margin, which is the amount the plant gain can change before the system becomes unstable, is theoretically infinite.

CLASSICAL FEEDBACK APPROACH



Best performance

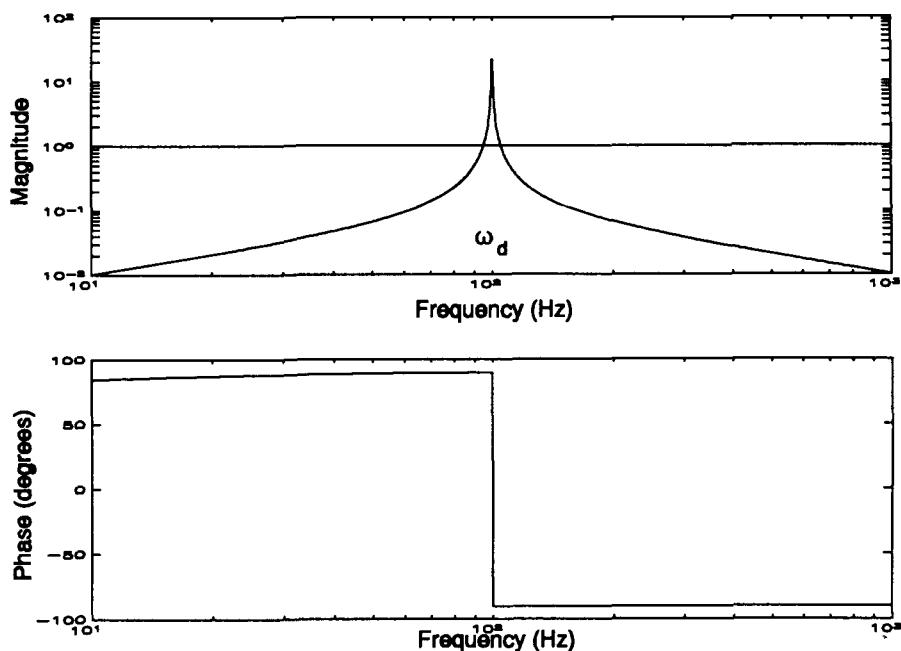
$$H(s) = k \frac{s}{\left(\frac{s}{\omega_d}\right)^2 + 1} = \frac{H_{\text{num}}(s)}{\left(\frac{s}{\omega_d}\right)^2 + 1}$$

Best stability

$$\angle G(j\omega_d) + \angle H_{\text{num}}(j\omega_d) = +90^\circ$$

These good stability margins were derived for a particularly simple plant that has constant gain. However, many of these good stability properties remain even under significantly relaxed assumptions about the plant. For a more general plant all we need know to design the compensator and analyze its stability properties is the maximum gain of the plant G_{\max} and the phase of the plant at the disturbance frequency $\angle G(j\omega_d)$. At frequencies away from the disturbance frequency, we can guarantee stability if the loop gain is kept below 0 db independent of the plant phase, that is we "gain stabilize" the plant at these frequencies. If the loop gain is less than one (0 db) it can never encircle the minus one point on the Nyquist plot, which is the stability condition for this system. At frequencies near the disturbance frequency, the loop gain becomes infinite and the best stability robustness will be achieved if the loop gain changes from +90 to -90 degrees. The undamped poles in the compensator will contribute a change in loop phase of -180 degrees to the loop gain at the disturbance frequency. Therefore at the disturbance frequency we want the plant phase and the numerator portion of the compensator to contribute +90 degrees of phase. This stability definition was shown on the previous page (ref. 3). The numerator of the compensator, is therefore designed to satisfy this equation, once the plant angle at the disturbance frequency is known. The angle of the compensator can be changed by changing the zero structure or, with a discrete time implementation, by the use of a pure time delay. The gain of the compensator is chosen so that the maximum loop gain in frequency ranges not close to the disturbance frequency gives a desired gain margin.

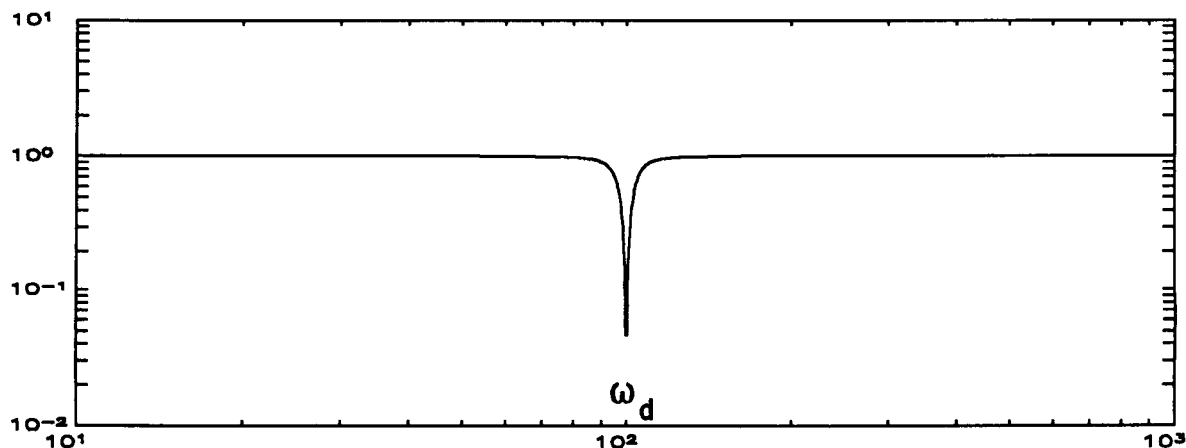
LOOP TRANSFER FUNCTION



More explicitly, the closed-loop performance of the compensator is given by the sensitivity transfer function below. If we assume for simplicity that the plant transfer function $G(s)$ is a simple unity gain, the closed-loop transfer function between the periodic disturbance $d(s)$ and the net output error $e(s)$ is given in the figure below. As expected, the error will be zero at the disturbance frequency, because of the infinite gain in the feedback compensator at this frequency. Note that although the shape of the closed-loop disturbance to error transfer function of the figure below is in general a function of the plant gain $G(s)$, it will always be zero at the disturbance frequency ω_d independent of the plant gain at this frequency $G(j\omega_d)$. This is assuming that the plant is reasonably well behaved at the disturbance frequency, in particular that it does not have undamped zeros at the disturbance frequency. The relatively simple compensator, therefore, exhibits "perfect" performance in rejecting the disturbance force, if it is stable.

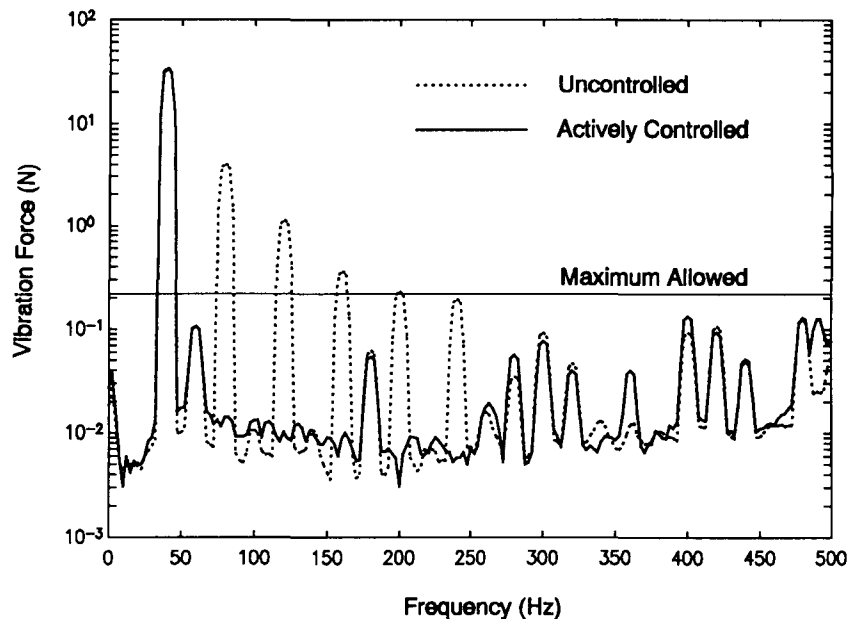
CLOSED LOOP TRANSFER FUNCTION

$$\frac{e(s)}{d(s)} = \frac{1}{1 + G(s)H(s)}$$



One application of this classical feedback narrowband control theory is to actively control a Stirling-cycle cryocooler compressor to cancel the higher harmonic forces produced by the linear motor (ref. 3). The linear motor is driven at a fundamental frequency of 40 Hz and produces higher harmonics that exceed the desired force vibration levels, as shown by the dotted plot in the figure below. The narrowband feedback compensation consists of five undamped oscillators, in parallel, at the higher harmonics of 80, 120, 160, 180, and 220 Hz. As shown in the figure, the forces at the target higher harmonics were driven into the noise floor of the force dynamometer, with over 40 db reduction at the 80 Hz harmonic.

AXIAL VIBRATION FORCE SPECTRA USING SELF-CANCELING CONFIGURATION: FIVE HARMONICS CANCELED



The previous discussion on narrowband control theory was assuming an open-loop stable plant. Attractive force magnetic bearings, however, are open-loop unstable. As a result, the loop transfer function cannot have small gains everywhere besides the disturbance frequency, as in the open-loop case, and still remain stable. There are numerous narrowband control approaches for synchronous vibration reduction of magnetic bearing systems, several of those are listed below (ref. 4,5,6). The remaining discussion will describe a SatCon hardware demonstration and introduce disturbance accommodating control theory as an effective narrowband approach for open-loop unstable plants.

NARROWBAND CONTROL FOR MAGNETIC BEARING SYSTEMS

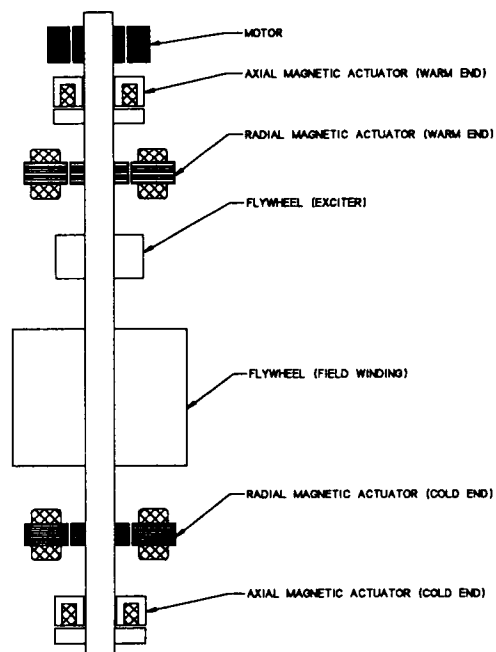
- o magnetic bearing systems are open-loop unstable plants**
- o gain margin approach breaks down for open-loop stable plants breaks down**

Approaches

- o Notch filter**
- o Open-loop dynamic balancing**
- o LQ frequency shaping**
- o Disturbance accommodating control**
- o Others**

The following discussion applies specifically to a hardware demonstration developed by SatCon Technology Corporation (ref 7). The system, shown in the figure below, is a one-fifth scaled model (by mass) of a cryogenic alternator. The figure is an axial cross-section of the shaft and several important components, namely the magnetic thrust and journal bearings, the motor and the flywheels. The magnetically suspended rotor/shaft assembly mass is approximately 82 kilograms. The axis of rotation is in the vertical direction, therefore its weight is supported entirely by the thrust bearings. The induction motor spins the entire rotor/shaft assembly at a maximum working rotational speed of 3600 rpm (60 Hz). The flywheel components are simply cylindrical masses that simulate the inertial effects of the exciter and generator on the full scale cryogenic alternator. During cryogenic operation, the lower radial and axial actuators and the corresponding sensors are immersed in liquid nitrogen to demonstrate working bearings at 77° K.

CROSS-SECTION OF ROTOR/SHAFT ASSEMBLY



mass = 82 kg

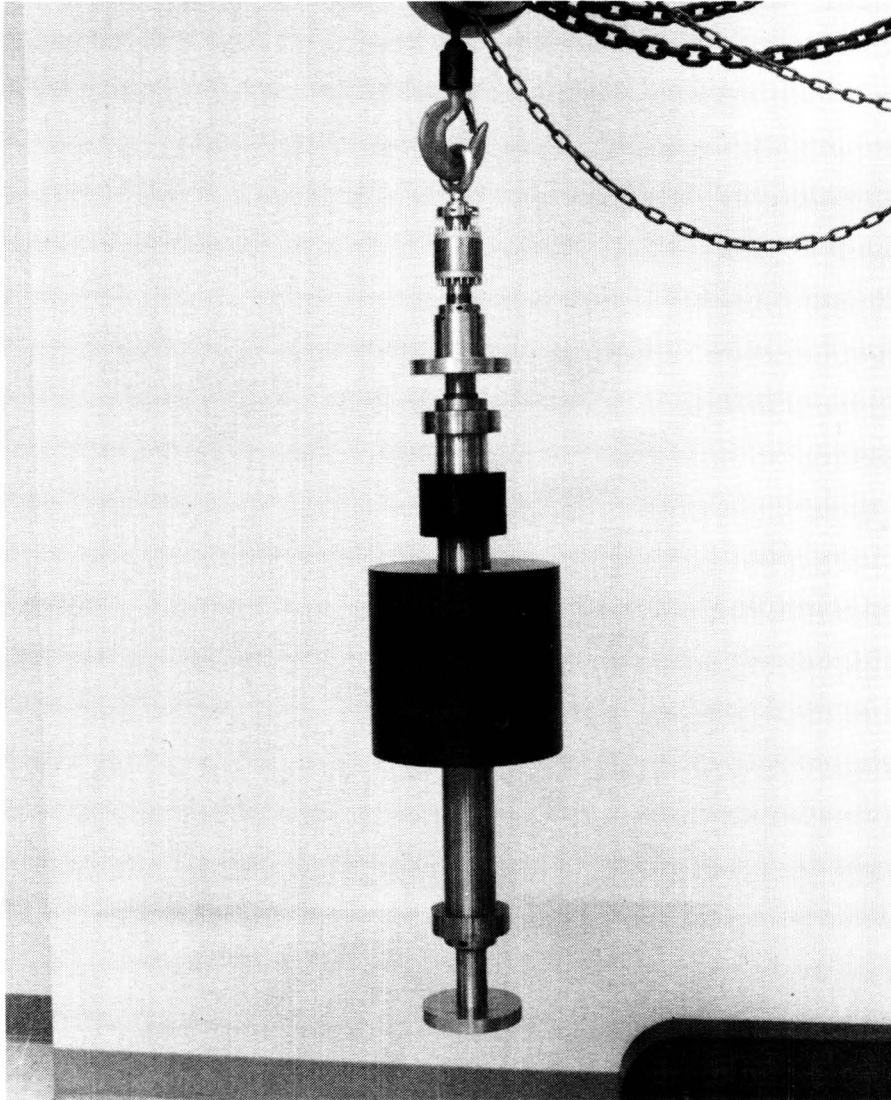
shaft length = 1.2 m (47 in)

rotational speed = 3600 rpm (60 Hz, 377 rad/sec)

thrust bearing force (max) \approx 800 N per bearing

radial bearing force (max) \approx 400 N per bearing

The figure below is a photograph of the actual shaft, again showing the important components. The rotor is equipped with an adjustable mass system. The mass imbalance distance is increased by dropping a small weight down an access hole in the center of the shaft. When the shaft spins, the weight moves up a plugged-end channel, which is cut into the large flywheel, and thereby increases the mass imbalance.



ORIGINAL PAGE
BLACK AND WHITE PHOTOGRAPH

A photo of the testbed structure is presented in the figure below. The shaft is vertical to accommodate for the cryogenic demonstration. As shown, a support stand provides the principal support and positioning of the entire system. A thick steel plate is bolted to the top of the stand. From this plate are hung the magnetic actuators, the rotating assembly, and the cryostat. During cryogenic operation, a level sensing system feeds liquid nitrogen to the cryostat from an external storage bottle. As a result, the bottom radial and axial magnetic actuators are submerged in liquid nitrogen and reach a constant temperature of 77°K . The magnetic actuator assembly consists of upper and lower housing structures which hold and accurately position the axial and radial actuators by the spacer also shown in the figure. Touch-down surfaces are also integrated into these housings in the event of interruption of power to the actuators. Various sensor systems including capacitive sensors for measuring radial and axial distances and accelerometers for measuring relative housing vibration are integrated into each housing.



ORIGINAL PAGE
BLACK AND WHITE PHOTOGRAPH

Disturbance accommodating control (DAC) theory is used to design controllers and estimators for systems with disturbances having waveform structure (ref. 8). The control of magnetic bearings is a natural application of DAC theory because the dominant disturbances are non-stochastic functions of the synchronous frequency, as previously described. DAC theory is used in the following discussion to develop a disturbance model of the measurement error. By combining the plant and disturbance models, an accurate estimate of the true center of mass position is created. Then the corresponding controller feeds back an uncorrupted estimate of the center of mass position, which results in the desired behavior of spinning about the center of mass.

DISTURBANCE ACCOMMODATING CONTROL (DAC)

Applications

- o disturbances have "waveform" structure**
- o non-stochastic methodology**

Approach

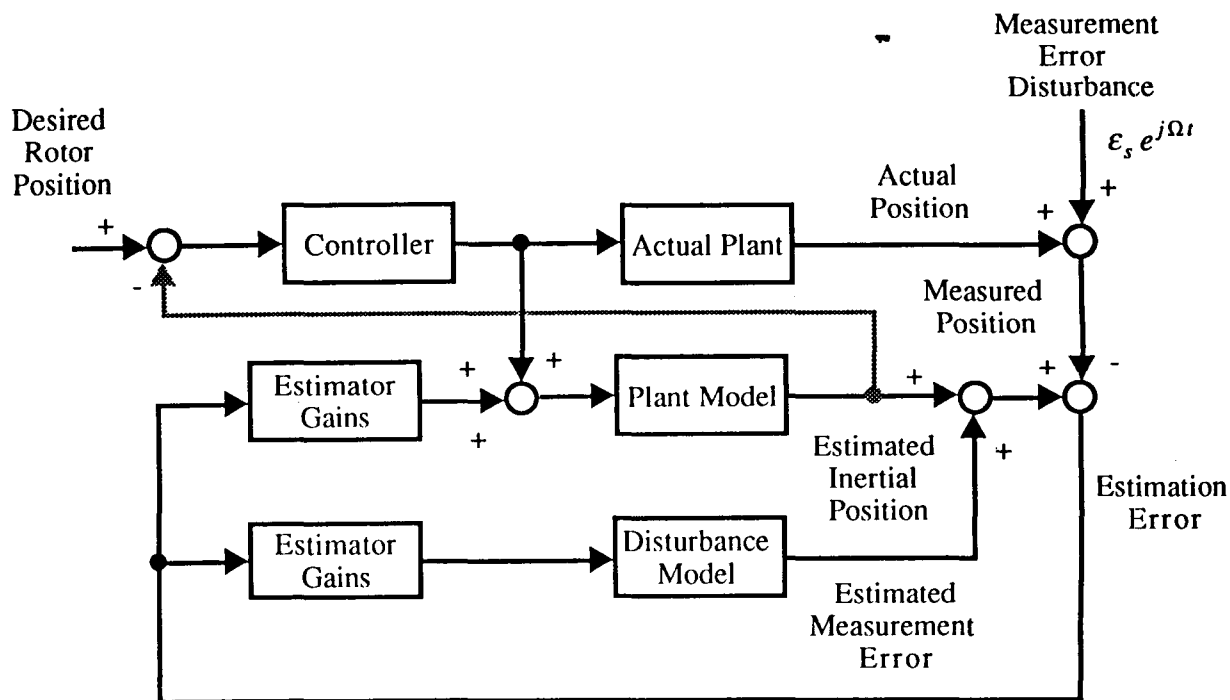
- o develop disturbance model**
- o combine plant and disturbance models to design estimator**
- o given this structure, use appropriate tools to design controller**

Attributes

- o good in rotor dynamic problems**
- o does not affect stability**
- o quick convergence of estimates**

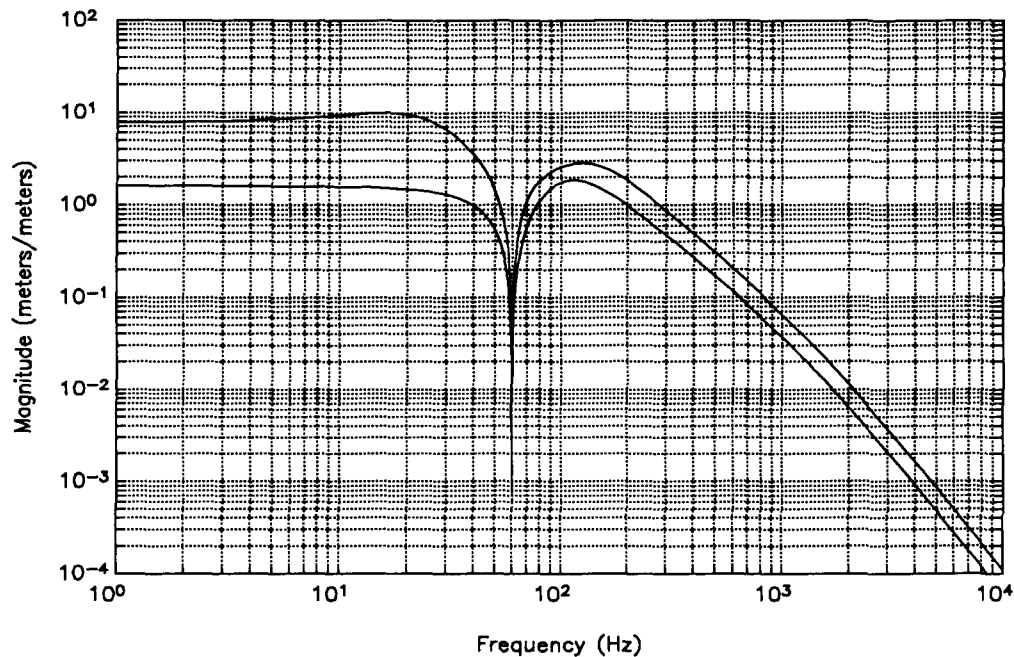
A block diagram of the closed loop DAC system is presented in the figure below. The system consists of the actual plant, the plant and disturbance models and the controller. The plant and disturbance models make up the DAC estimator. The disturbance model represents the measurement error disturbance at each sensor. The disturbance estimates are injected at the plant model output, thereby producing estimates of the corrupted measurements. The differences in the estimated and actual measurements are fed back through the estimator gains to drive the plant and disturbances estimation errors to zero. The purpose of the disturbance model is to be able to distinguish between the plant and disturbance states, in the presence of disturbances. By feeding back the estimated inertial positions, uncorrupted by the synchronous disturbances, the rotor will spin about its inertial axis. For a variable speed system, the rotational speed is fed to the controller to update the disturbance model. Hence, the oscillator will track the rotational speed and reduce the vibrations as the speed changes.

BLOCK DIAGRAM OF DAC SYSTEM



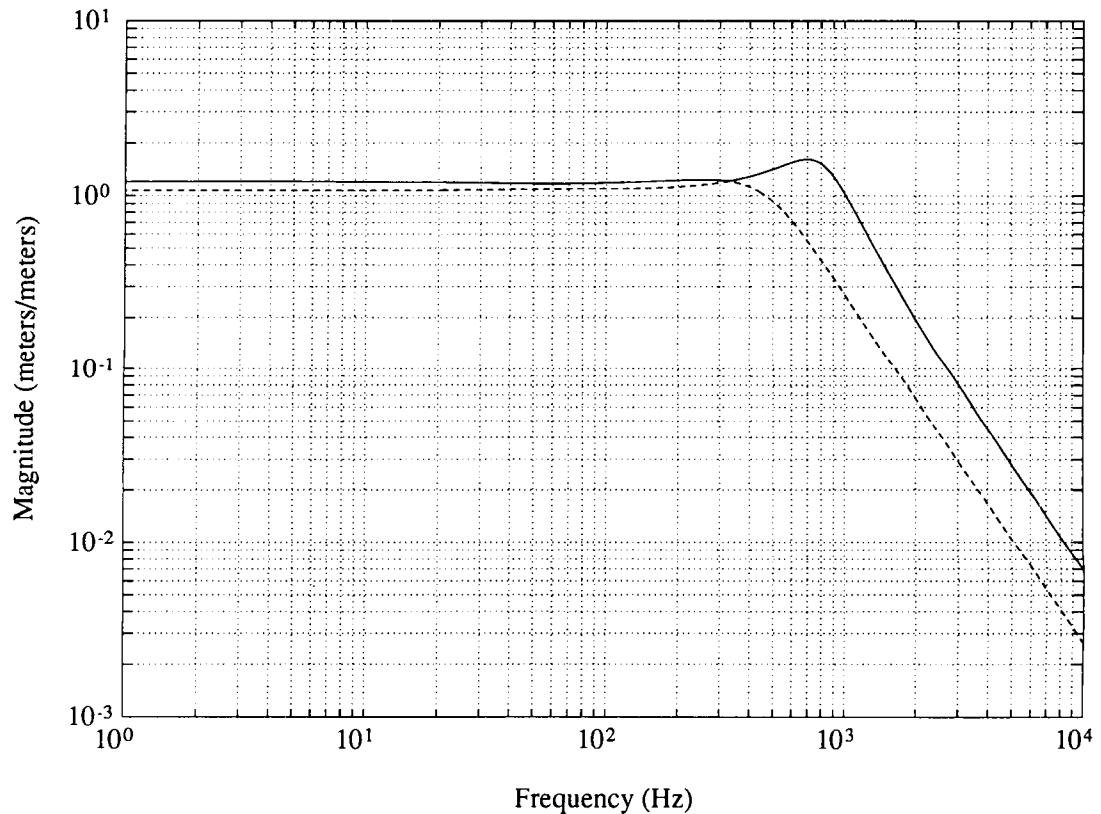
The figure below is a plot of the singular values of the closed loop transfer function matrix from the measurement error disturbance inputs to the inertial position outputs. The area of interest is at 60 Hz, the rotational frequency. The infinite notch at 60 Hz illustrates that the measurement error disturbance is completely removed from the system. It is important to note that both the maximum and the minimum singular values are zero at 60 Hz, resulting in complete ideal attenuation of the measurement error disturbances.

SINGULAR VALUE PLOT FROM MEASUREMENT ERROR DISTURBANCE TO INERTIAL POSITION



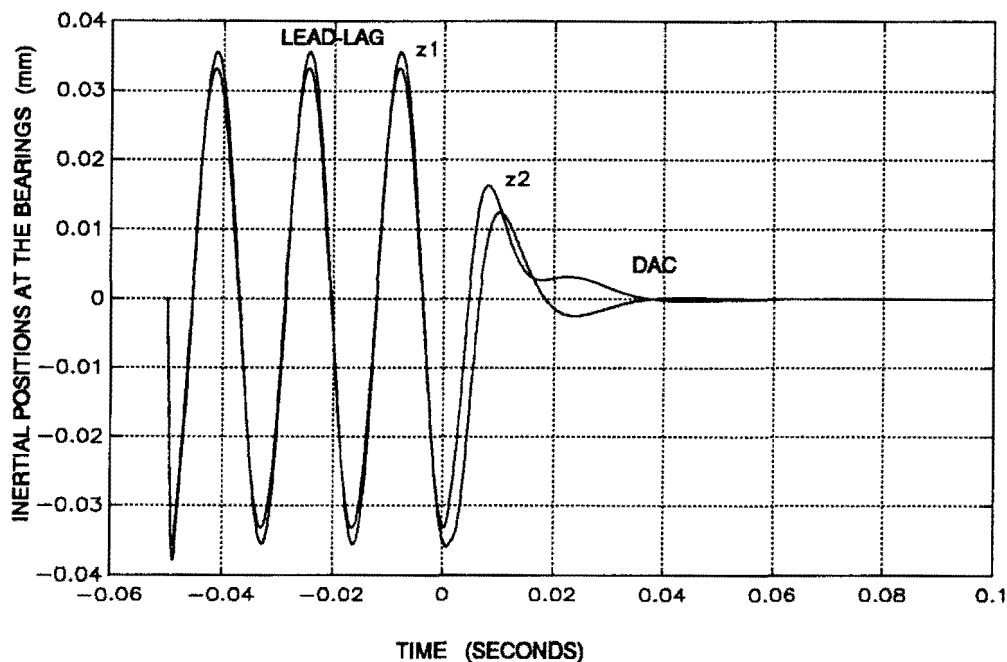
The notch does not occur in the transfer function between the commanded input and the inertial output as shown in the figure below. The DAC estimator, unlike a notch filter, rejects the synchronous disturbances without attenuating the control signals at 60 Hz. The system is therefore stable at all rotational speeds.

SINGULAR VALUE PLOT FROM COMMANDED INPUT TO INERTIAL POSITION



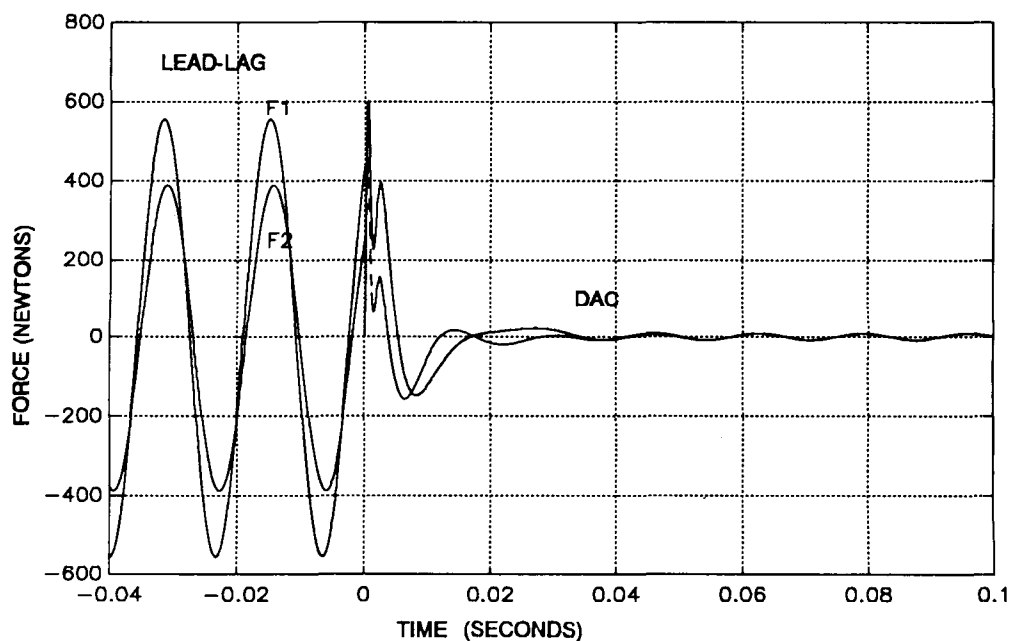
The figure presented below is the time simulation of the inertial position response to the measurement error disturbance input. At negative time, the rotor is spinning around its geometric center because the feedback variables are the measured positions. Then at time $t=0$, the DAC estimator is turned on and the feedback variable becomes the estimated center of mass position. As a result of the DAC estimator, the rotor quickly reaches the desired steady-state position, spinning about its inertial axis. This graph represents the motion of the inertial positions in the X plane. Due to symmetry, the Y plane is identical, 90 degrees out of phase.

CENTER OF MASS POSITION RESPONSE TO MEASUREMENT ERROR DISTURBANCE



The bearing force response to the measurement error disturbance is shown in the figure below, again illustrating the dynamics of the X plane. The DAC estimator is turned on at time $t=0$, hence the feedback variables are changed from the corrupted measurement positions to the estimated inertial positions. As shown, the forces on the rotor are reduced significantly.

CENTER OF MASS FORCE RESPONSE TO MEASUREMENT ERROR DISTURBANCE



References

1. Gaffney, M.S. "Synchronous Vibration Reduction In Magnetic Bearing Systems". S.M. Thesis, Massachusetts Institute of Technology, Cambridge, Massachusetts, June 1990.
2. Sievers, L.A., vonFlotow, A.H., "Comparison and Extensions of Control Methods for Narrowband Disturbance Rejection". NCA-Vol.8, A.S.M.E. Winter Annual Meeting, Dallas, Texas, November 1990
3. Johnson, B.G., Gaffney, M.S. "Demonstration of Active Vibration Control on the JPL Cryocooler Vibration Testbed". SatCon Technology Corporation Final Report R30-91, Cambridge, MA, August 1991
4. Johnson, B.G, Hochney, R.L., Misovec, K.M. "Active Synchronous Response Control of Rigid-Body Rotors". IMEchE 4th International Conference on Vibrations Machinery, September, 1988
5. Humphris, R.R., Knospe, C.R., Sundaram, S. "Dynamic Balancing With Open Loop Control of Magnetic Bearings". 26th Annual IECEC, Boston, MA, August 1991
6. Gaffney, M.S., Johnson, B.G., "Application of Disturbance Accommodation Control to Reduce Vibrations in Magnetic Bearing Systems". NCA-Vol.8, A.S.M.E. Winter Annual Meeting, Dallas, Texas, November 1990
7. Downer, J.R., et. al., "Cryogenically-Cooled Magnetic Journal Bearings". SatCon Final Report R08-91, Cambridge, MA, March 1991
8. Johnson, C.D., "Theory of Disturbance Accommodating Controllers, Chapter 7, Control and Dynamic Systems Vol. 12 (D.T. Leondes, Ed.), Academic Press, New York, 1976

N 9 2 - 2 7 7 3 0

**Dynamics and Control of High Precision
Magnetically Levitated Vibration Isolation Systems**

K. Youcef-Toumi and T-J Yeh

**Department of Mechanical Engineering
Massachusetts Institute of Technology**

**Mailing Address:
Kamal Youcef-Toumi
M.I.T. Room 35-233
77 Massachusetts Avenue
Cambridge, Massachusetts 02139
Telephone: (617) 253-2216**

Abstract

Vibration control of flexible structures has received a great deal of interest in recent years. Several authors have investigated this topic in the areas of robot manipulators, space structures and flexible rotors. Key issues associated with the dynamics and control of vibration isolation systems are addressed in this paper.

Among other important issues to consider in the control of such systems, the location and number of actuators and sensors are essential to effectively control and suppress vibration. In this paper, we first address the selection of proper actuator and sensor locations leading to a controllable and observable system. The Rayleigh-Ritz modal analysis method is used to develop a lumped-parameter model of a flexible vibration isolation table top. This model is then used to investigate the system's controllability and observability including the coupling effects introduced by the magnetic bearing. This analysis results in necessary and sufficient conditions for proper selection of actuator and sensor locations. These locations are also important for both controller system's complexity and stability point of views. A favorable pole-zero plot of the open loop transfer functions is presented. Necessary and sufficient conditions for reducing the controller complexity are derived. The results are illustrated by examples using approximate mode shape functions.

Contents

| | | |
|-----|---|-----|
| 1 | Introduction | 152 |
| 2 | Problem Formulation | 153 |
| 3 | Controllability and Observability | 156 |
| 3.1 | Analysis without the Coupling Effect of Actuator Dynamics | 156 |
| 3.2 | Analysis with the Coupling Effect of Actuator Dynamics | 159 |
| 3.3 | Examples of Locating Actuators (Sensors) to Achieve Controllability (Observability) | 161 |
| 4 | Control System Characteristics for Collocated and Noncollocated Configurations | 164 |
| 5 | Effects of Damping | 172 |
| 6 | Conclusion | 173 |
| A | Rayleigh-Ritz method | 173 |

1 Introduction

Sensitive instruments and precision machines have made it possible to investigate phenomena with dimensions of the nanometer scale. For example, current Michelson-type optical heterodyne interferometer can measure displacement with a resolution in the nanometer range [1]. Scanning Tunneling Microscopes (STM's) which use flexure linkage structures have Ångstrom resolution and range of motion on the order of one micron [2]. In these and other applications, vibration from ground motion and other disturbances, which may be in the micrometer level, will seriously degrade the overall system performance.

Traditional vibration isolation techniques can be generally divided into two categories: 1) passive and 2) active. Passive vibration isolation often involves the use of metal springs, elastomers, rubber, air springs or other passive elements to either absorb or dissipate vibration energy [3]. Passive techniques offer simple, inexpensive and reliable means to protect mechanical systems from environmental vibration. However, it is not possible for the passive vibration isolation methods to influence the system dynamics and adapt in real time. On the other hand, active vibration isolation techniques which use force generators that are adaptable to excitation and response characteristics of the system can actively counteract and cancel the undesirable vibration. In addition, the active system provides significantly superior vibration isolation performance. The control force is often realized by pneumatic or electromechanical actuators. For example, Sandercock [4] proposed to combine both the active controlled electromechanical actuators and passive elastomers in building a dynamic antivibration system and has already become a commercialized product. In this system, the electromechanical actuators offer the damping force proportional to the absolute velocity of the table top while the elastomers provide the required compliance. This system is said to achieve $3\mu\text{gs}$ (3 mgal) RMS acceleration isolation performance [5].

In addition to the isolation of ground vibration, the suppression of induced vibration of work surface (or the table top plate) is also an important factor in vibration isolation system design. Since the table plate is not a perfect rigid body and thus considered flexible, the resonant frequencies of the table can be excited by the environmental disturbances such as acoustic noise, payload change, or the motion of a positioning system on the table top. In this case, the vibration modes of the table top will be excited and the performance of the system may degrade.

The use of actively controlled magnetic bearings is considered to not only achieve ultra high performance vibration isolation from the environment but also to suppress the induced vibration of the table top. Because of the unstable nature of the magnetic bearing, robust control scheme is needed to guarantee the performance. But prior to the control system design, the sensors and magnetic actuators should be properly located so that the vibration can be reduced effectively. As far as the flexibility of the top plate is concerned, this is related to the mode shapes of different vibration mode. This paper focuses on the actuator and sensor locations from the system controllability and observability points of view.

Controllability and observability of distributed systems has been investigated by Hughes and Skelton [6], and Yang and Mote [7]. In [6] the controllability and observability condition of linear matrix-second-order systems are discussed. But since the orthogonality of mode shape functions wasn't used, no direct relationship between the mode line and the condition of controllability and observability is derived. In [7], although the locations of actuators and sensors were related to the modeshape functions, the examples discussed are the axially moving string with clamped ends and rotating circular disk with clamp rim and thus the rigid body motion is not considered. Also the sensors assumed in their derivation are the position and velocity sensors.

In this paper, it is of interest to investigate the controllability and observability of rigid body motion of a magnetically suspended vibration isolation table top. In the case, the table top will be modelled as a rectangular plate with free edges. Due to the importance of the inertial acceleration feedback in vibration isolation systems, the accelerometer outputs are also included in the derivation of the observability condition. Since the prototype design uses magnetic bearings for levitation and vibration control, the unstable nature of the actuators is coupled to the overall

system dynamics. The controllability and observability analysis presented in this work takes this fact into account. In order to apply the results to the system design, normalized frequencies and a map depicting the node lines corresponding to table top were approximated using the Rayleigh-Ritz method.

Improper placement of actuators and sensors can lead to complex control system designs even though these locations may correspond to a controllable and observable system. For example, a conventional flexible arm has zeros in the right half plane if the actuator and sensor are noncollated. This nonminimum phase nature adds additional phase lag to the system and results in poor system performance [8]. Such issues have motivated us to investigate the relationship between proper actuator/sensor locations and favorable open loop system behavior.

In this paper, the problem formulation is presented in section 2. The selection of proper actuator and sensor locations leading to a controllable and observable system is then discussed in section 3. A lumped-parameter model of a flexible vibration isolation table top is used to investigate the system's controllability and observability including the coupling effects introduced by the magnetic bearing. This analysis results in necessary and sufficient conditions for proper selection of actuator and sensor locations. Section 4 presents a favorable pole-zero plot of the open loop transfer functions. Necessary and sufficient conditions for reducing the controller complexity are derived. The results are illustrated by examples using approximate mode shape functions. Such information is important for the overall design of ultra high performance vibration isolation systems. For example, critical frequency regions in the transmissibility curves can be identified and taken into account in the control system design.

2 Problem Formulation

Consider a thin rectangular table top plate with free edges as shown in Figure 1, assuming that the plate is made of homogeneous, isotropic material, then the equation of motion is [9],

$$\rho h \ddot{w}(x, y, t) + D \nabla^4 w(x, y, t) = f(x, y, t) \quad (1)$$

where ρ is the density of the plate, h is the plate thickness, $w(x, y, t)$ is the transverse deflection, D is the flexural rigidity of the plate and is equal to $\frac{Eh^3}{12(1-\nu^2)}$, E is the Young's modulus, ν is Poisson's ratio and ∇^4 represents the biharmonic operator. Moreover, since we will first deal with the controllability and observability issues in this paper, only the control force is taken into account and other forces such as gravity and disturbances are not included. Therefore, in such a case $f(x, y, t)$ denotes the control force per unit area of the plate. Because there is no lateral constraint, the boundary conditions of the plate are given by [10],

$$\begin{aligned} (i) \quad & \frac{\partial^2}{\partial y^2} w(x, y, t) + \nu \frac{\partial^2}{\partial x^2} w(x, y, t) = 0 \Big|_{0 \leq x \leq a} & \text{for } y = 0, y = b \\ (ii) \quad & \frac{\partial^3}{\partial y^3} w(x, y, t) + (2 - \nu) \frac{\partial^3}{\partial y \partial x^2} w(x, y, t) = 0 \Big|_{0 \leq x \leq a} & \text{for } y = 0, y = b \\ (iii) \quad & \frac{\partial^2}{\partial x^2} w(x, y, t) + \nu \frac{\partial^2}{\partial y^2} w(x, y, t) = 0 \Big|_{0 \leq y \leq b} & \text{for } x = 0, x = a \\ (iv) \quad & \frac{\partial^3}{\partial x^3} w(x, y, t) + (2 - \nu) \frac{\partial^3}{\partial x \partial y^2} w(x, y, t) = 0 \Big|_{0 \leq y \leq b} & \text{for } x = 0, x = a \end{aligned} \quad (2)$$

The physical meaning of these four boundary conditions is that the bending moments, twist moments, and shear forces along the four edges are equal to zero.

In order to develop and implement a finite dimensional controller, a lumped parameter model of the system is needed for the distributed system described by Equation (1). Because the equation is a partial differential equation, in order to apply the control law, the system should be discretized to obtain a lumped-parameter model. To achieve this we consider only n modes in the dynamic equations and assume that the influence of the higher modes is negligible. The transverse deflection

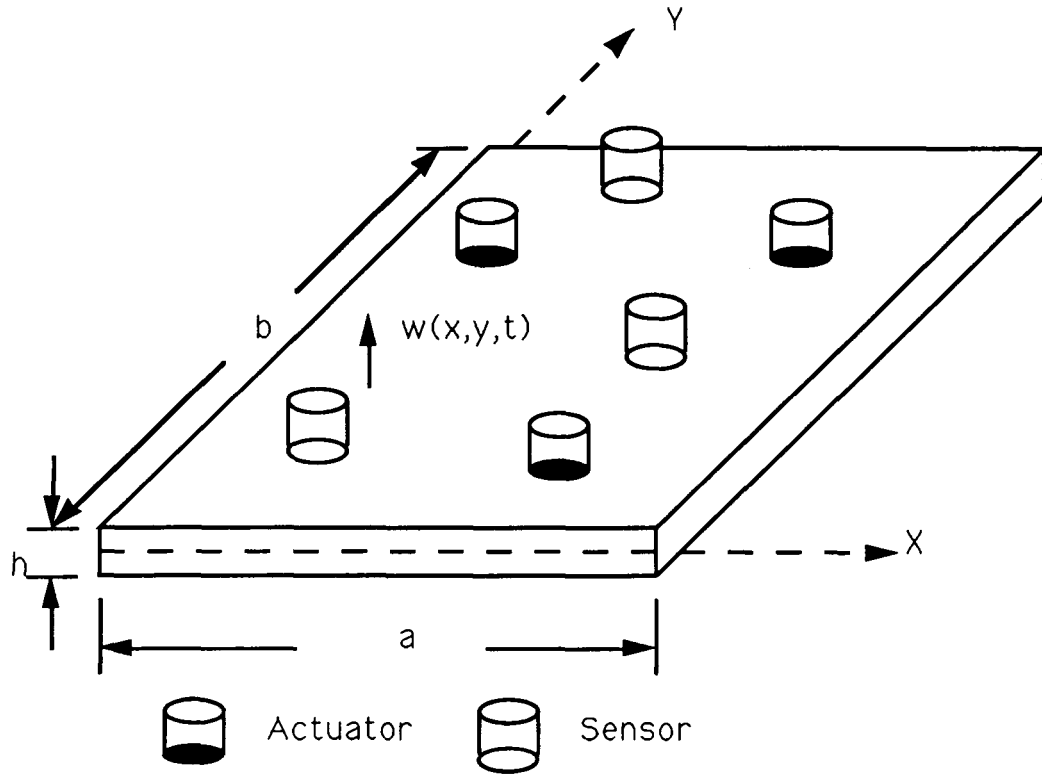


Figure 1: Thin rectangular plate with free edges

$w(x, y, t)$ can be represented by means of a series of n mode shape functions $\phi_i(x, y)$ of the system and expressed in the following form,

$$w(x, y, t) = \sum_{i=1}^n a_i(t) \phi_i(x, y) = \mathbf{a}^T(t) \mathbf{\Phi}(x, y) \quad (3)$$

where $a_i(t)$ ($i = 1, 2, \dots, n$) are the generalized coordinates. We further assume that the plate is supported by m discrete point force actuators located at (x_i, y_i) and $i = 1, 2, \dots, m$. Therefore the control force can be expressed as,

$$f(x, y, t) = \sum_{i=1}^m f_i(t) \delta_i(x, y) = \mathbf{f}^T(t) \mathbf{\Delta}(x, y) \quad (4)$$

where $f_i(t)$ is the control force exerted by the i th actuator and $\delta_i(x, y)$ is the impulse function at (x_i, y_i) . Using Equation (3), the kinetic energy \mathcal{T} and potential energy \mathcal{V} of the plate can be written in terms of generalized coordinates and mode shape functions as [9],

$$\begin{aligned} \mathcal{T} &= \frac{1}{2} \int_A \rho h \dot{w}^2(x, y, t) dA = \frac{1}{2} \int_A \rho h \left[\sum_{i=1}^n \dot{a}_i(t) \phi_i(x, y) \right]^2 dA \\ &= \frac{1}{2} \int_A \rho h (\dot{\mathbf{a}}^T \mathbf{\Phi}(x, y))^2 dA = \frac{1}{2} \dot{\mathbf{a}}^T(t) \mathbf{M} \dot{\mathbf{a}}(t) \end{aligned} \quad (5)$$

where the inertia matrix \mathbf{M} is given by,

$$\mathbf{M} = \rho h \int_A \mathbf{\Phi}(x, y) \mathbf{\Phi}^T(x, y) dA$$

and

$$\mathcal{V} = \frac{D}{2} \int_A [w_{xx}^2 + w_{yy}^2 + 2\nu w_{xx} w_{yy} + 2(1 - \nu)(w_{xy})^2] dA$$

$$\begin{aligned}
&= \frac{D}{2} \int_A [(\mathbf{a}^T(t) \Phi_{xx})^2 + (\mathbf{a}^T(t) \Phi_{yy})^2 + 2\nu \mathbf{a}^T(t) \Phi_{xx} \Phi_{yy}^T \mathbf{a}(t) \\
&\quad + 2(1-\nu)(\mathbf{a}^T(t) \Phi_{xy})^2] dA \\
&= \frac{1}{2} \mathbf{a}^T(t) \mathbf{K} \mathbf{a}(t)
\end{aligned} \tag{6}$$

where the stiffness matrix \mathbf{K} is given by ,

$$\begin{aligned}
\mathbf{K} = D \int_A &(\Phi_{xx} \Phi_{xx}^T + \Phi_{yy} \Phi_{yy}^T \\
&+ 2\nu \Phi_{xx} \Phi_{yy}^T + 2(1-\nu) \Phi_{xy} \Phi_{xy}^T) dA
\end{aligned}$$

Also the virtual work due to the m point force actuators is:

$$\begin{aligned}
\delta W &= \int_A f(x, y, t) \delta w(x, y, t) dA \\
&= \int_A \mathbf{f}^T(t) \Delta(x, y) \Phi^T(x, y) \delta \mathbf{a}(t) dA \\
&= \mathbf{f}^T(t) \left[\int_A \Delta(x, y) \Phi^T(x, y) dA \right] \delta \mathbf{a}(t) \\
&= \mathbf{f}^T(t) \mathbf{R} \delta \mathbf{a}(t)
\end{aligned} \tag{7}$$

where

$$\mathbf{R} = \begin{bmatrix} \phi_1^1 & \phi_2^1 & \dots & \phi_n^1 \\ \phi_1^2 & \phi_2^2 & \dots & \phi_n^2 \\ \vdots & \vdots & \dots & \vdots \\ \phi_1^m & \phi_2^m & \dots & \phi_n^m \end{bmatrix}$$

and ϕ_i^j indicates that the i th mode shape is evaluated at location (x_j, y_j) , that is $\phi_i(x_j, y_j)$. Substituting Equations (5), (6), (7) into the variation indicator of the system and applying Hamilton principle, the equations of motion are obtained as,

$$\mathbf{M} \ddot{\mathbf{a}}(t) + \mathbf{K} \mathbf{a}(t) = \mathbf{R}^T \mathbf{f}(t) \tag{8}$$

To transform Equation (8) into a state space form, a state vector $\mathbf{x}^T = [\mathbf{a}^T(t) \quad \dot{\mathbf{a}}^T(t)]$ is introduced so that Equation (8) can be written as,

$$\dot{\mathbf{x}} = \mathbf{A} \mathbf{x} + \mathbf{B} \mathbf{f} \tag{9}$$

where the matrices \mathbf{A} and \mathbf{B} of orders $2n \times 2n$ and $2n \times m$ respectively are given by,

$$\mathbf{A} = \begin{bmatrix} \mathbf{0} & \mathbf{I} \\ -\mathbf{M}^{-1} \mathbf{K} & \mathbf{0} \end{bmatrix}, \quad \mathbf{B} = \begin{bmatrix} \mathbf{0} \\ \mathbf{M}^{-1} \mathbf{R}^T \end{bmatrix} \tag{10}$$

Now that the system equations are formulated, we turn to the system outputs. We consider k sensors located at $(x_i, y_i)^1$ ($i = 1, 2, \dots, s$). Assuming that the first p sensors are position sensors, $(p+1)$ th to $(p+q)$ th sensors can measure the velocity of the individual points, and the last $s-p-q$ sensors are accelerometers. The outputs from the position sensors can be written as:

$$y_j(t) = \sum_{i=1}^n a_i(t) \phi_i(x_j, y_j) \quad j = 1, 2, \dots, p \tag{11}$$

¹Even though we use the same notation (x_i, y_i) 's to represent the locations for both actuators and sensors, the point (x_i, y_i) for i th actuator may not be the same as the point (x_i, y_i) for i th sensor.

The outputs from the velocity sensors are :

$$y_j(t) = \sum_{i=1}^n \dot{a}_i(t) \phi_i(x_j, y_j) \quad j = p+1, p+2, \dots, p+q \quad (12)$$

Finally, the accelerometer outputs are:

$$y_j(t) = \sum_{i=1}^n \ddot{a}_i(t) \phi_i(x_j, y_j) \quad j = p+q+1, p+q+2, \dots, s \quad (13)$$

Note that $\dot{a}_i(t)$ and $\ddot{a}_i(t)$ represent the first and second time derivatives of the generalized coordinate $a_i(t)$. The overall output equations can now be expressed in matrix form using Equation (11), (12) and (13),

$$\begin{aligned} \mathbf{y} &= \begin{bmatrix} \mathbf{P} & \mathbf{0} \\ \mathbf{0} & \mathbf{Q} \\ \mathbf{0} & \mathbf{0} \end{bmatrix} \mathbf{x}(t) + \begin{bmatrix} \mathbf{0} \\ \mathbf{0} \\ \mathbf{S} \end{bmatrix} \ddot{\mathbf{a}}(t) \\ &= \begin{bmatrix} \mathbf{P} & \mathbf{0} \\ \mathbf{0} & \mathbf{Q} \\ -\mathbf{SM}^{-1}\mathbf{K} & \mathbf{0} \end{bmatrix} \mathbf{x}(t) + \begin{bmatrix} \mathbf{0} \\ \mathbf{0} \\ \mathbf{M}^{-1}\mathbf{R}^T \end{bmatrix} \mathbf{f}(t) \\ &= \mathbf{Cx} + \mathbf{Df} \end{aligned} \quad (14)$$

where

$$\begin{aligned} \mathbf{P}_{p \times n} &= \begin{bmatrix} \phi_1^1 & \phi_2^1 & \dots & \phi_n^1 \\ \phi_1^2 & \phi_2^2 & \dots & \phi_n^2 \\ \vdots & \vdots & \dots & \vdots \\ \phi_1^p & \phi_2^p & \dots & \phi_n^p \end{bmatrix}, & \mathbf{Q}_{q \times n} &= \begin{bmatrix} \phi_1^{p+1} & \phi_2^{p+1} & \dots & \phi_n^{p+1} \\ \phi_1^{p+2} & \phi_2^{p+2} & \dots & \phi_n^{p+2} \\ \vdots & \vdots & \dots & \vdots \\ \phi_1^{p+q} & \phi_2^{p+q} & \dots & \phi_n^{p+q} \end{bmatrix} \\ \mathbf{S}_{s \times n} &= \begin{bmatrix} \phi_1^{p+q+1} & \phi_2^{p+q+1} & \dots & \phi_n^{p+q+1} \\ \phi_1^{p+q+2} & \phi_2^{p+q+2} & \dots & \phi_n^{p+q+2} \\ \vdots & \vdots & \dots & \vdots \\ \phi_1^s & \phi_2^s & \dots & \phi_n^s \end{bmatrix} \end{aligned}$$

Equation (9) and (14) can now be analyzed in order to determine the conditions of controllability and observability. These issues are addressed in the following section.

3 Controllability and Observability

3.1 Analysis without the Coupling Effect of Actuator Dynamics

The $2n$ th order system described by Equations (9) and (14) is controllable if and only if

$$\text{rank}(\mathcal{C}) = \text{rank} \begin{bmatrix} \mathbf{B} & \mathbf{AB} & \dots & \mathbf{A}^{2n-1}\mathbf{B} \end{bmatrix} = 2n \quad (15)$$

and the system is observable if and only if

$$\text{rank}(\mathcal{O}) = \text{rank} \begin{bmatrix} \mathbf{C}^T & \mathbf{A}^T\mathbf{C}^T & \dots & (\mathbf{A}^T)^{2n-1}\mathbf{C}^T \end{bmatrix} = 2n \quad (16)$$

In order to simplify the problem and deal with diagonal \mathbf{M} and \mathbf{K} matrices, the orthogonality of the eigenfunctions is used [11]. Under this assumption, the $n \times n$ inertia and stiffness matrices take

the form,

$$\mathbf{M} = \begin{bmatrix} M_1 & 0 & \dots & 0 \\ 0 & M_2 & \dots & 0 \\ \vdots & \vdots & \dots & \vdots \\ 0 & 0 & \dots & M_n \end{bmatrix}, \quad \mathbf{K} = \begin{bmatrix} K_1 & 0 & \dots & 0 \\ 0 & K_2 & \dots & 0 \\ \vdots & \vdots & \dots & \vdots \\ 0 & 0 & \dots & K_n \end{bmatrix} \quad (17)$$

where $M_i, K_i \geq 0$. The matrix $\mathbf{M}^{-1}\mathbf{K}$ is also diagonal with diagonal components corresponding to the system eigenvalues,

$$\mathbf{M}^{-1}\mathbf{K} = \begin{bmatrix} \lambda_1 & 0 & \dots & 0 \\ 0 & \lambda_2 & \dots & 0 \\ \vdots & \vdots & \dots & \vdots \\ 0 & 0 & \dots & \lambda_n \end{bmatrix} \quad (18)$$

The eigenvalues $\lambda_1, \lambda_2, \dots, \lambda_n$ are equal to the square of natural frequencies of the system. Because a thin plate with free edges is considered, the first three eigenvalues are equal to zero, i.e., $\lambda_1 = \lambda_2 = \lambda_3 = 0$. The modes associated with these eigenvalues correspond to the translation parallel to the z axis and rigid body rotations along x and y axes. In the following discussion, it is assumed that $n > 3$ so that the vibration modes are taken into account and all other eigenvalues $\lambda_4, \lambda_5, \dots, \lambda_n$ are positive. In order to investigate the condition for this system to be controllable and observable, the controllability and observability matrices are calculated and discussed as follows.

In our case, the controllability matrix has the form,

$$\mathbf{C} = \begin{bmatrix} 0 & \mathbf{H} & 0 & \mathbf{JH} & \dots & 0 & \mathbf{J}^{n-1}\mathbf{H} \\ \mathbf{H} & 0 & \mathbf{JH} & 0 & \dots & \mathbf{J}^{n-1}\mathbf{H} & 0 \end{bmatrix} \quad (19)$$

where

$$\mathbf{H}_{n \times m} = \mathbf{M}^{-1}\mathbf{R}^T = \begin{bmatrix} \frac{1}{M_1}\phi_1^1 & \frac{1}{M_1}\phi_1^2 & \dots & \frac{1}{M_1}\phi_1^m \\ \frac{1}{M_2}\phi_2^1 & \frac{1}{M_2}\phi_2^2 & \dots & \frac{1}{M_2}\phi_2^m \\ \vdots & \vdots & \dots & \vdots \\ \frac{1}{M_n}\phi_n^1 & \frac{1}{M_n}\phi_n^2 & \dots & \frac{1}{M_n}\phi_n^m \end{bmatrix}$$

$$\mathbf{J}_{n \times n} = -\mathbf{M}^{-1}\mathbf{K} = \begin{bmatrix} 0 & 0 & 0 & 0 & 0 & \dots & 0 \\ 0 & 0 & 0 & 0 & 0 & \dots & 0 \\ 0 & 0 & 0 & 0 & 0 & \dots & 0 \\ 0 & 0 & 0 & -\lambda_4 & 0 & \dots & 0 \\ 0 & 0 & 0 & 0 & -\lambda_5 & \dots & 0 \\ \vdots & \vdots & \vdots & \vdots & \vdots & \dots & \vdots \\ 0 & 0 & 0 & 0 & 0 & \dots & -\lambda_n \end{bmatrix}$$

Since there are $2n$ states (n position components and n velocity components), the controllability matrix should have rank $2n$ which means that $2n$ rows must be linearly independent. It is obvious that the upper $n \times 2mn$ matrix and the lower $n \times 2mn$ matrix are almost the same except that they are shifted by a series of $n \times m$ 0 matrices. Therefore, if n linearly independent rows can be obtained from the upper $n \times mn$ submatrix, the lower $n \times mn$ matrix will also have n linearly independent rows and these two sets of n linearly independent rows are linearly independent to each other. If we interchange the columns of the upper submatrix and put all the 0 columns to the right hand side without changing the rank of the submatrix, we can deduce that the system is controllable if and only if the $n \times mn$ matrix \mathbf{L} has rank n , where

$$\mathbf{L} = [\mathbf{H} \quad \mathbf{JH} \quad \dots \quad \mathbf{J}^{n-1}\mathbf{H}] \quad (20)$$

Therefore, the system is controllable if and only if $\text{rank}(\mathbf{L}) = n$. Due to the diagonal structure of \mathbf{J} matrix, the conditions for the \mathbf{L} matrix to have rank n are [12]:

1. For λ_i with no repeated eigenvalues, the i th row of the \mathbf{H} matrix should be a nonzero vector.
2. For repeated eigenvalues of multiplicity ℓ , $\lambda_{i+1} = \lambda_{i+2} = \dots = \lambda_{i+\ell}$, the $(i+1)$ th, $(i+2)$ th, \dots , $(i+\ell)$ th rows of \mathbf{H} should be linearly independent.

On the other hand, the observability matrix takes the form,

$$\mathcal{O} = \begin{bmatrix} \mathbf{P}^T & \mathbf{0} & \mathbf{J}\mathbf{S}^T & \mathbf{0} & \mathbf{J}\mathbf{Q}^T & \mathbf{0} & \dots & \mathbf{0} & \mathbf{J}^n\mathbf{Q}^T & \mathbf{0} \\ \mathbf{0} & \mathbf{Q}^T & \mathbf{0} & \mathbf{P}^T & \mathbf{0} & \mathbf{J}\mathbf{S}^T & \dots & \mathbf{J}^{n-1}\mathbf{P}^T & \mathbf{0} & \mathbf{J}^n\mathbf{S}^T \end{bmatrix} \quad (21)$$

To investigate the rank of this matrix, we rearrange it as follows:

$$\mathcal{O}' = \begin{bmatrix} \mathbf{P}^T & \mathbf{J}\mathbf{S}^T & \mathbf{J}\mathbf{Q}^T & \dots & \mathbf{J}^n\mathbf{Q}^T & \mathbf{0} & \mathbf{0} & \mathbf{0} & \dots & \mathbf{0} \\ \mathbf{0} & \mathbf{0} & \mathbf{0} & \dots & \mathbf{0} & \mathbf{P}^T & \mathbf{Q}^T & \mathbf{J}\mathbf{S}^T & \dots & \mathbf{J}^n\mathbf{S}^T \end{bmatrix} \quad (22)$$

For the system to be observable, the following two conditions must be satisfied,

$$\text{rank} [\mathbf{P}^T \quad \mathbf{J}\mathbf{S}^T \quad \mathbf{J}\mathbf{Q}^T \quad \dots \quad \mathbf{J}^n\mathbf{Q}^T] = \text{rank} [\mathbf{H}' \quad \mathbf{J}\mathbf{H}' \quad \dots \quad \mathbf{J}^{n-1}\mathbf{H}'] = n \quad (23)$$

where $\mathbf{H}' = [\mathbf{P}^T \quad \mathbf{J}\mathbf{S}^T \quad \mathbf{J}\mathbf{Q}^T]$, and

$$\text{rank} [\mathbf{P}^T \quad \mathbf{Q}^T \quad \mathbf{J}\mathbf{S}^T \quad \dots \quad \mathbf{J}^n\mathbf{S}^T] = \text{rank} [\mathbf{H}'' \quad \mathbf{J}\mathbf{H}'' \quad \dots \quad \mathbf{J}^{n-1}\mathbf{H}''] = n \quad (24)$$

where $\mathbf{H}'' = [\mathbf{P}^T \quad \mathbf{Q}^T \quad \mathbf{J}\mathbf{S}^T]$. By substituting the \mathbf{P} , \mathbf{Q} , and \mathbf{S} matrices, the \mathbf{H}' , \mathbf{H}'' matrices in Equation (23) and (24) can be represented as,

$$\mathbf{H}' = \begin{bmatrix} \phi_1^1 & \dots & \phi_1^p & 0 & \dots & 0 & 0 & \dots & 0 \\ \phi_2^1 & \dots & \phi_2^p & 0 & \dots & 0 & 0 & \dots & 0 \\ \phi_3^1 & \dots & \phi_3^p & 0 & \dots & 0 & 0 & \dots & 0 \\ \phi_4^1 & \dots & \phi_4^p & (-\lambda_4)\phi_4^{p+1} & \dots & (-\lambda_4)\phi_4^{p+q} & (-\lambda_4)\phi_4^{p+q+1} & \dots & (-\lambda_4)\phi_4^s \\ \vdots & \dots & \vdots & \vdots & \dots & \vdots & \vdots & \dots & \vdots \\ \phi_n^1 & \dots & \phi_n^p & (-\lambda_n)\phi_n^{p+1} & \dots & (-\lambda_n)\phi_n^{p+q} & (-\lambda_n)\phi_n^{p+q+1} & \dots & (-\lambda_n)\phi_n^s \end{bmatrix} \quad (25)$$

and

$$\mathbf{H}'' = \begin{bmatrix} \phi_1^1 & \dots & \phi_1^p & \phi_1^{p+1} & \dots & \phi_1^{p+q} & 0 & \dots & 0 \\ \phi_2^1 & \dots & \phi_2^p & \phi_2^{p+1} & \dots & \phi_2^{p+q} & 0 & \dots & 0 \\ \phi_3^1 & \dots & \phi_3^p & \phi_3^{p+1} & \dots & \phi_3^{p+q} & 0 & \dots & 0 \\ \phi_4^1 & \dots & \phi_4^p & \phi_4^{p+1} & \dots & \phi_4^{p+q} & (-\lambda_4)\phi_4^{p+q+1} & \dots & (-\lambda_4)\phi_4^s \\ \vdots & \dots & \vdots & \vdots & \dots & \vdots & \vdots & \dots & \vdots \\ \phi_n^1 & \dots & \phi_n^p & \phi_n^{p+1} & \dots & \phi_n^{p+q} & (-\lambda_n)\phi_n^{p+q+1} & \dots & (-\lambda_n)\phi_n^s \end{bmatrix} \quad (26)$$

Due to the similarity between the observability Equations (23), (24) and the controllability Equation (20), the system is observable if both \mathbf{H}' and \mathbf{H}'' matrices satisfy conditions (1) and (2). Therefore, the relation between the location of actuators (sensors) and controllability (observability) can be obtained. These results are summarized in the following theorems.

Theorem 3.1 *If the k th mode is controllable (observable), then there exists at least one actuator (sensor) not located on the corresponding node loci.*

Proof: In condition (1), the i th row vector of \mathbf{H} (\mathbf{H}' , \mathbf{H}'') should be a nonzero vector. This corresponds to the situation that for every mode shape function $\phi_i(x, y)$ with no repeated eigenvalue, there exists one actuator (sensor) location (x_j, y_j) such that $\phi_i(x_j, y_j) = \phi_i^j$ is nonzero. \square

Theorem 3.2 ℓ modes with the same natural frequency ($\lambda_{i+1} = \lambda_{i+2} = \dots = \lambda_{i+\ell}$) are controllable (observable) if there exists at least ℓ actuators (sensors) located at points $(x_{j_\alpha}, y_{j_\alpha})$ ($\alpha = 1, 2, \dots, \ell$) such that

$$\det \begin{bmatrix} \phi_{i+1}^{j_1} & \phi_{i+1}^{j_2} & \dots & \phi_{i+1}^{j_\ell} \\ \vdots & \vdots & \dots & \vdots \\ \phi_{i+\ell}^{j_1} & \phi_{i+\ell}^{j_2} & \dots & \phi_{i+\ell}^{j_\ell} \end{bmatrix} \neq 0 \quad (27)$$

where $\phi_{i+1}, \phi_{i+2}, \dots, \phi_{i+\ell}$ are the mode shape functions or the eigenfunctions corresponding to this natural frequency.

Proof: In condition (2), the $(i+1)th, (i+2)th, \dots, (i+\ell)th$ rows of \mathbf{H} ($\mathbf{H}', \mathbf{H}''$) are linearly independent if there are ℓ linearly independent columns in the submatrix formed by the $i+1th, i+2th, \dots, i+\ellth$ rows of \mathbf{H} matrix. This corresponds to the situation for which every set of ℓ mode shape functions $\phi_{i+1}, \dots, \phi_{i+\ell}$ corresponding to same eigenvalue $\lambda_{i+1} = \lambda_{i+2} = \dots = \lambda_{i+\ell}$, there should exist a set of $(x_{j_\alpha}, y_{j_\alpha})$ ($\alpha = 1, 2, \dots, \ell$) such that Equation (27) is satisfied. \square

A direct application of this result is that there should be at least α actuators (sensors) not located at the intersections of all the node lines of the same natural frequencies to make these modes controllable (observable).

Theorem 3.3 The modes of a flexible plate cannot be controlled (observed) with less than three actuators (position sensors), nor is it possible to control (observe) them with more than three collinear actuators (sensors).

Proof: Since there are three zero eigenvalues corresponding to rigid body motion, it can therefore be concluded that there should exist a set of three actuator (or position sensor, due to the 0 submatrix in the upper-right corners of \mathbf{H}' and \mathbf{H}'' matrices) locations $(x_{j_1}, y_{j_1}), (x_{j_2}, y_{j_2}), (x_{j_3}, y_{j_3})$ so that,

$$\det \begin{bmatrix} \phi_1^{j_1} & \phi_1^{j_2} & \phi_1^{j_3} \\ \phi_2^{j_1} & \phi_2^{j_2} & \phi_2^{j_3} \\ \phi_3^{j_1} & \phi_3^{j_2} & \phi_3^{j_3} \end{bmatrix} \neq 0 \quad \text{for some } j_1, j_2, j_3 \text{ between 1 and } m(p) \quad (28)$$

$\phi_1(x, y)$, $\phi_2(x, y)$ and $\phi_3(x, y)$ denote the first three mode shape functions of the plate which correspond to one parallel translation and two rigid body rotations. Assuming $\phi_1(x, y) = 1$, $\phi_2(x, y) = x$, $\phi_3(x, y) = y$, Equation (28) implies that there exists three actuator (position sensor) locations (x_{j_i}, y_{j_i}) ($i = 1, 2, 3$) such that,

$$\det \begin{bmatrix} 1 & 1 & 1 \\ x_{j_1} & x_{j_2} & x_{j_3} \\ y_{j_1} & y_{j_2} & y_{j_3} \end{bmatrix} \neq 0 \quad \text{for some } j_1, j_2, j_3 \text{ between 1 and } m(p) \quad (29)$$

which means that these three points are not collinear. \square

Corollary 3.1 The minimum number of properly located actuators (sensors) necessary to control (observe) the modes of a flexible plate is equal to $\max \{ 3, \text{multiplicity of eigenvalue of the modes to control (observe)} \}$.

Proof: This is the direct result from the previous three theorems. \square

3.2 Analysis with the Coupling Effect of Actuator Dynamics

In the previous discussion of controllability and observability, no actuator dynamics were considered in the system state equation. Since we are interested in using magnetically levitation techniques to control the vibration, the unstable nature of magnetic forces should be taken into account. This

instability comes from the negative stiffness existing between the levitated object and the magnetic bearing pole face. The introduction of magnetic bearings into the system will significantly affect the dynamic behavior. Therefore, in this section we reformulate the problem and investigate the influence of magnetic bearings on the controllability and observability conditions. In general, the nonlinear magnetic force equation is linearized about an equilibrium point. The incremental force can then be represented by,

$$f = k_z z + k_i i \quad (30)$$

where k_z is the unstable stiffness, z is the air gap distance, k_i is the current stiffness constant and i is the control current. Assuming m magnetic bearings are used as actuators in the vibration isolation system, then Equation (30) is written in vector form as,

$$f = \mathcal{K}_z z + \mathcal{K}_i i \quad (31)$$

In this equation, f, z, i denote the $m \times 1$ force, air gap distance, and control current vectors. \mathcal{K}_z^2 and \mathcal{K}_i are both nonsingular, $m \times m$ diagonal matrices. The diagonal elements of \mathcal{K}_z represent the unstable stiffness of each magnetic bearing while those of \mathcal{K}_i are the corresponding current stiffness constants. Substituting Equation (31) into Equation (9) and using the relation that $z = [R \ 0]x$, we can get the new state equation as,

$$\dot{x} = A' x + B' i \quad (32)$$

where

$$A' = \begin{bmatrix} 0 & I \\ J + H\mathcal{K}_z R & 0 \end{bmatrix}, \quad B' = \begin{bmatrix} 0 \\ H\mathcal{K}_i \end{bmatrix} \quad (33)$$

Using the same procedure as discussed previously, the system is controllable if and only if the matrix

$$L' = \begin{bmatrix} H\mathcal{K}_i & (J + H\mathcal{K}_z R)H\mathcal{K}_i & (J + H\mathcal{K}_z R)^2 H\mathcal{K}_i & \dots & (J + H\mathcal{K}_z R)^{n-1} H\mathcal{K}_i \end{bmatrix} \quad (34)$$

has rank n . A first result is stated in the following lemma.

Lemma 3.1 *Given an integer p and matrices J, H and W such that $p \in Z$, $J \in R^{n \times n}$, $H \in R^{n \times m}$ and $W \in R^{m \times m}$, The column space of the matrix $J^p H W$ is spanned by the column vectors of the matrix $J^p H$.*

Proof: Assuming that the matrix $H = [h_1 \ h_2 \ \dots \ h_m]$ where the h_i 's are column vectors of H . Let the elements of W be w_{ij} , then

$$\begin{aligned} J^p H W &= J^p [h_1 \ h_2 \ \dots \ h_m] W \\ &= J^p \left[\sum_{j=1}^m w_{j,1} h_j \quad \sum_{j=1}^m w_{j,2} h_j \quad \dots \quad \sum_{j=1}^m w_{j,n} h_j \right] \\ &= \left[\sum_{j=1}^m w_{j,1} J^p h_j \quad \sum_{j=1}^m w_{j,2} J^p h_j \quad \dots \quad \sum_{j=1}^m w_{j,n} J^p h_j \right] \end{aligned}$$

Because $J^p H$ can be expanded as $[J^p h_1 \ J^p h_2 \ \dots \ J^p h_m]$, it is obvious that the column space of $J^p H W$ is spanned by the column vectors of $J^p H$. \square

Now we state a controllability theorem for magnetically levitated vibration isolation system..

²Due to the instability of the magnetic bearing, \mathcal{K}_z is a positive definite matrix.

Theorem 3.4 *The system described by Equation (9) is controllable if and only if the system described by Equation (32).*

Proof: In order to show this, we need to prove that the rank of \mathbf{L}' is the same as that of \mathbf{L} . Since \mathcal{K}_i is a common factor in each element of \mathbf{L}' , we can factor it out and write the \mathbf{L}' matrix as,

$$\mathbf{L}' = \mathbf{L}'' \mathcal{K}_i$$

where $\mathbf{L}'' = \begin{bmatrix} \mathbf{H} & (\mathbf{J} + \mathbf{H}\mathcal{K}_z\mathbf{R})\mathbf{H} & (\mathbf{J} + \mathbf{H}\mathcal{K}_z\mathbf{R})^2\mathbf{H} & \dots & (\mathbf{J} + \mathbf{H}\mathcal{K}_z\mathbf{R})^{n-1}\mathbf{H} \end{bmatrix}$. Since \mathcal{K}_i is a non-singular diagonal matrix, \mathbf{L}'' has the same rank as the matrix \mathbf{L}' . We perform the algebraic manipulation on column vectors to reduce the \mathbf{L}'' matrix into the same form as the \mathbf{L} matrix. From the lemma for the case of $p = 0$, we can use the columns of \mathbf{H} , which is the first element of \mathbf{L}'' to eliminate $\mathbf{H}\mathcal{K}_z\mathbf{R}\mathbf{H}$ in the second element so that only the columns of $\mathbf{J}\mathbf{H}$ remains. Then expand the third element as $\mathbf{J}^2\mathbf{H} + \mathbf{J}\mathbf{H}\mathcal{K}_z\mathbf{R}\mathbf{H} + \mathbf{H}\mathcal{K}_z\mathbf{R}\mathbf{J}\mathbf{H} + \mathbf{H}\mathcal{K}_z\mathbf{R}\mathbf{H}\mathcal{K}_z\mathbf{R}\mathbf{H}$. The lemma again allows us to use the columns of first element \mathbf{H} and the new second element $\mathbf{J}\mathbf{H}$ to reduce the third element into $\mathbf{J}^2\mathbf{H}$. Applying the same column reduced procedure to the 4th, 5th, ..., nth elements of \mathbf{L}'' matrix. We can reduced the \mathbf{L}'' into the same matrix as \mathbf{L} . The algebraic manipulation of column vectors doesn't change the rank of the matrix \mathbf{L}'' , therefore we conclude that the \mathbf{L}'' matrix and the \mathbf{L} matrix have the same rank, which implies \mathbf{L}' matrix has the same rank as \mathbf{L} . \square

A direct application of the theorem is that the introduction of the magnetic bearings dynamics wouldn't influence the controllability condition discussed previously. And all the theorems mentioned before can be applied to the magnetic levitated vibration isolation systems.

For the observability part, using the same argument, we can prove the magnetic bearing dynamics wouldn't change the observability condition if there are m position sensors collocated with those m magnetic bearings. This is because if the m position sensors collocated with those m magnetic bearings used, the $m \times 1$ output vector becomes $\mathbf{y} = [\mathbf{R} \ 0] \mathbf{x}$. Using Equation (32), the observability condition can be deduced and is in fact similar to the controllability condition of Equation (34).

3.3 Examples of Locating Actuators (Sensors) to Achieve Controllability (Observability)

To apply the results obtained in the previous section, the eigenfunctions or the mode shape functions of the system need to be determined. Since there is no analytical solution for a flexible plate with free edges [13], approximate mode shape functions are found using with the Rayleigh-Ritz method. These mode shape functions allow us to get the node loci, which are the locus of points on the plate with zero amplitude corresponding to the normalized natural frequency. For the case of a square plate, the node loci of different normalized natural frequencies are shown in Figure 2. From the relationships obtained from the previous section, to control and observe the vibration of the plate, it can be inferred that we have to choose the actuators and sensors not located on the node loci associated with the desired frequency. Therefore, Figure 2 can be used as a guide line to properly locate the actuators and sensors so that the modes of interest may be controlled (observed) efficiently. Of course, it is necessary to check whether these locations satisfy the condition of linear independence for the modes with the same natural frequency.

In order to apply the results obtained from the discussion of controllability and observability, the first 9 node loci together as a node map are shown in Figure 3. Some examples of locating the actuators and sensors are illustrated as follows:

In Figure 4, the three actuators (sensors) are located in a straight line. Therefore, the rigid body rotation of the plate about this line cannot be controlled (observed).

As shown in Figure 5, although the three actuators (sensors) aren't collinear, they are all placed on the node line of the sixth mode. Therefore, this mode cannot be controlled (observed).

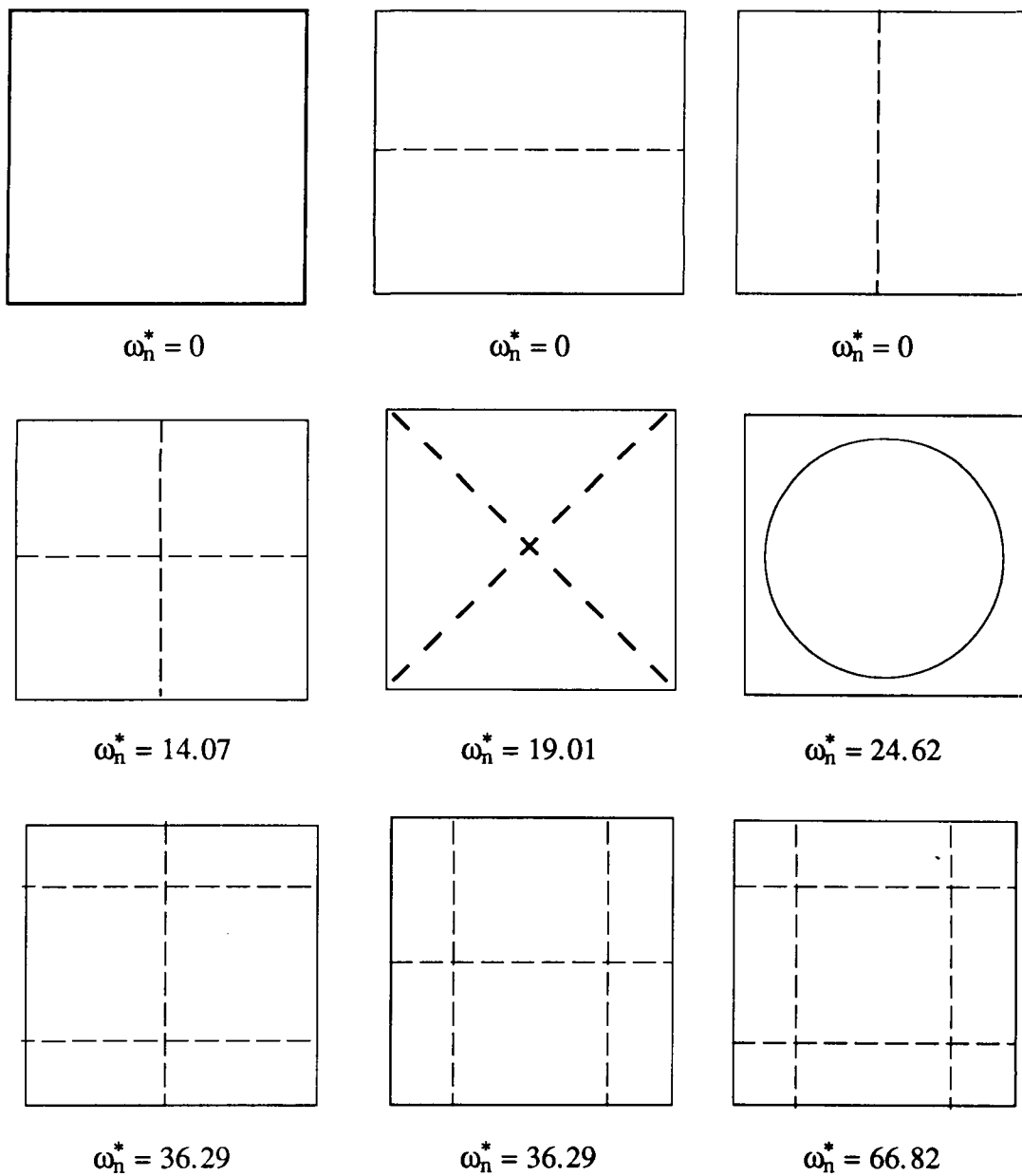


Figure 2: The node loci of the first nine normalized frequencies

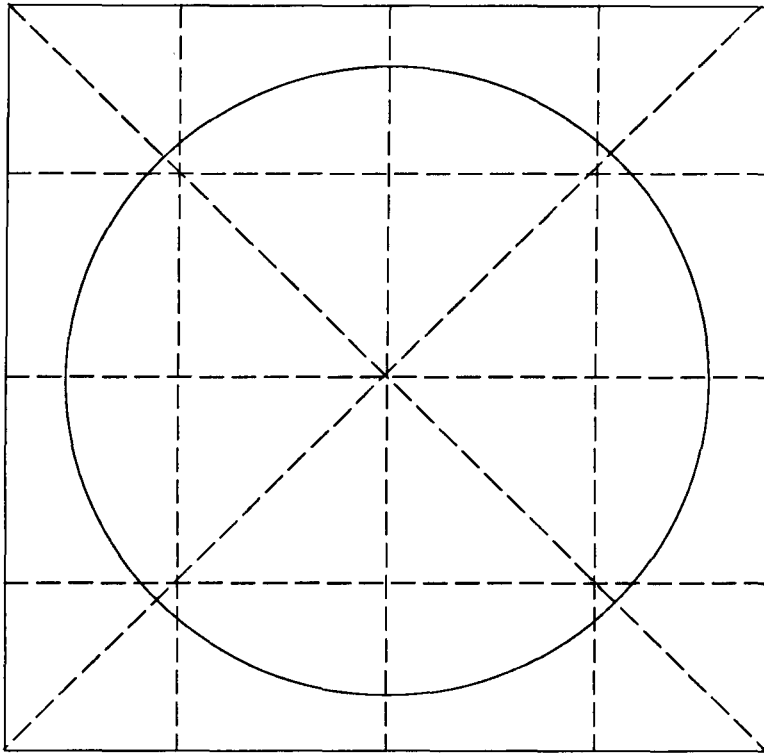
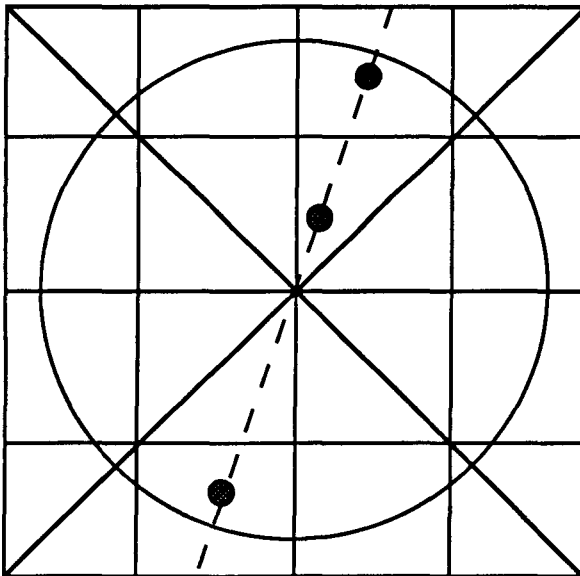
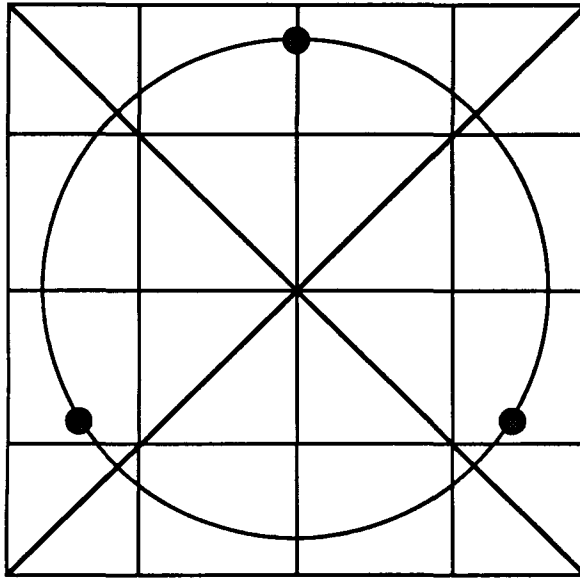


Figure 3: Node map of the first 9 modes of vibration



● Actuator/Sensor

Figure 4: Uncontrollability (unobservability) due to three collinear actuators (sensors)



● Actuator/Sensor

Figure 5: Uncontrollability (unobservability) of the sixth mode due to actuators (sensors) located on the node line of this mode

In Figure 6, since one actuator (sensor) is not located on any node line of the nine modes, it seems that all the nine modes are controllable (observable). However, due to the fact that the other two actuators and/or sensors are located at the intersections of the node line corresponding to the normalized frequency $\omega^* = 36.29$, the condition for repeated eigenvalues makes these two modes uncontrollable (unobservable).

Figure 7 shows four actuators (sensors) placed in symmetrical arrangement on the node line of the fourth mode. Therefore, the fourth mode is uncontrollable (unobservable).

Figure 8 shows three actuators (sensors) which are located unsymmetrically on the plate. All of the nine modes in this are controllable (observable) because none of the actuators (sensors) are located on the node lines.

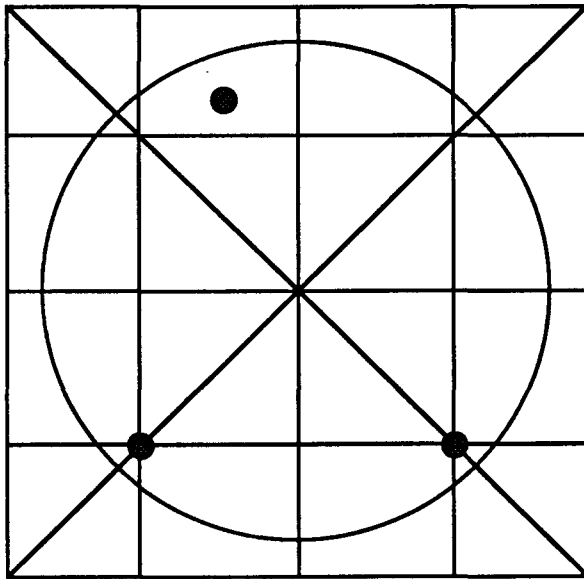
4 Control System Characteristics for Collocated and Non-collocated Configurations

In this section, we will examine proper actuator/sensor locations leading to a favorable open-loop system behavior. We will investigate the influence of the collocated and noncollocated actuator/sensor configuration on the control system characteristics, and then provide guide lines for achieving a favorable system behavior.

The open loop transfer function matrix of the $2n$ th order system described by Equations (9) and (14) is,

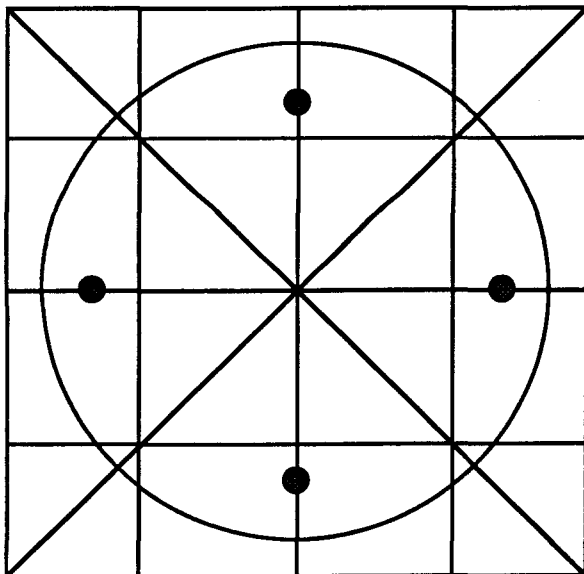
$$\mathbf{G}(s) = \mathbf{C}(s\mathbf{I} - \mathbf{A})^{-1}\mathbf{B} \quad (35)$$

In the following analysis, it is assumed that only position sensors are used which corresponds to that $\mathbf{C} = [\mathbf{P} \ 0]$. If the corresponding elements of matrices \mathbf{A} , \mathbf{B} and \mathbf{C} are substituted into the



● Actuator/Sensor

Figure 6: Uncontrollability (unobservability) of the seventh and eighth modes



● Actuator/Sensor

Figure 7: Uncontrollability (unobservability) of the fourth modes

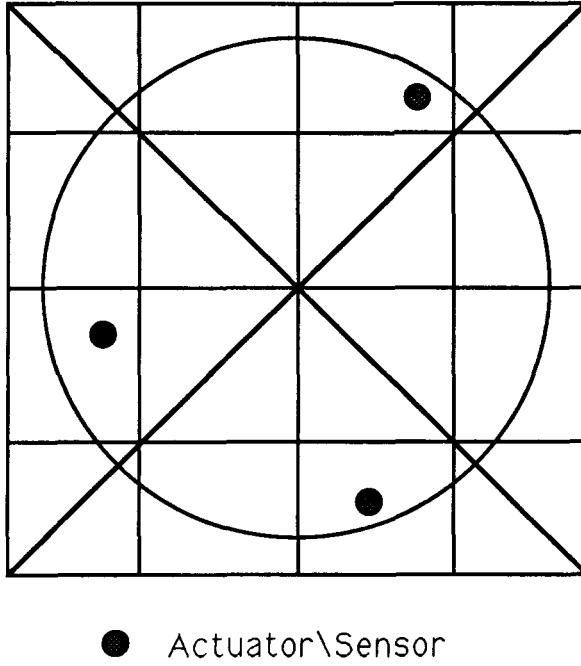


Figure 8: Controllability (observability) using three actuators (sensors)

right hand side of Equation (35), then the (i, j) th element of the $\mathbf{G}(s)$ matrix takes the form,

$$\begin{aligned}
 g_{i,j}(s) &= \sum_{k=1}^n \frac{\phi_k^{s_i} \phi_k^{a_j}}{M_k(s^2 + \omega_k^2)} \\
 &= \frac{\sum_{k=1}^n \left[\frac{\phi_k^{s_i} \phi_k^{a_j}}{M_k} \prod_{\ell=1, \ell \neq k}^n (s^2 + \omega_\ell^2) \right]}{\prod_{k=1}^n (s^2 + \omega_k^2)} \quad (36)
 \end{aligned}$$

$g_{i,j}(s)$ denotes the transfer function from the j th actuator at location (x_{a_j}, y_{a_j}) to the i th sensor at location (x_{s_i}, y_{s_i}) .

The transfer function $g_{i,j}(s)$, if without pole-zero cancellation, always has poles at $\pm j\omega_1, \pm j\omega_2, \dots, \pm j\omega_n$. If with pole-zero cancellation is possible, we can skip those cancellation pairs and focus only on the uncanceled ones. The numerator of Equation (36) has to be expanded as an $2(n-1)$ th degree polynomial and solved for the $2(n-1)$ zeros. Because the coefficients of this polynomial are real and the Laplace variable s always appear with even power, if there is any complex root $\alpha + j\beta$, then $\alpha - j\beta$, $-\alpha + j\beta$ and $-\alpha - j\beta$ are also the roots of the polynomial. Therefore, for the transfer function to be nonminimum phase, the zeros can't be any positive or complex numbers. This implies that the zeros, like the poles, should be on the imaginary axis. Although such information may be known, there are still many ways to locate the zeros. In order to decide on the most favorable type of pole-zero plot, the merits of a conventional PD controller are evaluated. The following lemma and theorem allow us to compare the relative performances of different types of pole-zero plots.

Lemma 4.1 *For a system with the transfer function in the form of Equation (36), if the i th pole located at $\pm j\omega_i$ is stabilized by a PD controller and there are $2\ell_i$ zeros at $\pm j\beta_1, \pm j\beta_2, \dots, \pm j\beta_{\ell_i}$, such that $\beta_1 < \beta_2 < \dots < \beta_{\ell_i} < \omega_i$, then $\ell_i - i = 2q_i - 1$ where q_i is an arbitrary integer.*

Proof: To prove this lemma, we look at the angle of departure of the i th pole. The angle of departure α_i of the i th pole is equal to $180^\circ - (\text{sum of the angles of vectors to this poles from other$

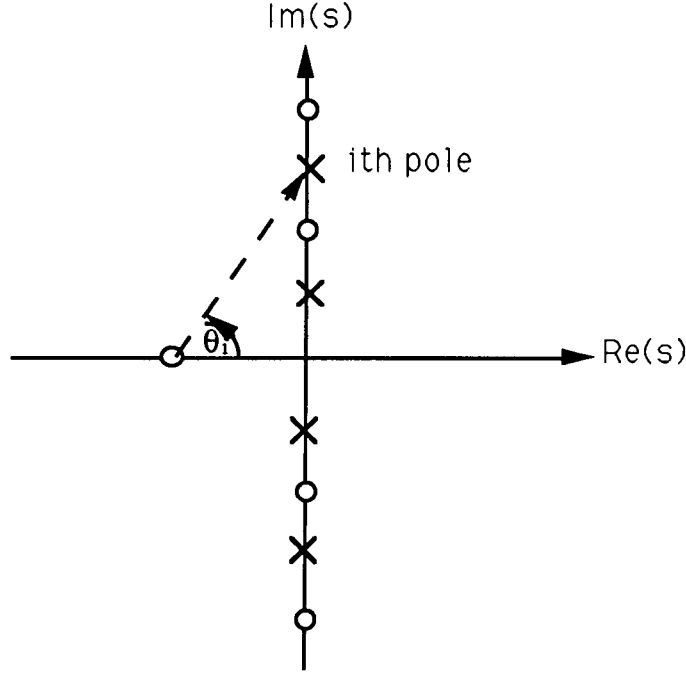


Figure 9: Calculation of the angle of departure for a PD controller

poles)+(sum of the angles of vectors to this pole from zeros) [14]. For the pole-zero plot shown in Figure (9), it can be shown that,

$$\begin{aligned}\alpha_i &= 180^\circ - [(n+i-1) \times 90^\circ - (n-i) \times 90^\circ] + [\theta_i + (n-1+\ell) \times 90^\circ - (n-1-\ell) \times 90^\circ] \\ &= 180^\circ + \theta_i + (2\ell - 2i + 1) \times 90^\circ\end{aligned}\quad (37)$$

Because a stable PD controller is used, $0 < \theta < 90^\circ$, which means $180^\circ + (2\ell - 2i + 1) \times 90^\circ < \alpha_i < 270^\circ + (2\ell - 2i + 1) \times 90^\circ$. It is obvious that if the root locus of the i th pole goes to the stable region, then $90^\circ \leq \alpha_i \leq 270^\circ$. Equation (37) can satisfy this angle condition only when $2\ell + 2i + 1 = 4q_i - 1$, that is, $\ell_i - i = 2q_i - 1$. \square

Theorem 4.1 *If all $2n$ poles $\pm j\omega_1, \pm j\omega_2, \dots, \pm j\omega_n$ in Equation (36) are stabilized by a PD controller, then there should be one and only zero located between two consecutive poles $j\omega_i, j\omega_{i+1}$ or $-j\omega_i, -j\omega_{i+1}$ for $i = 1, 2, \dots, n-1$. And the pole-zero plot should be the same as the one shown in Figure (10).*

Proof: For all the poles to be stabilized by a PD controller, Lemma 4.1 should be true for all poles. Take the poles located at $j\omega_i, j\omega_{i+1}$ or $-j\omega_i, -j\omega_{i+1}$ for example, the necessary condition becomes,

$$\ell_{i+1} - (i+1) = 2q_{i+1} - 1 \quad (a)$$

$$\ell_i - i = 2q_i - 1 \quad (b)$$

If (b) is subtracted from (a), we get $\ell_{i+1} - \ell_i = 2(q_{i+1} - q_i) + 1$ which implies that $\ell_{i+1} - \ell_i$ is an odd number. Since $\ell_{i+1} - \ell_i$ represents the number of zeros between these two poles and can't be a negative number. From above arguments, $\ell_{i+1} - \ell_i$ has to be greater than or equal to 1. This means that there is at least one zero between two poles $j\omega_i, j\omega_{i+1}$ or $-j\omega_i, -j\omega_{i+1}$. Because there is only $2(n-1)$ zeros for this transfer function and we have to place at least one zero in each of

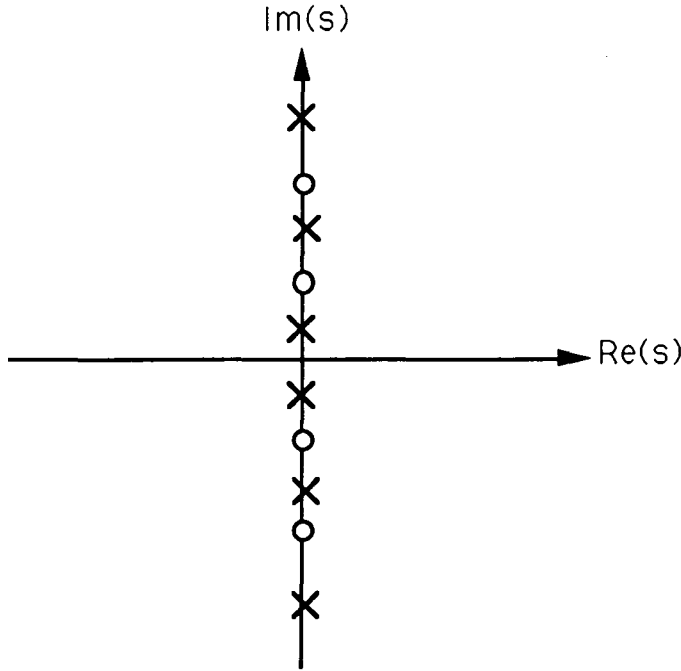


Figure 10: A favorable pole-zero plot

the $2(n-1)$ intervals between consecutive poles $j\omega_i, j\omega_{i+1}$ or $-j\omega_i, -j\omega_{i+1}$ for $i = 1, 2, \dots, n$, the only pole-zero type can be achieved is the alternating pole-zero plot shown in Figure (10). \square

Now we have proved that the only type of nonminimum phase pole-zero plot can be stabilized by a conventional PD controller is the alternating pole-zero plot. In what follows, we limit ourselves to this case and investigate the condition on the transfer function to have such a dynamic behavior. This condition can be obtained from the following theorem,

Theorem 4.2 *The transfer function of Equation (36) has an alternating pole-zero plot as in Figure (10) if and only if either one of the following conditions is true,*

$$\begin{aligned}
 & \text{(i)} \quad \frac{\phi_k^{s_i} \phi_k^{a_j}}{M_k} > 0 \quad \text{for any } k\text{th mode with no repeated eigenvalues} \\
 & \text{and} \quad \sum_{k=p+1}^{p+q} \left[\frac{\phi_k^{s_i} \phi_k^{a_j}}{M_k} \right] > 0 \quad \text{for } p+1\text{th}, p+2\text{th}, \dots, p+q\text{th modes with same} \\
 & \quad \quad \quad \text{repeated eigenvalues} \\
 & \text{or} \\
 & \text{(ii)} \quad \frac{\phi_k^{s_i} \phi_k^{a_j}}{M_k} < 0 \quad \text{for any } k\text{th mode with no repeated eigenvalues} \\
 & \text{and} \quad \sum_{k=p+1}^{p+q} \left[\frac{\phi_k^{s_i} \phi_k^{a_j}}{M_k} \right] < 0 \quad \text{for } p+1\text{th}, p+2\text{th}, \dots, p+q\text{th modes with same} \\
 & \quad \quad \quad \text{repeated eigenvalues}
 \end{aligned}$$

Proof: To simplify the notation, a_k 's are used to denote $\frac{\phi_k^{s_i} \phi_k^{a_j}}{M_k}$ and all the eigenvalues are different. This condition will be relaxed later. Then the numerator $Z(s)$ of Equation (36) can be written as,

$$Z(s) = \sum_{k=1}^n a_k \prod_{\ell=1, \ell \neq k}^n (s^2 + \omega_\ell^2) \quad (38)$$

The $2(n-1)$ roots of $Z(s)$ which are represented by $\pm jz_1, \pm jz_2, \dots, \pm jz_{n-1}$ correspond to the zeros of the transfer function. For the system to have alternating pole-zero plot, we should have $\omega_k < z_k < \omega_{k+1}$ for $k = 1, 2, \dots, n-1$. The necessary and sufficient condition for the above arguments to be true is,

$$Z(j\omega_k)Z(j\omega_{k+1}) = a_k a_{k+1} \prod_{\ell=1, \ell \neq k}^n (-\omega_k^2 + \omega_\ell^2) \prod_{\ell=1, \ell \neq k+1}^n (-\omega_{k+1}^2 + \omega_\ell^2) < 0$$

for $k = 1, 2, \dots, n-1$ (39)

Since $\omega_1 < \omega_2 < \dots < \omega_n$, the following product must be negative,

$$\begin{aligned} \text{sgn} \left[\prod_{\ell=1, \ell \neq k}^n (-\omega_k^2 + \omega_\ell^2) \prod_{\ell=1, \ell \neq k+1}^n (-\omega_{k+1}^2 + \omega_\ell^2) \right] &= \text{sgn} [(-1)^{k-1} (-1)^k] \\ &= -1 \end{aligned}$$

(40)

If this result is substituted into Equation (39), the necessary and sufficient condition becomes $a_k a_{k+1} > 0$ for $k = 1, 2, \dots, n-1$. This condition is the same as either $a_k > 0$ or $a_k < 0$ for any k , which means that all the a_k 's have the same sign. If there are $p+1$ th, $p+2$ th, \dots , $p+q$ th with the same natural frequency, then in Equation (36), all the $p+1$ th, $p+2$ th, \dots , $p+q$ th can be summed up together so that there is no repeated poles in the transfer function. As the case of no eigenvalue multiplicity and using a_p to represent $\sum_{k=p+1}^{p+q} [\frac{\phi_k^{*i} \phi_k^{*j}}{M_k}]$ and follow the same procedure, we can still conclude that a_k for $k = 1, \dots, p, p+q+1, \dots, n$, should be have the same sign. Even though we only discussed the case of one eigenvalue with multiplicity, if there are other repeated eigenvalues, the conclusion is the same as what stated in this theorem. \square

Remark:

1. If any $\frac{\phi_k^{*i} \phi_k^{*j}}{M_k}$ or $\sum_{k=p+1}^{p+q} [\frac{\phi_k^{*i} \phi_k^{*j}}{M_k}]$ in Equation (38) is equal to zero, pole-zero cancellation occurs for the pole $j\omega_k$ or $j\omega_p$.

2. For the special case of a collocated actuator and sensor pair, $\phi_k^{*i} = \phi_k^{*j}$, for $k = 1, 2, \dots, n$. The i th condition is obviously satisfied. Therefore, the collocated system always has an alternating pole-zero plot as that of Figure (10).

Finally, we prove the next theorem to guarantee the stability of a PD controller applied to the alternating pole-zero plot of the system in Equation (36).

Theorem 4.3 *The transfer function of Equation (36) has an alternating pole-zero plot if and only if it can be stabilized by a PD controller.*

Proof: The necessary condition of this theorem has already been proved in Theorem 4.1. For the sufficient part, first we formulate the closed loop characteristic equation as,

$$\prod_{k=1}^n (s^2 + \omega_k^2) + K_{pd}(s + c) \sum_{k=1}^n \left[a_k \prod_{\ell=1, \ell \neq k}^n (s^2 + \omega_\ell^2) \right] = 0 \quad (41)$$

where K_{pd} is the gain of the PD controller and $-c < 0$ is the zero introduced by the controller. In addition, the a_k 's have the same meaning as in Theorem 4.2. We have already shown in Theorem 4.1 that alternating pole-zero plot will make the angle of departure of all open loop poles pointing to the left hand plane. If we can prove that the root locus of this plot with a PD controller never cross the imaginary axis for any finite gain $|K_{pd}| < \infty$, then the stability is always guaranteed. Assuming the root locus crosses the imaginary axis at $j\omega$. By substituting $s = j\omega$ into Equation (41) and equate both the real and imaginary parts to zero, we have,

$$\prod_{k=1}^n (-\omega^2 + \omega_k^2) + K_{pd}c \sum_{k=1}^n \left[a_k \prod_{\ell=1, \ell \neq k}^n (-\omega^2 + \omega_\ell^2) \right] = 0 \quad (42)$$

and

$$K_{pd}\omega \sum_{k=1}^n \left[a_k \prod_{\ell=1, \ell \neq k}^n (-\omega^2 + \omega_\ell^2) \right] = 0 \quad (43)$$

Equation (43) is true only when

$$\text{or} \quad \sum_{k=1}^n \left[a_k \prod_{\ell=1, \ell \neq k}^n (-\omega^2 + \omega_\ell^2) \right] = 0 \quad \omega = 0$$

For the former case, if $\omega = 0$ is substituted into Equation (42), then the equation becomes,

$$\prod_{k=1}^n \omega_k^2 + K_{pd}c \sum_{k=1}^n a_k \prod_{\ell=1, \ell \neq k}^n \omega_\ell^2 = 0$$

Since all a_k 's have the same sign and if a K_{pd} of suitable sign is used, the equation can never be equal to zero. Therefore, 0 is not on the root locus. In the latter case, the solution of ω corresponds to the open loop zeros of the system. Then the equation is substituted into Equation (42) again. Equation (42) is true only when $K_{pd} = \infty$ or $K_{pd} = -\infty$ with the sign dependent on the sign of the a_k 's. This is due to the fact if finite value of K_{pd} is used, the first term of Equation (42) becomes zero while the second term is nonzero because of the alternating pole-zero plot (the open loop zeros can never be equal to the open loop poles). From above argument we have proved that the alternating pole-zero plot can always be stabilized by PD controller, which is the sufficient condition of this theorem. \square

In order to apply the above theorem and illustrate the consequence of a given actuator/sensor system configuration, we consider only the first vibration mode. Because the first three modes correspond to the rigid body motion with eigenvalue equal to zero, it can be shown from Theorem 4.2 that the transfer function between the i th input and j th output will have an alternating pole-zero plot if and only

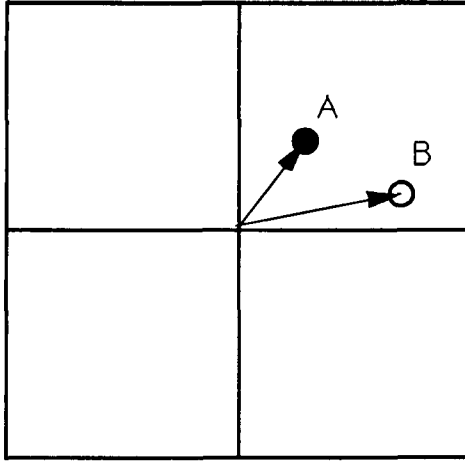
$$\begin{aligned} (i) \quad & \left(\frac{\phi_1^{*i} \phi_1^{aj}}{M_1} + \frac{\phi_2^{*i} \phi_2^{aj}}{M_2} + \frac{\phi_3^{*i} \phi_3^{aj}}{M_3} \right) \geq 0 \\ (ii) \quad & \frac{\phi_4^{*i} \phi_4^{aj}}{M_4} \geq 0 \end{aligned} \quad (44)$$

or

$$\begin{aligned} (i) \quad & \left(\frac{\phi_1^{*i} \phi_1^{aj}}{M_1} + \frac{\phi_2^{*i} \phi_2^{aj}}{M_2} + \frac{\phi_3^{*i} \phi_3^{aj}}{M_3} \right) \leq 0 \\ (ii) \quad & \frac{\phi_4^{*i} \phi_4^{aj}}{M_4} \leq 0 \end{aligned} \quad (45)$$

In order to gain more insight, the mode shape functions obtained from the Rayleigh-Ritz method are substituted in the above equations. Consider the case of a rectangle plate, if the length-to-width ratio $\frac{a}{b}$ is between 0.65 and 1.54, the first four mode shape functions can be calculated as $\phi_1(x, y) = 1$, $\phi_2(x, y) = f_{b_2}(y)$, $\phi_3(x, y) = f_{a_2}(x)$, $\phi_4(x, y) = f_{a_2}(x)f_{b_2}(y)$ and $M_1 = M_2 = M_3 = M_4$. If they are substituted, Equation (44) and (45) can be rearranged as,

$$\begin{aligned} (i) \quad & \frac{1}{12} + \left[\frac{1}{a}(x_{s_i} - \frac{a}{2}), \frac{1}{b}(y_{s_i} - \frac{b}{2}) \right] \left[\frac{1}{a}((x_{a_j} - \frac{a}{2}), \frac{1}{b}(y_{a_j} - \frac{b}{2})) \right] \geq 0 \\ (ii) \quad & \left(\frac{a}{2} - x_{s_i} \right) \left(\frac{a}{2} - x_{a_j} \right) \left(\frac{b}{2} - y_{s_i} \right) \left(\frac{b}{2} - y_{a_j} \right) \geq 0 \end{aligned} \quad (46)$$



- actuator
 ○ sensor

Figure 11: Case 1 for locating the actuator and sensor to achieve desirable alternating pole-zero type

and

$$\begin{aligned}
 (i) \quad & \frac{1}{12} + \left[\frac{1}{a}(x_{s,i} - \frac{a}{2}), \frac{1}{b}(y_{s,i} - \frac{b}{2}) \right] \left[\frac{1}{a}((x_{a,j} - \frac{a}{2}), \frac{1}{b}(y_{a,j} - \frac{b}{2})) \right] \leq 0 \\
 (ii) \quad & \left(\frac{a}{2} - x_{s,i} \right) \left(\frac{a}{2} - x_{a,j} \right) \left(\frac{b}{2} - y_{s,i} \right) \left(\frac{b}{2} - y_{a,j} \right) \leq 0
 \end{aligned} \tag{47}$$

Conditions (i) of Equation (46) and (47) can be interpreted geometrically as comparing $\frac{1}{12}$ with the inner product of two vectors. These two vectors have starting points at the center of the plate and end points at the locations at the actuator or sensor, but their x and y components are normalized with respect to a and b individually. If the rectangle plate are divided into four quadrants by the lines $x = \frac{a}{2}$ and $y = \frac{b}{2}$, then condition (ii) of Equation (46) is satisfied if the actuator and sensor are in the same quadrant or they are in opposite quadrant individually. However, condition (ii) of Equation (47) is satisfied if the actuator and sensor are in the adjacent quadrants individually. Therefore, for the transfer function to have an alternating pole-zero plot, there are basically three ways to locate the actuator and sensor. These three cases are described below.

- Case 1 : Locate actuator and sensor in the same quadrant as shown in Figure (11). Condition (i) of Equation (46) is satisfied automatically because the inner product of the two normalized vectors are always greater than zero. If either the actuator or sensor is located at the node lines of $\phi_4(x, y)$ which are composed of the lines $x = \frac{a}{2}$ and $y = \frac{b}{2}$, then the zeros cancel the two poles symmetrically on the imaginary axis and there are only two poles at the origin.
- Case 2 : Locate actuator and sensor in the opposite quadrants individually and check if condition (i) of Equation (46) is satisfied. For the special case of a square plate as shown in Figure (12), if the sum of $\frac{a^2}{12}$ and the inner product of vectors \vec{OA} and \vec{OB} is greater than 0, then the condition is satisfied. Also when the sum is equal to zero, then the zeros cancel the two poles at the origin and there are only two poles symmetrically on the imaginary axis.

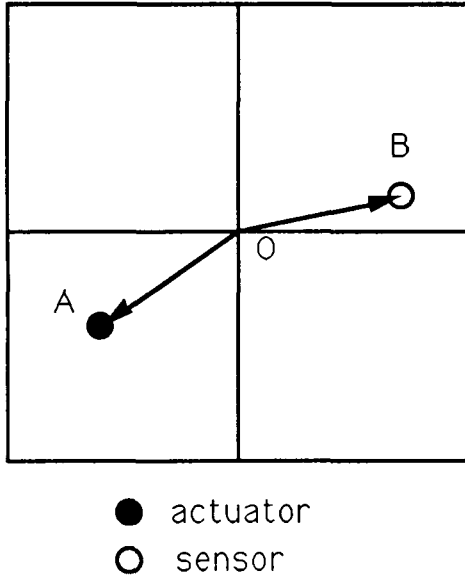


Figure 12: Case 2 for locating the actuator and sensor to achieve desirable alternating pole-zero type

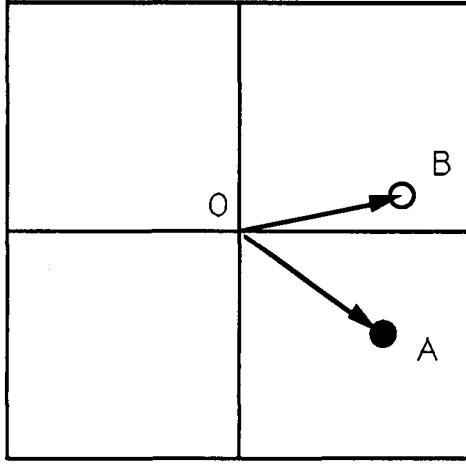
- Case 3 : Locate actuator and sensor in the adjacent quadrants individually and check if condition (i) of Equation (47) is satisfied. By the same argument in case 2, if the plate is square, the sum of $\frac{a^2}{12}$ and the inner product of vectors \vec{OA} and \vec{OB} of Figure (13) should be less than 0. One obvious result is that the angle between the two vectors has to be greater than 90 degrees. Also as in case 2, when the sum is equal to zero, then the zeros cancel the two poles at the origin and there are only two poles symmetrically on the imaginary axis.

5 Effects of Damping

In the above discussion, we assume that there is no energy dissipation or system damping in the vibration of a flexible plate. But damping normally exist in the physical systems. Especially in the vibration isolation table, damping is a favorable effect because with proper damping mechanism (e.g. viscoelastic material), the higher frequency vibrations that reach the table top can be attenuated rapidly.

For the case of weak damping effects, it can be guaranteed that the controllability and observability conditions obtained in Section 3 are still acceptable. This is because the controllability and observability are preserved under sufficient small perturbation such as the damping effect [15, 16]. However, when the damping is not negligible, the modes will couple with each other. Therefore, certain modes originally uncontrollable (unobservable) in the case of no damping may become controllable (observable) [6]. If the system damping is sufficiently large. It is also pointed out in [6] that the number of actuators (sensors) to achieve controllability (observability) are expected to be reduced because of the significant coupling effect.

On the other hand, the influences of damping on the system pole-zero plot is that the open loop poles are now placed in the left hand plane instead of being on the imaginary axis. The larger the damping, the further the poles are from the imaginary axis. Therefore damping tends to stabilize



- actuator
- sensor

Figure 13: Case 3 for locating the actuator and sensor to achieve desirable alternating pole-zero type

the overall system and make the controller easier to implement.

6 Conclusion

This paper investigated the relationships between actuator and sensor locations and the dynamics and control characteristics of a magnetically levitated vibration isolation system. The problem was formulated using orthogonal mode shape functions based on the Rayleigh-Ritz method. A lumped-parameter model of a flexible vibration isolation table top is used to investigate the system's controllability and observability including the coupling effects introduced by the magnetic bearing. The selection of proper actuator and sensor locations leading to a controllable and observable system were discussed. Necessary and sufficient conditions were derived for proper selection of actuator and sensor locations, and for reducing the controller complexity. The results are illustrated by examples using approximate mode shape functions. Such information is important for the overall design of ultra high performance vibration isolation systems.

A Rayleigh-Ritz method

Assuming that the plate is vibrating with a mode shape $\phi(x, y)$ and frequency ω , the Rayleigh-Ritz method proceeds by calculating the maximum potential energy from Equation (6),

$$V_{max} = \frac{D}{2} \int_A [\phi_{xx}^2 + \phi_{yy}^2 + 2\nu\phi_{xx}\phi_{yy} + 2(1-\nu)(\phi_{xy})^2] dA \quad (48)$$

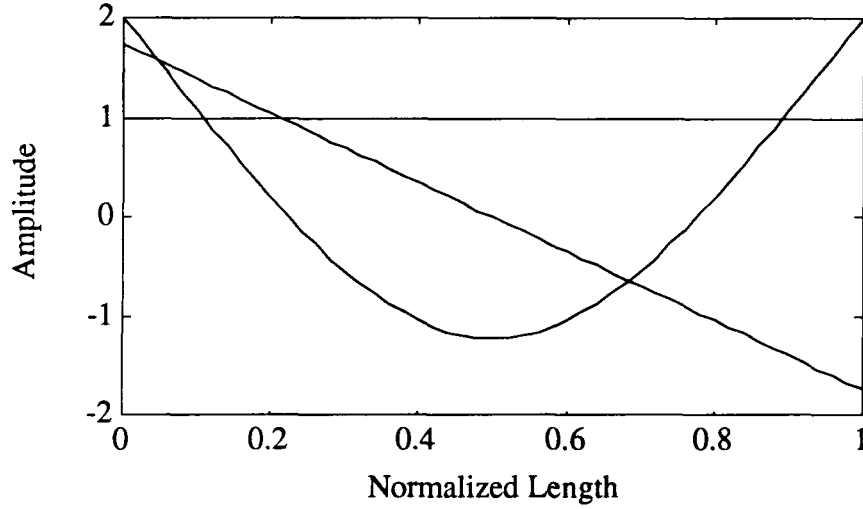


Figure 14: The first three modeshape functions of prismatic beam with free ends

Also the maximum kinetic energy from Equation (5) is given by,

$$\mathcal{T}_{max} = \frac{D}{2} \rho h \omega^2 \int_A \phi^2 dA \quad (49)$$

By equating the above two equations, an expression for the frequency ω is obtained,

$$\omega^2 = \frac{\rho h}{2} \frac{\mathcal{V}_{max}}{\int_A \phi^2 dA} \quad (50)$$

The Rayleigh-Ritz method assumes that the mode shape functions can be expanded by a linear series of “admissible” functions and adjusts the coefficients in the series to minimize Equation (50). For the case of rectangle plate with length a and width b , the mode shape function $\phi(x, y)$ is expanded as :

$$\phi(x, y) = \sum_{n=1}^3 \sum_{m=1}^3 A_{mn} f_{a_m}(x) f_{b_n}(y) \quad (51)$$

where the function $f_{\beta,i}(\cdot)$ is the i th mode shape function of a prismatic beam with free ends and length β . The first three mode shape functions are plotted in Figure 14. We can write these first three modeshape functions as : $f_{\beta_1}(\xi) = 1$, $f_{\beta_2}(\xi) = \sqrt{3}(1 - \frac{2\xi}{\beta})$, $f_{\beta_3}(\xi) = \cosh(\frac{4.73\xi}{\beta}) - \cos(\frac{4.73\xi}{\beta}) - 0.983[\sinh(\frac{4.73\xi}{\beta}) - \sin(\frac{4.73\xi}{\beta})]$. By substituting these into Equation (51), Equation (50) becomes a function of A_{mn} . Then we minimize it by taking the partial derivative with respect to each coefficient and equating to zero then follow the same procedure as in [17], we arrive at a set of equations each of which has the form,

$$\sum_{n=1}^3 \sum_{m=1}^3 [C_{mn}^{(ik)} - \lambda \delta_{mn}] A_{mn} = 0 \quad (52)$$

where

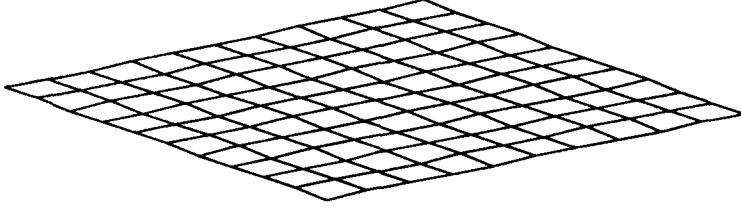


Figure 15: The 1st mode with normalized frequency 0

$$C_{mn}^{(ik)} = \nu \frac{a}{b} [E_{mi} E_{kn} + E_{im} E_{nk}] + 2(1 - \nu) \frac{a}{b} H_{im} H_{kn}, \quad \delta_{mn} = 1, \quad \text{for } mn \neq ik$$

$$C_{mn}^{(ik)} = \frac{b}{a} \epsilon_i^4 + \frac{a^3}{b^3} \epsilon_k^4 + 2\nu \frac{a}{b} E_{ii} F_{kk} + 2(1 - \nu) \frac{a}{b} H_{ii} H_{kk}, \quad \delta_{mn} = 1, \quad \text{for } mn = ik$$

and

$$E_{im} = \beta \int_0^\beta f_{\beta i}(\xi) \frac{d^2 f_{\beta m}(\xi)}{d\xi^2} d\xi, \quad H_{im} = \beta \int_0^\beta \frac{df_{\beta i}(\xi)}{d\xi} \frac{df_{\beta m}(\xi)}{d\xi} d\xi, \quad \epsilon_1 = \epsilon_2 = 0, \epsilon_3 = 4.730$$

The above set of linear equations is a typical eigenvalue problem in linear algebra. In this paper, we take the Poisson ratio ν as 0.3 and solve Equation (52) using the Matlab package and thus get nine approximate mode shape functions and corresponding normalized natural frequencies. For the special case of square plate, the nine mode shape functions and corresponding normalized natural frequencies were computed using Matlab and found to be,

$$\begin{aligned} \omega_1^* &= 0 & \phi_1(x, y) &= 1 \\ \omega_2^* &= 0 & \phi_2(x, y) &= f_2(y) \\ \omega_3^* &= 0 & \phi_3(x, y) &= f_2(x) \\ \omega_4^* &= 14.07 & \phi_4(x, y) &= f_2(x) f_2(y) \\ \omega_5^* &= 19.01 & \phi_5(x, y) &= 0.7071 f_3(y) - 0.7071 f_3(x) \\ \omega_6^* &= 24.62 & \phi_6(x, y) &= 0.7069 f_3(y) + 0.7069 f_3(x) + 0.0262 f_3(x) f_3(y) \\ \omega_7^* &= 32.69 & \phi_7(x, y) &= f_2(x) f_3(y) \\ \omega_8^* &= 32.69 & \phi_8(x, y) &= f_3(x) f_2(y) \\ \omega_9^* &= 66.82 & \phi_9(x, y) &= -0.0185 f_3(y) - 0.0185 f_2(x) + 0.9497 f_3(x) f_3(y) \end{aligned} \quad (53)$$

where the normalized frequency $\omega^* = \frac{\omega a^2}{h} \sqrt{\frac{12\rho(1-\nu^2)}{E}}$ and $f_j(\xi) = f_{\beta j}(\xi)$ as appeared in the appendix. Figure 15 to Figure 23 are the 3-D approximate modeshape functions of square plate.

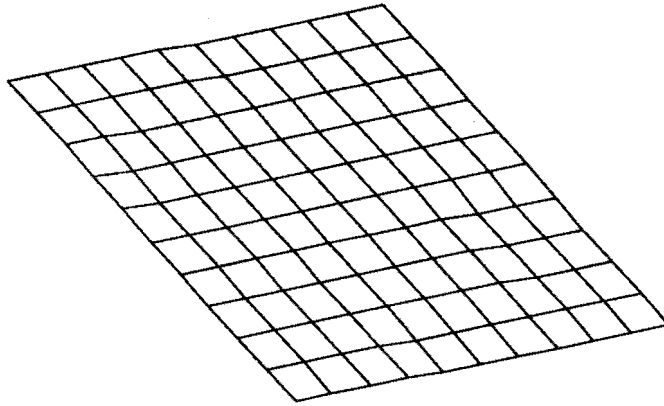


Figure 16: The 2nd mode with normalized frequency 0

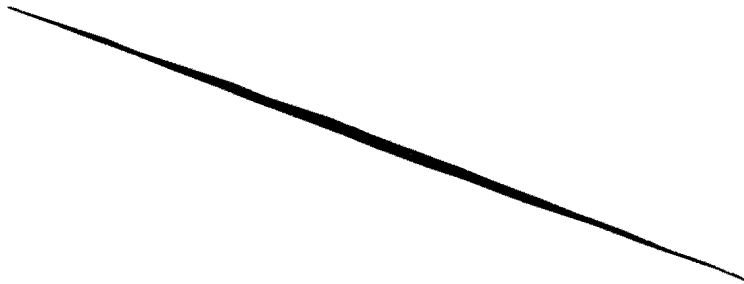


Figure 17: The 3rd mode with normalized frequency 0

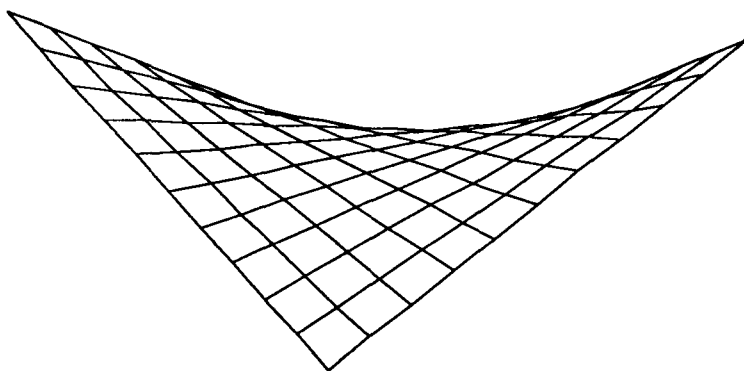


Figure 18: The 4th mode with normalized frequency 14.07

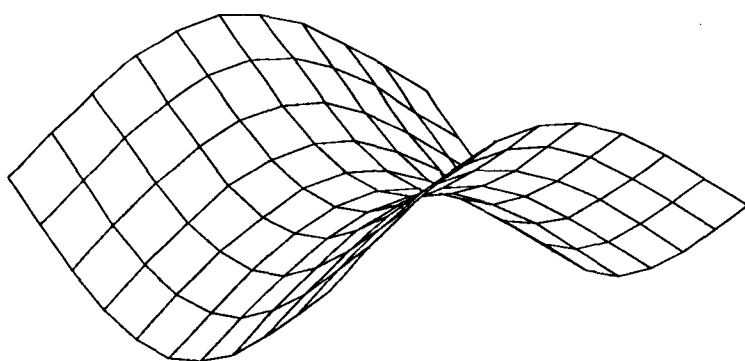


Figure 19: The 5th mode with normalized frequency 19.81

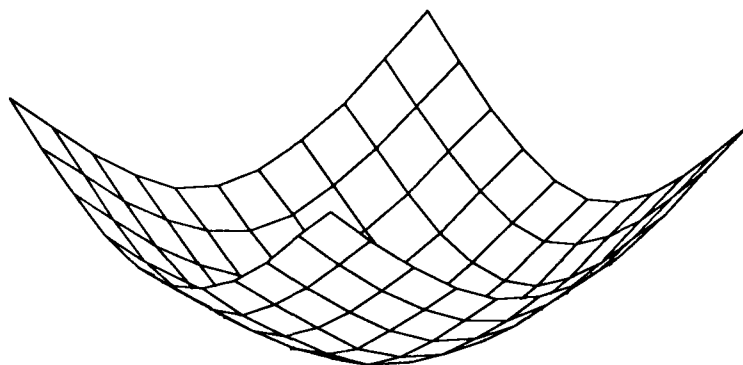


Figure 20: The 6th mode with normalized frequency 24.62

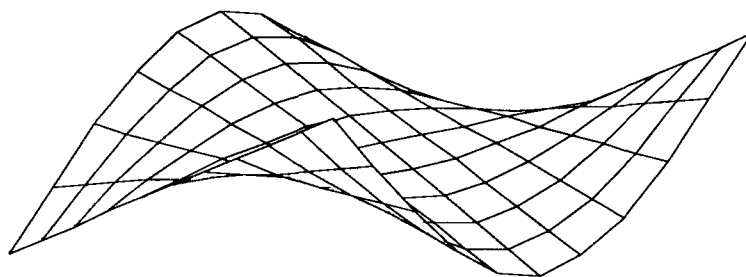


Figure 21: The 7th mode with normalized frequency 36.29

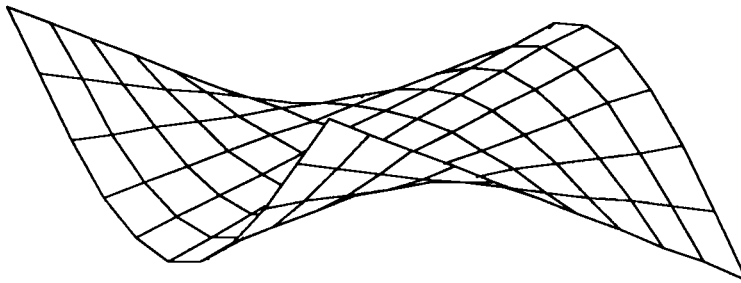


Figure 22: The 8th mode with normalized frequency 36.29

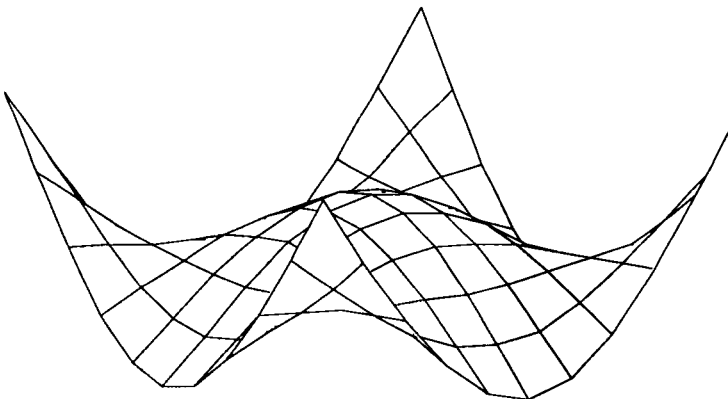


Figure 23: The 9th mode with normalized frequency 66.82

References

- [1] Slocum, A., *Precision Machine Design*, Draft, 1989.
- [2] Binnig, G., and Rohrer, H., "Scanning Tunneling Microscopy," *Helvetica Physica Acta*, Vol. 55, 1982, pp. 726-735.
- [3] Harris, C. M. and Crede, C. E., *Shock and Vibration Handbook*, McGraw-Hill Book Company, New York 1976.
- [4] Sandercock, J. R., "A Dynamic Antivibration System," *Proceedings of First International Conference of Vibration control in Optics and Metrology*, February 1987, London, England, pp. 157-165.
- [5] Newport Catalog in, "Vibration Isolation System," CA, 1990.
- [6] Hughes, P. C. and Skelton, R. E., "Controllability and Observability of Linear Matrix-Second-Order Systems," *Journal of Applied Mechanics*, Vol. 47, June 1980, pp. 415-420.
- [7] Yang, B. and Mote, C. D. Jr., "Controllability and Observability of Distributed Gyroscopic Systems," *Journal of Dynamic Systems, Measurement, and Control*, Vol. 113, March 1991, pp. 11-17.
- [8] Park, J-H and Asada, H., "Design and Control of Minimum-Phase Flexible Arms with Torque Transmission Mechanisms," *IEEE International Conference on Robotics and Automation*, May 1990, pp. 1790-1795.
- [9] Bennighof, J. K. and Meirovitch, L., "Active Vibration of a Distributed System With Moving Support," *Journal of Vibration, Acoustics, Stress, and Reliability in Design*, Vol. 110, 1988, pp. 246-253.
- [10] Timoshenko, S., *Theory of Plates and Shells*, McGraw-Hall Book Company, Inc., New York and London, 1940.
- [11] Soedel, W., *Vibrations of Shells and Plates*, Marcel Dekker, Inc. New York and Basel, 1982.
- [12] Chen, C-T, *Linear System Theory and Design*, Holt, Rinehart and Winston, 1984.
- [13] Timoshenko, S. and Young, D. H., *Vibration Problems in Engineering*, New York, Van Nostrand, 1975.
- [14] Ogata, K., *Modern Control Engineering*, Prentice-Hall Inc. 1990.
- [15] Balas, M. J., "Feedback Control of Flexible Systems," *IEEE Trans. Automatic Control*, Vol. AC-23, Aug. 1978, pp. 674-679.
- [16] Wonham, W., *Multivariable Control*, Springer, 1974.
- [17] Young, D., "Vibration of Rectangular Plates By the Ritz Method," *Journal of Applied Mechanics*, 17, 1950, pp. 448-453.

Bibliography

- [1] Hisatani, M., Inami, S., Ohtsuka, T. and Fujita, M., "Design and Testing of a Flexible Rotor-Magnetic Bearing System," *Proceedings of the Second International Symposium on Magnetic Bearings*, July 1990, Tokyo, Japan, pp. 131-138.
- [2] McCallum, D. C., "Dynamic Modelling and Analysis of a Magnetically Suspended Flexible Rotor," *NASA Conference in Aerospace Applications of Magnetic Suspension Technology*, September 1990, pp. 499-538.
- [3] Meirovitch, L., *Analytical Methods in Vibrations*, The Macmillan Co., New York, 1967.

N 9 2 - 2 7 7 3 1

**STABILITY AND PERFORMANCE OF NOTCH FILTER CONTROL FOR
UNBALANCE RESPONSE**

**C. R. Knospe
Department of Mechanical and Aerospace Engineering
University of Virginia
Charlottesville, Virginia 22901 USA**

May 28, 1991

ABSTRACT

Many current applications of magnetic bearings for rotating machinery employ notch filters in the feedback control loop to reduce the synchronous forces transmitted through the bearings. In this paper, the capabilities and limitations of notch filter control are investigated. First, a rigid rotor is examined with some classical root locus techniques. Notch filter control is shown to result in conditional stability whenever complete synchronous attenuation is required. Next, a nondimensional parametric symmetric flexible three mass rotor model is constructed. An examination of this model for several test cases illustrates the limited attenuation possible with notch filters at and near the system critical speeds when the bearing damping is low. The notch filter's alteration of the feedback loop is shown to cause stability problems which limits performance. Poor transient response may also result. A high speed compressor is then examined as a candidate for notch filter control. A collocated 22 mass station model with lead-lag control is used. The analysis confirms the reduction in stability robustness that can occur with notch filter control. The author concludes that other methods of synchronous vibration control yield greater performance without compromising stability.

NOMENCLATURE

| | |
|-----------|---|
| c | derivative feedback coefficient |
| c_r | rotor damping |
| \bar{C} | nondimensional bearing damping, c/c_r |
| e_u | unbalance eccentricity |
| F_b | bearing force |
| F_u | unbalance force |
| g | notch gain |
| H | feedback transfer function |
| k | proportional feedback coefficient |
| k_b | open loop magnetic bearing stiffness |
| k_{eq} | equivalent bearing stiffness |
| K_{eq} | nondimensional equivalent bearing stiffness, k_{eq}/k_s |
| k_s | shaft stiffness |

| | |
|----------------|---|
| j | $\sqrt{-1}$ |
| m | rotor mass |
| m_b | bearing rotor mass |
| m_d | disk rotor mass |
| M | mass ratio, $2m_b/m_d$ |
| N | notch filter transfer function |
| p | characteristic polynomial |
| p_e | even part of characteristic polynomial |
| p_o | odd part of characteristic polynomial |
| s | complex frequency variable |
| W | notch width |
| Z | rotor position |
| Z_1 | complex bearing displacement, $Z_1 = X_1 + j Y_1$ |
| Z_2 | complex midspan displacement, $Z_2 = X_2 + j Y_2$ |
| β | angle from PD zero to notch zero |
| ϕ | angle from notch pole to notch zero |
| θ | angle from notch pole to notch zero |
| ψ | angle of arrival of locus |
| ζ_d | notch pole damping |
| ζ_o | notch zero damping |
| ζ_r | rigid bearing shaft damping, $c_r/2\sqrt{k_s m_d}$ |
| ω_o | operating speed, notch center frequency |
| $\bar{\omega}$ | nondimensional operating speed, ω_o/ω_r |
| ω_r | rigid bearings critical speed, $\sqrt{k_s/m_d}$ |
| λ | nondimensional complex frequency, s/ω_r |

INTRODUCTION

In the last decade, active magnetic bearings for rotating machinery have moved from a promising concept to industrial application. Magnetic bearings have been installed in a variety of machines including pumps and compressors [1,2]. They have been employed successfully in several large rotating machinery applications including over 25 thousand hours of operation on a natural gas pipeline compressor [2]. While these initial experiences with industrial application of magnetic bearings have been encouraging, problems with their installation have been noted. Often, installation of current design of magnetic bearings requires several weeks of "tuning" of the controller [2]. Undoubtedly, as digital control becomes more widespread for magnetic bearings, this time will be shortened. However, the authors believe that the fundamental factor in the long controller installation time is the amount of tuning required to achieve stability and acceptable performance. Better analysis of the rotor dynamic and control issues of a particular application before installation should greatly reduce on-site tuning.

One area that the authors believe has undergone insufficient analysis is the use of notch filters. Many current applications of magnetic bearings have a notch filter in the

control feedback loop to suppress rotor synchronous response [3]. The notch frequency is placed at the operating speed and causes the bearings effective stiffness and damping at this speed to be greatly reduced. In principle, the bearings exert little harmonic force upon the rotor and the rotor spins about its inertial axis. Thus, a greatly reduced harmonic force is transmitted to the foundation. However, since the stiffness and damping of the bearings at the rotational speed is very small, the orbits at the bearings may become quite large. The notch filter technique is often referred to as "automatic balancing". This name may be misleading since the reduced bearing stiffness and damping are not analogous to conventional rotor balancing techniques. In conventional rotor balancing, correction weights are added to the shaft so as to reduce the residual unbalance. These weights produce forces which rotate with the shaft counteracting the forces due to the shafts unbalance distribution. Conventional balancing does not change the bearing properties. Thus, conventional balancing does not affect system stability or transient response. Notch filtering changes both these since it alters the bearing properties. With the notch filter, the unbalance distribution about the geometric axis is unaltered; however, the rotor spins about its inertial axis. In theory, the motion of the shaft is not transmitted to the foundation because of the very low stiffness and damping.

Since notch filters achieve synchronous attenuation through altering the magnetic bearing feedback loop, stability becomes an important issue. In practice, the stability issue has a profound impact upon the efficacy of notch filters as a solution to the unbalance response problem. This result has been reported by Beatty [4] for single mass flexible rotors with massless bearings. For the same reason, a notch filter controlled system may also have poor transient response.

The authors emphasize, however, that it is not necessary to use feedback modification to achieve unbalance response attenuation. Because the synchronous response is highly correlated, it can be reduced through an open loop (feedforward) scheme without altering the system transient response or stability. This method has been employed by many researchers [5,6,7,8]. Recently, the authors have demonstrated reductions in transmitted synchronous vibration of 42 dB (over one hundred fold) on an experimental rotor rig [9]. It is interesting to note that, to the authors' knowledge, open loop controllers are currently not in use on any commercial machines. The promise of these controllers will not be discussed further in this paper as the focus remains the examination of notch filter controllers which are widely employed in commercial machines.

In this paper, the stability and performance of notch filter control systems is examined. In Section II, a rigid rotor model is used to introduce the stability and performance issues of notch filter controllers. Section III examines an extended symmetric three mass rotor model and solves for a nondimensionalized characteristic equation and bearing response. In Section IV, the analysis' results are presented and the stability and performance of notch filter controllers is discussed. Section V examines the robustness of a 22 mass station model of a high speed compressor with notch filters in the feedback loop. Section VI closes with conclusions.

II. RIGID ROTOR ANALYSIS

A rigid rotor system with magnetic bearings is discussed here to introduce the instability that can be produced by notch filters in the feedback loop. A rigid rotor in magnetic bearings without stabilizing feedback may be described by a mass, m , attached to a negative spring [10], $k_b < 0$, with a transfer function between bearing force, F_b , and rotor position, Z

$$\frac{Z(s)}{F_b(s)} = \frac{1}{ms^2 + k_b} \quad (1)$$

A block diagram representation is shown in Figure 1. This system has poles at $\pm \sqrt{-k_b/m}$ and is unstable since one pole is in the right half of the complex plane. The system may be stabilized using proportional-derivative (PD) control

$$\frac{F_b(s)}{Z(s)} \equiv H(s) = cs + k \quad (2)$$

resulting in a stable closed loop system transfer function between unbalance force, F_u , and rotor position

$$\frac{Z(s)}{F_u(s)} = \frac{1}{ms^2 + cs + k_{eq}} \quad (3)$$

where $k_{eq} = k_b + k$, if c and k_{eq} are positive. As illustrated in Figure 2, a root locus diagram for the system, the PD control places a zero on the real axis in the left half of the complex plane at $-k/c$. Whether this zero is to the right or left of the pole at $-\sqrt{-k_b/m}$, the system will be stabilized provided $k > -k_b$. The bearing of the closed loop system will have equivalent stiffness k_{eq} and damping c .

The transfer function for a simple notch filter centered at the operating speed ω_o , characterized by its gain, g , and its width, W , is

$$N(s) = \frac{s^2 + 2\zeta_o \omega_o s + \omega_o^2}{s^2 + 2\zeta_d \omega_o s + \omega_o^2} \quad (4)$$

$$g = \frac{\zeta_o}{\zeta_d} \quad W = 2\zeta_d \omega_o \quad (5)$$

where ζ_o and ζ_d are the damping of the notch filter zeros and poles respectively. The notch gain g is the gain of a signal at frequency ω_o as it passes through the notch. The notch depth, D , $D = 1 - g$, specifies the amount of signal rejected at ω_o . Note that if the notch gain is zero then a signal at ω_o is completely removed by the filter. If the notch gain is one then the signal is completely passed. The notch width is the width of the frequency band where attenuation is greater than -3dB when the notch depth is one [4]. Figure 3 shows the magnitude plot of notch filters of various depths and widths.

A notch filter may be placed in the magnetic bearing feedback loop in essentially two fashions: (1) directly in serial with the PD control, and (2) in serial with PD control after the plant has been compensated for its negative bearing stiffness. In the first case, the controller transfer function is

$$\frac{F_b(s)}{Z(s)} \equiv H(s) = (cs + k) N(s) \quad (6)$$

and in the second case

$$\frac{F_b(s)}{Z(s)} \equiv H(s) = -k_b + (cs + k_{eq}) N(s) \quad (7)$$

In the first case, if the notch has a gain

$$g < -k_b/k$$

then the system will have a negative stiffness to vibrations at ω_o and will therefore be unstable. In the second case, the notch gain would have to be negative to produce an effective negative stiffness at frequency ω_o . Since it is simpler for explanation and no generality is lost, only the second case will be examined in this paper.

When the notch gain is zero, the bearings have no synchronous stiffness or damping and no synchronous vibration is transmitted to the foundation. In practice, however, k_b cannot be known precisely and one cannot cancel it exactly using feedback. It is likely that the bearings after this compensation would have some equivalent stiffness. This would limit the ability of the notch filter to attenuate the transmitted vibration. Thus, the assumption that k_b can be precisely canceled will yield the ideal performance for the notch filter. This ideal case is examined here since the problems associated with notch filters, as will be shown, are serious enough that even their idealized performance will discourage their continued use.

After feedback compensation for the negative bearing stiffness, the plant (rotor plus stabilizing stiffness $-k_b$) has the transfer function

$$\frac{Z(s)}{F_b(s)} = \frac{Z(s)}{F_u(s)} = G(s) = \frac{1}{ms^2} \quad (8)$$

and the notch filter feedback controller has the transfer function

$$H(s) = (k_{eq} + cs) N(s) \quad (9)$$

The plant has two poles at the origin of the complex plane while the controller has poles at

$$-\zeta_d \omega_o \pm j\omega_o \sqrt{1 - \zeta_d^2}$$

and zeros at

$$-\frac{k_{eq}}{c} \quad , \quad -\zeta_o \omega_o \pm j\omega_o \sqrt{1 - \zeta_o^2}$$

If the notch gain is zero ($\zeta_o = 0$) then the complex zeros of GH are on the imaginary axis. If the notch width is 20% of ω_o ($\zeta_d = 0.1$), a possible pole-zero structure and root locus is shown in Figure 4. Note that two closed loop poles are in the right half complex plane

and the system is unstable. Even though the poles of the notch filter are placed near the zeros, the loci stray into the right half plane.

Interestingly, the conditional stability of zero notch gain controllers can be examined through the classical root locus technique of the angle of arrival. The angle of arrival is the angle in the complex plane at which a locus approaches an open loop zero. Evans [9] first established that the sum of the angles from the open loop poles of the system to a point on a locus minus the sum of the angles from the open loop zeros to the same point must be 180° . From this, it is easy to calculate the angle of arrival of a locus at a zero. For the example, the loci must approach the imaginary zeros from the left to ensure unconditional stability. Thus, their angles of arrival must be between 90° and 270° . Given that the notch is thin ($\zeta_d < 1$), this yields a condition for stability of these roots in terms of the angle from the PD zero on the negative real axis to the open loop imaginary zero, β :

$$90^\circ < \beta < 270^\circ$$

Clearly, this condition is only satisfied when the zero on the real axis is in the right half plane. Thus, for a given ratio of equivalent stiffness to damping (which would be chosen by the designer for transient response since this determines the log decrement) the closed loop system with notch filter will go unstable as the stiffness is increased.

Indeed, it is easy to show that conditional stability of this kind will always result if the notch gain is zero for any notch width. Figure 5 illustrates the argument. Note that for any notch filter of the form Eqn. (4), the poles and zeros lie along a semi-circle of radius ω_0 in the left half plane. From geometry, the angle from any possible notch pole circumscribing the two undamped zeros is right (i.e. $\phi + \theta = 90^\circ$). The angles from the open loop poles to a point on the locus as it arrives at the notch zero are ϕ , θ , 90° , and 90° . The angles from the open loop zeros to the point are ψ , β , and 90° where ψ , the angle of arrival, must satisfy

$$90^\circ < \psi < 270^\circ$$

for unconditional stability. The angle of arrival condition

$$(\phi + \theta + 90^\circ + 90^\circ) - (\psi + \beta + 90^\circ) = 180^\circ$$

with

$$\begin{aligned} \phi + \theta &= 90^\circ, \\ -\psi &= \beta \end{aligned} \quad \text{yields}$$

and

$$90^\circ < \beta < 270^\circ$$

This establishes that conditional stability will always occur if the PD control zero is placed on the negative real axis (i.e., damping and stiffness are positive). Conditional stability can only be eliminated by having a notch gain greater than zero. However, as the notch is made more shallow, the attenuation of the transmitted synchronous vibration is reduced.

This conditional stability is not surprising since the notch filter introduces phase lag at frequencies below the center frequency. Thus, the feedback controller may not have phase lead at the rotor natural frequencies, resulting in instability.

III. FLEXIBLE ROTOR MODEL

A symmetric three mass rotor model with flexible shaft and notch filter controller is examined in this section. The model to be used, shown in Figure 6, is described by the Laplace domain dynamical equations

$$\begin{aligned} [m_b s^2 + \frac{1}{2} k_s + k_b + H(s)] Z_1(s) &= [\frac{1}{2} k_s] Z_2(s) \\ [m_d s^2 + c_r s + k_s] Z_2(s) &= [k_s] Z_1(s) + F_u(s) \end{aligned} \quad (10)$$

where m_b is the rotor bearing mass, m_d is the rotor disk mass, c_r is the rotor damping, k_s is the shaft stiffness, $Z_1(s)$ is the complex displacement at the bearing, $Z_2(s)$ is the complex displacement at midspan, $H(s)$ is the controller transfer function, and $F_u(s)$ is the unbalance force which is assumed to act at the midspan. The feedback controller transfer function is given by

$$H(s) = -k_b + (cs + k_{eq}) N(s) \quad (11)$$

where $N(s)$ is the notch filter transfer function defined in Eqn. (4). The characteristic equation for this system is given by

$$0 = [m_b s^2 + \frac{1}{2} k_s + k_b + H(s)] [m_d s^2 + c_r s + k_s] - \frac{1}{2} k_s^2 \quad (12)$$

With the nondimensional quantities ω_r , ζ_r , \bar{M} , \bar{C} , \bar{K}_{eq} , and $\bar{\omega}$ defined in the nomenclature, the characteristic polynomial, Eqn. (12), becomes

$$\begin{aligned} 0 = & \left[\frac{1}{2} \bar{M} \lambda^2 + \frac{1}{2} \right] [\lambda^2 + 2\zeta_r \lambda + 1] [\lambda^2 + 2\zeta_d \bar{\omega} \lambda + \bar{\omega}^2] \\ & + [2\bar{C} \zeta_r \lambda + \bar{K}_{eq}] [\lambda^2 + 2\zeta_r \lambda + 1] [\lambda^2 + 2\zeta_d \bar{\omega} \lambda + \bar{\omega}^2] \\ & - \frac{1}{2} [\lambda^2 + 2\zeta_d \bar{\omega} \lambda + \bar{\omega}^2] \end{aligned} \quad (13)$$

where λ is the nondimensional complex frequency, $\lambda = s/\omega_r$. This is a sixth order polynomial in λ which defines the closed loop poles of rotor-controller system,

$$p(\lambda) = p_6 \lambda^6 + p_5 \lambda^5 + p_4 \lambda^4 + p_3 \lambda^3 + p_2 \lambda^2 + p_1 \lambda + p_0 \quad (14)$$

where the coefficients are defined by

$$p_6 = \bar{M}/2$$

$$\begin{aligned}
p_5 &= \bar{M}\zeta_d\bar{\omega} + \bar{M}\zeta_r + 2\zeta_r\bar{C} \\
p_4 &= \frac{1}{2}\bar{M}\bar{\omega}^2 + 2\bar{M}\zeta_r\zeta_d\bar{\omega} + \frac{1}{2}(\bar{M}+1) + 4\zeta_r\zeta_o\bar{C}\bar{\omega} + 4\zeta_r^2\bar{C} + K_{eq} \\
p_3 &= \bar{M}\zeta_r\bar{\omega}^2 + (\bar{M}+1)\zeta_d\bar{\omega} + \zeta_r + 2\zeta_r\bar{C}\bar{\omega}^2 + 2\zeta_r\bar{C} + 2\zeta_rK_{eq} \\
&\quad + 2(4\zeta_r^2\bar{C} + K_{eq})\zeta_o\bar{\omega} \\
p_2 &= \frac{1}{2}(\bar{M}+1)\bar{\omega}^2 + 2\zeta_r\zeta_d\bar{\omega} + (4\zeta_r^2\bar{C} + K_{eq})\bar{\omega}^2 \\
&\quad + 4(\bar{C} + K_{eq})\zeta_r\zeta_o\bar{\omega} + K_{eq} \\
p_1 &= \zeta_r\bar{\omega}^2 + 2(\bar{C} + K_{eq})\zeta_r\bar{\omega}^2 + 2K_{eq}\zeta_o\bar{\omega} \\
p_0 &= K_{eq}\bar{\omega}^2
\end{aligned} \tag{15}$$

The unbalance force transmitted through the bearings to the foundation is, in terms of the nondimensionalized parameters,

$$\frac{F_b(\lambda)}{m e_u \omega_r^2} = \frac{[2\zeta_r\bar{C}\lambda + K_{eq}] N(\lambda)\bar{\omega}^2}{[\bar{M}\lambda^2+1 + 2(2\zeta_r\bar{C}\lambda + K_{eq}) N(\lambda)][\lambda^2 + 2\zeta_r\lambda+1] - 1} \tag{16}$$

Using the coefficients of the characteristic polynomial, an efficient procedure may be employed for finding the largest stabilizing notch depth as a function of the nondimensionalized parameters ζ_o , ζ_r , \bar{C} , K_{eq} , $\bar{\omega}$ and \bar{M} .

For a system to be stable, the roots of its characteristic polynomial must all lie in the left half of the complex plane. Polynomials satisfying this condition are called Hurwitz [11,12]. A method for determining the lowest possible notch gain for a stable rotor system is to continually check a Hurwitz stability condition as ζ_o is decreased starting with ζ_o equal to ζ_d (no notch filter). When the notch filter is absent from the feedback loop, the rotor system will be stable if \bar{C} and K_{eq} are positive. As the notch is made deeper for a given bearing (\bar{C} , K_{eq}), the closed loop poles will move continuously in the complex plane. When the notch becomes of sufficient depth, a complex pole will enter the right half plane. On a Nyquist plot, this will appear as a clockwise encirclement of the critical point, as discussed in Beatty [4]. As the notch becomes deeper, the encirclement will remain. Thus, the range of notch gains between zero and one is divided into a stable and an unstable interval.

IV. SIMPLE MODEL RESULTS

In this section, the degree of attenuation of synchronous transmitted force obtainable with a notch filter controller is examined. This is done to explore the limits of notch filters and not to suggest an actual method of implementation. Thus, while we show the attenuation possible over an entire speed range, we are not suggesting that this is in practice desirable or implementable.

Given the nondimensional parameters for the rotor (\bar{M} , ζ_r), the control (\bar{C} , K_{eq} ,

ζ_d), and the operating speed ($\bar{\omega}$), the notch of greatest possible depth (ζ_o) that may be employed while preserving system stability may be found by repeatedly checking stability. From the notch depth so determined, the magnitude of synchronous bearing force can be calculated using Eqn. (16). This is the minimum transmitted force due to unbalance that can be obtained using a notch filter in the feedback loop. (It is easy to demonstrate that maximizing notch depth minimizes transmitted force.) In cases with non-zero notch gain, the system has only marginal stability. In this case, a pair of poles lies along the imaginary axis. Thus, any transient to this system will cause it to 'ring' at this frequency. The only way to amend this undesirable behavior is to reduce the notch depth and thus the synchronous attenuation obtained. Note that in practice the degree of synchronous response attenuation indicated in this analysis cannot be obtained; any implemented feedback controller must have some stability margin.

The analysis was conducted for a three disk magnetic bearing rotor rig used at the University of Virginia. This rig has been used in various research projects and is well characterized [10,13,14]. The nominal values of the nondimensional parameters are

$$\begin{aligned} \bar{M} &= 1.466 & \zeta_r &= 0.0625 \\ \bar{C} &= 10.5 & K_{eq} &= 0.906 \\ \zeta_d &= 0.10 & (\text{Width} &= 20\% \omega_o) \end{aligned}$$

Figure 7 shows the theoretical non-dimensional transmitted synchronous force (without notch filtering) as a function of nondimensional operating speed $\bar{\omega}$ and nondimensional bearing damping \bar{C} . Note the two separate critical speeds at low damping. The limit imposed by stability to the attenuation of this synchronous transmitted force are now examined.

In Figure 8 the minimum notch gain that may be employed while maintaining stability is shown as a function of operating speed and damping. A very deep notch can be obtained above the first critical speed if a high degree of bearing damping is employed. However, if the bearing damping is less than five times the rotor damping, a notch in the region of the second critical cannot be 20 dB deep (gain of 0.1). To achieve this depth at the first critical, the bearing damping must be approximately twenty times the rotor damping. Unfortunately, the synchronous vibration problem is greatest at the critical frequencies where the notch must be the shallowest to maintain stability. In design of PD control for magnetic bearings, the damping is chosen to yield good transient performance and robustness to unmodeled destabilizing forces. It is not desirable to set the bearing damping so as to permit the use of a notch filter.

Figure 9 shows the minimum synchronous bearing force that can be achieved with a notch filter controller at each operating speed as a function of bearing damping. The notch employed at each operating speed and damping is the deepest that may be used with system stability maintained. As Figure 8 suggests, the attenuation of notch filter control when the bearing damping is light is poor near the rotor criticals, approximately 6 dB as can be seen in comparing Figures 7 and 9. When the nondimensional rotor damping is above 10, 20 dB (factor of 10) attenuation can be obtained at any operating speed.

Figure 10 shows the nondimensional bearing force (without notch) for the same three mass rotor model as before except that the bearing masses have been reduced to one quarter the midspan disk mass ($\bar{M} = 0.5$). Thus, this model acts more like a single mass

rotor. Note that the second critical speed is significantly higher. Figure 11 shows the minimum stabilizing notch gain as a function of the nondimensional rotational frequency and damping. Note that the range of operating speeds at low damping near the second critical speed requiring shallow notch filters is much broader than with the first rotor examined (Figure 8). Interestingly, the maximum transmitted force with the notch filter, Figure 12, does not occur at the same frequency as the second critical (without notch) or where the notch is the shallowest. While this seems counter-intuitive, the introduction of the notch filter alters the location of the closed loop poles in the complex plane. As discussed by Dorf [15], the synchronous response of a system is inversely proportional to the distance of the poles from the synchronous frequency on the imaginary axis. Thus, the maximum synchronous response of a synchronous notch system will not occur at the critical frequency of the system without notch since the closed loop pole locations have been altered by the introduction of the notch.

The author wishes to emphasize that the performance indicated here is ideal since it has been assumed that the unstable bearing stiffness can be precisely canceled through feedback and that notch filter controller-rotor system can operate without any stability margin. It should also be pointed out that the notch controller-rotor systems represented that are marginally stable possess a pole on the imaginary axis. Therefore, any disturbance acting at this asynchronous frequency will result in very large displacements.

V. ROBUSTNESS ANALYSIS

We now examine a more realistic rotor model to gauge the effect of notch filters on magnetic bearing system robustness. The 'rotor' employed for this analysis is a 22 mass station model of a high speed test rig constructed at the University of Virginia to simulate an aircraft compressor [16]. The designed operating speed range of this machine is 30,000 to 70,000 rpm. The model employs collocated sensors and actuators and local lead-lag control. The negative bearing stiffness is assumed to have been compensated. The magnetic bearings and the sensors are assumed to have infinite bandwidth. Gyroscopic terms are not included in the model. These assumptions were made so that the results are easier to analyze. We may fairly attribute changes in robustness with the introduction of notch filters to the notch filters themselves and not to the notch filters' interaction with other destabilizing mechanisms (e.g. non-collocation). The rotor with bearing locations is shown in Figure 13.

The structured singular value method is used to analyze the magnetic bearing system robustness with notch filters. Multiplicative uncertainty elements (Δ_1, Δ_2) are placed in the feedback path as shown in Figure 14. These uncertainties are complex numbers and therefore represent some gain and phase change to the signals in the feedback loop. A notch filter operating speed is fixed and the structured singular values of this plant (rotor, phase lead control, notch filters) with respect to the multiplicative uncertainty is computed [17]. The structured singular value is the inverse of the size of the smallest complex uncertainty matrix $\Delta = \text{diag}(\Delta_1, \Delta_2)$ which destabilizes the system. Thus, the structured singular value can be thought of as the inverse of the gain/phase margin at each frequency. Large structured singular values in a frequency range indicates poor stability robustness to unmodeled dynamics in this frequency band.

In this analysis, the maximum structured singular values over frequency is found for the rotor system with and without notch filters. This serves as our robustness measure. We examine this measure as a function of the center frequency of the notch filter. Robustness is therefore examined as a function of notch filter/rotor operating speed much as in Section IV.

In the first analysis, a narrow notch with a notch gain of 0.1 is used. Figure 15 shows the maximum structured singular value as a function of notch center frequency. Also shown is the maximum structured singular value for the system without notch filters. Note that the maximum structured singular value (" μ ") is highest in the region of the rotors critical speeds without notches (first critical: 5530 rpm; second: 10910 rpm; third: 22350 rpm; fourth 55800 rpm). Thus, if a notch filter with 20 dB attenuation were used on this rig near one of these speeds, the system would be much more prone to destabilization due to uncertainties in each feedback loop. The use of notch filters in this operating speed range will make the rotor system much more sensitive to components in the feedback loop (sensors, filters, amplifiers, and actuators). This may help to explain the difficulties experienced in "tuning" magnetic bearing systems.

The maximum structured singular value can be converted to either gain margin or phase margin specifications. These margins are guaranteed margins; that is the system will be stable for at least the amount of variation specified by the margin. Because the system we are examining is a resonant system (which is always stabilized by collocated phase-lead control), closed loop stability is much more sensitive to phase changes. Thus, it is reasonable to expect that the actual multivariable phase margin is not much greater than the guaranteed phase margin specified by the maximum structured singular value. Figure 16 shows the guaranteed phase margin as a function of notch center frequency. Note that without notch filters, the system has 41° phase margin. However, with a notch filter included, the phase margin drops considerably, especially near critical speeds. It should be noted that most control systems are designed to have phase margins greater than 20°. In the author's opinion, a healthy phase margin is necessary for a properly running magnetic bearing system.

This analysis was also carried out with a notch filter with 40 dB depth. The maximum structured singular value as a function of notch center frequency for this case is shown in Figure 17. Below approximately the third critical speed the rotor is unstable (without any multiplicative uncertain). As the notch center frequency is increased, the system becomes less sensitive to phase/gain changes in the feedback loops. Figure 18 shows the corresponding guaranteed phase margin of the system with and without notch filters as a function of notch center frequency. Note that at no frequency in the rotors operating speed range will the system with notch filters have a phase margin of 20°.

VI. CONCLUSIONS

Analysis of synchronous notch filter controllers for unbalance response attenuation of magnetically suspended rotors demonstrates that the introduction of a notch filter into the feedback loop has a profound affect on system stability and robustness. It was shown that for a rigid rotor complete attenuation was impossible without conditional stability. For flexible rotors, notch depth was restricted by instability near the critical speeds. If the bearing damping is low, transmitted force attenuation is small near the critical speed. When set for a given operating speed, asynchronous disturbances can cause large displacements since the notch filter controlled rotor may be marginally stable. This is an important consideration for practical rotor systems which have subharmonic excitations due to cross coupled effects such as seals. Structured singular value analysis was used to show the reduced robustness that may occur when notch filters are introduced into the feedback loop. This analysis examined the robustness with respect to the simultaneous independent gain/phase changes in each loop. Notch filter controllers may also have poor robustness to changes in the rotor (for example, thermal induced changes in Young's modulus) and destabilizing fluid forces which are not representable by this structure.

Due to these problems with notch filter controllers, the author strongly recommends that magnetic bearing users employ open loop (feedforward) control strategies for synchronous vibration reduction. These controllers have been demonstrated by many researchers to yield superior vibration attenuation with no stability problems.

REFERENCES

- [1] Imlach, J., Humphris, R., Blair, B., Allaire, P., and Lewis, D., "Testing of a Magnetic Bearing Equipped Canned Motor Pump for Installation in the Field," 2nd International Symposium on Magnetic Bearings, Tokyo, Japan, July 12–14, 1990, pp. 39–45.
- [2] Foster, E., Kulle, V., and Peterson, R., "The Application of Active Magnetic Bearings to a Natural Gas Pipeline Compressor," ASME Paper 86–GT–1, presented at International Gas Turbine Conference and Exhibit, Dusseldorf, West Germany, June 8–12, 1986.
- [3] Haberman, H. and Brunet, M., "The Active Magnetic Bearing Enables Optimum Damping of Flexible Rotors," ASME Paper 84–GT–117, 1984.
- [4] Beatty, R., "Notch Filter Control of Magnetic Bearings to Improve Rotor Synchronous Response", Master's Thesis, MIT, May 1988.
- [5] Burrows, C.R., Sahinkaya, N., Traxler, A., and G. Schweitzer, "Design and Application of a Magnetic Bearing for Vibration Control and Stabilization of a Flexible Rotor," Proceedings of the First International Symposium on Magnetic Bearings, ETH Zurich, Switzerland, June 6–8, Springer–Verlag, 1988.
- [6] Higuchi, T., Mizuno, T., and Tsukamoto, M., "Digital Control System for Magnetic Bearings with Automatic Balancing," Proceedings of the 2nd International Symposium on Magnetic Bearings, Tokyo, Japan, July 12–14, 1990.
- [7] Kanemimtsu, Y., Ohsawa, M., and Watnabe, K., "Real Time Balancing of a Flexible Rotor Supported by Magnetic Bearings," Proceedings of the 2nd International Symposium on Magnetic Bearings, Tokyo, Japan, July 12–14, 1990.
- [8] Nonami, K., and Kawamata, S., "Feedforward Control to Unbalance Force Cancellation for Flexible Rotor Systems," Proceedings of the International Symposium on Advanced Computers for Dynamics and Design (ACD&D), Tsuchiura, Japan, Sept. 6–8, 1989.
- [9] Knospe, C.R., Humphris, R.R., and Sundaram, S., "Flexible Rotor Balancing using Magnetic Bearings," Proceeding of the Conference on Recent Advances in Active Control of Sound and Vibration, Blacksburg, VA., April 15–17, 1991. Techomics Publishing, Lancaster, PA, pp. 420–429, 1991.
- [10] Humphris, R., Allaire, P., Lewis, D., and Barrett, L., "Diagnostic and Control Features with Magnetic Bearings," Proc. of the 24th Intersociety Energy Conversion Engineering Conference, Washington, D.C., August 6–11, 1989, pp. 1491–1498.
- [11] Evans, W., Control–System Dynamics, McGraw–Hill, New York, 1954, pp. 96–121.
- [12] Bhattacharyya, S. P., Robust Stabilization Against Structured Perturbations, Lecture Notes in Control and Information Sciences, Vol. 99, Springer Verlag, Berlin, 1987, pp. 14–22.
- [13] Humphris, R., Kelm, R., Lewis, D., and Allaire, P., "Effect of Control Algorithms on Magnetic Journal Bearing Properties," Journal of Engineering for Gas Turbines and Power, Vol. 108, Oct. 1986, pp. 624–632.

- [14] Williams, R., Keith, F., and Allaire, P., "Digital Control of Active Magnetic Bearings," IEEE Transactions on Industrial Electronics, Vol. 37, No. 1, February 1990, pp. 19–27.
- [15] Dorf, R., Modern Control Systems, Addison–Wesley, Reading, MA, 1967, pg. 190.
- [16] Maslen, E., Allaire, P., Scott, M., and Herman, P., "Magnetic Bearing Design for a High Speed Rotor,"
- [17] Doyle, J.C., "Analysis of Feedback Systems with Structural Uncertainties", IEE Proceedings, Part D., Volume 129, No. 6, pp. 242–250, Nov. 1982.

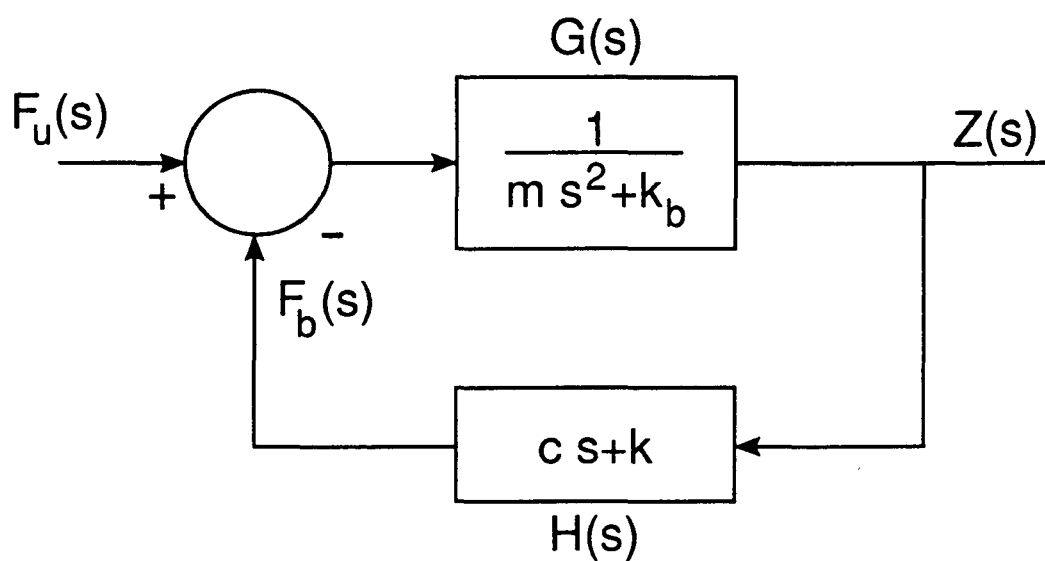


Figure 1: Block diagram of rigid rotor system in magnetic bearings

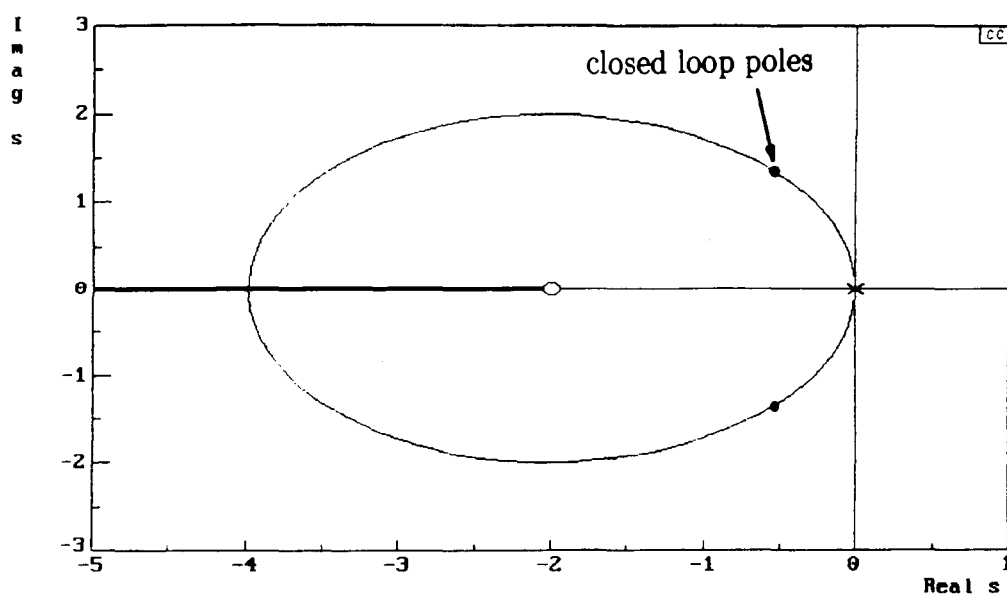
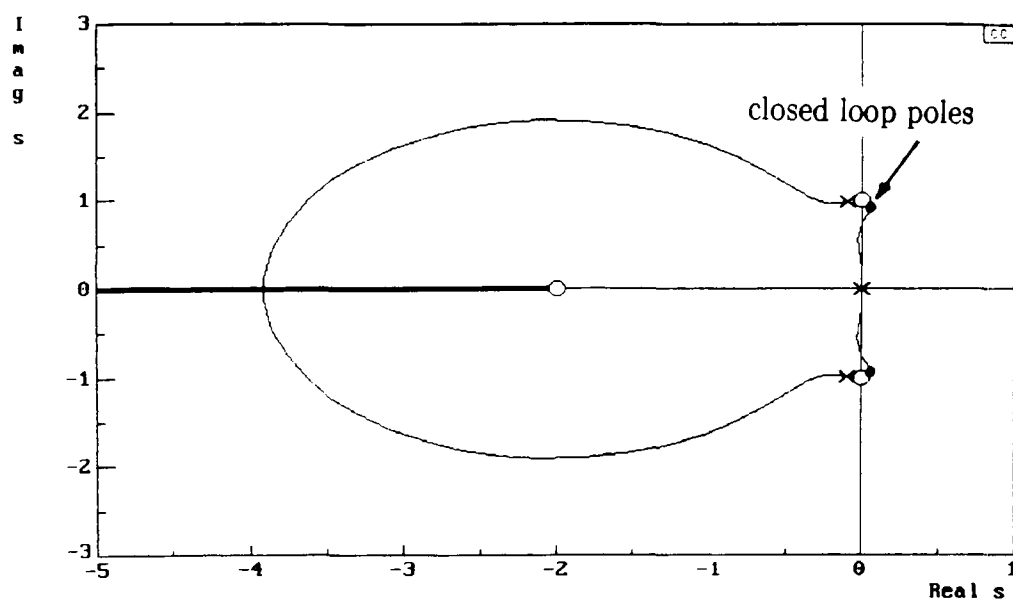
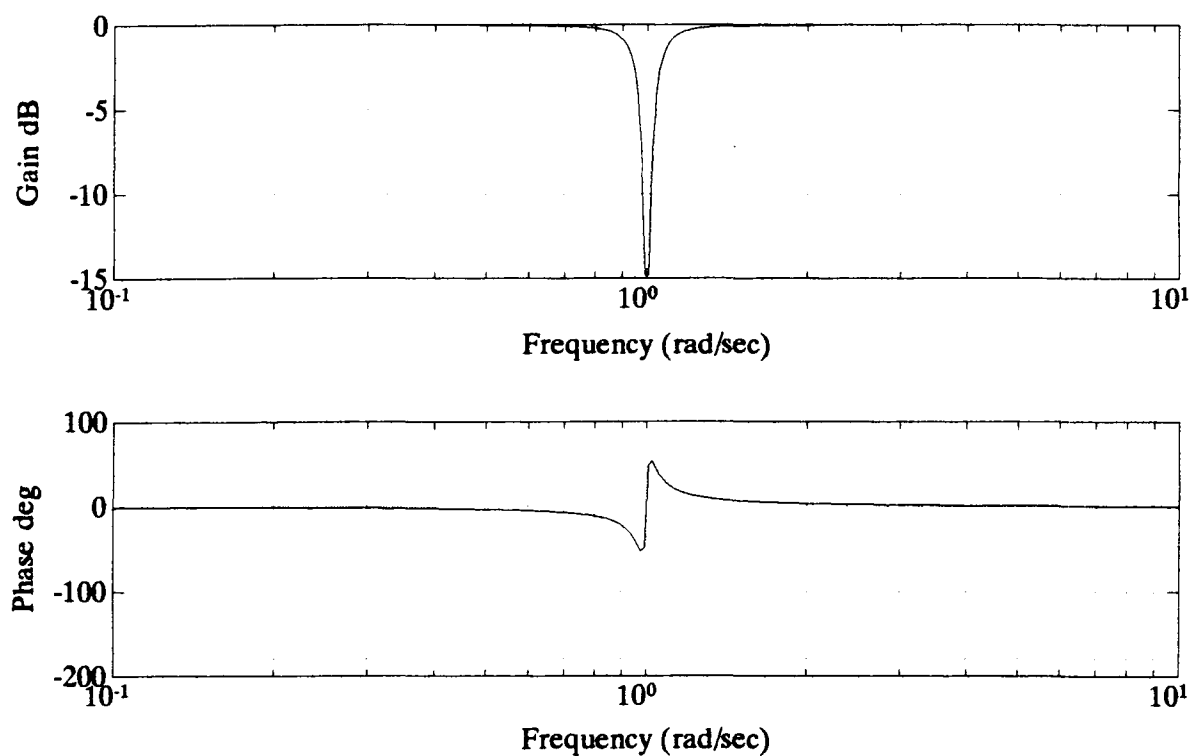


Figure 2: Root locus for PD control of a rigid rotor



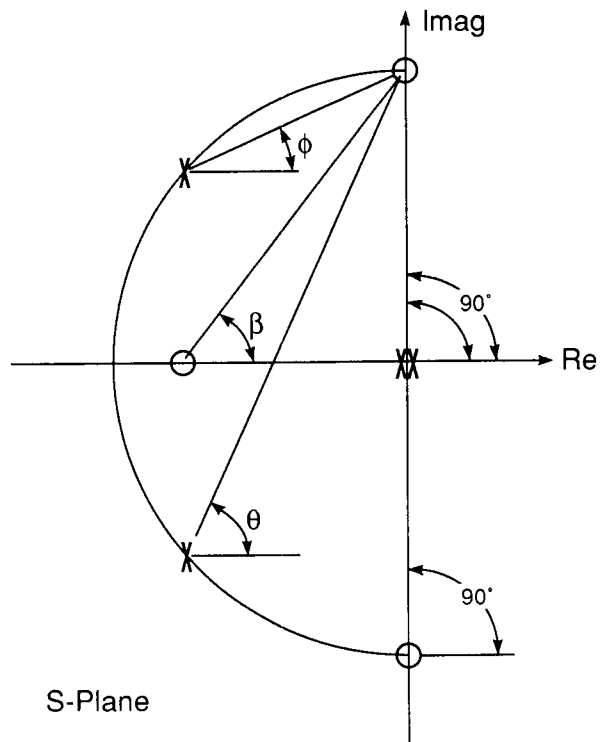


Figure 5: Locus angle for arrival condition ($\zeta_o = 0$, $\zeta_d \leq 1$)

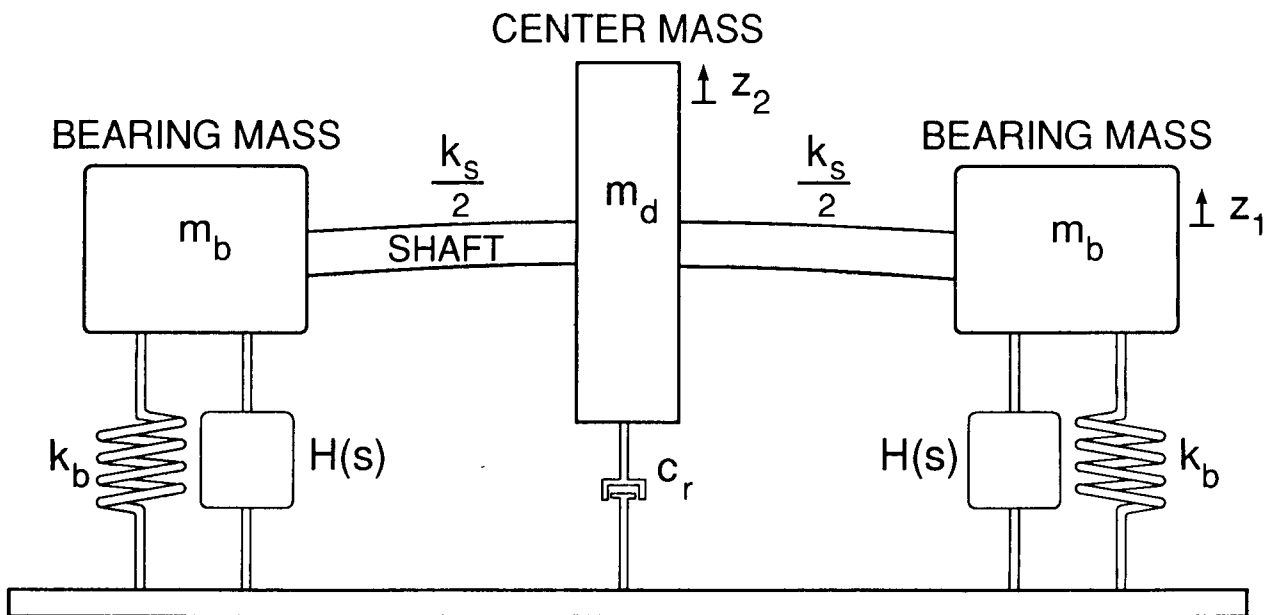


Figure 6: Symmetric three mass rotor model

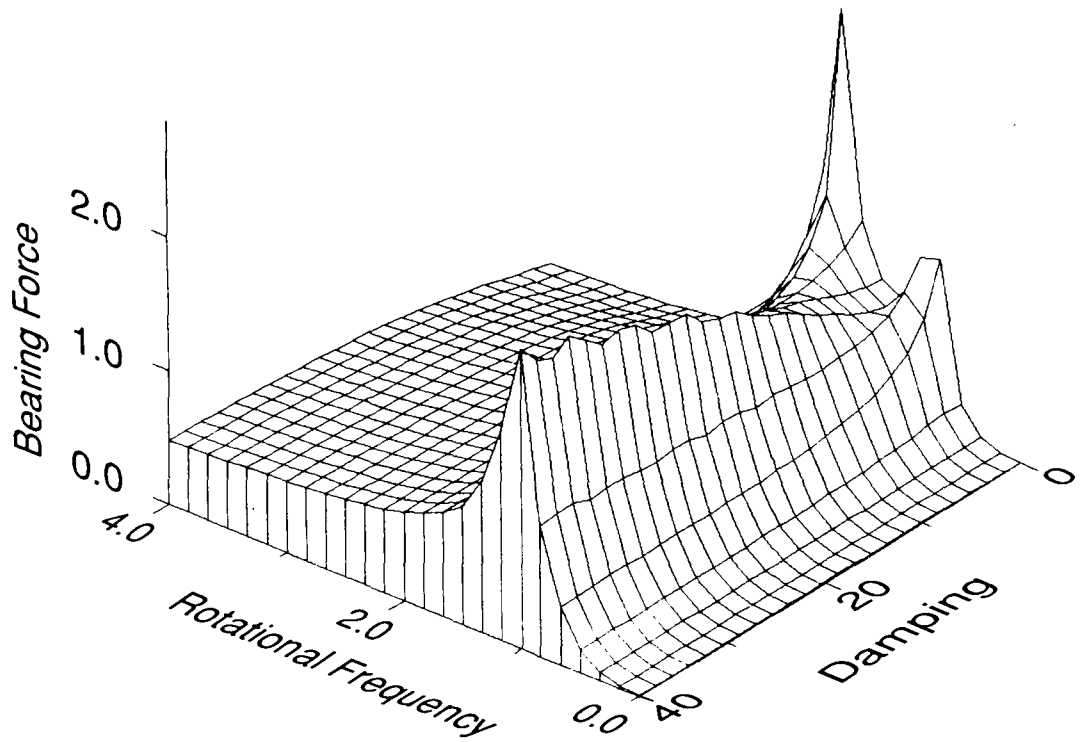


Figure 7: Nondimensional transmitted synchronous force at each nondimensional operating speed as a function of nondimensional bearing damping
($\bar{M} = 1.466$, $\zeta_d = 0.1$)

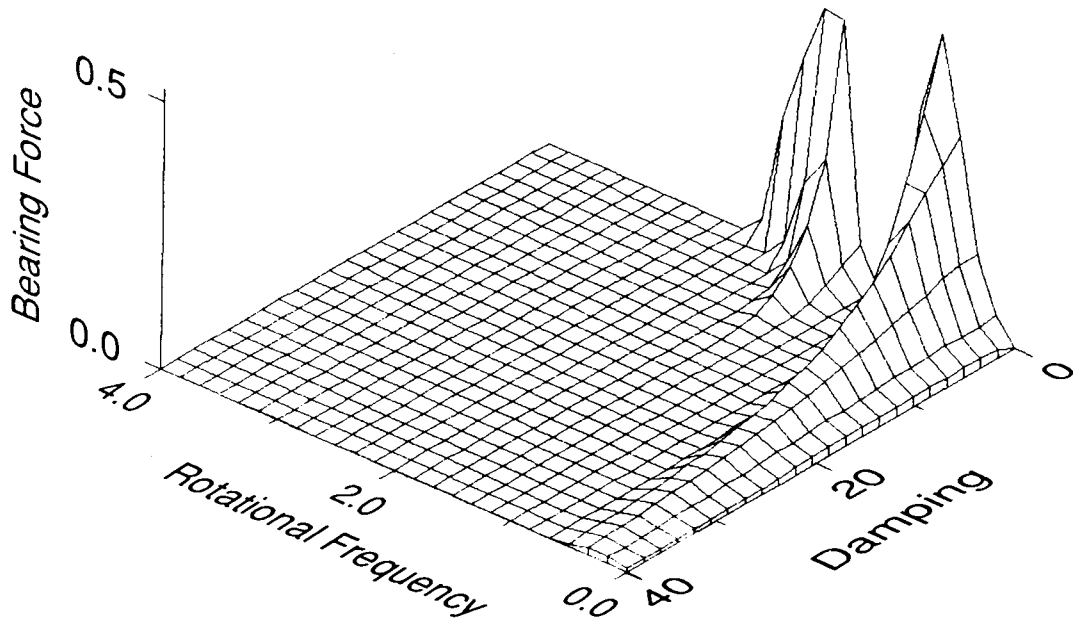


Figure 8: Minimum notch gain at each nondimensional operating speed as a function of nondimensional bearing damping ($\bar{M} = 1.466$, $\zeta_d = 0.1$)

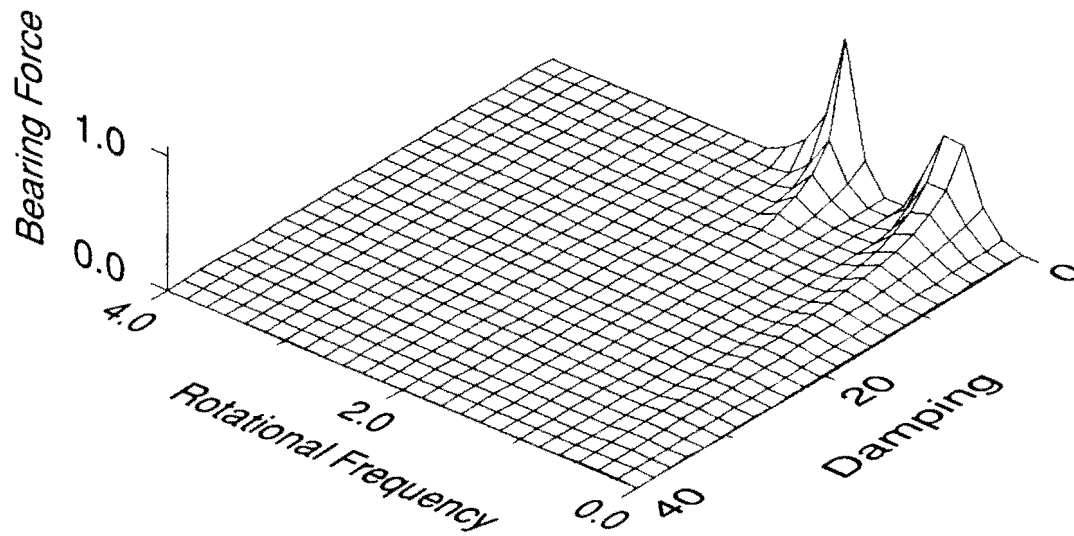


Figure 9: With notch filter control: Nondimensional transmitted synchronous force at each nondimensional operating speed as a function of nondimensional bearing damping ($\bar{M} = 1.466$, $\zeta_d = 0.1$)

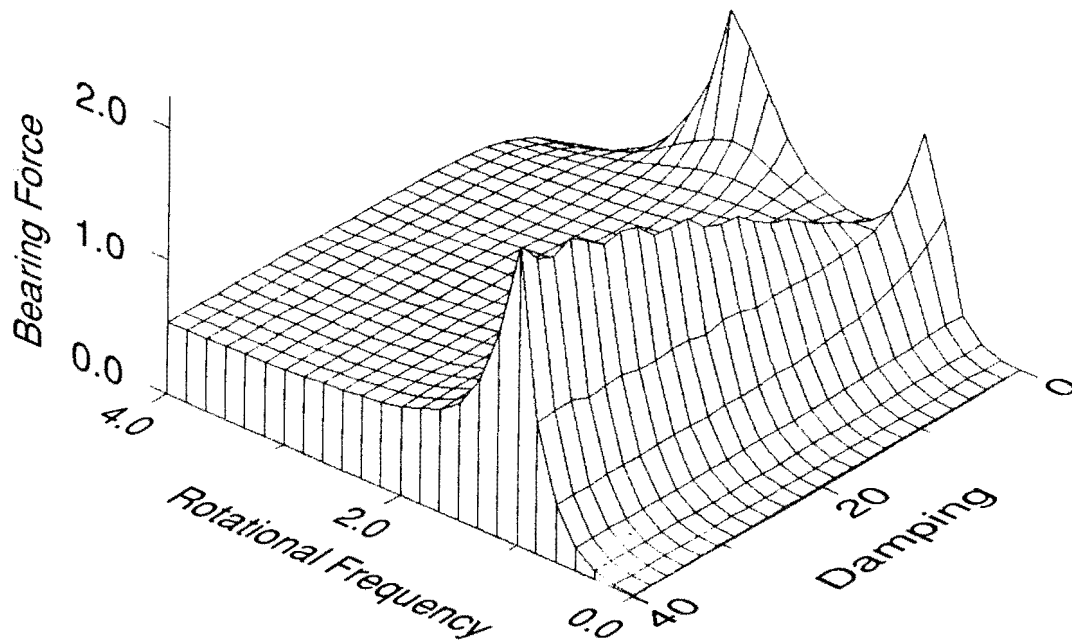


Figure 10: Nondimensional transmitted synchronous force at each nondimensional operating speed as a function of nondimensional bearing damping ($\bar{M} = 0.5$, $\zeta_d = 0.1$)

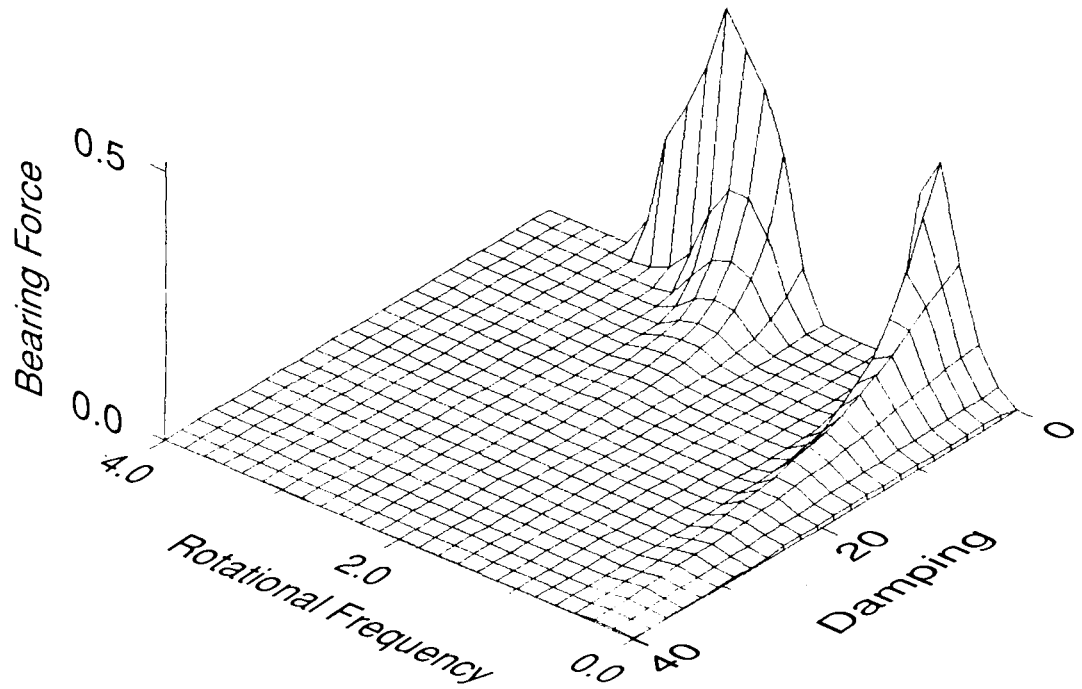


Figure 11: Minimum notch gain at each nondimensional operating speed as a function of nondimensional bearing damping ($\bar{M} = 0.5$, $\zeta_d = 0.1$)

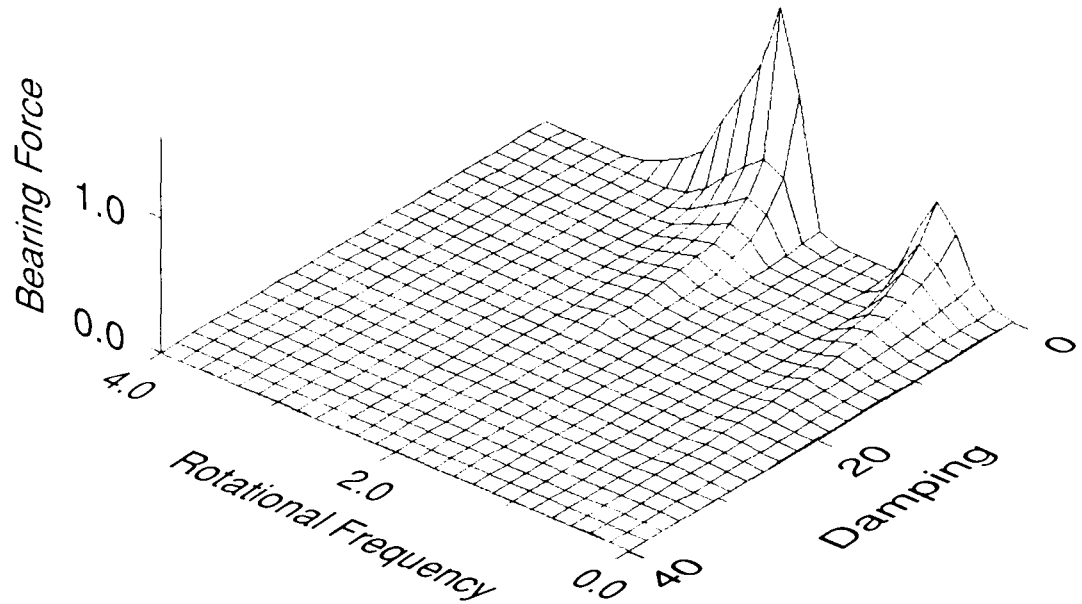


Figure 12: With notch filter control: Nondimensional transmitted synchronous force at each nondimensional operating speed as a function of nondimensional bearing damping ($\bar{M} = 0.5$, $\zeta_d = 0.1$)

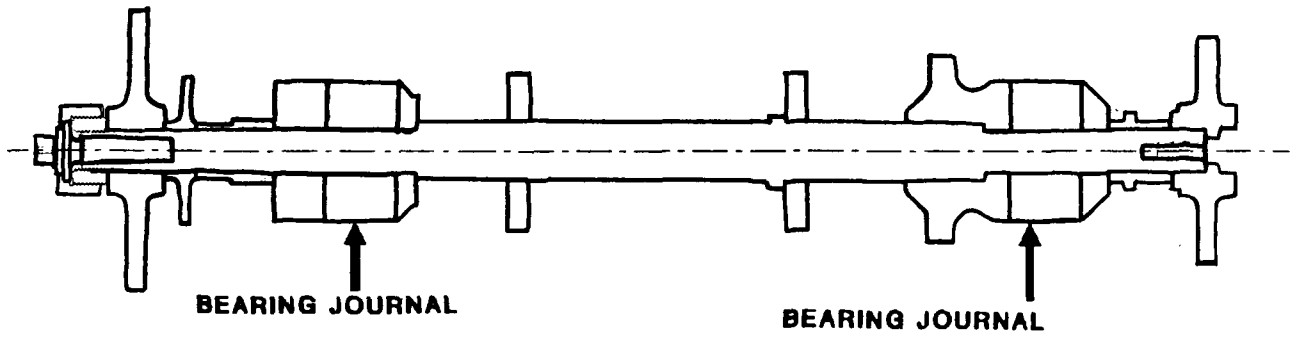


Figure 13: High speed rotor for model aircraft compressor

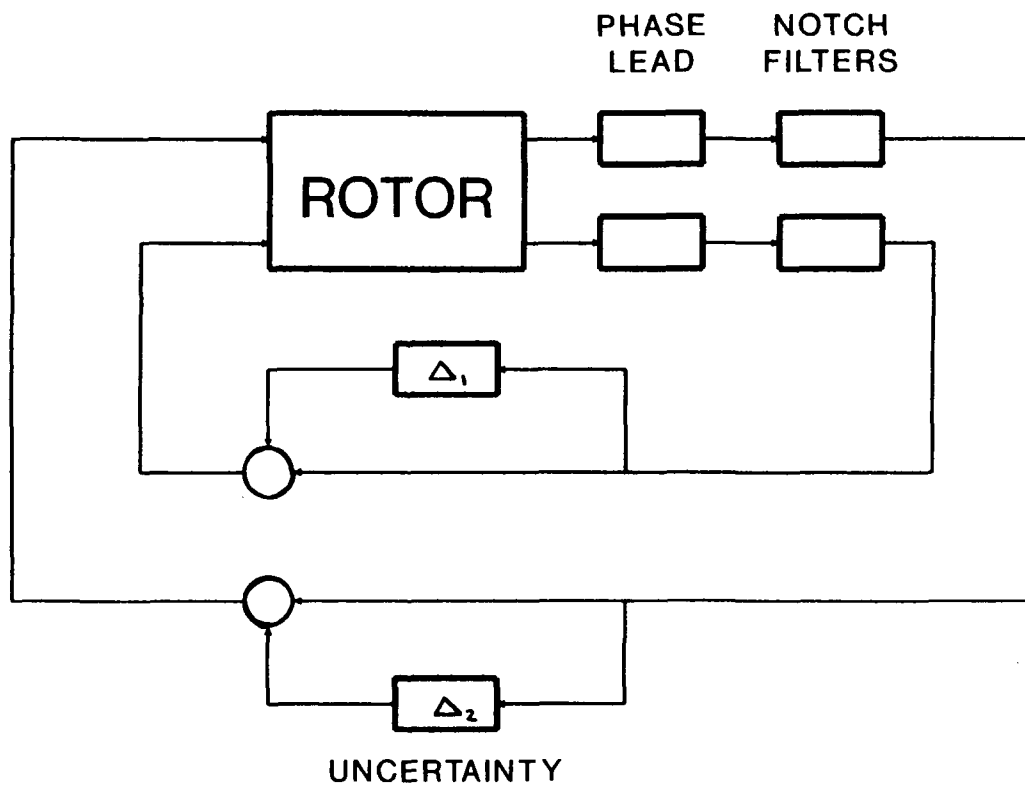


Figure 14: Uncertainty elements in feedback path

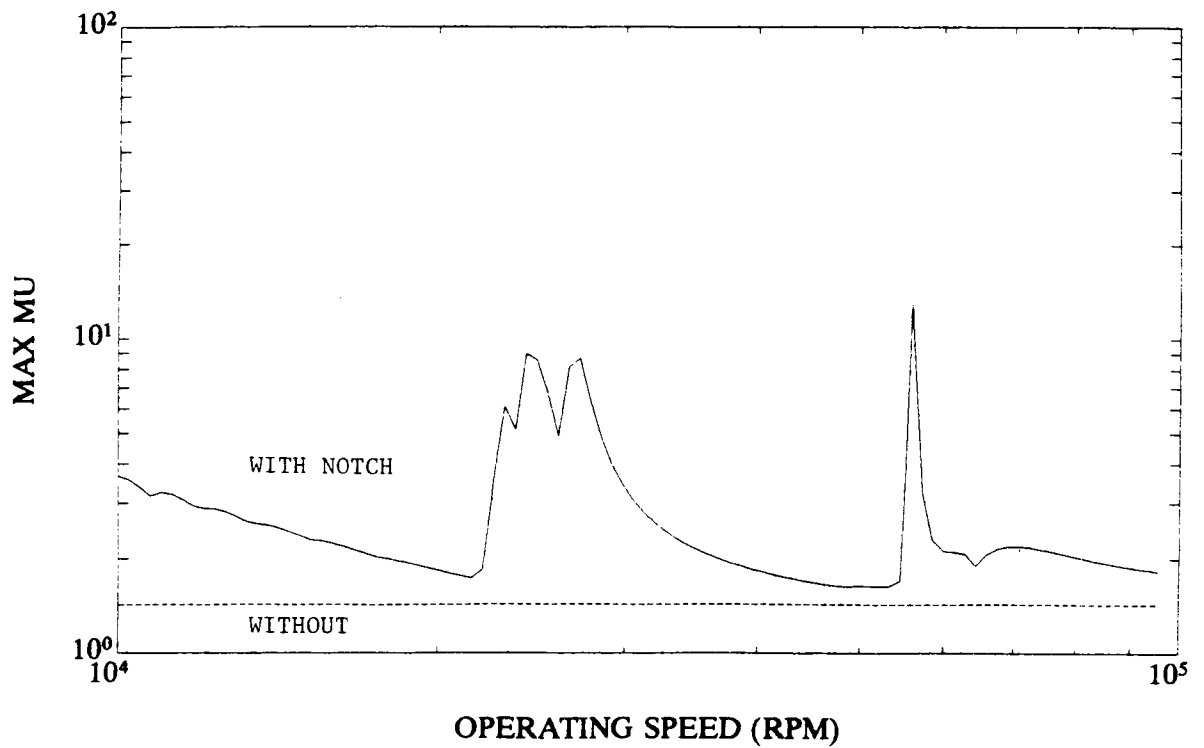


Figure 15: Maximum structured singular value with and without notch filters as a function of operating speed (notch gain = 0.1)

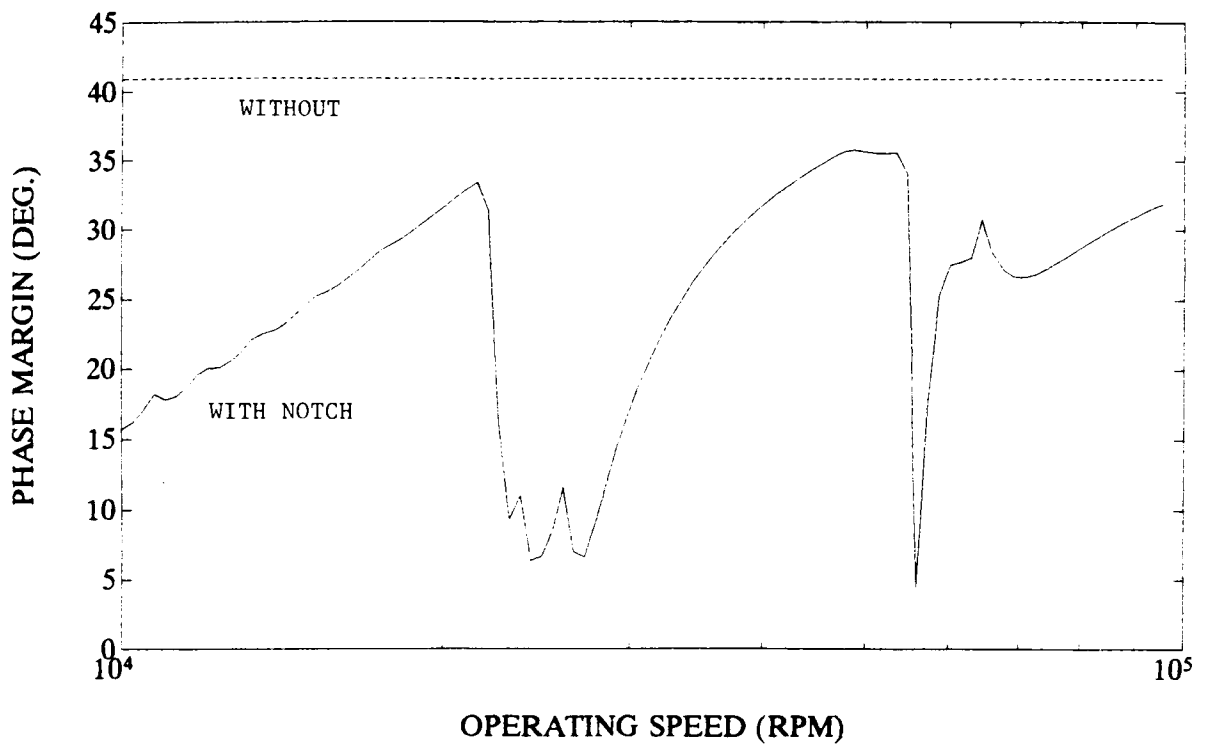


Figure 16: Guaranteed Phase margin with and without notch filters as a function of operating speed (notch gain = 0.1)

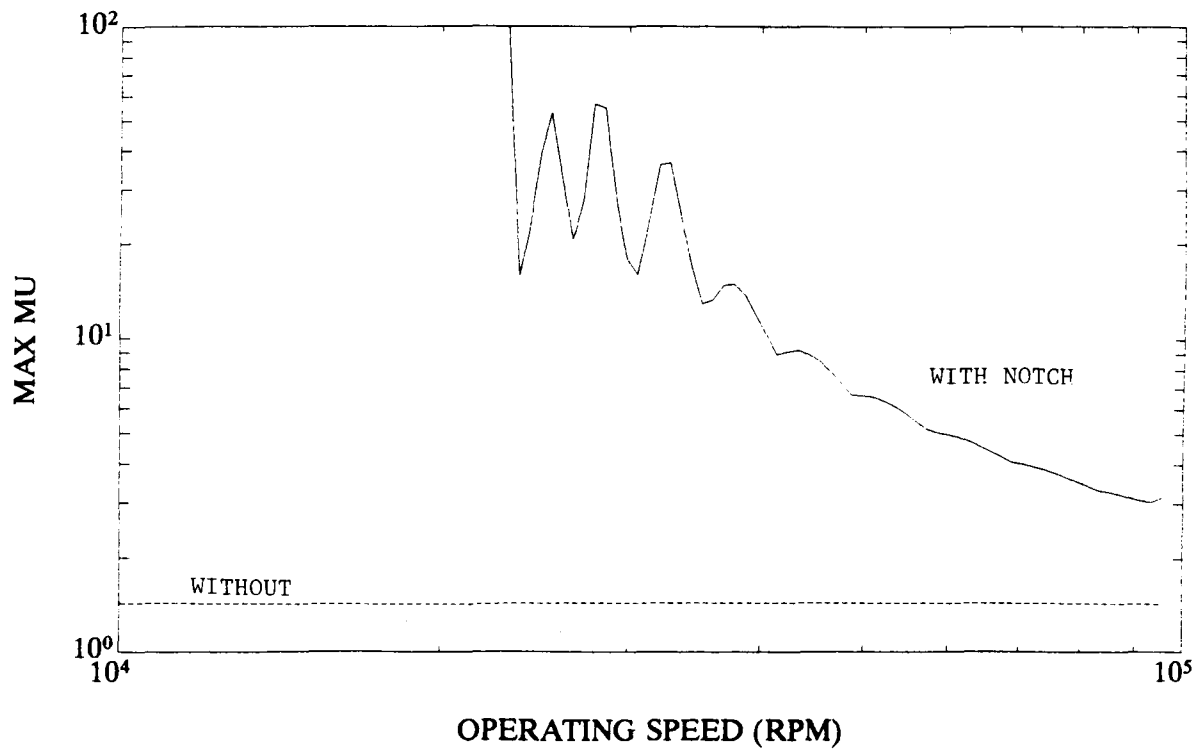


Figure 17: Maximum Structural singular value with and without notch filters as a function of operating speed (notch gain = 0.01)

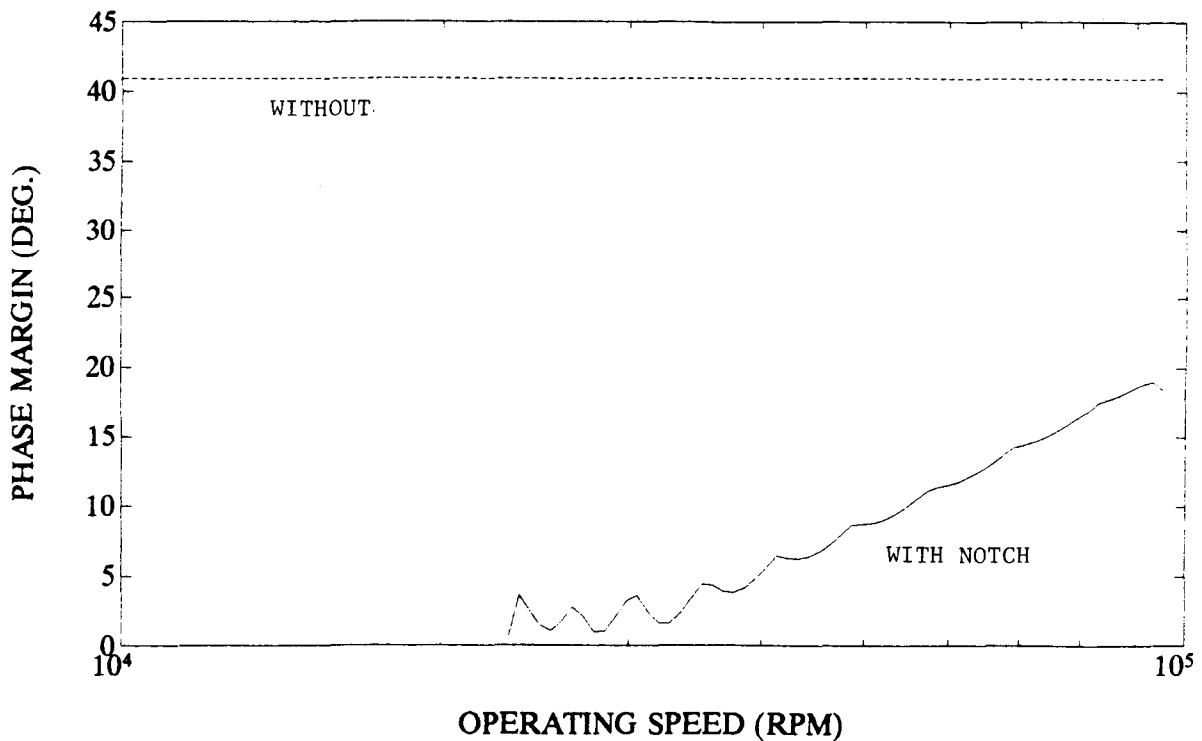


Figure 18: Guaranteed Phase Margin with and without notch filters as a function of operating speed (notch gain = 0.01)

Session 4

MICROGRAVITY AND VIBRATION ISOLATION 1

Chairman - Mike Scott
NASA Langley Research Center

**A Six Degree-of-Freedom Magnetic Bearing for
Microgravity Vibration Isolation ***

**A. Peter Allan and Carl R. Knospe
Department of Mechanical and Aerospace Engineering
University of Virginia**

August 20, 1991

1 Introduction

The authors have previously presented a conceptual design for a coarse-fine actuator pair and discussed its efficacy in the microgravity vibration isolation application[1]. The coarse stage comprises a Stewart platform [2] which is mounted in a spacecraft and isolates low frequency, high amplitude vibrations. The fine stage is a novel magnetic bearing mounted on the Stewart platform (between the legs for compactness) and levitates the experiment to isolate all frequencies at low amplitudes. The combination is illustrated in Figure 1.

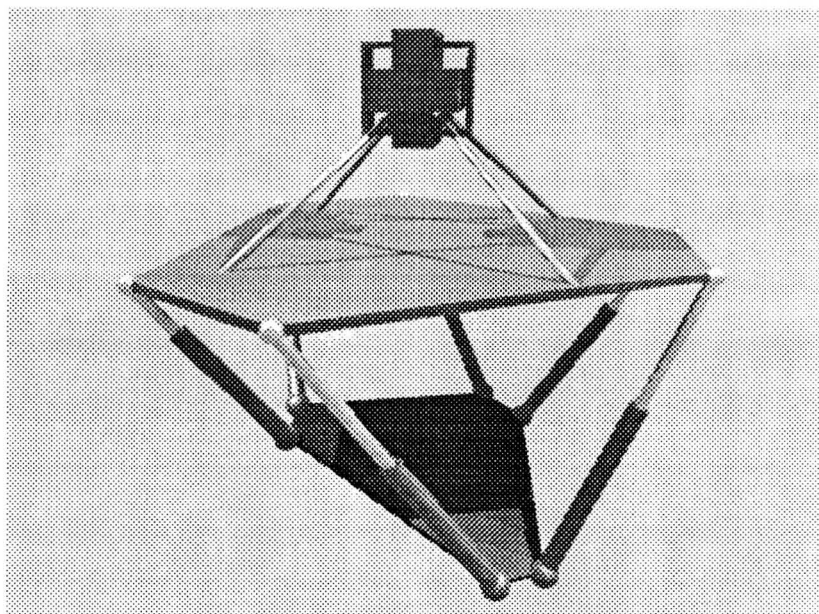


Figure 1: Coarse-Fine Actuator Pair

This paper will present a survey of published 6 DOF levitation designs and discuss a novel magnetic bearing in terms of design, predicted performance, and control issues.

*Supported in part by the NASA Lewis Research Center and the Commonwealth of Virginia's Center for Innovative Technology.

2 Survey of Published Designs

Several designs for 6 DOF levitation are discussed in the literature. A comparison of the specifications for these designs is given in Table 1.

| <i>Group</i> | <i>Trans.</i> | <i>Rot.</i> | <i>Force</i> | <i>Envelope</i> | <i>Weight</i> | <i>Actuator</i> | <i>Sensor</i> |
|--------------|---------------|----------------------------|--------------------|-----------------------------|---------------|-----------------|---------------|
| Honeywell | ± 5 mm | $\pm 1.6^\circ$ | 43 N | 27x34x50 cm | 36 kg | Mag. Brng. | Eddy & Flux |
| N. Wales | ± 5 mm | $< \pm .2^\circ$ | .04 N ^a | 100x100x100 cm ^b | ? | Lorentz | Capacitive |
| NASA | ± 4 mm | $\pm 3^\circ$ ^c | 445 N | 30x30x15 cm ^c | ? | Mag. Brng. | Eddy |
| SatCon | ± 10 mm | $\pm 8^\circ$ ^c | 4 N | 40x40x12 cm ^c | 4.9 kg | Lorentz | Eddy |
| IBM | ± 5 mm | $\pm 4^\circ$ | 32 N | 25x25x15 cm ^c | ? | Lorentz | Optical |
| Toshiba | ± 2 mm | $\pm 1.5^\circ$ | 20 N ^c | 25x25x20 cm | 8 kg | Mag. Brng. | Eddy |

^aRequirement, not limitation

^bIncludes experiment package

^cEstimated by authors

Table 1: Comparison of Published Designs

Four designs specifically for microgravity isolation have been published. Honeywell [3] has a well developed system called FEAMIS with which they have demonstrated impressive isolation performance. The system is designed for the Space Shuttle experiment configuration. The University College of North Wales [4] also has a well developed system designed for the European Space Agency experiment configuration. NASA [5] and SatCon [6] both have laboratory levitation systems.

Two levitation designs were developed for different applications, but they are mentioned here because they are similar and could be easily adapted to the isolation application. IBM [7] has a laboratory levitated robot "wrist" which enhances robot accuracy and performance. Toshiba [8] has a satellite antenna pointing system which is fully developed. Both devices have demonstrated positional accuracies on the order of $1 \mu\text{m}$.

Isolation of vibrations with large amplitudes — typically occurring at low frequencies — requires a large translational range. SatCon's system has the largest range, but there is a significant tradeoff with the device's force capability. A coarse-fine approach would allow both a large range, provided by the coarse stage, and a high force capability, since the levitation gaps are small. There is no available data on the rotational range requirements of the application. Isolation with an umbilical disturbance requires a high force capability as is offered by the systems from Honeywell, NASA, IBM, and Toshiba. Space and weight should be minimized in any spacecraft. SatCon, IBM, and Toshiba's systems offer advantages in envelope space and weight.

The choice of the actuator technology between Lorentz force and magnetic bearings has no definitive advantage. Lorentz actuators offer linearity, simplicity, and compactness. Magnetic bearings offer higher force capability and lower power consumption, particularly if gaps are minimized.

Four position sensor technologies offer promising performance. Eddy current position probes are simple and robust, but bulky and heavy for large gaps. Capacitive sensors are simple and light weight, but can be noisy in unconstrained environments. Optical lateral effect photo-diodes are compact and quiet, but they require substantial supporting electronics. Hall effect flux sensors can be used with magnetic bearing designs both to linearize the control problem, and to measure position.

3 Design

The magnetic bearing proposed has two parts: a stator which is attached to the spacecraft, and a surrounding "flotor" to which the experiment is attached.

The stator is illustrated in Figure 2. It has twelve pole pieces and coils arranged around the surface of a cube. The cube and pole pieces are ferromagnetic. Each pair of pole pieces and the region of the cube to which they are attached comprise a typical “horseshoe” electromagnet causing an attractive force toward the nearby flotor. Magnetic flux through the center of the cube will cause an imbalance in the flux levels of a pair of pole pieces, resulting in a net torque on the flotor. Differential Hall effect sensors will be located in the cube side of each pole piece to measure the local flux. All electrical connections will be to the stator.

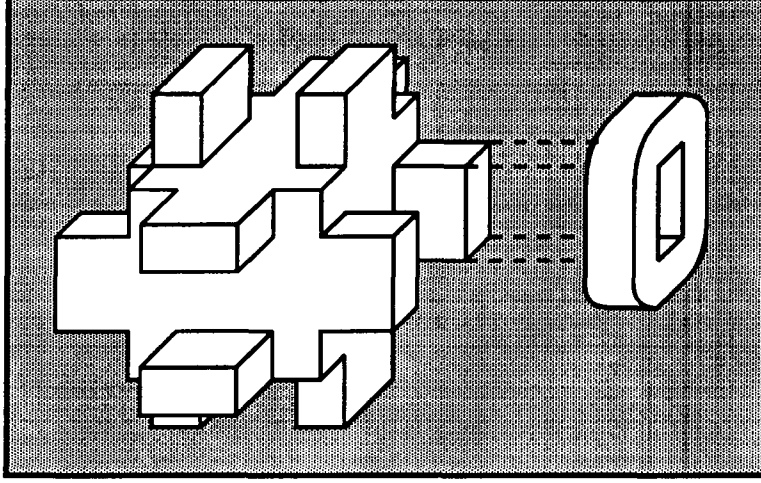


Figure 2: Stator and Typical Coil

The flotor is illustrated in Figure 3. Three ferromagnetic bands are rigidly attached to each other, but form independent flux paths. The bands are thicker in the region near the pole pieces to avoid saturation. Flux which passes through the center of the cube is returned through the remaining portion of the bands.

Four mounting posts will attach to corners of the cube, and pass through clearances in the flotor. These posts could carry cooling fluid to be circulated through the stator if it is required.

Design equations relating force and moments to the coil currents will be derived below referring to Figure 4. The figure shows a schematic slice through the stator and flotor with appropriate nomenclature and sign convention information. It should be noted that a complete model comprises three such systems, but they are identical and orthogonal, so only one will be analyzed.

The relationship between coil currents (i_1, \dots, i_4) and the force and moment generated in one slice of the stator (F_y, M_z) can be derived from Maxwell's Equations. The first Maxwell equation (1), which relates magnetic field intensity (\mathbf{H}) around a closed path to the electric current density (\mathbf{J}) through that path, is discretized and applied to closed loops drawn through the slice. N is the number of turns in each coil, and G_i are the air gap lengths which are dependent on the stator's position relative to the flotor. The iron flux paths are ignored because their reluctance is low relative to that of the air gaps. Many such equations can be written (2), but only three are independent.

$$\oint_C \mathbf{H} \cdot d\mathbf{l} = \int_S \mathbf{J} \cdot d\mathbf{a} \quad (1)$$

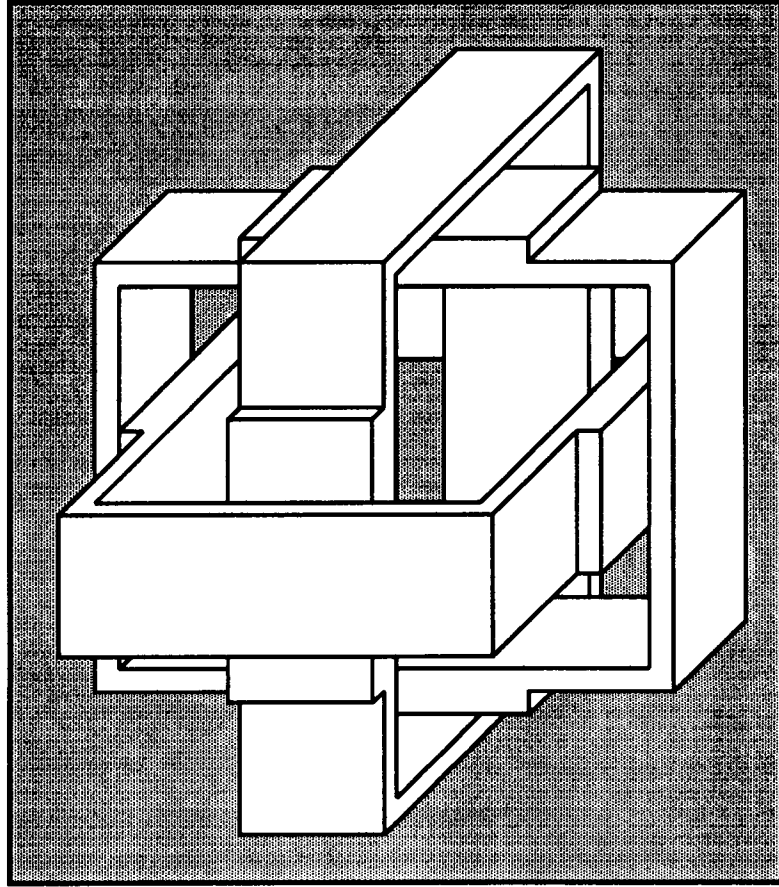


Figure 3: Flotor

$$\begin{aligned}
 H_1 G_1 - H_2 G_2 &= N(i_1 - i_2) \\
 -H_3 G_3 + H_4 G_4 &= N(-i_3 + i_4) \\
 -H_1 G_1 - H_4 G_4 &= N(-i_1 - i_4) \\
 -H_2 G_2 - H_3 G_3 &= N(-i_2 - i_3) \\
 &\vdots
 \end{aligned} \tag{2}$$

The second Maxwell equation (3), which ensures conservation of magnetic induction (\mathbf{B}), is used to obtain a fourth independent equation (4).

$$\nabla \cdot \mathbf{B} = 0 \tag{3}$$

$$B_1 + B_2 - B_3 - B_4 = 0 \tag{4}$$

We can assume linear magnetization in the air gaps (5), where μ_0 is the permeability of free space, to obtain a relation between magnetic induction in the gaps and coil currents (6).

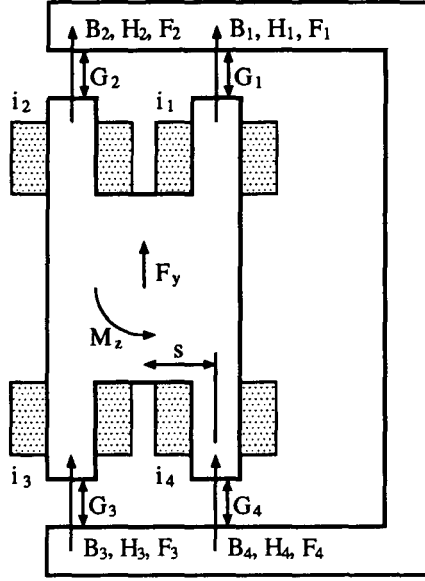


Figure 4: Schematic Cross Section of Magnetic Bearing

$$H_i = \frac{B_i}{\mu_0} \quad i = 1, \dots, 4 \quad (5)$$

$$\begin{Bmatrix} B_1 \\ B_2 \\ B_3 \\ B_4 \end{Bmatrix} = \frac{N\mu_0}{G_1G_2G_3 + G_1G_2G_4 + G_1G_3G_4 + G_2G_3G_4} \begin{bmatrix} G_2G_3 + G_2G_4 + G_3G_4 & -G_3G_4 & G_2G_4 & G_2G_3 \\ -G_3G_4 & G_1G_3 + G_1G_4 + G_3G_4 & G_1G_4 & G_1G_3 \\ G_2G_4 & G_1G_4 & G_1G_2 + G_1G_4 + G_2G_4 & -G_1G_2 \\ G_2G_3 & G_1G_3 & -G_1G_2 & G_1G_2 + G_1G_3 + G_2G_3 \end{bmatrix} \begin{Bmatrix} i_1 \\ i_2 \\ i_3 \\ i_4 \end{Bmatrix} \quad (6)$$

The four gaps are geometrically related to the offset of the stator with respect to the rotor by the relations (7) which assume small angles.

$$\begin{aligned} G_1 &= G_0 - y - s\theta \\ G_2 &= G_0 - y + s\theta \\ G_3 &= G_0 + y - s\theta \\ G_4 &= G_0 + y + s\theta \end{aligned} \quad (7)$$

G_0 is the air gap length with the stator centered in the rotor.

The magnetic energy stored in the magnetic bearing (ω_m) is found from (8) where A_g is the area of the pole faces.

$$\begin{aligned}\omega_m &= \frac{1}{2} \int_{\infty} \mathbf{B} \cdot \mathbf{H} dV \\ &= \frac{A_g}{2\mu_0} (B_1^2 G_1 + B_2^2 G_2 + B_3^2 G_3 + B_4^2 G_4)\end{aligned}\quad (8)$$

The force and moment on the stator are found from the relations (9) and (10).

$$F_y = \frac{\partial \omega_m}{\partial y} \quad (9)$$

$$M_z = \frac{\partial \omega_m}{\partial \theta} \quad (10)$$

After considerable algebraic manipulation, and introduction (without loss of generality) of the linear current transformations (11) we obtain the force and moment relations sought (12) and (13).

$$\begin{aligned}j_1 &= i_1 + i_2 + i_3 + i_4 \\ j_2 &= i_1 - i_2 + i_3 - i_4 \\ j_3 &= i_1 - i_2 - i_3 + i_4\end{aligned}\quad (11)$$

$$F_y = \frac{A_g N^2 \mu_0 (G_0 j_2 + \theta s j_1 + y j_3) (G_0^2 j_3 - \theta^2 s^2 j_3 + G_0 y j_2 + \theta s y j_1)}{4 G_0 (G_0^2 - \theta^2 s^2 - y^2)^2} \quad (12)$$

$$M_z = \frac{A_g N^2 s \mu_0 (G_0 j_2 + \theta s j_1 + y j_3) (G_0^2 j_1 + G_0 \theta s j_2 + \theta s y j_3 - y^2 j_1)}{4 G_0 (G_0^2 - \theta^2 s^2 - y^2)^2} \quad (13)$$

The current j_2 is analogous to the bias current in a conventional bidirectional thrust bearing and could be fixed at a constant value — nominally half of the maximum current. The force generated is predominantly driven by j_3 and the moment by j_1 . The system is unstable (negative stiffness) in both translation and rotation. The currents i_1, \dots, i_4 can be found by a pseudo-inverse technique from j_1, j_2, j_3 . Closed form analytic inverses to (12) and (13) have been found for a known position.

4 Predicted Performance

The equations of the previous section were used to predict the performance of a specific design. The design has a center cube of 2 in. on a side, pole faces of 1 x .5 in., and pole length of 2 in. Maximum current is determined by allowing a coil current density of 5000 amp/in² which is known to be conservative from previous designs. The gap in the centered position was chosen to be .125 in. plus an allowance of .030 in. for inclusion of flux sensors and a protective layer on the inside of the bands. The resulting specifications for the design are presented in Table 2. The 53 N force is a continuous worst case, with the stator moved away from the flotor in the direction of the force. The continuous force capability in the centered position is 175 N. Intermittent force capability is limited only by the current capability of the amplifiers, and the saturation limit of the magnetic material used. Using Vanadium Permadrur with this design, saturation would occur at about 1000 N. Of the 4.5 kg weight, the flotor comprises only 1.2 kg.

| <i>Trans.</i> | <i>Rot.</i> | <i>Force</i> | <i>Envelope</i> | <i>Weight</i> |
|---------------|---------------|--------------|-----------------|---------------|
| ± 3.2 mm | $\pm 7^\circ$ | 53 N | 15x15x15 cm | 4.5 kg |

Table 2: Specification of UVA Design

When compared with the designs presented in Table 1, the UVA design has several advantages. The envelope is substantially smaller than any of the previous designs, while the performance is similar. In addition to saving space, this compactness allows the flotor to be naturally rigid, and thus avoids control problems with structural dynamics. The design is quite dense in comparison with the others, but it is lighter than the lightest for which data were available.

5 Control

A regulator has been designed to reject the disturbances caused by the umbilical connection to the experiment. A schematic is shown in Figure 5. Nonlinearities in the magnetic bearing are eliminated by using flux feedback in a minor loop [3]. Six accelerometers mounted on the flotor produce a generalized acceleration signal which is fed back through a linear controller. More details on the controller are available in [9]. The desired control force is processed through an inverse magnetic circuit model to obtain a desired flux signal. This model could be either a digital algebraic model, or an appropriately trained neural network.

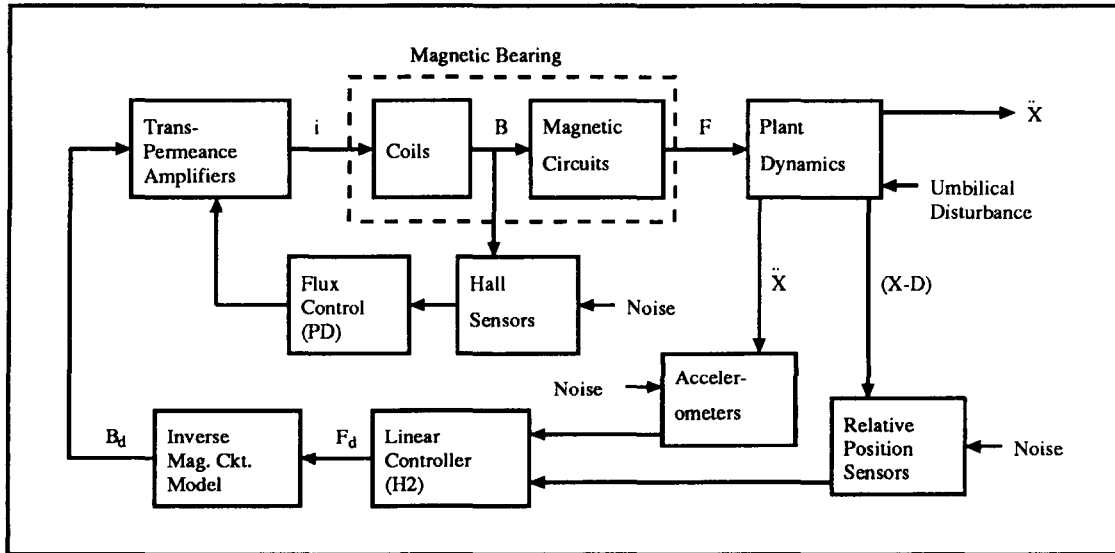


Figure 5: Control Schematic

A relative position sensor has not been chosen but the optical scheme used in IBM's design is a strong candidate. Alternatively, the current and flux signals could be processed to infer position [10]. The purpose of the relative position signal is only to prevent collision with the walls, so accuracy demands are relatively low.

6 Conclusion

A design for a novel magnetic bearing, proposed as the fine stage of a coarse-fine actuator for microgravity vibration isolation, has been presented. The bearing is novel in that it uses a geometry that has just three independent flux path systems. This contrasts the twelve flux path systems (six bidirectional thrust bearings) used in conventional designs. The novel design results in compactness, light weight and high performance, when compared with the published designs. A control system is proposed to reject disturbances caused by an umbilical connection to the experiment.

Future work will focus on building a laboratory version of the bearing and control system.

References

- [1] A. Peter Allan and Carl R. Knospe. A six degree-of-freedom actuator design for microgravity vibration isolation. In *International Workshop on Vibration Isolation Technology for Microgravity Science Applications*, Cleveland, Ohio, April 23-25, 1991. NASA Lewis Research Center.
- [2] D. Stewart. A platform with six degrees of freedom. *Proceedings of the Institute of Mechanical Engineers*, 180(1):371-386, 1965.
- [3] Terry S. Allen, Douglas D. Havenhill, and Kevin D. Kral. FEAMIS: A magnetically suspended isolation system for space-based materials processing. In *Annual AAS Guidance and Control Conference*, Keystone, Colorado, February 1-5, 1986. Rocky Mountain Section, American Astronautical Society.
- [4] D. I. Jones, A. R. Owens, and R. G. Owen. A microgravity isolation mount. *Acta Astronautica*, 15(6/7):441-448, 1987.
- [5] Carlos M. Grodsinsky. Development and approach to low-frequency microgravity isolation systems. Technical Paper 2984, NASA, August 1990.
- [6] Ralph Fenn and Bruce Johnson. A six degree of freedom Lorentz force vibration isolator with nonlinear controller. In *International Workshop on Vibration Isolation Technology for Microgravity Science Applications*, Cleveland, Ohio, April 23-25, 1991. NASA Lewis Research Center.
- [7] Ralph L. Hollis, S. E. Salcudean, and A. Peter Allan. A six degree-of-freedom magnetically levitated variable compliance fine-motion wrist: Design, modeling and control. *IEEE Transactions on Robotics and Automation*, 7(3):320-332, 1991.
- [8] Kenichi Takahara, Tamane Ozawa, Hiroshi Takahashi, Shitta Shingu, Toshiro Ohashi, and Hitoshi Sugiura. Development of a magnetically suspended, tetrahedron-shaped antenna pointing system. In *22nd Aerospace Mechanisms Symposium*, Hampton, VA, May 4-6, 1988. NASA Langley Research Center.
- [9] R. D. Hampton and Carl R. Knospe. Extended H_2 synthesis for multiple-degree-of-freedom controllers. In *International Symposium on Magnetic Suspension Technology*, Hampton, VA, August 19-23, 1991. NASA Langley Research Center.
- [10] D. Zlatnik and A. Traxler. Cost-effective implementation of active magnetic bearings. In *2nd International Symposium on Magnetic Bearings*, Tokyo, Japan, July 12-14, 1990. Institute of Industrial Science, University of Tokyo.

**A SIX DEGREE-OF-FREEDOM LORENTZ FORCE VIBRATION ISOLATOR
WITH NONLINEAR CONTROLLER**

**INTERNATIONAL SYMPOSIUM ON
MAGNETIC SUSPENSION TECHNOLOGY
NASA LANGLEY RESEARCH CENTER**

August 19-23, 1991

Ralph C. Fenn

**SatCon Technology Corporation
12 Emily Street
Cambridge, MA 02139
(617) 661-0540**

The other major contributors to this project were Michael Gerver, physicist, and Bruce Johnson, Dynamic Systems and Controls Division Leader at SatCon. The project was sponsored by NASA Marshall Space Flight Center.

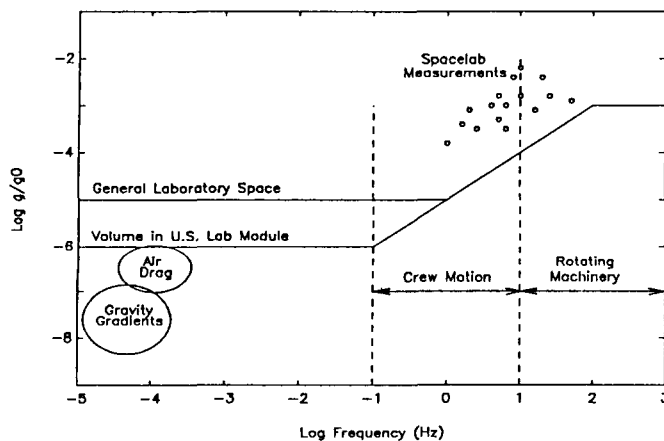
This paper presents the results of a Phase II Small Business Innovation Research program sponsored by NASA Marshall Space Flight Center. Technology is developed for isolating acceleration sensitive "microgravity" experiments from structural vibrations of a spacecraft, such as Space Station. Two hardware articles were constructed, a six degree of freedom Lorentz force isolator, and a one degree of freedom low acceleration testbed capable of tests at typical experiment accelerations.

PRESENTATION OVERVIEW

- o Microgravity experiment isolation requirements**
- o Six degree of freedom suspension specifications**
- o SatCon six degree of freedom Lorentz force isolator**
 - Prototype space based system**
 - Design**
 - Hardware**
 - Test results**
- o SatCon single degree of freedom testbed**
 - Low acceleration precision test facility**
 - Design**
 - Hardware**
 - Test results**
- o Nonlinear control**
 - Simulations**
 - Test results**

The need for isolation of microgravity experiments has been established recently based on Spacelab measurements and modeling of experiment requirements. Low frequency accelerations, caused by air drag and gravity gradients, small and fall below experiment acceleration limits. High frequency vibrations, caused by rotating machinery, require isolation, but simple mechanical isolators are adequate. The difficult vibrations at moderate frequencies, caused by crew motion, require a combination of large stroke and relatively low crossover frequency that is best provided by active suspensions. Isolation above approximately 0.04 Hz is required.

EXPERIMENT REQUIREMENTS VS THE ENVIRONMENT

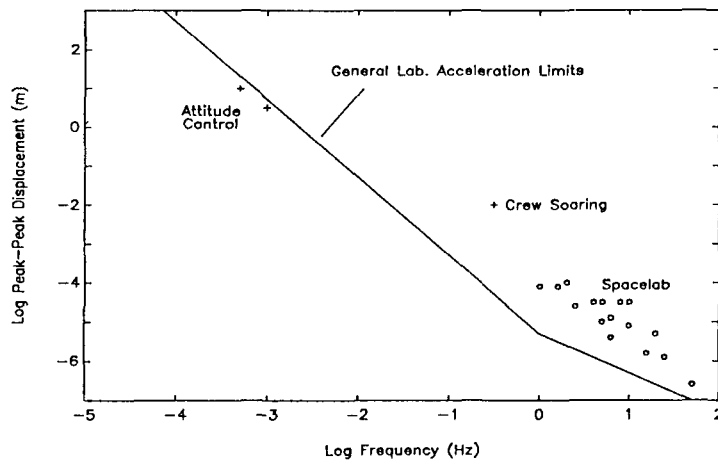


CHARACTERISTIC FREQUENCY RANGES

- o LOW FREQUENCIES DON'T REQUIRE ISOLATION
- o HIGH FREQUENCIES (10-100Hz) REQUIRE ISOLATION BUT EASY MECHANICAL SUSPENSIONS
- o MIDDLE FREQUENCIES (0.04-10Hz) HARDEST; CREW MOTION
 - LOW CROSSOVER
 - LARGE STROKE
- o INTERSECTION OF ENVIRONMENT AND REQUIREMENT PLOTS AT .04 Hz

The previous plot shows the acceleration environment and limits. Given the 0.04 Hz maximum base following bandwidth from the previous plot, the required suspension stroke can be determined. This figure shows that a peak-to-peak actuator displacement of 2 cm is required for desired isolation.

VIBRATION AMPLITUDE MEASUREMENTS AND LIMITS



- o SOLID LINE IS THE VIBRATION POSITION AMPLITUDE LIMIT
- o ± 1 cm STROKE IS REQUIRED FOR ISOLATION DOWN TO 0.04 Hz

Both attractive and Lorentz force actuators were considered for this application. Because of the large stroke requirement, the typical mass penalty of Lorentz force actuators did not exist. Many other advantages of Lorentz force actuation are beneficial in this application as listed below.

THE ADVANTAGES OF LORENTZ FORCE ACTUATORS

(FORCE \propto CURRENT TIMES FLUX DENSITY)

- o **OPEN-LOOP STABILITY (FACILITATES NON-LINEAR CONTROLLERS)**
- o **INHERENT ZERO GRAVITY ISOLATION AT ZERO CURRENT**
- o **CAN ISOLATE TO LOWER FREQUENCIES THAN FERRO-ATTRACTIVE ACTUATORS**
- o **MECHANICAL SIMPLICITY FACILITATING SIX DOF DESIGNS**
- o **EASY INTEGRATION WITH STANDARD ELECTRONICS**
- o **EQUIVALENT MASS PER UNIT FORCE WITH ATTRACTIVE ACTUATORS DUE TO LARGE STROKE**
- o **SATURATION DOES NOT LIMIT FORCE LIKE ATTRACTIVE ACTUATORS**

The previous figures showed how the stroke, base following bandwidth, actuator bandwidth and force requirements were formulated, as summarized here.

ISOLATOR FUNCTIONAL REQUIREMENTS

- o **STROKE (X, Y, AND Z)** **± 1 cm**
- o **MAXIMUM BASE-FOLLOWING FREQUENCY
(MAXIMIZE "FREE FLYING")** **4×10^{-2} Hz**
- o **MINIMUM ACTUATOR BANDWIDTH
(COUNTERBALANCE DIRECT FORCES)** **10^2 Hz**
- o **FORCE FOR 500 KG EXPERIMENT** **1 N**

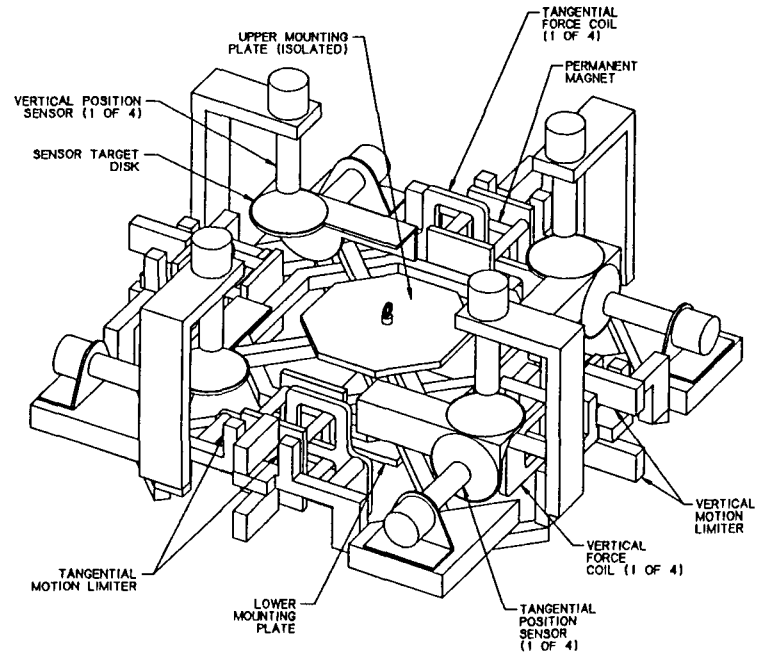
A prototype six degree of freedom (DOF) isolator was constructed that had the characteristics listed below. The width and depth were scaled approximately to typical orbiter locker size. Weight was reduced to some degree by aluminum construction, but further reductions are possible. The prototype force capability was sized for very large 500 kg experiments. This capacity could be reduced, giving a substantial mass savings.

SIX DOF ISOLATOR DESIGN

| | |
|-------------------------------|-----------------------------------|
| FORCE | 4 N (EXCEEDS REQUIREMENTS) |
| DIMENSIONS: | |
| STROKE | ±1 CM |
| WIDTH AND DEPTH | 45 CM |
| HEIGHT AT CENTER | 8 CM |
| WEIGHT: | |
| SUSPENDED PLATFORM | 5.0 KG |
| BASE STRUCTURE | 4.5 KG |
| TOTAL | 9.5 KG |
| ISOLATOR POWER: | |
| 1 N Z AXIS | 1 W |
| 1 N X OR Y AXIS | |
| (EXPER CG 15 CM UP) | 4 W |
| OPEN-LOOP ACTUATOR BW: | > 100 HZ |

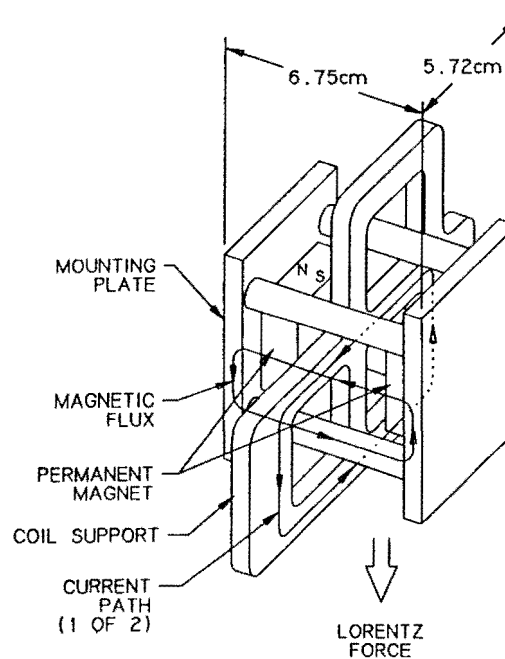
The prototype suspension shown below has four actuators, supplying eight forces, and eight position sensors. Each of the four isolator sides is identical, which provides symmetry and reduces controller complexity. Four Lorentz force actuators in the center of each side produce vertical and tangential forces. Two mounting plates are provided, one for the experiment on top, and the second for Space Station attachment below. Eddy current position sensors measure the vertical and tangential position at each corner.

SATCON SIX DOF MAGNETIC SUSPENSION



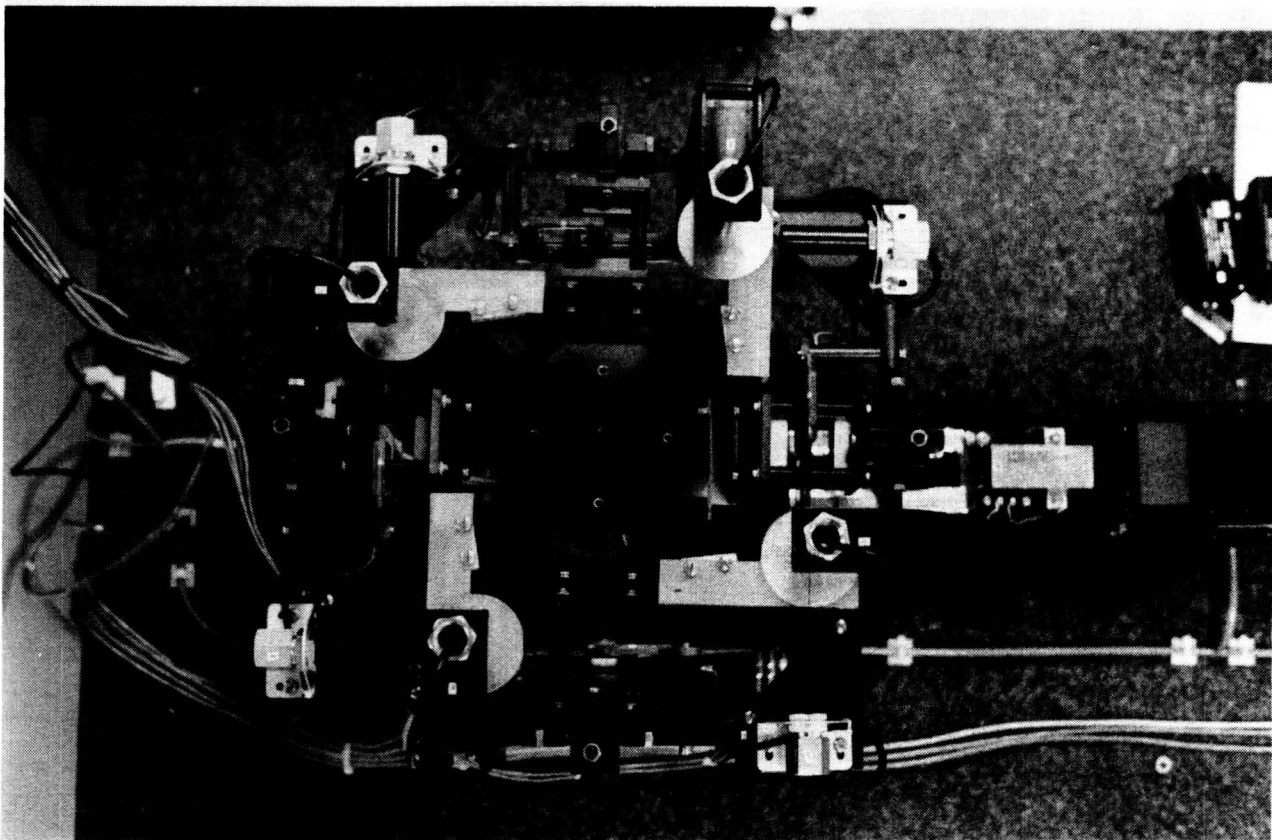
The actuator shown below has two permanent magnets that produce flux in the central air gap, where the coils cross. The flux returns through the four posts at the corners of the mounting plates. "L" shaped coil mounts comprised of separate horizontal and vertical coils are laced through the gap. The return current returns outside the gap. The force constant is 1 Newton per ampere and the coil resistance is 9 ohms. Force capacity depends entirely on the duty cycle because the actuators are heat limited.

ONE OF THE SIX DOF ISOLATOR ACTUATORS



This top view of the isolator shows the upper mounting plate surrounded by the position sensors and circular targets, and the actuators on the center of each side.

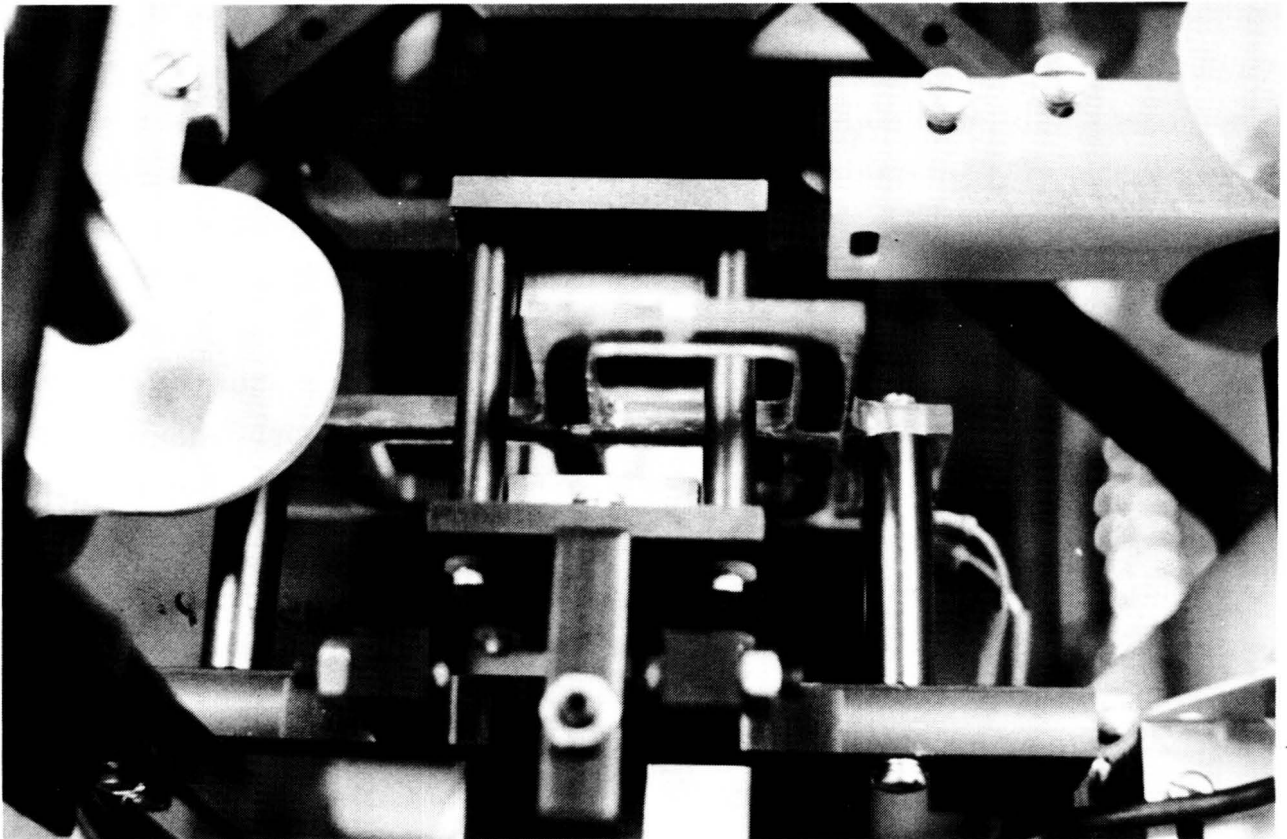
THE COMPLETED SIX-DOF ISOLATOR



ORIGINAL PAGE
BLACK AND WHITE PHOTOGRAPH

A photograph of one of the actuators is shown below. The crossing point of the coils is visible in the center of the gap, between the permanent magnets. One of the aluminum foil eddy current sensor targets is also shown.

AN ACTUATOR INSTALLED ON THE SIX-DOF ISOLATOR

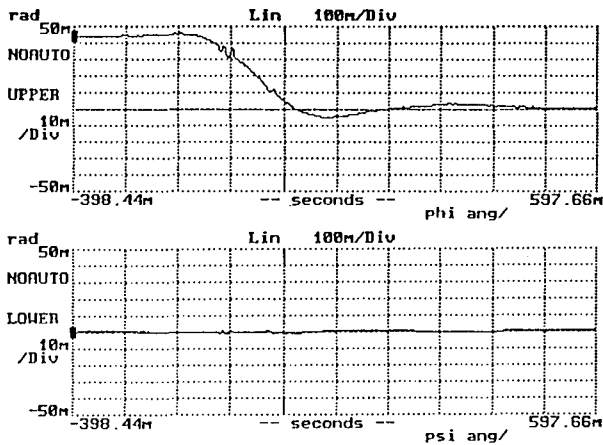


ORIGINAL PAGE
BLACK AND WHITE PHOTOGRAPH

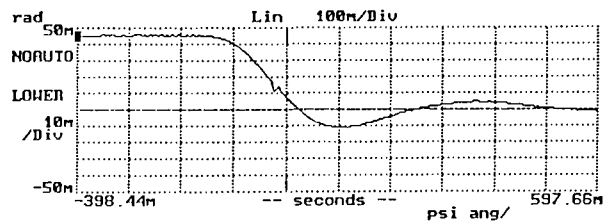
These plots show experimental data for initial condition responses of roll of the suspended platform. A long, soft spring was used to unload the gravity force and give a nominally centered coil position within the gap. The top two plots are concurrent traces of the x axis and y axis roll motions (ϕ and ψ). The second plot shows that the roll axes are decoupled by the controller. Good damping characteristics are also exhibited.

INITIAL CONDITION RESPONSE OF ROTATIONAL AXES

(a) phi

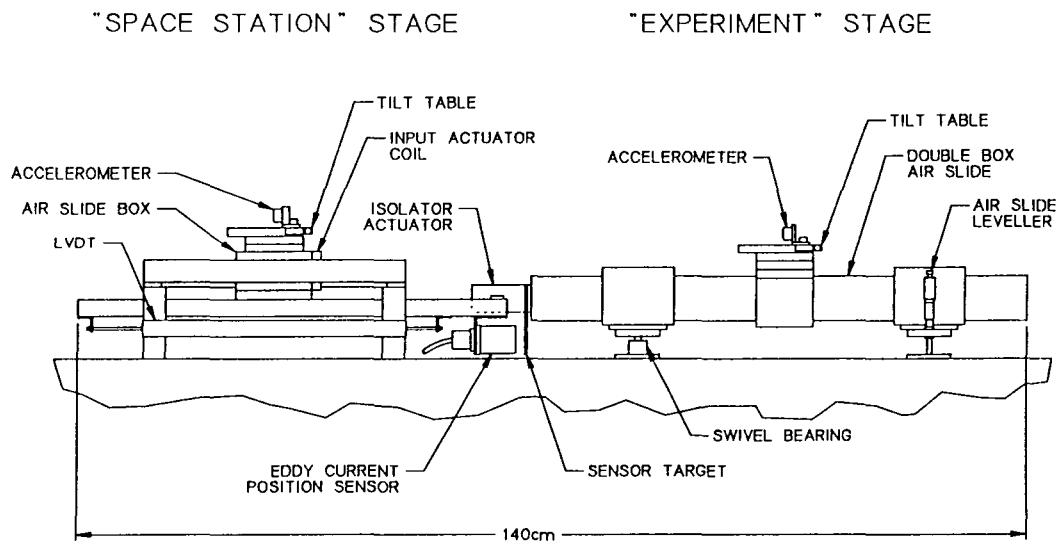


(b) psi



The second article of hardware constructed is a one degree of freedom testbed to simulate on orbit accelerations and test controllers. The figure below shows an integrated Lorentz force motor / air slide on the left, which produces expected Space Station accelerations. On the right is another air slide supported by two air boxes, which simulates the floating experiment mass. The relative position of the "experiment" stage and the "Space Station" stage is controlled to maximize isolation in one DOF while preventing "bottoming out" of the central isolation actuator. This apparatus is useful for testing nonlinear controllers and determining the effect of signal noise levels throughout the control system.

ONE DEGREE OF FREEDOM TESTBED



**PRECISION LOW ACCELERATION TEST FACILITY MICROGRAVITY LEVEL
ACCELERATIONS**

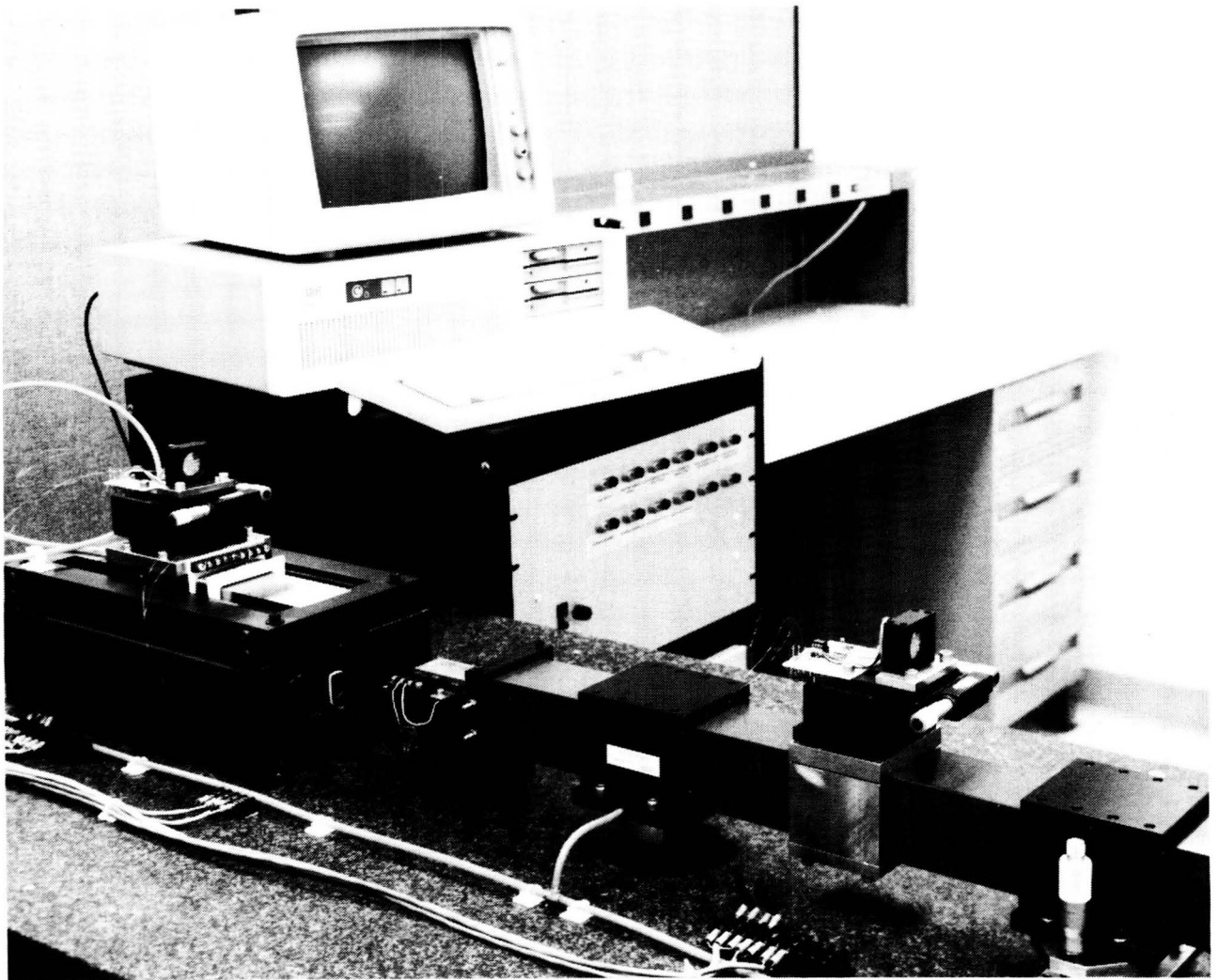
The single digit microgravity background accelerations were produced using noncontacting actuators, sensors and mechanical suspensions where possible. The only connection to the sensitive Space Station stage are several thirty four gage wires carrying the accelerometer power and signals.

ONE DOF TESTBED

- o **INPUT STAGE SIMULATES SPACE STATION VIBRATIONS.**
- o **EXPERIMENT STAGE IS ISOLATED BY LINEAR ACTUATOR IN CENTER.**
- o **EACH STAGE HAS POSITION AND ACCELERATION FEEDBACK.**
- o **SIMULATE TYPICAL SPACE ACCELERATIONS AND SIGNAL LEVELS:
IMP. FOR NONLINEAR CONTROL TESTS, SENSOR AND ACTUATOR TESTS.**
- o **NONCONTACTING HARDWARE:**
 - **AIR SLIDES: ACCURATE SPACE STATION ACCELERATION REPLICATION
W/O STICTION AND SENSITIVE ISOLATION EVALUATION**
 - **NONCONTACTING POSITION SENSORS**
 - **NONCONTACTING INPUT MOTOR AND ISOLATION ACTUATOR**
 - **AIR LINES ON NONMOVING PART**
 - **ONLY ACCELEROMETER LEADS CONNECT TO EXPERIMENT**
- o **VERY STIFF STRUCTURE**

This figure shows the one DOF testbed mounted on the granite surface plate. The accelerometers mounted on top of each stage are visible. One of the two 0.12 μm resolution differential micrometers is shown on the right.

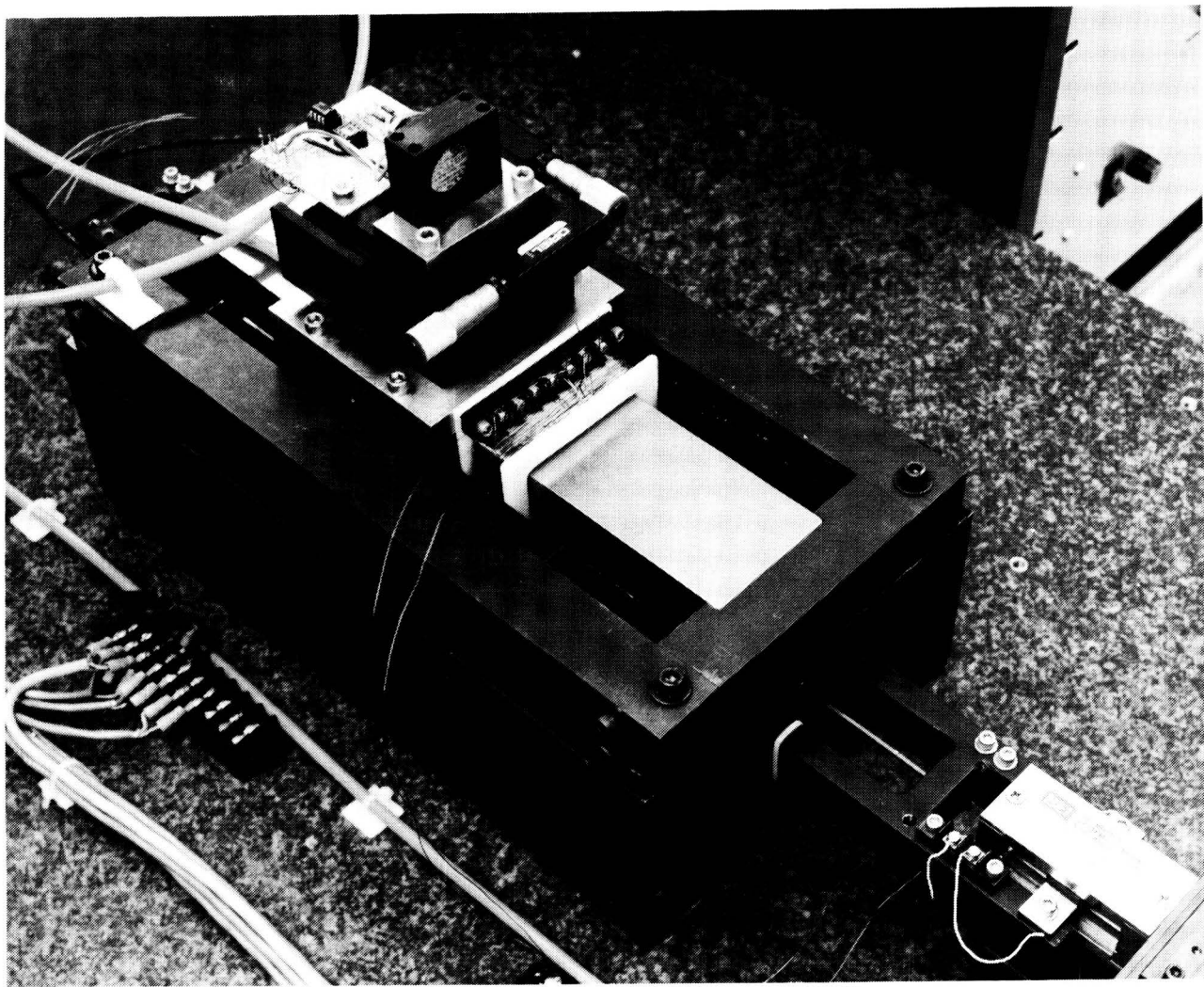
ONE DOF TESTBED



ORIGINAL PAGE
BLACK AND WHITE PHOTOGRAPH

The integrated Lorentz force motor / air slide is shown below. An eight inch long permanent magnet lies on each side of the central air slide. Flux crosses the gap and returns through the airslide and backiron holding the magnets. A coil passes through the gap and encircles the air slide. The Lorentz force on the coil, which is mounted on the air slide, creates the desired Space Station accelerations.

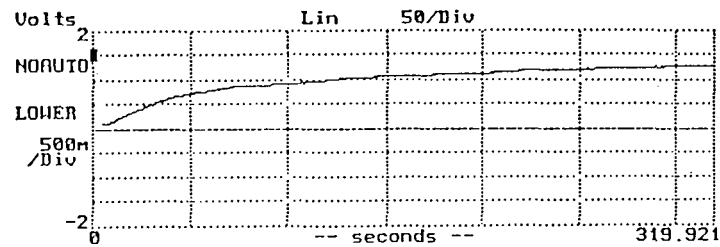
LORENTZ FORCE INPUT MOTOR AND INSTRUMENTATION



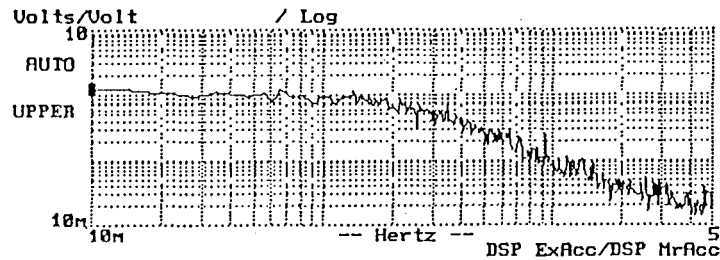
ORIGINAL PAGE
BLACK AND WHITE PHOTOGRAPH

The figures below show experimental data from the one DOF testbed with the desired 0.04 Hz crossover linear controller. The step response shows the desired low friction characteristics that facilitate controller testing using expected on orbit parameters. The frequency response of the system on the lower plot shows crossover to be somewhat higher than the design value of 0.04 Hz. This may be due to unmodeled viscous damping in the air slide.

STEP RESPONSE OF THE 0.04 Hz BANDWIDTH POSITION CONTROL



TRANSFER FUNCTION OF 0.04 Hz BANDWIDTH POSITION CONTROL



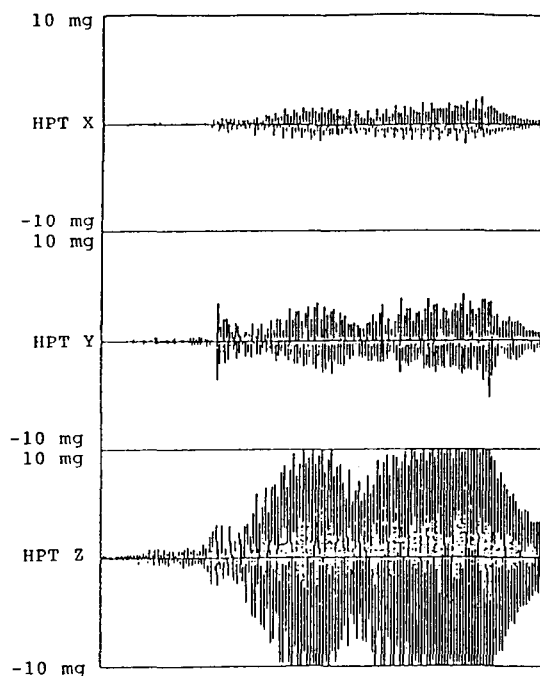
Nonlinear controllers offer many advantages over linear designs. In this application no weight is given to the location of the coil in the gap, as long as the coil does not hit the stops. An ideal controller would not apply forces to the suspended platform carrying the experiment unless the suspension was likely to bottom out. This actuator nonlinearity suggests a nonlinear controller that has a gain that is position dependent. When the suspension is centered, the controller should "turn off" and not apply undesirable forces. The gain should increase when infrequent environmental accelerations are very large so that the experiment must be forced to follow the spacecraft. Such a controller can allow an experiment to free fly at all frequencies, given limits to the position amplitude of the vibrations.

NONLINEAR CONTROLLER ADVANTAGES

- o **ALL ACTUATORS HAVE SATURATION NONLINEARITY**
- o **A LINEAR CONTROLLER APPLIES EXCESSIVE FORCES**
- o **A NONLINEAR CONTROLLER CAN FREE FLY AT ALL FREQUENCIES (AT SMALL AMPLITUDES)**
- o **THE SUSPENSION COULD BE STIFFENED BY GAIN SCHEDULING ANTICIPATING LARGE BASE MOTIONS**
- o **ADVANCED CONTROLLERS COULD MINIMIZE A COST FUNCTION OF STROKE AND FORCE USING A STOCHASTIC MODEL OF EXPERIMENT SENSITIVITY AND THE ENVIRONMENT**

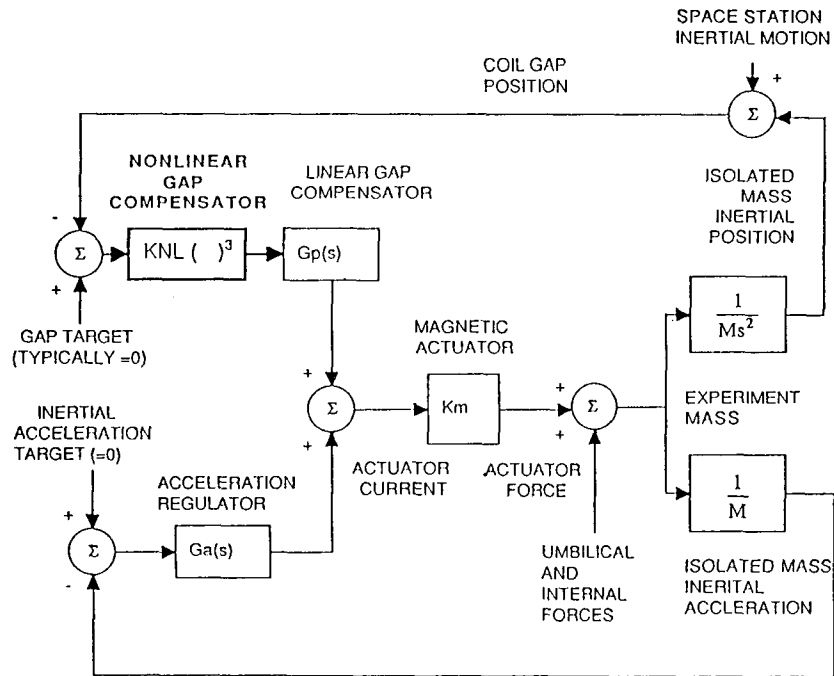
This figure showing D3 mission data illustrates the advantage of a variable gain controller. The vast majority of time has quiescent acceleration levels that are orders of magnitude lower than the peak values. These typical low levels are shown at the left of the plots here. During the great majority of the time that the experiments run, there are no large accelerations requiring isolator action. However, if a linear suspension controller is used, every small but finite motion will produce a proportional and unwanted experiment acceleration. These low level but frequent controller induced accelerations may cause the majority of experiment damage, rather than the much more infrequent large accelerations.

LARGE VIBRATION DYNAMIC RANGE BUT LOW AVERAGE VALUE



A controller having the desired "dead zone" characteristic without limit cycling behavior is the cubic error controller shown below. The only alteration to a linear position controller is the addition of one operation that cubes the position error before it enters the linear compensator. This cube operation approximates a dead zone but is smoother.

CONTROL SYSTEM EXAMPLE WITH CUBIC NONLINEARITY



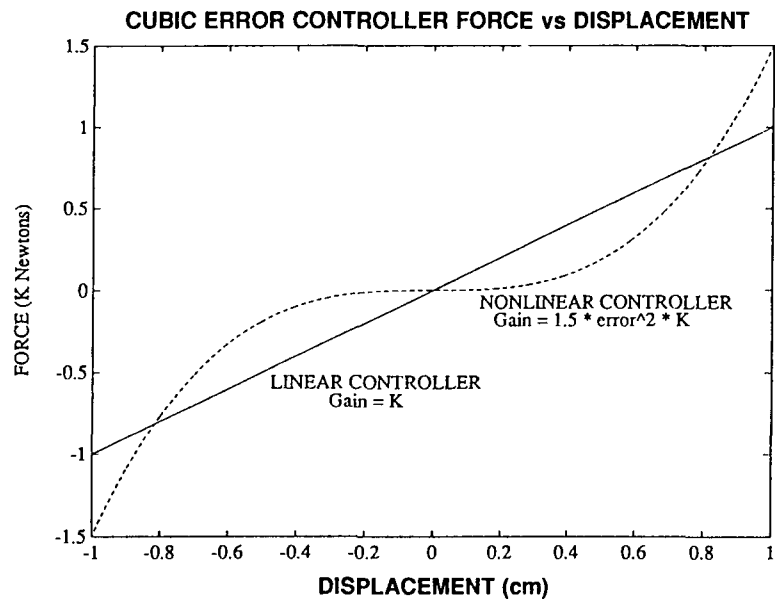
The block diagram on the previous page shows how both position control and acceleration control are used to isolate base vibrations and reject direct forces. The actuator gap position control has a very low bandwidth of 0.04, as developed in the first viewgraphs from environmental accelerations and experiment requirements. The acceleration loop should have a bandwidth of 100 Hz to counterbalance the major directly applied forces. The one degree of freedom testbed has position and acceleration control while the six DOF isolator as constructed has only position feedback, but could be easily modified to add acceleration control. Describing function analysis can be used to model the cubic nonlinearity as $\frac{3}{4} (\text{amplitude})^2$. This shows explicitly that the loop gain is reduced dramatically for small excursions. The gain during one DOF cubic controller tests was chosen to provide just slightly more force at maximum stroke than the linear design.

A CUBIC GAP ERROR NONLINEAR CONTROLLER

- o **GAP LOOP IS LOW PASS (0.04 HZ) BASE FOLLOWING.**
- o **ACCELERATION LOOP IS BANDPASS REGULATOR (TARGET = 0) REJECTS DIRECT FORCES.**
- o **THE NONLINEAR CONTROLLER REDUCES UNNEEDED FORCES DURING LOW AMPLITUDE MOTIONS.**
- o **THE NONLINEAR GAIN GIVES THE SAME LOOP GAIN AT MAXIMUM DISTURBANCE AMPLITUDE (AND THE SAME BANDWIDTH).**
- o **THE DESCRIBING FUNCTION ALLOWS LINEAR ANALYSIS WHEN THE INPUT FUNDAMENTAL PREDOMINATES.**
- o **THE DESCRIBING FUNCTION OF $(A \cdot \sin(WT))^3$ IS $\frac{3}{4} A^2$.**
- o **THE GAP LOOP GAIN BECOMES PROPORTIONAL TO THE ERROR².**
- o **A STOCHASTIC DESCRIBING FUNCTION FOR (RANDOM)³ IS $3 \cdot \sigma^2$. USE FOR GAIN SELECTION FOR STOCHASTIC NONLINEAR CONTROLLER.**

The force for small fractions of the maximum displacement is greatly reduced by the nonlinear controller. For the gains shown here, the ability of the two controller designs to absorb large accelerations is nearly identical. The nonlinear controller applies larger forces at large, but infrequent, disturbances than the linear design. In this way, the lack of action at small displacements is compensated for.

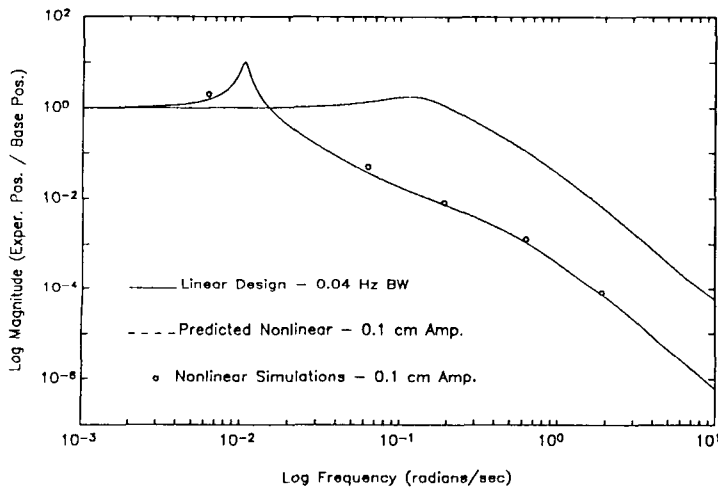
CUBIC ERROR CONTROLLER FORCE vs DISPLACEMENT



NO FORCE IS APPLIED FOR SMALL DISPLACEMENTS

The continuous plots here show the predicted linear response and the predicted nonlinear response using describing functions. Nonlinear simulation data points are also plotted. It shows that the describing function discussed above approximates very closely the nonlinear response of the system. The plot shows the desirable behavior of reduced base following bandwidth for small position disturbances. Low bandwidth gives better isolation and less experiment damage.

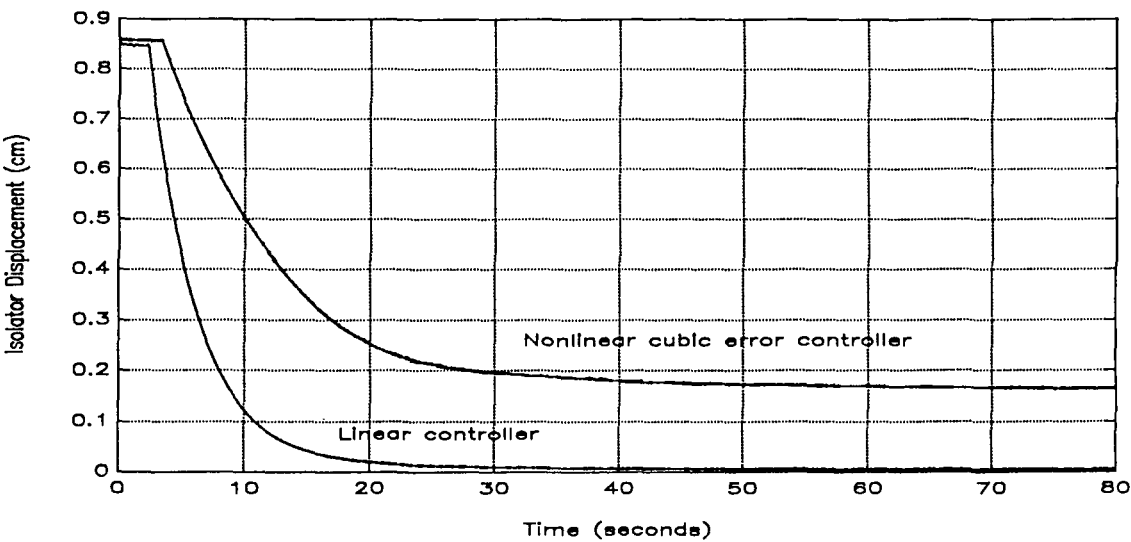
CONTROL SYSTEM EXAMPLE WITH NONLINEAR SIMULATION DATA



- 1) COMPARES EXPERIMENT ACCELERATIONS FOR 10% FULL-SCALE BASE MOTION
- 2) CUBIC NONLINEARITY IS AN ADJUSTABLE GAIN - DOWN BY A FACTOR OF 90
- 3) ISOLATION FREQUENCY REDUCED BY A FACTOR OF 17
- 4) NONLINEAR CONTROLLER PRODUCES LOWER EXPERIMENT ACCELERATIONS IF BASE RMS VIBRATION IS MUCH SMALLER THAN PEAK VALUES

This time plot shows how the nonlinear controller essentially "turns off" when the coils are within 15% of the centered position. Because this application has no penalty for small steady state position errors, this behavior is preferable because of the lower forces applied to the experiment by the controller.

CUBIC ERROR AND LINEAR INITIAL CONDITION RESPONSES



MEASURED DATA FROM SINGLE-DEGREE-OF-FREEDOM TESTBED

The paper shows that microgravity isolation will be required on Space Station, and that current technology can satisfy this need. Lorentz force actuation with nonlinear controls is a good match to the requirements of this application.

SUMMARY

- o **MICROGRAVITY ISOLATORS ARE REQUIRED.**
- o **0.04 HZ ISOLATION AND ± 1 CM STROKE ARE REQUIRED.**
- o **BOTH BASE ISOLATION AND DIRECT FORCE REJECTION ARE DESIRABLE.**
- o **LORENTZ FORCE ACTUATORS ARE WELL SUITED FOR THIS APPLICATION.**
- o **A NEW TWO DEGREE OF FREEDOM ACTUATOR WAS DESIGNED.**
- o **A SIX DEGREE OF FREEDOM SUSPENSION WAS DESIGNED, CONSTRUCTED AND TESTED.**
- o **NONLINEAR POSITION CONTROLLERS CAN REDUCE EXPERIMENT ACCELERATIONS.**
- o **A ONE DOF MICROGRAVITY ACCELERATION TESTBED WAS BUILT. INVESTIGATE ACCELERATION DISTURBANCES PRODUCED BY CONNECTIONS TO THE EXPERIMENT:**
 - **POWER**
 - **SIGNAL**
 - **COOLING**

Session 5

SUPERCONDUCTIVITY 1

Chairman - Jim Downer
SatCon Technology Corporation

**Recent Progress Towards Developing a High Field, High- T_c
Superconducting Magnet for Magnetic Suspension
and Balance Systems.**

L. Pierre de Rochemont, Carlton E. Oakes, Michael R. Squillante
Radiation Monitoring Devices, Inc.
44 Hunt Street
Watertown, MA 02172

Hong-Min Duan, Allen M. Hermann
Center for Applied Superconductivity
University of Colorado, Boulder
Boulder, CO 80303

Robert J. Andrews
Rome Laboratory
Solid State Sciences Directorate
Hanscom AFB, MA 01731

Roger B. Poeppel
Materials and Components Technology Division
Argonne National Laboratory
9700 South Cass Avenue
Argonne, IL 60439-4838

Victor A. Maroni
Chemical Technology Division
Argonne National Laboratory
9700 South Cass Avenue
Argonne, IL 60439-4838

Ingrid A. Carlberg and Warren C. Kelliher
Engineering Laboratory
NASA Langley Research Center
Hampton, VA 23665-5225

I. INTRODUCTION.

The initial discovery of the high- T_c superconducting ceramics in 1986 [Bednorz and Müller], rapidly followed by the subsequent development of compositional families which exhibited zero resistance transition temperatures at 90 K [Wu], 125 K [Hermann], and recently as high as 132 K [Hongbao et al., Chandrachood et al.], heralded predictions for major breakthroughs in mankind's technical mastery of the universe. Images of high-speed magnetically levitated trains racing across the continent or inexpensive electricity transported thousands of miles over resistanceless power lines littered the pseudo scientific literature to popularize these new observations. As had been the case when the first type-I low- T_c superconductors were identified in 1911 [Onnes], a more thorough investigation of the intrinsic properties of these materials fostered sobering attitudes within the technical and engineering communities as practical limitations to the application of this technology were identified.

In the 50 years succeeding the discovery of superconductivity, the physical foundations upon which an understanding of the onset and preservation of the resistanceless conductive state were constructed. This arduous research path led to the commercialization of superconductors for applications as diverse as low field magnetometry, high field magnetism, and charged particle acceleration throughout the 1960's, -70's, and -80's. Although superconductors remain a modest industry by global business standards, their reliability and unique performance capabilities in medical and extremely high-cost experimental physics apparatus has demonstrated feasibility for their integration into complex systems where down time spells disaster.

There is a clear need for the development of the high- T_c superconductors. Relieving the constraint of systems operation at liquid helium cryogenic temperatures makes the application of superconducting devices more broadly possible on the basis of overall system cost and simplicity. At present, NASA has identified interest in applying high- T_c superconducting magnets to the following aerospace technology applications: vibrational isolation, high accuracy pointing, and magnetic suspension in wind tunnel testing. The most challenging system requirements for these application orientations will be found in the suspension and balance systems used in conjunction with cryogenic wind tunnels. Levitation is required in this test apparatus to remove aerodynamic interference caused by a mechanical support under conditions of dynamic or unsteady testing. Superconducting magnets for this application will have to be capable of maintaining DC fields on the order of 6 - 8 Tesla, in addition to an overlapping large amplitude ac sinewave field at 5 Hz, superposed by higher frequency (50 Hz to 60 Hz) 0.1% maximum field strength signals which are critical to system control.

This paper will briefly review superconducting magnet and high- T_c superconducting oxide ceramic materials technology to identify areas of fundamental impasse to the fabrication of components and devices that tap what are believed to be the true potential of these new materials. Fortunately a great knowledge base on the subject of superconductivity and superconductive devices has already been acquired through the development of low- T_c superconductor components. However, the high- T_c ceramics pose problems in fundamentally different areas which have to be solved. We will map out an experimental plan designed to research process technologies which, if suitably implemented, should allow us to overcome many of these deficiencies. We will conclude with an assessment of where and on what regimes magnetic system designers should focus their attention to advance the practical development of systems based on these new materials.

II. FUNDAMENTAL CONSIDERATIONS TO THE DESIGN OF SUPERCONDUCTING MAGNETS.

The superconductive state is a thermodynamic phase of material systems susceptible to "delicate" and complex internal electronic interactions. The phase space mapped out by the superconducting state is defined through the following parameters of state: temperature, T , magnetic field, H , and current density, J . Critical values for each of these parameters mark the transition of the material from its superconducting phase to its *normal* resistive phase. The critical values for each of these state parameters are dependent upon the thermodynamic weighting of the other state variables through a system of Lagrangian constraints. That is, the highest critical load that can be sustained by this thermodynamic phase, be it thermal, magnetic, or electrical, is obtained through the application of minimal stress on the other two state variables.

Zero electrical resistance can be maintained at the highest temperatures in the absence of any applied or generated magnetic field, and through the passage of minimal current densities. The superconductive phase will persist under the weight of high magnetic fields at the coldest temperatures and with minimal current densities, and so on and so forth. While both temperature, T , and magnetic field, H , are fundamental thermodynamic state variables defined by the internal dynamics and energies intrinsic to a specific materials system, critical current densities, J_c , are far more susceptible to influences extrinsic to the material system and can generally be increased through improved materials processing.

The objective in designing and constructing a high field superconducting magnet is essentially to run the gambit. It is necessary to construct a superconductive surface topology which allows the material system to sustain its thermodynamic phase through the application of maximal stress on at least two, and many times all three of the state parameters. **Figure 1** shows a topological design using a tape/ribbon conductor. The tape is constructed to have a surface coverage of superconducting material. As diagrammed, the poles of the magnet will be subject to considerable thermodynamic stress. Maximum magnetic load will be fundamentally limited by the effects of strain produced in this "stress node" of the magnet. Magnetic field densities in the superconductor will be greatest in those regions where the radial field lines loop back down through the core of the magnet. A high current will induce a strong magnetic field. The ultimate field density in the core of the magnet is proportional to the current passing through the coil and defined by a *shape factor* which relates the surface current paths to the induced field strength. The generation of these fields which penetrate through the superconductor, will in turn *pinch-off* the critical current densities passing through the conductor at these stress points in the coil, and, as a result, start limiting the maximum field.

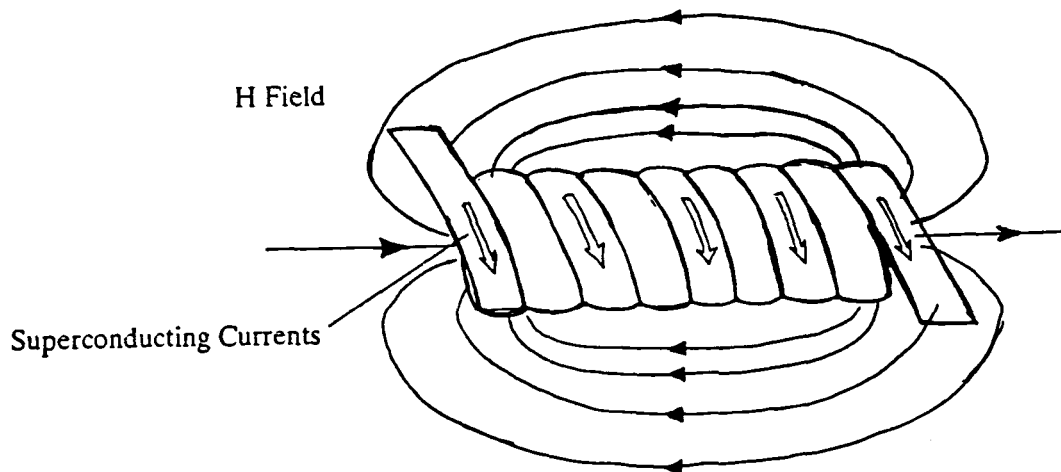


Figure 1. Magnetic coil based on a ribbon composite-conductor design. The high- T_c superconducting ceramic is either embedded as a sheet within the ribbon, or is applied as a surface coverage to the structure.

It is therefore necessary for the superconductor to be magnetically hardened at the poles. When magnetic flux bundles, fluxoids, penetrate the superconductor they will interact with the supercurrents through Lorentz forces. Greater fluxoid densities, will activate the frequency of these interactions. This interaction will deflect the supercurrents from their intended path and exert an equal and opposite force upon the fluxoid. (See **Figure 2**). Fluxoids will move in response to this force, and if they drift through the material they will dissipate their energy into the superconductor. Their energy is ultimately converted to heat, which in turn applies greater

stress to this thermodynamic phase of the material. However, if the fluxoids are *pinned* by potentials greater than the interaction energy of the Lorentz forces, their movement will be prevented and less heat is dissipated into the system.

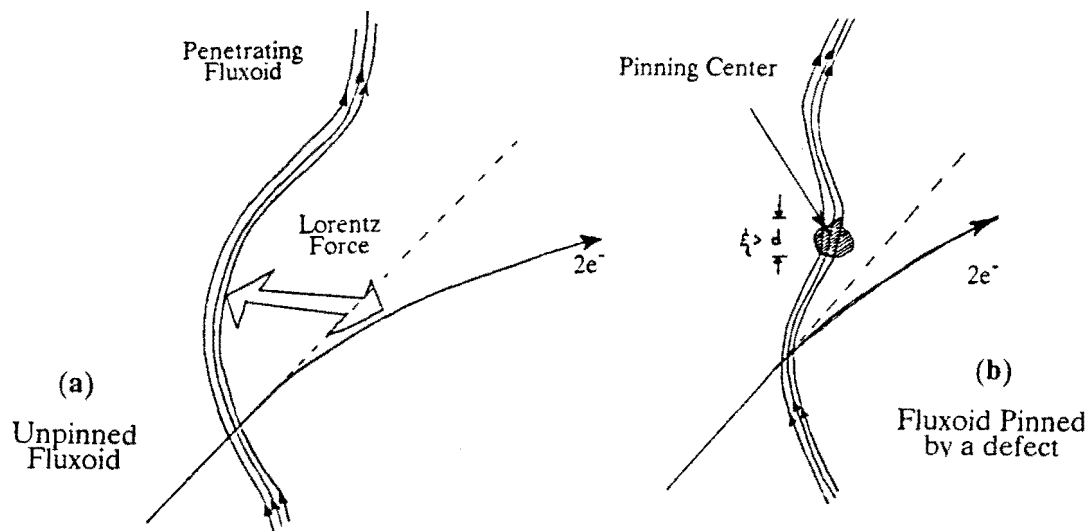


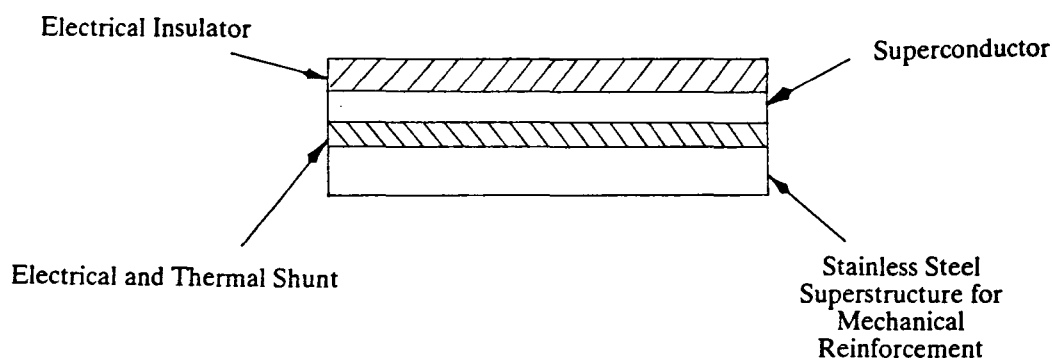
Figure 2. Lorentz force interaction between a penetrating fluxoid and supercurrents within the conductor (a). Fluxoids can be pinned within the superconductor to prevent heat generation by defects having physical dimensions smaller than the coherence lengths of the superconducting Cooper pair (b).

The conducting surface topology given in **Figure 1** is attractive in researching these new materials for a number of reasons. It allows the entire superconductor to be bathed completely in the thermal reservoir, thereby effecting more uniform control over the thermal load applied to, or generated within, the superconductor. If continuous ribbons of tape are used, this design reduces the potential need for spliced joints between segments of the coil. Spliced joints electrically connect superconducting segments of tape through the application of normal conductor material. They would certainly be needed if edge wound ribbon conductor coils are considered. When high currents are applied to these joints they can also generate heat sufficient to drive normal state transitions and *quench* the superconducting state along the entire coil.

Implicit to the successful design of a high- T_c superconducting magnet is the design of the conductor ribbon. A composite structure to these conductors is required. (See **Figure 3**). First, the superconductor needs to be intimately contacted to a metallic substrate material. This metal must have a high thermal conductivity so heat generated within the material can be quickly transported out of the superconducting medium. This thermal shunt is necessary to reduce the occurrence of normal state transitions and to avoid generating conditions which could precipitate a quenched coil. Secondly, the metal enveloping the superconductor must also be an excellent electrical conductor. In the event the coil does quench an electrical shunt is needed to drain the current in the system.

In addition to anticipating problems related to quenching the superconductor coil, the ribbon design must also anticipate the enormous pressures under which it is likely to be subject when incorporated into the design of a high field magnet. Differences in the field densities across a coil as it generates strong magnetic fields can exert enormous mechanical stress on the coil. Fields of 6 Tesla are known to exert mechanical pressures upon coils on the order of 140 atm, which is equivalent to pressures contained within gas cylinders. Magnetic fields approaching 10 Tesla can generate pressures equivalent to 520 atm, which approaches the yield strength of annealed copper. Therefore, it is imperative that a strong mechanical superstructure be

embedded within the ribbon. This can be accomplished by having a stainless steel base. Stainless steel has electrical and thermal properties which are not sufficient to accommodate shunt characteristics required in the structure. Finally, this entire structure should be encapsulated by a good electrical insulator to avoid high voltage arc discharges between various windings within the coil, or the coil and its confinement chamber.



Tape Cross-Section

Figure 3. Schematic design of the superconducting ribbon to be applied to the construction of a high field magnet.

III. FUNDAMENTAL PROPERTIES OF THE HIGH- T_c CERAMIC OXIDE SUPERCONDUCTORS.

The challenge presented to the materials engineer trying to overcome the natural difficulties posed by these materials systems is formidable. The difficulties involved can be appreciated by examining the "compositional windows" over which high- T_c superconductivity is observed to occur in these ceramics. High- T_c superconductivity is now known to occur in a number of ceramic materials systems with the perovskite crystal structure. Current understanding of the high- T_c ceramic oxides has been developed upon the observation that the superconducting compositions in these material systems are located over a compositional domain between adjacent semiconducting (insulating) and metallic manifestations of these *complex* metal oxides [Kitazawa, 1990]. (See Figure 4).

1. ELECTRONIC STRUCTURE OF THE CERAMIC SUPERCONDUCTORS.

The current focus in the scientific literature mainly emphasizes that the evolution of superconductivity, which is nestled in the vicinity of a semiconductor-to-metal compositional transition, is triggered by high-level carrier doping in a semiconductor (insulator) which has a nonconventional energy gap at the half-filled position of its conduction band. The energy gap involved in these systems has its origin in strongly correlated multi-body interactions: charge density waves (CDW) in the barium bismuthates (BaBiO_3) or electronic correlation in the case of the cuprates.

The electronic properties of the superconducting cuprates are fundamentally characterized by a two-dimensional network of covalent Cu-O bonds which form a CuO_2 square lattice in the a-b (basal) plane of the perovskite crystal structure. Cu-O bonding along the c-axis is believed to be ionic and electrical conduction is essentially two-dimensional along the a-b plane and can be modeled by assuming a pile of alternating ultra-thin metallic and insulating layers. (See Figure 5). The chemistry within the ionic layer controls the amount of charge carriers transferred into the superconducting sheets, which in turn, influences whether or not the superconductive phase will

form and at what temperature it occurs if it does [Cava *et al.*, Jorgensen]. As a result, these layers have come to be known as "electronic doping" regions. (See Figure 5).

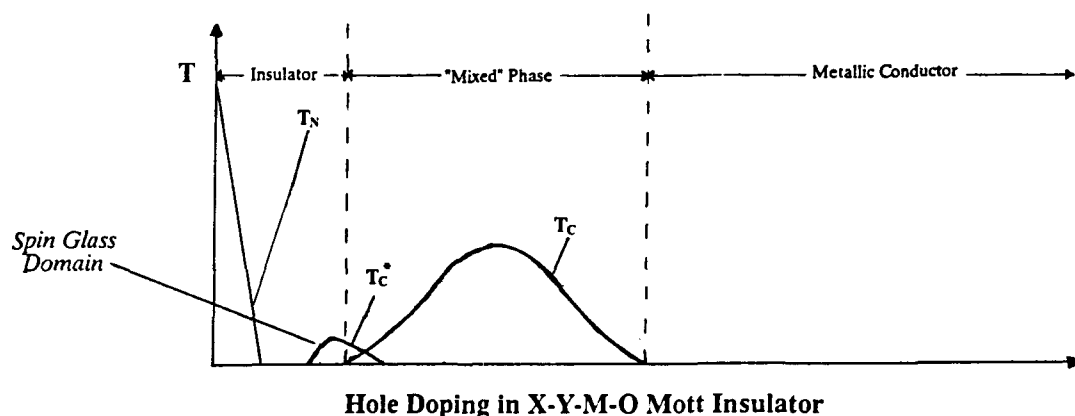


Figure 4. Compositional dependence on the electrical phase of high- T_c superconducting ceramic cuprates.

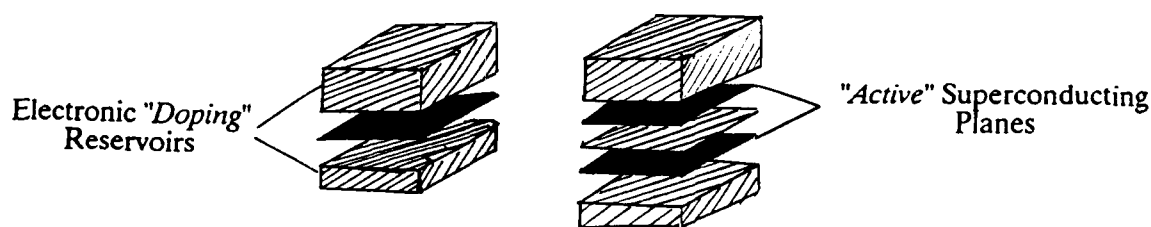


Figure 5. Electronic structure of the high- T_c superconducting cuprates.

The transfer probability from a metallic plane to the adjacent one across the intervening insulating layer(s) seems to be a very sensitive function of the nature of the ionic layer. As a result of these structural features, superconducting parameters in the cuprates are highly dependent upon interlayer coupling, and are consequently anisotropic. A fundamental consideration to making these systems work in high field magnet applications will be to maintain specific

crystallographic orientations *vis-à-vis* the applied magnetic field and the superconducting current path. This requires the entire ceramic to have a "textured" quality. That is, its c-axis must be oriented relative to the metallic substrate surface on a macroscopic scale.

T_c in these materials can depend sharply on composition, and the emergence of superconductivity is observed to be in a compositional domain located between insulating (semiconducting) and metallic manifestations of these material systems. The unit cell structures for these materials is indeed quite complex. **Figure 6** shows the unit cells for 6 of the superconducting phases which have been identified for the Tl-Ba-Ca-Cu-O superconducting system. The most interesting phases have the most complex structures. The primary task goal in manufacturing a single phase tape will be to replicate one of these atomic structures throughout a surface layer 20-50 μm thick, 1 cm wide, and 10-100 m long.

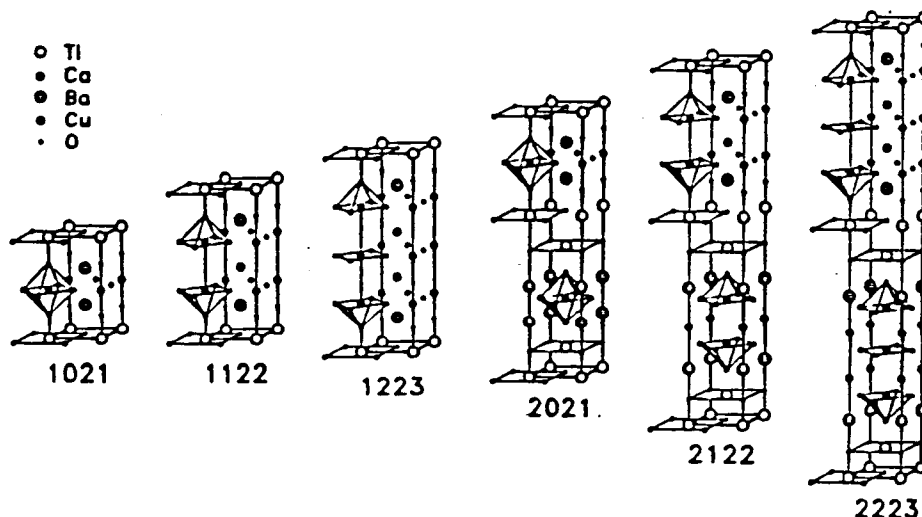


Figure 6. Six of the superconducting phases identified in the Tl-Ba-Ca-Cu-O system.

While depositing the proper stoichiometry in the film or coating is a necessary prerequisite, it will not assure the formation of the desired phase. During synthesis these materials have to be processed over wide temperature ranges. Over different thermal regimes various phases of the material will have stronger tendencies to form. For instance, if the 2223 stoichiometry is deposited but the material is processed at temperatures which favor the formation of the lower T_c 2021 phase, the material will phase separate into this phase and an equal stoichiometric blend of barium and copper oxides which can be insulating. As a general rule, it appears that the more interesting compositions have the narrowest synthesis windows to form phase stabilized solids and are the most difficult to form. Consequently, once phase separation has been initiated the coatings will have poor electrical properties and be of little use to fabricating a magnet.

2. INTRINSIC MAGNETIC PROPERTIES OF THE HIGH- T_c CERAMICS.

The truly magnificent property of these materials is their magnetic hardness. While actual values for the upper critical magnetic fields for these materials is still not yet known, for many of the different systems they are believed to be on the order of many hundreds, if not more than a thousand, of Tesla for many of the different compositional families [Kang *et al.*, Larbelestier]. Current impediments towards achieving an accurate appraisal for these properties has involved many complex issues related to defects. Defects in these materials can be both beneficial and detrimental to their ultimate performance. When point defects are arrayed into a structured lattice dramatic increases in transition temperature, upper critical field, and, most significantly, critical current density can be achieved. However, larger defects located in the path of the

superconducting currents can severely degrade their capacity to carry supercurrents as well as their performance in magnetic fields.

3. EXTRINSIC MAGNETIC PROPERTIES OF THE HIGH- T_c CERAMICS.

Many of the same "tricks" used to develop high quality low- T_c superconductors, such as the deliberate generation of defects to serve as flux pinning centers, can be adapted to the high- T_c superconducting ceramics. Flux pinning centers improve critical current densities by preventing the free motion of penetrating fluxoids, which dissipate their kinetic energies into the system through Lorentz force interactions with the supercurrents. Although this approach can be applied to high- T_c conductors, it must be done on a significantly different physical scale. The coherence length (ξ)--(nominally defined as the maximal separation of two electrons in a *Cooper pair*, beyond which they split and revert back to normally resistive charge conductors)--is anisotropic in the cuprates and are orders of magnitude shorter in the high- T_c materials. Typical values are found to be on the order of 2-4 Å for ξ parallel to the perovskite c-axis and $\xi = 16-30$ Å along the a-b plane. This compares unfavorably to coherence lengths of up to a couple microns for some of the low- T_c materials [Doss].

Deliberately induced defects will only serve as flux-pinning centers if they have a spatial extent less than the coherence length of the *Cooper pair*, (see **Figure 2**), otherwise they will stimulate pair transitions to the normal state. Flux pinning point defects can be generated in these films using high-energy particle irradiations. This treatment will form defects by slightly perturbing the location of an ion from its equilibrium position in the lattice. It can raise the critical current density in films from 10^5 to 10^7 A/cm² [Venturini *et. al.*, van Dover, *et al.*, 1989, 1990]. Unfortunately, these techniques are only useful in samples exhibiting good *texture*, for instance, single crystals or high quality epitaxial films. A materials synthesis process, like spray pyrolysis, capable of producing large area films will produce inherently polycrystalline films which could conceivably be dominated by weak link intergranular connections. The ultimate success of any large area deposition process will be strongly influenced by its ability to control the orientation of these individual grain granules.

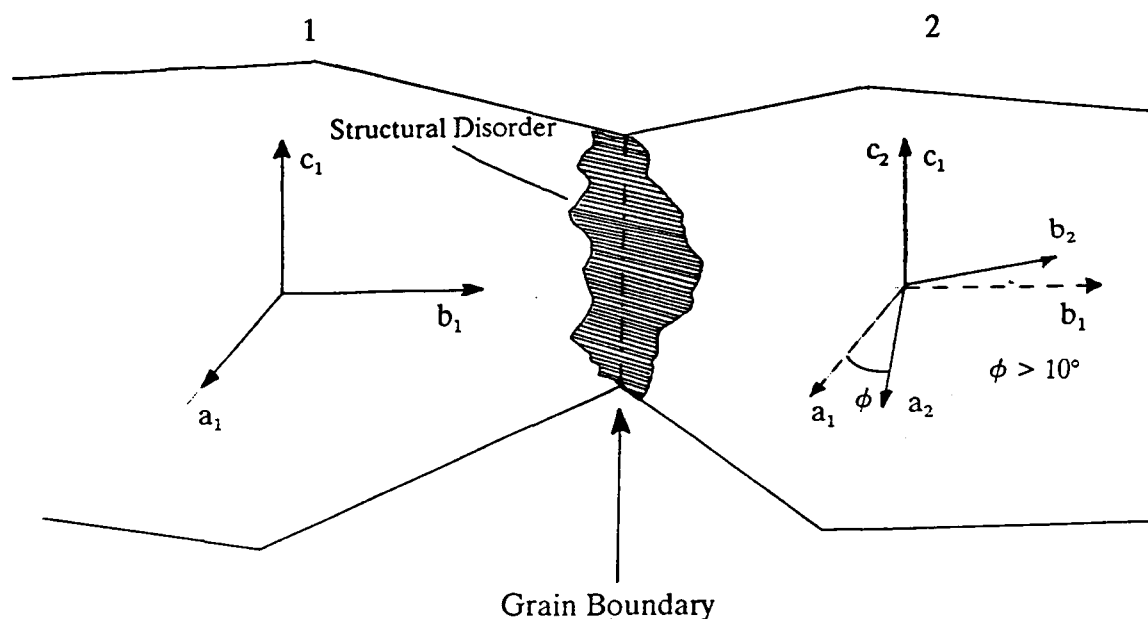


Figure 7. Superconducting-Insulating-Superconducting (SIS) junctions at the boundaries between grains limit critical current densities in c-axis aligned polycrystalline ceramics.

In view of the strong anisotropy and poor conductivity of the cuprate superconductors in directions parallel to the perovskite c-axis, a necessary, but not sufficient requirement, will be to orient all the individual grains with their c-axes perpendicular to the current paths in the conductor, i.e., in the plane of the substrate. It has been shown that the relative orientation of the basal (a-b) planes in c-axis aligned bicrystals can greatly influence the critical current densities transported across the grain boundary [Dimos *et al.*, 1988]. Grain boundaries in which the c-axes are perfectly aligned but have the orientation of their basal planes skewed by a screw rotation of more than 10° behave as Josephson junctions and will have relatively low and highly magnetic field dependent critical current densities. (See **Figure 7**). This occurrence can greatly inhibit the performance of the superconductor in magnetic applications.

The formation of these superconductor-insulator-superconductor (SIS) junctions is believed to be the result of structural disorder at the grain boundary which occurs as a natural consequence of the need to accommodate the lattice mismatch at the boundary plane [Dimos *et al.*, 1990]. One would expect that this region of *insulating structural disorder* to be on the order of 10's of angstroms, and that tunneling current densities through these effective Josephson junctions will depend directly on the degree of coupling between the superconducting regions. Polycrystalline films loaded with these superconductor-insulator-superconductor (SIS) junctions will have relatively low and highly magnetic field dependent critical current densities which cannot be improved through the generation of radiation induced defects. This occurrence can greatly inhibit the performance of the superconductor in high field magnet applications.

Consequently, the suitability of using high- T_c superconducting ceramics in high field magnet applications will likely depend upon the selection of a materials system based on a number of intrinsic properties. As a result of the sensitivity of these grain boundaries to magnetic fields, intrinsic parameters other than transition temperature will likely play a more determinant role in selecting the materials systems for a high field magnetic component. Since charge transport through the insulator is a tunneling process, higher critical current densities across the grain boundary are likely to be obtained using a materials system exhibiting longer coherence lengths. If one of the electrons in a Cooper pair has tunneled through the barrier, but its coherence length is long enough to remain bound to the other electron in the superconducting paired state across the insulating region, the probability for supercurrent transport across the junction is greatly enhanced. (See **Figure 8**). In general, coherence lengths seem to follow an inverse relationship to the T_c of the material.

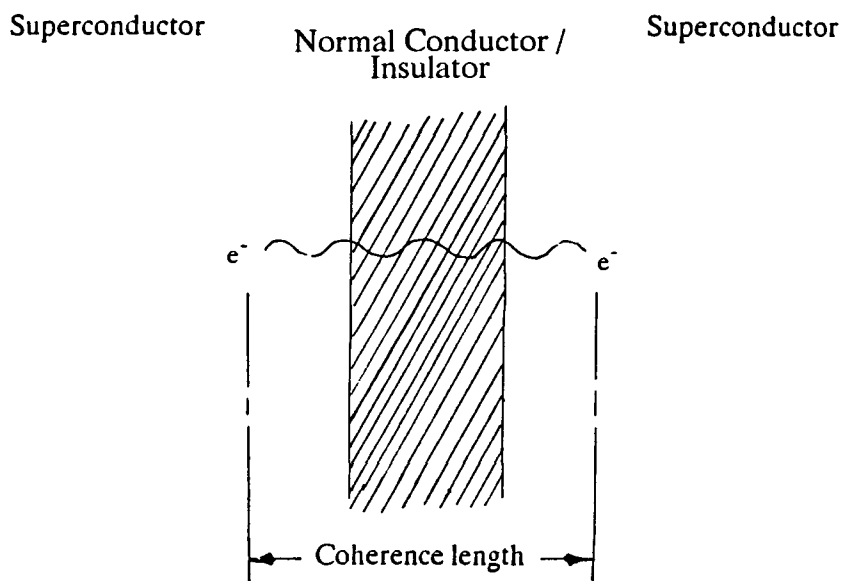


Figure 8. Tunneling of a paired electron state through an insulating barrier.

4. CHEMICAL SENSITIVITIES OF HIGH- T_c SUPERCONDUCTING CERAMICS.

All of the high- T_c superconducting ceramics are known to participate in thermodynamically unstable reactions with carbon dioxide (CO_2) and water (H_2O) [Sleight]. They generally have favorable chemical reactivities with oxygen. As a result of the unstable reactions, a finished film with a nice sharp high- T_c transition will degrade over time as lower T_c knees grow into the transition region, and insulating regions metamorphose within the grain boundaries to pinch-off critical current densities (J_c). Water is known to attack the Y-Ba-Cu-O superconductor by preferentially dissolving barium, so the use of organic solvents is now preferred in solution bulk processes [Trolrier *et al.*]. However, the use of organic solvents will increase the likelihood that CO_2 remains trapped in the lattice and corrodes the lattice through other reaction paths. CO_2 is created in the lattice during the initial firing of these organic laden ceramic formulations.

It has recently been confirmed that the presence of either H_2O or CO_2 will deteriorate critical current densities in these films by altering the surface properties of individual grains, thereby degrading current transport across their boundaries. The formation of BaCO_3 , insulating Y_2BaCuO_5 , Y_2O_3 , and CuO have been observed to occur at various temperatures and pressures as the Y-Ba-Cu-O ceramic oxides react with CO_2 which evolves during firing [Poeppel *et al.*, 1990a]. However, substantial improvements in J_c and thermodynamic phase stabilization can be achieved if CO_2 is efficiently removed from the lattice. It has been confirmed that the kinetics of CO_2 removal from these ceramics is strongly influenced by the partial pressure of CO_2 gas over the solid. Low-pressure high oxygen (O_2) flow rate treatments or low pressure annealing in ozone (O_3) have produced large, multilayer Y-Ba-Cu-O coils with acceptable critical current densities [Poeppel *et al.*, 1990a, 1990b].

IV. CHEMICAL SPRAY PYROLYSIS AND CERAMIC MATERIALS PROCESSING.

This research program will focus on adapting chemical spray pyrolysis to the manufacture of superconducting ribbons. Spray pyrolysis is a process where soluble precursor salts are dissolved in a solution which is then sprayed on to a hot surface. The cationic salts then precipitate out of solution and react together to form a coating of the desired compound, as the solvent, used to transport the reactants to the substrate, is evaporated from the surface. The high- T_c superconductors comprise a fairly complex materials system, not yet fully understood, and have very unique chemical properties (sensitivities) which must be respected if good quality films are to be produced. The entire synthesis process is composed of three basic steps: deposition, calcination, (where the precursor by-products are broken down and driven out of the film), and sintering, (where the stoichiometric mix is annealed to drive local atomic displacements to form a stabilized superconductive phase).

1. Strategies Towards Achieving Stoichiometric Control at the Molecular Level.

As is evident upon inspecting the electronic-structure properties of the high- T_c superconducting crystal structure, any bulk process capable of producing good quality films or coating must exert stoichiometric control at the molecular level. Although solution processes are attractive for the homogeneous mixing they can provide, not all of the precursor salts exhibit good or similar solubility in the solvent. Therefore, the likelihood for single species agglomerations to form as the salts precipitate out of solution and into the films near the hot substrate surface is real.

In the first phase of this development we countered the possibility for single phase agglomeration by preparing stoichiometric solutions which used an organic (glycerol) as a chemical binder. The objective was to find ways to "gel" all the different precursors together though an organic chain(s). This approach greatly enhanced the chemical uniformity of the sprayed films, as determined by backscattered scanning electron microscopy. On the basis of thermal analysis it appears as though we are forming derivatized salt complexes. **Figure 9** shows individual thermogravimetric (TGA) spectra of the various precursors used in our process. TGA measures the percentage weight changes in a compound residue versus temperature and allows the experimentalist to determine at which temperature regimes the material is likely to outgas and to infer what chemical decomposition species are forming on the basis of molar percentage weight changes.

As is clearly evident in the figure the decomposition spectra is seen to change from the

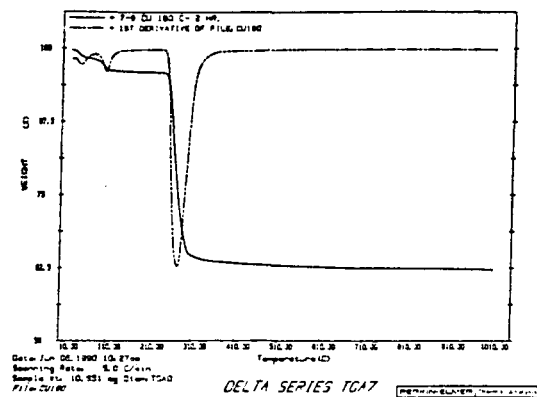
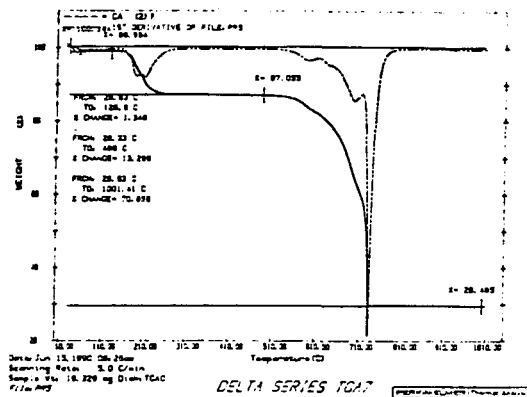
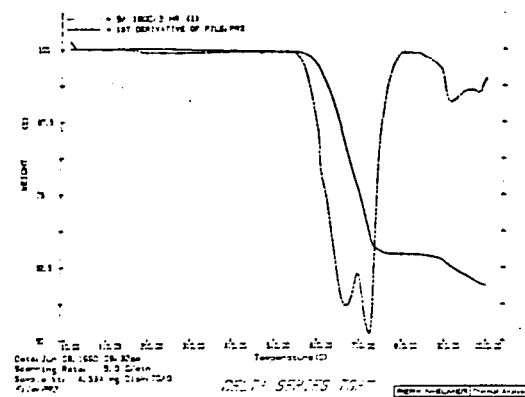
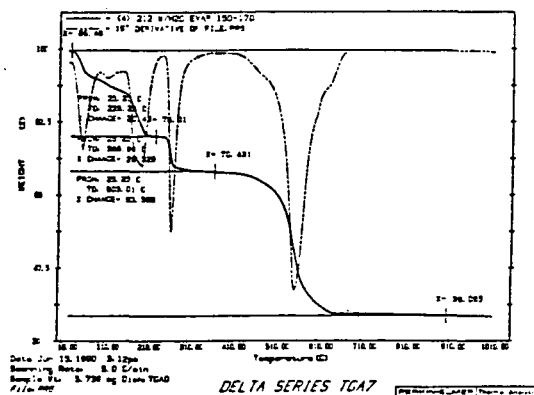
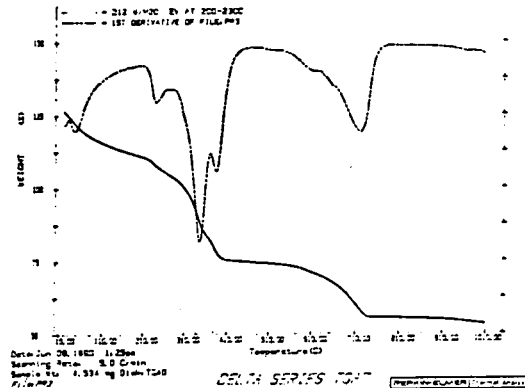

 $\text{Cu}_2(\text{OH})_3 - (\text{NO}_3)$

 $\text{Ca}(\text{NO}_3)_2$

 $\text{Ba}(\text{NO}_3)_2$

 212 Ba-Ca-Cu- $(\text{NO}_3)_2$ in H_2O only

 212 Ba-Ca-Cu- $(\text{NO}_3)_2$ in H_2O with
20% Glycerol Binder by volume

Figure 9. Thermal decomposition spectra of residues dried from aqueous salt solutions containing $\text{Ba}(\text{NO}_3)_2$, $\text{Ca}(\text{NO}_3)_2$, $\text{Cu}(\text{NO}_3)_2$, only, and solution mixtures of the three salts with and without an organic binder.

single species cases. In aqueous solution both $\text{Ba}(\text{NO}_3)_2$ and $\text{Ca}(\text{NO}_3)_2$ appear to have an affinity for each other and complex together. This is verified through the loss of their individual spectra, and by percentage weight changes which indicate that they are decomposing simultaneously. However, the $\text{Cu}(\text{NO}_3)_2$ aqueous salt derivative decomposes independently in the case of aqueous only, and aqueous/20%-ethanol by volume solutions. When the glycerol is added the spectra for the $\text{Cu}(\text{NO}_3)_2$ aqueous salt derivative is observed to shift to higher temperatures as the $\text{Ca}(\text{NO}_3)_2/\text{Ba}(\text{NO}_3)_2$ complex shifts to lower temperatures.

Our objective in performing this work is to identify the conditions which derivatize all of the salts into a "single complex" which decomposes simultaneously at an intermediate temperature. This eventuality would allow all of the metal oxide components in superconductor to form together and to be located physically close to one another to facilitate the sintering process.

Figure 10 shows the R-T curve for films prepared in the first phase of the research effort. In this instance Ba-Ca-Cu-O precursor films were spray pyrolyzed using a nitrate salt aqueous solution which contained 20% glycerol as a chemical binder. Tl_2O_3 was diffused into the film to form the superconducting Tl-Ba-Ca-Cu-O phase. While these results represent, to our knowledge, the highest zero resistance temperatures for films prepared using this process, the films were phase unstable. Over time lower- T_c knees grew into the transition to zero resistance. We attribute this phase instability to the likely presence of water and CO_2 , formed in the material during processing, which are naturally abundant as a result of our aqueous/organic solution chemistry.

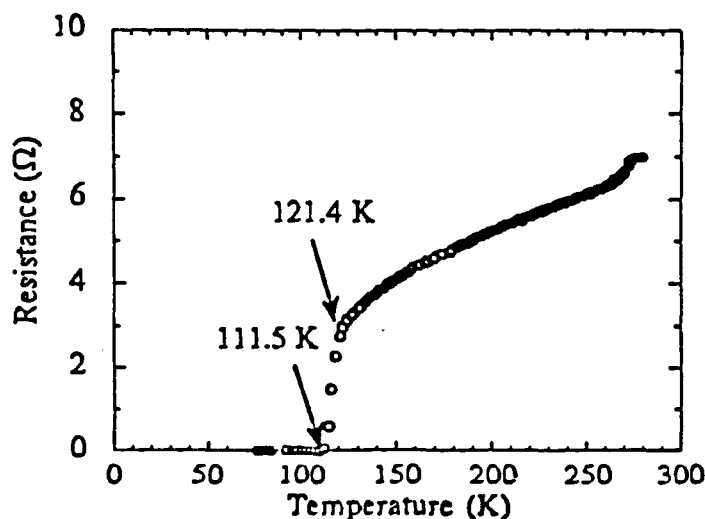


Figure 10. R-T curve of a film prepared by spray pyrolyzing Ba-Ca-Cu-O and diffusing Tl_2O_3 to form superconducting Tl-Ba-Ca-Cu-O.

A current objective of our work is to reduce the amount of water used in the process. While investigating other nonaqueous solvents we have found that formamide, (H_3CCN) , is an excellent solvent for non-transition metal salt precursors. It should be noted that extreme care must be exercised when mixing $\text{Cu}(\text{NO}_3)_2$ with organics. The redox active copper atom can catalyze the formation of some very explosive compounds. However, these reaction pathways appear to be shunted when the less reactive salts are mixed into the organic prior to the introduction of $\text{Cu}(\text{NO}_3)_2$.

2. CALCINATION--FORMING THE SUPERCONDUCTING CERAMIC.

The sprayed films are not initially superconducting. Solution stoichiometries could be maintained in the precipitated surface residue by spraying at surface temperatures which did not

pyrolyze the salt compounds into their respective oxides, even though these films had been dried of most of their solvents. Once the appropriate stoichiometry had been deposited on to the surface it could then be converted into its oxide form through calcination.

Over the course of the next year this development will focus on how gas pressure and atmosphere flow rates can be optimized during the calcination process to efficiently remove CO₂ from the lattice. It has been confirmed that the kinetics of CO₂ removal from these ceramics is strongly influenced by the partial pressure of CO₂ gas over the solid. Low-pressure high oxygen (O₂) flow rate treatments or low pressure annealing in ozone (O₃) have produced large, multilayer Y-Ba-Cu-O coils with acceptable critical current densities [Poeppel *et al.*, 1990a, 1990b].

Once optimal solution chemistries have been identified, studies into the calcination process will be performed at Argonne National Laboratories, Argonne, IL. ANL, through the Superconductivity Pilot Center Program, will examine outgassing products during the thermal conversion processing step to determine optimal gas atmosphere and pressure parameters for this stage of the process. This work will involve *in situ* diffuse reflectance infrared Fourier transform (DRIFT) spectroscopic and gas chromatographic investigations to probe the chemical transformations that take place when the spray pyrolyzed high-T_c superconducting ceramic formulations are calcined and converted to superconducting films and coatings. The dried salt-complex residues obtained from the spray pyrolysis process will be placed in a controlled environment DRIFT cell (CEDC), (see Figure 11), and the thermal treatment schedule will be monitored by recording the infrared spectra of the solid residue and the gases evolving from the residue. The outgassing species will also be monitored downstream of the DRIFT cell using on-line gas chromatography. Thermal treatment parameters, such as heating rate and gas atmosphere, will be varied in a systematic manner designed to optimize product properties. The useable range of the DRIFT technique is normally limited to $\leq 550^{\circ}\text{C}$ and total pressures near atmospheric; however, ANL will attempt (on a best effort basis) to perform DRIFT studies of the thermal treatment process under reduced pressure conditions.

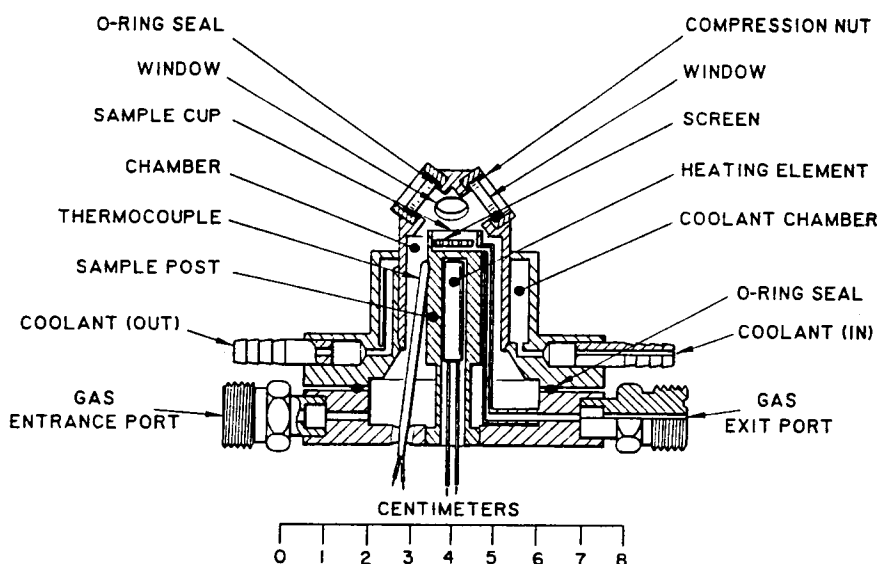


Figure 11. Schematic of the Argonne National Laboratory, DRIFT cell to be used to study the calcination process of the high-T_c superconducting ceramics.

3. TEXTURING THE CERAMIC.

Films prepared via solution processes are inherently porous and in fact need to have a spongy texture in order to allow the outgassed products a pathway to efficiently escape the lattice.

It is therefore necessary to densify the film after calcining. This can be accomplished by cold pressing the ceramic under pressures which densify the film to roughly 10% of its initial thickness. This process is essential to obtaining good c-axis alignment and texture in these ceramics. (See **Figure 12**). Texture can be loosely defined as c-axis alignment and excellent grain boundary alignment.

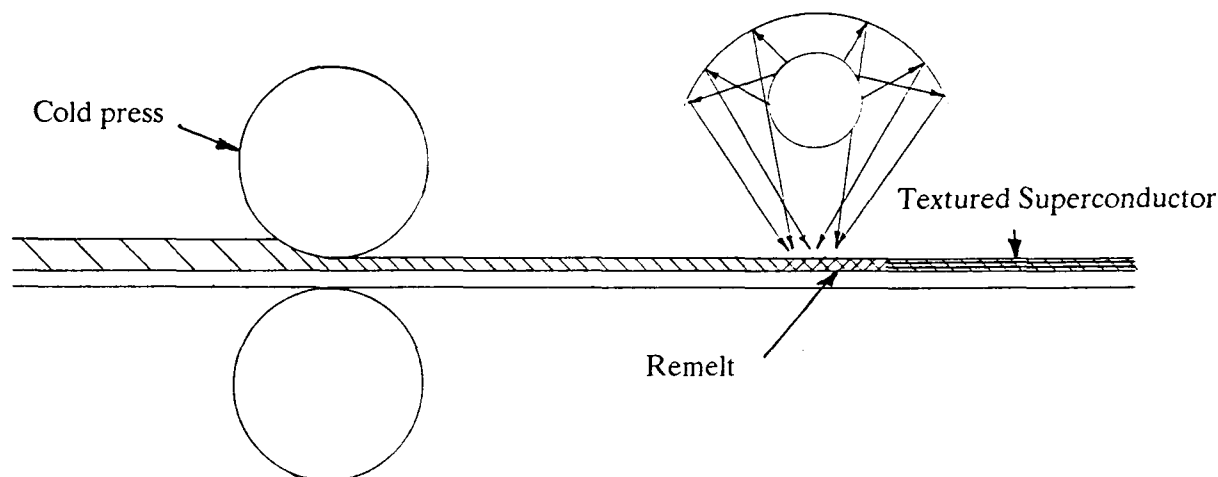


Figure 12. Densification and melt processing leads to films with improved texture.

Once the films have been pressed they should be subject to partial remelt. The purpose of this remelt is to locally rearrange atomic configurations into a phase-stabilized superconducting crystalline phase. A key objective to this aspect of the process is to improve supercurrent transport across the grain boundary.

V. FLUX PINNING IN HIGH- T_c SUPERCONDUCTORS

The generation of flux pinning centers is a critical aspect of high- T_c superconducting magnet technology. Flux pinning centers are deliberately induced defects embedded within the superconductor which have physical dimensions shorter than the coherence length(s) of superconducting Cooper pairs. If they were to have dimensions larger than the coherence length they would induce transitions to the normal state. Fluxoids pinned at a defect center will be prevented from dissipating their kinetic energy through the generation of heat in the system. A difficulty of working with the high- T_c ceramics is that their coherence lengths are very short. However, flux pinning centers can be introduced in these systems using ionizing radiation to randomly introduce point defects throughout the medium.

Researchers at Oak Ridge National Laboratory, Oak Ridge, TN, have recently shown that high energy, heavy-ion ($Z \approx 30$) irradiations can increase intragranular critical current densities to magnitudes of 10^8 A/cm^2 in 5-10 Tesla fields [Christian]. The orientation of the incident irradiation must be aligned parallel to the orientation of the penetrating magnetic flux lines. This irradiation is capable of producing a line (or lattice) of correlated point defects in the crystal roughly 3 to 5 microns in length. (See **Figure 13**). This kind of flux pinning can be likened to a seamstress' hem. A hem made with a greater number of stitches is more resistant to tearing than one made with a single stitch. Analogously, a fluxoid pinned by a single point defect will be more responsive to stress imposed by Lorentz forces than a fluxoid pinned along a line of defects. Increases in the flux pinning potentials appear to be independent upon the crystallographic orientation and are solely dependent on the relative orientation of the line defect to the orientation of penetrating lines of flux.

While this technology represents some major breakthrough, both in terms of assessing the quality of these new materials and focusing attention on how strong a role correlated forces play in these systems, they may not be useful at all in films lacking any kind of texture. The susceptibility of polycrystalline films to magnetic fields at grain boundaries is a far greater problem which does not appear to be remedied through the generation of defects with improved flux pinning potentials.

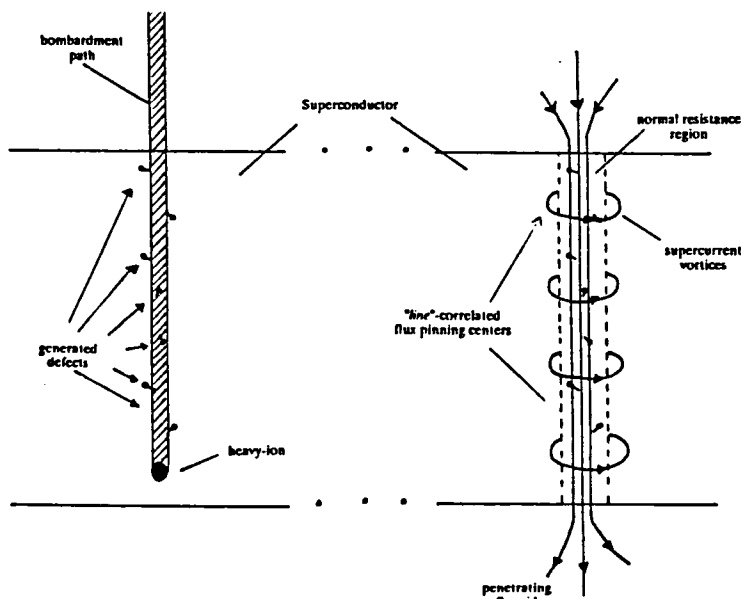


Figure 13. Heavy-ions accelerated to high energy leave a trail of point defects within the crystal along their bombardment path. Enhanced flux pinning will result when the penetrating flux lines are oriented parallel to this defect string.

VI. COMMENTS ON THE SELECTION OF WHICH MATERIALS SYSTEMS

At present there are a number of different compositions in the perovskite crystal family which exhibit high- T_c superconductivity. Each family has been observed to have intrinsic properties unique to its compositional domain. Some are observed to have higher transition temperatures, others have lower anisotropy, and yet others, those with the lower T_c 's have longer coherence lengths. Table I lists these various properties for some of the more well known and technologically important oxide superconductors. All of these factors come into play when considering the practical design and construction of a high field, high- T_c magnet. There is not one single property which can be used to evaluate the relative merits of one materials system over another. The timing of the development of a magnetic coil using various materials systems should immediately take into account the volume of data available on materials processing. Delivery of a coil or component can be severely hampered in cases where insufficient data is available of the temperature-compositional phase relationships and chemical sensitivities of the materials system. Most significantly, more pragmatic development may result if the current focus of development were to shift from transition temperature and more towards coherence lengths and relative isotropy as the alluring intrinsic properties.

VII. COMMENTS ON WHERE TO FOCUS SYSTEM DESIGNS TO TAKE ADVANTAGE OF THESE MATERIALS.

Even though the high- T_c superconductors may still be many years from widespread application in systems the engineering community should start taking a good look now on how to take advantage of these systems. At this stage, and perhaps on into the future, the concept of liquid nitrogen-cooled **high field** superconducting magnets does not appear relevant to any of the materials systems under study. **Figure 14** shows data collected by researchers at Oak Ridge

Table 1

| Material System | T_c(K) | Coherence Length (Å) | Known Synthesis Properties |
|---|-------------------------|-----------------------------|-----------------------------------|
| <i>Isotropic</i> | | | |
| (Ba,K)BiO ₃ | 20-30 | 43 | Difficult, (Hygroscopic) |
| YBa ₂ Cu ₃ O _x | 60-90 | 31 | Most well Known |
| Tl/A/Cu/O | 90-120 | 16-30 | Toxic, Not Well Known |
| (Nd,Ce) ₂ CuO _{4+x} | 22-30 | 70 | Not Well Known |
| Bi-Sr-Pb-Ca-Cu-O | 88-110 | 30-40 | Relatively Well Known |
| Bi-Sr-Sb-Ca-Cu-O | 90-132 | ----- | Unknown |
| <i>Most Anisotropic</i> | | | |

National Laboratory and the General Electric Research Laboratory, Schenectady, NY, on the magnetic dependence of c-axis oriented Tl-Ba-Ca-Cu-O films prepared by diffusing Ti_2O_3 in spray pyrolyzed Ba-Ca-Cu-O. It is clear that even though this system has one of the highest T_c superconducting phases, and on the basis of its single crystal properties is one of the hardest magnetic materials of this new class of crystals, it is not capable of sustaining a magnetic load until it is cooled to lower temperature. This plot does not describe the upper critical fields which this material system can sustain, rather it diagrams the irreversibility field conditions provoked by defect structures which are extrinsic to the material system itself.

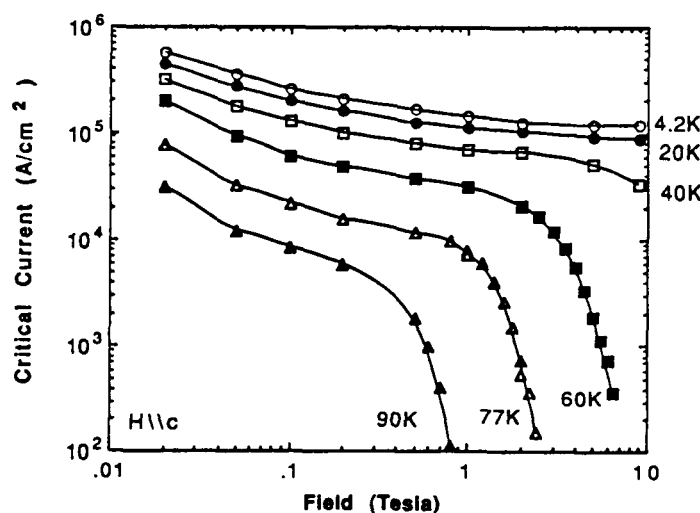


Figure 14. Critical current density versus magnetic load in c-axis aligned polycrystalline Tl-Ba-Ca-Cu-O films. (After Tkaczyk et al.)

Similar behavior has been observed in the Bi-Sr-Pb-Ca-Cu-O family of oxide superconductors which also have T_c 's greater than 100 K. This family of superconductor is generally considered to be the most anisotropic. The anisotropy of these materials is a matter of serious concern to high field magnet design engineers. However, again at lower temperature the anisotropy of this system appears to be lifted and the relative orientation of the crystal *vis-à-vis* the application of thermodynamic stress on the system is less of a problem. (See **Figure 15**).

The points at which these recently discovered materials really come into their own is in the niche of low temperature, very high field applications. By low temperature we include temperatures up to 25-30 K. **Figure 16** compares the magnetic load performance of Bi-Sr-Ca-Cu-O (BiSCCO) superconductors to niobium-titanium (Nb-Ti) and niobium-tin (Nb_3Sn) at 77 K and 4.2 K. Even though the low- T_c superconductors do not operate at liquid nitrogen temperatures, critical current densities in this high- T_c superconductor drop very rapidly with increasing load. However, at liquid helium temperatures the BiSCCO systems can sustain 10^5 A/cm² critical current densities to fields well beyond the operating potential of the conventional superconductors. This mapping should define the design parameters for systems which take advantage of the advances in technology which can be exploited by these new materials systems. As it is now possible to purchase cryostats capable of reaching ≈ 10 K at reasonable cost, the attraction of the high- T_c superconducting ceramics should not emphasize liquid nitrogen operation as much as high magnetic load capability.

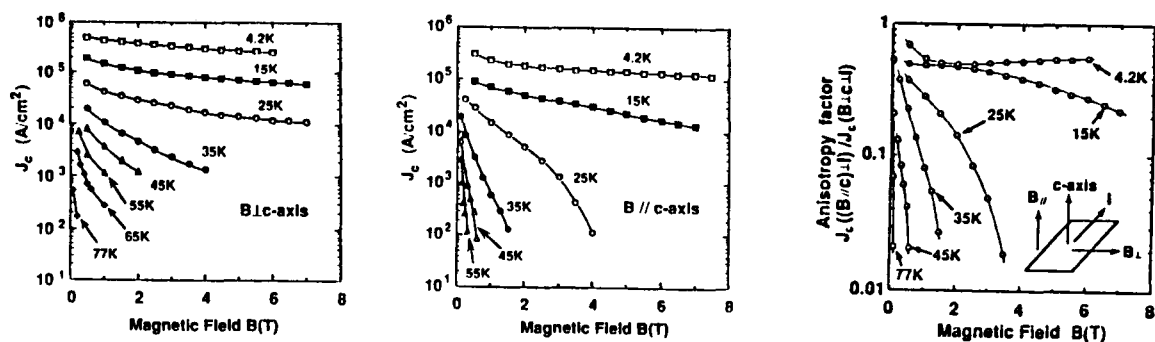


Figure 15. Temperature dependence of the critical current density anisotropy factor for textured 2212 BiSCCO tape [After Kumakura et al.].

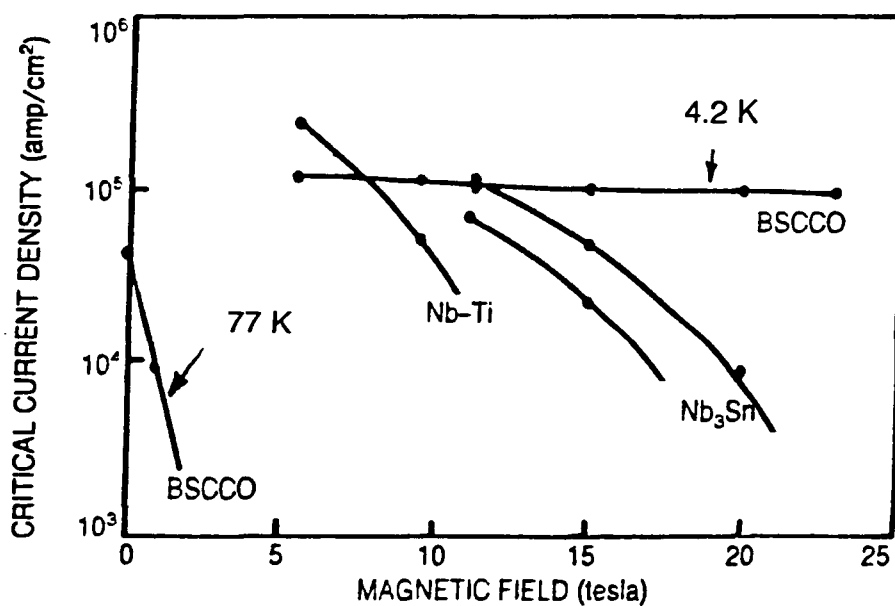


Figure 16. Critical current density versus magnetic load in BiSCCO wires. [After Larbalestier]

References:

- Bednorz, J.G., Müller, K.A., Z. Phys. **B64**, 189 (1986).
- Cava, R.J., Hewat, A.W., Hewat, E.A., Batlogg, B., Marezio, M., Rabe, K.M., Krajewski, J.J., Peck, W.F., Jr., and Rupp, L.W., Jr., Physica C **165**, 419 (1990).
- Chandrasekhar, M.R., Mulla, I.S., and Sinha, A.P.B., Appl. Phys. Lett. **55**(14), 1472 (1989).
- Christian, David, Oak Ridge National Laboratory, Oak Ridge, TN, Private communication, July 15, 1991.
- Dimos (1988), D., Chaudhari, P., Mannhart, J., LeGoues, F.K., Phys. Rev. Lett. **61**(2), 219 (1988).
- Dimos (1990), D., Chaudhari, P., Mannhart, Phys. Rev. B **41**(7), 4038 (1990).
- Doss, J.D., "Engineer's Guide to High-Temperature Superconductivity", John Wiley & Sons, New York, 1989.
- Hermann, A.M., and Sheng, Z.Z., "The High High-Tc Tl-Ba-Ca-Cu-O Superconducting System", presented at the SERI Thin Film Conference, Solar Energy Research Institute, Boulder, CO, November, 1988.
- Hongbao, L., Liezhao, C., Ling, Z., Zhiqiang, M., Oxian, L.X., Zhidong, Y., Bai, X., Xianglei, M., Guien, Z., Yaozhong, R., Zhaojia, C., and Yuheng, A., Solid State Commun. **69**, 867 (1989).
- Jorgensen, J.D., "Defects and Superconductivity in the Copper Oxides", Physics Today **44**(6), 34 (1991).
- Kitazawa, A., "Electronic Structures of Oxide Superconductors Development of Concepts", in Earlier and Recent Aspects of Superconductivity, J.G. Bednorz and K.A. Müller, (eds.), Springer Series in Solid-State Sciences 90, Springer-Verlag, New York, 1990, p. 45 - 65.
- Kumakura, H., Togano, K., Maeda, Kase, J., and Morimoto, T., Appl. Phys. Lett. **58**(24), 2830 (1991).
- Larbalestier, D., "Critical Currents and Magnet Applications of High-T_c Superconductors", Physics Today, **44**(6), 74 (1991).
- Onnes, H.K., "The resistance of pure mercury at helium temperatures", Comm. Leiden. 120b (28 April 1911).
- Poeppel (1990a), R.B., et al., "Fabrication Advances for Improved Performance of Long Lengths of High-Temperature Superconducting Wire and Tape", Proc. 1990 Appl. Superconductivity Conf., Snowmass Village, CO, Sept. 24-28, (1990). To be published in IEEE Trans. Magn., vol. 27 (March 1991).
- Poeppel (1990b), R.B., et al., "Atmosphere Control During Preparation of YBa₂Cu₃O_{7-x} Magnetic Windings", Proc. 3rd Intnatl. Symp. on Superconductivity, Sendai, Miyagi Prefecture, Japan, Nov. 6-9, 1990.
- Sleight (1991), A.W., "Comparison of High-Tc Superconducting Compounds: Implications for Applications", paper B1.1, Industrial and Competitiveness Consortia, Materials in Washington Forum, Washington D.C., February 28 to March 1, 1991, (sponsored by the Materials Research Society, Pittsburgh, PA).
- Tkaczyk, J.E., et al., 1990 Fall Meeting of the Mater. Res. Soc., Boston, MA.
- Trolier, S.E., et al., Am. Ceram. Soc. Bull. **76**, 759 (1988).
- van Dover (1989), R.B., Gyorgy, E.M., Schneemeyer, L.F., Mitchell, J.W., Rao, K.V., Puzniak, R., and Waszczak, J.V., Nature **342**, 55 (1989).
- van Dover (1990), R.B., Gyorgy, E.M., White, A.E., Schneemeyer, L.F., Felder, R.J., and Waszczak, J.V., Appl. Phys. Lett. **56**(26), 2681 (1990).
- Venturini, E.L., Barbour, J.C., Ginley, D.S., Baughman, R.J., and Morosin, B., Appl. Phys. Lett. **56**(24), 2456 (1990).
- Wu, M.K., Ashburn, J.R., Torng, C.J., Hor, P.H., Meng, R.L., Gao, L., Huang, Z.J., Wang, Y.Q., and Chu, C.W., Phys. Rev. Lett. **58**, 908 (1987).

N 9 2 - 2 7 7 3 5

LEVITATION OF $\text{YBa}_2\text{Cu}_3\text{O}_{7-x}$ SUPERCONDUCTOR IN A VARIABLE
MAGNETIC FIELD

Alexander N. Terentiev and Anatoliy A. Kuznetsov
Institute of Chemical Physics Academy of Sciences of the USSR,
117977 Moscow USSR

SUMMARY

The influence of both a linear alternating and rotational magnetic field component on the levitation behavior of a $\text{YBa}_2\text{Cu}_3\text{O}_{7-x}$ superconductor was examined. The transition from a plastic regime of levitation to an elastic one, induced by an alternating field component, was observed. An elastic regime in contrast to a plastic one is characterized by the unique position of stable levitation and field frequency dependence of relaxation time to this position. It was concluded that vibrations of a magnet levitated above the superconductor can induce a transition from a plastic regime of levitation to an elastic one. It was found that a rotational magnetic field component induces rotation of a levitated superconductor. Rotational frictional motion of flux lines is likely to be an origin of torque developed. A prototype of a motor based on a levitated superconductor rotor is proposed.

INTRODUCTION

The discovery of high T_c superconductivity stimulated a study of passive levitation phenomenon in a system consisting of a permanent magnet and high T_c superconductor. This levitation phenomenon is of great importance for passive contactless magnetic bearings. High T_c superconductors are type 2 superconductors exhibiting low values of the first critical field. These specific features of the new superconductors result in the fact that in magnetic bearings a high T_c superconductor is in the mixed state and a magnetic field penetrates inside the superconductor in the form of flux lines. Flux lines do not freely exist in a superconductor body but are pinned by lattice inhomogeneities. Strong pinning leads to hysteresis of the magnetization curve. Hysteresis of the magnetization curve due to the pinning of flux lines is the origin of two unusual levitation effects. The first effect is the possibility of stable suspension of the superconductor below a permanent magnet, first discovered with an $\text{YBa}_2\text{Cu}_3\text{O}_{7-x}$ sample doped with silver oxide (ref. 1). This effect is the consequence of large magnetic hysteresis leading to a positive superconductor magnetization after the external field decreased. The second effect is friction in levitated superconductors resulting in a continuous range of stable levitation positions and orientations (ref. 2).

ELASTIC LEVITATION

Another class of unusual magnetomechanical levitation effects was discovered by applying a variable magnetic field component to a superconductor levitated above the permanent magnet. A schematic diagram of the experiment is represented in fig. 1. The superconducting specimen was levitated above the ring-shaped permanent magnet, magnetized along the axis. In order to create an alternating field component at the sample position, an electric coil was placed inside the magnet so that the coil axis coincided with the magnet axis. The permanent magnet containing the coil was placed at the bottom of the bath with liquid nitrogen. In the case of superconductor levitation in the

static magnetic field of the permanent magnet so-called dry magnetic friction is observed. There is a continuous range of levitation positions. After the displacement of the sample along Z-axis from the initial levitation position the new position is also stable for levitation. There is no visible mechanical relaxation to the original position. This is the rigid or plastic type of levitation described in (ref. 2). The superconductor levitated in this regime is similar to the load on an inclined plane rested due to friction. When alternating current is applied to the coil, a new levitation behavior appears. In this case a unique position of stable levitation having height h_0 is observed. If the initial position of levitation is beyond h_0 , the superconductor is forced to float up off the magnet. If it is higher than h_0 the superconductor is forced to float down. Therefore the superconductor displacement from the equilibrium position generates a restoring force and the sample returns to the original position. In this regime a levitated superconductor is similar to a spring-suspended weight. Therefore a variable magnetic field induces the transition from a plastic type of levitation to an elastic one, characterized by a single position of stable levitation. Switching off the alternating field component leads to the inverse transition from an elastic levitation to a plastic one. It was found that the time of relaxation to the unique position of levitation in the elastic levitation regime depends strongly on the variable field frequency. The experiment was the following. The superconductor levitated in a variable magnetic field was displaced by means of non-magnetic pincers 2 mm down from the equilibrium position; then the superconductor was liberated from pincers and the time of relaxation to the original position was measured. The results are represented in fig. 2. One can subdivide the field frequency dependence of the relaxation time in two parts. In the low frequency range (0–100 Hz) the relaxation time decreases with increasing field frequency. In the high frequency range, (100–5000 Hz) the relaxation time is constant. Let's consider the structure of the hysteresis loop of a high T_c superconductor. Due to the irreversibility, magnetization of the superconductor is not a simple function of the external field. Consequently, the mechanical force in the inhomogeneous magnetic field depends not only on the field intensity but also on the magnetic history of the sample. The hysteresis loop of the superconductor consists of two curves (fig. 3): the upper-curve $m^+(H)$ corresponds to increasing the magnetic field and the down-curve $m^-(H)$ corresponds to decreasing the magnetic field. The existence of two different curves is a consequence of the irreversible part of magnetization of superconductors with pinning. According to the Bean critical state theory (ref. 3) these curves correspond to the different directions of the critical current inside the superconductor. From this it is obvious that increasing the external magnetic field by a value exceeding $2H_p$, where H_p is the field value resulting in the penetration of the magnetic field to the center of the superconductor, leads to the transition of sample magnetization from the $m^-(H)$ curve to the $m^+(H)$ curve if initial magnetization is related to the $m^-(H)$ curve. Decreasing the field to the same value leads to the inverse transition. These transitions between the curves form the minor loop. Due to hysteresis the superconductor magnetization can exhibit any value ranging from m^+ to m^- under a given field intensity. Hysteresis of magnetization leads to the hysteresis of repulsive force acting on a superconductor so that repulsive force can exhibit any value from r^+ to r^- under a given levitation height. The appearance of a unique position of levitation in the elastic regime is clearly seen when the amplitude of the alternating component is large enough to induce the cycle transitions between the $m^+(H)$ and $m^-(H)$ curves of the hysteresis loop. The magnetization value of the superconductor in this case is the following:

$$m = (m^+ + m^-)/2 + 0.5(m^+ - m^-) \sin 2\pi ft \quad (1)$$

where f is field frequency. One can see from (1) that after applying an alternating field the average value of magnetization equals to the reversible magnetization value $(m^+ + m^-)/2$ having no hysteresis. This means that the origin of the continuous range of levitation points disappeared and only the unique point of levitation occurs. However in the experiment the elastic regime of levitation is observed when the amplitude of an alternating field is low compared to the H_p parameter. Elastic levitation is likely to occur even when the alternating field is low compared to the H_p parameter and

the flux lines motion is induced only in the thin surface layer of superconducting grains. Thus the microscopic origin of the transition from the plastic type of levitation to the elastic one is the flux lines motion induced by the variable field. In the elastic regime the levitation height is determined by the reversible magnetization of superconductor $(m^+ + m^-)/2$ see (1). This conclusion is of importance because the reversible magnetization is low compared to the irreversible one in high quality oxide superconductors. This means that the load capacity in the elastic regime of levitation is less than that in the plastic regime. In order to explain the field frequency dependence of relaxation time in elastic regime of levitation consider the evolution of the point representing the state of the superconductor in the plane repulsive force - levitation height plane (r - h plane) see fig. 4. Consider for simplicity that the alternating component has the form of rectangular pulses and the inhomogeneity of the alternating field may be neglected compared to the one of the static field. In this case the magnetic moment of a superconductor will oscillate and the representing point will be displaced instantaneously vertically up or vertically down after each change of the sign of an alternating component. This means that the value of repulsive force, acting on the superconductor, changes without any change in the levitation height. Let's suppose that the field frequency is rather low so that after each change of the sign of alternating field the superconductor occupies the new equilibrium position which we called the local equilibrium point. Therefore the point representing the state of the superconductor reaches the line $r=mg$ after each change of the alternating field sign. In the elastic regime the global equilibrium height h_0 is determined as the crosspoint of the lines $r=mg$ and $(r^+ + r^-)/2$. Displacement of the superconductor from the global equilibrium point h_0 induces the relaxation motion of a superconductor. During this motion alternating field pulses having different signs displace the operating point in the different directions along the line $r=mg$ (see fig. 4). But the contributions of the pulses of different signs are not equivalent because when the operating point is in the local equilibrium the distance between the lines r^+ and $r=mg$ is not equal to the one between r^- and $r=mg$ lines. Due to these differences in the contributions of impulses of opposite signs the operating point is displaced towards the global equilibrium point h_0 until reaching it. When the superconductor occupies the global equilibrium point the contribution of the impulses with opposite signs becomes equivalent and the superconductor oscillates near this point without the resulting displacement. From this consideration one can conclude that at low frequencies each cycle of the alternating field induces the particular displacement of a superconductor. If in order for the superconductor to reach the global equilibrium, N cycles is required, the relaxation time will be equal to N/f . One can see that the relaxation time is inversely proportional to the field frequency in the low frequency regime, so that at zero frequency the relaxation time is infinite. This means the transition to the plastic regime of levitation in a static field. Therefore the considerations of the relaxation process of a superconductor in a variable magnetic field presented here explain the increase of time relaxation observed in the experiment in the low frequency range.

Now let's consider the vibrations of the magnet levitated above the superconductor. The levitated magnet generates an inhomogeneous magnetic field in the surrounding space. Due to the field inhomogeneity a vibrational motion of the magnet induces a change of the magnetic field value near the magnet. Therefore the vibrating magnet generates a variable field component in surrounding space. Since the superconductor providing the levitation is placed in the vicinity of the magnet, the variable magnetic field affects it. The variable magnetic field forces the flux lines to move inside the superconductor and as a consequence induces the transition from the plastic regime of levitation to the elastic one. Therefore the transition from the plastic regime of levitation to the elastic one may be induced when the permanent magnet levitated above the superconductor is forced to vibrate relative to the superconductor. This conclusion is of great importance because in using such a bearing, for instance in aerospace applications, variations in load, attitude and speed occur. These disturbances will induce vibration of the levitated magnet, and as a consequence, change the levitation height and decrease the load capacity of the bearing. It should be noted that the inverse situation occurs when a superconductor levitated above a magnet is forced to vibrate

relative to a rested magnet and is physically equivalent to the one considered above. Thus all the conclusions made in the case of the magnet levitated above the superconductor are true for a superconductor levitated above a magnet.

ROTATION OF LEVITATED SUPERCONDUCTOR

The second interesting effect is rotation of a levitated YBCO superconductor due to a rotational magnetic field. For the rotation experiment, two ceramic samples $\text{YBa}_2\text{Cu}_3\text{O}_{7-x}$ (YBCO) and $\text{YBa}_2\text{Cu}_3\text{O}_{7-x}\text{Ag}_2\text{O}$ (YBCO-Ag) prepared by means of ordinary ceramic technology were used. The first sample was a ring shape with these dimensions: outer diameter 7 mm, inner diameter 4 mm, thickness 2 mm. The second sample was a parallelepiped shape with dimensions $5.5 \times 1.0 \times 1.0 \text{ mm}^3$. A ring-shaped permanent magnet (SmCo_5) magnetized along the z-axis was the source of the inhomogeneous field. The Z-axis coincided with the magnet symmetry axis. The magnet had dimensions of 34 mm outer diameter, 10 mm inner diameter and 5 mm thickness. The experiment was carried out with the apparatus illustrated in fig. 5. A glass tube containing the superconductor was attached to the vacuum main. This tube was placed inside the Dewar with liquid nitrogen. The special external platform containing the ring-shaped magnet and four air coils provided the levitation of the magnet and creation of the rotational field component. An infrared beam passed through the tube and provided the registration of the rotation by infrared detector. The output of the detector was connected to the rotating-mirror oscillograph. An AC generator connected to the two equivalent power amplifiers was used to supply the current through the coils to create the rotational field.

At low rotational magnetic fields, rotation of the levitated superconductor was not observed. As the field intensity was increased, torsion oscillations of the superconductor appeared. When the rotational magnetic field intensity exceeded the critical value, the levitated superconductor began to rotate in the XY plane. In all of the experiments the superconductor rotated in the direction of field rotation. It was found that the rotation frequency increases with the increase of rotating field intensity until the rotation frequency achieves a certain value of about 10 Hz. Then the rotating frequency stops increasing and the further growing of the rotational field intensity causes considerable superconductor oscillations in the XY plane. The subsequent increase of rotating field intensity causes the rotation to be unstable. In this regime chaotic-like radial oscillations were observed. Active deceleration of the rotational superconductor (YBCO sample) and the subsequent active acceleration by the rotational field (10 Oe 50 Hz) is represented in fig. 6. One can see the rotational field develops considerable torque acting on the levitated superconductor. Superconductors' spin rate decay vs time in a static field is represented in fig. 7. Here we see a clear straight line decay. Note that the sample doped with silver oxide exhibits considerably stronger friction torque compared to the undoped sample. The torque acting on a levitated superconductor in a rotating magnetic field can arise from 1) diamagnetic geometric form effects, 2) rigid sample magnetization due to trapped flux lines, 3) anisotropy of type 2 superconductor, leading to transverse magnetization of the Abrikosov lattice, or 4) frictional rotational motion of flux lines induced by the rotating magnetic field. In cases 1) – 3) only synchronous rotation of the superconductor can occur. Only in case 4), when frictional rotational motion of flux lines drives the rotation of the superconductor, the rotational frequency of the superconductor may be less than the external field frequency and be independent of it. In this case the flux lines rotate with a frequency equal to the field frequency. Moving vortices develop a frictional torque which acts on the superconducting body inducing rotation. However, the rotational frequency of the specimen is controlled by external friction (in our case magnetic friction) and may be substantially less than the field frequency. In all our experiments the superconductor rotational frequency was

less (substantially) than field frequency. From this we concluded that frictional rotational motion of flux lines inside the superconductor is an origin of superconductor rotation.

While a superconductor is rotating around a center of a homogeneously magnetized ring, no changes of the magnetic field in a superconductor occur. Consequently no flux lines motion occurs in the superconductor. Real magnets, however, have some magnetization inhomogeneity leading to the existence of the asymmetry of a magnetic field with respect to their vertical axis. In that case during rotation the magnetic field in the specimen does not remain constant causing the flux lines motion. As a result a magnet friction torque occurs (ref. 4). Moving over an atomic lattice, flux lines are acted upon by two different microscopic forces (ref. 5): 1) The pinning force, which does not depend on the motion speed of a flux line and is analogous to the dry friction force, 2) The viscous force, which is directly proportional to the flux line speed. The superconductor rotational rate decay is observed to be linear (see fig. 7); i.e. the friction torque does not depend upon the rotational frequency. This conforms with the data obtained by F. Moon et al. (ref. 4) in the experiments with the high frequency rotation of the magnet levitated above the superconductor. Thus, it may be concluded that the pinning force acting upon moving flux lines is the origin of the macroscopic rotational torque developed by the rotational magnetic field. The magnitude of the viscous force is negligible. It should be noted that different superconducting samples exhibit different friction torque during free rotation (see fig. 7). One can see that friction torque increases as pinning force decreases. The magnitude of angular acceleration of the levitated superconductor in the case of active acceleration of the superconductor by the rotational field is directly proportional to the torque acting on the superconductor. Similar to that case the magnitude of angular deceleration of the freely rotating superconductor is proportional to the magnetic friction torque. By using the slopes of this dependency (see fig. 6,7) we calculated that **rotational field torque / friction torque** = 40 for YBCO sample and rotational magnetic field 10 Oe, 50 Hz. This conclusion is of great importance because it means that magnetic friction in levitated superconductors is not the factor restricting the rotational speed and in principle one can reach considerably higher speed magnitude. The instability of the rotating superconductor in a horizontal plane is likely to be the origin of low rotation rate. It was observed that the maximal rotation frequency of the levitated superconductor is approximately equal to the radial resonance frequency of the superconductor. Therefore, one can suppose that low frequency natural resonance restricts the rotational frequency.

The apparatus represented in fig. 5 may be considered as the prototype of a new motor based on a superconductor levitated rotor. We called this type of motor a superconductor hysteresis motor because the rotational field develops the torque acting on the superconductor due to the pinning of flux lines. Pinning of flux lines leads to the hysteresis of superconductor magnetization and the occurrence of a non-zero angle between the vector of magnetization and the vector of a rotational field. The occurrence of this angle results in the development of torque acting on a superconductor. This method of torque generation qualitatively differs from that used in the ordinary motor based on a magnet levitated above a superconductor as a rotor (ref. 6). In a magnet levitated motor there is an additional small magnet connected with the main magnet providing the levitation. The small magnet is acted upon by the rotational field to induce rotation. In contrast, in hysteresis, the superconductor motor rotational field acts on the levitated superconductor rotor immediately. Another important feature of the hysteresis motor is independence of the torque generated upon the relation between the superconductor rotation frequency and field frequency. It is required only that field frequency exceed the rotation frequency. This property makes initiation of rotor rotation effortless.

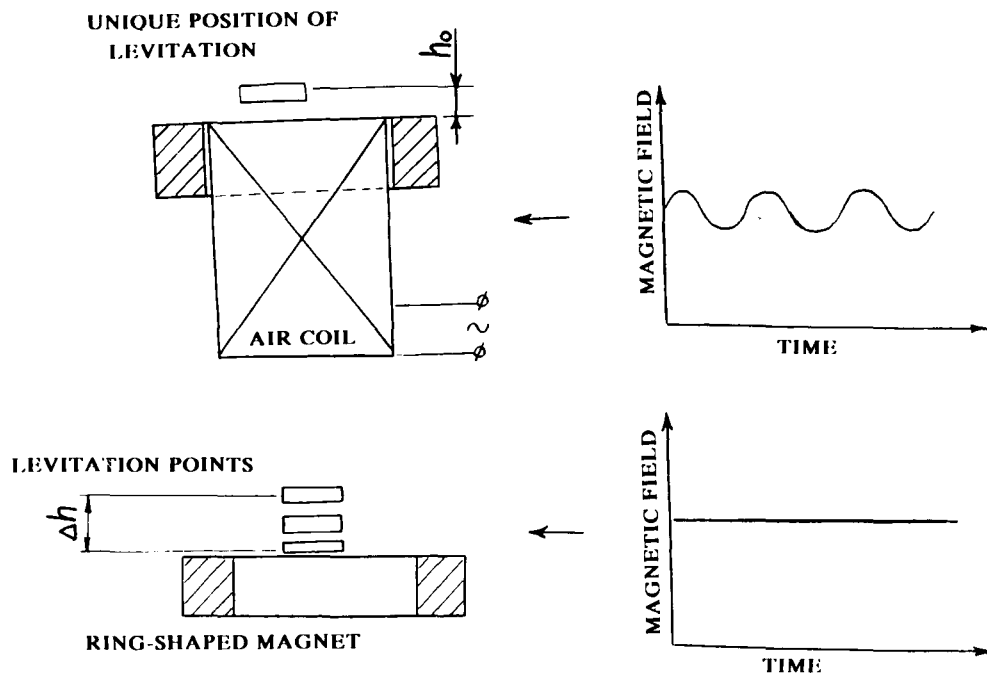
CONCLUSIONS

Influence of both linear alternating and rotational magnetic field components on a levitation behavior of $\text{YBa}_2\text{Cu}_3\text{O}_{7-x}$ superconductor was examined. The transition from a plastic regime of levitation to an elastic one, induced by an alternating field component was discovered. In contrast to plastic levitation, elastic levitation is characterized by a unique position of levitation and field frequency dependence of relaxation to the equilibrium position after disturbance. The elastic type of levitation exhibits low load capacity compared to the plastic one. It was concluded that vibrations of a magnet levitated above the superconductor can induce the transition from plastic levitation to an elastic one.

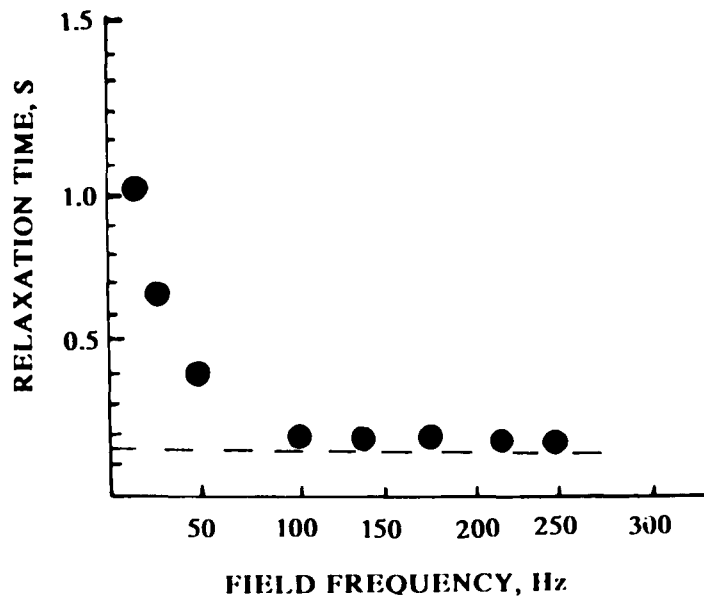
The rotational field component causes the levitated superconductor to rotate. Rotational frictional motion of flux lines is likely to be an origin of the torque developed. Frictional torque developed during rotation of the superconductor is low compared to the torque developed by the rotational field. Instability of the rotating superconductor in a horizontal plane restricts the maximal rotational frequency. A new type of motor based on the superconductor levitated rotor was proposed.

REFERENCES

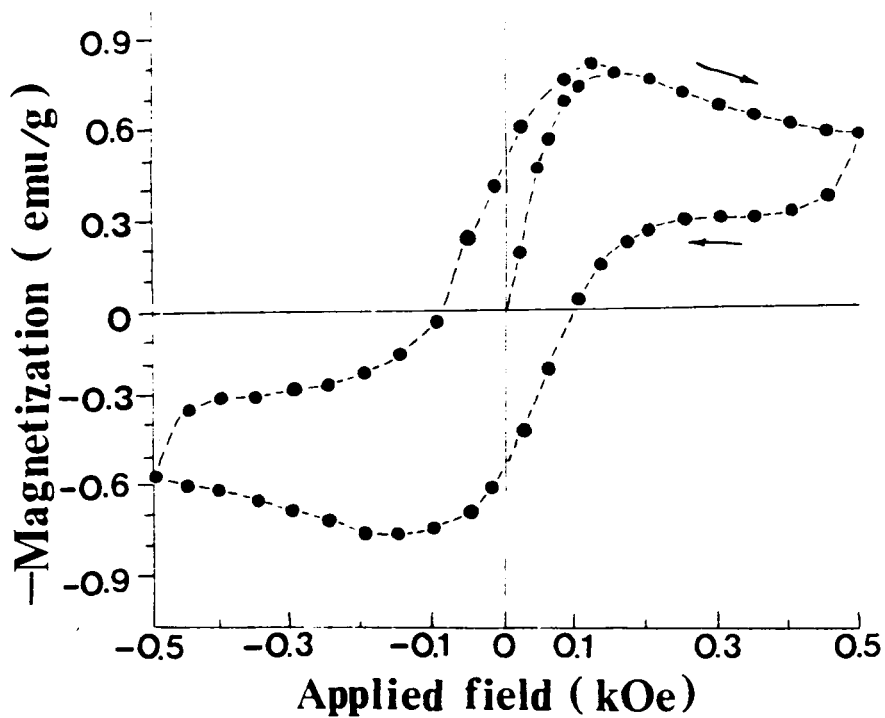
1. Shapira, Y., C. Y. Huang, E. J. McNiff, Jr., P. N. Peters, B. B. Schwartz, M. K. Wu: Magnetization and magnet suspension of $\text{YBa}_2\text{Cu}_3\text{O}_x\text{-AgO}$ ceramic superconductors. *J. Mag. & Mag. Materials.*, vol. 78, 1989, pp. 19-30.
2. Brandt, E. H.: Friction in levitated superconductors. *Appl. Phys. Lett.*, vol. 53, no. 16, 1988, pp. 1554-1556.
3. Bean, C. P.: Magnetization of hard superconductors. *Phys. Rev. Lett.*, vol. 8, no. 6, 1962, pp. 250-253.
4. Moon, F. C., and Chang, P.-Z.: High-speed rotation of magnets on high T_c superconducting bearing. *Appl. Phys. Lett.*, vol. 56, no. 4, 1990, pp. 397-399.
5. Matsushita, T.: Electromagnetic phenomena and hysteresis losses in superconductors. *Cryogenics.*, vol. 30, 1990, pp. 314-323.
6. Weinberger, B. R., Lynds, L., Hull, J. R.: Magnetic bearings using high-temperature superconductors: some practical considerations. *Supercond. Sci. Technol.*, vol. 3 1990, pp. 381-388.



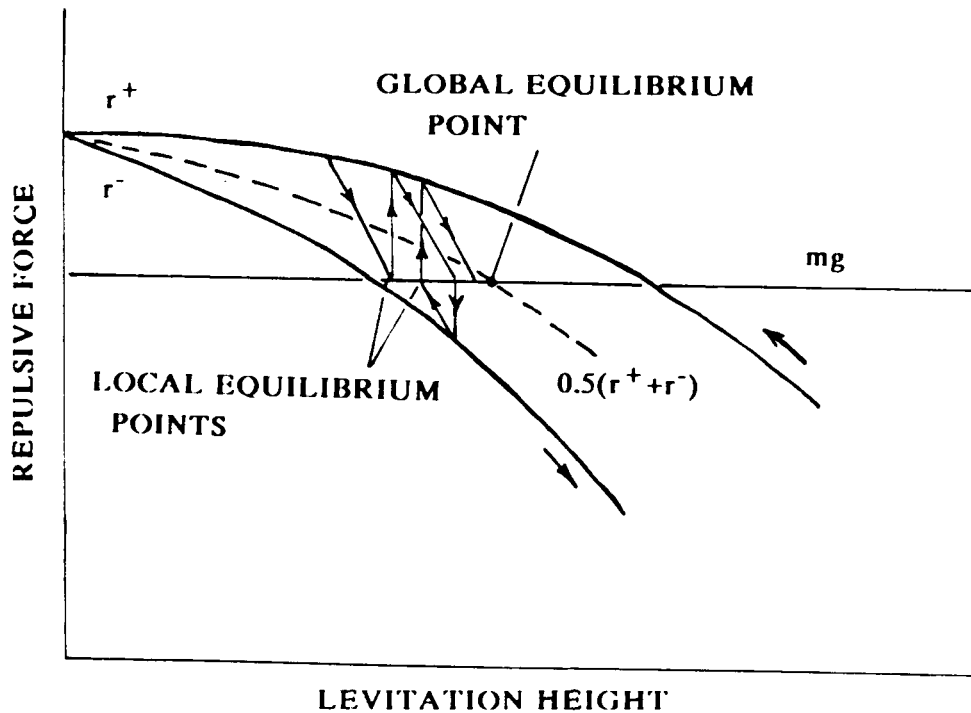
1. Apparatus for levitation experiment in the variable magnetic field



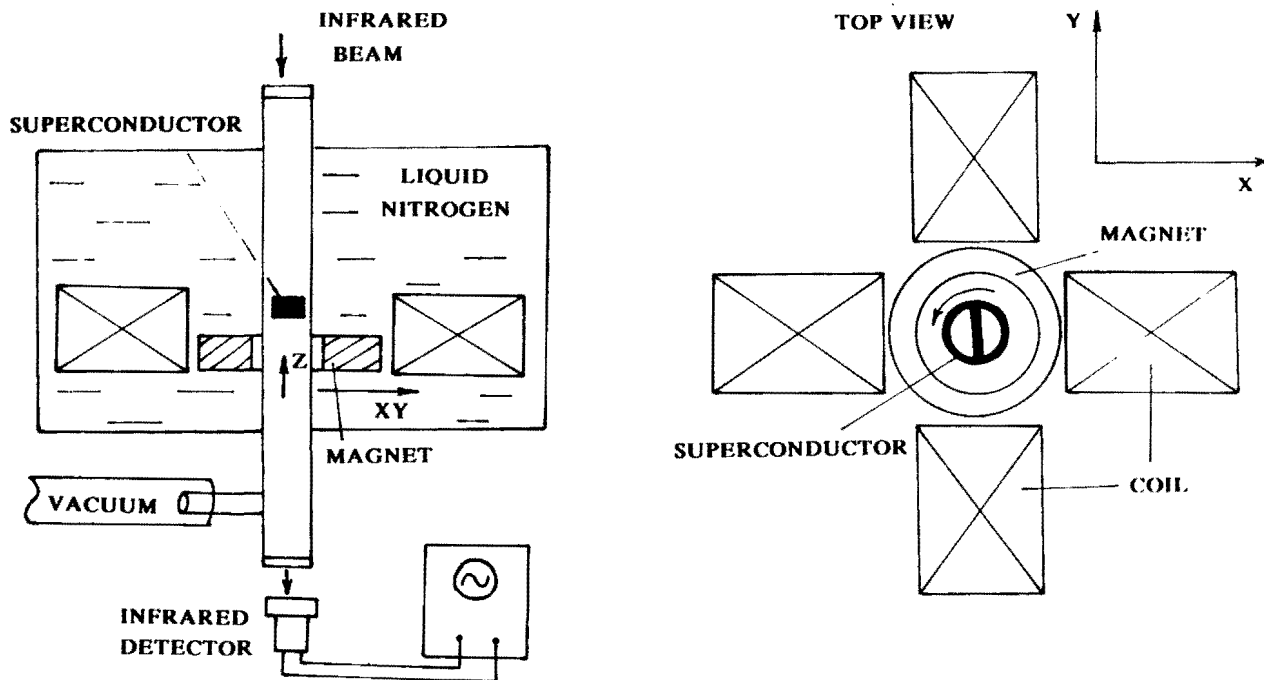
2. Field frequency dependence of the relaxation time of the superconductor to the unique position of stable levitation in elastic levitation regime.



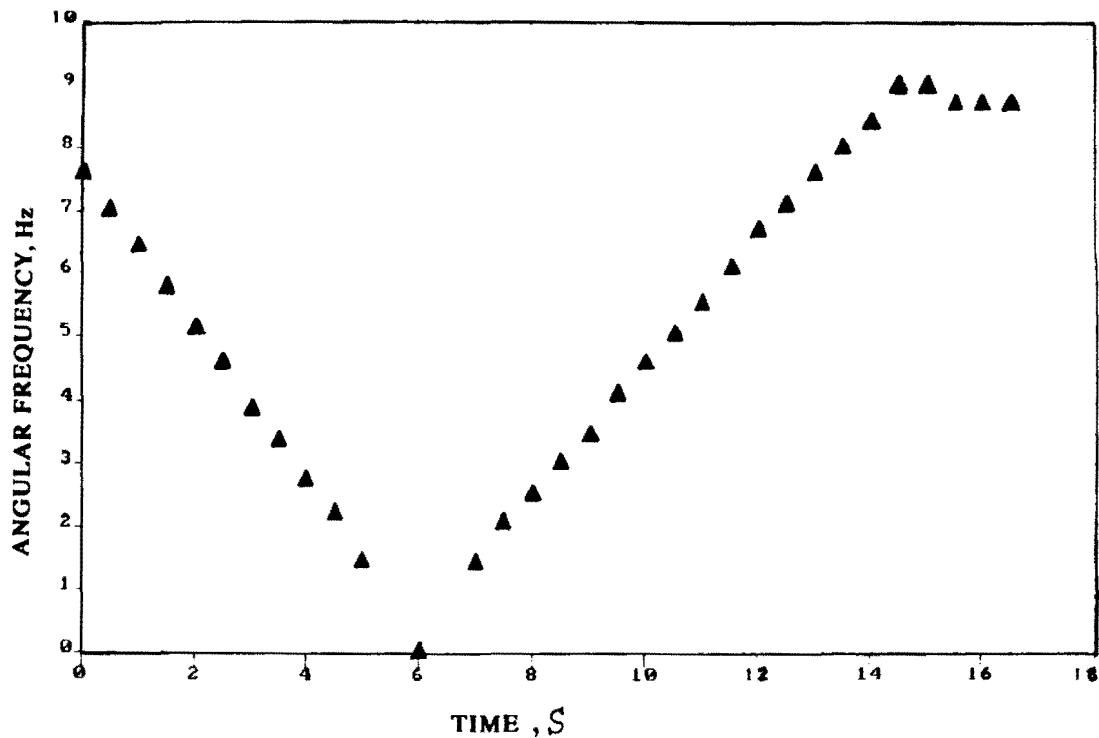
3. Hysteresis loop of YBCO superconductor used in the levitation experiment. $T=77\text{K}$.



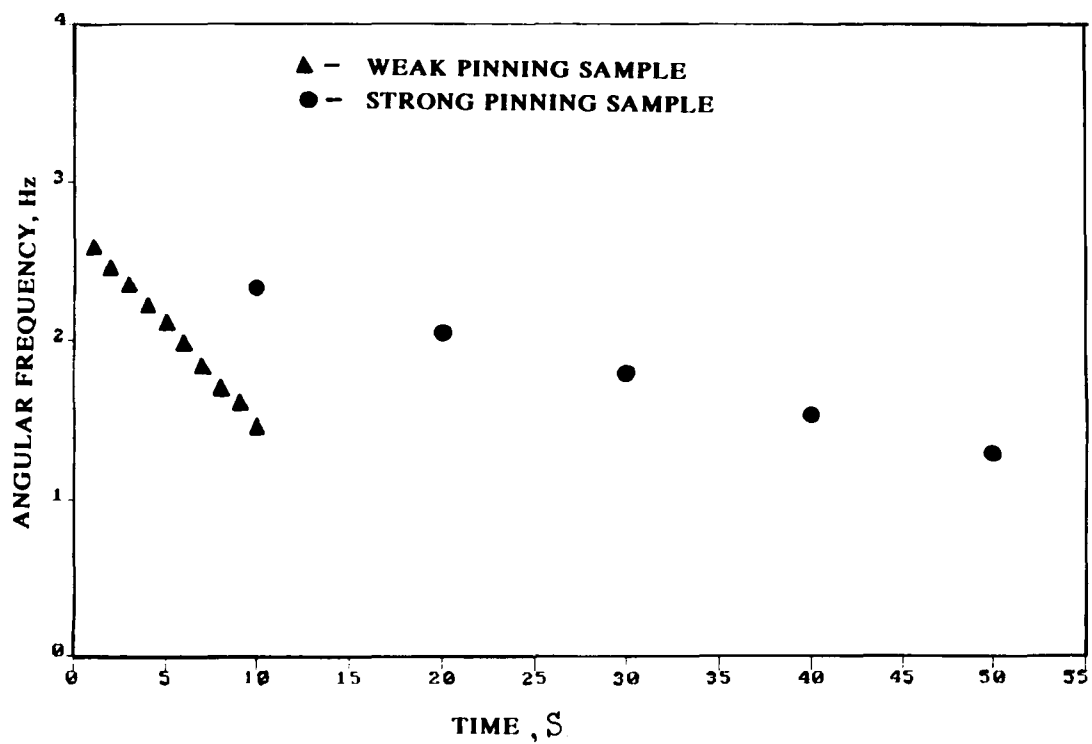
4. Relaxation of superconductor to the unique position of levitation in elastic levitation regime. Alternating field has the form of rectangular pulses.



5. Apparatus for rotation experiment.



6. Active deceleration and acceleration of rotating superconductor induced by rotational magnetic field (50 Hz, 10 Oe).



7. Superconductor rotation frequency decay in static magnetic field.

Hybrid Superconducting Magnetic Bearing (HSMB) For High Load Devices

C. K. McMichael^(a) , K. B. Ma, M. A. Lamb^(b) , M. W. Lin^(c) , L. Chow,
R. L. Meng, P. H. Hor, and W. K. Chu
Texas Center for Superconductivity at the University of Houston (TCSUH)

- (a) C. K. McMichael is an undergraduate fellow from the University of Houston.
- (b) M. A. Lamb is an undergraduate fellow from the University of Houston.
- (c) M. W. Lin is an undergraduate fellow from the California Institute of Technology.

SUMMARY

Lifting capacities greater than 41 N/cm² (60 psi) at 77 K have been achieved with a new type of levitation (hybrid) using a combination of permanent magnets and high quality melt-textured Y₁Ba₂Cu₃O_{7-δ} (YBCO). The key concept of the hybrid superconducting magnetic bearing (HSMB) is the use of strong magnetic repulsion and attraction from permanent magnets for high levitation or suspension forces in conjunction with a superconductor's flux pinning characteristics to counteract the inherent instabilities in a system consisting of magnets only. To illustrate this concept, radial and axial forces between magnet/superconductor, magnet/magnet, and magnet/superconductor/ magnet, were measured and compared for the thrust bearing configurations.

INTRODUCTION

The objectives of developing a more viable high temperature superconductor (HTS) bearing are to achieve higher stiffness and higher load lifting capacity while maintaining high vibration damping and low rotational dissipation at a temperature of 77 K. The origin of the inefficiency in previous systems utilizing active magnetic suspension, such as electrical feed back controls or complex pneumatic gas bearing systems, lies in their continuous energy consumption. Superconductors in their present-day bulk form are good candidates for simple superconducting magnetic bearing (SMB) devices [1, 2, 3] such as a levitated magnet over a disk of YBCO. However, this simple type of bearing arrangement yields limited levitation, limited suspension, and low magnetic stiffness. This is due to the finite rotor magnetic field and the finite J_c of the superconducting stator. In view of the fact that zero field cooling (ZFC) results in force creep (gap creep) [4] and low radial stiffness for such magnetic bearings, field cooled conditions (FC) should be addressed. In addition, it is impractical to cool the bearing elements (superconductors) before assembling the bearing device (magnetic rotor). Under FC conditions, a negligible static levitation force occurs when no external load is applied in any direction. In contrast, a much higher magnetic stiffness for radial displacement is found in FC as compared to ZFC conditions.

In this report, a simple approach to improve upon the limitations of the SMBs is presented. Higher levitation, suspension, and stiffness forces are needed to implement SMBs into a wider range of applications. This is achievable in a passive magnetic bearing system composed of strong permanent magnets with a design that alleviates the inherent instability as stated in Earnshaw's theorem [5]. The HSMB design overcomes the magnet/magnet instability by using high quality continuously processed melt-textured YBCO material [6] placed between the rotor and stator magnets. This design allows for greater stiffness values and maintains a much higher static load-lifting capacity compared to magnet/superconductor bearings.

ABBREVIATIONS

| | |
|-------|---|
| HTS | high temperature superconductor |
| FC | field cooled |
| ZFC | zero field cooled |
| SMB | superconducting magnetic bearing |
| HSMB | hybrid superconducting magnetic bearing |
| T_c | critical temperature |
| J_c | critical current density |
| YBCO | $Y_1Ba_2Cu_3O_{7-\delta}$ |

EXPERIMENTAL

A dipole permanent magnet (1.27 cm length, 0.95 cm diameter, 0.426 T surface field) used in a rotor was attached to a static force measurement system [7] incorporating an elastic beam with strain gauges. This cantilever beam was fixed to a motorized stage controlled by a computer. A stationary cold stage held fixed on an optical table was used with liquid nitrogen (77K) to cool the superconductor and, when needed, an opposing permanent magnet. The collected data was converted into static forces and force hystereses versus displacement, for both radial and axial movement with the thrust bearing configuration.

For comparison between ZFC and FC conditions, the axial force creep and the radial stiffness between the rotor magnet and a YBCO disk (0.47 cm

thick, 2.23 mm diameter) was measured and the results are displayed in Figs. 1 and 2, respectively.

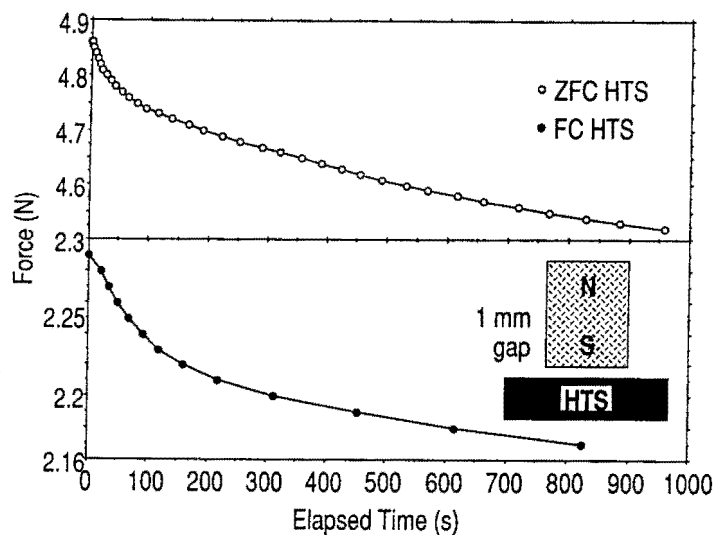


Fig. 1 Force creep - force between magnet and HTS as a function of time under ZFC and FC conditions.

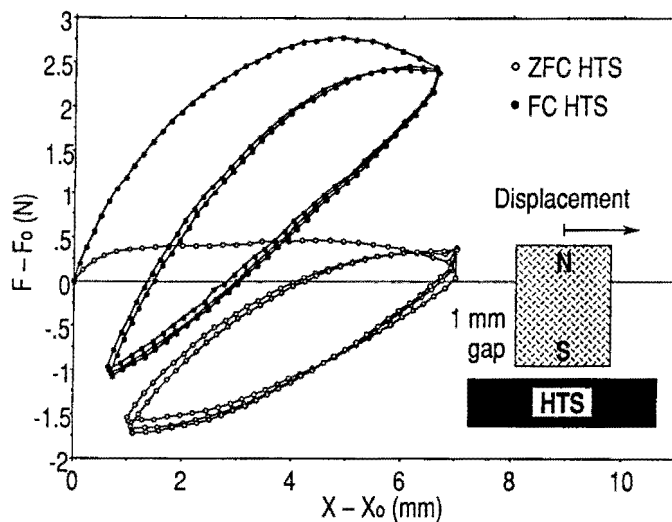


Fig. 2 Radial hysteresis loops - change of force from the initial setup value (different for FC and ZFC cases) as magnet is displaced across an HTS disk, as a function of the displacement from the initial point.

Radial and axial force hysteresis measurements were also taken from the same YBCO disk starting at a fixed distance of 0.25 mm from the surface of the rotor magnet. These results are shown in Figs. 3-5.

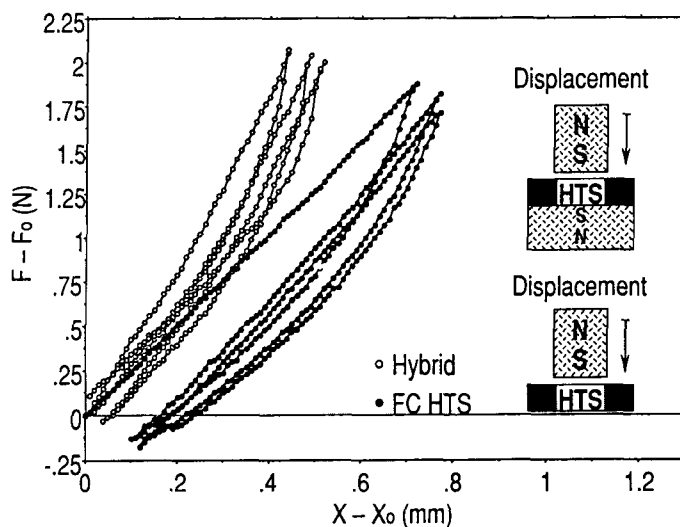


Fig. 3 Axial hysteresis loops - change of force from the initial setup value (different for FC HTS and hybrid cases) as the magnet is pressed onto the HTS disk, as a function of the displacement from the initial point.

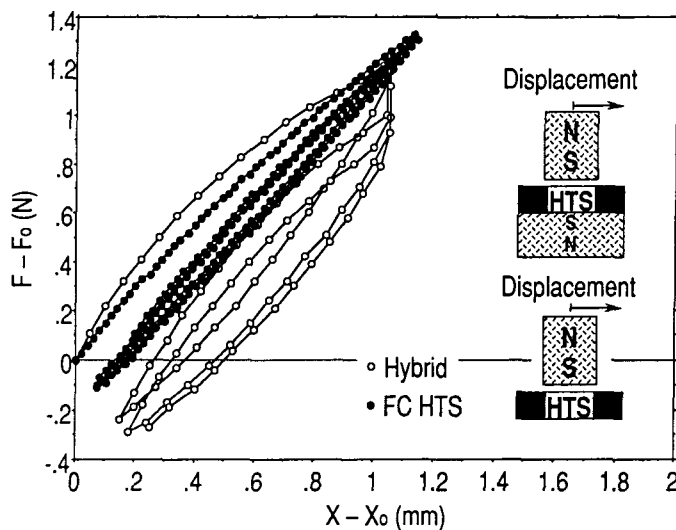


Fig. 4 Radial hysteresis loops - change of force from the initial setup value (different for FC HTS and hybrid cases) as the magnet is displaced across the HTS disk, as a function of the displacement from the initial point near the center.

A permanent magnet (0.95 cm diameter, 1.27 cm length, 0.416 T surface field) was fixed at the bottom of the apparatus as a stator with polarity attracting the rotor magnet. At 77 K, measurements (Fig. 6) were taken of the negative shear stiffness (N/mm) and correlated directly to the repulsion force.

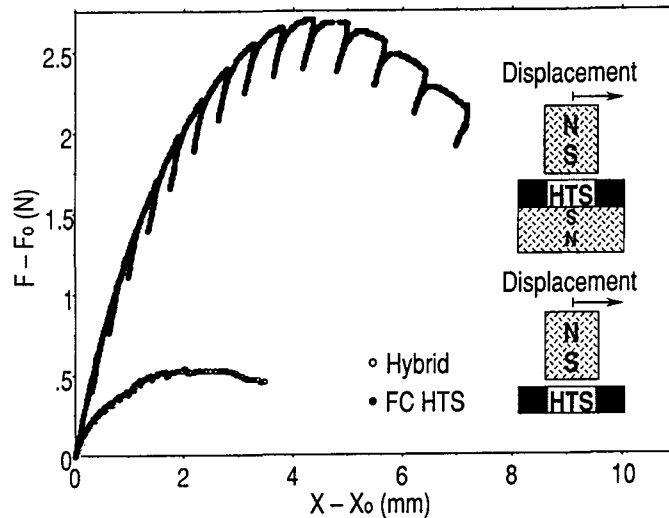


Fig. 5 Radial force versus displacement with minor hysteresis loops - change of force from the initial setup value (different for FC HTS and hybrid cases) as the magnet is displaced across the HTS disk, as a function of the displacement from the initial point near the center.

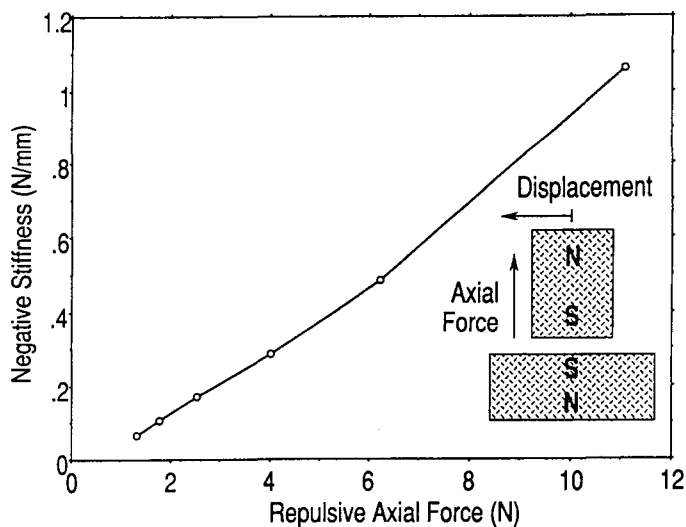


Fig. 6 Stability versus thrust for the stator magnet - the negative stiffness in the radial direction is used as a measure of the instability that has to be overcome if the stator magnet is to provide a given amount of thrust.

Then the rotor magnet was held fixed over a superconductor placed on top of the stator magnet to form a prototype HSMB (magnet / superconductor / magnet) non-rotating setup. Radial and axial force hysteresis measurements were made for this HSMB setup with a 6 mm gap between both magnets and compared with the corresponding results for the FC SMB in Figs. 3-5.

RESULTS AND DISCUSSION

It is known that the force between a magnet and an HTS disk is much smaller under FC conditions than under ZFC conditions. This is no longer a disadvantage for FC conditions, since our central idea is to use magnets to provide the thrust force, with the HTS providing the required stabilization. For example, our FC SMB provided practically zero lifting force, while the HSMB can provide up to 8.88 N. What we have shown in Fig. 1 is that the force creep under similar load is almost the same for both ZFC and FC conditions. The time scale in which the creep occurs is also similar. In 10 minutes, the magnet/HTS force decreased by 5.3% of its initial value for ZFC conditions, whereas, the decrease was only 4.8% for FC conditions. Since forces required for stabilization purposes can be expected to be smaller than that of the main thrust, this translates into an advantage for the FC case. This is further supported by our measurements of the retaining force against a displacement in the radial direction, as shown in Fig. 2. The stiffness that comes from FC conditions is bigger, and so is the maximum force that can be sustained before it yields.

Since we would have to supply the required thrust using additional magnets, the next question concerns whether the presence of this extra magnet would annul these advantages of higher stability. To investigate this, we have put a magnet below the HTS disk and measured changes of the forces as the rotor magnet above the HTS disk is displaced in the axial and radial directions. The negative stiffness (instability) in the radial direction due to this additional stator magnet is plotted as a function of the thrust that it can provide at various gap distances in Fig. 6. This instability is the inherent instability if we used the magnets only. This is to be overcome by placing the HTS disk in between the two magnets. We have definitely shown that this can be accomplished in Figs. 4 and 5. The effects

of the stator magnet are not apparent until displacements as large as a significant fraction of a millimeter from the original position are reached. Although there is no instability to be overcome in the axial direction, we have also included measurements in this direction in Fig. 6, to show the final stiffness that can be achieved in the magnet/superconductor/magnet system. This axial stiffness is similar to that of the magnet/magnet system with the same gap distance between magnets, but is definitely inferior to the magnet/magnet system that has the same gap as the top magnet/superconductor pair in our hybrid system.

In conclusion, we have shown that the HSMB allows us to increase the thrust over that which can be provided by SMBs. The stiffness that can be achieved is similar to magnet/magnet systems with the same magnet/magnet gap distance. Thus, higher stiffnesses can be attained if we decrease this gap, but then the thickness of the intervening HTS disk would be decreased accordingly. The radial stability would be compromised. An optimum HTS thickness would have to be determined.

REFERENCES

1. F. C. Moon and P.-Z Chang, Appl. Phys. Lett. 56, 397 (1990).
2. B. R. Weinberger, L. Lynds, and J. R. Hull, Supercond. Sci. Technol. 3, 381 (1990).
3. C. K. McMichael, K. B. Ma, M. W. Lin, M. A. Lamb, R. L. Meng, Y. Y. Xue, P. H. Hor, and W. K. Chu, to be published in Appl. Phys. Lett.
4. F. C. Moon and J. R. Hull, 25th IECEC 3, 425 (1990).
5. S. Earnshaw, "On the Nature of the Molecular Forces which Regulate the Constitution of the Luminiferous Ether," Trans. Camb. Phil. Soc. 7, pp. 97-112, (1842).
6. R. L. Meng, C. Kinalidis, Y. Y. Sun, L. Gao, Y. K. Tao, P. H. Hor and C. W. Chu, Nature 345, 326 (1990).
7. F. C. Moon, M. M. Yanoviak, and R. Ware, Appl. Phys. Lett. 52, 1534 (1988).

CHARACTERIZATION
OF
SUPERCONDUCTING MAGNETIC BEARINGS
(Dynamic stiffness and damping coefficient in axial direction)

Ryoichi Takahata, Hirochika Ueyama
Koyo Seiko Co., Ltd.
24-1 Kokubuhiganjo, Kashiwara, Osaka 582, Japan

Tsutom Yotsuya
Osaka Prefectural Industrial Technology Research Institute
2-1-53 Enokojima, Nishi-ku, Osaka 550, Japan

ABSTRACT

High-Tc superconductor as a stator and permanent magnets for a rotor were assembled into a superconducting magnetic bearing. The dynamic stiffness and the damping coefficient of the superconducting magnetic bearing in axial direction were measured. The dynamic stiffness depended on an axial gap between superconductor and permanent magnet. The superconducting magnetic bearings are advantageous for a passive bearing, because they have a vibration damping effect that a permanent magnet bearing does not have. The tendency of its vibration damping coefficient indicated an increase as the resonant frequency increased.

INTRODUCTION

Since a high-Tc superconductor was discovered, many efforts have been made on developing a superconducting magnetic bearing (SMB) (ref.1). The SMB has been appreciated by several factors, levitation pressure, dynamic stiffness (ref.2), damping coefficient, and the rotational speed (ref.3).

Recently a melt process on bulk $\text{YBa}_2\text{Cu}_3\text{O}_x$ has been improved (ref.4) and a levitation pressure has also become large.* The SMB has been able to support a rotor weighing about 1 kg, rotating at a speed of 5,000rpm.†

One of the purpose of this work is to examine the dynamic stiffness and the damping coefficient of SMB in axial direction. They are very significant for bearing design.

EXPERIMENT

Construction of SMB

A superconducting magnetic bearing can be assembled by using high-Tc superconductor as a stator and permanent magnets for a rotor. The superconductor used in this test was a bulk $\text{YBa}_2\text{Cu}_3\text{O}_x$ prepared by quench and melt growth (QMG) process. The diameter of the bulk was 43mm and 12mm in thickness, and was made by Nippon Steel Corporation. The rotor had 4 permanent magnets (Nd-Fe-B, Sumitomo Special Metal Co., Ltd.). The surface flux density of the magnets was 0.45T. Each of the permanent magnets has 20mm in diameter and 4mm in thickness.

* K.Miyamoto and K.Sawano et al. : "Quench and Melt Growth (QMG) Processed Superconducting Materials for Levitation and Magnetic Flux Trapping", Submitted to Proc. ISS'90 (1990) in Sendai, Japan

† R.Takahata, H.Ueyama and T.Yotsuya : "Load Carrying Capacity of Superconducting Magnetic Bearings", Submitted to Proc. The International Symposium on Application of Electromagnetic Forces (1991) in Sendai, Japan

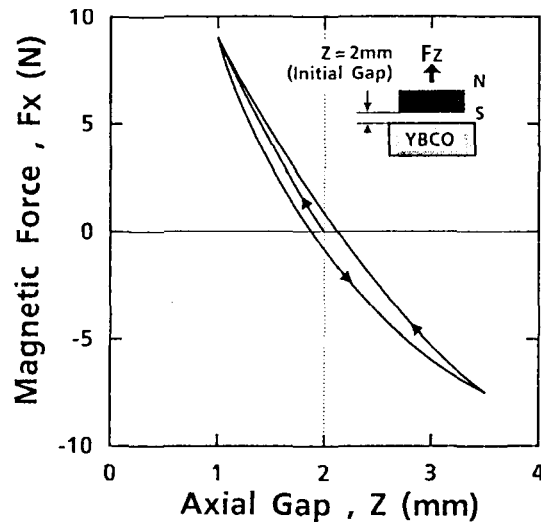


Fig.1 Static stiffness of SMB

The maximum carrying load capacity of the tested bearing was 5 kg in axial direction and the levitation pressure was 3.4N/cm^2 . Its value was measured by means of road cell, when the magnet approached the surface of bulk $\text{YBa}_2\text{Cu}_3\text{O}_x$ cooled down to liquid nitrogen temperature.

The static stiffness of tested bearing was 9N/mm as shown in Fig.1. It was also measured by means of road cell when the magnets were moved slowly in axial direction after the bulk $\text{YBa}_2\text{Cu}_3\text{O}_x$ was cooled down by liquid nitrogen at 2mm axial gap between magnet and superconductor.

Test equipment

The apparatus shown in Fig.2 was constructed to measure the vibration damping and the dynamic stiffness of SMB in axial direction. A shaft having permanent magnets on its lower side was located vertically above the bulk $\text{YBa}_2\text{Cu}_3\text{O}_x$. The shaft was able to be supported with no mechanical contact by active magnetic bearings in radial direction and by SMB in axial direction. To decrease the damping effect brought about by eddy current, conducting materials were located as far from permanent magnets as possible. The total mass of the shaft was 1.118 kg.

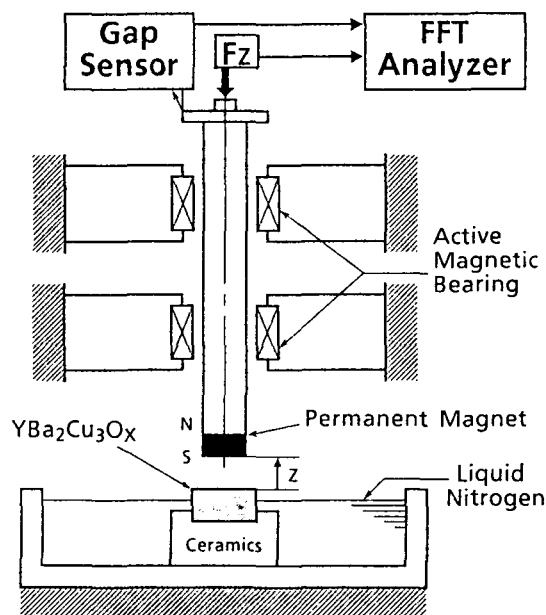


Fig.2 Dynamic stiffness measuring apparatus

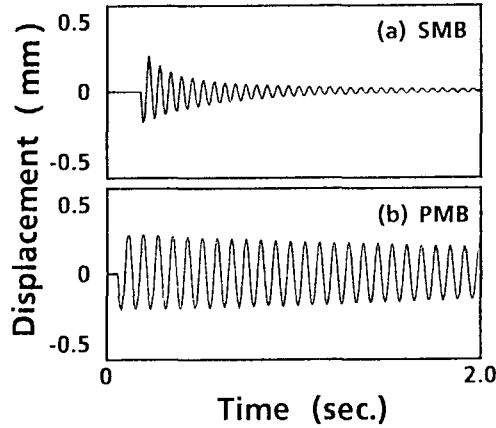


Fig.3 Vibration of shaft in axial direction ;
(a) in the case of SMB, (b) in the case of PMB

Test Procedure

The shaft was supported by active magnetic bearings in radial direction and fixed at initial gap Z_0 in axial direction; then the bulk $\text{YBa}_2\text{Cu}_3\text{O}_x$ was cooled down to about 77K by liquid nitrogen. After above field cooling, the shaft was released and supported with no mechanical contact. At that time an axial gap of SMB decreased to $Z < Z_0$. That is the equilibrium position.

RESULT AND DISCUSSION

SMB model in one degree of freedom

A vibration of the shaft in axial direction was measured by gap sensor when an external impulse force F_z acted on the shaft that was supported by SMB. It is shown in Fig.3(a). Fig.3(b) shows a vibration of the shaft supported by a permanent magnet bearing (PMB) by the same procedure. The vibration damping of SMB was larger than that of PMB using repulsive forces of permanent magnets. Therefore an SMB model in one degree of freedom can be shown in Fig.4(b). The motion of this model can also be described by equation (1).

$$m\ddot{z} + c\dot{z} + kz = F_z \quad (1)$$

In this equation m is the mass of shaft, k is the spring constant and c is the damping coefficient respectively.

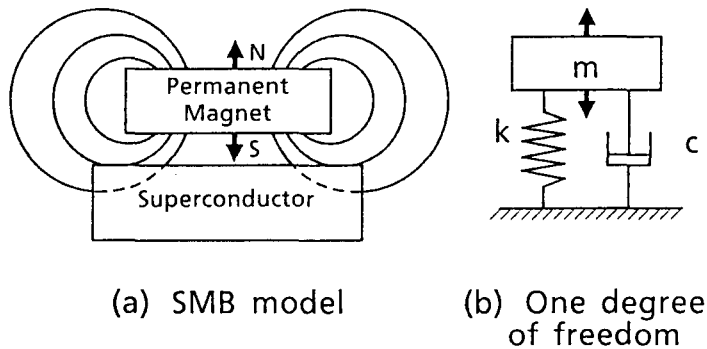


Fig.4 SMB model in 1 degree of freedom

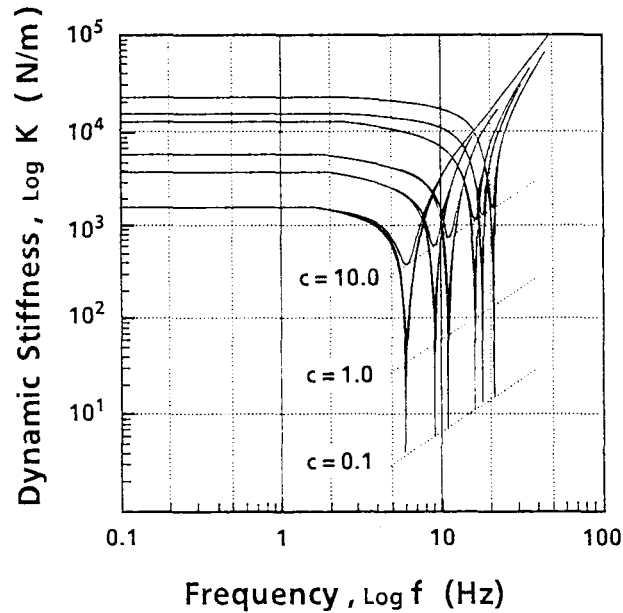


Fig.5 Dynamic stiffness vs vibration frequency (simulation)

The dynamic stiffness K of axial displacement for external force Fz can be also described by equation (2).

$$|K| = \sqrt{(k - m\omega^2)^2 + \omega^2 c^2} \quad (2)$$

where ω is the angular velocity. Arbitrary values ($k=1.6, 3.7, 5.4, 11.5, 14.2, 20.0 \times 10^3 \text{N/m}$, $c=0.1, 1.0, 10.0 \text{Ns/m}$) in equation (2) are simulated and the results are shown in Fig.5. The minimum value of dynamic stiffness appears at resonant frequency ω_0 that depends upon only spring constant k ($\omega_0 = \sqrt{k/m}$). And that minimum value is decided by the damping coefficient c . So it is possible to estimate the damping coefficient by means of measuring dynamic stiffness.

Measured spring constant, k

When the shaft was struck by an impulse hammer in axial direction, the axial vibration of it was measured at several gaps of Z . The values of Z of SMB were 0.8, 1.3, 1.9 mm which corresponded to the initial gap $Z_0 = 2.0, 3.0, 4.0 \text{mm}$ respectively. Z did not change after the hammering

Spring constant of axial direction is able to be given by equation (3)

$$k = 4\pi^2 \cdot m \cdot f_0^2 \quad (3)$$

where f_0 is the resonant frequency.

The value of spring constant k calculated from equation (3) using the measured f_0 is shown in Fig.6. The spring constant increased as the axial gap decreased. The value of spring constant was $15,000 \text{N/m}$ at $Z=1 \text{mm}$.

Measured damping coefficient, c_s

It is also possible to estimate damping coefficient c_s from the decreasing characteristics of vibration amplitude. Damping coefficient c_s can be described by equation (4).

$$c_s = 2m \cdot \beta \quad (4)$$

where β is a natural logarithm of damping ratio per second in vibration amplitude.

Measured damping coefficient, c_s is shown in Fig.7. Damping coefficient c_s also increased as an axial gap decreased.

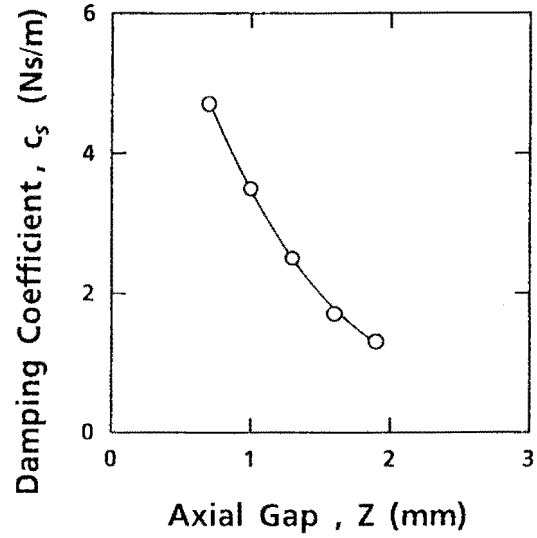
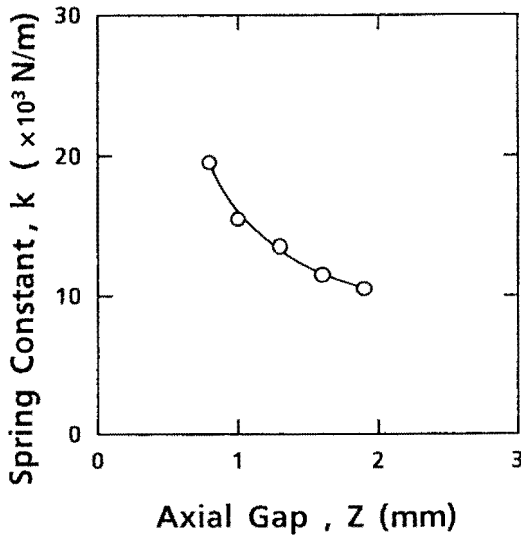


Fig.6 Change in spring constant with axial gap Fig.7 Change in damping coefficient with axial gap

But in this test equipment, c_s included the intrinsic damping coefficient c_i in addition to the damping coefficient $c_{(SMB)}$ due to SMB was caused by eddy current loss and air resistance in a vibration of the shaft. It was clear that the vibration of the shaft supported by the permanent magnet bearing, not having a damping factor, had actually a little damping as shown in Fig.3(b). The damping coefficient $c_{(SMB)}$ is given by equation (5).

$$c_{(SMB)} = c_s - c_i \quad (5)$$

Measured dynamic stiffness, $K(\omega)$

We also measured dynamic stiffness $K(\omega)$ of SMB directly by means of FFT analyzer and frequency changeable external force $Fz(\omega)$ acting on the shaft with no mechanical contact. That force was attractive force generated by an electromagnet and swept sine-wave excitation current $I(\omega)$.

The dynamic stiffness can be measured as the transfer function from the external force $Fz(\omega)$ to the displacement $Z(\omega)$ of the shaft as shown in equation (6).

$$K(\omega) = Fz(\omega) / Z(\omega) \quad (6)$$

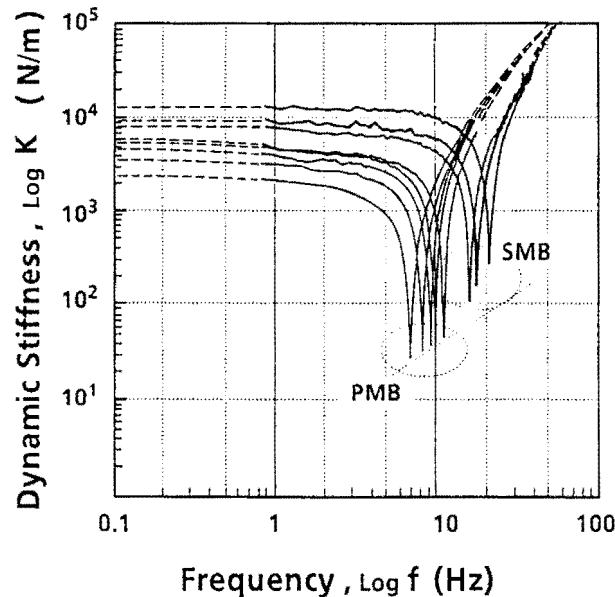


Fig.8 Dynamic stiffness vs vibration frequency in the SMB and PMB

The measured dynamic stiffness of SMB and PMB are shown in Fig.8. The damping coefficient of PMB was constant independently of frequency by judging from the minimum value of dynamic stiffness in comparison with Fig.5. Its value of damping coefficient was 0.6Ns/m and seemed to indicate the value of c_i , while the values of c_s were 1.0, 1.3, 1.9 Ns/m at resonant frequency $f_0 = 16.0, 17.75, 21.0\text{Hz}$ respectively, so $c_{(SMB)}$ were calculated from equation (5), $c_{(SMB)} = 0.4, 0.7, 1.3(\text{Ns/m})$. The value of $c_{(SMB)}$ seems to increase as the resonant frequency f_0 increased.

These values of c_s in this test are a little smaller than the damping coefficients c_s , measured by hammering, shown in Fig.7, because here $K(\omega)$ was measured by taking $I(\omega)$ instead of $Fz(\omega)$ in equation (6). As $I(\omega)$ is swept sine-wave excitation current, the actual $Fz(\omega)$ acting on the shaft in this test is proportional to $I(\omega)^2$ and is larger than $I(\omega)$ for vibration at resonant point so that the measured dynamic stiffness appearing in Fig.8 seems to be a little smaller than actual dynamic stiffness. Therefore we think it is necessary to linearize $I(\omega)$ for $Fz(\omega)$ in the next step.

Bearing design

Measured damping coefficients of SMB were smaller at least by one order of magnitude than that of active magnetic bearings. It is very important for bearing design to improve the damping coefficient. This damping factor of SMB seemed to be dependent on hysteresis loop shown in fig.1. Therefore an improvement of $\text{YBa}_2\text{Cu}_3\text{O}_x$ materials with a larger hysteresis loop and stiffness than that is expected for one of the ways to develop a practical SMB. If the material improvement is impossible, it will be necessary to add another damping mechanism for SMB to be used in a cryogenic environment.

CONCLUSIONS

Dynamic characteristics of the superconducting magnetic bearing, using high-Tc superconductor as a stator and a permanent magnet for a rotor, in axial direction were measured.

- (1) Dynamic stiffness and damping coefficient of SMB were dependent on an axial gap.
- (2) SMB had a damping factor that had never been observed on PMB.
- (3) Damping coefficients of SMB increased as the resonant frequency increased. These values were smaller at least by one order of magnitude than that of the active magnetic bearing.

It is very significant for bearing design to clarify the dynamic stiffness and damping coefficient of SMB. Accordingly the test equipment will be more improved to measure those factors exactly.

ACKNOWLEDGMENTS

The authors wish to thank Dr.K.Sawano and Mr.K.Miyamoto of Nippon Steel Corporation for supplying bulk $\text{YBa}_2\text{Cu}_3\text{O}_x$ in this test.

REFERENCE

1. F.C.Moon and P.-Z.Chang : Appl. Phys. Lett. 56 (4), 397 (1990)
2. F.C.Moon, K.-C.Weng, and P.-Z.Chang : J. Appl. Phys. 66(11) (1989), 5643
3. R.Takahata and T.Yotsuya : IEEE Trans. on magn., 27 (2), 2423 (1991)
4. M.Morita, K.Miyamoto, and K.Sawano et al. : Physica C 172 (1990), 383

Session 6

BEARINGS 2

Chairman - Claude Keckler
NASA Langley Research Center

FEASIBILITY OF MAGNETIC BEARINGS FOR ADVANCED GAS TURBINE ENGINES*

David Hibner, Senior Project Engineer
United Technologies Corporation, Pratt & Whitney
East Hartford, Connecticut 06108

Lewis Rosado, Project Engineer
Wright Laboratory
Wright-Patterson AFB, Ohio 45433

ABSTRACT

The application of active magnetic bearings to advanced gas turbine engines will provide a product with major improvements compared to current oil lubricated bearing designs. A re-thinking of the engine rotating and static structure design is necessary and will provide the designer with significantly more freedom to meet the demanding goals of improved performance, increased durability, higher reliability, and increased thrust-to-weight ratio via engine weight reduction. The product specific technology necessary for this high speed, high temperature, dynamically complex application has been defined. The resulting benefits from this innovative approach to aircraft engine rotor support and the complementary engine changes and improvements have been assessed.

INTRODUCTION

The aircraft gas turbine engine represents the most challenging application of active magnetic bearings. It is the most technologically advanced, high speed rotating machinery operational in the world today. Compared to all other turbomachinery, the gas turbine engine demonstrates higher levels and larger cyclic variations of stress and temperature primarily because of the stringent requirements for thrust/weight, fuel consumption, reliability, and durability. Rolling element bearings, both ball and roller, have always been used for turbojet and turbofan gas turbine engine main shafts because of their long service life, high load capacity, tolerance to oil contamination, and their survivability to short-term loss of oil. A change from this fundamental and proven technology will only result if significant benefits of a better technology can be demonstrated and if the limits of rolling element bearings are reached.

Studies made by Pratt & Whitney and the U. S. Air Force have shown the feasibility of using main shaft active magnetic bearings as a replacement for oil lubricated rolling element bearings in advanced military aircraft engines. The studies have also shown that significant benefits including weight reduction, improved performance, improved durability, reduced external vibration, and unlimited bearing life are possible. Technology readiness by the turn of the century can be achieved by maturing existing technology. Magnetic bearing technology has advanced significantly in the past 25 years, particularly in recent years with digital controls, higher power density, and more power-efficient designs. Magnetic bearings have been applied successfully to over 100 large ground-based turbomachines such as natural gas compressors, turbo expanders, and gas, steam, and water turbines. This equipment is in operation worldwide and has demonstrated high reliability, improved performance, durability, and unexcelled vibration control with many years and hundreds of thousands of hours of successful operation. Large ground-based turbomachinery, among the 1500+ pieces of rotating equipment with magnetic bearings operating today, are cited because of their similarity to gas turbine engines. While these machines with S2M or MBI magnetic bearings compare well with gas turbine engines in size, weight, power, speed, thrust and radial loads, and general operation, there are major differences in gas turbine engine operating temperatures, dynamic loads, and other factors unique to flight conditions. It is these unique requirements that need to be addressed during the next ten years.

*Magnetic Bearing Feasibility and Development, Wright Laboratory Contract F33615-87-C-2701.

The need for an improved bearing for gas turbine engines has evolved from future fighter aircraft requirements of increased thrust-to-weight ratio over the best engines available today. A 100% increase in this important engine parameter must be achieved while increasing fuel efficiency in order to increase range, improve engine component durability, and reduce life-cycle cost. To achieve these goals, the Air Force has embarked on a major long-range initiative. The Integrated High Performance Turbine Engine Technology (IHPTET) Initiative is aimed at developing the technology necessary to meet future weapon system propulsion requirements. Aggressive propulsion system goals have been jointly established by the Air Force and Pratt & Whitney and have set the focus of the engine component technology initiatives. Conceptual far-term engine designs have been initiated to determine the overall engine cycle flow path geometry and technology features that are needed to satisfy the above goals. These studies have indicated that the resulting rotor speeds will be significantly increased over the current state-of-the-art designs. Consequently, unconventional main shaft support systems, such as magnetic bearings that are able to operate at higher speeds and temperatures, become very desirable. In addition, magnetic bearings have better damping characteristics than squeeze film dampers to control shaft dynamics and reduce engine vibration.

Advanced engine designs which are being studied under the IHPTET Initiative will require advancements in rolling element bearing technology that may not be possible within the required time frame. Rolling element bearings used in current production engines are operating at speeds up to 2.4 million DN (DN = shaft diameter in mm x shaft rpm). With the recent development of a high fracture tough bearing material (M50 NiL), it is now feasible to operate rolling element bearings at speeds up to 3.0 million DN. The advanced engine designs being studied under the IHPTET Initiative will require the bearings to operate well above 3.0 million DN and at temperatures that exceed the bearing material capability (hot hardness) and the liquid lubricant thermal stability. Bearing compartment seal durability will be adversely affected by a high temperature environment, and higher engine speeds will produce higher seal sliding velocities and cause seal wear problems. Blade tip and labyrinth seal designs will have to be improved to control operating clearances. In addition, these engines will require bearings that have superior fatigue life and better damping characteristics. Magnetic bearings have the potential for meeting these requirements since they do not require a liquid lubricant and there is no physical contact between the rotor and the mount structure. Consequently, there is no wear mechanism to limit operational life.

Contained herein are the results of the Air Force sponsored magnetic bearing feasibility program. It includes, in addition to the potential benefits of gas turbine engines with active magnetic bearings, the results of a literature search which was conducted to define the state of the art, a feasibility study wherein advanced magnetic bearings were designed for an advanced military aircraft engine, and a technology requirement assessment which defined the technology necessary to further enhance the application of magnetic bearing rotor support systems for Air Force propulsion needs.

POTENTIAL BENEFITS OF GAS TURBINE ENGINES WITH ACTIVE MAGNETIC BEARINGS

The active magnetic bearing represents an innovative approach to aircraft engine rotor support with the potential to provide significant benefits not possible with rolling element bearings. An engine with a full complement of radial and thrust magnetic bearings combined with electrical accessories would add a new dimension to the design of aircraft gas turbine engines. This magnetic bearing engine would incorporate many electrical components, some of which are necessary because of the elimination of a mechanical power takeoff, i.e., the tower shaft and the accessory gearbox. An integral, main shaft starter/generator and electric fuel pumps for both main and augmentor supplies are required. Other components such as electric vane and nozzle actuators become attractive for this "mostly" electric engine. The successful application of magnetic bearings would result in future engines with the following features:

- Reduced engine weight
- Elimination of oil and hydraulic systems
- Improved fire/safety survivability
- Simplified, less costly bearing compartment seals

- Elimination of the tower shaft
- Elimination of the accessory gearbox
- Higher rotor speed potential
- Reduced blade tip and seal clearances
- Reduced rotor-to-case deflections due to aircraft maneuvers
- Reduced secondary airflow for cooling and thrust balance
- Reduced bearing power consumption
- Superior engine vibration response control
- System health monitoring
- Virtually unlimited bearing life.

These features would reduce the propulsion system fuel consumption and maintenance requirements, and increase thrust-to-weight and reliability, thus providing greater aircraft capability with lower life cycle cost. The improvements in reliability, durability, and vibration control are exemplified by the dramatic change in the engine external components relative to a conventional engine of today, as is shown in Figures 1 and 2. The incorporation of magnetic bearings and other electrical components will produce an engine with significantly less plumbing and mechanical structure which is susceptible to vibration and fatigue failure. The elimination of a majority of the failure-prone hardware alone will provide a greater than 2:1 improvement in reliability. With the anticipated superior vibration control of magnetic bearings, the durability of the remaining structure (e.g., fuel and bleed air lines) will be significantly improved. Improvements in maintainability of the external engine structure are readily apparent primarily because of the resulting simplicity. The remaining components only include the engine and magnetic bearing electronic control system, electric fuel pumps and associated delivery systems, electric actuators, and the air bleed and service systems.

Increased Thrust-to-Weight Ratio

Among the most fundamental means to increase engine specific thrust and, therefore, thrust-to-weight is to increase the speed of the rotating components in the engine. Since the aerodynamic work interactions of the turbomachinery within the engine are proportional to the square of the tip speed of the blading, increased rotational speed has a dramatic effect on the performance of an engine. The stress levels in the blading material also increase with the square of the tip speed, thereby requiring improved materials with increased working stress levels and reduced densities. The current operating speed capability of rolling element bearings used in today's engines could be increased to values of 3.0 million DN if improvements in lubrication technology and the materials used in the elements, races, and cages are realized. While progress in rolling element bearing technology will continue, active magnetic bearing systems have already demonstrated DN values of more than 4.5 million, a significantly higher level. The limitation of operating speed and DN of a magnetic bearing is dependent upon centrifugal stresses generated in the materials used for rotor construction, and does not involve the frictional heating and fatigue limits associated with rolling element bearings. Considering recently demonstrated developments in magnetic bearing technology, step increases in rotor speed and gas turbine engine performance are believed to be achievable within the time frame consistent with IHPTET Initiative goals. Thus, higher speed, longer life turbine engines are achievable with active magnetic bearings.

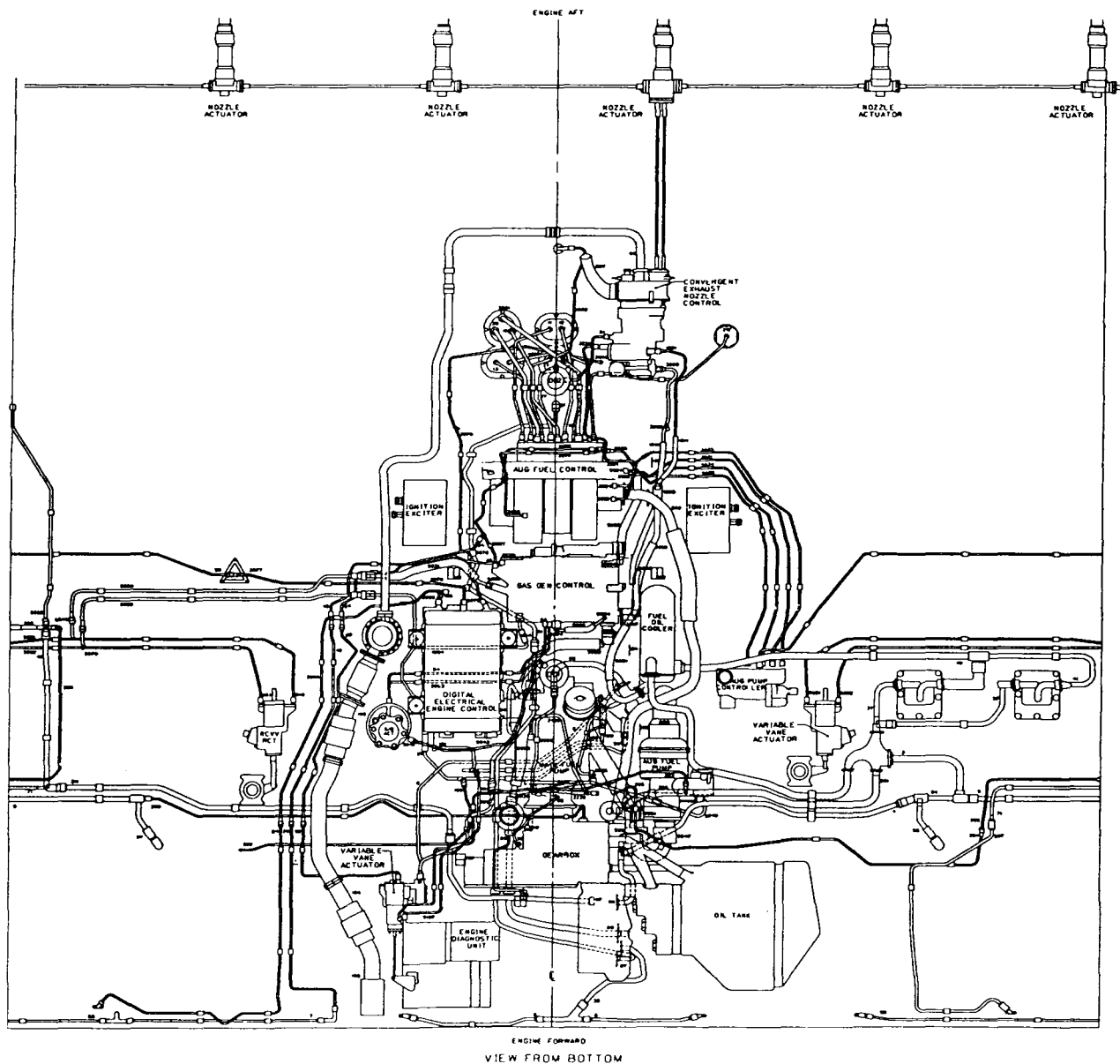


Figure 1. Conventional Engine External Components

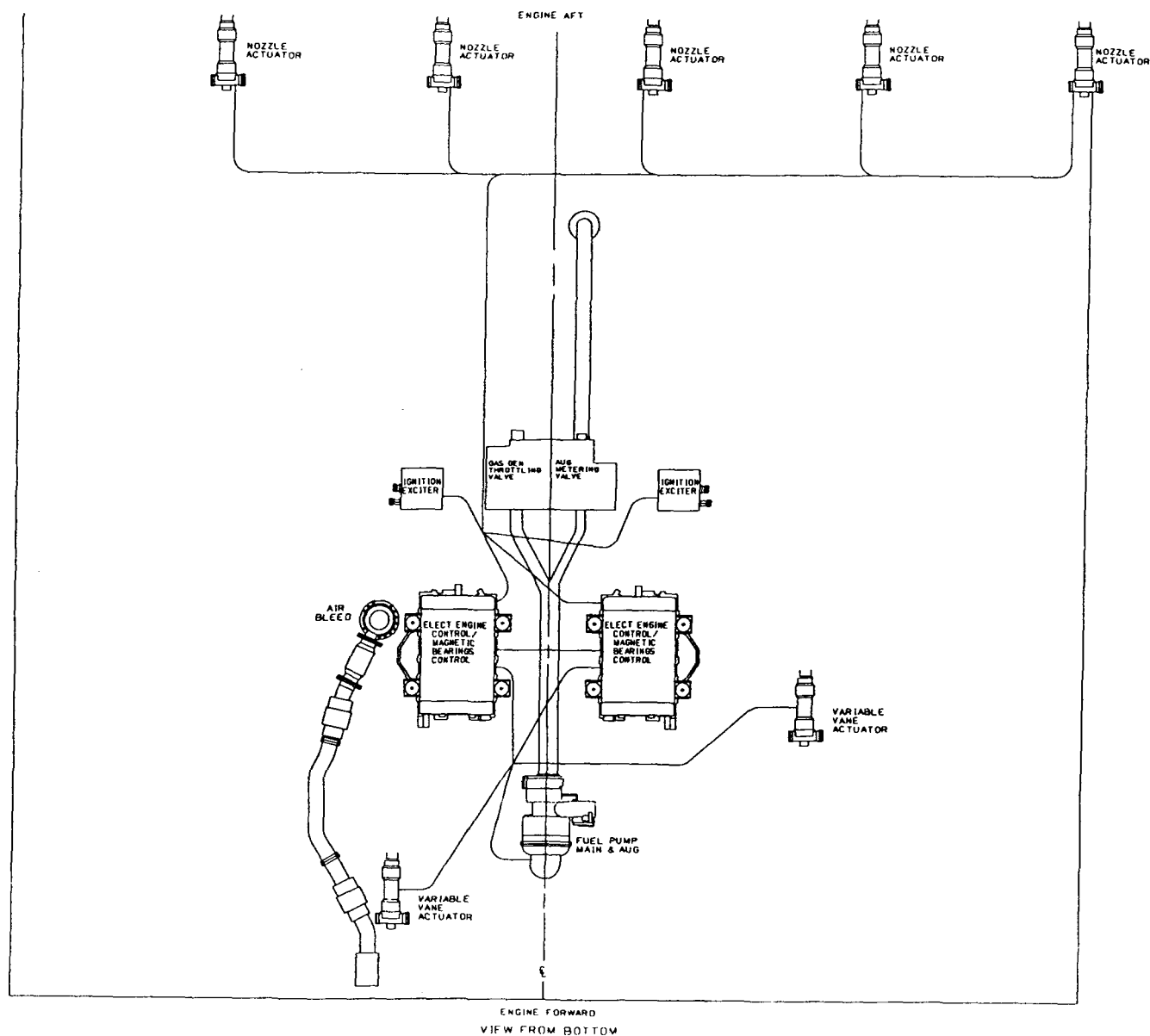


Figure 2. Magnetic Bearing Engine External Components

Design and Aerodynamic Advantages

The higher DN capability of magnetic bearings will increase the allowable bearing-limited speed for a shaft of a given size, or permit larger shafting for a specific operational speed, thus increasing shaft stiffness and providing more design freedom. Since magnetic bearings do not require lubrication, the overall engine design could be quite different. No oil tank, supply or scavenge pumps, oil piping or coolers would be required. Weight savings and additional design freedoms could accrue. Bearing compartment temperature limits related to lubricants could be raised significantly since magnetic bearings can be made to operate in temperature environments exceeding 1000°F if magnetic material and insulation research continue to extend the temperature range of the most promising materials. Further design advantages in the use of magnetic bearings for aircraft gas turbine engines are possible by electronically varying the stiffness and damping of each bearing. The rotor could be made to rotate about the inertial axis rather than the

geometric axis, and thereby reduce the structural vibration caused by rotor imbalance. The axial position of the rotor could also be controlled by the magnetic thrust bearing. With more sophisticated digital controller algorithms, it will be possible to improve performance by closing blade tip and seal clearances in a manner similar to currently employed thermal methods, but more efficiently.

Operational Impact

Magnetic bearings in a high performance turbine engine will provide important operational benefits. The elimination of lubrication oil in an all-magnetic bearing engine has logistic and supply advantages, and eliminates the need for filters and the possibility of contamination. It also eliminates oil servicing and sampling. Bearing life is essentially unlimited, and higher temperature operation is possible. Energy losses associated with the friction and the lubrication systems in rolling or sliding element bearings are eliminated; the electrical power required for magnetic bearing operation is relatively small. Signals for system diagnostics already exist in the electronic control of the magnetic bearing. Both the radial and axial bearing control sensors may be used not only for vibration and position control, but also for monitoring imbalance level. As rotor imbalance increases due to erosion or foreign object damage, the levels can be monitored to prevent set limits from being exceeded. Signals proportional to bearing current can be used as measures of bearing load. Using these data, the net axial thrust load on the rotor can be determined. With magnetic bearings, improvements in engine health monitoring will be possible.

LITERATURE SURVEY OF MAGNETIC BEARING TECHNOLOGY (1988)

A literature survey, which identified and defined the current state of the art relative to design, analysis, manufacture, operability and use of magnetic bearings, focused on bearing load capacity, damping characteristics, electronic control systems, power requirements, and size and weight of both the bearing and the control system. Of prime importance was determining future development trends in digital control technology, high saturation flux magnetic materials, high temperature insulation materials, and high strength rotor lamination materials. The literature survey showed three types of magnetic bearings: passive, active, and hybrid concepts. Passive magnetic bearings employ high-energy permanent magnets configured either for repulsion or attraction. Because of their low load capacity and lack of damping, these bearings were not considered suitable for aircraft engine applications. Active magnetic bearings of the "attractive force" type are the dominant design in most commercial installations. They employ closed-loop analog control systems. Hybrid magnetic bearings use both permanent magnets and electro magnets wherein the permanent magnets generate the static (bias) force and the electro magnets generate the dynamic force. Negative features of hybrid bearings are low stiffness and the need for larger air gaps to control permanent magnet related stabilities. However, because of the lower power consumption requirements, imaginative hybrid design configurations could have the potential to enhance significantly the application of these bearings for aircraft engine applications (Ref. 1). Because the current design philosophy of commercially operating active magnetic bearing systems is dictated by land-based applications, size and weight considerations do not play a primary role. These magnetic bearings and analog control systems are bulky and heavy and are not suitable for aircraft engine applications. The literature survey has, however, revealed that advanced magnetic materials, such as Supremendur, and coil current densities similar to those presently achieved in aircraft electric power generators can be used to design magnetic bearings with significant size and weight reductions necessary for aircraft engine applications. Order of magnitude reductions in control system size and weight are also achievable by replacing the analog controls with digital controls. Miniaturized digital controls with adaptive algorithms, which are necessary for the dynamically complex gas turbine engine, can be developed. These developments in control technology have the potential to provide weight and size reductions of the electric generators, heat exchangers, power amplifiers, and even the magnetic bearing structure. Key development areas, which are critical for the advancement of magnetic bearing technology for aircraft engines, include: magnetic bearing control technology, high saturation flux magnetic materials, high temperature insulation materials, and high strength rotor lamination materials. Major conclusions on each of these areas are discussed below.

Magnetic Bearing Control Technology for Aircraft Gas Turbine Engines

Most magnetic bearing controllers use analog circuits which have inherent size, weight, and versatility disadvantages. Digital controllers, however, have the potential to overcome many of the drawbacks associated with

analog controllers and, therefore, will be more suitable for aircraft engine applications. Significant development effort would, however, be required before a miniaturized digital control system can be produced. The previously uncompetitive weight and size of magnetic bearing systems, compared with rolling element bearing systems, has precluded their application to rotor support in aircraft turbine engines. This literature survey showed that the basic technology now exists for implementing an aircraft magnetic bearing system with weight and size competitive with conventional bearings. Significant reductions in the magnetic bearing design loads result from using a microprocessor implementation of a model follower control strategy having disturbance estimation and eccentricity offset capabilities (Ref. 2). By forcing the rotor geometric center to orbit around its mass center during operation at any speed (including shaft critical speeds) and with a limited degree of imbalance (including blade loss), the magnetic bearing need only be designed to withstand aircraft maneuver loads. These loads are a small fraction of the rotor imbalance loads that must be reacted. The reduced loads made possible by this new control technology would permit significant reductions in weight and size of the magnetic bearings, their control circuitry, power amplifiers, and the generators needed to power them. The application of magnetic bearing systems to support the rotors of aircraft turbine engines should result in more predictable rotor damping, nearly zero dynamic force transmitted to the support structure, elimination of most in-flight shut-downs (IFSDs) caused by high engine vibration, and improved engine reliability (dual channel electronics with no single point failure).

High Saturation Flux Magnetic Materials

Iron-cobalt materials like Vanadium Permendur and Supermendur have immediate applications for significant size and weight reductions in active and hybrid magnetic bearings. Magnetic saturation flux densities of 2.4 teslas appear possible (Refs. 3-5). Thus, with small air gaps (10 mils), large weight reductions appear practical. Optimization design analyses will be necessary to determine achievable weight and size reductions, and development will be necessary to improve heat treatment procedures for optimal magnetic and mechanical properties.

High Temperature Insulation Materials

State-of-the-art high temperature winding insulation materials are ceramics, polyimides, polyesters, silicones and epoxy Novolac. While ceramics have up to 2000°C maximum useful temperature, the other high temperature insulation materials have maximum useful temperatures between 250°C and 315°C. Cracking problems in the ceramic and epoxy encapsulants may be handled using special curing schemes and fillers including glass microspheres. Vacuum pressure impregnation can eliminate cracking problems but provides less mechanical and chemical protection for the windings. Numerous IEEE and ASTM standard test procedures for electric rotating machine insulation may be used to evaluate high temperature insulation systems for active magnetic bearings. When operating requirements are specified, appropriate insulation can be selected and developed to provide the required life for aircraft engine environmental conditions.

High Strength Rotor Lamination Materials

Iron-cobalt-vanadium-nickel and specially heat treated iron-cobalt-vanadium alloys appear to be very attractive high speed rotor lamination materials. Flux densities of 2 teslas at 50 to 100 oersteds and yield strengths of 100,000 psi have been reported (Ref. 6). A commercially available iron-cobalt-vanadium-nickel alloy is Rotelloy, but the properties of Rotelloy are not well documented. Reported values of mechanical and magnetic properties were not referenced to any standard test procedures. Currently available alloys appear to be adequate for high DN rotor applications, but it will be necessary to document the heat treatment procedures and the reported mechanical and magnetic properties.

ENGINE AND MISSION SELECTION FOR THE FEASIBILITY STUDY

Under an Air Force sponsored program, Pratt & Whitney conducted configuration definition and long-range planning studies to define required propulsion system technologies for future weapon systems. The study involved extensive Pratt & Whitney and airframer coordination to meet the IHPTET goals of doubling current propulsion system capability. Representative advanced engine preliminary designs capable of meeting the IHPTET goals, and

realistic missions for these engines were selected. Mechanical component operating conditions were also predicted. A far-term advanced engine, which had been optimized for a Mach 3.0 Interceptor Aircraft, was selected for the magnetic bearing feasibility study. The magnetic bearing system requirements in terms of bearing loads, bearing compartment size, operating temperature, bearing stiffness and damping, and shaft diameter and rotational speeds were predicted. These design requirements were dictated by the selected mission profile. This engine was selected for the magnetic bearing feasibility study because the bearing compartment temperatures and bearing loads were much higher than other engines, thereby dictating an advanced level of magnetic bearing technology to meet these stringent requirements.

The far-term engine conventional bearing design incorporated five main shaft bearings, one of which was an intershaft roller bearing. Because it appears not to be technically feasible to incorporate an intershaft magnetic bearing, a modification to the engine bearing arrangement was made. The bearing was changed from intershaft to a conventional case supported radial bearing. This is the arrangement for which the operating conditions were predicted. Specifically, the bearing damping and stiffness, maximum load, maximum operating temperatures, and bearing compartment constraints were used for the design of magnetic bearings for advanced IHPTET engines.

FEASIBILITY STUDY

The purpose of the feasibility study was to apply the knowledge gained from the literature survey and determine if magnetic bearings could be designed under the conditions and within the constraints imposed by the selected engine and mission. The literature survey provided the current level of technology and offered insight into possible advancements in required technology areas such as digital controls, high temperature winding wire insulation, high strength rotor lamination materials, and high saturation flux magnetic materials. The selected far-term engine (Figure 3), which had the requirement of meeting IHPTET goals, was a particularly challenging target because of very high rotor speed, high bearing compartment operating temperatures, and high rotor thrust. In addition, space was at a premium for both the bearing compartments and the externally mounted digital electronic control. By applying state-of-the-art technology, it was concluded that a practical design which would meet advanced military aircraft engine requirements could not be achieved. Significant modifications including excessive cooling air requirements, the inclusion of thrust balance air, changes to the rotor construction, and the placement of generators on both rotors were necessary. This resulted in a very uncompetitive design compared to rolling element systems. An all-barriers-removed design could meet the advanced engine requirements and could be achieved by developing existing basic technology. Technology programs are essential to develop flight worthy digital controls, reliable auxiliary bearings, high power density starter/generators, high flux density magnetic materials, high temperature position sensors, and durable wire insulation. It is concluded that, with a firm commitment to the technology, the application of active magnetic bearings to military aircraft engines could be demonstrated within a time frame consistent with the objectives of the IHPTET Initiative.

State-of-the-Art Magnetic Bearing Design

The state-of-the-art design of magnetic bearings for the far-term engine was based on the philosophy that the bearings and the integral starter generator could be built using existing technology. It was concluded that the design would not fit into the limited bearing compartment space and environment without compromising performance, weight, and engine configuration. This was based upon limitations in material properties, insulation capabilities, and the analog control systems which are well known today. The integral starter/generator also did not fit into the available space forward of the No. 2 bearing, thereby requiring an additional generator to be placed on the low rotor. The analog controller was also found to be excessively large and heavy. Table I presents a summary of the state-of-the-art magnetic bearing design dimensions. The state-of-the-art bearing dimensions as designed with the full thrust and radial load requirements were considerably beyond the bearing compartment envelopes. A reduction in the thrust bearings capabilities was necessary to fit the envelope and resulted in a compromise in the engine thrust balance system. Full rotor thrust could not be taken by the thrust bearings but needed to be offset by conventional thrust balancing which imposed a performance penalty. Minor modifications were also required in the rotating and static structure to accommodate these large bearings. The saturation flux density level of the materials used in this state-of-the-art design was based on proven technology. Levels of 1.5 teslas to 1.7 teslas were assumed and are considered entirely feasible based on experience at these levels in other electro magnetic equipment.

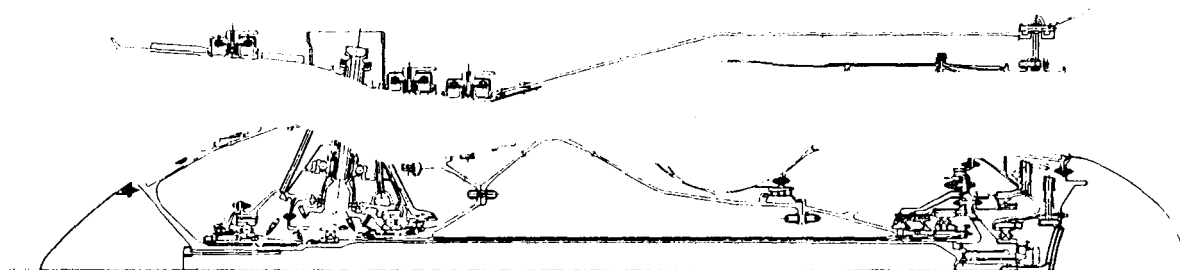


Figure 3. Conventional Bearing Engine Design

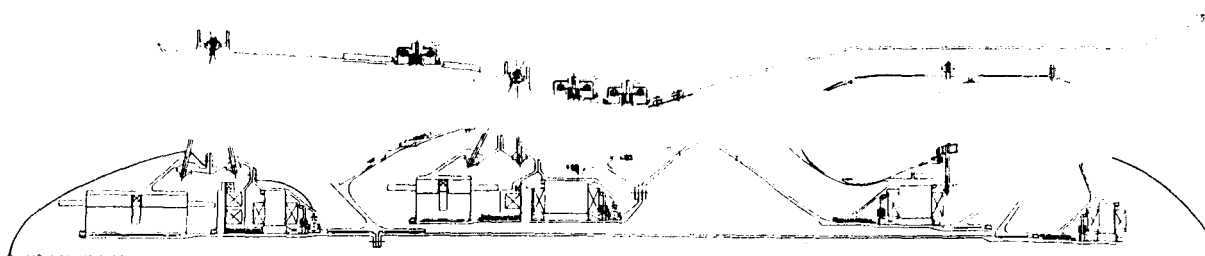


Figure 4. State-of-the-Art Magnetic Bearing Engine Design

TABLE I. STATE-OF-THE-ART AND ALL-BARRIERS-REMOVED DESIGN DIMENSION SUMMARY

| Bearing Number | Available Axial Length (inches) | Available OD (inches) | State-of-the-Art | | All-Barriers-Removed | |
|---------------------------------|---------------------------------|-----------------------|------------------|-------------|----------------------|-------------|
| | | | Length (inches) | OD (inches) | Length (inches) | OD (inches) |
| Radial/thrust No. 1, low rotor | 4.0 | 10.0 | 5.18 | 9.8 | 3.58 | 9.8 |
| Radial No. 4, low rotor | 3.5 | 7.75 | 3.18 | 7.7 | 1.41 | 7.7 |
| Radial/thrust No. 2, high rotor | 3.0 (4.5) | 11.0 (10.0) | 7.26 | 10.4 | 4.66 | 10.4 |
| Radial No. 3, high rotor | 3.5 | 9.5 | 4.25 | 10.1 | 1.95 | 10.1 |

The environmental temperatures in the bearing compartments (860°F, 1450°F) are considered very severe with today's proven insulation technology. While there are published data on ceramic impregnants capable of withstanding these temperatures, their use in this type of application is not proven. To keep the risk to a reasonable level, proven epoxy encapsulants were used in the state-of-the-art design. This required the use of cooling air to keep the bearing compartments under 400°F, a temperature comparable to conventional bearing compartments. Cooling air to accomplish this requires an external cooling system since ambient air can be as high as 640°F during parts of the assumed mission. A 20 mil and 15 mil radial air gap for the thrust and radial bearings, respectively, were used for the state-of-the-art design. Reduction of this gap would allow a size reduction in the bearings but would increase the likelihood of contacting the auxiliary bearings during aircraft maneuvers. With the current proven flux density capability, the 20 mil and 15 mil gaps provided a lower risk design. Nickel plated copper wire was assumed for the state-of-the-art design. This plating prevents oxidation of the copper and has been proven in a 550°F environment.

The analog electronic controller for the state-of-the-art bearing design would see temperatures in excess of 640°F if it were placed on the side of the engine without a means to cool it. An analog controller would require cooling air to create the environment currently seen by engine fuel control systems. A volume estimate of the analog controller and power switching electronics would be approximately 2.5 cubic feet. This 2 to 1 size reduction of current production controllers would be accomplished by high density packaging. However, a system this large would present a severe performance penalty if mounted on the engine within the nacelle. To minimize this performance penalty and that associated with cooling air requirements, it was assumed to be airframe mounted.

The auxiliary bearings, which are necessary for preventing magnetic bearing contact during high but temporary axial and radial loads, were designed to provide limited life during conditions such as surge, high aircraft maneuvers, or hard landings. The clearance between the shaft and the auxiliary bearing was set at one-half the magnetic bearing clearance enabling the auxiliary bearing to support the excessive load without damaging the magnetic bearing. Under conditions of prolonged heavy loading, bearing life would be severely compromised if they were not oil lubricated. The auxiliary bearings designed for the state-of-the-art magnetic bearing engine would have a life measured in minutes. This requires an engine shutdown if loads exceed the magnetic bearing support capability as would be expected during a significant blade failure. The state-of-the-art magnetic bearing engine cross section (Figure 4) shows two types of auxiliary bearings which are considered necessary for intermittent overload and safe shutdown. The sleeve bearings, consisting of dissimilar materials with high lubricity (e.g., carbon and silicon nitride), are designed to contact first and react the momentary high loading. The two solid lubricated ball bearings would provide the thrust and radial support during shutdown after a failure.

With the elimination of the oiling system, the tower shaft and external gearbox were also removed. This results in a cleaner flow path and requires the mechanically driven externals to be electrical. Starting the engine must be accomplished with a high rotor mounted integral starter/generator. Considering the temperature and space constraints imposed by the far-term engine and the selected mission, a single permanent magnet starter/generator could not be designed for the power requirements of the aircraft (250 KVA) using state-of-the-art technology. The alternative was

to place a starter/generator on the high rotor and place a second generator on the low rotor forward of the No. 1 bearing in the nose cone. This also required an additional support structure at the inlet and added significant weight and complexity to the engine.

Design Technology Shortfalls

The application of state-of-the-art magnetic bearing technology to the far-term engine did not provide a practical design that would meet all the requirements of this advanced aircraft engine. Significant modifications to the configuration were necessary and severe performance and weight penalties were anticipated. As a result of the state-of-the-art configuration study, technology shortfalls were identified in the magnetic bearing, the associated controls, the starter/generator, and the auxiliary bearings. Specifically, the shortfalls were a direct result of high environmental temperature, load and power requirements, size and weight constraints, and life requirements. Each of the items is addressed below in order to provide an understanding of the deficiencies and the development necessary to overcome these technology shortfalls.

Magnetic Bearings. The primary problems associated with the magnetic bearing are size, weight and temperature capability. Load capacity was achieved in the state-of-the-art design by increasing the size and, therefore, the weight. Load capacity measured in terms of unit volume or unit weight must be increased significantly for magnetic bearings to become practical. Significant improvements in soft magnetic materials for both the stator and the rotor lamination materials to increase the flux density are essential. The bearing compartment environmental temperature for the state-of-the-art design was assumed to be maintained below 400°F primarily because of the lack of durable, high temperature wire insulation materials. Development in this area is also required and appears to be feasible at temperatures approaching the magnetic material Curie point.

Controller. With state-of-the-art technology, the controller (analog design) is significantly heavy and too large to be mounted within the nacelle. Miniaturized digital control systems with expanded control capability are essential for advanced aircraft engine designs. Integration of this control system with the engine electronic fuel control will offer additional benefits.

Starter/Generator. The space and temperature constraints imposed by the far-term engine required the incorporation of a homopolar generator into the state-of-the-art design. This design would be capable of operating in the engine environment but only half as efficient in size and weight as a permanent magnet design; thus, the engine required an additional generator on the low rotor. The weight and performance penalties associated with this approach were expected to be unacceptable. A high temperature, high efficiency starter/generator must be developed. Advanced materials and insulation capabilities required for the magnetic bearing could also be used in the starter/generator.

Auxiliary Bearings. The state-of-the-art auxiliary bearing limitation was primarily low life. There is a need for a fail-safe backup bearing to allow, in addition to intermittent heavy loading, engine operation during failure of the magnetic bearing system. The goal of sufficient life to enable the pilot to return to base requires extensive development of a solid lubricant bearing capable of operating at temperature levels approaching 1500°F.

All-Barriers-Removed Magnetic Bearing Design

The all-barriers-removed design of magnetic bearings for the far-term engine was based upon the philosophy that the bearings and integral starter/generator could be built within a time frame consistent with the objectives of the IHPTET Initiative by developing basic technology which exists today. It does not, for example, depend upon unexpected breakthroughs such as high temperature super-conductivity or the development of specialized magnetic materials which have Curie temperatures much greater than available today. Development in the areas cited above or in related fields is currently in progress; what is required is the extension or redirection of these efforts toward the specific needs of active magnetic bearings in the gas turbine engine application. Table I presents a summary of the all-barriers-removed magnetic bearing design dimensions.

The all-barriers-removed bearing designs were successfully incorporated into the far-term engine (Figure 5). The forward bearings (Nos. 1 and 2) were designed to operate at the maximum environmental temperature of 860°F and

handle the full radial and thrust load without thrust balance air. The rear bearings (Nos. 3 and 4) were designed to operate at a maximum temperature of 1450°F in order to keep below the Curie temperature of the magnetic materials. Cooling air was required for the No. 3 bearing location where surrounding environmental temperatures exceed 3500°F. The required load capacity of these advanced bearings was achieved by assuming saturation flux densities of 2.4 teslas. Further increases in load capacity were achieved with air gap reductions to 10 mils radial, approximately half the gap of the state-of-the-art design. With advanced, adaptive digital controls, full dynamic control and stability with this small clearance should be achievable.

With the magnetic bearings operating at temperatures of 1450°F, ceramic insulation is necessary. The development of ceramic impregnation and encapsulation techniques need to be developed to guarantee the life requirements of these bearings. At high temperatures, the copper wire would experience a significant increase in electrical resistivity causing increased power consumption due to higher I^2R losses. It is, therefore, desirable to keep the resistivity as low as possible either through the use of high thermal insulation, compact cooling systems, or a change of material (e.g., silver). Silver wire has been assumed for the high temperature bearing locations in the all-barriers-removed design. A miniaturized digital controller was assumed for the all-barriers-removed design. The development of a flight worthy reliable controller one-fifth to one-tenth the size assumed in the state-of-the-art design appears to be technically possible. This is based on experience obtained from engine control system designs. With a volume of 0.5 to 0.25 cubic feet, placement on the engine with cooling schemes used today for the engine digital electronic controller will make the magnetic bearing system very attractive from a weight and performance standpoint. The auxiliary bearings for the all-barriers-removed design, as shown in Figure 5, appear to be essentially the same as the state-of-the-art design. The difference lies in their temperature and life capability. Development in this important area is critical to the success of the active magnetic bearing and the schemes shown are only representative of a concept requiring extensive development. The starter/generator shown on the all-barriers-removed design is a permanent magnet design with the full capability to supply all aircraft required power. This 250 KVA system, which resides in a 640°F environment, would require development but is considered achievable within the IHPTET time frame.

Technology Readiness Development

In order to achieve technology readiness within the IHPTET time frame, development in seven key areas is required.

(1) Digital Controls and Control Algorithms

Commercially available active magnetic bearings employ analog controllers. Since these active magnetic bearings are for ground-based applications with minimal space and weight constraints, the analog controllers have not been optimized and are large and heavy. To meet the requirements of the advanced aircraft engine bearings, the controller must be engine mountable, compact, lightweight, and very reliable in addition to being adaptive and integrable with the associated engine/flight systems. These conditions determine a dictated digital control system design not available as a commercial unit. The payoffs of using digital controllers include size and weight reductions and the benefits of combining digital active magnetic bearing controllers with digital electronic engine controllers. The digital active magnetic bearing controller will lead to improved reliability without increase in size through the incorporation of redundancies in the hardware and software. Digital controllers will make it possible to take advantage of "modern" control methodologies like digital filters for replacing lead compensation networks. Finally, digital controls can employ unusual control algorithms to improve system performance and not be limited to traditional control approaches like proportional-integral-derivative circuits. Considerable development work will be necessary to provide a fault-tolerant, miniaturized military quality digital active magnetic bearing controller capable of surviving the stringent engine load and temperature environment.

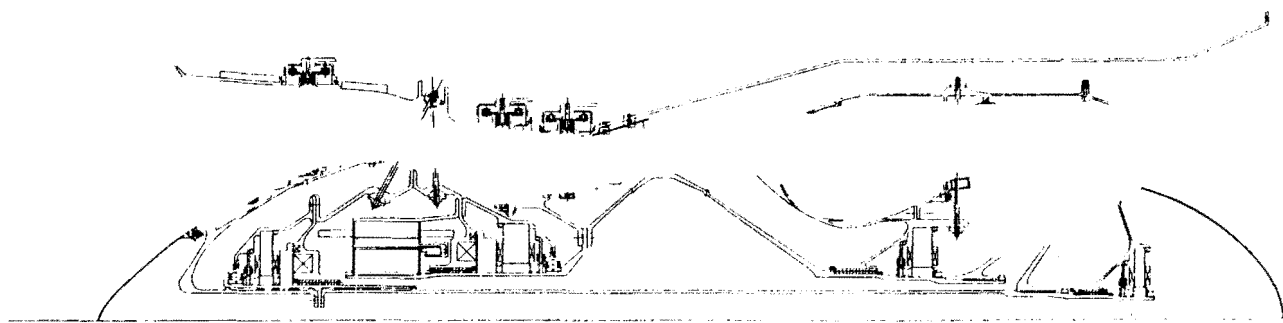


Figure 5. All-Barriers-Removed Magnetic Bearing Engine Design

(2) Magnetic Bearing Power Electronics

The size and weight of present, commercially available electronic power amplifiers for magnetic bearings are unsuitable for use in advanced aircraft engines. To fully utilize the superior capabilities of an active magnetic bearing system as compared to the rolling element bearings, power amplifier package weight and volume must be reduced by at least an order of magnitude. No commercially available power amplifier can presently operate in the 640°F ambient and 20 G vibration environment required for the targeted engine application. Lightweight, high power density, fault tolerant power electronics with sufficient gain and bandwidth to meet the acceleration rates commensurate with high shaft speeds and engine G loads must be developed. It must be engine mounted and be capable of surviving the high load and temperature environment.

(3) High Strength, High Flux Magnetic Materials

Advanced aircraft engines will require bearings to operate above 3.0 million DN and to require minimum space. Active magnetic bearings have the potential to exceed these requirements. Active magnetic bearings for advanced engine applications require magnetic materials with high saturation flux densities to provide the highest performance while occupying minimum space. Additionally, the rotor lamination magnetic materials must have mechanical yield strengths between 30,000 and 70,000 psi for DN values between 3 and 5 million mm-rpm. Therefore, there is a need to develop heat treatment procedures to produce rotor magnetic materials with yield strengths of 70,000 psi and higher and magnetic saturation flux densities of 2.0 teslas and higher. High mechanical strength, high saturation flux magnetic materials (i.e., Vanadium Permendur and Vanadium Permendur/Nickel) must be optimized to maximize these properties and minimize alternating current losses. Heat treatment procedures need to be developed to provide consistent quality material which meets the required specifications.

(4) High Temperature Winding Insulation

Electrical windings for magnetic bearings require impregnation systems for supplementary electrical insulation, mechanical support against vibrations and chemical protection. For engine temperatures (550°F to 1500°F), ceramic impregnation appears to be a promising candidate. High temperature (up to 1500°F) insulation materials for the bearing electrical windings, capable of withstanding a vibratory and changing thermal environment without degrading, are required for magnetic bearing engines.

(5) Improved Rotor Position Sensors

A key magnetic bearing component requiring reexamination is the position sensor used as the feedback element. The concept and the design of the position sensor used in magnetic bearing controls need to be reexamined in the light of the unique requirements for the advanced engines and in light of new understanding on the requirements for magnetic bearing sensors. Present commercially available sensors for magnetic bearings were designed for ground-based applications with minimal space restrictions but with major limitations on cost. For the aircraft engine applications, the size of the sensors needs to be reduced significantly because the radial bearing sensor represents about 20 percent of the bearing/sensor length. Thus, there is a need for sensor size reduction without sacrifices in reliability or accuracy. The proof of the new design concept verification of the sensor designs would also be required under the severe conditions imposed by advanced engine applications. Additionally, the availability of extensive control capabilities through digital controls and adaptive control methodologies calls for a re-thinking of sensor concepts and possibly a replacement of the sensor feedback with electronically synthesized feedback signals. The development of new or improved position or velocity sensors with significant improvements in accuracy and capable of operating in the high speed, high temperature engine environment is necessary. They must be space efficient and potentially capable of measuring relative rotor position at the center of the bearing applied force.

(6) Integral Electric Starter/Generator

This study has produced size, weight, and power requirements for an advanced engine generator. The generator was mounted on the high speed engine rotor with the overall size envelope being 11-inch OD, 4.8-inch ID, and 6-inch length. The power requirements were 247 KVA continuous (including 40 KVA isolated windings for engine functions), 371 KVA 5-minute rating, and a 467 KVA 10-second rating. Additionally, the minimum ambient air temperature for

the subject aircraft was projected to be about 640°F which is quite stringent as compared to currently available generator winding temperature capabilities. Existing aircraft electric power generators utilize a wound rotor design with rotating rectifiers. Because these rectifiers cannot be used in the 640°F environment anticipated for the targeted engine application, and rotor cooling below this temperature is not feasible, new generator technology must be developed. In addition to providing electric power for aircraft services and dual, fully capable isolated windings for engine requirements, the generator will be operated as an electric motor and used to start the engine. If the full potential of active magnetic bearings is to be realized, a main shaft starter/generator must replace the engine tower shaft, gearbox, and associated mechanical drive systems. Improvement on existing high speed motor and generator technology to meet the engine/aircraft needs and to operate reliably in the high temperature engine environment is necessary.

(7) Auxiliary Support Bearings

Advanced fail-safe auxiliary bearing technology has been identified as a critical need. In an aircraft engine configuration wherein the primary support for the main shaft rotor is provided by an active magnetic bearing system, the auxiliary bearings would serve as a fail-safe support mechanism. The unlevitated rotor will be statically supported by the auxiliary bearings. In the event of a power failure in the magnetic bearing control circuit or during excessive bearing loading caused by the accidental loss of a turbine blade or severe aircraft maneuvers, the auxiliary bearings must be capable of withstanding these high loads to prevent contact between the magnetic bearing rotor and stator. The auxiliary bearings, under these high loading conditions, must have sufficient life to enable the pilot to fly the aircraft safely to the nearest airbase. Auxiliary bearings must also be capable of withstanding magnetic bearing overloads for a limited time period in the high temperature bearing compartment. Silicon nitride ball bearings (steel races) have shown promise at very high DN levels but at room temperature. The development of non-liquid lubricated sleeve bearings could significantly reduce the high weight associated with the rolling element bearing design.

PARAMETRIC ANALYSIS

The IHPTET engine designed with all-barriers-removed magnetic bearings formed the basis for studies which ascertained the benefits for an advanced military aircraft engine. Parametric analyses were conducted using state-of-the-art design/analysis tools. The parametric analyses showed that the incorporation of magnetic bearings into a far-term IHPTET military engine could provide a 16% engine weight savings when compared with a current technology IHPTET base type conventional bearing engine. This more-electric engine would be oil free and have an integrated full authority digital electronic control and magnetic bearing control system. This weight savings could provide improvements in aircraft takeoff gross weight (TOGW) and mission range. A 5.6% weight savings was calculated in comparison with a far-term engine with high temperature, liquid lubricated conventional mount rolling element bearings and many of the other projected "electric" engine improvements. This weight savings is considered to be a very high payoff for advanced engine technology for IHPTET.

The incorporation of magnetic bearings into a far-term military engine would provide other major benefits which are known to be positive, but are difficult to quantify. These include reliability, durability, maintainability, vibration control, fire safety, reduced heat rejection, and cost. The improvements in reliability, durability, and vibration control are exemplified by the dramatic change in the engine external components relative to a conventional engine of today. The incorporation of magnetic bearings and other associated more-electric components would produce an engine with significantly less plumbing and mechanical structure which is susceptible to vibration fatigue failure. The elimination of a majority of the failure-prone hardware alone will provide a greater than 2:1 improvement in reliability. With the anticipated superior vibration control of magnetic bearings, the durability of the remaining structure (e.g., fuel and air lines) would be significantly improved. Improvements in maintainability of the engine external structure is readily apparent primarily because of simplicity. Remaining components only include the full electronic control system, electric fuel pump and associated delivery systems, electric actuators, and the air bleed and service systems.

The elimination of oil and hydraulic fluids would greatly improve the fire safety of the aircraft. The total impact of this benefit has not been assessed. Heat generation within the bearing and power section of the control system has also not been assessed in detail, but in comparison with rolling element bearings, reductions of more than 5:1 are expected. This is particularly important for high Mach number aircraft which utilize fuel/oil coolers and air/oil heat

exchangers at the expense of range and fuel burn. The issue of system cost was not addressed in this study, but if the historical trends in changeovers from mechanical to electronic systems are an indication, lower cost is anticipated.

Within the scope of this program, the search for penalties associated with the implementation of magnetic bearings into an advanced military engine did not surface anything significant. A magnetic bearing engine would be dramatically different than today's engines, and before full-scale engine development can be initiated, technology shortfalls must be addressed to achieve technology readiness within the IHPTET time frame. Much of this development represents a maturing of known technology and does not require significant breakthroughs. However, technology development must be pursued to reduce the risk to a level commensurate with the time frame associated with 21st century engine development. The payoff potential of magnetic bearing engines is significant and achievable.

CONCLUSIONS

Active magnetic bearings as replacements for conventional oil lubricated rolling element bearings in advanced military aircraft engines is feasible for 21st century applications. The engine feasibility study described herein provided invaluable insight into active magnetic bearings for advanced military engines. It is concluded that the application is practical and the required technologies could be matured to achieve technology readiness by the turn of the century. Many benefits have been defined and, in particular, have shown that significant weight savings are possible, increased reliability and durability are achievable, and higher levels of overall engine performance could result. The successful application of this concept would result in engines with no lubrication system, higher rotor speeds, reduced blade tip and seal clearances, reduced cooling and thrust balance air, reduced system weight, and enhanced rotor dynamic control. These features would, in turn, enhance propulsion system fuel consumption, thrust-to-weight ratio, maintenance, and reliability, thus providing greater aircraft capability with lower life cycle cost.

ACKNOWLEDGEMENTS

The authors acknowledge the diligent efforts of John Miner, Prem Bansal, Carol Shurick, Allan Carlson, and Paul Wawrzonek of Pratt & Whitney; and Messrs. Howard Moses, Donatus Ohanehi, Frank Pinckney, John Connelly, and David Bourke of MBI.

REFERENCES

1. Meeks, C. and V. Spencer, "Development of a Compact, Light Weight Magnetic Bearing," ASME Paper 90-GT-240, presented at the Gas Turbine and Aeroengine Congress and Exposition, Brussels, Belgium, June 11-14, 1990.
2. Reinig, K. D. and Desrochers, A. A., "Disturbance Accommodating Controllers for Rotating Mechanical Systems," ASME Transactions, *Journal of Dynamic Systems, Measurement, and Control*, Vol. 108, No. 1, March 1986, pp. 24-31.
3. Chen, Chih-Wen, Magnetism and Metallurgy of Soft Magnetic Materials, Dover Publications, Inc., New York, 1986, pp. 390-397.
4. Cullity, B. D., Introduction to Magnetic Materials, Addison-Wesley Publishing Company, Reading, Massachusetts, 1972, "Special Alloys," pp. 525-531.
5. Metals Handbook, Ninth Edition, American Society for Metals, 1980, "Magnetically Soft Materials," pp. 597-614.
6. Major, R. V., Martin, M. C. and Branson, M. W., "The Development of Cobalt-Iron Soft Magnetic Alloys with Improved Mechanical Properties for Use in Electrical Generators," Second Conference on Advances in Magnetic Materials and Their Applications, IEE, September 1-3, 1976, pp. 53-56.

**Low Power Magnetic Bearing Design
For High Speed Rotating Machinery**

**P. E. Allaire, E. H. Maslen,
and R. R. Humphris,
Department of Mechanical and Aerospace Engineering
University of Virginia
Charlottesville, VA 22901**

**C. K. Sortore
Aura Systems, Inc.
El Segundo, CA 90245**

**P. A. Studer
Magnetic Concepts
Silver Springs, MD 20901**

SUMMARY

Magnetic suspension technology has advanced to the point of being able to offer a number of advantages to a variety of applications in the rotating machinery and aerospace fields. One strong advantage of magnetic bearings over conventional bearings is the decrease in power consumption. The use of permanent magnets, along with electromagnets, is one appealing option which can further reduce the power consumption of the bearing.

The design and construction of a set of permanent magnet biased, actively controlled magnetic bearings for a flexible rotor is presented. Both permanent magnets and electromagnets are used in a configuration which effectively provides the necessary fluxes in the appropriate air gaps, while simultaneously keeping the undesirable destabilizing forces to a minimum. The design includes two radial bearings and a thrust bearing.

The theoretical development behind the design is briefly discussed. Experimental performance results for a set of operating prototype bearings is presented. The results include measurements of load capacity, bearing stiffness and damping and the dynamic response of the rotor. With few exceptions, the experimental measurements matched very well with the predicted performance. The power consumption of these bearings was found to be significantly reduced from that for a comparable set of all electromagnetic bearings.

INTRODUCTION

Magnetic bearings have a number of strong advantages. One most obvious advantage is their non-contacting, virtually friction-free characteristics. Entire lubrication systems and the need for mechanical oil seals, which add to friction losses and instabilities associated with cross coupled bearing coefficients, can be eliminated by using these types of bearings. The life expectancy of a magnetic bearing, in many cases, can be much higher than that of a conventional bearing. Due to the non-contacting nature of the bearings, mechanical parts do not wear out. This can obviously increase system reliability and decrease costly repairs and necessary maintenance which interrupt profitable machine operation. If designed properly, a magnetic bearing can perform under much harsher conditions and environments for extended periods of time which would not be possible with other types of bearings. One further advantage of the frictionless characteristic of these bearings is that of power loss. The power consumption of a conventional fluid-film bearing is in many cases much more than for a magnetic bearing. Power loss reductions of one order of magnitude or more can be expected when a machine is converted from using conventional bearings to magnetic bearings.

A variety of work has been accomplished on a number of different applications and aspects of magnetic bearings. An extensive amount of research has been performed by a number of university and industry researchers on the development of magnetic bearings in an industrial canned motor pump [1]. A number of other successful industrial applications of magnetic bearings has been reported by Weise [2]. Burrows et. al. [3] presents the development and application of a magnetic bearing specifically designed for the vibration control of a flexible rotor. Keith, et. al. [4] successfully developed a PC-based digital controller for magnetic bearings. Continuing research is being performed in the areas of digital and adaptive controls for magnetic bearings. In researching the use of permanent magnets in combination with electromagnets, of particular interest are two patents credited to Philip Studer [5, 6]. These patents contain a number of features, primarily dealing with permanent magnets, which have useful application to the bearings discussed in this paper. Wilson and Studer [7] have also applied the permanent magnet bias concept to a linear motion bearing. Ohkami et. al. [8] have performed some interesting comparison studies of magnetic bearings of various configurations which use permanent magnets. Another paper by Tsuchiya et. al. [9] studies and comments on the stability of a high speed rotor which is suspended in magnetic bearings biased with permanent magnets. Meeks [10] has also performed a comparison of the various magnetic bearing design approaches and concludes that the combining of actively controlled electromagnets with permanent magnets results in a superior magnetic bearing in terms of size, weight and power consumption. The rare earth permanent magnets of today, in particular Sm-Co and Nd-Fe-B magnets, offer very high performance characteristics in terms of magnetic strength, energy product and thermal qualities. The magnet designer is able to concentrate a very large amount of magnetic energy in a small package, making more efficient use of available space.

The design concept for the permanent magnet biased magnetic bearing design discussed in this paper is a variation on research and development reported by Studer [5, 6]. The following two sections give a brief description of how the bearings conceptually operate.

Radial Magnetic Bearing Description

A diagram of a permanent magnet biased radial magnetic bearing is shown in Figure 1. This bearing is designed to operate at one end of the rotor and control radial forces only. Four axially magnetized arc segment magnets are positioned circumferentially adjacent to the stator. The bias flux generated by the permanent magnets passes down the laminated stator pole leg, through the working air gap, axially along the shaft, then returns to the permanent magnet via

a radial bias pole piece. The active control flux generated by the coils also passes down the stator pole leg and through the working air gap. The return path for the active flux is then circumferentially around the stator, as shown in Figure 1. This design requires only four poles and four coils, unlike an all electromagnetic design which generally requires eight. In addition, since the coils for each bearing axis are connected in series, the bearing control system requires only five current amplifier channels, which is half as many as required of the all electromagnetic bearing.

Combination Radial/Thrust Magnetic Bearing Description

A schematic of this bearing design, revealing the various magnetic paths, is shown in Figure 2. This bearing combines control of both radial and thrust forces. The radial portion of the bearing is identical to that which was described in the previous section. The thrust control however, is implemented by a unique magnetic flux configuration. The permanent magnet bias flux passing along the shaft splits equally between the two thrust poles before returning to the permanent magnet. A single active coil produces a magnetic flux, in the shape of a toroid, which symmetrically adds or subtracts to the bias flux in the working air gaps between the thrust disk and thrust poles.

Design Concept

The bearings designed for this project are different from all electromagnetic bearing designs in that they employ both permanent magnets and electromagnets. Permanent magnets generate the bias flux in the working air gaps and electromagnets are used to modulate this flux.

The purpose of establishing a bias flux in the working air gaps is to linearize the governing force equation of the magnetic actuator. The bias flux is a nominal flux density about which the control flux is varied. If a bias flux of zero is used, (only one opposing actuator is operated at a time,) then the force generated by the actuator on the rotor follows a quadratic force law, i.e., the force will be proportional to the square of the flux density in the air gaps. Consequently, the force slew rate will be zero when the rotor is in the nominal balanced position and the transient response will be adversely effected. If, however, the bearing fluxes are modulated about a non-zero bias flux, (with opposing actuators symmetrically perturbed,) it is easily shown that the force becomes linearly related to the control flux. The following section demonstrates this important relation.

Force Relationships

The force generated in an air gap of area A_g and length g by a magnetic actuator can be expressed by the direct relation

$$F = \frac{1}{2\mu_0}(B_g)^2 A_g \quad (1)$$

where B_g is the flux density in the air gap and μ_0 is the permeability of free space. If only a single axis of the bearing is considered, then the net force acting on the shaft will be the difference of the two opposite acting actuator forces. Assuming the areas of the two opposing air gaps are the same, the force acting on the shaft by the magnetic bearing can be expressed as

$$F_{\text{shaft}} = \frac{1}{2\mu_0}(B_{g1}^2 - B_{g2}^2) A_g \quad (2)$$

The flux density in the air gaps is being supplied by two sources, i.e., the permanent magnet and the coil. In order to properly provide differential control, the fluxes in the two gaps are symmetrically perturbed so that the flux in one gap is increased while the flux in the opposite gap is decreased by the same amount. This implies that

$$B_{g1} = B_{pm} + B_c \text{ and } B_{g2} = B_{pm} - B_c \quad (3,4)$$

where B_{pm} is the flux density generated by the permanent magnet and B_c is the flux density generated by the coil. Substituting Eqs. (3, 4) into Eq. (2), expanding and simplifying, the force acting on the shaft can now be expressed as

$$F_{shaft} = \frac{2}{\mu_0} B_{pm} B_c A_g \quad (5)$$

By expressing the equation for the force on the shaft in this form, it is interesting to note that the force is not only proportional to the bias level, B_{pm} , but it is also linearized with respect to the control flux, B_c .

Open Loop Stiffness and Actuator Gain

The force generated by the bearing in the horizontal direction, F_x , can be accurately approximated by the truncated Taylor series expansion in the following way:

$$F_x \approx F_x \Big|_{\substack{x=0 \\ i_c=0}} + \frac{\partial F}{\partial x} \Big|_{\substack{x=0 \\ i_c=0}} x + \frac{\partial F}{\partial i_c} \Big|_{\substack{x=0 \\ i_c=0}} i_c \quad (6)$$

If the magnetic circuit is balanced, then the first term in Eq. (6) is equal to zero and

$$F_x = K_x x + K_i i_c \quad (7)$$

where x represents the rotor displacement and i_c represents the control current in the electromagnetic coil. The parameters K_x and K_i are defined as

$$K_x \equiv \frac{\partial F_x}{\partial x} \Big|_{\substack{x=0 \\ i_c=0}} \text{ and } K_i \equiv \frac{\partial F_x}{\partial i_c} \Big|_{\substack{x=0 \\ i_c=0}} \quad (8,9)$$

The quantity K_x is referred to as the open loop stiffness and represents the change in the horizontal force due to horizontal displacement. The open loop stiffness is always negative which implies that the bearing is unstable in the open loop control configuration. Unlike a actual spring with a positive stiffness, a positive displacement of the rotor toward the magnet will increase the attractive force. The quantity K_i represents the actuator gain of the bearing. It represents changes in the horizontal force due to control current, i_c . Equivalent expressions exist for the components of the vertical force expression. Expressions for the open loop stiffness and the actuator gain are determined by performing the appropriate differentiation of the force expression. These expressions take on the form

$$K_x = -\frac{2\mu_0 L^2 H^2 A_g}{g^3} \quad (10)$$

and

$$K_i = -\frac{\mu_0 L H N A_g}{g^2} \quad (11)$$

where L and H represent the length and demagnetization force, respectively, of the permanent magnet and N is the number of turns in the electromagnetic coil.

Control System Description

The control elements of this system are those components which detect the motion of the shaft, determine the required control force and generate a coil current required by the magnetic bearing to generate this force. The magnetic bearing system consists of four distinct components: the magnetic actuator, the displacement sensors and associated conditioning circuits, the analog PID controller and the power amplifier.

The actual magnetic bearing mainly consists of the electromagnetic coils, iron pole pieces, rotor and permanent magnets. The signal conditioning component consists of the eddy current induction displacement sensors, signal amplification and coordinate transformation circuits. The analog controller primarily consists of three separate components. The components take the form of proportional (P), integral (I) and derivative (D) compensation networks. These three parallel stages are added together through a summing amplifier to produce the output of the analog controller. The last component in the control loop is the power amplifier. The amplifier, upon request of the controller, supplies the required current to magnetic coils to produce the necessary fluxes in the bearing.

The dynamics of the bearing-rotor system can be combined with the operating characteristics of the control electronics to form a closed-loop control system. This control system is shown in a simplified block diagram form in Figure 3. The displacement sensor characteristics, analog controller and amplifier make up the relatively complex transfer function of the feedback controller, $G_c(s)$. The feedback controller relates the rotor position to the actuator current. The closed-loop transfer function for this magnetic bearing system, as determined from this block diagram, is given by

$$\frac{X(s)}{F_x(s)} = \frac{1}{ms^2 + K_x + K_i G_c(s)} \quad (12)$$

where m is the mass of the rotor supported by the bearing.

Prototype Bearing Construction

The four-pole radial bearing stators, as shown in the diagrams of Figures 1 and 2, were designed to be identical for both bearings. The stators and rotors were constructed of 3% silicon-iron lamination material which had a thickness of 0.007 inches. Each laminated component consists of approximately 100 laminations. The laminations were glued together using a two part activator/resin adhesive and the shape was machined by wire EDM (electric discharge machining.) The bearing stators have an outside diameter of approximately 3.0 inches and an

axial length of approximately 0.7 inches. The outside diameter of the laminated rotor is approximately 1.5 inches. The thrust bearing components were machined from soft magnet iron. The high energy permanent magnets, made out of a geodymium-Iron-Boron alloy, have a maximum energy product of 30 MG-Oe. The bearings support a shaft weighing approximately 3.7 lbm.

Load Capacity

Measurements of the maximum load applied to the shaft, before falling out of support, are plotted as a function of proportional controller gain, K_p , in Figure 4. The force in this test was applied by hanging weights on the shaft. A pulley system was constructed in such a way that the force could be applied in the desired direction. The force in the plots represents forces applied along the bearing axes.

The variation of the maximum load at lower proportional gains is actually a measure of the stability threshold of the system. It is noted in Eq. (8) that the open loop stiffness, K_x is defined at a nominal operating point, i.e., rotor position and control current equal to zero. However, as the bearing is loaded with a static force, the steady state current begins to increase. It can be shown analytically that K_x is a function of the operating point of the control current. That is, as the control current increases, K_x also increases. Increasing proportional gain has the effect of compensating for this increase in K_x and consequently increasing the stability of the system.

The measurements made at higher proportional gains represent a more accurate measure of the actual load capacity of the bearing. Enough stability is provided so that magnetic saturation is reached in the bearing pole structures. The maximum predicted loads in the plots of Figure 4 are calculated at the point of magnetic saturation.

Equivalent Bearing Stiffness and Damping

Measurements of the equivalent stiffness of the bearings are shown in Figure 5. This simple measurement was performed by applying a constant force, ΔF , and noting the displacement, Δx , of the shaft (controller integrators turned off.) The stiffness then is given simply by $K_{eq} = \Delta F / \Delta x$. A linear regression was performed on the measured data, which resulted in very good correlation, as can be observed in the plots. It is noted that the proportional gain has a direct effect on the stiffness of the bearings, as has been previously demonstrated by Humphris, et. al. [11].

Relative damping in the bearings was investigated from a white noise frequency response analysis of the bearing and rotor. The analysis was performed by injecting noise, composed of all frequencies of interest, into one axis of the turbine-end radial bearing, and performing a FFT (Fast Fourier Transform) analysis on the vibration response of that axis. This linear frequency response, composed of 100 averages, is shown in Figure 6. The derivative controller gain, K_r was varied through a range of values as noted in the plot. As expected, the derivative gain had a direct effect on the damping in the bearings [11]. The first large spike represents the first two modes of shaft vibration. They are very close together in frequency and essentially indistinguishable. The frequency of the second spike is the third mode of vibration and the third small spike at approximately 60,000 cpm is the fourth mode. It is noted that the variation of the derivative gain strongly effects the first two modes, has a small effect on the third mode and virtually no influence on the vibration amplitude of the fourth mode.

Critical Speeds and Rotor Response

The damped synchronous critical speeds of the flexible shaft supported by these bearings can be approximately determined from the white noise frequency response plots of Figure 6. These values, however, represent the zero speed natural frequencies, and the gyroscopic stiffening effects of any attached disks would not be included. Since the natural frequency is given by $\omega_n = \sqrt{k/m}$, where k is the shaft stiffness and m is the modal mass of the rotor, it is of course expected that the observed critical speeds, when the shaft was spinning, would be higher.

Plots showing the vibration magnitude and phase for the shaft speeds that were obtained is included in Figure 7. Amplitude information was taken directly from the magnetic bearing sensors and a key-phase sensor was used to provide the phase information. According to the maximum vibration amplitudes observed in Figure 7, the first vibration mode is observed to occur at approximately 10,000 rpm and the second at approximately 13,000 rpm.

Power Consumption

Finally, a number of power consumption measurements were made. Measurements of the power were taken with a wattmeter for a number of cases. This meter is used with the assumption that the measured voltage and current being supplied to the control electronics is sinusoidal in nature. In addition, it is realized that it represents a somewhat gross measurement as it includes all the inefficiencies of the various electronic components. Table 1 summarizes the results. The non-essential electronic diagnostic components of the bearing system were observed to consume only about 7 watts. These measurements represent a significant improvement over the 500 watts of approximate total power consumed by a comparable current biased all electromagnetic bearing design.

CONCLUSIONS

The brief theory which was presented in this paper established the basic electromagnetic and mechanical relationships necessary to develop a set of permanent magnet biased magnetic bearings. The design involved both radial and thrust bearings. The availability of newer rare-earth high energy permanent magnets made it possible to effectively provide the necessary bias fluxes in the bearing.

The bearings and rotor were successfully constructed and operated. A number of tests and experiments were performed on the bearing-rotor system. The tests consisted of load capacity, stiffness and damping measurements. The results proved to be very positive in that the theoretical predictions and the observed performance matched reasonably well, giving credibility to the models which were used to perform the analysis. Of particular interest for this study was the measured power consumption of the bearings. It clearly demonstrates that the use of permanent magnets can improve the operating efficiency of an active magnetic bearing.

It was successfully observed and demonstrated that these bearings have strong potential for future use as efficient, reliable bearings. However, further research and development is required in the areas of controls, magnetic materials and actuator design before it is possible to install them into a useful industrial application.

REFERENCES

1. Allaire P.; Imlach, J.; McDonald, J.; Humphris, R.; Lewis, D.; Banerjee, B.; Blair, B.; Clayton, J.; Flack, R.: "Design, Construction and Test of Magnetic Bearings in an Industrial Canned Motor Pump," Pump Users Symposium, Texas A & M, Houston, TX, May 1989.
2. Weise, D. A.: "Present Industrial Applications of Active Magnetic Bearings," Presented at the 22nd Intersociety Energy Conversion Engineering Conference, Philadelphia, Pennsylvania, August 1987.
3. Burrows, C. R., Sahinkaya, N.; Traxler, A.; and Schweitzer, G.: "Design and Application of a Magnetic Bearing for Vibration Control and Stabilization of a Flexible Rotor," Proceedings of the First International Magnetic Bearings Symposium, ETH Zurich, Switzerland, June 1988.
4. Keith F. J., Williams, R. D.; Allaire, P. E.; and Schafer, R. M.: "Digital Control of Magnetic Bearings Supporting a Multimass Flexible Rotor," Presented at the Magnetic Suspension Technology Workshop, Hampton, Virginia, February 1988.
5. Studer, P. A.: NASA, Magnetic Bearing, Patent 3865442, Patent Application 100637, February 1975.
6. Studer, P. A.: NASA, Linear Magnetic Bearing, Patent 4387935, Patent Application 214361, December 1980.
7. Wilson, M.; and Studer, P. A.: "Linear Magnetic Bearings," Presented at the International Workshop on Rare Earth—Cobalt Magnets and Their Applications, Roanoke, Virginia, June 1981.
8. Ohkami, Y., Okamoto, O.; Kida, T.; Murakami, C.; Nakajima, A.; Hagihara, S.; and Yabuuchi, K.: "A Comparison Study of Various Types of Magnetic Bearings Utilizing Permanent Magnets," Presented at the International Workshop on Rare Earth—Cobalt Permanent Magnets and Their Applications, Roanoke, Virginia, June 1981.
9. Tsuchiya, K.; Inoue, M.; Nakajima, A.; Ohkami, Y.; and Murakami, C.: "On Stability of Magnetically Suspended Rotor at High Rotational Speed,," Presented at the Aerospace Sciences Meeting, Reno, Nevada, January 1989.
10. Meeks, C.: "Trends in Magnetic Bearing Design," Paper presented at Naval Sea Systems Command Magnetic Bearing Forum, Washington, D. C., July 1989.
11. Humphris, R. R.; Kelm, R. D.; Lewis, D. W.; and Allaire, P. E.: "Effect of Control Algorithms on Magnetic Journal Bearing Properties," *Journal of Engineering for Gas Turbines and Power*, Vol. 108, October 1986.

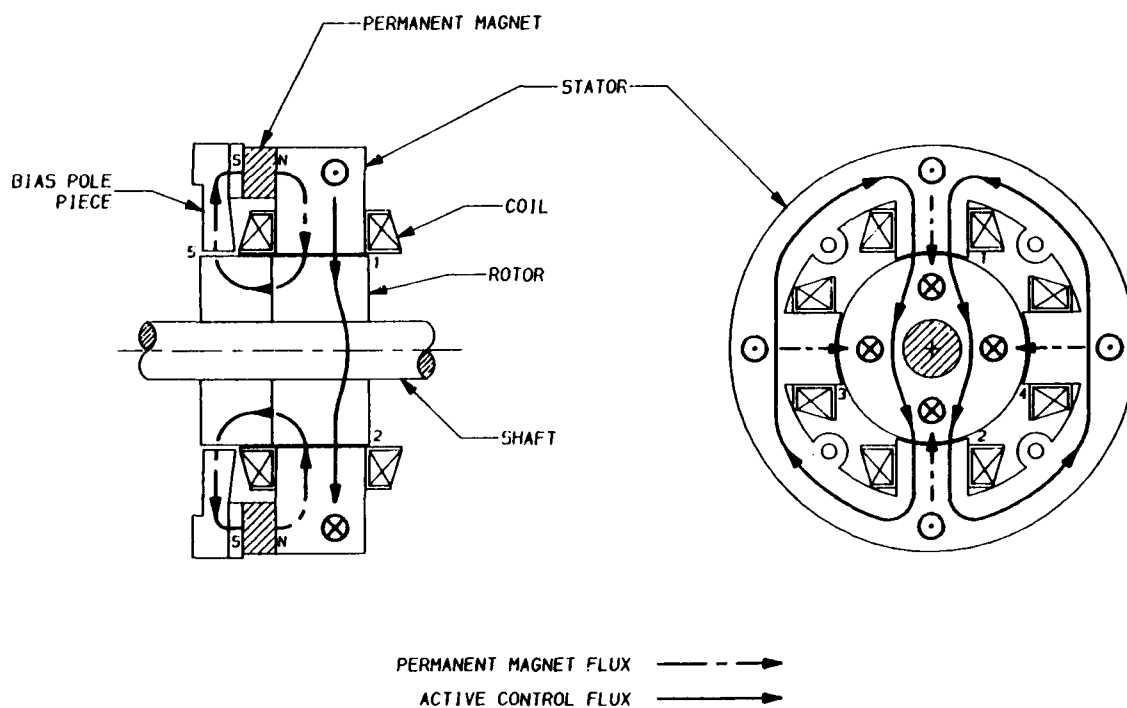


Figure 1 – Permanent Magnet Biased Radial Magnetic Bearing Flux Paths

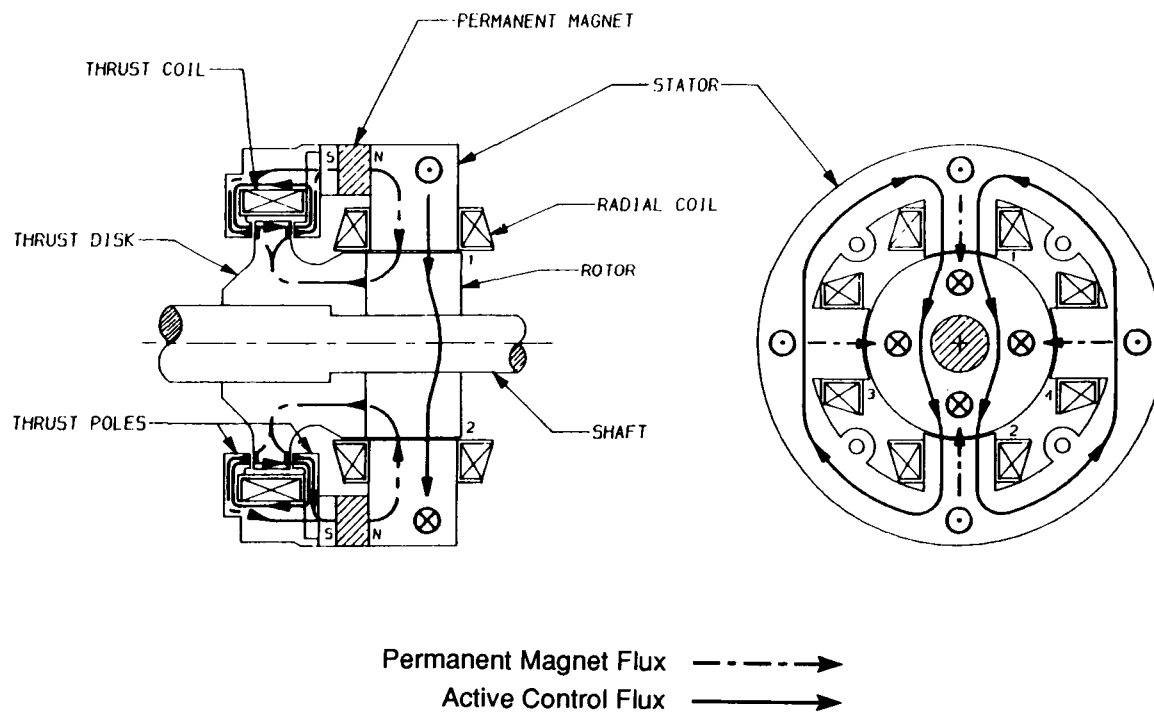


Figure 2 – Permanent Magnet Biased Radial/Thrust Magnetic Bearing Flux Paths

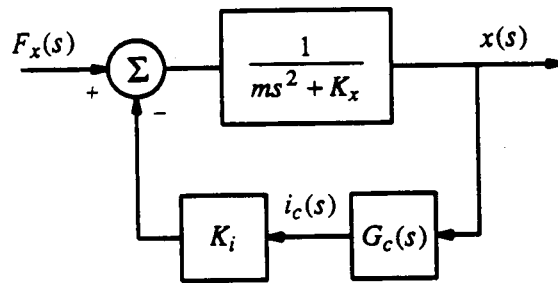


Figure 3 – Closed-Loop Magnetic Bearing Control System

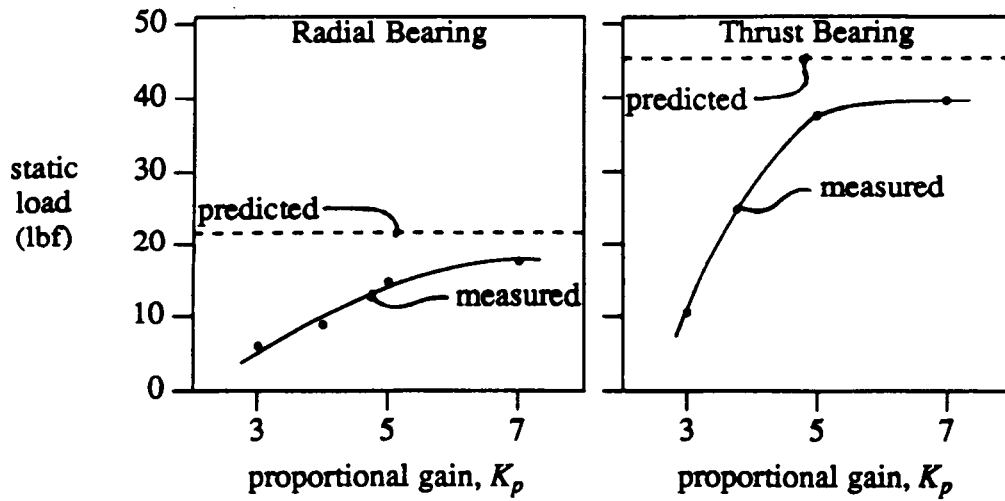


Figure 4 – Maximum Load Capacity

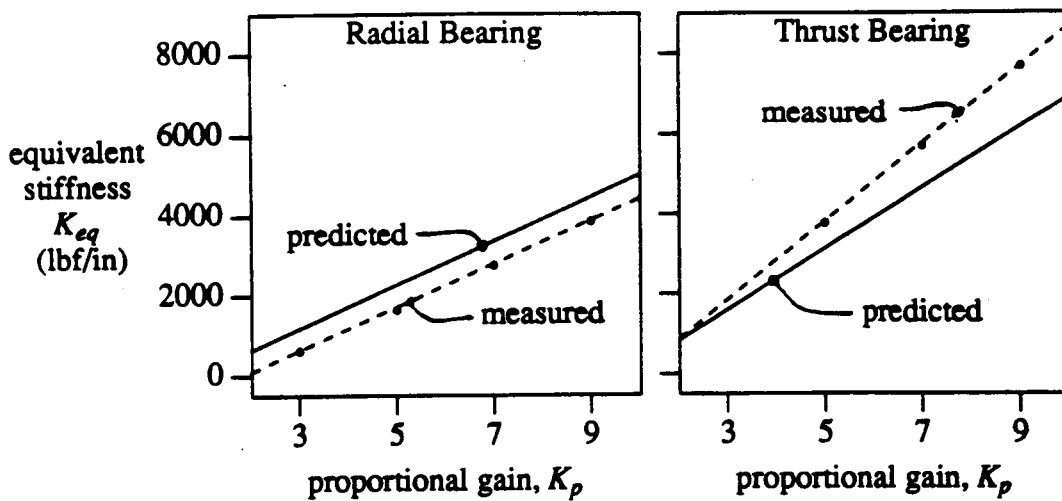


Figure 5 – Equivalent Bearing Stiffness

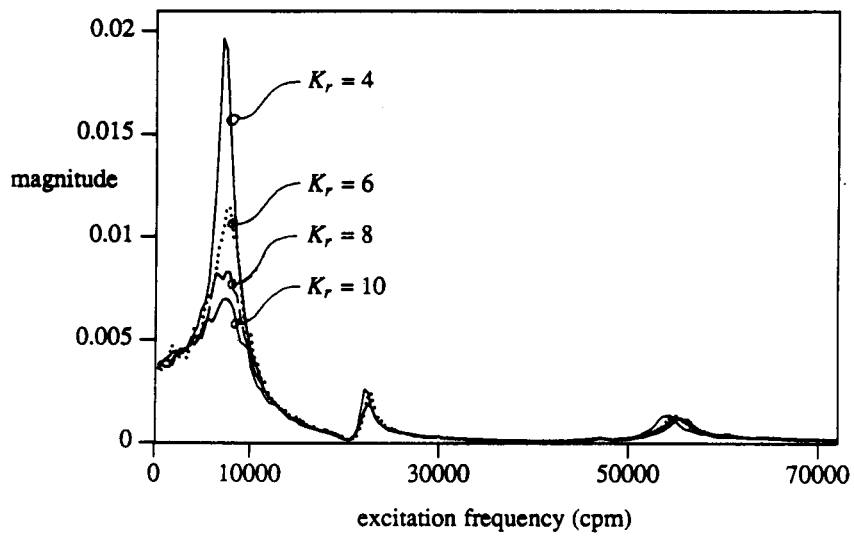


Figure 6 – Measured White Noise Linear Frequency Response

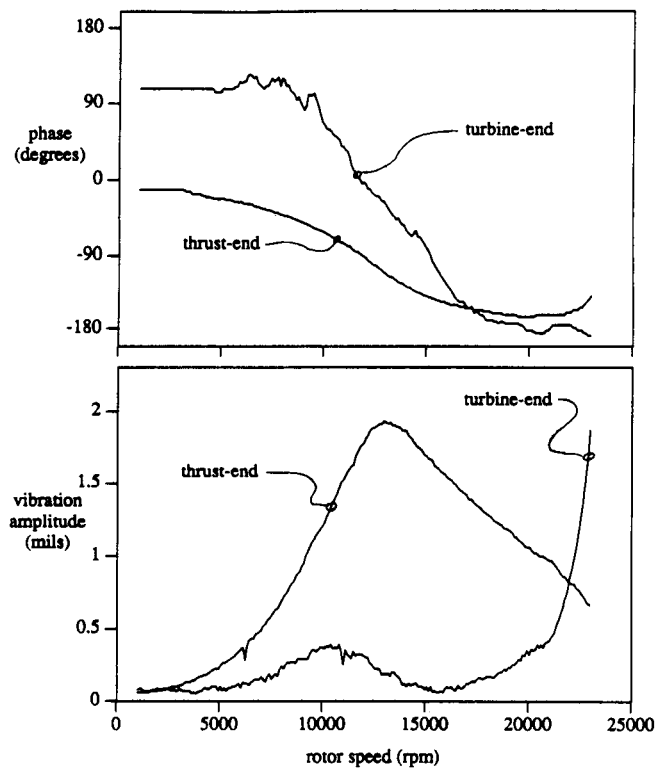


Figure 7 – Rotor Runup Response

**PROGRESS OF MAGNETIC SUSPENSION SYSTEMS
AND MAGNETIC BEARINGS IN THE USSR**

Kuzin A.V.

Moscow Aviation Technological Institute

SUMMARY

This paper traces the development and progress of magnetic suspension systems and magnetic bearings in the USSR. The paper describes magnetic bearings for turbomachines, magnetic suspension systems for vibration isolation, some special measuring devices, wind tunnels and other applications. The design, principles of operation and dynamic characteristics of the systems are presented.

INTRODUCTION

Due to increase of range, speed and operation life of moving objects, gain in accuracy of instruments and machines and growth of rotational speeds of their individual elements, the problem of improving the quality of bearing assemblies and suspensions becomes ever more acute.

Modern bearings should meet the following requirements: they must have capacity for long-duration and stable operation in any environment at low and high speeds, should have moments close to zero, and must consume a small quantity of energy; they should be easily producible and not too expensive. Quite a number of different bearings and suspensions, to one degree or another, satisfy some of the above-mentioned requirements.

These problems find their most exhaustive solution in electromagnetic suspensions (EMS) in which the weight of a suspended body and loads acting on it are counterbalanced by the magnetic field strength.

Free levitation of bodies in an electromagnetic field ensures functioning of suspensions at super-high speeds bringing about extremely small disturbing moments. The service life of EMS is determined mainly by the operation life of electronic equipment whose failure-free performance may last for dozens of years. Absence of contact, wear, noise and vibrations, ability to function in vacuum and corrosive mediums, wide temperature range, and low energy demand offer conditions for provision of high accuracy and operating longevity of instruments and devices incorporating EMS and make EMS ever more perspective.

Theoretical studies in the field of noncontact electromagnetic suspension began (approximately) in 1839 when English scientist Earnshaw proved that a static system of bodies which repel one another or have an attraction for each other, with a force inversely proportional to the square of the distance between them, is unstable (ref. 1).

Exactly one century later (in 1939) Brounbeck corroborated this inference, except that in his opinion stable spatial suspension of bodies in stationary magnetic and electric fields is possible but refers only to bodies having relative magnetic permeability or relative dielectric permittivity less than a unit (ref. 2).

Arkadiev V.K. was the first Russian scientist who demonstrated electromagnetic suspension. He suspended a permanent magnet measuring $4 \times 4 \times 10$ mm and weighing about 1.2 g in the space above the concave surface of a superconductive metallic disk whose diameter was 40 mm and was immersed in a vessel filled with liquid helium (ref. 3). Ponizovsky V.M. (Perm State University) (ref. 4) was one of the first Russian scientists who put into practice magnetic suspension with an external control system. Following American scientist J. Beams (ref. 5) in 1957 he built up an EMS set for suspension of steel balls whose diameters were from 2 to 5 mm. The balls were rotated in a vacuum by means of

a rotating magnetic field with the aim of conducting strength tests of steel balls and various coatings. Ponizovsky V.M. has been engaged in research work in the field of EMS for more than 20 years. One of his essential achievements manifested itself in double magnetic suspension of ferromagnetic rotors which is described in his work (ref. 6) and one version of which is presented on fig. 1. 1,2 - suspended rotors; 3,4 - servo systems of control of currents in solenoid 7 containing movable magnetic core 9 and damper 10, and in solenoid 11 containing core 12; 5,6 - rotors position inductive pickups.

The double magnetic suspension may be used for studying stability of motion of a liquid between two spheres rotating at different angular velocity and for studying stability of fluid film on the surface of a rotating sphere.

During the last two decades the main achievements in the field of magnetic suspension have been connected with creation of new precision measuring instruments of control systems and navigation of moving objects, high-speed turbomachines and electric machines using magnetic bearings, effective vibration isolation systems incorporating EMS and EMS intended for windtunnel studies.

EMS OF GYROSCOPIC INSTRUMENTS

Cardinal improvement of accuracy of gyroscopic devices can be attained through replacement of conventional suspensions by noncontact suspensions.

Many works are devoted to the discovery of stability conditions of a solid body (a gyroscope, rotor in particular) in noncontact suspension. Such interest in this problem is connected with the principal nature of stability of a solid body in noncontact suspension.

Passive noncontact suspensions in which the stability of the equilibrium position of a solid body is ensured by the special choice of parameters of resonant circuits that were studied rather minutely.

In their book (ref. 7) the scientists of the Moscow Technical College (MTC) discuss the questions of theory and application of instrument EMS. They generalize the principles of construction of EMS, analyse main alternative schemes and designs, offer methods of study and the designing of power, dynamic and moment characteristics. Figs. 2 and 3 present designs of two-axle octapole and three-axle magneto resonant suspensions used in gyroscopic instruments of the moment and attitude sensors type, the floated integrating gyroscope type, and the gyroscopic accelerometer type.

Quite a number of works are devoted to analysis of noncontact suspensions incorporating servo systems changing the field of forces of a suspension depending upon position of the body (refs. 8-16).

For twenty years the scientists of the Scientific Research Institute of Applied Mathematics and Cybernetics affiliated with the Gorky State University have been studying and designing nonbearing assemblies for measuring instruments.

Fig. 4 presents a functional diagram of the magnetic suspension which is employed by gyrocompass (refs. 9, 10). In this instrument the sensing element consists of a nonmagnetic rod, the upper part of which accommodates ferromagnetic sphere 1 and the lower part carries hydrochamber 2 with a fast moving rotor, 3 - body position pickup; 4 - controller; and 5 - electromagnet. In the mock-up of this suspension a body whose mass was 1-1.5 kg was suspended, being attached to a ferromagnetic sphere whose mass was 70-120 g.

Fig. 5 presents a functional diagram of the magnetic suspension used in torque magnetometer (ref. 11) in which ferromagnetic sphere 3, whose mass is 20-200 g, and which is tested for anisotropic properties, is suspended in the field of two coaxial electromagnets 1, 2; 4 - body position pickup; and 5 - controller.

Fig. 6 presents a functional diagram of the instrument in which magnetic suspension is used for noncontact suspension of sensing element 1, whose mass is 0.5-1.5 kg, by attaching it to two ferromagnetic spheres 2, 3 in the field of two coaxial electromagnets 4, 5 (ref. 17).

A peculiarity of the regulation processes in electromagnetic suspension devices is the natural instability of the suspended object. Existence of limitations for value of control voltage on windings of electromagnets leads to limited domain of the object's stability in space and to limited range of permissible external disturbances. Domain of states of stability in space is one of the most important characteristics of systems having a naturally unstable object of control which determines optimization for synthesis of control algorithms (ref. 12). In papers (refs. 13-17) the authors synthesize control algorithms for magnetic suspension systems presented on figs. 4, 5, 6 in accordance with the criterion of maximum domain of stability of the object which is suspended in space, make analysis of different systems of control with allowance for non-linearity of characteristics of power amplifier, and discuss rigidity dependences and values of permissible external disturbances induced by system parameters.

Fig. 7 shows a block diagram of a magnetic suspension optimum control system; the diagram is reduced to dimensionless form (ref. 17), where 1 - transfer function of the object being suspended; 2 - electromagnet; 3 - power amplifier; 4 - transfer function of optimum controller; 5 - link of electromagnet x_3 current negative feedback; x_4 displacement of the object; T - ratio of electromagnet time constant to selected scale of time coinciding with the object time constant; and p - differentiation statement.

Stability of a rotor in electromagnetic suspension with allowance for sluggishness of its circuits is analysed in a paper (ref. 18) in which the authors discovered the condition of damping of nutation

oscillations of the rotor. In ref. 19 the author discusses nonlinear resonances occurring with combined radial, axial and angular oscillations at different frequencies, where energy transfer between motions of a gyroscope rotor takes place.

Noncoincidence of the rotor shape of a noncontact gyroscope with a sphere provokes occurrence of moment relative to the centre of the mass of the rotor and therefore induces gyroscope drifts. Calculation of moment of forces applied to an ellipsoidal rotor in electromagnetic suspension is demonstrated in ref. 20. The moment of forces applied to a rotor whose shape differs little from spherical form is calculated in refs. 21-23.

The questions of gyroscope dynamics with noncontact suspensions arranged on a vibrating mounting are discussed in refs. 24-26.

Increase of mass and dimensions of structural elements of magnetic suspensions and application of resilient suspension for attachment of a useful load to the suspended body necessitate consideration of the resilient properties of a structure when designing suspension stabilization systems. Usage of a regulator synthesized without allowance for these properties may lead to diminution of domain of attraction, i.e., a region of absolute stability of the equilibrium state in the phase space of variables of the system which is always limited due to instability of the object of regulation and limitedness of control, and even to loss of stability of the equilibrium state. In ref. 27 the author, assuming that the power characteristics of an electromagnet are linear, synthesizes the control algorithm of the system of stabilization (of magnetic suspension) with allowance for resilient properties of its construction, providing maximum domain of attraction and absolute stability of the equilibrium state. The author discusses a three-mass model of magnetic suspension which takes into account the elasticity of the bearing and suspended body (fig. 8). A characteristic feature of the controller providing maximum domain of attraction and absolute stability in the discussed case when only clearance and current are measured, necessitates introducing additional correction of sensor signals which occurs when second order active filters tuned to the particular frequencies of elastic vibrations of the bearing and suspended body are used.

In ref. 28 the author gives quantitative estimates of permissible application of the simplest magnetic suspension regulator which does not allow for elasticity of mounting in a two-mass model.

The application of gyroscopes to noncontact suspensions is not limited by navigation and control of moving objects. Such gyroscopes are used in delicate physical experiments, in particular, for measurement of the effects of the general theory of relativity onboard a satellite which is free from drift. In this case it is necessary to measure gyroscope drift equal to 7 seconds of arc a year. Such exceptional accuracy requires taking account of extremely small moments acting on the gyroscope. In particular,

when analysing motion of the rotor it is necessary to take into account the oscillations of atoms inside the body of the gyroscope, i.e., to determine the so called heat barrier to gyroscope accuracy. Refs. 29 and 30 are devoted to solving this problem.

Ref. 31 is devoted to determining the principal vector and principal moment of forces acting on a confined superconductive body in a magnetostatic field.

The approximate calculation procedure of the power characteristics for suspension of a cryogenic gyroscope which allows us to obtain final formulae for forces and rigidity of suspension in a case when supporting coils of unspecified form are used, is suggested in ref. 32.

SYSTEMS OF MAGNETIC SUSPENSION IN FINAL-CONTROL DEVICES DESIGNED FOR ORIENTATION OF SPACE VEHICLES (SV)

Nowadays there is widespread application of magnetic suspension, i.e., inertia engine-flywheels allowing stabilization and changes of angular position in space without use of a propulsive mass which is always limited onboard satellites and is replenished with difficulty. Space Vehicles (SV) move in the conditions of space where damping is absent.

The basis of an electromechanical orientation control system consists of rotating the inertia mass-flywheel.

When the engine rotates the flywheel, then, according to the law of conservation of momentum the SV should rotate in the opposite direction at an angular velocity as low as the moment of inertia of the flywheel is in comparison with the moment of inertia of the SV. The main disadvantages of the systems with inertia flywheels are limited operation life and aptitude to enter saturation mode. The first disadvantage is explained by the presence of friction parts in bearings, and the second drawback is referred to maximum permissible rotational speed. These considerations have induced designers of inertia flywheels to give paramount importance to the questions of increasing the operation life and rotational speed accompanied by reduction of energy consumption, mass and dimensions of the system. Since the mass of the flywheel is in reverse relationship to rotational speed, there is a tendency to choose maximum possible speed of rotation.

Operation life of ordinary bearings is a function of the number of revolutions, and as in all phenomena connected with friction, it is characterized by wide scatter of the value of mean-time-between failures and value of moments of friction. Here selection of proper lubrication is of great importance. Usage of liquid or gas lubrication in cosmos conditions requires construction of hermetic casing, the mass of which may constitute a considerable part of the system's total mass.

There is potential for application of magnetic bearings in the gyroscopes and flywheels of space vehicles' attitude control systems. About twenty five years ago a group of specialists with the All-union Scientific Research Institute of Electromechanics (ASRIE, Moscow) under the leadership of academician Sheremetievsky N.N. began research works on an EMS problem for orientation of space vehicles. The result was the creation of an original spherical electromotor-flywheel for the orientation system of orbital station "Salut-5" and powered gyroscopes which are successfully used in the orientation system installed in orbital station "Mir" (refs. 33, 34, 35).

Fig. 9 displays an actuator device of the attitude control system where 1 - a support-free spherical rotor-flywheel of a three-axle electromotor acts as three flywheels simultaneously. The system of electromagnetic suspension incorporating electromagnets 2 through 7 creates an electromagnetic field which solely holds the flywheel in support-free state at the centre of the stator body of three collector-free electromotors: 8, 9, and 10. The spherical flywheel has a number of advantages in comparison with conventional flywheels fitted along three axes: it allows control of angular motion of SV about three axes simultaneously, it is not connected with the body gyroscopically, and it has lesser mass and dimensions.

The main parameters of a spherical electromotor-flywheel (ref. 36) are mass - 230 kg; rotor diameter - 0.64 m; rotation speed - 800 r.p.m.; maximum kinetic moment - 200 Nms; control moment - 3 Nm.

Further development of endeavors in this direction will be creation of an electromagnetic bearing for high-speed powered gyroscopes. Main parameters are mass of gyroscope - 160 kg; rotor diameter - 0.4 m; rotation speed - 10000 r.p.m.; kinetic moment - 1000 Nms; control moment - 200 Nm; and precession angle - unlimited.

The system of automatic protection of EMS has been worked out in the ASRIE and was used for protection of a number of big-size rotor mechanisms with magnetic suspension of the rotor, such as an electro-gas blowing system for gas-cooling nuclear reactor "EG-90/1.25" ($P=1500$ kW, $n=3000$ r.p.m.; $M_r=1500$ kg), turbo-compressor for gas main "GPA-C-16" ($P=16000$ kW, $n=5300$ r.p.m.; $M_r=1200$ kg), diametral fan "DV" ($P=100$ kW, $n=3000$ r.p.m.; $M_r=300$ kg) (ref. 37).

EMS may be successfully used as a ball support of the dynamic stand designed for physical modelling of different flight conditions of SV under space conditions. The dynamic stand is a movable platform which accommodates tested equipment including power units imparting angular motion. Suspension of the dynamic stand platform should provide three rotary degrees of freedom and absence of resistance to angular motion, i.e., real conditions in which a space vehicle operates. Nowadays the dynamic stand platform is suspended mainly with the aid of spherical gasdynamic bearings having significant disturbing moments. Application of an electromagnetic bearing in the dynamic stand allows it to have

disturbing moment which is far smaller than in the case when gasdynamic bearings are used. In the Moscow Aviation Institute specialists from the Electrical Engineering Department have designed and constructed a magnetic bearing for the dynamic stand which at a suspending mass of 1000 kg has adverse friction moment not exceeding 0.3 g.cm at lateral rigidity of 6000 N/m; i.e., its performance satisfies the requirements specified for dynamic stands of SV (refs. 38-40).

MAGNETIC SUSPENSION FOR TURBOMACHINES

Modern level development of engineering puts forward more and more contradictory requirements for bearings of rotor machines, which in a number of cases are practically unrealisable if we use existing rolling-contact bearings and plain bearings. First of all there is a substantial increase in rotational speed and operation in extreme conditions; second, there is a reduction of noise and vibrations, a gain in accuracy of rotation, an increase in operation life, and a decrease of mass dimensions and losses from friction. Magnetic bearings with an external control system are regarded as an alternative to existing rolling-contact bearings and plain bearings. Owing to the absence of mechanical contact there is no necessity for lubrication. The bearings can operate in a vacuum or in corrosive mediums as well as over a wide range of temperatures; there are no friction problems of wear, or noise; these bearings allow development of maximum rotational speeds, and it is worth mentioning that the operation life of magnetic bearings does not depend on rotational speed; it is determined only by the operation life of the control system that may amount to several dozen years. The control system ensures high accuracy of rotation (tenth fractions of micron), high rigidity at static loads (2000 N/ μ m), active damping of oscillations, low requirements to accuracy of balancing and assembly of rotor, easy control of static and dynamic rigidities.

The research works package of the Pskov Branch of the Leningrad Polytechnical Institute scientific group is devoted to creation of magnetic bearings for a high-speed grinding electrospindle (refs. 41-45). Super-high-speed grinding allows us to raise labour productivity, increase operation life of tools and ensure higher quality of the work surface. Fig. 10 displays the block diagram of a designed experimental model of a high-speed electrospindle with active magnetic bearings (AMB). The model was designed on the basis of a production-type grinding electrospindle 3W-120/0.4 (120000 r.p.m.; 0.4 kW) by means of substitution of active magnetic bearings for ball bearings. The driving part of the spindle consists of an induction motor having stator 6 and squirrel-cage rotor 12. Radial AMB consists of trunnion 13 fitted on shaft 1, the core of stator 3 with windings 4 and inductive pickup 5 of radial translations of the trunnion. The stator core is stacked sheets of electrical-sheet steel and has eight poles. Axial AMB consists of two ring electromagnets, 7 and 9, ferromagnetic disk 8 fitted on the shaft, and inductive pickup 10 of axial translations of the rotor. When suspension is switched off, or in emergencies, the rotor rests on emergency bearings 2 and 11 with bronzegraphite inserts. Fig. 11 shows the block diagram of a radial magnetic bearing coordinate Y optimum regulator ensuring minimum integral square error of regulation

in the presence of limitation of the maximum value of the integral square manipulated variable in transient processes in the absence of disturbances. $K_1, K_2, T_1, T_2, T_3, T_4, T_5$ - synthesized parameters of the regulator; I_{iv}, V_{iv} , - variable components of signals; I_{ic}, V_{ic} - direct components of signal; $\beta = I_{2c}/I_{1c}$ (ref. 44).

The production test results of the electrospindle model with AMB in operations of high-speed grinding prove the high efficiency of AMB.

There is potential for AMB application in metal-cutting machine tools where usage of super-speed cutting regimes allows considerable decrease in wear of tools and improves accuracy of the work surface. The results of research work relating to development of the high-speed spindle of a metal-cutting machine tool using magnetic bearings which is carried out in the Experimental Science Research Metal-cutting Machine Tools Institute, Moscow are presented in refs. 46-49.

Today there is an actual problem, i.e., the problem of AMB application in cooling life-support system turbines of flying vehicles where for development of maximum efficiency, rotational speed of the rotor should amount to 150000-180000 r.p.m. Research work relating to this theme was carried out in the Moscow Aviation Institute and the results of the work are presented in refs. 50-53.

MAGNETIC SUSPENSION OF NONCONTACT ELECTRIC MOTORS

Beginning in 1970 a scientific group of the Electric machines department of the Moscow Energetics Institute has been engaged in development and study of magnetic suspension of high-speed rotors of high-frequency electric motors with the aim of increasing their operational life. Such studies were needed because with the increase of rotational speed, operation life of rolling-contact bearings dwindles sharply to several hundred hours. Air-gas-cushion (aerostatic and aerodynamic) bearings are rather difficult to manufacture and, as a rule, for their normal operation they need an air compressor and air purifiers to clean air from moisture and dust. The scientific group suggested a design of magnetic suspension of a high-speed rotor in a rotating magnetic field (ref. 54), which has two functions simultaneously: it provides magnetic suspension forces of the rotor and creates electromagnetic moment of rotation as in an ordinary electric motor.

In accordance with this principle scientists have developed magnetic suspension of a disk-type rotor of a front electric motor (fig. 12) and of a cylindrical rotor of an electric motor (fig. 13) (ref. 55). On fig. 12 two stators (1 and 2) flank two-core disk-type rotors (3 and 4) of the face motor. Its active parts are connected by means of a hollow non-magnetic bush (5) inside which shaft (6) is rigidly secured. The rotor represents a bobbin designed to take up yarn. During starting and/or stoppage the rotor rests on safety bronze rings (7) and safety ball bearings (8) whose outer races do not contact the stator during magnetic stabilization of rotor position. The mass of the rotor is 1 kg. Fig. 13 displays a block

diagram of a combined magnetic suspension of a one-core rotor of a longitudinal axis autoregulation motor: 1, 2 - upper permanent magnets; 3, 4 - lower permanent magnets; 5 - electromagnet; 6 - rotor position inductive pickup; 7 - core of stator with winding; 8 - rotor; and 9 - shaft.

The suggested suspension of the rotor in a rotating magnetic working field with an autoregulation resonance circuit has the following advantages: economical operation, simplicity of design and suspension regulation scheme, absence of complicated control servo systems and special structural assemblies for rotor magnetic suspension. Feasibility of magnetic suspension of a rotor in a working rotating field was experimentally substantiated in 1973.

VIBRATION ISOLATION DEVICES WITH MAGNETIC SUSPENSION

In many cases the EMS may help essentially to solve the problem of vibration isolation of objects exposed to dynamic or kinematic vibrational and impact actions. At present mechanical elastic couplings prevail in vibration isolation engineering. When mechanical couplings are objectionable and therefore are replaced by electromagnetic suspension, in many cases it becomes necessary to provide effective protection of a suspended object against vibrations. High efficiency of EMS vibration isolation devices may be secured through implementation of wide potentialities of formation of desired dynamic suspension characteristics by the selection of proper algorithms to regulate voltages and currents of windings of power electromagnets in accordance with the characteristics of motion of the suspended object and mounting. Not many papers (refs. 56-61) are devoted to studies of EMS vibration isolation properties and to the development of vibration isolation devices incorporating EMS.

In ref. 56 the authors analyse types, characteristics and perspectives of application of magnetic vibration isolators.

In ref. 61 the author discusses vibration isolation properties of EMS devices of different designs. He has established dependences of these properties on parameters and transfer functions of stabilization circuits.

A group of scientists from the Scientific Research Institute of Applied Mathematics and Cybernetics has developed vibration-isolated magnetic suspension of a body with a ferromagnetic disk. Refs. 57-59 contain a description of the design and a functional diagram of the system of automatic regulation of magnetic suspension of a body which is suspended in a magnetic field by means of a ferromagnetic disk attached to it; diameter of the disk is 300 mm and clearance between the disk and electromagnet is 5 mm. Experimenters suspended a body, mass 10 kg, with watt consumption being 100 W. The frequency of body oscillations in the horizontal plane was 0.25-1 herz. Fig. 14 presents a diagrammatic representation of the suspension: A - front view; B - top view; 1 - electromagnets; 2 - first channel

pickup coil; 3 - coils of pickups of the second and third channels; 4 - suspending body; and 5 - conductive disk.

The functional diagram of the suspension control system is shown on fig. 15; it consists of three channels: channel 1 - body vertical stabilization and two identical channels 2, 3 - stabilization of the body according to angle of inclination and stabilization of the body in accordance with displacements in directions going via opposite electromagnets ΘM . Each channel has its own inductive pickup Δ . Signals of pickups Δ are transduced by amplifying-and-converting links $Y\Pi$ into voltages of direct current, the value and polarity of which are determined by values and directions of displacements of the body along corresponding coordinates. To ensure stability channels 2 and 3 are supplemented with forcing links Φ and channel 1 is provided with correcting feedback OC responding to the sum of currents of ΘM . $Y M$ - power amplifiers. T - links time constants; p - differentiation statement.

The suspension, if recommended for application in vibration isolation of instruments when mounting, is exposed to horizontal oscillations.

Present-day main features of gravimetric measurements consist of stringent requirements as to their accuracy. This is attributed to the fact that changes of gravitational force are small and from the pole to the equator they do not exceed 0.5%. The biggest anomalies do not exceed 0.05% of the value of free-fall acceleration. Urgency is attached to the problem of measuring gravitational force on a moving base (ship, aircraft, etc.). The specifics of a moving base assume that measurements are made against the background of inertia interferences, the value of which are considerably higher than variations of free-fall acceleration. One of the main methods of eliminating the influence of inertia interferences is suppression of the interferences by means of vibration isolation devices. On the strength of equivalence of gravitational and inertia forces it is principally impossible to derive a desired signal from gravimeter readings, i.e. to segregate free-fall acceleration from disturbing accelerations. For separation of inertia acceleration and free-fall acceleration scientists exploit their differing characteristics. Accelerations of motion change with relatively high frequency, whereas free-fall acceleration changes slowly. Using this phenomenon we may apply frequency filtering of the disturbances.

Vibration isolation of a ballistic gravimeter using an interferometric method of measurements may be effected by installing an auxiliary corner reflector on the vibration damper which has the capacity for filtering low frequencies.

The Kharkov Scientific Research Metrology Institute, in cooperation with the Moscow Aviation Institute, has developed a vibration isolation device in which, for construction of the vibration damper, the initiators suggested the use of a solenoid magnetic suspension effecting the elastic coupling of the isolated object with the vibrating base and possessing a significant extent of tractive characteristic and

zone of stable equilibrium in the absence of an external system of regulation (ref. 60). Fig. 16 displays a diagram of a ballistic gravimeter, showing 1 - accelerometer; 2 - vibration damper; 3 - regulator; 4 - auxiliary corner reflector; 5 - interferometer; 6 - ballistic unit; 7 - test body; 8 - electromagnetic centering system; 9 - laser; and 10 - photodetector. The accelerometer senses disturbed motion of the isolated object and reacts accordingly; from the accelerometer output the signal, via the filter of upper frequencies, enters the input of the correcting circuit which produces the law of control of feedback force action regulating the position of the movable part of the vibration damper. The regulator is a proportionally-integrally-differential regulator. The regulator incorporates an accelerometer in which elastic coupling of the inertia element with the body is effected with the aid of a magnetic support with a resonant circuit. For damping of motion of the inertia element all mechanical coupling is filled with oil. The accelerometer has small weight and dimensions. The developed vibration damper incorporates a combined system of electromagnetic centering with resonant circuits and additional active electromagnetic damping which ensures horizontal stabilization of the movable part of the vibration damper, having a weight of 200 g and an initial clearance of 0.15 mm at accelerations equal to 0.1 g. Design of the device also allows angular stabilization, the factor which is rather important for interferential methods of measurements. An experimental test of the vibration damper in conjunction with the ballistic gravimeter has shown that the vibration damper eliminates the effect of inertia interferences, thus permitting improvement of accuracy of determination of free-fall acceleration under real test conditions by 2.5-7 times.

SYSTEMS OF MAGNETIC SUSPENSION FOR WIND TUNNELS

Absolute absence of mechanical contacts with the suspended object (test model) allows us to solve the principal problems of aerodynamics which cannot be solved by conventional means: measurement of aerodynamic loads acting on the model without the effect of mechanical supporting devices, wake studies, study of base pressure, etc.; these opportunities stimulate growing interest to EMS engineering (ref. 62).

At present there are two systems of electromagnetic suspension for wind tunnels in the USSR. One was constructed in 1983 as a result of a collaboration between the Moscow Aviation Institute and the Central Aero-Hydrodynamic Institute and was intended for studies of models with six degrees of freedom in a subsonic wind tunnel, the working part of which measured 400 mm \times 600 mm (ref. 63).

The second system was created in the Moscow Aviation Institute in 1989; it is designed for laboratory investigations and for the development of magnetic suspension technology. The suspension has six degrees of freedom and its working part measures 300 mm \times 400 mm. Fig. 17 displays a model suspended in the suspension system of the Moscow Aviation Institute (ref. 64).

Both systems comprise seven electromagnets which are arranged as shown on fig. 18.

The optical system for determination of model position is based on usage of photodiode regions. Rays of light of special form cross the model as shown on fig. 19. Position of the model can be calculated by measuring the position of the model shadow on the surfaces of the detectors. The original design of the sensitive system (ref. 65) ensures determination of vertical and horizontal displacements of the model in one optical channel (fig. 20).

Both systems of electromagnetic suspension have analog control systems. Their design adopted control algorithms which provide maximum domain of stability of the suspended object in the presence of limitations of control actions (refs. 66, 67). Model roll stabilization is effected by passive means.

All electromagnets have copper windings with natural cooling and are provided with bipolar transistorized power sources. In the process of calibration, known values of static forces and moments are applied to the model and position of the model and currents of electromagnets are measured. Aerodynamic loads are computed by means of a digital minicomputer on the basis of established empirical dependences between currents of electromagnets, position of the model and external loads (ref. 68).

The current research efforts are directed at realization of the following technical problems:

1. Tests of models at high angles of attack, dynamic tests;
2. Development of a digital control system;
3. Perfection of means and methods of measurements.

MAGNETICALLY LEVITATED TRAINS

Nowadays there exists an essential problem - to create a new principal means of ground transport, the characteristics of which would be as follows: unlimited speed of movement, high economy index, absence of pollution and a minimum of noise emission. The solution of this problem is connected with high-speed ground transport (HSGT) using magnetic levitation.

Since 1976 the USSR has been addressing the problem of HSGT. Up to 1980 general areas and geographical directions of HSGT introduction were defined. Models of various systems were constructed and tested, such as linear engines and magnetic suspension systems as well as their feeding and control parts, and general normal and alarm breaking power supply systems. Also, there were elaborations of technical assignments for experimental carriages of 40 tons weight and for prototypes with electromagnetic suspension EMS added with one-side linear asynchronous engine OLAE and

with electrodynamic suspension system EDS added with linear synchronous engine LSE. Experimental HSGT-system "HE-01" was created in the city of Novochoerkassk. The system "HE-01" has L-way with permitted loading of 10 tons, air gap is 0.02-0.025 m, EMS, the number of electromagnets is at four each; the lifting force of the electromagnetic system is 29.4 kN; the side force - 14.72 kN.

The prototype for HSGT in Ramenskoye city has a track of 600 metres in length for motion testing. In 1979 the first in the USSR with a carriage of 10 tons weight on constant magnets was tested at a distance of 120 metres.

From 1980 on that prototype and the main parts of new devices of HSGT were tested. In 1985 an experimental carriage of 14 tons weight with EMS was created. In 1986 complex testing began on a prototype route, and a speed of 30 km per hour was reached.

The main technical characteristics of the USSR's HSGT systems which are working out in the USSR are given in table 1 (refs. 69, 70). Here "Soyus-E" is HSGT-train with EMS and OLAE, "Soyus-D" is HSGT-train with EDS and LSE.

CONCLUSION

The presented article reflects the main technical applications and the main directions of development of magnetic suspension systems and magnetic bearings but it does not pretend to completely cover the discussed problem. The analysed advantages of magnetic suspension systems and ever more increasing requirements to bearing assemblies of instruments, mechanisms and machines promote wider and wider introduction of noncontact systems of magnetic suspension.

The author expresses his gratitude to Dr. R. A. Kilgore (NASA Langley) and to the Organizing Committee of ISMST for their support and for giving us the opportunity to present this work to the Symposium.

Table 1.

| Parameters | Parameters' Value for HSGT-systems | | |
|---|------------------------------------|----------|-----------|
| | HE - 01 | Soyus-E | Soyus-D |
| Size, m : - length | 4.12 | 25 | 25 |
| - width | 1.77 | 3.6 | 3.6 |
| - height | 1.48 | 4.2 | 4.2 |
| Number of carriages in train | 1 | up to 10 | up to 10 |
| Carriage mass, tons | 3 | 40 | 40 |
| Maximum speed, km per hour | 50 | 400 | 400 |
| Number of passengers in train armchairs | 2 | 870 | 870 |
| Working period of time in a day, hours | - | 18 | 18 |
| Duration of stand, min | - | 3 | 3 |
| Passenger passing ability in a day, passenger-km | - | 5.48 | 5.48 |
| Acceleration when starting, m. per sq.sec. | - | up to 1 | up to 1.5 |
| Slowing down when braking, m. per sq.sec.: - normal | - | up to 1 | up to 1 |
| - alarm | - | up to 3 | up to 3 |
| Traction power, mW | - | 50 | 50 |

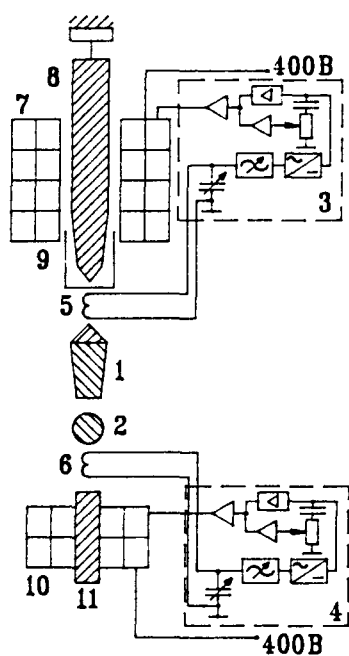


Fig. 1

Double magnetic suspension

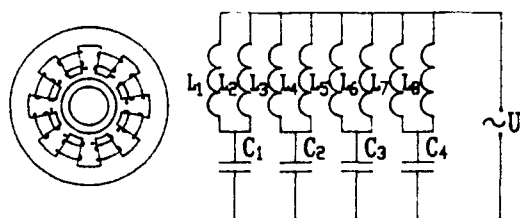


Fig. 2

Two-axle magnetoresonant suspension

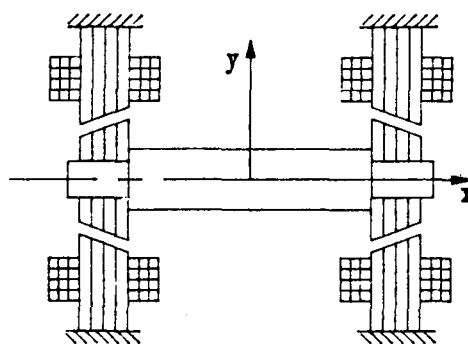


Fig. 3

Three-axle magnetoresonant suspension

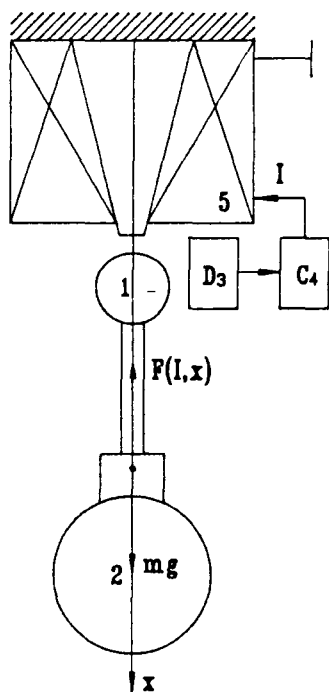


Fig. 4

EMS for gyrocompass

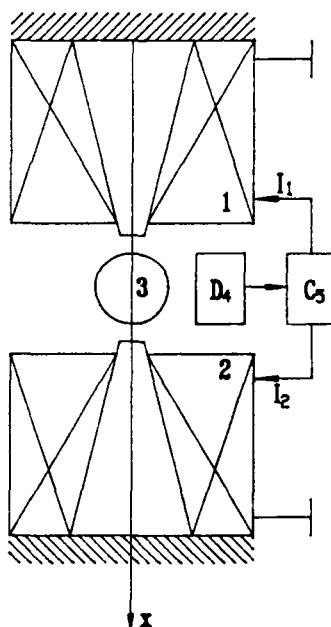


Fig. 5

EMS for torque magnetometer

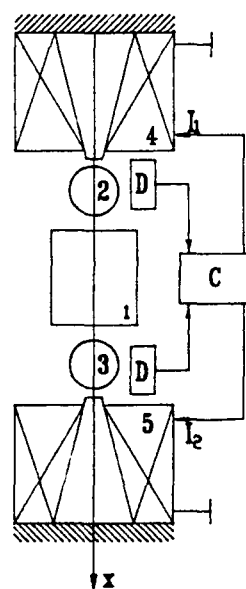


Fig. 6

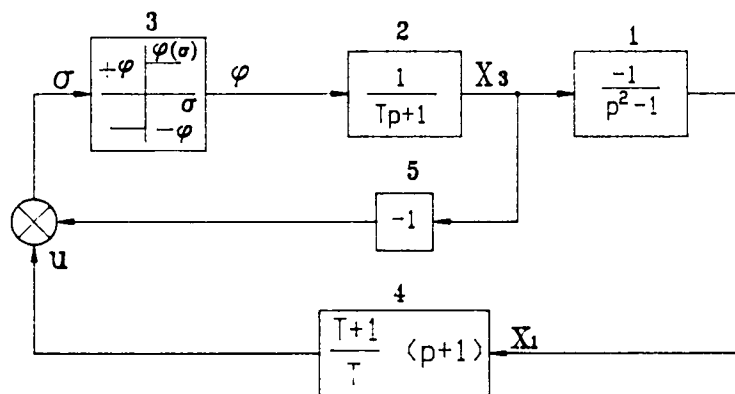


Fig. 7 Block diagram of EMS optimal control system

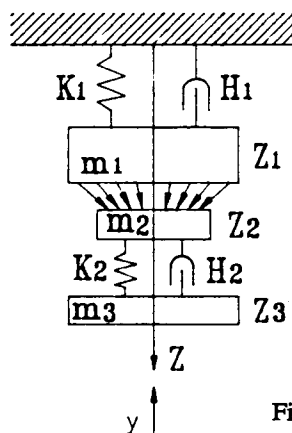


Fig. 8 Three-mass model of EMS

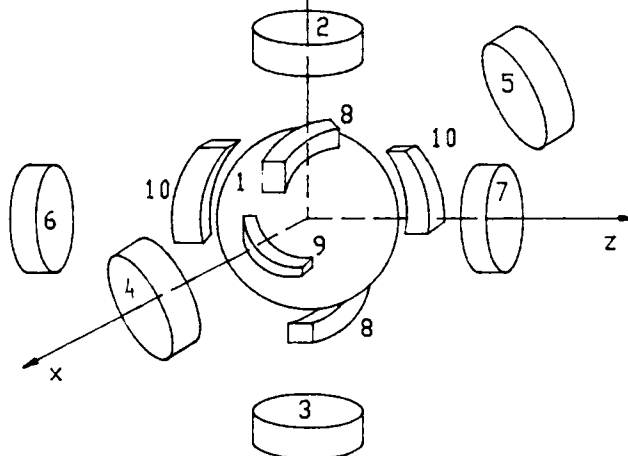


Fig. 9 An actuator device of the attitude control system for orientation of space vehicles

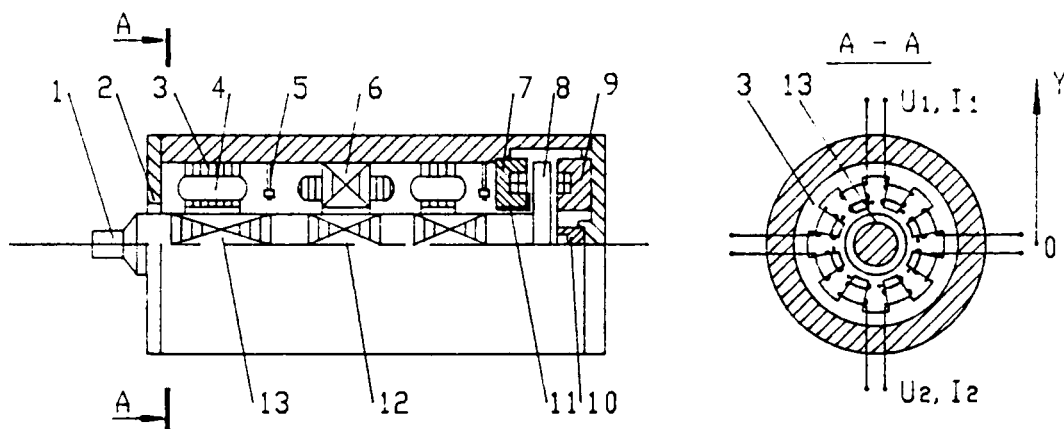


Fig. 10

Block diagram of high-speed electrospindle

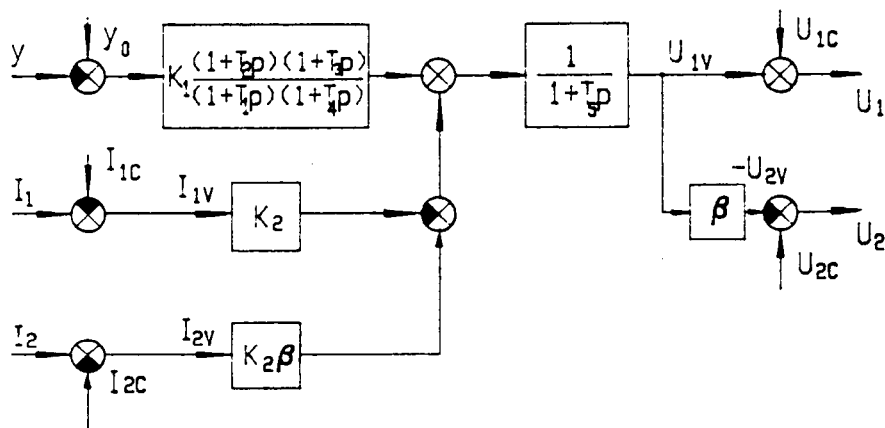


Fig. 11

Block diagram of a radial magnetic bearing coordinate
Y optimum regulator

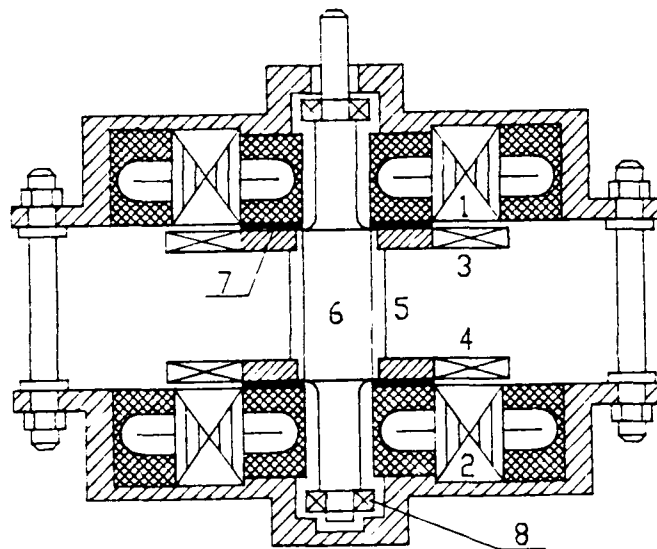


Fig. 12

EMS of disk-type rotor of front electric motor

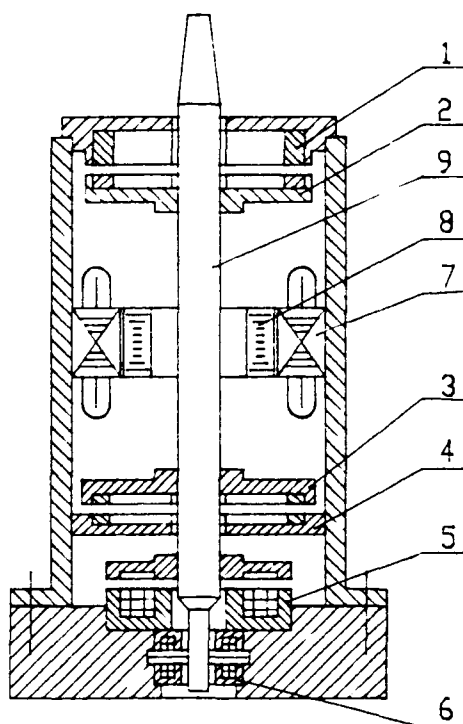


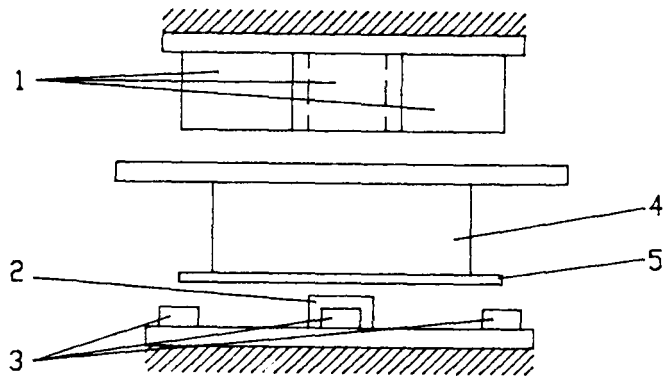
Fig. 13

EMS of cylindrical rotor of electric motor

Fig. 14

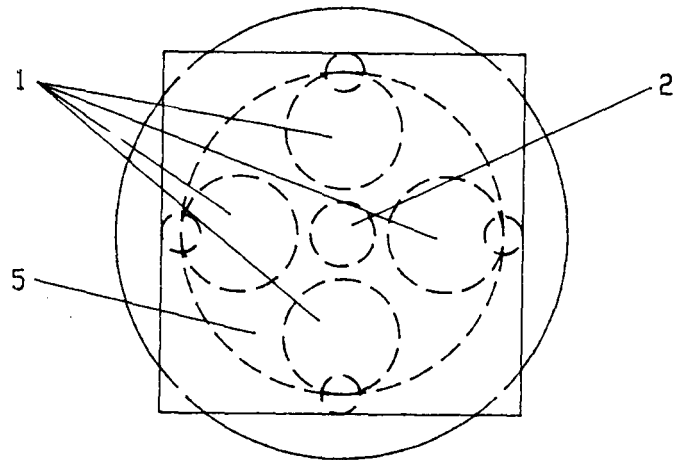
Vibration isolation
EMS of body with
ferromagnetic disk

A) Front view



A)

B) Top view



B)

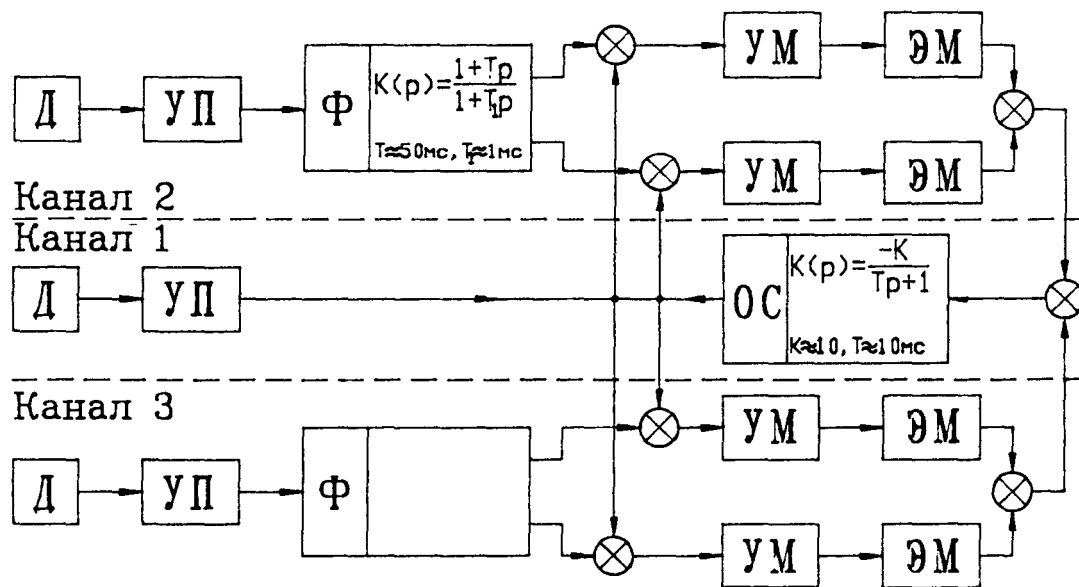


Fig. 15

Functional diagram of the suspension control system

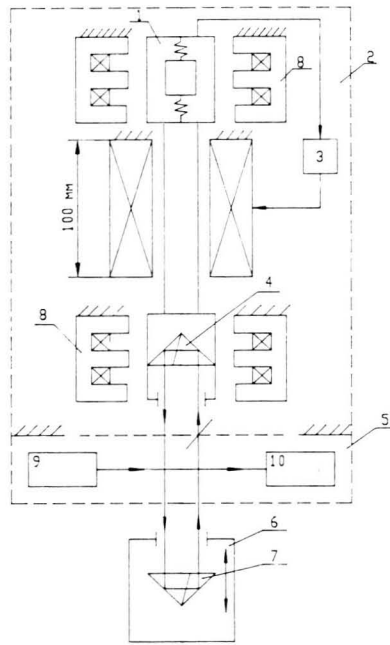


Fig. 16 Vibration isolation of a ballistic gravimeter



Fig. 17 Model suspended in suspension system of the MAI

ORIGINAL PAGE
BLACK AND WHITE PHOTOGRAPH

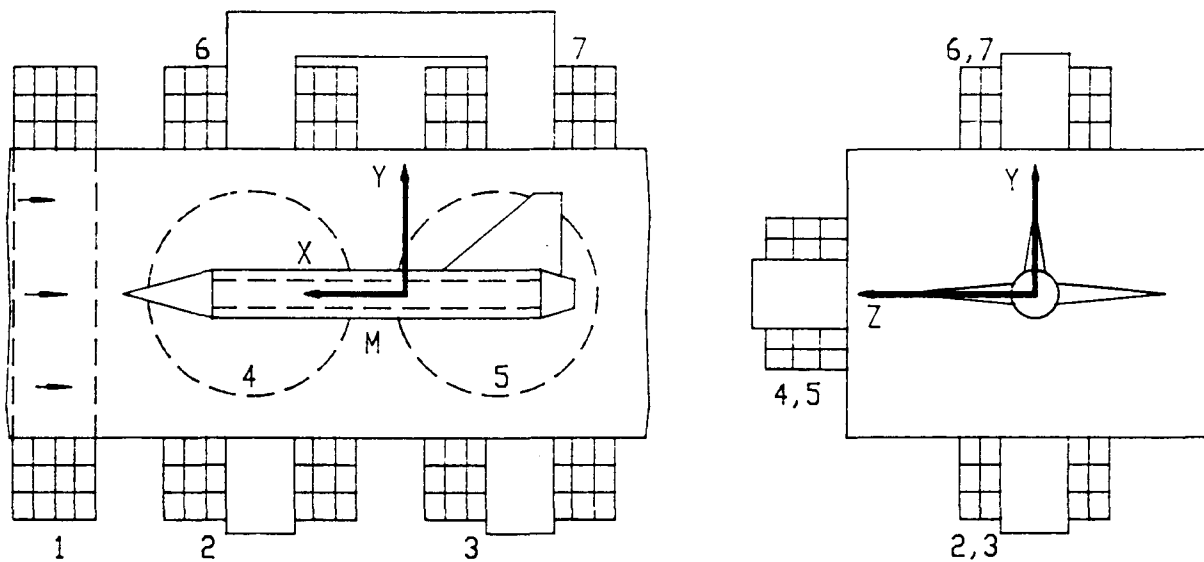


Fig. 18 EMS for wind tunnel

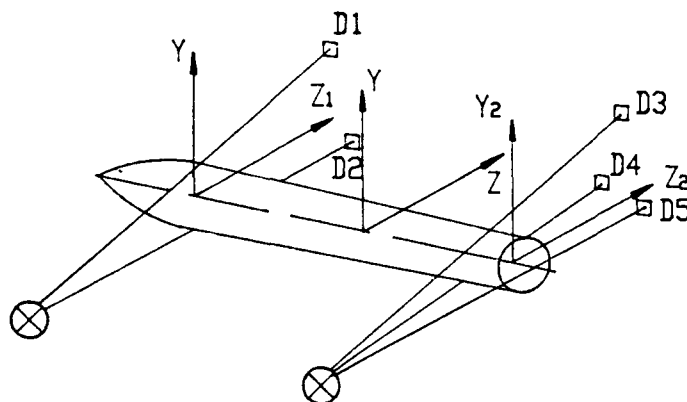


Fig. 19 Position sensing system

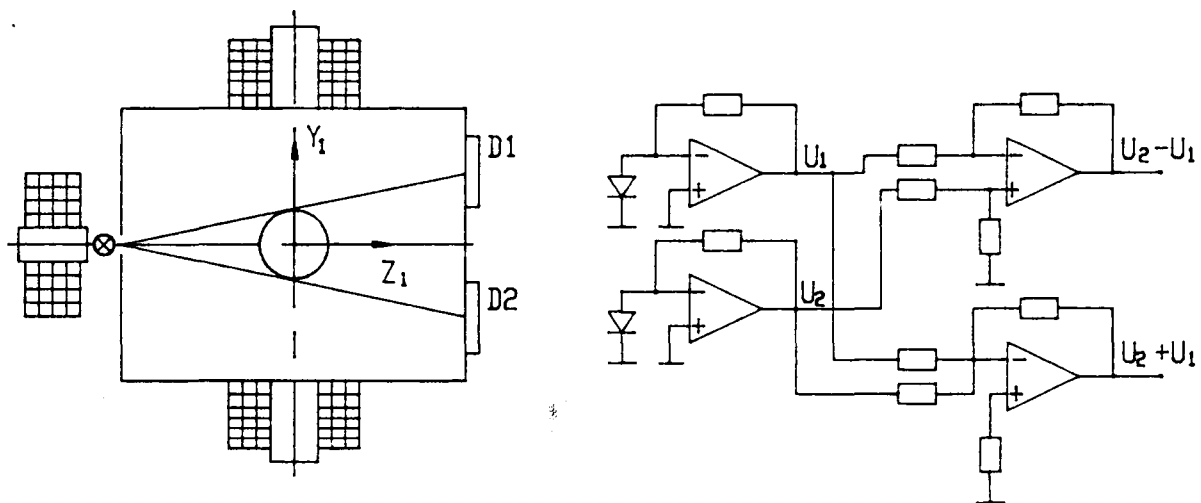


Fig. 20 Signal processing

REFERENCES

1. Earnshaw S. On the Nature of the Molecular Forces - Transactions of Cambridge Philips Society - 1842 - v.7.
2. Brounbeck W. Freischuebende Korperin Electriscen und Magnetischen Feld. - Ztschr. f. Physik. - 1939 - Bd 112 - H.7, 8.
3. Arkadiev V.K. A Floating Magnet. - Nature - 1947 - v.160.
4. Ponizovsky V.M. Induction of Large Centrifugal Fields // - Instruments and Technique of Experiment (ITE). - 1957 - No.7 - pp. 69-72.
5. Beans J.W., Joung J.J., Moore J.W., Journal of Applied Physics - 1946 - v.17.
6. Ponizovsky V.M. Double Magnetic Suspension of Ferromagnetic Rotors // ITE - 1976 - No.1 - pp. 181-183.
7. Osokin Y.A., Gerdy V.N., Maikov K.A., Stankevitch H.H. Theory and Application of Electromagnetic Suspensions - Moscow (M.): Machine Building. 1980 - 288 p.
8. Vyshkov Y.D., Ivanov B.I. Magnetic Bearings in Automatics - M.: Energy - 1978 - 160 p.
9. Voronkov V.S., Pozdeev O.D., Sandalov V.M. On Dynamics of Magnetic Suspension // Transactions of Colleges, Electromechanics - 1974 - No.10 - pp. 1082-1089.
10. Ganiev R.F., Vorobiev V.M., Liuty A.I. Resonance Oscillations of Gyroscopic Systems - Kiev: Scientific Thought - 1979 - 186 p.
11. Denisov G.G., Posdeev O.D., Khimin Y.A. On Rotary Hysteresis in Variable Magnetic Fields // Transactions of Colleges, Physics - 1978 - No.5 - pp. 64-67.
12. Stepaniants G.A., Tararoschenko N.S. On Structure of Laws of Control Providing Absolute Stability of Control Systems with Unstable Object // Reports of Academy of Sciences of the USSR. - 1970 - No.4 - pp. 774-776.
13. Voronkov V.S., Posdeev O.D. Effect of High Frequency Disturbances on Operation of Magnetic Suspension // Transactions of Colleges, Electromechanics - 1979 - No.9 - pp. 945-950.
14. Voronkov V.S., Pozdeev O.D. Optimization of System of Stabilization of Magnetic Suspension // Transactions of Colleges, Instrument Engineering - 1979 - No.9 - pp. 53-57.

15. Voronkov V.S., Pozdeev O.D. Investigation of Systems of Stabilization of Magnetic Bearing // Transactions of USSR Academy of Sciences, Magnetism of Rigid Body (MRB) - 1980 - No.4 - pp. 30-39.
16. Voronkov V.S. Synthesis of System of Stabilization of Magnetic Suspension and Experimental Investigation of its Dynamics // Transactions of Colleges, Instrument Engineering - No.8 - pp. 32-37.
17. Voronkov V.S. Synthesis and Analysis of Systems of Stabilization of Magnetic Suspension: Author's Essay of Dissertation of Candidate of Technical Sciences - M. - 1982.
18. Sorin V.M. Stability of Rotor in Electromagnetic Suspension with Allowance for Sluggishness of its Circuits // Works of Leningrad Polytechnical Institute (LPI) - 1969 - No.307 - pp. 46-53.
19. Sorin V.M. Some Types of Vibrations of Rotor in Electromagnetic Suspension // Works of LPI - 1982 - No.386 - pp. 94-98.
20. Sorin V.M. Moments Acting on Non-spherical Body in Electromagnetic Suspension // Engineering Journal, MRB - 1968 - No.2 - pp. 31-39.
21. Martynenko Y.G. Drifts of Electrostatic Gyroscope Provoked by Non-sphericity of Rotor // Transactions of USSR Academy of Sciences, MRB - 1970 - No.1 - pp. 10-18.
22. Urman Y.M. Moment of Forces Provoked by Rotor Non-sphericity in Cryogenic Suspension // Transactions of Colleges, Instrument Engineering - 1974 - No.11 - pp. 87-92.
23. Urman Y.M. Drifting moments provoked by rotor nonsphericity in suspension having axial symmetric field // Transactions of USSR Academy of Sciences, MIT - 1973 - No.1 - pp. 24-31.
24. Martynenko Y.G., Savchenko T.A. Resonance Motions of Gyroscope with Noncontact Suspension on Vibrating Base // Transactions of USSR Academy of Sciences, MRB - 1977 - No.6 - pp. 16-23.
25. Savchenko T.A. Stability of Motion of Gyroscope with Noncontact Suspension at Angular Vibrations of the Base // Transactions of USSR Academy of Sciences, MRB - 1979 - No.3 - pp. 7-14.
26. Savchenko T.A. Resonance Motions of Gyroscope with Noncontact Suspension in the Presence of Two-component Vibration of the Base // Transactions of USSR Academy of Science, MRB - 1980 - No.6 - pp. 9-16.
27. Voronkov V.S., Pozdeev O.D. Synthesis of System of Stabilization of Magnetic Suspension with Allowance for Elasticity of Elements of its Construction // Transactions of Colleges, Instrument Engineering - 1987 - No.2 - pp. 61-65.

28. Voronkov V.S. Analysis of Dynamics of System of Stabilization of Elastic Base Magnetic Suspension // Transactions of Colleges, Instrument Engineering - 1988 - No.7 - pp. 41-45.
29. Ishlinsky A.Y., Zhuravlev V.F., Klimov D.M. Heat Barrier of Accuracy of Gyroscopes Having Noncontact Suspension // Present-day Problems of Mathematics and Mechanics and Appendices - M.: Moscow Physicotechnical Institute - 1983 - pp. 21-28.
30. Kobrin A.I., Martynenko Y.G. Effects of Heat Oscillations of Crystal Lattice on Accuracy of Gyroscope in Noncontact Suspension // Moscow Energetics Institute (MEI) works. - 1983 - No.14 - pp. 10-15.
31. Ryabov A.B. Determination of Main Vector and Main Moment of Forces Acting on Superconductive Body in Magnetic Field // Transactions of USSR Academy of Sciences, MRB - 1969 - No.6 - pp. 34-37.
32. Zhuravlev V.F., Rudenko V.M. Referring to Analysis of Power Characteristics of Suspension of Cryogenic Gyroscope // Transactions of USSR Academy of Sciences, MRB - 1983 - No.1 - pp. 9-15.
33. Sheremetievsky N.N. Problems of Construction of Flywheel-motor (spherical type) for Control of Position of Space Object // Report to World Electrotechnical Congress - 1977 - p. 15.
34. Veinberg D.M., Vereschagin V.P., Danilov-Nitusov N.N., Sheremetievsky N.N. Systems of Magnetic Suspension in Executive Organs of Control of Orientation of Space Vehicles // Transactions of USSR Academy of Science, MRB - 1981 - No.3 - pp. 152-157.
35. Sheremetievsky N.N., Veinberg D.M., Vereshchagin V.P., Danilov-Nitusov N.N. Powered Gyroscope with Electromagnetic Bearings for the Orientation System of Orbital Stations // Transactions of USSR Academy of Sciences, Space Researches - 1983 - Vol. 21 - No.1 - pp. 10-16.
36. Sheremetievsky N.N. Electromechanics and Peace Cosmos // Electrotechnics - 1987 - No.6 - pp. 10-16.
37. Sheremetievsky N.N. Magnetic Suspension of Rotors of the Electric Machines and Mechanisms // Works of ASRIE - 1989 - Vol. 89.
38. Vyshkov Y.D., Zheltov V.P., Korobkov V.P. Identification of Power Characteristics of Electromagnets of Dynamic Stands // Works of Moscow Aviation Institute - 1974 - No.305 - pp. 74-78.
39. Vyshkov Y.D., Korobkov V.P. Moment of Electromagnetic Friction in Spherical Rotor Magnetic Suspension System. - In book: Automatization of Technological Processes in Different Branches of National Economy - Kuibishev - 1975 - pp. 279-280.

40. Vyshkov Y.D., Ivanov V.I., Korobkov V.P. Investigation of Braking Moments Acting on Spherical Rotor in Electromagnetic Suspension - In book: Present-day Methods and Means of Balancing of Machines and Instruments - Yaroslavl - 1976 - pp. 6-7.
41. Zhuravlev Y.N. Electromagnetic Forces in Conical Radial Thrust Electromagnetic Bearing // Electricity - 1982 - No.11 - pp. 61-63.
42. Zhuravlev Y.N., Vetlitsin A.M., Khmylko N.V. Experimental Investigation of Electromagnetic Bearings for High-speed Rotors // Machines and Tools - 1982 - No.5 - pp. 13-14.
43. Zhuravlev Y.N. Synthesis of Linear Optimum System of Control of Magnetic Suspension of Rigid Rotor // Science of Machines - No.4 - 1987 - pp. 49-56.
44. Zhuravlev Y.N., Khmylko N.V. Dynamic Optimization of Linear System of Control of Active Magnetic Bearing // Transactions of Colleges, Electromechanics - No.12 - 1987 - pp. 74-82.
45. Zhuravlev Y.N. Control of Dynamics of Flexible Rotor in Active Magnetic Bearings // Transactions of Colleges, Instrument Engineering - 1988 - No.6 - pp. 7-12.
46. Averianov O.I., Betin V.N., Eisenshtock G.I. System of Control of Electromagnetic Bearings of Spindle // Machines and Tools - 1985 - No.11 - pp. 19-20.
47. Vasiliev A.V., Betin V.N., Eisenshtock G.I. Electromagnetic Bearings with External Automatic Stabilization // Machines and Tools - 1985 - No.9 - pp. 16-18.
48. Betin V.N., Eisenshtock G.I. Dynamic of Radial Motion Spindle on Magnetic Bearings // Machines and Tools - 1988 - No.5 - pp. 20-22.
49. Vasiliev A.V., Eisenshtock G.I. Calculation of Parameters of Electromagnetic Bearings // Machines and Tools - 1989 - No.2 - pp. 16-19.
50. Shleenkin L.A. Radial Electromagnetic Suspension of High-speed Rotors // Electromechanical. Electromagnetic and Electronic Devices of Systems of Electrical Equipment of Flying Vehicles - M.: Moscow Aviation Institute - 1984 - pp. 44-47.
51. Shleenkin L.A. Synthesis of System of Stabilization of Active Magnetic Bearing - In book: Electronic Devices of Systems of Electrical Equipment of Flying Vehicles - M.: Moscow Aviation Institute - 1985 - pp. 42-46.
52. Bushuev V.A., Kuznetsov V.V., Shleenkin L.A. Radial Magnetic Bearings of Electrospondels - In book: Electric Drive and Automatization in Machine Building - M.: All-union Correspondence-course Machine Building Institute - 1985.

53. Shleenkin L.A. Multichannel System of Stabilization of High-speed Rotor - In book: On-board Converters of Systems of Electrical Equipment of Flying Vehicles - M.: Moscow Aviation Institute - 1986 - pp. 13-18.
54. Sharov V.S., Galkin V.I. Gyromotor with Magnetic Suspension of Ferromagnetic Rotor // Works of MEI - 1974 - No.187 - pp. 128-131.
55. Sharov V.S. Features of Design of Magnetic Suspension of Rotors of High-speed Electromotors - M.: MEI - 1982 - p. 85.
56. Piatin Y.M., Taisov V.N. Magnetic Vibration Isolators. Types, Characteristics and Perspectives of Application // Works of MADI - 1978 - No.139 - pp. 90-92.
57. Vorobjev V.M., Vorobjev-Obukhov A.V., Dmitriev A.Y., Pozdeev O.D. Magnetic Suspension of Body with Ferromagnetic Disk // ITE - 1976 - No.5 - pp. 245-247.
58. Vorobjev V.M., Vorobjev-Obukhov A.V., Pozdeev O.D. Vibration Isolated Electromagnetic Suspension - In book: Vibration Isolation of Man-operator and Vibrations in Machines - M.: Science - 1977 - pp. 57-61.
59. Vorobjev-Obukhov A.V. Investigation of Stability of Magnetic Suspension with Ferromagnetic Disk // Transactions of Colleges, Electromechanics - 1978 - No.12 - pp. 1300-1305.
60. Shurubkin V.D. Investigation and Development of Ballistic Gravimeter Magnetic Suspension Vibration Damper, (the Gravimeter is Designed for Determination of Absolute Values of Free Fall Acceleration on a Movable Base): Author's Essay of Dessertation of Candidate of Technical Sciences - M.: Moscow Aviation Institute - 1981.
61. Vyshkov Y.D. Vibration Isolation Properties of Electromagntic Suspension Devices // Transactions of Colleges, Instrument Engineering - 1985 - No.9 - pp. 49-54.
62. Beliaev L.B., Shirmanov P.M. Magnetic Suspension of Models in Wind Tunnels // Reviews of Central Aero-Hydrodynamic Institute - 1979 - No.557 - p. 58.
63. Vyshkov Y.D., Kovalnogov S.A., Usachov V.N., Shapovalov G.K. Magnetic Suspension and Balance System for Low-speed Wind Tunnel // Scientific Notes of Central Aero-Hyrodynamic Institute - 1986 - No.4 - pp. 94-97.
64. Kuzin A.V. Magnetic Suspension System for Aerodynamic Researches // Instruments and Technique of Experiment - 1990 - No.4 - pp.

65. Kuzin A.V. Photoelectrical Sensors of the Magnetic Suspension Systems // Transactions of Colleges, Instrument Engineering - 1990 - No.4 - pp. 63-67.
66. Kuzin A.V., Vyshkov Y.D. Optimization of Control in Multicomponental System of Electromagnetic Suspension // Transactions of Colleges, Instrument Engineering - 1987 - No.11 - pp. 44-49.
67. Kuzin A.V. Synthesis of the Magnetic Suspension Stabilization System for the Models in Wind Tunnel // Transactions of Colleges, Electromechanics - 1990 - No.5 - pp. 48-57.
68. Vyshkov Y.D., Kuzin A.V., Usachov V.N. Force Measurement Using Electromagnetic Suspension of Boaded Object. Paper presented at the 2nd Conference, Force Measurements. Modern Methods and Means - Novosibirsk - 1986 - pp. 43-44.
69. Bocharov V.I. High-Speed Ground Transport with Linear Drive and Magnetic Suspension // M.: Transport - 1985 - 279 p.
70. Bocharov V.I. Transport with Superconductive Magnets // Rostov-na-Donu: University of Rostov - 1988 - 152 p.

Session 7

SENSORS AND CONTROLS 2

Chairman - Monique Gaffney
SatCon Technology Corporation

N 9 2 - 2 7 7 4 1

EXTENDED H_2 SYNTHESIS
FOR MULTIPLE DEGREE-OF-FREEDOM CONTROLLERS

R. David Hampton
Carl R. Knospe

Center for Innovative Technology
University of Virginia

August 16, 1991

SUMMARY

H_2 synthesis techniques are developed for a general multiple-input-multiple-output (MIMO) system subject to both stochastic and deterministic disturbances. The H_2 synthesis is extended by incorporation of anticipated disturbance power-spectral-density information into the controller-design process, as well as by frequency weightings of generalized coordinates and control inputs. The methodology is applied to a simple single-input-multiple-output (SIMO) problem, analogous to the type of vibration isolation problem anticipated in microgravity research experiments.

INTRODUCTION

The vibration environment onboard current and planned manned orbiters requires isolation for microgravity science experiments. The disturbance frequencies are sufficiently low, and the attenuation requirements sufficiently great, so as to preclude a solely passive isolation system (ref. 1).

Since the disturbances to be attenuated are three-dimensional (ref 2, p.2), the isolation actuator must be capable of acting over six degrees of freedom. The requisite multiple-degree-of-freedom (MDOF) controller is much more difficult to design than a single-degree-of-freedom (SDOF) controller, because the isolation system has many inputs (actuator forces) and outputs (measured displacements and accelerations). Multiple-input-multiple-output (MIMO) designs can be very susceptible to unmodeled cross-coupling between channels of input or output (ref. 3), a problem not encountered in SDOF design. The control forces used must therefore be properly coordinated if the controller's performance is to be sufficiently insensitive to unmodeled dynamics (i.e., *robust*). The design of a robust MIMO control system requires the iterative use of synthesis and analysis tools, the former for controller design and the latter for system performance and stability evaluation (ref. 4).

A particular vibration isolation problem may involve different kinds of undesirable outputs, such as excessive absolute accelerations and unacceptable relative displacements. Some of these undesired outputs may be more important than others, and the degree of undesirability may vary with direction or frequency. For example, rattlespace constraints may be highly directional. Or a crystal-growth experiment may be particularly sensitive to accelerations at certain frequencies (ref. 2, p. 7) or in certain directions. One of the

goals, then, must be to design a controller capable of minimizing selected plant outputs as dictated by these considerations.

Plant outputs, however, cannot be minimized apart from consideration of the associated control costs, because any active control both consumes power and releases heat. Since both of these costs are of concern in a space environment, the control effort used should not be excessive. And at higher frequencies control effort should also be minimized in order to limit controller bandwidth for the sake of robustness concerns (ref. 5, p. 218).

This paper describes a design procedure, known as extended H_2 synthesis (ref. 5, p. 267), for developing active isolation system controllers. A single-input-multiple-output design problem is then addressed using the presented procedure.

BASIC PROBLEM AND SOLUTION

Problem Statement

We will use Linear Quadratic Gaussian (LQG) theory to design the MDOF controller. This theory has been extensively studied and used. LQG is chosen as a synthesis procedure since the quadratic performance index relates well to root-mean-square statistics and power spectral density.

When linearized, the differential equations of motion of the plant can be representable in state-space form by the first order system of equations

$$\begin{aligned}\dot{\underline{x}} &= A\underline{x} + B\underline{u} + E_d \underline{f}_d + E_s \underline{w}_s & (1a) \\ \underline{y} &= C\underline{x} + D\underline{u} & (1b) \\ \underline{z} &= \underline{y} + M\underline{n} & (1c)\end{aligned}$$

where \underline{x} is the state vector, \underline{y} is the output vector, \underline{z} is the measurement vector, \underline{u} is the control vector, \underline{f}_d is a known or measurable disturbance vector, and \underline{w}_s and \underline{n} are process- and sensor noise respectively. We begin by making a series of reasonable mathematical assumptions. Assume that not all states are accessible, so that $\text{rank } C \leq \dim \underline{x}$. Let the initial conditions on the state vector be $\underline{x}(0) = \underline{x}_0$; let \underline{x}_0 , \underline{w}_s , \underline{n} , and \underline{f}_d be independent and bounded; let \underline{x}_0 be Gaussian (ref. 6, p. 272); and let \underline{n} and \underline{w}_s be zero-mean white Gaussian, with $\text{cov}[\underline{w}_s(t), \underline{w}_s(\tau)] = V_1 \delta(t-\tau)$ and $\text{cov}[\underline{n}(t), \underline{n}(\tau)] = V_3 \delta(t-\tau)$ (ref. 6, p. 272). Assume that $\{A, B\}$ and $\{A, E_s V_1^{1/2}\}$ are stabilizable, where $V_1 = V_1^{1/2} V_1^{1/2*}$ (the asterisk here means "conjugate transpose"); and that $\{C, A\}$ is detectable (ref. 5, p. 226). Let V_1 and V_3 be positive semidefinite (PSD) and positive definite (PD), respectively.

We choose a performance index of the form

$$J = \mathcal{E} \left\{ \lim_{T \rightarrow \infty} \frac{1}{T} \int_0^T \left\langle \begin{bmatrix} \underline{x}' & \underline{u}' \end{bmatrix} \begin{bmatrix} W_1 & W_2 \\ W_1' & W_3 \end{bmatrix} \begin{Bmatrix} \underline{x} \\ \underline{u} \end{Bmatrix} \right\rangle dt \right\} \quad (2)$$

where W_1 is PSD and W_3 is PD (ref. 6; pp. 272, 276). " \mathcal{E} " is the expected-value operator, needed since the system is excited stochastically by \underline{w}_s . The cost rate functional form

(with " $\lim_{T \rightarrow \infty} \frac{1}{T}$ ") is used to allow both for the white noise disturbance \underline{w}_s and for the non-dwindling disturbance \underline{f}_d .

If $\underline{Z}(t)$ is defined by $\underline{Z}(t) = \{\underline{z}(\tau), 0 \leq \tau \leq t\}$; and if $\underline{u}(t) = \underline{\alpha}[t, \underline{Z}(t), \underline{f}_d]$ defines the set of admissible controls (ref. 6, p. 272), where $\underline{\alpha}$ is a vector operator that is linear in terms of its arguments; the basic problem objective is to find an admissible control function $\underline{u}^*(t)$ which minimizes J with respect to the set of admissible control functions $\underline{u}(t)$. [The asterisk here indicates optimality, in the sense defined by Eqn. (2).]

Problem Decomposition

The basic problem, as stated in Eqns. (1) and (2), can be decomposed into two parallel subproblems, one stochastic and the other deterministic. Suppose that $\underline{x} = \underline{x}_s + \underline{x}_d$, where \underline{x}_s is the portion of the system response due to disturbance \underline{w}_s , and where \underline{x}_d is the portion of the response due to \underline{f}_d . Let \underline{y}_s , \underline{y}_d , \underline{z}_s , \underline{z}_d , \underline{Z}_s , \underline{Z}_d , \underline{u}_s , and \underline{u}_d be correspondingly defined.

$$\text{Then } J = \lim_{T \rightarrow \infty} \frac{1}{T} \int_0^T \left\{ \mathcal{E} \left\langle [\underline{x}'_s + \underline{x}'_d] \begin{bmatrix} W_1 & W_2 \\ W'_2 & W_3 \end{bmatrix} \begin{Bmatrix} \underline{x}_s + \underline{x}_d \\ \underline{u}_s + \underline{u}_d \end{Bmatrix} \right\rangle \right\} dt \quad (3a)$$

can be reduced to $J = J_s + J_d$, where

$$J_s = \lim_{T \rightarrow \infty} \frac{1}{T} \int_0^T \left\{ \mathcal{E} \left\langle [\underline{x}'_s + \underline{u}'_s] \begin{bmatrix} W_1 & W_2 \\ W'_2 & W_3 \end{bmatrix} \begin{Bmatrix} \underline{x}_s \\ \underline{u}_s \end{Bmatrix} \right\rangle \right\} dt \quad (3b)$$

$$\text{and } J_d = \lim_{T \rightarrow \infty} \frac{1}{T} \int_0^T \left\langle [\underline{x}'_d + \underline{u}'_d] \begin{bmatrix} W_1 & W_2 \\ W'_2 & W_3 \end{bmatrix} \begin{Bmatrix} \underline{x}_d \\ \underline{u}_d \end{Bmatrix} \right\rangle dt \quad (3c)$$

The problem is now separable into a stochastic— and a deterministic subproblem, each of which has an analytical solution. The two subproblems are stated, and their solutions presented (without development) below.

Stochastic Subproblem and Solution

Statement:

$$\text{Given: } \dot{\underline{x}}_s = A \underline{x}_s + B \underline{u}_s + E_s \underline{w}_s \quad (4a)$$

$$\underline{y}_s = C \underline{x}_s + D \underline{u}_s \quad (\text{rank } C \leq \dim \underline{x}_s) \quad (4b)$$

$$\underline{z}_s = \underline{y}_s + M \underline{n} \quad (4c)$$

$\{A, B\}$ is stabilizable, $\{C, A\}$ is detectable

$\underline{x}_s(0) = \underline{x}_{s0}$ is Gaussian with zero mean

\underline{x}_{s0} , \underline{w}_s , and \underline{n} are independent and bounded

$$\text{such that } \text{cov}[\underline{w}_s(t), \underline{w}_s(\tau)] = V_1 \delta(t-\tau) \quad (4d)$$

$$\text{and } \text{cov}[\underline{n}(t), \underline{n}(\tau)] = V_3 \delta(t-\tau) \quad (4e)$$

where V_1 is PSD and V_3 is PD

$$J_s = \lim_{T \rightarrow \infty} \frac{1}{T} \left\{ \int_0^T \left\langle \begin{bmatrix} \underline{x}_s' & \underline{u}_s' \end{bmatrix} \begin{bmatrix} W_1 & W_2 \\ W_2' & W_3 \end{bmatrix} \begin{Bmatrix} \underline{x}_s \\ \underline{u}_s \end{Bmatrix} \right\rangle dt \right\} \quad (4f)$$

where W_1 is PSD and W_3 is PD

$$\underline{Z}_s(t) = \{\underline{z}_s(\tau), 0 \leq \tau \leq t\}, \underline{u}_s(t) = \underline{u}_s[t, \underline{Z}_s(t)] \quad (4g)$$

defines the set of admissible controls

Find: An admissible control function $\underline{u}_s^*(t)$ which minimizes J_s with respect to the admissible control functions $\underline{u}_s(t)$

Solution (See ref. 6, pp. 272–277; and ref. 7, ch. 11):

$$\underline{u}_s^*(t) = -K \tilde{\underline{x}}_s(t) \quad (5a)$$

where $\tilde{\underline{x}}_s$ is an estimate of \underline{x}_s using a Luenberger observer (ref. 7, pp. 288–289) having observer gain matrix L

$$K = W_3^{-1} (B'P + W_2') \quad (5b)$$

P is the unique PD solution to

$$PA + A'P - (PB + W_2) W_3^{-1} (PB + W_2)' + W_1 = 0 \quad (5c)$$

$$L = QC' (M V_3 M')^{-1} \quad (5d)$$

Q is the unique PD solution to

$$AQ + QA' - QC' (M V_3 M')^{-1} CQ + E_s V_1 E_s' = 0 \quad (5e)$$

P exists if $\{A, B\}$ is stabilizable and $\{C, A\}$ is detectable

or if the system is asymptotically stable

Q exists if $\{A, E_s V_1^{1/2}\}$ is stabilizable and $\{C, A\}$ is detectable

or if the system is asymptotically stable

Deterministic Subproblem and Solution

Statement:

$$\text{Given: } \underline{x}_d = A \underline{x}_d + B \underline{u}_d + E_d \underline{f}_d \quad (6a)$$

$$\underline{y}_d = C \underline{x}_d + D \underline{u}_d \quad (\text{rank } C \leq \dim \underline{x}_d) \quad (6b)$$

$$\underline{z}_d = \underline{y}_d \quad (6c)$$

$\{A, B\}$ is stabilizable, $\{C, A\}$ is detectable

$$\underline{x}_d(0) = \underline{x}_{d0}$$

\underline{x}_{d0} and \underline{f}_d are independent and bounded

$$J_d = \lim_{T \rightarrow \infty} \frac{1}{T} \int_0^T \left\langle \begin{bmatrix} \underline{x}_d' & \underline{u}_d' \end{bmatrix} \begin{bmatrix} W_1 & W_2 \\ W_2' & W_3 \end{bmatrix} \begin{bmatrix} \underline{x}_d \\ \underline{u}_d \end{bmatrix} \right\rangle dt \quad (6d)$$

where W_1 is PSD and W_3 is PD
 $\underline{Z}_d = \{\underline{z}_d(\tau), 0 \leq \tau \leq t\}, \underline{u}_d(t) = \underline{u}_d[t, \underline{Z}_d(t), \underline{f}_d]$
defines the set of admissible controls (6e)

Find: An admissible control function $\underline{u}_d^*(t)$ which minimizes J_d with respect to the set of admissible control functions $\underline{u}_d(t)$

Solution (refs. 8; 9; and 10, pp. 156–157):

$$\underline{u}_d^*(t) = -K \underline{x}_d - W_3^{-1} B' \int_t^\infty \exp[-\bar{A}'(t-\tau)] P E_d \underline{f}_d(\tau) d\tau \quad (7a)$$

where $K = W_3^{-1} (B'P + W_2')$ (7b)

P is the unique PD solution to

$$PA + A'P - (PB + W_2) W_3^{-1} (PB + W_2)' + W_1 = 0 \quad (7c)$$

P exists if $\{A, B\}$ is stabilizable and $\{C, A\}$ is detectable
or if the system is asymptotically stable

Combined Solution to Basic Problem

When $\text{rank } C < \dim \underline{x}_d$, an estimate $\tilde{\underline{x}}_d$ of \underline{x}_d must be used in the feedback. If one uses an asymptotic (i.e., Luenberger) observer, with gains L chosen to give an optimal solution to the stochastic subproblem, he can then combine the stochastic and deterministic subproblem solutions so as to use the same observer and regulator. This allows the optimal solution (feedback portion) to be realized physically. If such a choice is made,

$$\underline{u}^*(t) = \underline{u}_d^*(t) + \underline{u}_d^*(t) = -K \tilde{\underline{x}}(t) - W_3^{-1} B' \int_t^\infty \exp[-\bar{A}'(t-\tau)] P E_d \underline{f}_d(\tau) d\tau \quad (8a)$$

where $\tilde{\underline{x}}$ is an estimate of \underline{x} using a Luenberger observer

having observer gain matrix L

$$K = W_3^{-1} (B'P + W_2') \quad (8b)$$

$$L = QC'(M V_3 M')^{-1} \quad (8c)$$

P, Q , and \bar{A} are as defined previously

If \underline{f}_s and \underline{n} are correlated by $\mathcal{E} [\underline{f}_s(t), \underline{n}(\tau)] = V_2 \delta(t-\tau)$, then the above solution has the modification (ref. 7, pp. 414–417) that

$$L = (QC' + E_s V_2)(M V_3 M')^{-1} \quad (8d)$$

where Q is the unique PD solution to

$$\bar{A}Q + Q\bar{A}' - QC'(M V_3 M')^{-1} CQ + E_s \bar{V}_1 E_s' = 0 \quad (8e)$$

$$\text{for } \tilde{A} = A - E_s V_2 V_3^{-1} C \quad (8f)$$

$$\text{and } \tilde{V}_1 = V_1 - V_2 V_3^{-1} V_2' \quad (8g)$$

PROBLEM EXTENSIONS

Frequency Weighting

Suppose now that it is desired to frequency weight the states \underline{x} and the control \underline{u} in the cost rate functional, so that the weightings vary with frequency (ref. 11). Let \underline{x} be considered to be the input to a filter $\mathcal{W}_1(s)$ of which ${}^1\underline{x}$ is the output, and let $\mathcal{W}_1(s)$ have a state-space representation defined by $\{A_1, B_1, C_1, D_1\}$ [i.e., $\mathcal{W}_1(s) = C_1(sI - A_1)^{-1}B_1 + D_1$].

Then

$$\dot{\underline{z}}_1 = A_1 \underline{z}_1 + B_1 \underline{x} \quad (9a)$$

$${}^1\underline{x} = C_1 \underline{z}_1 + D_1 \underline{x} \quad (9b)$$

expresses ${}^1\underline{x}$ in terms of \underline{x} , employing pseudostates \underline{z}_1 . Similarly, if \underline{u} is considered to be the input to a filter $\mathcal{W}_3(s)$ of which ${}^1\underline{u}$ is the output, and if $\mathcal{W}_3(s)$ has a state-space representation defined by $\{A_2, B_2, C_2, D_2\}$, ${}^1\underline{u}$ can be expressed in terms of \underline{u} , employing pseudostates \underline{z}_2 :

$$\dot{\underline{z}}_2 = A_2 \underline{z}_2 + B_2 \underline{u} \quad (10a)$$

$${}^1\underline{u} = C_2 \underline{z}_2 + D_2 \underline{u} \quad (10b)$$

Suppose now that these frequency-weighted states (${}^1\underline{x}$) and controls (${}^1\underline{u}$) are further weighted by constant weighting matrices W_1 and W_2 , respectively. The resulting state equations and performance index are as follows:

$$\dot{\underline{\bar{x}}} = {}^1A \underline{\bar{x}} + {}^1B \underline{u} + {}^1E_d \underline{f}_d + {}^1E_s \underline{w}_s \quad (11a)$$

$$\underline{y} = {}^1C \underline{\bar{x}} + D \underline{u} \quad (11b)$$

$$\underline{z} = \underline{y} + M \underline{n} \quad (11c)$$

$${}^1J = \mathcal{E} \left\{ \lim_{T \rightarrow \infty} \frac{1}{T} \int_0^T \left\langle \begin{bmatrix} \underline{\bar{x}}' & \underline{u}' \end{bmatrix} \begin{bmatrix} {}^1W_1 & {}^1W_2 \\ {}^1W_2' & {}^1W_3 \end{bmatrix} \begin{Bmatrix} \underline{\bar{x}} \\ \underline{u} \end{Bmatrix} \right\rangle dt \right\} \quad (11d)$$

$$\text{where } \underline{\bar{x}} = \begin{bmatrix} \underline{x} \\ \underline{z}_1 \\ \underline{z}_2 \end{bmatrix} \quad (11e)$$

$${}^1A = \begin{bmatrix} A & O & O \\ B_1 & A_1 & O \\ O & O & A_2 \end{bmatrix} \quad (11f)$$

$${}^1B = \begin{bmatrix} B \\ O \\ B_2 \end{bmatrix} \quad (11g)$$

$${}^1C = [C \ O \ O] \quad (11h)$$

$${}^1E_d = \begin{bmatrix} E_d \\ O \\ O \end{bmatrix} \quad (11i)$$

$${}^1E_s = \begin{bmatrix} E_s \\ O \\ O \end{bmatrix} \quad (11j)$$

$${}^1W_1 = \begin{bmatrix} D_1'W_1D_1 & D_1'W_1C_1 & O \\ C_1'W_1D_1 & C_1'W_1C_1 & O \\ O & O & C_1'W_3C_2 \end{bmatrix} \quad (11k)$$

$${}^1W_2 = \begin{bmatrix} O \\ O \\ C_2'W_3D_2 \end{bmatrix} \quad (11l)$$

$${}^1W_3 = [D_2'W_3D_2] \quad (11m)$$

Disturbance Accommodation

Suppose further that the stochastic disturbance is not \underline{w}_s but \underline{f}_s , where \underline{f}_s is a stochastically modeled disturbance with power spectral density $S_f(\omega) = S_f^{1/2}(j\omega)S_f^{1/2*}(j\omega)$. Defining $H_f(j\omega)$ by $S_f^{1/2}(j\omega) V_1^{1/2}$, one can consider \underline{f}_s to be the output of a filter $H_f(s)$ excited by zero-mean white Gaussian noise \underline{w}_s (ref. 12) with power V_1 (i.e., $\text{cov}[\underline{w}_s(t), \underline{w}_s(\tau)] = V_1 \delta(t-\tau)$).

In state-space form,

$$\dot{\underline{\xi}} = A_s \underline{\xi} + \underline{w}_s \quad (12a)$$

$$\underline{f}_s = C_s(sI - A_s)^{-1} \quad (12b)$$

such that $H_f(s) = C_s(sI - A_s)^{-1}$ (12c)

Incorporating these new pseudostates ($\underline{\xi}$) into the state equations and performance index

yields

$$\dot{\underline{x}} = {}^2A \hat{\underline{x}} + {}^2B \underline{u} + {}^2E_d \underline{f}_d + {}^2E_s \underline{w}_s \quad (13a)$$

$$\underline{y} = {}^2C \hat{\underline{x}} + D \underline{u} \quad (13b)$$

$$\underline{z} = \underline{y} + M \underline{n} \quad (13c)$$

$${}^2J = \mathcal{E} \left[\lim_{T \rightarrow \infty} \frac{1}{T} \int_0^T \left\langle [\hat{\underline{x}}' \ \underline{u}'] \begin{bmatrix} {}^1W_1 & {}^1W_2 \\ {}^1W_2' & {}^1W_3 \end{bmatrix} \begin{Bmatrix} \hat{\underline{x}} \\ \underline{u} \end{Bmatrix} \right\rangle dt \right] \quad (13d)$$

$$\text{where} \quad \hat{\underline{x}} = \left\{ \frac{\bar{\underline{x}}}{\underline{\xi}} \right\} \quad (13e)$$

$${}^2A = \begin{bmatrix} A & O & O & E_s C_s \\ B_1 & A_1 & O & O \\ O & O & A_2 & O \\ O & O & O & A_s \end{bmatrix} \quad (13f)$$

$${}^2B = \begin{bmatrix} B \\ O \\ B_2 \\ O \end{bmatrix} \quad (13g)$$

$${}^2C = [C \ O \ O \ O] \quad (13h)$$

$${}^2E_d = \begin{bmatrix} E_d \\ O \\ O \\ O \end{bmatrix}$$

$${}^2E_s = \begin{bmatrix} O \\ O \\ O \\ I \end{bmatrix} \quad (13j)$$

$${}^2W_1 = \begin{bmatrix} D_1' W_1 D_1 & D_1' W_1 C_1 & O & O \\ C_1' W_1 D_1 & C_1' W_1 C_1 & O & O \\ O & O & C_2' W_3 C_2 & O \\ O & O & O & O \end{bmatrix} \quad (13k)$$

$${}^2W_2 = \begin{bmatrix} O \\ O \\ C_2'W_3D_2 \\ O \end{bmatrix} \quad (13m)$$

$${}^2W_3 = [D_2'W_3D_2] \quad (13n)$$

The solution to this problem has been given previously.

SYNTHESIS MODEL

The model given at the close of the previous section is the model from which the controller is synthesized. The synthesis involves the determination of observer gains L and regulator feedback gains K . Preview gains K_{FF} can also be determined, if desired, to approximate the Duhamel integral term of the optimal control. One approach to determining these preview gains has been presented in reference 9. Further study of the determination and use of these gains is needed.

ANALYSIS MODEL

Once the controller has been selected, it must be connected to the actual plant and the resulting "analysis model" used to evaluate closed-loop-system performance and stability. For constant gain matrices K , L , and K_{FF} the open loop transfer function from

\underline{Y} to $\underline{U}_{FB} [= -K \underline{X}]$ is

$$\mathcal{H}_{\underline{U}_{FB}\underline{Y}}^{OL}(s) = \left[\begin{array}{c|c} {}^2A - {}^2BK - L^2C & L \\ \hline -K & O \end{array} \right], \quad (14a)$$

where the form

$$\left[\begin{array}{c|c} A & B \\ \hline C & D \end{array} \right]$$

indicates $C(sI - A)^{-1}B + D$. The closed loop transfer functions, respectively, from \underline{F}_d and \underline{F}_s to \underline{X} , are

$$\mathcal{H}_{\underline{X}\underline{F}_d}^{CL}(s) = \left[\begin{array}{cc|c} A & -BK & E_d + BK_{FF} \\ LC & {}^2A - {}^2BK - L^2C & {}^2BK_{FF} \\ \hline I & O & O \end{array} \right] \quad (14b)$$

$$\text{and } \mathcal{H}_{\underline{X}\underline{F}_s}^{CL}(s) = \left[\begin{array}{cc|c} A & -BK & E_s + BK_{FF} \\ LC & {}^2A - {}^2BK - L^2C & {}^2BK_{FF} \\ \hline I & O & O \end{array} \right] \quad (14c)$$

The return ratio matrices (ref. 4) at the $\underline{Y}(s)$ and $\underline{U}(s)$ nodes, respectively, for $D \equiv O$, are

$$L_2(s) = \left[\begin{array}{cc|c} A^2 - BK - L^2C & 0 & L \\ -BK & A & O \\ \hline O & -C & O \end{array} \right] \quad (15a)$$

$$L_1(s) = \left[\begin{array}{cc|c} {}^2A - {}^2BK - L^2C & LC & O \\ O & A & B \\ \hline K & O & O \end{array} \right] \quad (15b)$$

The corresponding return difference matrices and inverse return difference matrices (ref. 4) are as follows:

$$I + L_2(s) = \left[\begin{array}{cc|c} {}^2A - {}^2BK - L^2C & O & L \\ -BK & A & O \\ \hline O & -C & I \end{array} \right] \quad (15c)$$

$$I + L_1(s) = \left[\begin{array}{cc|c} {}^2A - {}^2BK - L^2C & LC & O \\ O & A & B \\ \hline K & O & I \end{array} \right] \quad (15d)$$

$$I + L_2^{-1}(s) = I + [K(sI - {}^2A + {}^2BK + L^2C)^{-1}L]^{-1}[C(sI - A)^{-1}B]^{-1} \quad (15e)$$

$$I + L_1^{-1}(s) = I + [C(sI - A)^{-1}B]^{-1}[K(sI - {}^2A + {}^2BK + L^2C)^{-1}L]^{-1} \quad (15f)$$

The singular values of these matrices can be used to evaluate system noise and disturbance attenuation, stability margins, and sensitivity (ref. 4). Iterative application of the synthesis— and analysis models can be used to produce the desired controller.

EXAMPLE PROBLEM

Suppose one wishes to develop a controller to isolate a space experiment of mass m and position $x(t)$, from a unidirectional acceleration disturbance $\ddot{d}(t)$. Assume that a wall having position $d(t)$ acts on m through an umbilical with stiffness k and damping c . (See figure 1). Suppose further that rattlespace constraints require the transmissibility to be unity below 10^{-3} Hz, and that it is desired to attenuate the disturbance by at least two orders of magnitude between 0.05 and 10 Hz. Let a linear actuator, applying a force that varies with control current i , be connected between the wall and the experiment in parallel with the umbilical.

For this problem, it is desirable at low frequencies to penalize the relative displacement of the experiment heavily, so that the experiment "tracks" the wall. At intermediate frequencies, however, the absolute acceleration of the experiment should be heavily penalized to accomplish the desired disturbance rejection. The state space model,

then, should have relative position $x-d$ and absolute acceleration \ddot{x} as states, allowing them to be frequency-weighted in the performance index.

The system equation of motion is

$$\ddot{x} = -\hat{k}(x-d) - \hat{c}(\dot{x}-\dot{d}) - \hat{\alpha}i, \text{ where } \hat{k} = \frac{k}{m}, \hat{c} = \frac{c}{m}, \text{ and } \hat{\alpha} = \frac{\alpha}{m} \quad (16a)$$

In state-space form, the equations can be written as

$$\begin{Bmatrix} \dot{x}_1 \\ \dot{x}_2 \\ \dot{x}_3 \end{Bmatrix} = \begin{bmatrix} 0 & 1 & 0 \\ -\hat{k} & -\hat{c} & 0 \\ -\omega_h \hat{k} & -\omega_h \hat{c} & -\omega_h \end{bmatrix} \begin{Bmatrix} x_1 \\ x_2 \\ x_3 \end{Bmatrix} + \begin{Bmatrix} 0 \\ -\hat{\alpha} \\ -\omega_h \hat{\alpha} \end{Bmatrix} i + \begin{Bmatrix} 0 \\ -1 \\ 0 \end{Bmatrix} \ddot{d} \quad (16b)$$

$$\begin{Bmatrix} y_1 \\ y_2 \end{Bmatrix} = \begin{bmatrix} 1 & 0 & 0 \\ 0 & 0 & 0 \end{bmatrix} \begin{Bmatrix} x_1 \\ x_2 \\ x_3 \end{Bmatrix} \quad (16c)$$

$$\begin{Bmatrix} z_1 \\ z_2 \end{Bmatrix} = \begin{Bmatrix} y_1 \\ y_2 \end{Bmatrix} + \begin{Bmatrix} n_1 \\ n_2 \end{Bmatrix} \quad (16d)$$

where

$$\begin{aligned} x_1(t) &= x(t) - d(t) \\ x_2(t) &= \dot{x}(t) - \dot{d}(t) \\ x_3(s) &= \left(\frac{\omega_h}{s + \omega_h} \right) s^2 X(s), \omega_h \text{ high,} \\ &\text{so that } x_3(t) \approx \ddot{x}(t) \text{ for } \omega \ll \omega_h \end{aligned} \quad (16e)$$

Frequency-weighting the states so that

$$\begin{Bmatrix} {}^1X_1(s) \\ {}^1X_2(s) \\ {}^1X_3(s) \end{Bmatrix} = \begin{bmatrix} \frac{\omega_3}{s} & 0 & 0 \\ 0 & 1 & 0 \\ 0 & 1 & \frac{\omega_2 s}{(s + \omega_1)(s + \omega_2)} \end{bmatrix} \begin{Bmatrix} X_1(s) \\ X_2(s) \\ X_3(s) \end{Bmatrix} \quad (17a)$$

(where $\omega_1 < \omega_2$) results in a performance index that penalizes x_1 more highly at low frequencies and x_3 more highly at intermediate frequencies. If the control is frequency-weighted so that

$${}^1U(s) = \left(\frac{\omega_4 s}{s + \omega_4} \right) U(s) \quad [\omega_4 < \omega_h], \quad (17b)$$

at higher frequencies the control will be more heavily penalized. This is desirable both for the sake of robustness and since x_3 approximates \ddot{x} only at frequencies sufficiently below ω_h . Finally, let the input acceleration be considered to come from zero-mean Gaussian white noise filtered through $\frac{\omega_f}{s + \omega_f}$.

The resultant state equations are as indicated on page 8, where

$$A_1 = \begin{bmatrix} 0 & 0 & 0 \\ 0 & -(\omega_1 + \omega_2) & -\omega_1 \omega_2 \\ 0 & 1 & 0 \end{bmatrix} \quad (18a)$$

$$B_1 = \begin{bmatrix} 1 & 0 & 0 \\ 0 & 0 & 1 \\ 0 & 0 & 0 \end{bmatrix} \quad (18b)$$

$$C_1 = \begin{bmatrix} \omega_3 & 0 & 0 \\ 0 & 0 & 0 \\ 0 & \omega_2 & 0 \end{bmatrix} \quad (18c)$$

$$D_1 = \begin{bmatrix} 0 & 0 & 0 \\ 0 & 1 & 0 \\ 0 & 0 & 0 \end{bmatrix} \quad (18d)$$

$$A_2 = -\omega_4$$

$$B_2 = 1$$

$$C_2 = -\omega_4^2$$

$$D_2 = \omega_4$$

$$A_s = -\omega_f$$

$$B_s = 1$$

$$C_s = \omega_f$$

$$D_s = 0$$

Assume that $\text{cov} [w_s(t), w_2(\tau)] = 1 \delta(t - \tau)$
 $\text{cov} [n_1(t), n_1(\tau)] = 0.001 \delta(t - \tau)$
 and $\text{cov} [n_2(t), n_2(\tau)] = 0.001 \delta(t - \tau).$

Since A_1 has a zero [1st] column, 2A will have a corresponding zero [4th] column. To make the frequency-weighted system $\{^2C, ^2A\}$ observable, obtain $\int (x-d) dt$ as a measured state (i.e., the first pseudostate, Z_{11}) and modify 2C accordingly. Let the measurement noise associated with Z_{11} be n_3 , such that

$$\text{cov} [n_3(t), n_3(\tau)] = 0.0001$$

Gain matrix W_1 can be varied to "tune" the optimal control to give the most satisfactory results. The transmissibility between $\ddot{d}(t)$ and $\ddot{x}(t)$ is given in figure 2. The control uses feedback (and observer) gains obtained from system parameters and weightings as indicated on the figure. Note that the low-frequency transmissibility is unity, as desired, and that for intermediate frequencies the transmissibility rolls off with a slope of -1 .

If a different frequency-weighting of x_3 is used, it is to be anticipated that the transmissibility curve will change as well.

$$\text{For } {}^1X_3(s) = \frac{\omega^2 s}{(s+\omega_1)^2(s+\omega_2)^2} X_3(s) \quad (19)$$

the resultant selected transmissibility curve is given in figure 3. The low-frequency transmissibility again, is unity; but now for the intermediate frequencies the transmissibility rolls off with a slope of -2 , as expected. Adding another pole at ω_1 and at ω_2 to the $X_3(s)$ frequency weighting would further improve the intermediate-frequency roll-off. The present controller, however, meets the design specifications.

$$\text{If state frequency-weightings of } {}^1X_1(s) = \frac{\omega_3}{s+\omega_3} X_1(s) \quad (20a)$$

$$\text{and } {}^1X_3(s) = \frac{\omega^2 s}{(s+\omega_1)^2(s+\omega_2)^2} X_3(s) \quad (20b)$$

are used, the results (figure 4) are similar to those given previously in figure 3. Note that with this latter choice of frequency weighting however, (i.e., without any "rigid body poles"), the frequency-weighted system $\{{}^2C, {}^2A\}$ is observable, without augmenting the actual plant output y as was previously necessary. Consequently this is the preferred control.

DISCUSSION

H_2 synthesis, as the example problem indicates, provides a highly versatile loop-shaping tool. It is especially useful in controller development for SIMO and MIMO systems, where classical loop-shaping methods are most lacking. Once the designer has expressed the system equations in terms of states for which he has an intuitive feel, and of measurable outputs, the design process becomes relatively easy. He frequency weights (i.e., filters) the states and control inputs according to his engineering experience and intuition, to indicate the relative importance of each as a function of frequency. Then he weights these frequency-weighted states and controls relative to each other. The H_2 synthesis methodology automatically provides him with a set of regulator and observer gains that are optimal with respect to the chosen weightings, given a quadratic performance index. Known aspects of the input disturbances and sensor noise can be incorporated into the design as well. Singular value checks provide the ability to evaluate system robustness. With a few iterations, the skillful engineer can complete his design. Excellent computer software packages already exist to assist in the task.

The frequency weighting tells the H_2 synthesis machinery how much "cost" to place on a state or control input at any frequency, relative to its cost at other frequencies. If, for example, absolute acceleration is undesirable only in a particular frequency range, that is where it should be most heavily weighted. The subsequent weighting of the frequency-weighted states and control inputs tell the synthesis machinery how much cost to place on each frequency-weighted state or control relative to the others.

In the example problem changing the relative weighting between absolute acceleration and relative displacement caused the frequency range of unit transmissibility to vary. An increase in the sharpness of the bandpass filter, used in the acceleration frequency weighting, resulted in a corresponding increase in the rate of gain roll-off. Increasing the weighting of relative velocity added damping to the system, as expected; and adjusting the acceleration bandpass filter's lower pole location allowed fine tuning of the unit transmissibility upper frequency limit. Use of a high-pass filter for control weighting produced a control which responds favorably (i.e., minimally) at higher frequencies, where the plant models typically are invalid.

CONCLUDING REMARKS

The extended H_2 synthesis method has been developed and applied to a one-dimensional microgravity vibration isolation problem, for which it seems particularly well-suited. Research continues toward the application of H_2 synthesis to the full six-degree-of-freedom isolation problem.

SYMBOLS AND ABBREVIATIONS

Alphabetical Symbols

| | |
|------------------------------|--|
| A | System dynamic matrix |
| B | System control input matrix |
| c | Umbilical damping |
| C | Systems State output matrix |
| D | Control transmission matrix |
| E | System disturbance input matrix |
| \underline{f} | Disturbance vector |
| H | Stochastic-disturbance input filter |
| $\mathcal{H}(s)$ | Transfer function matrix |
| i | Control current |
| I | Identity matrix |
| j | Square root of -1 |
| J | Performance index |
| K | Control feedback gain matrix |
| L | Observer gain matrix |
| m | Experiment mass |
| M | Sensor noise input matrix |
| \underline{n} | Sensor noise vector |
| O | Zero matrix |
| P | Algebraic Riccati Equation solution for regulator feedback gains |
| Q | Algebraic Riccati Equation solution for observer gains |
| s | Laplace variable |
| S(s) | Stochastic-disturbance power-spectral-density matrix |
| t | Time |
| \underline{u} | Control vector |
| V | Covariance matrix |
| \underline{w} | White-noise disturbance vector |
| $\underline{W}, \mathcal{W}$ | Weighting matrix |
| α | Actuator proportionality constant |
| $\underline{\alpha}$ | Admissible-control function |
| δ | Dirac delta function |
| \mathcal{E} | Expected-value operator |
| $\underline{\xi}$ | Disturbance-accommodation pseudostates |
| ω | Circular frequency |
| Capitalization | Laplace transform, indicated by context |

Abbreviations

| | |
|------|--------------------------------|
| CL | Closed loop |
| cov | Covariance |
| FF | Feedforward (preview) gain |
| MDOF | Multiple-degree-of-freedom |
| MIMO | Multiple-input-multiple-output |
| OL | Open loop |
| PD | Positive definite |
| PSD | Positive semidefinite |
| SDOF | Single-degree-of-freedom |
| SIMO | Single-input-multiple-output |

Subscripts, Superscripts, and Diacritical Marks

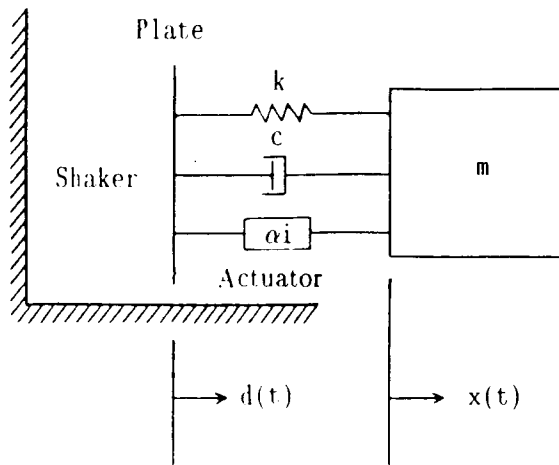
| | |
|----------------------|---|
| postsubscript 0 | Value at time $t=0$ |
| postsubscript 1 | With A,B,C,D,z: related to state–frequency weighting state–space description With L: return ratio matrix at control node With V: process noise covariance With w,W, \mathcal{W} : state (or pseudostate) weightings, applied subsequent to any frequency weighting |
| postsubscript 2 | With A,B,C,D,z: related to state–frequency–weighting state–space description With L: return ratio matrix at output node. With V,W: cross–weightings |
| postsubscript 3 | With V: measurement noise covariance With W, \mathcal{W} : control weightings |
| postsubscript d | Related to deterministic disturbance |
| postsubscript f | Related to filter for stochastic disturbance |
| postsubscript s | Related to stochastic disturbance |
| postsuperscript 1/2 | Square root or spectral factorization |
| postsuperscript ' | Transpose |
| postsuperscript -1 | Inverse |
| postsuperscript * | Optimum or conjugate transpose |
| underline $_$ | Vector |
| overbar $_$ | With A: closed loop system dynamic matrix With \bar{x} : augmented with frequency–weighting pseudostates |
| overhat $\hat{_}$ | Augmented with frequency–weighting– and disturbance–accommodation pseudostates |
| overtilde \sim | Estimated or associated with cross–correlation |
| presuperscript 1 | With \underline{x} , \underline{X} , \underline{u} , or \underline{U} : frequency–weighted With other symbols: related to system augmented by frequency weighting |
| presuperscript 2 | Related to system augmented by frequency–weighting and disturbance–accommodation |

ACKNOWLEDGEMENTS

This work was supported in part by the NASA Lewis Research Center and by the Center for Innovative Technology of the Commonwealth of Virginia.

REFERENCES

1. Grodsinsky, C.M.; and Brown, G.V.: "Non-intrusive Inertial Vibration Isolation Technology for Microgravity Space Experiments." NASA TM-201386, January 1990.
2. Nelson, E.S.: "An Examination of Anticipated g-Jitter on Space Station and Its Effects on Materials Processes." NASA TM-103775, April 1991.
3. Knospe, C.R.; Hampton, R.D., and Allaire, P.E.: "Control Issues of Microgravity Vibration Isolation." Acta Astronautica, accepted for publication.
4. Safonov, M.G.; Laub, A.J.; and Hartmann, G.L.: "Feedback Properties of Multivariable Systems: The Role and Use of the Return Difference Matrix." IEEE Trans. on Automatic Controls, Vol. AC-26, No. 1, February 1981, pp. 47-65.
5. Maciejowski, J.M.: Multivariable Feedback Design. Addison-Wesley Publishing Company, Inc., Wokingham, England, 1989.
6. Sage, A.P.; and White, C.C., III: Optimum Systems Control, 2nd ed. Prentice Hall, Inc., Englewood Cliffs, New Jersey, 1977.
7. Friedland, B.: Control System Design: An Introduction to State-Space Methods. McGraw-Hill, Inc., New York, 1986.
8. Salukvadze, M.E.: "Analytic Design of Regulators (Constant Disturbances)." Translated in Automation and Remote Control, Vol. 22, No. 10, October 1961, pp. 1147-1155. Originally published in Avtomatika i Telemekhanika, Vol. 22, No. 10, February 1961, pp. 1279-1287.
9. Hampton, R.D.; Knospe, C.R.; Allaire, P.E.; Lewis, D.W.; and Grodsinsky, C.M.: "An Optimal Control Law for Microgravity Vibration Isolation." Workshop on Aerospace Applications of Magnetic Suspension Technology, September 25-27, 1990, NASA Conference Publication 10066, Part 2, March 1991, pp. 447-476.
10. Bryson, A.E., Jr.; and Ho, Yu-Chi: Applied Optimal Control. Hemisphere Publishing Corporation, Washington, D.C., 1975.
11. Gupta, N.K.: "Frequency Shaped Cost Functionals: Extension of Linear - Quadratic-Gaussian Design Methods." AIAA Journal of Guidance and Control, November/December 1980, pp. 529-535.
12. Johnson, C.D.: "Further Study of the Linear Regulator with Disturbances - The Case of Vector Disturbances Satisfying a Linear Differential Equation." IEEE Trans. on Automatic Control (Short Papers), Vol. AC-15, April 1970, pp. 222-228.



$m = 75 \text{ lbm}$
 $k = 1.544 \text{ lbf/ft}$
 $c = 0 \text{ lbf-sec/ft}$
 $\alpha = 2 \text{ lbf/amp}$

FIGURE 1: Example-Problem Model

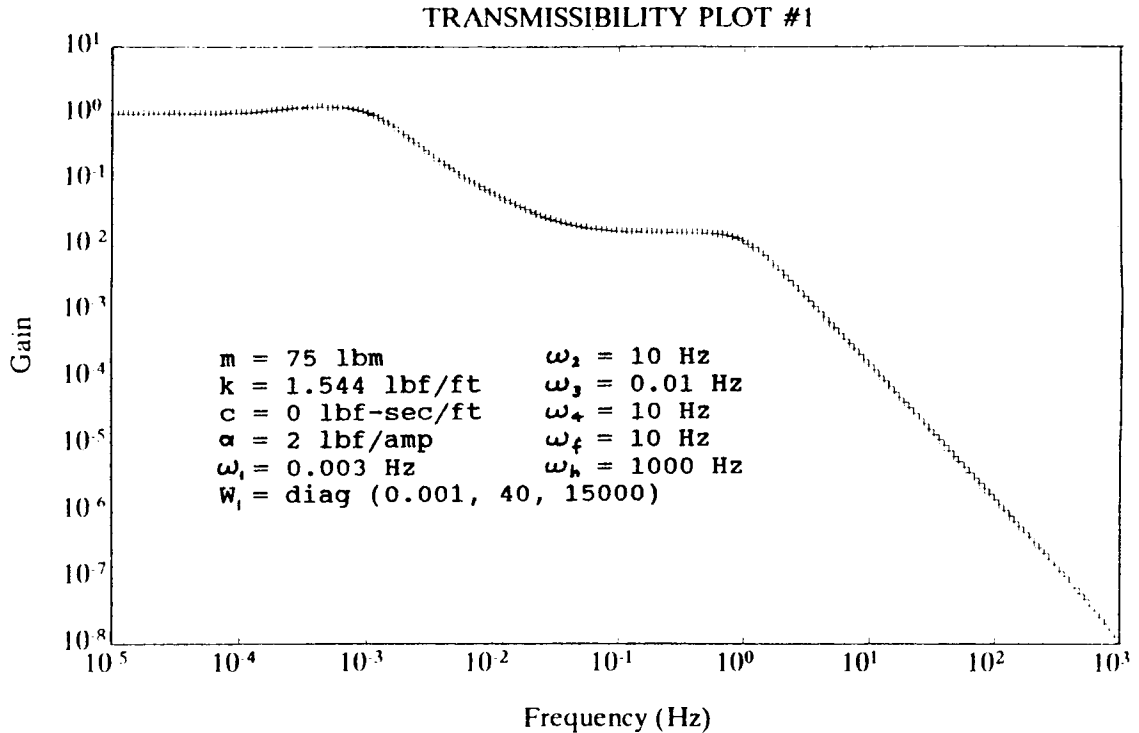


FIGURE 2: Transmissibility Plot for 1st Control Weighting

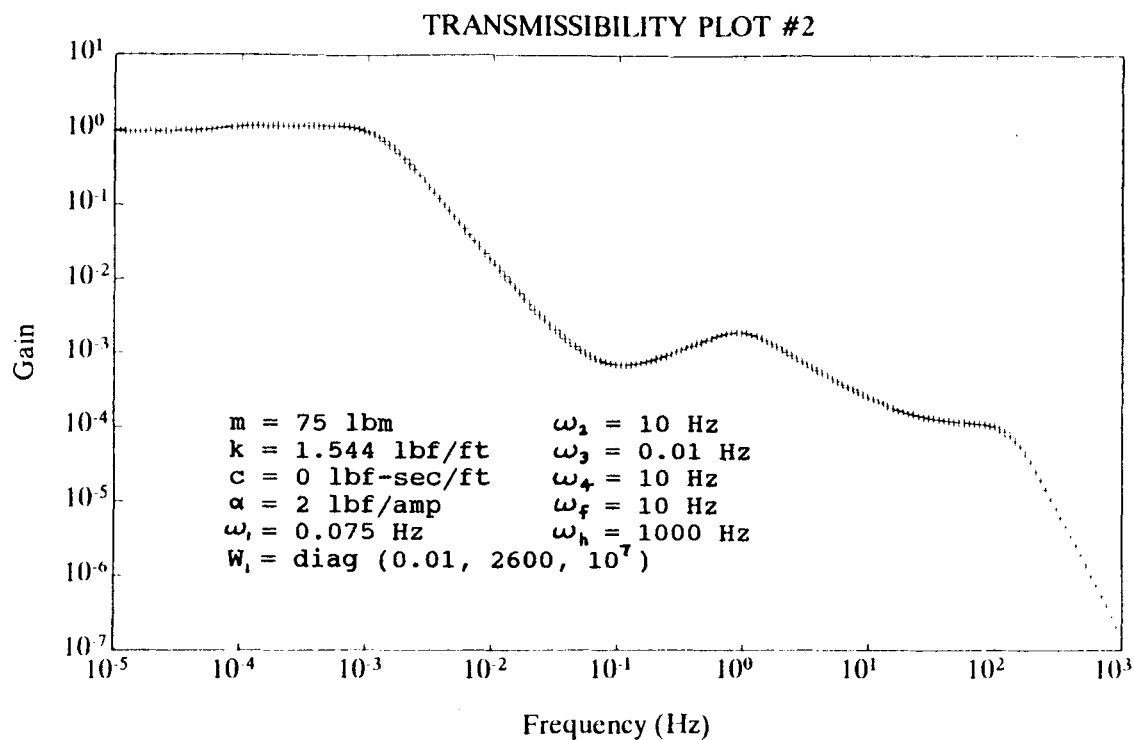


FIGURE 3: Transmissibility Plot for 2nd Control Weighting

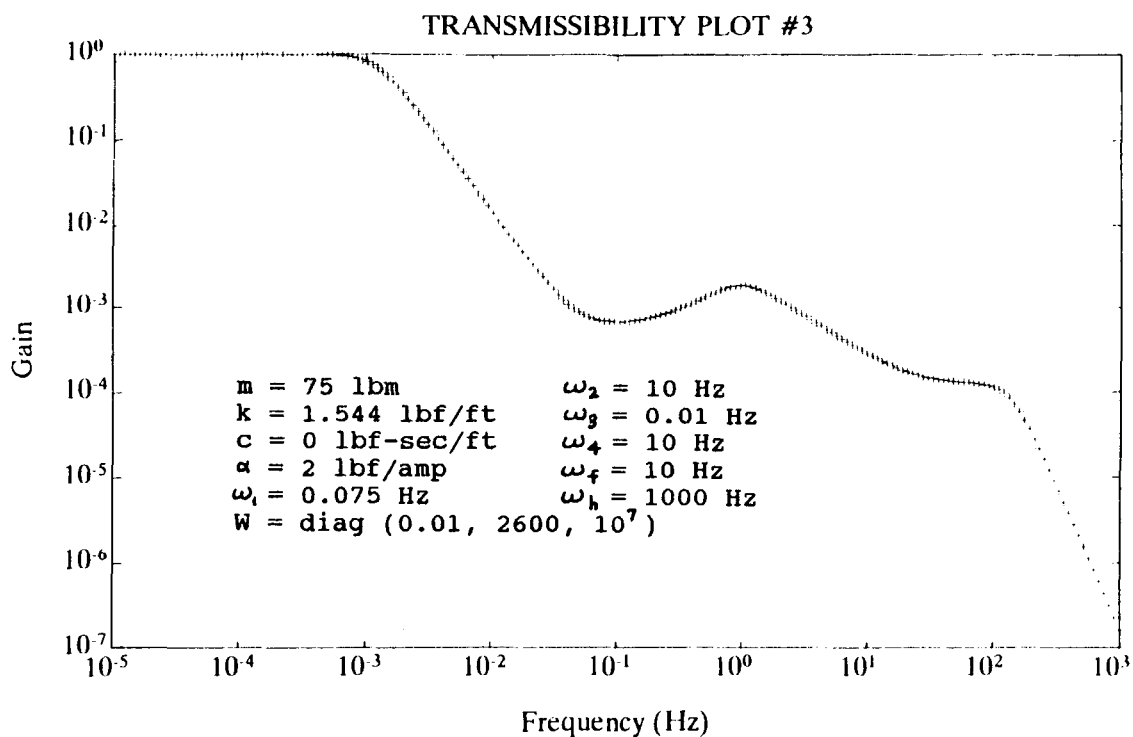


FIGURE 4: Transmissibility Plot for 3rd Control Weighting

N 9 2 - 2 7 7 4 2

Experimental Results in Nonlinear Compensation
of a
One Degree-of-Freedom Magnetic Suspension

David L. Trumper, James C. Sanders, Tiep H. Nguyen, and Michael A. Queen
Dept. of Electrical Engineering
Univ. of N. Carolina at Charlotte
Charlotte, NC 28223

1 Introduction

Nonlinear control techniques are of increasing interest in magnetic bearing applications. A one-degree-of-freedom magnetic suspension system has been constructed to serve as a test system for nonlinear control. The objective of this effort is to build an accurate model for the nonlinear suspension dynamics and to show the advantages of compensating for these nonlinearities by using a nonlinear controller. The results obtained with a nonlinear controller are experimentally demonstrated as superior to those obtained with a linear controller. Specifically, a controller which contains a force-control block yields transient responses which are largely independent of the operating point air gap.

A block diagram for the suspension system is shown in Figure 1. As shown in the figure, a one inch steel ball is suspended below a 3500-turn solenoid wound on a one inch steel core. The solenoid is driven by a hysteretic switching current drive. The ball position is sensed using a photodiode array illuminated by an array of infrared LEDs. The system is controlled by a PC-based algorithm and data acquisition system. Within the control algorithm, corrections are made for sensor nonlinearities and for the solenoid nonlinear force characteristics.

Theory for feedback linearization is presented in [1-4]. The application of linearization to magnetic suspension systems has been discussed in [5-10]. The results presented herein are an experimental investigation of ideas presented in [10]. Here, feedback linearizing transformations are demonstrated for second-order and third-order models of a one-degree-of-freedom magnetic suspension. Simulated responses are presented, but no experimental results are given. This is due to two shortcomings. First, the optical sensor used in [10] is not sufficiently stable to allow accurate position measurements which are required to linearize the suspension. Second, the force measurement scheme consists of a balance beam which allows only static force measurements. These deficiencies have been rectified in the present effort, allowing the presentation of experimental results verifying the advantages of using nonlinear compensation for magnetic suspensions.

In the following sections the design of the position sensor, switching power amplifier, force measurement fixture, and nonlinear controller are presented, along with experimental results for the power amplifier, force measurements, and suspension dynamics.

2 Position Sensor

The position sensor works by arranging for the suspended ball to cast a shadow on a 16-element linear photodiode array. The array is illuminated by a vertical linear array of four infrared light emitting diodes. In order to reduce interference from external optical sources, the photodiode array is covered by a piece of red plastic taken from a display bezel, and shielded with a closed-ended tube, in which end a slit has been cut of width sufficient to admit the LED illumination but block most other external light.

In initial work, the individual photodiode currents were used to study the uniformity of illumination, but in operation, all sixteen currents are summed together at the virtual ground input of a transresistance amplifier. The vertical spacing of the LEDs was adjusted to achieve the minimum nonuniformity, but a significant amount remains. Because of this, the sensor output is not purely linear with ball position.

This uniformity is measured by making use of a test fixture which is depicted in Figure 2.

Here a test ball is glued into an adapter ring which connects it with a piezoelectric load cell which is itself mounted on an adapter ring which is epoxied onto the anvil of a differential thread micrometer. With this fixture, the ball can be vertically translated with a resolution of better than 10 μm . Simultaneously, the force acting on the ball can be measured via the load cell. Because the piezoelectric load cell is very stiff, the combined system has a resonant frequency of about 5 kHz, which allows the load cell output to be interpreted as measuring applied force for all frequencies of interest. Force measurements are described in more detail in Section 4. Here, the test fixture was used to set a known air gap, and thereby calibrate the position sensor. Because the ball enters the beam from below, the test fixture does not interfere with the optical path when performing this calibration.

Measurements of the uncorrected sensor output indicate a deviation from the best-fit straight line of about ± 1 mm. Samples of the measured data are stored in a table in the control computer, and used to linearly interpolate position, in order to remove this deviation. The controller samples the sensor voltage and updates the control law output at a 1 kHz rate. At each sample, the data table is used to interpolate position by using a bisection algorithm. This corrected position is fed to the lead compensation block and thus to the rest of the loop.

Following this correction, the sensor corrected output shows deviations from a best-fit straight line of about ± 0.1 mm. The largest remaining error term is due to instability of the LED intensity, primarily with respect to temperature. This instability limits the accuracy of the data table used for interpolation. In future implementations, it would be advantageous to design a sensor in which absolute intensity is not of first-order importance to the measurement. One approach would be to use a lateral effect photocell, in which the location of the illumination rather than its intensity is the important parameter. In any case, the sensor linearity is satisfactory for the current purposes.

3 Power Amplifier

A schematic for the solenoid current drive is shown in Figure 3. The power amplifier is of the

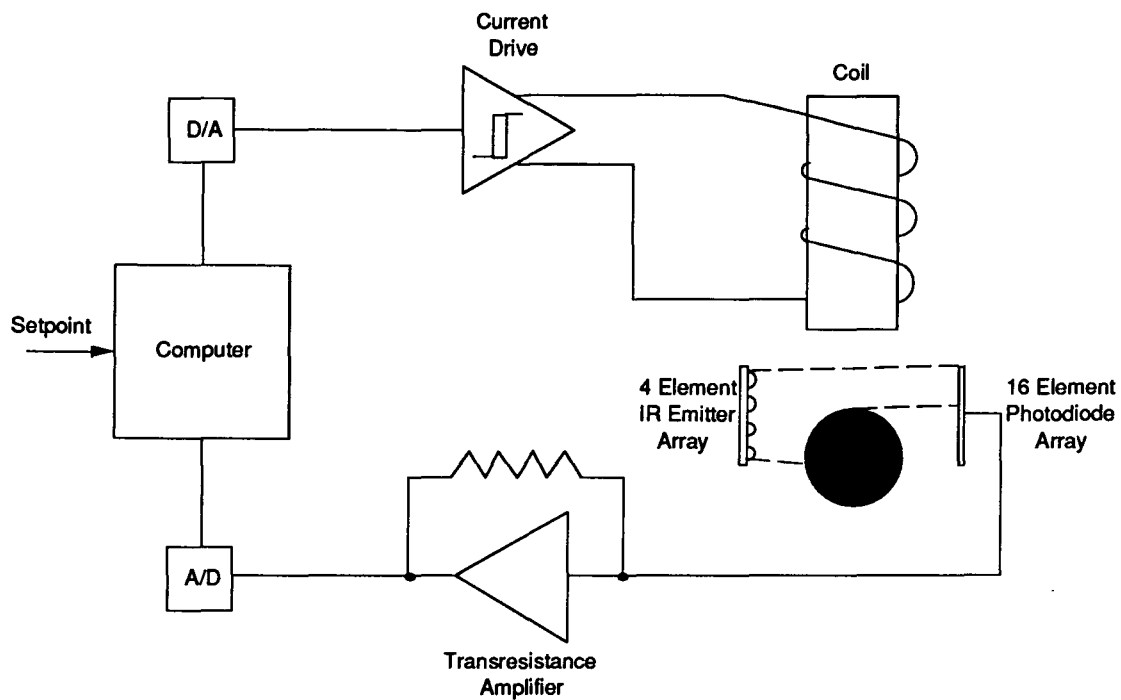


Figure 1: Control loop block diagram.

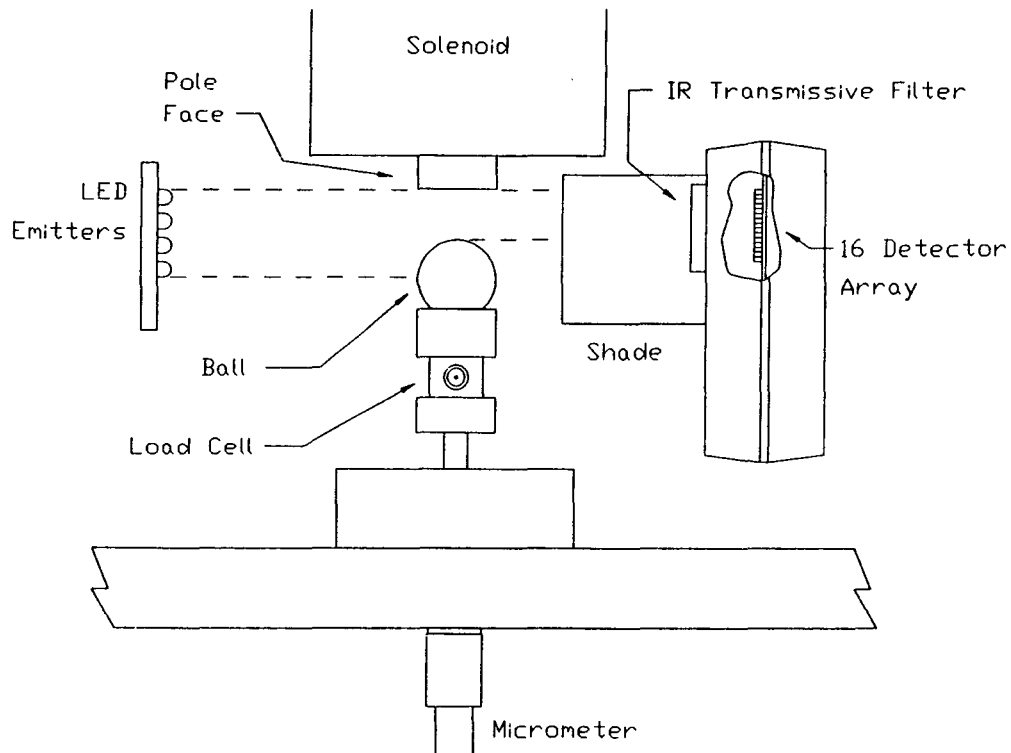


Figure 2: Micrometer and load cell fixture.

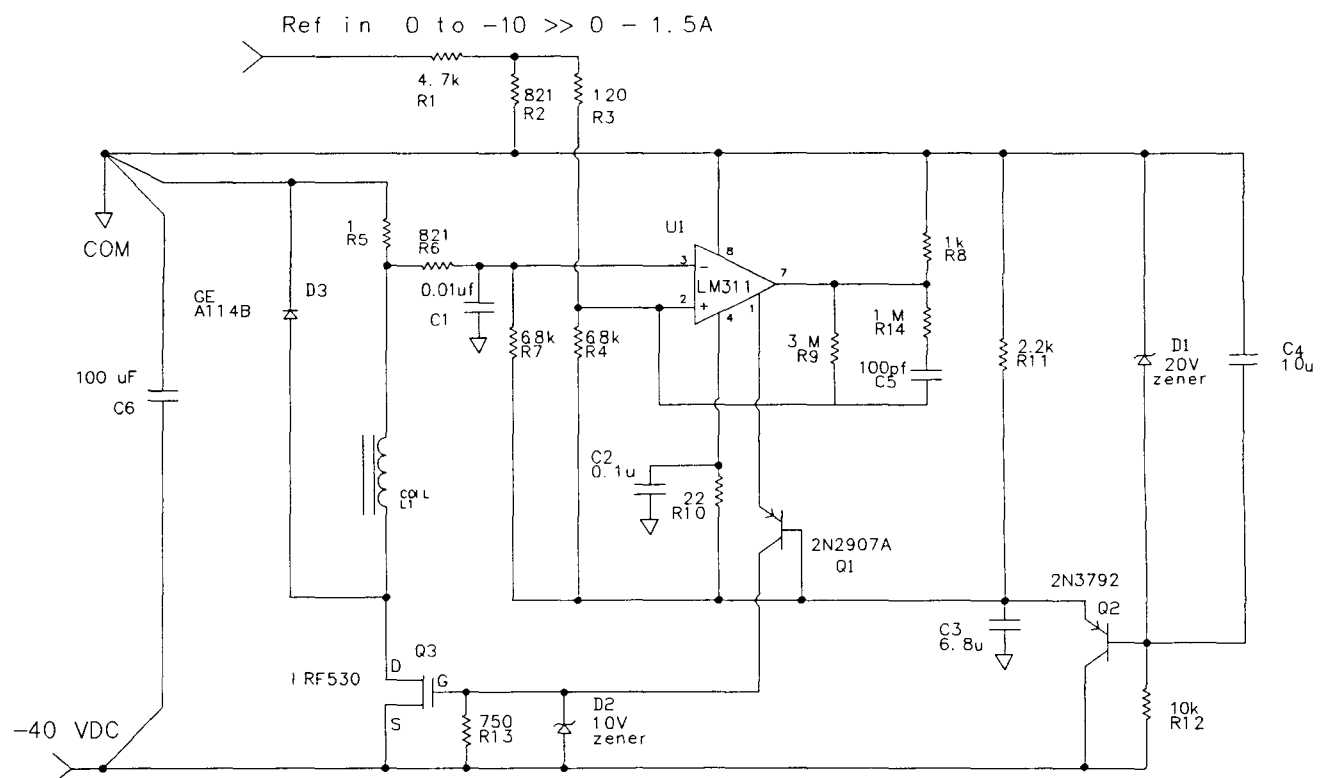


Figure 3: Current drive schematic.

hysteretic type. A comparison of this type of converter to sample/hold and minimum pulse width converters is given in [11]. The operation of the amplifier is described as follows.

The coil voltage is controlled by transistor Q_3 acting as a switch. When Q_3 is on, 40 volts is applied to the coil, thereby increasing the coil current. When Q_3 is off, the coil current freewheels through the flyback diode D_3 , thereby decreasing the coil current. The switching of Q_3 is controlled by comparator U_1 through the common base transistor Q_1 which provides level shifting, and the gate-network D_2 – R_{13} which limits the gate voltage to 10 volts when Q_1 is on and provides a turn-off path when Q_1 is off.

Comparator U_1 switches on and off based upon the difference between the reference level as scaled by the input network R_1 – R_4 and the actual current level as measured by sense resistor R_5 . The switching has a hysteretic component determined by the feedback network R_9 , R_{14} , and C_5 . Components R_{14} and C_5 are included to eliminate a burst of oscillation which occurred on the comparator switching transients and which resulted in undue heating of the power FET Q_3 . The R_6 – C_1 low pass filter serves to attenuate spikes due to stray inductance in R_5 and feedthrough capacitance in the solenoid coil L_1 . Without this filter, the supply oscillates at about 1 MHz.

A goal of this design is to operate with only a single external power supply. Thus transistor Q_2 and its bias network are used to supply -20 volts to the low side of comparator U_1 . Through resistors R_7 and R_4 this -20 volt supply is used to offset the comparator input voltages to within the allowable common mode range of the comparator. Resistors R_7 and R_4 are adjusted relative to the values in the rest of the input network in order to reject changes in the -20 volt supply level. This prevents transients on the -20 volt supply from disturbing the switching thresholds. One additional consequence of the chosen topology is that the reference voltage must go negative to set an increase in the coil current.

The solenoid consists of 3500 turns of #22 wire, with a room temperature resistance of $R_L = 28$ Ohms. This resistance rises to about $R_L = 33$ Ohms at the typical operating temperature ($i_L = 0.6$ A). If the solenoid is alternately switched between 0 and 40 Volts, the resulting current waveform has an exponential time constant of about 60 msec, implying a low-frequency coil inductance of about 2 H. However, based upon measurements at the 10 kHz supply mid-point operating frequency, the coil demonstrates a high-frequency incremental inductance of 200 mH. This value is used in the analysis which follows.

In operation, the coil current will oscillate between a low-threshold current I_1 and high-threshold current I_2 . This oscillation will take the form of an asymmetric triangle wave, with I_1 and I_2 set by the reference voltage and the amount of comparator hysteresis. Neglecting the flyback diode voltage drop, the cycle time T for this oscillation is given by

$$T = -\tau \ln \left(\frac{I_1(I_F - I_2)}{I_2(I_F - I_1)} \right) \quad (1)$$

where $\tau = L_1/(R_5 + R_L)$, and $I_F = 40/(R_5 + R_L)$ is the full scale current which results if the switch Q_1 remains closed. For the design values,

$$I_1 = -0.1488V_{ref} - 5.605 \times 10^{-3} \quad (2)$$

and

$$I_2 = -0.1488V_{ref} - 9.766 \times 10^{-4} \quad (3)$$

There is thus $I_2 - I_1 \approx 4.6$ mA of switching ripple, and the current remains within about 2.3 mA of the setpoint for all inputs which do not exceed the current slew rate limit imposed by the finite supply voltages. This latter limitation has a significant impact on closed-loop operation as discussed in Section 5.

The switching frequency is given by $1/T$. Using the results from (1)–(3), the switching frequency as a function of average current $(I_1 + I_2)/2$ is calculated and compared to the measured frequency in Figure 4. Note that the frequency is zero at both zero and full-scale currents, and peaks at about the mid-scale current. The measured frequency was recorded as the current was increased from zero to full scale, and closely matches the calculated frequency. However the actual frequency exhibits significant hysteresis dependent upon the time history of supply current. This effect is due to the magnetic hysteresis in the solenoid core, and can be as large as 2 kHz at the maximum frequency point.

4 Force Measurements

The electromagnet force as a function of position and current is measured with the load cell and micrometer fixture which was used to calibrate the optical sensor. With the micrometer at a fixed position, the electromagnet current is cycled from zero to full scale and then back to zero, with a triangular time dependence. Over multiple cycles, the load cell amplifier output is measured at about 200 points within each cycle and averaged at each point over the multiple cycles. The form of the resulting data is shown in Figure 5.

The force curves exhibit significant hysteresis, which is due to using cold-rolled steel as the core material. In future designs, a magnetically-softer material should be used. Also note that the hysteresis curves have essentially constant width in current, independent of air gap. This is explained by the fact that the ball is only weakly coupled to the core and thus the core flux is largely independent of ball position.

The measured force rises as the square of current for low currents, as would be predicted by a first order field analysis, and then rises less strongly at higher currents, due to saturation in the core. In the low-current region ($i < 0.4$ A), the force is well modeled by

$$F = C \left(\frac{i}{x + 0.0025} \right)^2 \quad (4)$$

where F is the electromagnet force in Newtons, i is the coil current in amps, x is the air gap in meters, and $C = 6.5 \times 10^{-4}$ Nm²/A². Note that the actual air gap plus 2.5 mm is used in this law. This accounts for the fact that the force does not become infinite at zero air gap. Beyond 0.4 Amps, saturation becomes significant, and a more complex model is required.

The force curves exhibit significant hysteresis, which is due to using cold-rolled steel as the core material. In future designs, a magnetically-softer material should be used. Also note that the hysteresis curves have essentially constant width in current, independent of air gap.

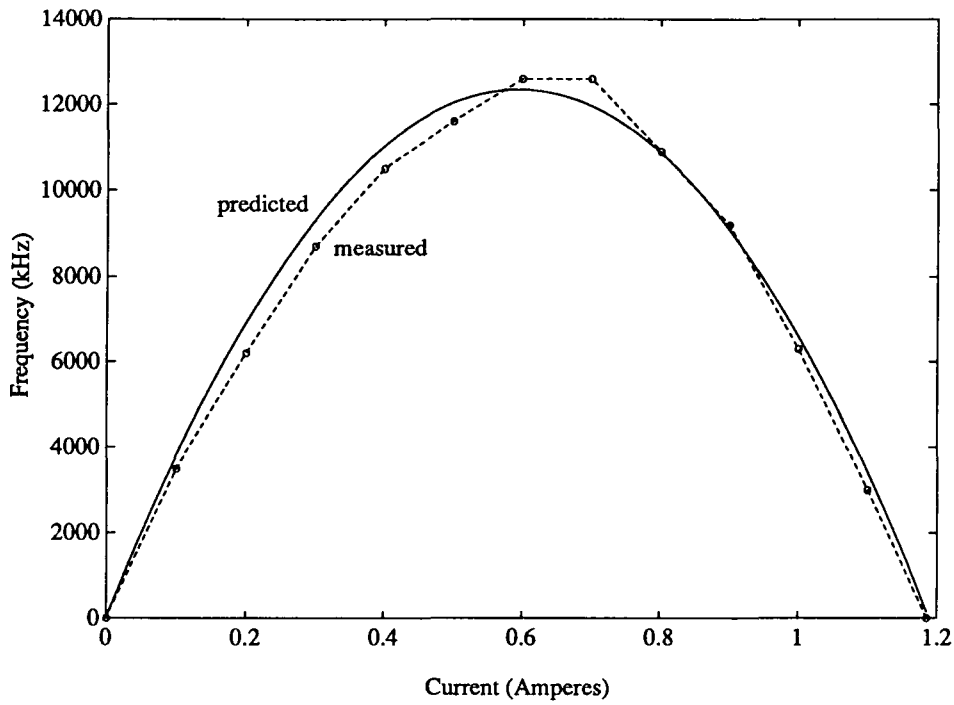


Figure 4: Switching frequency as a function of current.

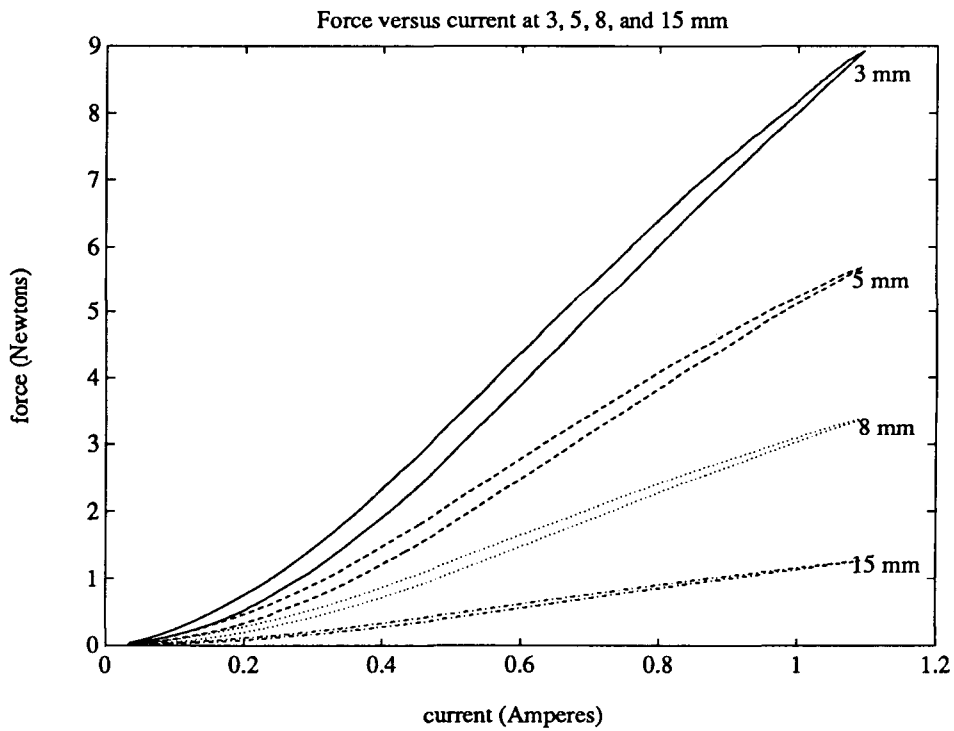


Figure 5: Uncompensated electromagnet force as a function of current at air gaps of 3, 5, 8, and 15 mm.

This is explained by the fact that the ball is only weakly coupled to the core and thus the core flux is largely independent of ball position.

However, this model is not developed in the i - F plane, since for the present purpose of nonlinear compensation what is required is a function which, given the air gap x and a desired force F_d , yields the current in Amperes necessary to realize this force. At low forces relative to the air gap, this function is found by inverting (4), and thus increases linearly with air gap and as the square root of desired force. At higher forces, the current must grow more strongly with desired force. A reasonable fit to the data has been empirically found to be

$$i_s = (x + 0.0025)\sqrt{\frac{F_d}{C}} + \left(0.0195e^{\left(\frac{x-0.002}{0.006}\right)} - 2.5(x - 0.01)\right) F_d + 400(x - 0.002)^2 F_d^2 \quad (5)$$

This function fits the data well over the operating range of the suspension.

The quality of the fit achieved by (5) is determined experimentally by writing a test program which cyclically ramps the desired force up and down while measuring the actual force with the load cell fixture. The results of this experiment are shown in Figure 6. The four traces shown in the figure are for air gaps of 3, 5, 8, and 15 mm; these traces essentially overlay, showing the success of the compensation (5). There is however, an error of about 10% in the gain, and the force drops off slightly from a straight line at high current and the smaller air gaps. The source of the gain error has not yet been adequately identified, as the data has only recently been acquired. However, hysteresis represents the most significant error term, particularly at small air gaps, where the force hysteresis magnitude approaches the weight of the ball. As mentioned above, this error term can best be addressed by using a magnetically- softer core material.

The results of the above force modeling are used to design the nonlinear compensator, which is described in the next section.

5 Nonlinear vs. Linear Control

A block diagram for the nonlinear compensation control loop is shown in Figure 7. The blocks labelled Sensor Compensator, Lead Compensator, Gain, and Nonlinear Compensator are implemented in floating point arithmetic within the control computer, which is an 80386/80387-based system with a processor clock frequency of 20 MHz. The A/D and D/A converters both have 12-bit resolution, and reside on a circuit card within the computer. The current drive, electromagnet, and sensor have been described in detail above. The mass of the ball $M = 0.06$ kg times the acceleration of gravity g is equal to approximately 0.6 Newtons. This force sums with the electromagnet force as the input to the block labelled $1/Ms^2$ which has air gap x as its output.

All the blocks within the control computer algorithm are updated at a 1 kHz rate. The Nonlinear Compensation block implements (5) appropriately scaled for the 12-bit D/A converter, and for the algorithm air gap representation in millimeters. The anticipated gravity load of 0.6 N is added to the error signal to give $F_d = F_e + 0.6$ which is input to the Nonlinear Compensation block as the force to be maintained on the ball. Adding the gravity load at this

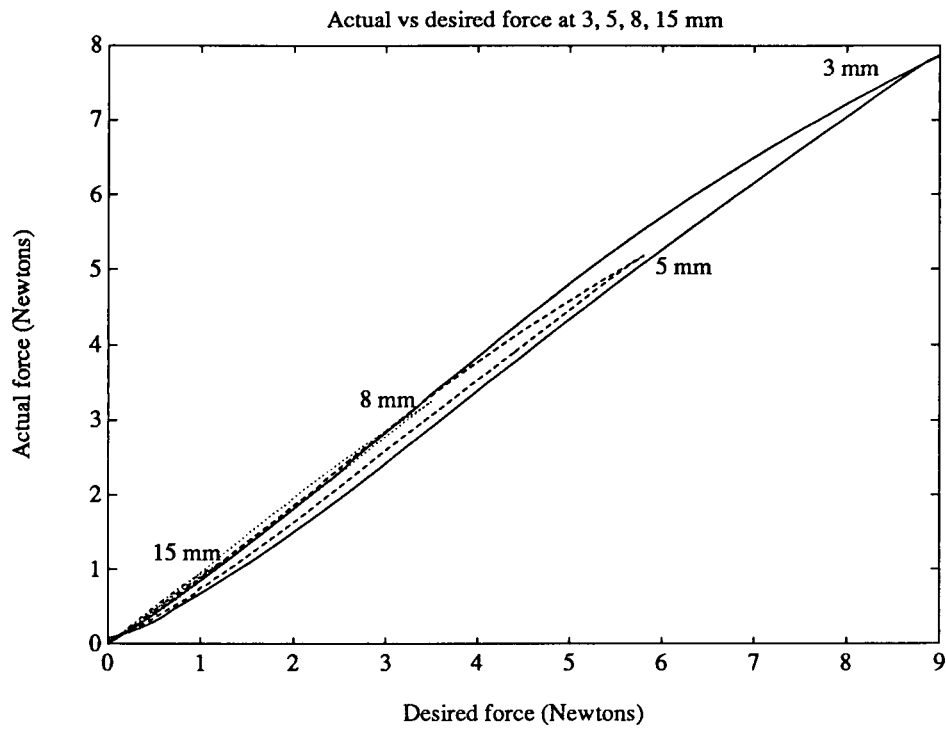


Figure 6: Compensated electromagnet force as a function of desired force at air gaps of 3, 5, 8, and 15 mm.

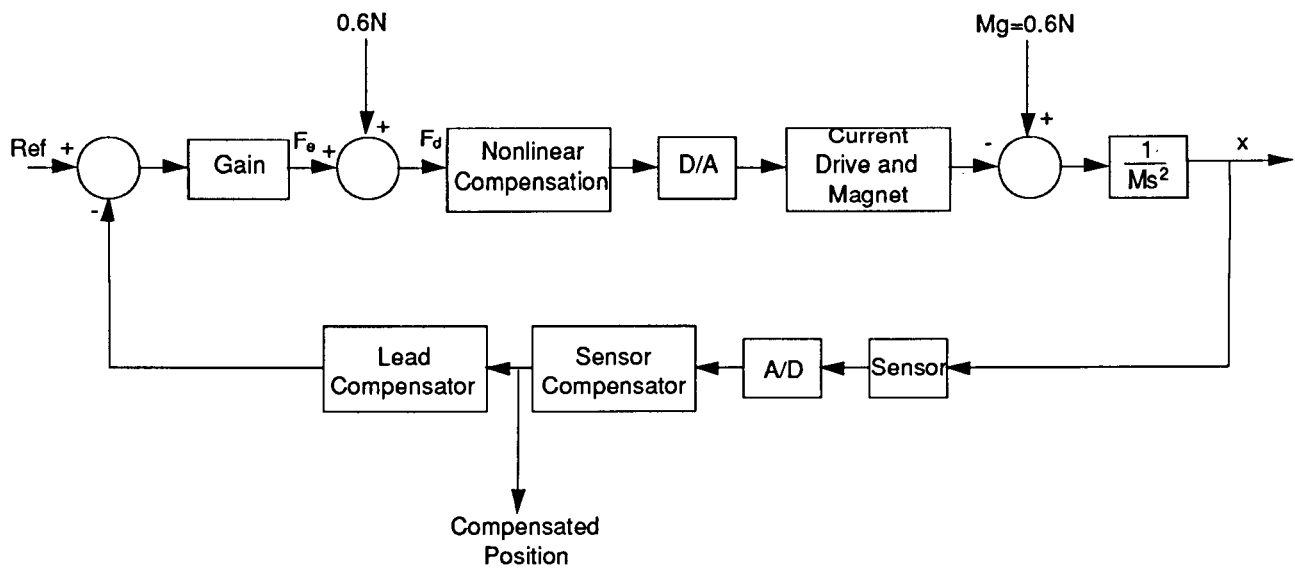


Figure 7: Nonlinear compensated control loop block diagram.

point greatly reduces the static error in suspension, since the loop uses only lead compensation and thus is of type 0. The reference signal is subtracted from the output of the lead compensator to yield the force error F_e . The loop lead compensation is placed in the feedback path in order to reduce the amplitude of the transient under step inputs as compared with placing the lead compensator in the forward path. The lead compensator has a zero at $z = 0.94$, a pole at $z = 0$, and a DC gain of unity.

The linear loop uses the same lead compensation singularity locations, but differs from the nonlinear loop in that the nonlinear compensation operation is replaced by a constant gain. Additionally, it is not possible to add a constant force offset term in the linear case. The error under Type 0 linear compensation has been found to reach 4–5 mm at the largest air gaps. Thus, in the linear compensation, the reference input is manually reset to achieve a desired air gap. All results are reported herein in terms of actual air gap.

A comparison of the loop performance under linear and nonlinear compensation is made as follows. At an air gap of 14.6 mm, both the linear and nonlinear compensator gains are adjusted to achieve essentially identical step responses with approximately 26 msec rise time. Then these gains are left unchanged as the air gap is set to 8.4 mm, 5.7 mm, and 3.7 mm. The resulting transients for the nonlinear and linear compensated systems are shown in Figure 8. In each of the figures, the top trace represents the compensated air gap as output by the Sensor Compensation block, with a sensitivity of 0.1 mm per division. Thus the steps shown represent a change in position of approximately 0.25 mm. The lower trace in each figure is the coil current as measured by a hall effect probe. This trace is AC coupled, and has a sensitivity of 50 mA per division.

As shown in the figures, the nonlinear compensated loop maintains a nearly constant step response as the air gap is reduced by about a factor of four, whereas the linear compensated loop performance deteriorates significantly. One measure of this change is the asymmetry between the positive going and negative going transients. Since the top trace represents the air gap which increases as the ball moves away from the pole face, the positive-going transient is associated with the ball moving away from the pole face, and likewise the negative-going transient is associated with the ball moving toward the pole face.

Another measure is the variation in rise and fall times as indicated on each trace. The rise and fall times for the nonlinear compensation loop remain symmetric at approximately 25 msec for all responses except at 3.7 mm where a small amount of asymmetry is visible, and the rise time increases slightly to about 29 msec. By comparison, the rise and fall times for the linear compensation loop change dramatically and exhibit significant asymmetry, as shown in the figure. The associated current traces also show significant asymmetry under the linear compensator, but remain symmetric under the nonlinear compensator. Note that as the air gap is reduced, the magnitude of the current transient decreases, since the incremental current-to-force gain of the electromagnet increases at smaller air gaps.

The transients shown in Figure 8 are the result of averaging 32 traces. This was done to eliminate a baseline limit-cycle noise of approximately 50 mV. The magnitude and dominant frequency of this noise depend strongly upon the controller gain, lead-zero location, and operating point air gap. The cause of this limit cycle has not yet been thoroughly

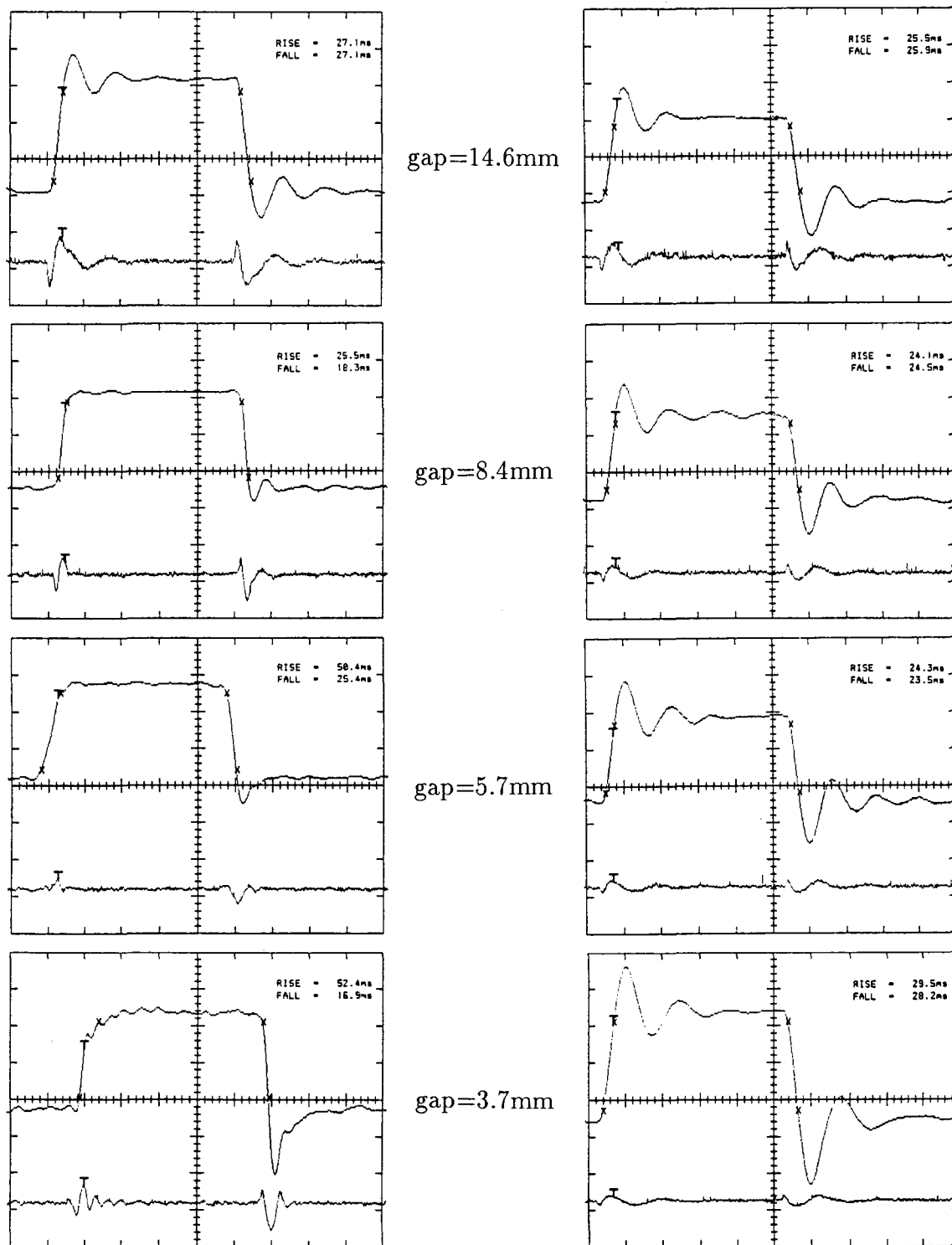


Figure 8: Step responses of linear and nonlinear compensated loops at air gaps of 14.6, 8.4, 5.7, and 3.7 mm (top to bottom). Left column shows response with linear compensator. Right column shows response with nonlinear compensator. In both columns, the top trace is incremental air gap, 0.1 mm/div, and the bottom trace is coil current, 50 mA/div. The time base is 100 msec/div for all traces.

investigated; however it is believed to be due to the finite quantization levels of the 12-bit converter used in these experiments. This is physically reasonable, since for the ± 10 volt range of the converter, the least significant bit represents about 5 mV, and thus the limit cycle entails a total span of about 10 least significant bits. For an open-loop unstable system such as this suspension, some amount of limit cycling is inevitable in the presence of amplitude quantization. A describing-function analysis of the quantized loop and simulation experiments are planned to verify quantization as the cause of this behavior.

Another destabilizing effect, which can be observed if the current trace is examined in detail, is voltage saturation of the current drive. The current drive operates from a unipolar 40 volt supply. Thus, especially at small air gaps when the current required for suspension is small, the maximum negative slew rate is highly constrained. This slew rate limiting becomes significant when the ball is stepped towards the pole face. Initially, current is increased to draw the ball toward the pole face, but then must be rapidly decreased to stop the ball at its new closer position. If the current cannot be rapidly decreased, the ball strongly overshoots. This effect contributes significantly to the asymmetric transients observed for the linear compensator in Figure 8, and also can degrade the stability of the nonlinear compensated loop if the gain is increased much above the value used in Figure 8. In the describing function sense, the lagging current which occurs in saturation adds negative phase shift which degrades the loop stability.

At small air gaps, the current source voltage saturation can lead to loss of control as shown in Figure 9. Here, the linearly compensated system is operating at a gain higher than that shown in Figure 8, but still within the short-term stability boundary. However, once every few minutes, stability is lost. The trace shown in this figure captures that process. The transient is negative-going, and thus toward the pole face. As the transient is initiated, the current is increased to draw the ball upward, and then enters voltage saturation in which the current source power FET is shut off for approximately 30 msec, during which time the trace takes the form of a decaying exponential, since the coil voltage is constant and equal to zero minus the flyback diode voltage drop. In the second and later transients, the current actually does reach zero. By this process, the ball diverges from suspension.

To avoid this effect, it is clear that the current source must be modified to be capable of applying bipolar voltages to the coil. This can be accomplished within the framework of the present hysteretic design by replacing the single power FET with an H-bridge driver. These are available from a number of manufacturers in integrated form.

6 Conclusions and suggestions for further work

The experimental results presented herein demonstrate the effectiveness of using nonlinear compensation for variable reluctance magnetic suspensions. Several improvements are suggested within the text. The most significant of these is to adopt a current source which has a bipolar voltage capability, so as to avoid the current slew-rate saturation which has been shown to destabilize the loop under certain conditions. The quantization-driven limit cycles which were observed require more investigation; it is likely that a higher-resolution

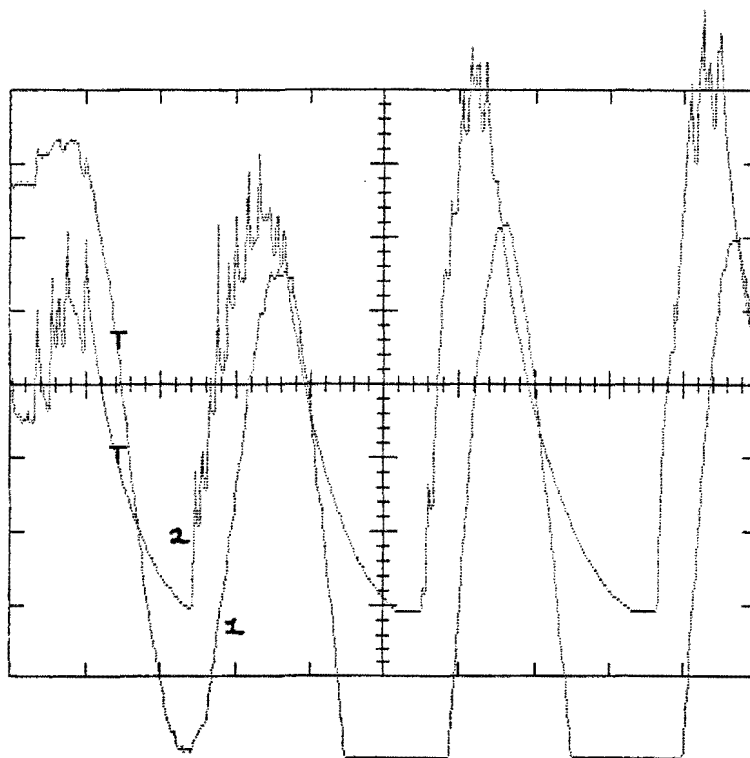


Figure 9: Loss of suspension due to current source voltage saturation. Trace 1 is position at 0.05 mm/div, and trace 2 is current at 20 mA/div. The time base is 20 msec/div.

converter would reduce the magnitude of these cycles. The core should be replaced with a lower-hysteresis material in order to improve the accuracy of the force correction. At very small air gaps (< 1 mm), this remanent magnetization is sufficient to lift the ball, and control is lost. Also, the pole face should be made somewhat conical, in order to more strongly center the ball. At very small air gaps, the ball was observed to pull out to the corner of the pole face where the field is more concentrated. Finally, the optical sensor stability could be improved, perhaps by using a lateral effect photo-sensor.

7 References

- [1] Slotine, J. E., and Li, W., *Applied Nonlinear Control*, Prentice-Hall, 1991
- [2] Spong, M., and Vidyasagar, M., *Robot Dynamics and Control*, Wiley, 1989, pp. 259-283.
- [3] Su, R., "On the linear equivalents of nonlinear systems," *Systems and Control Letters*, vol. 2, No. 1, pp. 48-52, July, 1982.
- [4] Hunt, L.R., Su, R., and Meyer, G., "Global Transformations of Nonlinear Systems," *IEEE Transactions on Automatic Control*, Vol. AC-28, No. 1, Jan., 1983.
- [5] Jayawant, B.V., Hodgkinson, R.L., Wheeler, A.R., and Whorlow, R.J., "Transducers and Their Influence in the Design of Magnetically Suspended Vehicles," *I.E.E. Conf. on Control Aspects of New Forms of Guided Land Transport*, I.E.E. Publication No. 117, Aug., 1974, pp. 200-206.
- [6] Jayawant, B.V., Sinha, P.K., Wheeler, A.R., and Whorlow, R.J., "Development of 1-ton Magnetically Suspended Vehicle Using Controlled D.C. Electromagnets," *Proc. I.E.E.*, Vol. 123, No. 9, Sept., 1976.
- [7] Groom, N.J., and Waldeck, G.C., "Magnetic Suspension System for a Laboratory Model Annular Momentum Control Device," *AIAA Paper No. 79-1755*, 1979.
- [8] Traxler, A., Meyer, F., and Murbach, H., "Fast Digital Control of a Magnetic Bearing with a Microprocessor," *International Kongress Mikroelektronik*, Munich, Nov 13-15, 1984, pp 94-102.
- [9] Trumper, D.L., "Magnetic Suspension Techniques for Precision Motion Control," Ph.D. Thesis, Dept. of Elec. Eng. and Comp. Sci., M.I.T., Camb., Mass., Sept., 1990.
- [10] Trumper, D.L., "Nonlinear Compensation Techniques for Magnetic Suspension Systems," *NASA Workshop on Aerospace Applications of Magnetic Suspension Technology*, Hampton, VA, Sept. 25-27, 1990.
- [11] Keith, F. J., et al. , "Switching Amplifier Design for Magnetic Bearings," *Proceedings of the Second International Symposium on Magnetic Bearings*, Tokyo, Japan, July 12-14, 1990, pp. 211-218.

CONTROL CONCEPTS
FOR
ACTIVE MAGNETIC BEARINGS

R. SIEGWART^{1,2}, D. VISCHER¹, R. LARSONNEUR^{1,2},
R. HERZOG¹, A. TRAXLER², H. BLEULER¹, G. SCHWEITZER¹

¹ Mechatronics Lab, Swiss Federal Institute of Technology (ETH), 8092 Zürich, Switzerland

² MECOS Traxler AG, CH-8400 Winterthur, Switzerland

Active Magnetic Bearings (AMB) are becoming increasingly significant for various industrial applications. Examples are turbo-compressors, centrifuges, high-speed milling and grinding spindles, vibration isolation, linear guides, magnetically levitated trains, vacuum and space applications. Thanks to the rapid progress and drastic cost reduction in power- and micro-electronics, the number of AMB applications is growing very fast.

Industrial use of AMBs leads to new requirements for AMB-actuators, sensor systems and rotor dynamics. Especially desirable are new and better control concepts to meet demands such as low cost AMB, high stiffness, high performance, high robustness, high damping up to several kHz, vibration isolation, force-free rotation and unbalance cancellation.

This paper surveys various control concepts for active magnetic bearings and discusses their advantages and disadvantages. Theoretical and experimental results are presented.

1. INTRODUCTION

Basics and feasibility of Active Magnetic Bearings (AMBs) were first shown by Beams, Young and Moore in 1946 [Beams et al. 46]. Considerable progress has been made since, though the basic principle is still the same.

This basic principle gives no general information on how the displacement is measured, how the controller is designed or how the AMB-actuator (electromagnetic coil) is controlled.

Up to now, most AMB-systems made use of **current** amplifiers to drive the electromagnetic coils and mainly **analog PD / PID controllers** were applied.

For today's and tomorrow's demanding AMB-applications, new **control concepts** for the actuator and the main controller have to be taken into consideration.

The AMB controller design can be divided into two levels. The first level involves the choice of the input and output variables of the AMB-actuator. This can be denoted as the "**actuator control configuration**". The following rough classification can be made:

- current control
- voltage control
- flux measurement and flux density control
- "self-sensing" control (operation without displacement sensor)

The second level is concerned with the "**main controller**" itself, i.e. the relation between measured signals and actuator input signals. Design approaches for the main controller are:

- PD, PID (root locus)
- LQR, LQG, pole placement (observer based)
- direct low order controller design (SPOC-D, chapter 4.3)
- H^∞ and other frequency-domain methods

Furthermore, a so called "feed forward controller" can be added to the standard feedback loop. This subject is not addressed in this paper.

Prior to the choice of the actuator control configuration and the controller layout, the AMB-engineer should carefully analyze and optimize the configuration of the plant (rotor). The configuration of the plant is basically given through the observability, the controllability, the structural dynamics and the AMB-actuator design [Keith et. al 90], [Siegwart et al. 90]. These aspects are not addressed in this paper.

Starting with the general model of the AMB-actuator (section 2), different actuator control configurations are outlined (section 3). The principles of current, voltage, flux-density and self-sensing control are described, and their advantages and disadvantages are discussed.

Section 4 gives a general overview on the design specifications of the main controller and the different controller layout approaches. PD/PID controllers are widely used low order controllers for applications where performance requirements are not very demanding. For high performance requirements, observer based LQR/LQG regulators are well suited. However, there is still a computational on-line burden because of high order and full coupling in the MIMO case. To close the gap, a tool for direct low order controller design (SPOC-D, chapter 4.3) is shown. Demanding applications, e.g. high performance control of flexible shafts, lead to sophisticated control specifications, mostly in frequency domain. This is the motivation for H^∞ control (chapter 4.4).

Some of the new concepts for actuator control configurations and main AMB controller design discussed in this paper are already used at the Swiss Federal Institute of Technology (ETH) and by the Swiss AMB system manufacturer MECOS Traxler AG. Theoretical and experimental results are presented in section 5.

2. THE BASIC AMB-EQUATIONS

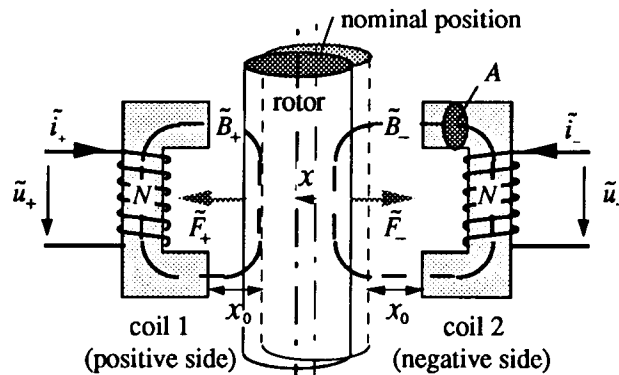


Figure 1: Notations for a two-sided actuator with one mechanical degree of freedom, rotor displacement x . A displacement to the left is defined positive, for $x=0$ the air gaps are x_0 . More symbols are listed in table 1 on the next page.

The basic AMB equations are obtained from Maxwell's laws [Breinl 80], [Traxler 85], [Vischer 88]. The derivations are not shown here. Neglecting secondary effects such as copper resistance, stray fields and saturation, and assuming that the complete energy of the magnetic field is concentrated within the active air gap, we get the following well-known equations for an AMB:

According to figure 1 and to the notation in table 1 we find an electromagnetic force F proportional to the square of the current i in the coil divided by the air gap. The force can also be described by the flux density B .

$$\begin{aligned}\tilde{F}_+ &= \frac{N^2 A \mu_0}{4} \frac{\tilde{i}_+^2}{(x_0 - x)^2} = \frac{A}{\mu_0} \tilde{B}_+^2 \\ \tilde{F}_- &= \frac{N^2 A \mu_0}{4} \frac{\tilde{i}_-^2}{(x_0 + x)^2} = \frac{A}{\mu_0} \tilde{B}_-^2\end{aligned}\tag{2.1}$$

The relation for the voltage u in the coil can be found as

$$\begin{aligned}\tilde{u}_+ &= \frac{N^2 A \mu_0}{2} \frac{d}{dt} \left(\frac{\tilde{i}_+}{x_0 - x} \right) = NA \frac{d}{dt} (\tilde{B}_+) \\ \tilde{u}_- &= \frac{N^2 A \mu_0}{2} \frac{d}{dt} \left(\frac{\tilde{i}_-}{x_0 + x} \right) = NA \frac{d}{dt} (\tilde{B}_-)\end{aligned}\quad (2.2)$$

Usually AMB actuators are operated around a constant operating point. The operating point is defined through the following nominal values:

$$x_0, i_0, B_0 = \frac{N \mu_0 i_0}{2 x_0}, u_0 = 0$$

Around the operating point the relations for the AMB actuator can be linearized for $x \ll x_0$ and $i \ll i_0$:

$$\begin{aligned}\tilde{F}_+ &= \frac{L_0 i_0^2}{2 x_0} + \frac{L_0 i_0^2}{2 x_0^2} x + \frac{L_0 i_0}{2 x_0} i_+ = \frac{A}{\mu_0} B_0^2 + \frac{2A}{\mu_0} B_0 B_+ \\ \tilde{F}_- &= \frac{L_0 i_0^2}{2 x_0} - \frac{L_0 i_0^2}{2 x_0^2} x + \frac{L_0 i_0}{2 x_0} i_- = \frac{A}{\mu_0} B_0^2 + \frac{2A}{\mu_0} B_0 B_- \end{aligned}\quad (2.3)$$

$$\begin{aligned}u_+ &= \frac{d}{dt} \left(L_0 \frac{i_0}{x_0} x + L_0 i_+ \right) = NA \frac{d}{dt} B_+ \\ u_- &= \frac{d}{dt} \left(-\frac{i_0}{x_0} L_0 x + L_0 i_- \right) = NA \frac{d}{dt} B_- \end{aligned}\quad (2.4)$$

By arranging the AMB in axially opposed pairs of coils (figure 1), as it is usually done, the linearized force F and voltage u result in

$$F = \tilde{F}_+ - \tilde{F}_- = 2L_0 \frac{i_0^2}{x_0^2} x + 2L_0 \frac{i_0}{x_0} \left(\frac{i_+ - i_-}{2} \right) = k_s x + k_i i \quad (2.5)$$

$$u = \frac{u_+ - u_-}{2} = \frac{x_0}{2i_0} \frac{d}{dt} \left[2L_0 \frac{i_0^2}{x_0^2} x + 2L_0 \frac{i_0}{x_0} \left(\frac{i_+ - i_-}{2} \right) \right] = \frac{x_0}{2i_0} \frac{d}{dt} F \quad (2.6)$$

$$F = 2NA \frac{i_0}{x_0} \left(\frac{B_+ - B_-}{2} \right) = 2NA \frac{i_0}{x_0} B \quad (2.7)$$

$$u = NA \frac{d}{dt} \left(\frac{B_+ - B_-}{2} \right) = NA \frac{d}{dt} B \quad (2.8)$$

Substituting force and voltage in equation (2.5) and (2.6) by the corresponding quantities in equation (2.7) and (2.8), displacement x from the nominal position can be described as a function of B , i and u .

$$x = \frac{2}{N \mu_0} \cdot \frac{x_0^2}{i_0} \cdot B - \frac{x_0}{i_0} \cdot i \quad (2.9)$$

$$x = \frac{1}{L_0} \cdot \frac{x_0}{i_0} \cdot \int u dt - \frac{x_0}{i_0} \cdot i \quad (2.10)$$

Applying equation (2.9), the displacement signal x can therefore be directly calculated from the flux density B , measured for instance by a hall-effect sensor, and the current in coil i (chapter 5.1, [Zlatnik & Traxler 90]). Similarly, one could derive the displacement through current i and the integration of voltage u . From

control theory, however, it is known that the output of an integrator is not observable by its input. Thus it is not possible to reconstruct the air gap of a magnetic bearing by directly using equation (2.10). Nevertheless, it will be shown later (chapter 3.5) that, by closing the loop with the mechanical model, it becomes possible to stabilize the AMB-system by the measurements of u and i only.

| Operating point | | Basic bearing constants: | |
|----------------------------------|---|---|---|
| x_0 | : Nominal airgap | N | : Number of windings |
| i_0 | : Nominal current | A | : Iron cross-sectional area |
| $B_0 = \frac{N\mu_0 i_0}{2 x_0}$ | : Nominal flux density | $(\mu_0 = 1.257 \cdot 10^{-6} \text{ Vs / Am})$ | : permeability of air) |
| Variables (functions of time) | | Secondary bearing constants: | |
| \tilde{F}_+ ; \tilde{F}_- | : Electromagnetic force | $L_0 = \frac{N^2 A \mu_0}{2 x_0}$ | : Inductance at $x = \text{const.} = 0$ |
| \tilde{B}_+ ; \tilde{B}_- | : Flux density | $k_i = 2 L_0 \frac{i_0}{x_0}$ | : Force-current factor |
| \tilde{u}_+ ; \tilde{u}_- | : Voltage | $k_s = k_i \frac{i_0}{x_0}$ | : Force-displacement factor |
| $\tilde{i}_+ = i_0 + i_+$ | : Currents in the coils (corresponding relations for F, B and u) | | |
| $\tilde{i}_- = i_0 + i_-$ | | | |

Table 1: Notations

3. AMB-ACTUATOR CONTROL CONFIGURATION

An AMB-actuator usually consists of a pair of coils (fig. 1) and two power amplifiers. The actuator control configuration determines how the AMB-actuator is controlled. Starting with a general state space model of an AMB-system, the basic ideas of current, flux-density, voltage and self-sensing control are derived and discussed in this section.

State-Space Model

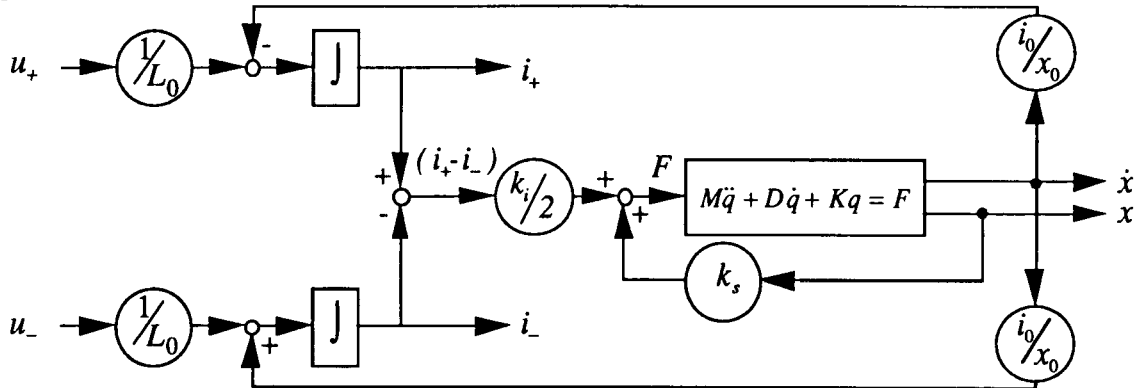


Figure 2: Linearized state-space model for one mechanical degree of freedom and two coils according to figure 1. The two currents (i_+ , i_-), in each coil of the bearing, rotor velocity \dot{x} and displacement x are selected as state variables.

The complete state-space model for the AMB system includes at least two mechanical states (velocity and displacement). In addition, each electromagnet contributes one state variable to the model. In the case of two-sided actuators (fig. 1), two state variables, for example the currents in the coils, are necessary for each mechanical degree of freedom to completely describe the behavior of the open loop system.

Figure 2 and 3 show the state-space model of an AMB actuator acting on a general mechanical system. For simplicity we assume in chapter 3, that the mechanical system is an unbound mass m with one degree of freedom x . According to Newton's law we get the following differential equation:

$$m\ddot{x} = F \quad (3.1)$$

(For a rigid body rotor, m would stand for an equivalent rotor mass effective at the actuator.)

The MIMO-system (*Multiple Input Multiple Output*) shown in figure 2 is observable from the current measurements i_+ , i_- alone. Using the voltage inputs u_+ , u_- , it is also controllable. This means that the **measurement of the rotor displacement x is not needed** for control.

This has been demonstrated in practical setups by Vischer and in several student projects at ETH [Jordil & Volery 90], [Colloti & Kucera 91]. A patent [Vischer, Traxler & Bleuler 88] has been applied for.

A simpler state space model is found choosing B_+ and B_- as state variables rather than i_+ and i_- (fig. 3).

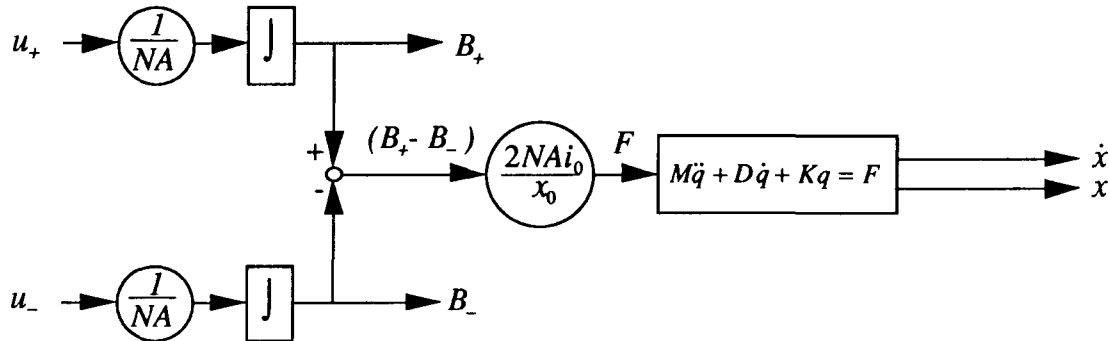


Figure 3: Linearized state-space model for one mechanical degree of freedom and two coils according to figure 1. The two flux densities (B_+ , B_-) in each coil of the bearing, rotor velocity \dot{x} and displacement x are selected as state variables.

3.1 Voltage Control

The state space models shown in figure 2 and 3 can now be used to design a bearing control with voltage instead of current as input variable. This will be called "voltage control". Voltage control has been investigated thoroughly by many authors [Ulbrich & Anton 84], often in the context of magnetically levitated vehicles (e.g. [Jayawant 81], [Breinl 80]).

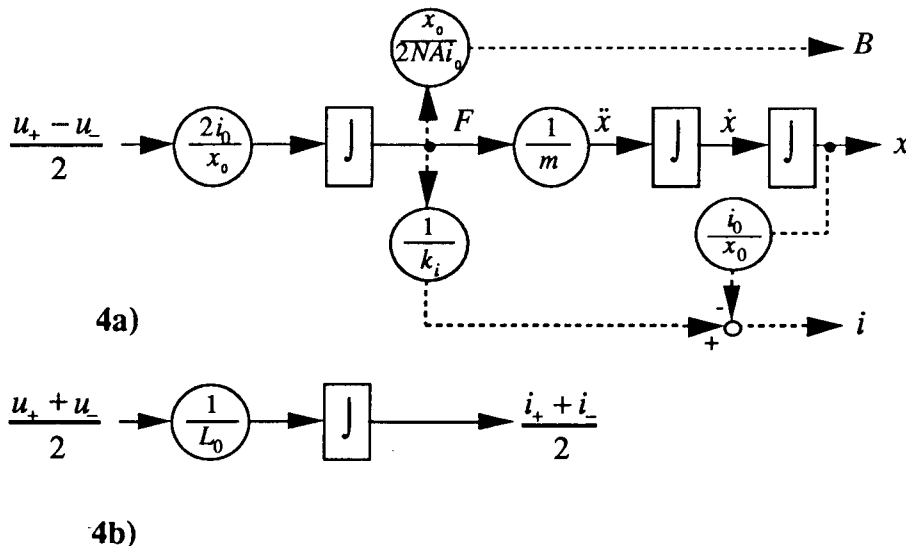


Figure 4: Transformed state-space model for the system of figure 2 with a single mass model of the mechanical system. This choice of state variables produces two decoupled subsystems, figure 4a (with states x , \dot{x} and F) and figure 4b with the single state variable $(i_+ + i_-)/2$. Figure 4b shows that the body movement only depends on the difference between the two input voltages u_+ and u_- , whereas the sum of the currents $i_+ + i_-$ is only a function of the sum $u_+ + u_-$.

The system of figure 2 is observable if at least two of the three outputs (i_+ , i_- and x) are available to the controller. The following two cases, both of which have some advantages for AMB applications, will be examined further:

- voltage control combined with three measurements (i_+ , i_- , and x)
- voltage control combined with the current measurements only ("self sensing" bearing)

The system of figure 3 is observable if x and either B_+ or B_- are available to the controller.

One way to control the above systems is to implement a Luenberger observer and a state feedback controller. The full state-feedback matrix has 8 coefficients (2 inputs, 4 states). Some additional control parameters are used for the Luenberger observer. Such controllers were built and tested at ETH.

As we deal only with a single mechanical degree of freedom, we seek to simplify this controller. It is possible to describe the plant (fig. 2 and 3) as a set of two SISO-systems (Single Input Single Output), as shown in fig. 4. If the four values $(i_+ + i_-)/2$, x , \dot{x} and F [Gottzein & Crämer 77] or [Gottzein et al. 77]) are used as state variables instead of i_+ , i_- , x and \dot{x} , the MIMO-system can be replaced by a 3rd order and a first order SISO-system. The transfer function of the first subsystem (fig. 4a) is

$$x = \frac{2i_0}{x_0 m} \frac{1}{s^3} u \quad (3.2)$$

which is a simple triple integrator. The transfer function of the second subsystem (fig. 4b) is

$$\frac{i_+ + i_-}{2} = \frac{1}{L_0} \frac{1}{s} \left(\frac{u_+ + u_-}{2} \right) \quad (3.3)$$

which is a first order system independent of the rotor movement.

Thus, a controller for the voltage-controlled bearing consists of two independent sub-controllers according to the two subsystems of figure 4. For the subsystem in figure 4b a simple proportional controller is suitable. Since its main function is to keep the premagnetization current $(i_+ + i_-)/2$ at a nominal value i_0 , we like to refer to it as "operating point controller".

The extension to a full order system with multiple mechanical degrees of freedom is straightforward. As seen before, each pair of opposing electromagnets is separated into two subsystems. The subsystem of figure 4b remains independent of the mechanical system.

The influence from one mechanical degree of freedom to another acts just like an **additional force input** at the corresponding summation points in figures 2 or 3. Decentralization, i.e. the implementation of local feedback based on a complete model, is feasible in most practical cases [Bleuler 84], with the obvious implications on the model order used for analysis. With such a layout approach, the on-line computing power requirements grow only proportional to the number of control channels.

In many cases, it is even possible to simplify one step further and to base control layout itself on a decentralized model, which brings us back to the simple models described in this chapter.

3.3 Current Control

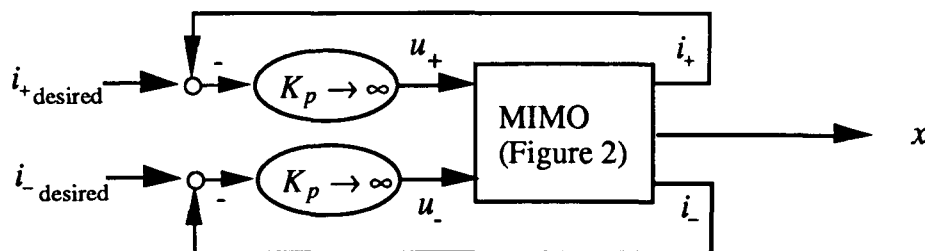


Figure 5: AMB-system with current controlled actuator

Strictly speaking, the term "current-controlled bearing" designates a special voltage-controlled bearing consisting of two current controllers as inner loops and a position control as outer loop. Because magnet current in reality is a state variable, the dynamics of the inner control loop is usually neglected for treatment of the outer loop with current as plant-input.

The inner control loops keep the two currents at their desired values, which is possible as long as the voltages are not saturated and the assumption of infinite inner loop gains K_P is legitimate. The transfer characteristic is given by equation (2.5) as

$$i_{+ \text{ desired}} = i_{+} \text{ and } i_{- \text{ desired}} = i_{-} \Rightarrow F = k_s x + k_i \left(\frac{i_{+} - i_{-}}{2} \right) = k_s x + k_i i \quad (3.4)$$

Equation (3.4) shows that the current controlled bearing can be interpreted as a "force-source", which is not entirely perfect due to the undesirable term ($k_s x$) corresponding to a spring with a negative stiffness k_s . This negative stiffness term only turns up in the context of current control.

3.4 Flux Density Control

Quite similar to the current control, the flux density measurements can also be used to directly control the flux densities B_{+} and B_{-} in the air-gaps to desired values by means of two inner loops, as shown in figure 6.

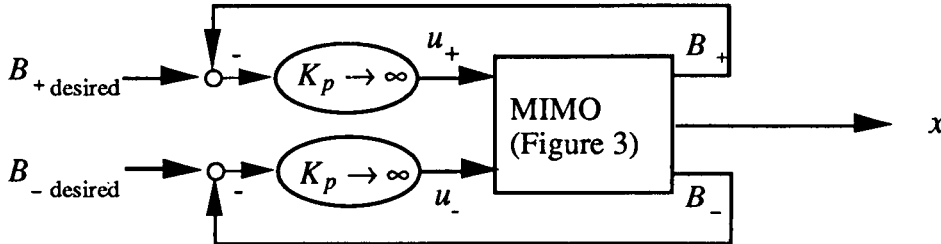


Figure 6: AMB-system with flux density controlled actuator

The behavior of the flux density controlled bearing is then given by equation 2.7.

$$B_{+ \text{ desired}} = B_{+} \text{ and } B_{- \text{ desired}} = B_{-} \Rightarrow F = 2NA \frac{i_0}{x_0} \left(\frac{B_{+} - B_{-}}{2} \right) = 2NA \frac{i_0}{x_0} B \quad (3.5)$$

The advantages of this actuator control configuration is that it yields an almost perfect "force-source" without the negative bearing stiffness associated with the current control. Furthermore the relation between force and flux density is linear, as opposed to current control and voltage control, where the assumed equations are only valid around the operating point and some other specific locations in the work space.

As we could see in equation (2.9), the displacement x can be calculated from the flux density and the current in the coil. This type of indirect displacement measurement is excellently suited for large air gaps (chapter 5.1).

3.5 Comparison of Actuator Control Configurations

Current control has the advantage that the two states associated with the two magnetic coils can be neglected under certain conditions (see chapter 3.3). It makes the design of the main controller a little easier (e.g. PD control is feasible).

When voltage control is employed, only one of the two states is taken care of by an inner actuator loop, whereas the second state has to be considered in the layout of the main controller.

Voltage controlled AMBs, however, have the advantages that the open loop system has no negative stiffness k_s (highly instable open loop system). It is known from control theory, that a highly instable open

loop system is very sensitive to time lag and noise in the measurement. Detailed description can be found in [Vischer 88]. Future comparison involving other criteria is shown in figure 7.

| Criteria | Voltage Control | Current Control | Flux Control |
|---|-----------------|-----------------|--------------|
| Sensitivity to Timelag in the Measurement | ⬆ | ⬇ | ⬆ |
| Sensitivity to Noise in the Measurement | ⬆ | ⬇ | ⬆ |
| Copper Resistance | ■ | ⬆ | ⬆ |
| Stray Field | ■ | ⬆ | ⬆ |
| Saturation of Iron | ⬆ | ⬇ | ⬆ |
| Validity of Linearization | ■ | ■ | ⬆ |

⬆ Advantage ■ Minor Disadvantage ⬇ Disadvantage

Figure 7: Comparison of actuator control configurations

Flux density control: *Force-source* (eq. 2.2)

Current Control: "*Force-source*" & negative stiffness (eq. 2.5)

Voltage control: "*Force derivative source*" if the the rotor is approximated by one mass (eq 2.7 and 2.8)

3.5 Self-Sensing AMB

The transfer function (3.8) from input $u=(u_+-u_-)/2$ to output $i=(i_+-i_-)/2$ nicely shows the operating principle and the feasibility of the self-sensing bearing.

$$i = \frac{\frac{1}{L_0} s^2 - \frac{2i_0^2}{x_0^2 m}}{s^3} u \quad (3.8)$$

Both transfer functions (3.3) & (3.8) are of full order; therefore it can be deduced that the voltage controlled AMB-plant is observable and controllable from the measurements of the current (i_+-i_-) and i only.

Figure 8 shows the corresponding simple state-space model.

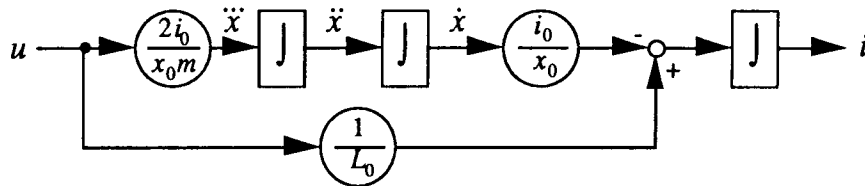


Figure 8: Transformed state-space model of the SISO-plant of figure 4 for self-sensing operation. (State variables: $i=(i_1-i_2)/2$, \dot{x} and \ddot{x}) This system together with the subsystem of figure 4b can be used to design a simple linear controller for the self-sensing bearing.

It can be shown, that the simplest linear main controller for the self-sensing bearing is

$$u = \frac{b_2 s^2 + b_1 s + b_0}{a_1 s + a_0} i \quad (3.9)$$

4. DESIGN OF THE MAIN CONTROLLER

The controller is generally a part of a mechatronic (electro-mechanical) system. It feeds back some sensed signals of the system to the actuators of the system. Thus, the controller is involved with the whole system and can never be regarded isolated. The system design starts with the design of the plant and the design and placement of the sensors and actuators, called control configuration. Next, an appropriate model of the system has to be derived and control layout specifications have to be defined. Thereby, the modelling and the control design cannot be treated as separate problems [Skelton 89]. After the controller layout, the controller has to be implemented and tested.

Thus, the main controller layout is only a part of the whole AMB-system design and has to be done in tight cooperation with rotor design, sensor and actuator design and placement, modelling and implementation. The good controller layout leads only to good performance if the system configuration (actuator, sensor, mechanical structure etc.) is optimized.

AMB-systems can usually be modelled as quite linear systems, even if the AMB-actuator is not absolutely linear. A suspended flexible structure can lead to a high order model. We therefore assume, that the plant, P , and the controller, C , are linear and time-invariant (LTI).

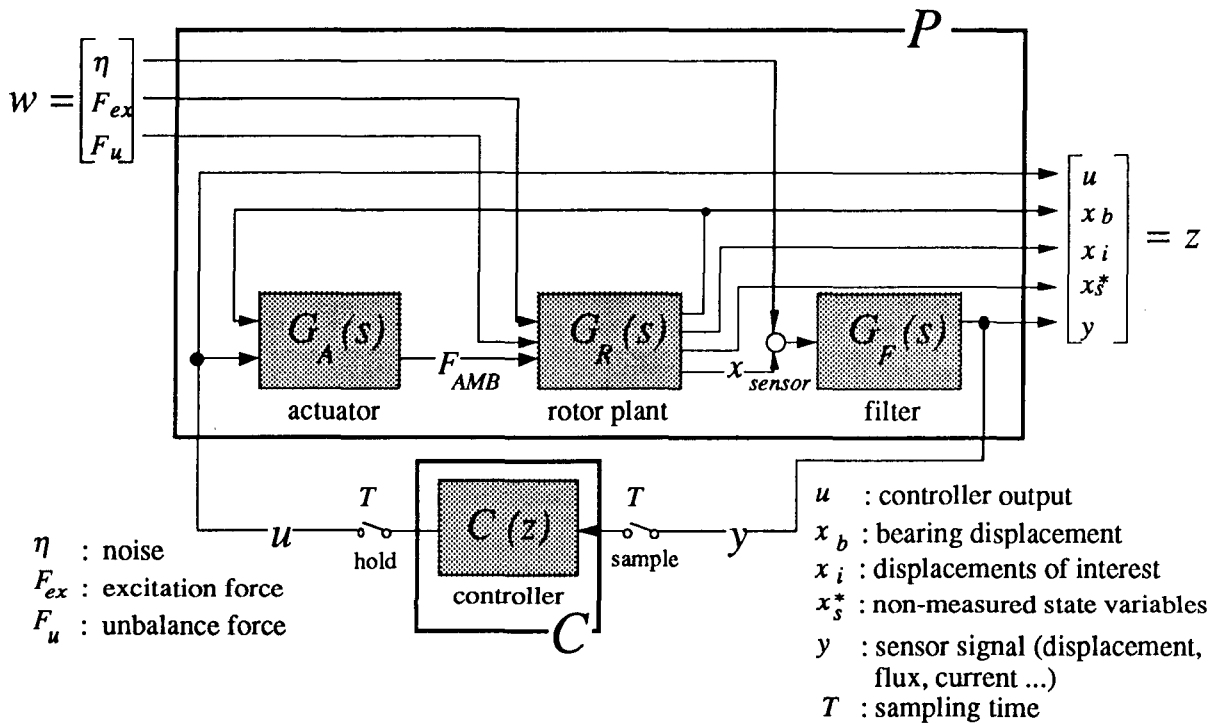


Figure 9: Block scheme of a typical AMB-system

Figure 9 shows a general AMB system, where $G_A(s)$ is the transfer matrix of the AMB-actuator, $G_R(s)$ that of the rotor plant (suspended body) and $G_F(s)$ that of the sensor and signal filtering. The transfer matrices $G_A(s)$, $G_R(s)$ and $G_F(s)$ describe the AMB-plant P . $C(z)$ is the transfer matrix of the controller C which has to be designed. The controller C is assumed to be time discrete.

The inputs to the plant are divided into two vector signals:

- The *actuator input vector* u , consisting of those inputs to the plant which can be manipulated by the controller.
- The *exogenous input vector* w , consisting of all other input quantities such as noise, excitation forces, etc.

The output of the plant consists of two vector signals:

- The *measured output vector* y , consisting of those measured signals which are accessible to the controller.
- The *regulated output vector* z , consisting of all outputs of interest such as actuator input, rotor displacements, measured and non measured state variables.

This notation of the plant includes more details about the AMB system than is common in classical control [Boyd et al. 90]. The exogenous inputs and regulated variables contain each signal subject to constraints or specification, whether it is measured or not.

Some general examples of specifications for AMB-systems can be found in the next paragraph.

4.1 Specifications for the Controller Layout

The controller layout of an AMB system is always restricted by different specifications. The specifications have to be defined by the AMB-engineer and include e.g. physical aspects of the plant and specifications on the system performance. Common examples are:

- closed loop stability
- maximum stiffness over a given frequency band [Herzog & Bleuler 90]
- limitation of the amplifier's bandwidth [Keith et al. 90], [Siegwart & Traxler 90]
- noise rejection, noise filtering
- force free rotation around the inertial axis [Higuchi et al 90]
- damping to cross critical speed
- vibration rejection
- robustness (changes in the plant, modelling errors, nonlinearities)

The constraints and specifications often define upper and lower bounds for the input-output behavior of the AMB-system shown in figure 9.

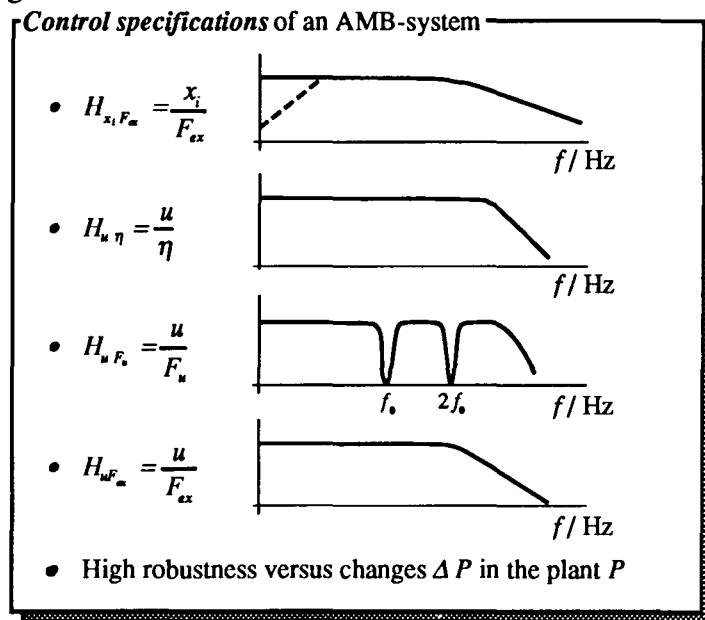


Figure 10: An example for the specifications given for an AMB system.

Possible specifications of input-output transfer function of AMB-systems are shown in figure 10. Unfortunately, the different specifications often are in opposition to each other. It is up to the talented control engineer to find an acceptable compromise. After defining the bounds of the controller layout, different *design tools* help to find an optimal solution to the control problem.

4.2 On Different Controller Design Approaches

Modern AMB controllers will almost certainly make use of digital control with its well-known advantages such as large flexibility in controller structure changes during machine installation or easy implementation of additional controller features ("feedforward" control, automatic adaptation to changing plant parameters, machine monitoring etc.).

In the process of controller design, the control engineer has either to find a control law that meet the design specifications (chapter 4.1) or determine that none exists. If there is no controller meeting the specifications, the control engineer has to change the specifications and/or the system configuration. Thus, a good controller design tool should allow an account of all design specifications of the given design problem and consider the specific control configuration of the system.

Specific control features of AMB systems are:

- only very few system states, most often the displacements at the coils, are measured.
⇒ observer based controller (LQG, LQR, H^2 , H^∞)
- the controller often has to be of much lower order than an adequate plant model
⇒ direct low order controller design (PD, PID, SPOC-D)
- many control specifications have to be considered (see chapter 4.1)
⇒ H^∞ , 'convex optimization' of the class of all stabilizing controller, SPOC-D

Many different control approaches for linear and time-invariant (LTI) are available and it is up to the control engineer to choose the most appropriate to solve his control problem. Some of them, namely the PD, PID, LQG, LQR and the more advanced direct low order controller design (SPOC-D) and H^∞ methods are discussed in the following.

PD, PID controller layout

PD and PID controllers are the most common and most used controllers. The basic idea is to use a feedback similarly to 'a mechanical spring and damper'. The big advantages are, that they are easy to understand and easy to implement (even in analog technique). In many applications they are fairly robust due to the positive real transfer function of a PD controller. However, with PD and PID the controller has always to be decentralized for MIMO-systems. Only very few specifications can be met by PD / PID controllers and closed-loop stability can not be guaranteed. PD / PID is a predefined low order approach which does usually not account for high demanding specifications of high order plants.

Observer Based High Order Controller

As stated before, a typical property of many practical AMB systems is the fact that only very few system states, most often the displacements at the AMB-coils, are measured. This is the case especially with flexible rotors, where the order of an appropriate plant model is much higher than the number of sensor signals available. The well-known consequence is:

A high order observer-based state feedback must be implemented including the full dynamics of the plant. Stability and good performance of the nominal closed-loop system may then be achieved by an appropriate controller design method such as the well-known LQR and LQG methods (Linear Quadratic Riccati resp. Linear Quadratic Gaussian).

One crucial drawback of this controller design approach, however, is that this high order control scheme will require a considerable amount of computation time for the estimation of the non-measured state variables and for the calculation of the corresponding controller output signals. The consequence is either the need of a sophisticated and expensive multi-processor or the acceptance of low sampling rates whenever single-processor implementations are used.

Hence, *low order* discrete-time *dynamic output control schemes* must be sought in order to simplify the control task. The most general approaches for such a *low order controller* are summarized in figure 12:

Controller Reduction and Practical Aspects of Low Order Controller Implementation:

According to figure 11 the three basic ways to achieve a practically implementable discrete-time controller are:

- model reduction prior to the controller design
- controller reduction after controller design
- direct low order controller design

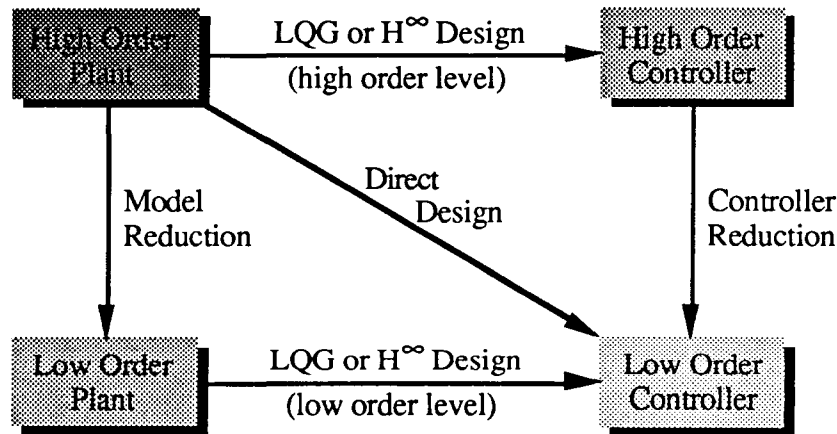


Figure 11: Basic principles of low order controller design (figure from [Anderson & Liu 89])

Many among the first two mentioned reduction techniques can be denoted as so called "open-loop" reduction methods. This means that stability of the resulting closed-loop system is *not* an intrinsic property of the reduction process. A practical example, well-known to any AMB control engineer, is that *high frequency bending eigenmodes* will often turn out to be unstable when reduced order controllers or controllers relying on reduced models are used.

The common way out of this is post layout on-site "tuning" of the nominal AMB controller or filtering of non-desired signal components by means of notch-filters in the feedback loop

Both listed approaches of a practical implementation of reduced AMB controllers are quite *ineffective*: On the one hand, "tuning" is a time-intensive and therefore expensive job, and obtained results can hardly be transferred to any other type of machine. On the other hand, notch-filtering of bending eigenmodes has a drastically deteriorating impact on the overall controller performance, since the necessary controller phase lead is degraded even in the rigid body (i.e. low frequency) range. Thus, the use of notch-filters makes the following controller tuning a necessary task, and, roughly spoken, renders the preceding LQR or LQG controller layout often very unqualified.

Another, more sophisticated way is to account for the neglected plant dynamic in the controller design specifications. Such specifications can be included in H^∞ and 'convex optimization' of the class of all stabilizing controller.

This approach seems very promising, especially because all neglected plant dynamic of the real physical plant, not only of an appropriate model, can be included in the control specifications.

Direct Design of Low Order Dynamic Compensators:

A promising and most practical solution to the problem of obtaining *low order controllers* for *high order plants* is the *direct low order controller design*: [Bernstein & Hyland 84], [Larsonneur 90]:

Order and structure of the discrete-time controller for the nominal high order (i.e. not reduced) plant model are predefined prior to the controller layout (structurally constrained controller). This predefinition is made according to practical needs such as physical considerations, complexity constraints, decentralization, symmetry etc.

This approach is, in fact, very common in AMB applications where, quite often, discrete-time low order approximations of traditional continuous-time P(I)D control schemes are implemented. The most simple discrete-time PD approximations are the following ones (controller output u , measured plant output y , sampling time T , time event k , proportional respective differential control coefficients P and D):

$$u_i(k) = \left(P + \frac{D}{T} \right) y_i(k) - \frac{D}{T} y_i(k-1) \quad (4.1)$$

$$u_i(k) = \left(P + \frac{3D}{2T} \right) y_i(k) - \frac{4D}{2T} y_i(k-1) + \frac{D}{2T} y_i(k-2) \quad (4.2)$$

Such P(I)D controller schemes exactly match above direct design definition: the controller order (e.g. 1st or 2nd order) and a decentralized structure (sensor signal y_i is fed back on actuator input u_i only) are predefined prior to the controller layout (determination of P resp. D). The control parameters P and D can then be obtained by numerical simulations or, again, by on-site "tuning" of the AMB system.

In many cases, no set of control parameters (P, D) can be found stabilizing both low frequency rigid body and higher frequency bending eigenmodes. More sophisticated approaches for direct low order controller design, namely the so called SPOC-D approach, are therefore required (see next paragraph).

4.3 Structure-Predefined Optimal Control for Discrete Systems (SPOC-D)

Lately, a direct low order controller design method for discrete-time systems named SPOC-D (*Structure-Predefined Optimal Control for Discrete Systems*) has been developed at the Swiss Federal Institute of Technology (ETH). This method has a strongly practical orientation. Similar to the LQR/LQG design methods, SPOC-D uses a quadratic performance criterion to be optimized, accounting for a high order plant model as well as for the controller dynamics. The fundamental difference to these classical methods, however, is that the controller order and structure are *not a result* of the controller design process, as it is the case for LQR/LQG or familiar methods, where high order plants generally lead to high order controllers (see figure 11). The SPOC-D method combines the advantages of a system optimization including the full plant dynamics on the one hand and possibly simple low order dynamic compensator schemes on the other hand and, thus, closes the gap between the classical LQR/LQG or pole placement methods and the more practical and less sophisticated P(I)D approaches.

The main features of SPOC-D can be summarized as follows:

- discrete-time controller order and structure are freely predefinable according to practical needs (low or high order, fully coupled or completely decentralized, etc.)
- determination of an optimal set of control parameters by minimizing a quadratic performance criterion involving both, the full plant and the controller dynamics
- analytical description of the performance criterion (by Lyapunov equations) and corresponding vector gradient allowing for an efficient numerical optimization process
- consideration of *additional* linear or nonlinear *control specifications* in order to achieve specific controller properties of practical importance (stiffness, noise reduction at high frequencies, band pass filtering, symmetries, etc.)

A detailed description of the SPOC-D method is not presented in this paper but can be found in [Larsonneur 90]. However, controller layout results for a high speed AMB milling spindle are presented in chapter 5.3.

4.4 H^∞ : A MiniMax Approach to Control

Cultural Remarks and Motivation for H^∞ Control

An intuitively most appealing motivation for H^∞ control is supplied by its differential game analogy [Doyle et al. 89]: consider a plant with two inputs. These two inputs which are also called players are set up in opposition. The first player $u(t)$ (that's you in fact !) is the control input generated by the controller (your strategy). The second player $w(t)$ (your adversary) is an *exogenous* input signal which could represent some disturbance. Of course, this exogenous input signal is a priori unknown to you; the only available signal for the controller input is the measured plant output $y(t)$. Your objective is to *minimize* the "*worst case*" disturbance, that is to *minimize* the disturbance which causes the *maximal* "damage" (in terms of energy) to the plant output $z(t)$. This "*minimax*" optimization problem characterizes H^∞ control. Note that figure 9 in section 4 exactly matches the situation described above.

Practical Aspects of Designing and Implementing H^∞ Controllers

The *off-line* effort for computing H^∞ controllers has been drastically reduced recently by the "state space approach" in [Doyle et al. 89], where the resulting controller is basically given in terms of two algebraic Riccati equations. H^∞ software packages are already available [Matlab], and algorithms are being improved and standardized. These advances have a common desirable consequence: the H^∞ approach is nowadays available to a broader section of the control community. However, there is still a computational *on-line* burden because standard H^∞ designed MIMO (multiple input multiple output) controllers are fully coupled, and their order is roughly the same as the order of the plant. That is why there remains a strong need to keep up with the latest developments in special purpose controller architectures, in modern "closed-loop" controller reduction schemes [Anderson & Liu 89], [Mustafa & Glover 91], and in decentralized control [Wu 90].

Experimental implementations of H^∞ designed controllers for AMB systems (especially for high performance AMB milling spindles) will be effectuated soon at our institute. The AMB milling spindle is a particularly challenging application example of H^∞ control since the cutting forces of the milling process appear as a highly unpredictable exogenous input which may cause intolerable vibrations of the milling tool. Some theoretical considerations to this problem were carried out in [Herzog & Bleuler 90]. In [Matsumura et al. 90] experimental results based on the H^∞ "mixed sensitivity" approach were shown. A theoretical example is shown in chapter 5.4.

5. THEORETICAL AND EXPERIMENTAL RESULTS

5.1 Displacement Sensing by Flux Density Measurement

The laboratory prototype crystal-growth system shown on figure 13 makes use of equation (2.9) for the displacement measurement [Zlatnik & Traxler 90]. The flux density measurement together with a current measurement is used for the displacement sensing. The lack of a special displacement sensor is specially useful for large air-gaps, lower costs and encapsulated rotor systems. A liquid phase epitaxy centrifuge in a similar arrangement and with a totally encapsulated rotor, is currently installed at MECOS Traxler AG. The temperature at the front end of the rotor goes up to 800° Celsius.

5.2 Self-sensing AMB Systems

One way to build a self-sensing bearing is to design a Luenberger observer for the voltage controlled system of 4th order according to figure 4. The observer can be tuned by comparing the estimated air gap with the measurement of a position sensor. A state feedback can then be implemented and self-sensing operation is achieved by switching position feedback from the measured signal to the estimated one. This was implemented in [Jordil & Volery 90] on a signal processor with a sampling time of 120 μ s.

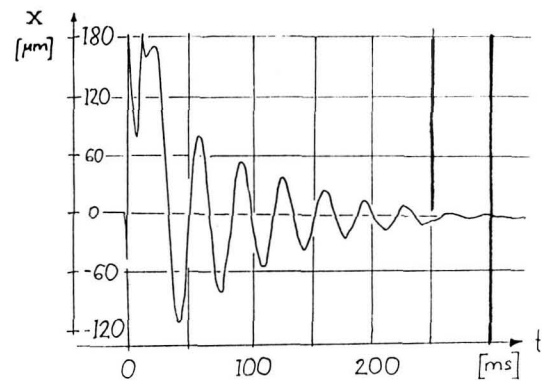
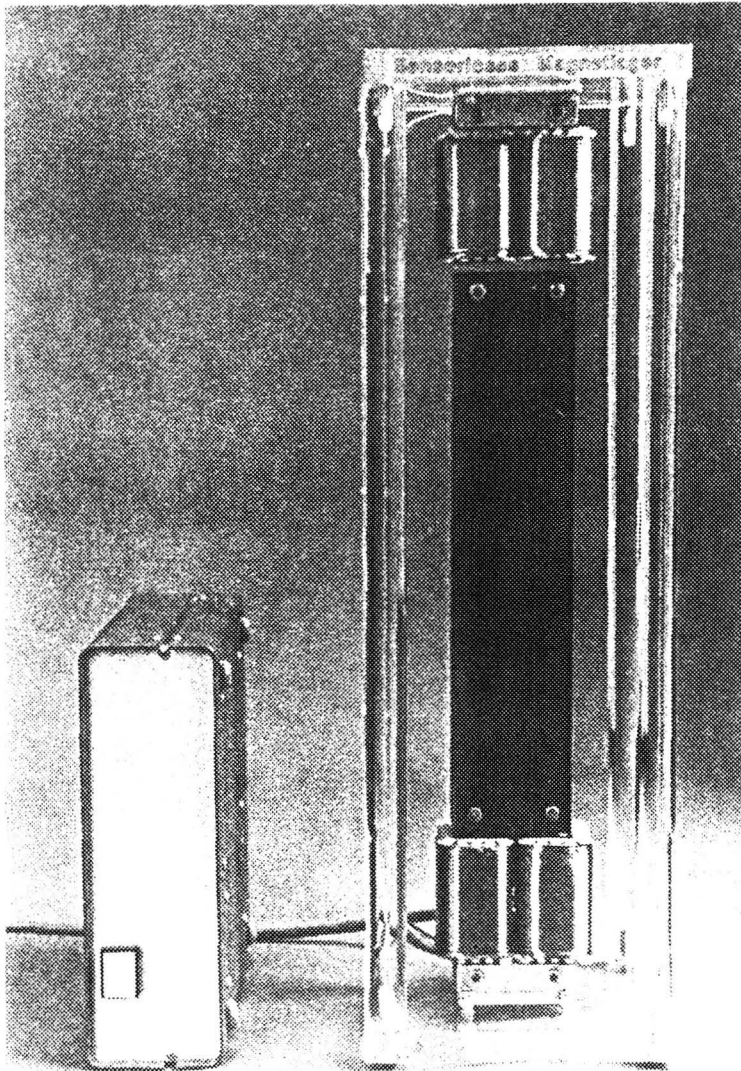


Figure 12a: Demonstration model of the self sensing bearing with one controlled degree of freedom. The Box on the right contains power amplifier, power supply and controller.

Figure 12b: Measurement of impact response (hammer) of position signal of a self-sensing AMB. The air gap of the bearing is 0.7 mm, rotor mass is 8 kg, bearing diameter is 78 mm, bias current is 0.5 A and maximum force is over 100N. The static behavior is satisfactory, similar to the current controlled bearing. The dynamic response is still not exciting, and has to be improved.

An analog realization of a self-sensing bearing was successfully completed as a student project [Colloti & Kucera 91]. The controller makes use of the separation shown in figure 4. The complete circuit needs very few electronic components. A good robustness of the bearing was achieved.

The measurement result of figure 12 shows the system response to an impact force, a blow with a hammer on the rotor. Maximum rotor displacement of this measurement was about 0.3 mm which is almost maximum rotor clearance in the auxiliary bearing and about 50% of the total air gap in the bearing magnet. Further technical data of this system is given in the figure caption

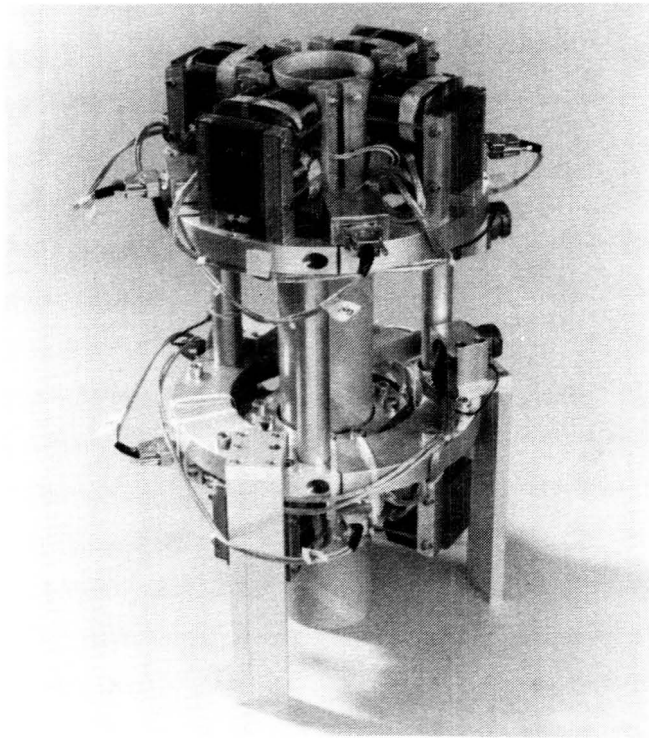


Figure 13 Laboratory set-up of a crystal-growth system with displacement sensing by flux and current measurement.

5.3 Optimal Control of a Stiff AMB System using the SPOC-D Method

The example in this chapter is from an actually realized system, a high performance AMB milling spindle, controlled by a single digital signal processor (DSP) [Sieewart et al. 90]. It illustrates the large variety of control goals offered by the SPOC-D method.

The procedure to obtain an appropriate controller fulfilling the desired requirements can be summarized as follows (see details in [Larsonneur 90]):

1. Step: Predefinition of discrete-time controller structure and order according to the practical feasibility. For the milling spindle example, two decentralized dynamic compensators, each of 4th order, have been chosen (sampling frequency 10kHz). This yields the following IIR (*Infinite Impulse Response*) controller transfer function in the z -domain:

$$g(z) = \frac{u(z)}{y(z)} = \frac{d_0 + d_1 z^{-1} + d_2 z^{-2} + d_3 z^{-3} + d_4 z^{-4}}{1 + c_1 z^{-1} + c_2 z^{-2} + c_3 z^{-3} + c_4 z^{-4}} \quad G(z) = \begin{bmatrix} g_1(z) & 0 \\ 0 & g_2(z) \end{bmatrix} \quad (4.3)$$

Note that this controller predefinition uses two decentralized 4th order controllers $g(z)$ for a plant of *total order 14* (including sensor and anti-aliasing filter state variables), and involves *only 18 control coefficients*, whereas a full state observer for this plant would require *56 control coefficients* and corresponding multiplications.

2. Step: Introduction of *additional control specifications* in order to achieve requirements of *important practical relevance*. Here, the *static bearing stiffness* (without integrator feedback), *suppression of rotation-synchronous AMB force components* (analogous to notch-filters) and *noise suppression* at high frequencies are introduced as parameter constraints. This results in an *interdependence* of the control parameters. For the given case, four control coefficients of each dynamic compensator will be dependent on the other five.

Note that the conditions of bearing stiffness, unbalance and noise suppression or other parameter constraints are *directly* introduced into the controller design process *before*

optimization and not achieved by any specific choice of weighting matrices during the controller optimization process.

3. Step: Determination of the independent and dependent control parameters by numerical minimizing a quadratic performance criterion (which includes the parameter constraint equations). Efficient numerical minimizing procedures can be used since vector gradients are formulated analytically.

The resulting controller transfer function of this optimization process for the AMB milling spindle is shown in the following figure:

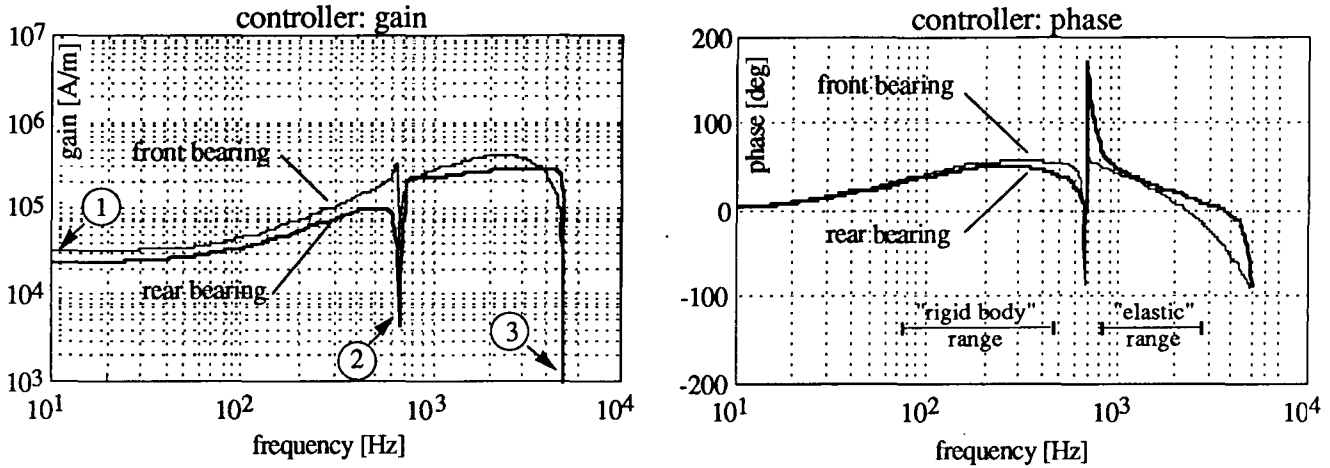


Figure 14: Transfer functions of the SPOC-D optimized decentralized discrete-time controller (4th order) at rear and front AMB of the high speed milling spindle. The conditions of static bearing stiffness (1), unbalance force suppression (2) and noise suppression (3) are introduced by control parameter constraints.

As can be seen from above results the SPOC-D optimized decentralized low order controller perfectly accounts for the the desired spindle requirements: high stiffness, unbalance and noise suppression and large "damping" (positive controller phase lead) in the low frequency rigid body range as well as in the higher frequency bending eigenmode range. This is made possible by optimally using the design freedom offered by low order dynamic compensators in a most practical and straightforward way, instead of "tuning" otherwise obtained controllers so that they match the desired requirements.

5.4 Stiff AMB Control: H^∞ versus PD

Comparing different controller layout methods is not an easy task. Clearly, any comparison must be made with respect to a *common* performance index. There is an erroneous and prejudiced opinion stating that PD controllers are mostly "nearly optimal" in "some" sense, and that modern control theory only allows small "performance improvements" at the expense of extremely high sophistication. Our illustrative example here proves the contrary.

Consider the controlled AMB system in figure 15. The two mass oscillator P stands for a simple electromagnetically supported *flexible* shaft. The system is assumed to be subjected to an *unknown* disturbance force $w(t)$ acting on the bottom mass m_1 . Let $z(t)$ denote the displacement of m_1 caused by $w(t)$, and let $T(s)$ be the frequency-domain compliance: $z(s) = T(s) w(s)$. Let the objective of controller $C(s)$ be to stabilize $P(s)$ and to maintain the magnitude of dynamic compliance $|T(i\omega)|$ uniformly below a given bound α , i.e. $|T(i\omega)| < \alpha$ for all frequencies ω . The main feature of this example is that the disturbance and actuator forces are *not* acting on the *same* mass. This implies the following drawback for PD control $C(s) = -(p + d s)$: *neither low nor high* (p, d) gains are appropriate for very stiff control, i.e. for a small value of α . Note that high (p, d) gains lead to a *rigid top* mass m_2 , whereas the *bottom* mass m_1 is nearly *undamped*, which produces a high resonance peak of dynamic compliance $|T(i\omega)|$.

Obviously, "optimal" (p, d) tuning leads to investigating $\max_{\omega} |T(i\omega)|$ as a function of (p, d), see figure 16. It can be concluded from this example that PD controllers may give poor performance results especially

if the actuator and disturbance forces are not acting on the same place. Now, what is the answer of H^∞ to all this? In [Herzog & Bleuler 90] we derived the following result:

For the above example, there exist stabilizing controllers $C(s)$ enabling an *arbitrarily* low compliance peak bound $\alpha > 0$.

Of course, a low value of α implies high controller authority. Actually there is a *trade-off* between *several* requirements. This trade-off reasoning is absolutely fundamental to control engineering. PD control disguises this fact since high (p, d) gains do not necessarily lead to high performance. The freedom offered by PD tuning is only a tiny little subset of the freedom offered by the set of all stabilizing controllers. However, if the performance specifications are *not* very demanding, the reduced freedom of PD controllers is mostly sufficient.

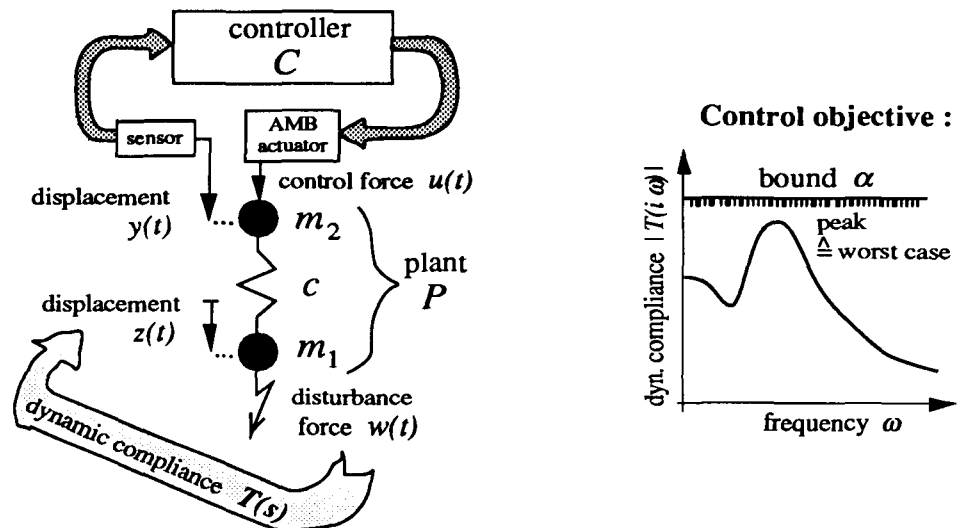


Figure 15: Control problem and objective

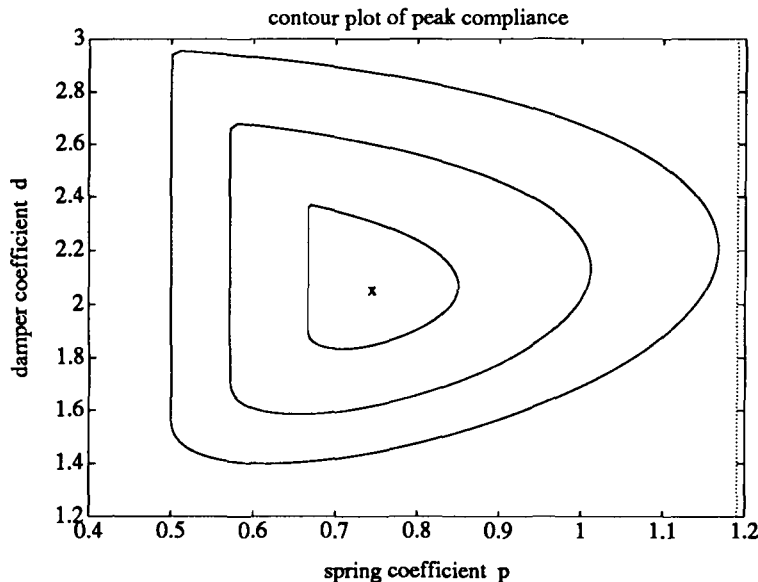


Figure 16: Contour plot for the following peak level values: $\{3, 2.75, 2.5\}$. The cross marks the optimum (p, d) tuning $p_{opt} \approx 0.7444$, $d_{opt} \approx 2.0478$. The corresponding (p, d) -optimal peak compliance is about $\max_{\omega} |T(i\omega)| \approx 2.3438$. Parameter values of plant P : $m_1 = m_2 = c = 1$.

6. CONCLUSION AND OUTLOOK

Various control configurations of AMB-actuators have been presented. Voltage and flux density control are promising for many applications, advantages are clearly indicated by theory. Extended experimental comparisons remain to be done.

A self-sensing AMB has been presented in theory and realization, i.e. an AMB using no sensing hardware in the bearing [Bleuler & Vischer 91]. Self-sensing AMB are a promising solution for low cost applications or applications where conventional sensing hardware is expensive.

The control layout is regarded as a key point of AMB system design. However, a good control layout alone cannot guarantee a good system behavior when the "conditioning" of the control plant is bad.

New approaches to control design as they have been outlined in this paper have many advantages compared to the widely used PD and PID control. With new control design tools such as *direct low order controller design* [Larsonneur 90], H^∞ or 'convex optimization' over the set of all stabilizing controllers [Boyd et al. 90], controller specifications can be met, which are not achievable by PD/PID or even by LQG/LQR approaches. Some examples show the advantages of the new design techniques.

A successful control layout, especially for high performance systems, is still a very challenging engineering problem. There are thousands of problems to be solved. New AMB-systems, with better control configurations have to be designed, better sensor and actuator hardware has to be developed and new control design methods have to be investigated. To improve the performance of AMB systems it is essential that the whole system is treated as a mechatronic product where all parts are interdependent. Not the isolated design of AMB components, but smart integration of all parts into the overall system will result in successful products.

7. REFERENCES

- [Anderson & Liu 89] Anderson B.D.O and Liu Y.: Controller Reduction: Concepts and Approaches, IEEE Transactions on Automatic Control, Vol. 34, No. 8, pp. 802-812, 1989
- [Beams et al. 46] Beams J.W., Young J.L. and J.W. Moore: The Production of High Centrifugal fields, Journ. of Appl. Physics, Vol 17, pp 886-890, 1946
- [Bernstein & Hyland 84] Bernstein D.S. and D.C. Hyland: The Optimal Projection Equations for Fixed-Order Dynamic Compensation, IEEE Trans. AC, Vol. 29, No. 11, 1984
- [Bleuler 84] Bleuler H: Decentralized Control of Magnetic Bearing Systems, Doctor thesis no 7573, ETH Zürich 84
- [Bleuler & Vischer 91] Bleuler H., Vischer D.: Magnetic Bearing Systems with Minimal Hardware Requirement, ROMAG '91 Magnetic Bearing & Dry Gas Seals, Int. Conf., Alexandria Va., March 91
- [Boyd et al. 90] Boyd S., Barratt C. and S. Norman: Linear Controller Design: Limits of Performance Via Convex Optimization, Proceedings of the IEEE, Vol. 78, March 1990.
- [Breinl 80] Breinl W.: Entwurf eines unempfindlichen Tragregelsystems für ein Magnetschwebefahrzeug. Fortschrittbericht der VDI-Zeitschriften, Reihe 8, Nr. 34, München, 1980.
- [Colloti & Kucera 91] Colloti A. and L. Kucera: Low Cost Magnetic Bearings, Semesterarbeit IfR 1991.
- [Doyle et al. 89] Doyle J.C., Glover K., Khargonekar P.P., and B. A. Francis: State Space Solutions to Standard H^2 and H^∞ Control Problems, IEEE Trans. AC, Aug. 1989, Vol. 34, No. 8, p. 831-847.
- [Gottzein & Crämer 77] Gottzein E. and W. Crämer: Critical Evaluation of Multivariable Control Techniques based on MAGLEV Vehicle Design. IFAC Symposium on Multivariable Technological Systems, Canada, July 1977.

- [Gottzein et al. 77] Gottzein E., Miller L. and R. Meisinger: Magnetic Suspension Control System for High Speed Ground Transportation Vehicles. World Electrical Congress, Moscow, June 1977.
- [Herzog & Bleuler 90] Herzog R. and H. Bleuler: Stiff AMB Control using an H^∞ Approach, 2nd Int. Symp. on Magnetic Bearings, Tokyo 1990
- [Higuchi et al. 90] Higuchi T., Mizuno T. and M. Tsukamoto: Digital Control System for Magnetic Bearings with Automatic Balancing, 2nd Int. Symp. on Magnetic Bearings, Tokyo 1990
- [Jayawant 81] Jayawant B.V.: Electromagnetic Levitation and Suspension Techniques, London, Arnold, 1981
- [Jordil & Volery 90] Jordil P. and F. Volery: Régulation d'un palier magnétique sans senseur de position, Student's diploma project, Feb. 1990, Inst. for Robotics, ETH Zürich
- [Keith et al. 90] Keith F.J., Maslen E.H., Humphris R.R., and R.D. Williams: Switching Amplifier Design for Magnetic Bearings, 2nd Int. Symp. on Magnetic Bearings, Tokyo 1990
- [Larsonneur 90] Larsonneur R.: Design and Control of Active Magnetic Bearing Systems for High Speed Rotation, Doctoral Thesis No. 9140, ETH Zürich, 1990
- [Matlab] Chiang R.Y. and M.G. Safonov: User's Guide of the Robust Control MATLAB Toolbox, The Mathworks Inc., Natick, MA 01760
- [Matsumura et al. 90] Matsumura F., Fujita M. and M. Shimizu: H^∞ Robust Control Design for a Magnetic Suspension System, 2nd Int. Symp. on Magnetic Bearings, Tokyo 1990
- [Mustafa & Glover 91] Mustafa D. and K. Glover: Controller Reduction by H^∞ Balanced Truncation, IEEE Trans. AC, June 1991, Vol. 36, No. 6, p. 668-682.
- [Siegwart & Traxler 90] Siegwart R. and A. Traxler: Performance and Limits of AMB-Actuators Illustrated on an Electromagnetically Suspended Milling Spindle, Proc. 25th Intersociety Energy Conversion Engineering Conference. Nevada, August 1990
- [Siegwart et al. 90] Siegwart R., Larsonneur R. and A. Traxler: Design and Performance of a High Speed Milling Spindle in Digitally Controlled Active Magnetic Bearings, 2nd Int. Symp. on Magnetic Bearings, Tokyo 1990
- [Skelton 89] Skelton R.E.: Model Error Concepts in Control Design, Int. J. Control, Vol. 49, No. 5, 1989
- [Traxler 85] Vischer D.: Eigenschaften und Auslegung von berührungsfreien elektromagnetischen Lagern, Doctor Thesis No. 7851, ETH Zürich, 1985
- [Ulbrich & Anton 84] Ulbrich H. and E. Anton: Theory and Application of Magnetic Bearings with Integrated Displacement and Velocity Sensors, The Inst. of Mech. Eng., C299/84, Cambridge 1984
- [Vischer 88] Vischer D.: Sensorlose und spannungsgesteuerte Magnetlager, Doctor Thesis No. 8665, ETH Zürich, 1988
- [Vischer, Traxler & Bleuler 88] Vischer D., Traxler A., Bleuler H.: "Magnetlager", patent No. 678090, 22.11.88, Switzerland
- [Wu 90] Wu Q.: An Application of H^∞ Theory to Decentralized Robust Control, thesis ETH Zurich, No. 9116
- [Zlatnik & Traxler 90] Zlatnik D. and A. Traxler: Cost-Effective Implementation of AMB, 2nd Int. Symp. on Magnetic bearings, Tokyo, 1990

COMPUTER AIDED DESIGN OF DIGITAL CONTROLLER
FOR RADIAL ACTIVE MAGNETIC BEARINGS *

Zhong CAI[†] Zupei SHEN[†] Zuming ZHANG[‡] Hongbin ZHAO[†]
[†]Lab. of Mechatronics and Control, Department of Engineering Physics,
Tsinghua University, Beijing, P.R. China
[‡]Beijing Institute of Printing, Beijing, P.R. China

Abstract

A five degrees of freedom Active Magnetic Bearings (AMB) system is developed in Tsinghua University, which is controlled by digital controllers.

The model of the radial AMB system is linearized and the state equation is derived. Based on the state variables feedback theory, digital controllers are designed. The performance of the controllers are evaluated according to experimental results.

The Computer Aided Design (CAD) method is used to design controllers for magnetic bearings. The controllers are implemented with a digital signal processing (DSP) system. The control algorithms are realized with real-time programs. It is very easy to change the controller by changing or modifying the programs.

In order to identify the dynamic parameters of the controlled magnetic bearings system, a special experiment was carried out. Also, the on-line Recursive Least Squares (RLS) parameter identification method is studied. It can be realized with the digital controllers. On-line parameters identification is essential for the realization of adaptive controller.

Introduction

A magnetic bearings system with electromagnetic attractive force is an inherently open-loop unstable system. The uncontrolled magnetic force provides a negative stiffness to the magnetic

bearings system, i.e., when the gap between rotor and bearing is reduced, the magnetic force will be increased. In this case, compensation to such a system is necessary. The AMB controllers can eliminate the negative stiffness and provide positive stiffness and damping to the AMB system. Therefore, the performance of the controllers is a decisive factor to the performance of the AMB system. Many papers have described design of the control system. [1, 2, 3, 4]

In order to design a practical AMB controller, which is easy to implement and has relatively good performance, some control algorithms are studied on a computer system.

Design of digital controllers can be divided into several steps. Firstly, the discrete model and state equation of the system are obtained according to the original system. Secondly, a controller is designed with the CAD method according to the selected control algorithm. Thirdly, the designed controller can be simulated with computer before implemented as a real-time control program. Lastly, the coefficients of the control programs are tuned to reduce the effects of deviations of the system model. And, if necessary, the system model is modified and the controller is re-designed.

In our magnetic bearings system, the rotor has five degrees of freedom need to control, one axial degree of freedom and four radial degrees of freedom. Generally, the axial AMB system can be considered as a single degree of freedom system, i.e. it is uncoupled with the radial AMB system. In our early work, digital and analog controllers for axial AMB had been studied. [5]

The axial AMB controllers are Single-Input

*Supported by the National Natural Science Foundation of China

$$f = k_p x + k_i i \quad (1)$$

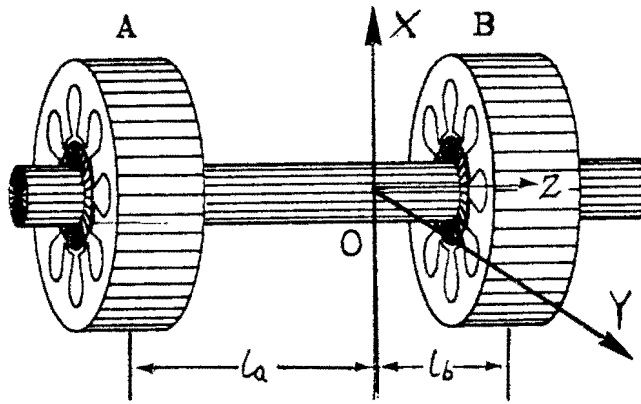


Figure 1: Structure of Radial Magnetic Bearings

Single-Output (SISO) controllers, which can be analyzed and designed with the classical control theory. However, it is difficult to design the Multi-Input Multi-Output (MEMO) controllers, as used for a radial AMB system, with the classical control theory.

In this paper, we focus our study on the radial AMB controllers with the state variables feedback theory.

Radial Bearings System

Figure 1 shows the schematic structure of radial magnetic bearings used in our experiment. The horizontal rotor is supported by two radial magnetic bearings, A and B. Each bearing controls two motion directions of rotor, x and y , in the fixed Cartesian coordinates. The origin of the coordinates, O is at the mass center of the rotor. The electromagnetic force of each direction is produced by two opposite magnets. The magnets in y direction provide an additional force to support the weight of the rotor.

In actual magnetic bearings, the relationship between magnetic force and control current and rotor position are nonlinear. However, when the rotor position is near the reference position, the relationship can be linearized as:

where,

k_p —position stiffness

k_i —current stiffness

x —displacement from reference position

i —control current

The total current in magnets can be divided into control current and bias current. The bias current makes the magnets work in the linear range of magnetizing curve. [6]

Taking state variables vector as,

$$\mathbf{X} = (x_a, x_b, y_a, y_b, \dot{x}_a, \dot{x}_b, \dot{y}_a, \dot{y}_b)^T$$

control variables vector as,

$$\mathbf{U} = (i_{xa}, i_{xb}, i_{ya}, i_{yb})^T$$

The state equation of the magnetic bearings system is,

$$\dot{\mathbf{X}} = \mathbf{A}\mathbf{X} + \mathbf{B}\mathbf{U}$$

where, state matrix,

$$\mathbf{A} = \begin{pmatrix} 0 & 0 & I & 0 \\ 0 & 0 & 0 & I \\ L & 0 & 0 & -M \\ 0 & L & M & 0 \end{pmatrix}$$

control matrix,

$$\mathbf{B} = \frac{k_i}{k_p} \begin{pmatrix} 0 & 0 \\ 0 & 0 \\ L & 0 \\ 0 & L \end{pmatrix}$$

The 2×2 submatrixes O, I are zero and identity matrixes, respectively, and,

$$\mathbf{L} = \frac{k_p}{m} \begin{pmatrix} 1 + \frac{ml_a^2}{J_x} & 1 - \frac{ml_a l_b}{J_x} \\ 1 - \frac{ml_a l_b}{J_x} & 1 + \frac{ml_b^2}{J_x} \end{pmatrix}$$

$$\mathbf{M} = \frac{J_z \Omega}{J_x(l_a + l_b)} \begin{pmatrix} l_a & -l_a \\ -l_b & l_b \end{pmatrix}$$

Generally, $J_z/J_r \ll 1$, when the rotor rotates at the low speed, submatrix \mathbf{M} can be considered as zero matrix, i.e., the gyroscopic effects can be omitted.

The rotor positions in each direction are measured by four eddy-current displacement sensors mounted near radial bearings. In the linear range of the sensors, the outputs of sensors, which are produced by analog circuits, are DC voltages proportional to the displacement of the rotor in each direction. When the rotor is at reference positions in bearings, all the outputs of the sensors are zero. Therefore, the output equation of the magnetic bearings system is,

$$\mathbf{Y} = \mathbf{C}\mathbf{X}$$

where,

$$\mathbf{Y} = (x_a, x_b, y_a, y_b)^T$$

output matrix,

$$\mathbf{C} = \begin{pmatrix} I & O & O & O \\ O & I & O & O \end{pmatrix}$$

Design of Control System

The CAD method is used to design digital optimal state variables feedback control system. [7]

For a continuous time system, the performance index to be minimized is,

$$J = \int_0^\infty [\mathbf{X}^T(t)\mathbf{Q}\mathbf{X}(t) + \mathbf{U}^T(t)\mathbf{R}\mathbf{U}(t)]dt$$

where, \mathbf{Q} and \mathbf{R} are the state weighting matrix and control weighting matrix, respectively.

Given sampling period T , the state equation can be discretized as,

$$\mathbf{X}(k) = \mathbf{F}\mathbf{X}(k-1) + \mathbf{G}\mathbf{U}(k-1)$$

where, \mathbf{F} and \mathbf{G} are the discrete state matrix and control matrix, respectively.

And the performance index can be discretized as,

$$J = \sum_{k=0}^{\infty} [\mathbf{X}^T(k)\mathbf{Q}_1\mathbf{X}(k) + 2\mathbf{X}^T(k)\mathbf{Q}_3\mathbf{U}(k) + \mathbf{U}^T(k)\mathbf{Q}_2\mathbf{U}(k)]$$

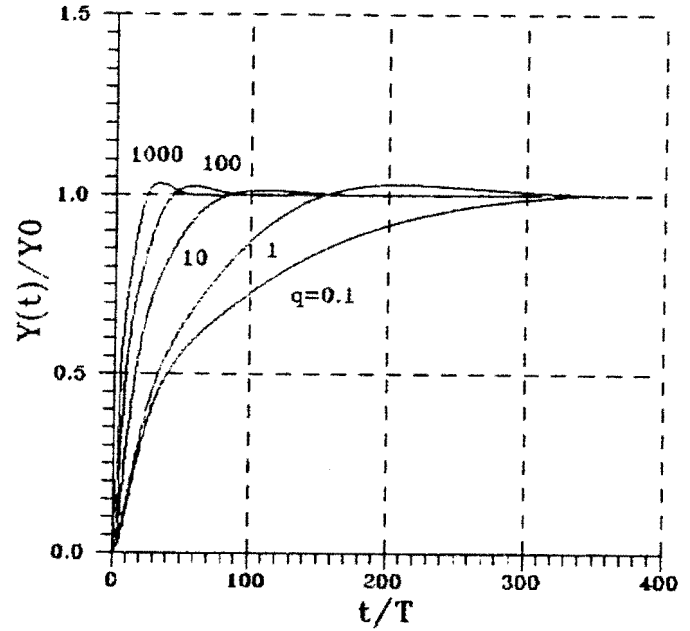


Figure 2: Simulation Results of Step Response

where, \mathbf{Q}_1 , \mathbf{Q}_2 and \mathbf{Q}_3 are the discrete state weighting matrix, control weighting matrix and cross weighting matrix, respectively.

Given the continuous state equation, weighting matrixes \mathbf{Q} and \mathbf{R} , and sampling period T , a computer program is available to compute the optimal state variables feedback gain matrix \mathbf{K} for digital controller. The choices of weighting matrixes \mathbf{Q} and \mathbf{R} have decisive effects to the dynamics of a magnetic bearings system.

We choose the matrixes,

$$\mathbf{Q} = \text{diag}(q, q, q, q, 0, 0, 0, 0),$$

$$\mathbf{R} = \mathbf{I}$$

where, $q > 0$ and \mathbf{I} is a 4×4 identity matrix. These choices mean that only the squares of displacements and control currents are weighted in the performance index J .

The simulation of step response of the magnetic bearings system controlled by controllers with different values of q are shown in Figure 2.

The simulation results shows that a big q corresponds fast response of the system.

Identification of System Parameters

The optimal state variables feedback control theory is very suitable for designing AMB control

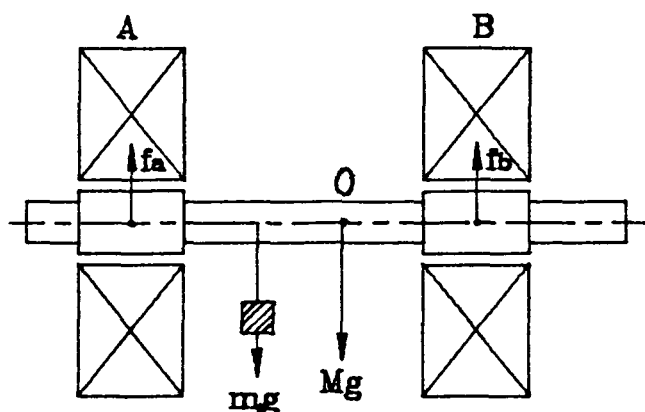


Figure 3: Parameters Identification Experimental System

system from the given system model. However, if the parameters of the system are not accurate enough, the designed control system will not be optimal or even make controlled system unstable.

Because the AMB system is open-loop unstable and nonlinear, some important parameters of system, such as position stiffness k_p and current stiffness k_i , are strongly dependent on operating point of AMB system. It is difficult to measure the system parameters accurately from an open-loop system. However, when a simple controller, like PD controller, can suspend the rotor stably, the parameters can be measured from the close-loop system.

Figure 3 shows a schematic experimental system. The horizontal rotor, with rotation speed $\Omega = 0$, is suspended stably. Setting this working state as the operating point of the magnetic bearings system, the reference position of rotor in bearings, the currents in bearing coils can be measured and the bearing forces can also be decided according to the structure of magnetic bearings and the rotor.

When a small weight m_1 is loaded to the rotor, it will have small displacements from the reference position. The displacements of rotor and the currents in bearings can be measured directly. The changes of bearing forces can also be

decided. Changing the weight to m_2 ($m_2 \neq m_1$), another set of data can be obtained in the same way. According to the linear assumption, bearing forces are expressed as Eq. (1). Therefore, a set of equations is obtained. Consequently, the k_p and k_i can be obtained by solving these equations.

Another close-loop measurement method, called Recursive Least Squares (RLS) parameters identification method, is also studied. This method can be realized on-line with a digital controller and the difference equations of an AMB system can be obtained directly.

Consider a single degree of freedom rotor, the motion equation,

$$m\ddot{x} = k_p x + k_i i$$

can be transformed to a difference equation,

$$x(k) = a_1 x(k-1) + a_2 x(k-2) + b_1 i(k-d) + \eta(k)$$

where,

$$a_1 = 2 + \frac{k_p T^2}{m} \quad (2)$$

$$b_1 = \frac{k_i T^2}{m} \quad (3)$$

$$a_2 = -1$$

$d = 2$ — delay number of sampling period

$\eta(k)$ — random noise at sampling time kT

T — sampling period

The predicted system output is,

$$\begin{aligned} \hat{x}(k) &= \alpha_1 x(k-1) - x(k-2) + \beta_1 i(k-d) + \eta(k) \\ &= -x(k-2) + \mathbf{V}^T(k-1)\theta(k-1) + \eta(k) \end{aligned}$$

where, the input and output vector,

$$\mathbf{V}(k-1) = [x(k-1), i(k-d)]^T$$

predicted parameters vector,

$$\theta(k-1) = [\alpha_1, \beta_1]^T$$

From the control inputs i and system outputs x , at k th sampling period, the predicted system parameters are,

$$\theta(k) = \theta(k-1) + \mathbf{N}(k)[x(k) - \hat{x}(k)]$$

where, $x(k)$ is the rotor displacement measured at kT th time.

And the matrix

$$\mathbf{N}(k) = \frac{\mathbf{P}(k-1)\mathbf{V}(k-1)}{1 + \mathbf{V}^T(k-1)\mathbf{P}(k-1)\mathbf{V}(k-1)}$$

the positive definite covariance matrix

$$\mathbf{P}[k] = \mathbf{I} - \mathbf{N}[k]\mathbf{V}^T[k-1]\mathbf{P}[k-1]$$

The initial iteration values are,

$$\mathbf{P}(0) = \alpha \mathbf{I}, \quad \alpha = 5 \sim 10^4$$

$$\theta(0) = 0$$

The simulation results of RLS parameters identification with a PD controller are shown in Figure 4. The predicted system parameters converge to the real system parameters stably. i.e.,

$$\alpha_1 = a_1, \quad \beta_1 = b_1$$

From the identified parameters α_1, β_1 and Eq. (2) and (3), the parameters k_p, k_i can be computed.

It is the advantage of the on-line parameters identification that the difference equation of the system is obtained directly, and according to the difference equation an on-line control output can be calculated. Based on this idea, the adaptive controller can be designed.

Implementation of Digital Control System

As we know, the radial AMB system has 8 state variables and 4 control variables. The feedback gain matrix is a 4×8 matrix. When the optimal control algorithm is directly realized in a real-time program, at least 32 multiplications and additions have to be done within an interrupt period. And, counting in the calculation of observing state variables, the control program will be very large.

In our test-rig, a TMS32010 DSP system was used to implement the control algorithm.

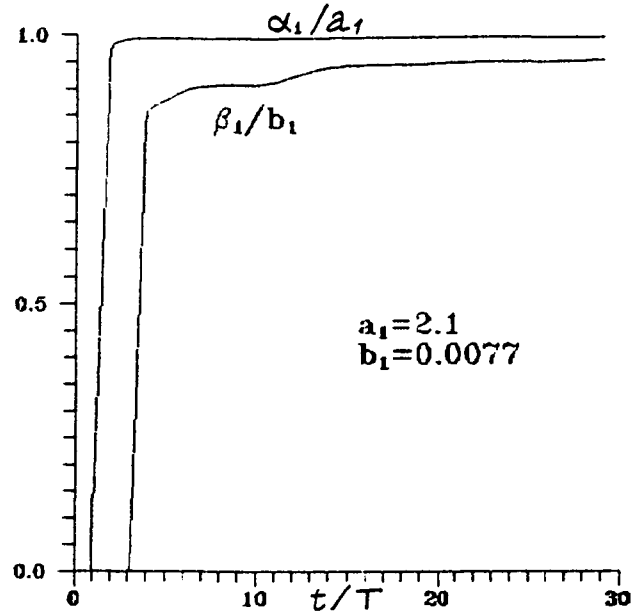


Figure 4: Simulation of On-line Parameters Identification with PD Digital Controller

TMS32010 can do a multiplication or addition in a 200ns instruction cycle. However, the limitation of in-chip data RAM makes it difficult to run the optimal control program, which needs many data RAM for controller coefficients. To simplify the structure of the control system, a decentralized controller is used, which is obtained by simply omitting all the coupling elements in the optimal feedback gain matrix.

For our magnetic bearings system, at low rotation speed of rotor, the coupling elements in optimal feedback gain matrix \mathbf{K} are very small compared with the uncoupling elements. Therefore, it is believable that this simplification will not cause large degradation of system performance compared with the optimal central control. Figure 5 shows the step response of radial magnetic bearings controlled by the decentralized controller and the optimal central controller. And this result has also been verified in some other papers. [8]

To obtain velocity of the rotor, which can not be measured directly, the digital differentiators are used. A modified differentiators algorithm is,

$$u_d(k) = \frac{1}{6T}[x(k) + 3x(k-1) - 3x(k-2) - x(k-3)]$$

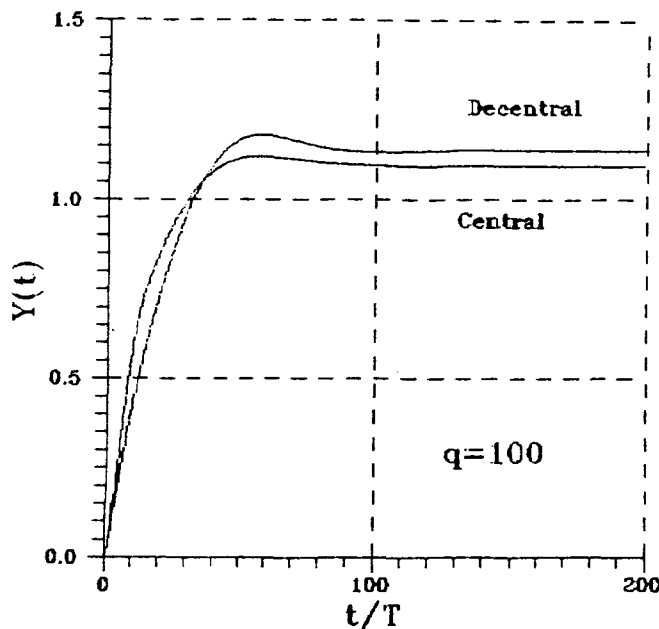


Figure 5: Comparison of Central and Decentralized Controllers

where,

T —sampling period

$x(k)$ —input displacement at sampling time kT

This algorithm can reduce the effects of input noise to system performance.

The block diagram of control system is shown in Figure 6. The digital control system consists of displacement sensors, switching power amplifiers, DSP system and a host computer. The control program can be loaded to the memory of the DSP. The structure and parameters of the controllers can be changed easily in the memory. The flowchart of the real-time control program is shown in Figure 7. In this digital system, only one A/D converter and one D/A converter are used. Four input and output ports are switched by two multiplexers. This simplification is economic use of hardware, but increases the time of interrupt service program.

Experimental Results

According to the designed controller, the feedback parameters are tuned. The step responses of the radial magnetic bearings with different feedback parameters are measured. In fact, when the velocities of the rotor are obtained by differentiators, the decentralized radial AMB con-

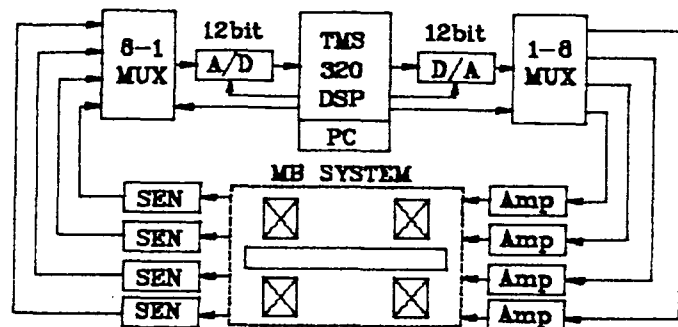


Figure 6: Block Diagram of Control System

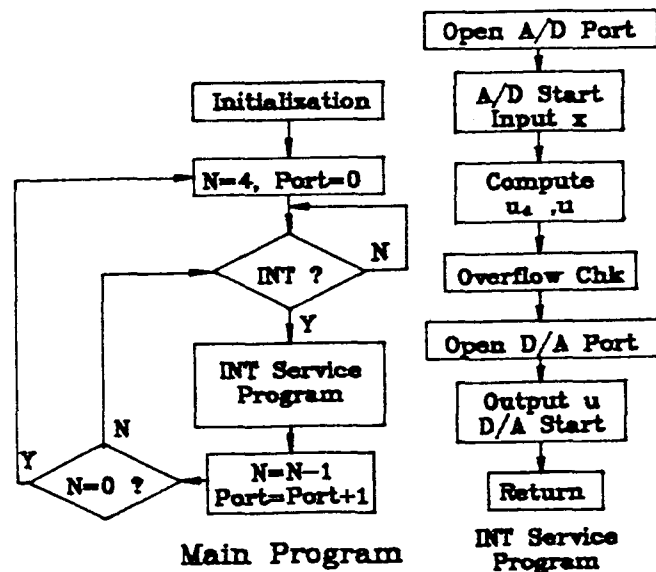


Figure 7: Flowchart of the Real-time Control Program

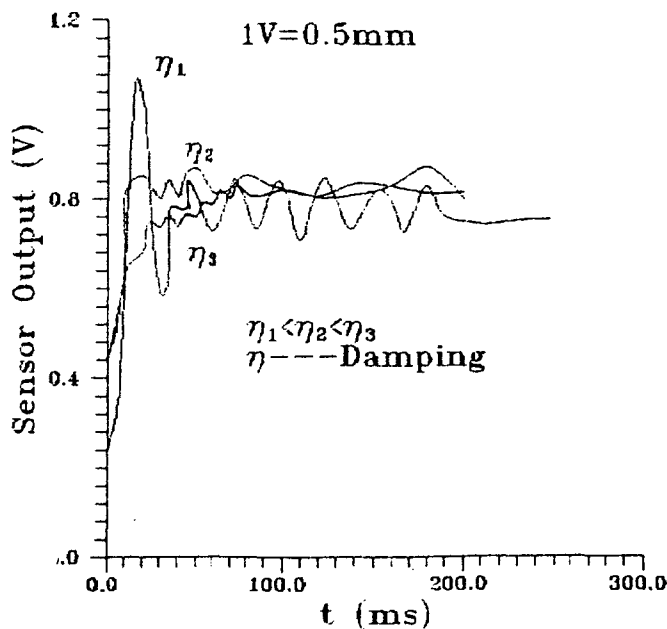


Figure 8: Step Response of the Radial AMB System

troller can also be considered as four PD controllers. From the view of PD controller, changing of gains of proportional and differential paths means changing of stiffness and damping of system. Figure 8 shows a set of step responses curves with different damping η and same stiffness.

Conclusions

Computer Aided Design method is very suitable for the design of radial magnetic bearings control system. The designed controller can be simulated with the simulation program before implemented as a practical AMB controller. And, the effects of controller coefficients to the system performance can be revealed by simulation. For example, increasing of position weights in a performance index will increase the speed of system response. With the CAD method, the development cycle of AMB controller is shorter.

The experimental results show that the simple decentralized state variables feedback digital controllers also have relatively good performance. This control system has simple structure and is easy to implement in a digital control system.

When the static rotor is suspended stably, the close-loop measurement can be carried out

to identify the system parameters. The on-line parameters identification is an advanced parameters identification method. Based on this method, an adaptive controller can be realized.

References

1. Humphris, R.R., Allaire, P.E., "Effect of Control Algorithms on magnetic Journal Bearing properties", *J. Eng. Gas. Turb. Pow.*, vol. 108 pp.624 (1986)
2. Keith, F.J., Williams, R.D., Allaire, P.E., "Digital Control of Magnetic Bearings Supporting a Multimass Flexible Rotor", *Tribology Trans.*, vol.33, no.3, pp.307-314, (1990)
3. Hisatani, M., Inoue, Y., Mitsui, J., "Development of Digitally Controlled Magnetic Bearings", *Bulletin of JSME*, vol.29, no.247, pp.214-220, (1986)
4. Youcef-Toumi, K., "A Digital Time Delay Controller for Active Magnetic Bearings", 2nd Intern. Symp. on Magnetic Bearings, pp.15. (1990)
5. Cai, Z., Zhang, Z.M., Zhao, H.B., "Performance of the Active Magnetic Bearings", *Proc. of the 2nd Intern. Symp. on Magnetic Bearing*, Tokyo, Japan, pp.251-255 (1990)
6. Cai, Z., Zhao, H.B., et al, "Design of Digital Active Magnetic Bearings Controllers", 2nd Symp. on Modern Design Methodology, Wuxi, China, (1990)
7. Sun, Z.Q., et al, "Computer Aided Design of Control System", Tsinghua University Press, (1988)
8. Bleuler, H., "Decentralized Control of Magnetic Rotor Bearing Systems" Ph.D. Dissertation, ETH, Switzerland, (1984)

Session 8

MICROGRAVITY AND VIBRATION ISOLATION 2

**Chairman - Ralph Fenn
SatCon Technology Corporation**

PRECEDING PAGE BLANK NOT FILMED

N92-27745

A MICROGRAVITY VIBRATION ISOLATION RIG

Bibhuti B. Banerjee
Carl R. Knospe
Paul E. Allaire

Center for Magnetic Bearings/ROMAC
University of Virginia
Charlottesville, VA 22903 USA

PRECEDING PAGE BLANK NOT FILMED

1. ABSTRACT

It is well-known that the spacecraft environment deviates from a state of zero gravity due to various random as well as repetitive sources. Science experiments that require a microgravity environment must therefore be isolated from these disturbances. Active control of noncontact magnetic actuators enables such isolation. A one-degree-of-freedom test rig has been constructed to demonstrate the isolation capability achievable using magnetic actuators. A cylindrical mass on noncontacting electromagnetic supports simulates a microgravity experiment on board an orbiter. Disturbances generated by an electrodynamic shaker are transmitted to the mass via air dashpots representing umbilicals. A compact Lorentz actuator has been designed to provide attenuation of this disturbance.

2. INTRODUCTION

Space exploration was initiated for the investigation of space itself, ranging from the planetary system to the limits of the universe. Resulting benefits of this effort include satellite communications and earth observation and imaging systems.

The scope of space exploration widened in the early eighties with the development of the space shuttle — a system capable of transporting a large cargo to a low earth orbit, and recovering the payload or frequently servicing it in space. A parallel development was the gradual change in the role of man in space, starting with the primarily technical function of a pilot and evolving into a more active involvement encompassing interactive work and scientific experimentation in space.

Space-based laboratories like the Skylab and the Spacelab were flown to utilize the "vanishingly low" gravitational forces available for extended periods of time. The results, however, were mixed at best, and disappointing in certain cases. This can be explained in part by the fact that the environment aboard the spacecrafts deviates considerably from the ideal of zero gravity due to disturbances produced by machinery and people on board, thruster fire, and other factors.

The incentives for performing science experiments in space include the investigation of phenomena that are influenced by gravity on earth, the development of novel materials and the improvement of processes like crystal

This work was supported in part by the NASA Lewis Research Center and the Center for Innovative Technology of the Commonwealth of Virginia.

growth [1]. In theory, a freely orbiting spacecraft offers a state of zero gravity to objects inside it, since the gravitational force is balanced by the centrifugal force [2]. However, in practice, there are various residual forces that disturb the environment.

Attempts to estimate these residual forces have been made in the past few years [3–10]. The orbital microgravity environment can be divided into three classes, as detailed in Table 1. Quasi-steady accelerations are generated by three sources — gravity gradient, aerodynamic drag and rotational acceleration. Any point of an orbiting structure that is at a distance from the structure's center of mass experiences a gravitational field that is different from that at the spacecraft center of mass. Aerodynamic drag due to the earth's atmosphere represents the absolute lower limit of the achievable background microgravity level, if the effect of light pressure is neglected. Finally, in order to keep the same vertical orientation on the space station with respect to the earth, the station must maintain a constant pitch rate about its center of mass. This creates a centripetal force that results in a rotational acceleration.

Orbital thruster fire and the steady-state operation of machinery like fans and pumps on board a spacecraft are among the sources of periodic accelerations, which occur at known frequencies. Impulsive disturbances like crew push-off and the start-up and shut-down of machinery create non-periodic accelerations. The irregular, unpredictable nature of these accelerations complicates attempts at isolation.

Theoretical acceleration requirements for various processes and experimental conditions have been investigated [3,7,11]. The common feature of curves depicting the frequency-dependent requirements is that, for a given process, the acceleration threshold is lowest from steady-state to about (0.01 — 0.1) Hz, depending upon the type of experiment. The acceptable acceleration then increases linearly with increasing frequency, up to (1 — 10) Hz. Subsequently, it increases as the square of the frequency. The acceleration tolerance also typically scales inversely with the volume that characterizes the process. The slopes and breakpoints result from fundamental aspects of a process, and the shape of the curve can be considered to be characteristic of a family of experiments. The acceleration level thresholds range from an extreme level of (10^{-7} — 10^{-8}) g_0 for some material science and fluid science experiments, to only 10^{-3} g_0 for the majority of biology and biotechnology experiments.

A comparison of the microgravity requirements with the actual environment available on the spacecraft indicates the need for vibration isolation. Moreover, the frequency range of interest spans several decades, thus requiring the use of multiple strategies for isolation.

For the high frequency range, passive isolators can serve adequately. Since these are relatively simple and cheap, they can be placed at each interface between a disturbance source and the space station. It should be noted that the sensitivity of various categories of experiments to high frequency disturbances is also comparatively low.

In the quasi-static frequency range, the extremely low stiffness and large motion required make attempts at isolation very difficult. Rattlespace constraints prohibit the occurrence of such large relative motions between the payload and the spacecraft. This imposes a fundamental limitation upon vibration isolation. Consequently, efforts at minimizing the input disturbances, like reducing the surface area presented to the atmosphere so as to reduce atmospheric drag and locating

payloads as close to the spacecraft's center of mass as possible, are necessary. Owens and Jones have also suggested the possibility of canceling such disturbances by continuous thruster control of the whole spacecraft [11].

At intermediate frequencies — approximately between 0.01 Hz and 1 Hz — no passive isolation scheme can be effective due to the displacements and isolation levels required. Only active vibration isolation at the payload-spacecraft interface allows the synthesis of the desired isolator properties and the adjustment of these properties using a control loop.

The actuator used to implement an active control scheme in the intermediate frequency range should ideally be noncontacting. The ideas of acoustic, electrostatic and electromagnetic (Lorentz force) levitation have been considered in the context of containerless processing of materials in a low gravity environment [12–15]. The first two techniques are limited to small objects. Lorentz forces are utilized by placing an electrically conductive sample within a suitably designed coil excited by a radio frequency current. Currents induced in the sample interact with the magnetic field of the coil to produce forces that tend to move the sample away from regions of high magnetic flux density. These currents also tend to heat the sample, which is often utilized to melt it. However, the inability to control this heating effect independently of the coil current required for levitation is a limitation of this technique. Some unwanted stirring of a melt by the induced currents also occurs.

Noncontact magnetic actuators, utilizing electromagnets or permanent magnets, appear to be the best solution for vibration isolation in the intermediate frequency range [16]. These actuators produce relatively large forces and can be applied to the isolation of a variety of science experiments. An active magnetic isolation system can be "tuned" by simply changing control law gains to accommodate changes in the payload or the expected disturbance environment, or to produce improved performance once in orbit. Such experiments need only be enclosed in a container, and can have umbilicals connecting them to the spacecraft.

A Long Action Magnetic Actuator (LAMA) has been proposed for this purpose [17]. This is a magnetic thrust bearing modified to accommodate longer strokes than those found in typical industrial applications. The pole-faces are inclined at an acute angle to the axis of motion, instead of being perpendicular to it. Detailed studies of magnetic thrust bearing design and use have been made [18–20]. The LAMA would be suitable for those intermediate frequencies that require motions not exceeding about a hundred miles. Since the forces called for are of the order of a few pounds at most, such actuators can be quite compact, the size being primarily determined by the stroke required.

A single-axis magnetic actuator similar to a magnetic thrust bearing has been described in [21]. The authors compared various sensing options to close the actuator control loop — gap and current sensing, force sensing and flux sensing. In their experiment, the authors achieved force linearization using flux feedback. Due to shaker and accelerometer limitations, the lowest recorded frequency of their measured data was 5 Hz. A subsequent paper described a similar isolation system extended to six degrees-of-freedom, called the Fluids Experiment Apparatus Magnetic Isolation System (FEAMIS) [22].

An interesting dual-mode approach to vibration isolation of large payloads over long displacements has been discussed in [23]. It was intended to provide the high performance active isolation of noncontact magnetic suspension technology without the limitations on articulation imposed by the small air gaps used in such

systems. In such a tandem system, a "coarse" motion actuator was controlled as a followup actuator, always attempting to keep the gap displacement for the magnetic actuator within its design limits. The magnetic actuator functioned as a "fine" motion actuator, ignoring the presence of the other, coarse actuator. The performance requirements on the coarse actuator were not very stringent, since the imperfections of its motions would be attenuated by the fine actuator.

The operation of microgravity science experiments is likely to require the use of an umbilical. An example is a plastic tube formed into a helical shape and carrying a coolant. Acceleration control to reject disturbances caused by the compliance of the umbilical has been theoretically investigated [24]. The umbilical was assumed to have stiffness, but not damping. The microgravity quality deteriorated with increasing umbilical stiffness, as expected. Acceleration control improved disturbance rejection greatly when compared to position-only control, but there was a price to be paid in the form of a more complicated control system. An active umbilical control strategy, in which the extension of the umbilical is minimized by making one end track the other, was also analyzed. It was found to be effective in principle and comparable in performance to the acceleration control loop technique.

3. EXPERIMENTAL RIG

An experimental rig to demonstrate vibration isolation down to microgravity levels in one degree-of-freedom has been constructed, and is shown in Figures 1 and 2. An innovative long stroke Lorentz actuator, described in detail in the next section, will be used to implement the isolation scheme.

An electrodynamic shaker with a long, peak-to-peak stroke of 6.25 inches represents the space platform. The shaker is mounted, via aluminum plates, on a concrete block resting on the laboratory floor. The shaker can generate sinusoidal, random or impulse waveforms at frequencies down to DC, thus simulating the disturbances typically produced on a space station that require active isolation.

The umbilicals connecting a science experiment to the space platform are expected to be flexible hoses and wires. These will be modeled by air dashpots with adjustable stiffness and damping coefficients. This type of dashpot has been evaluated at NASA Lewis in a single-degree-of-freedom mass-spring-damper system in a fixed-fixed mounting configuration [25]. The test indicated the possibility of a nonlinear stiffness/damping mechanism in these air dashpots. The vibration isolation rig has been designed so that different kinds of umbilicals may be employed, including actual hoses used for fluid transfer. This is important, since very little work has been done to date on vibration isolation to microgravity levels in the presence of an actual physical connection between the experiment and the space platform.

The long stroke Lorentz actuator, in parallel to the umbilical(s), connects the shaker armature to the mass representing a microgravity science experiment in space. This mass is a solid steel cylinder weighing 75 pounds, which is a typical weight for such an experiment. The cylinder is horizontally suspended in space by the magnetic forces generated by a noncontact electromagnetic support system. Similar to radial magnetic bearings, the support system consists of two eight-pole structures, mounted on a concrete base, at the two ends of the cylindrical mass. This concrete base is massive compared to the "experiment" mass, and rests on the same laboratory floor as the separate concrete block on which the shaker is

mounted. Eddy current probes sense the radial position of the cylinder and complete the feedback loop supplying current to the electromagnets. When the electromagnetic support system is turned off, the cylinder rests on a pair of touchdown pedestals made of delrin.

The axial acceleration of the cylinder will be sensed off a sensory plate mounted at its free end, using a very low frequency accelerometer with a maximum resolution of $1\text{ }\mu\text{g}$. Provision has been made for the use of other types of accelerometers, and the sensing of other states of the system, like position. The accelerometer signal will be fed to a feedback control circuit that determines the current required in the electromagnetic actuator to isolate the cylinder from the disturbances generated by the shaker. A control strategy for such an isolation system with multiple degrees-of-freedom is discussed in [26].

The background vibration levels on the concrete base on which the cylinder is mounted have been measured over twenty-four-hour periods, in both the horizontal and the vertical directions. These vibrations are of the order of milli-g's, the quietest period occurring from late in the night to early in the morning. Operating at this time will yield the highest degree of reproducibility in our results. Figures 3 and 4 show the frequency spectrum of the background acceleration in the horizontal and vertical directions. The vertical vibration shows acceleration components corresponding to natural frequencies of the mounting plate. The horizontal vibration has significant content at 45 Hz. The authors believe this is a floor mode.

4. THE LONG-STROKE LORENTZ ACTUATOR

A compact long-stroke Lorentz Actuator has been designed, built and tested in the laboratory. An intermediate version of the design was presented at the Workshop on Aerospace Applications of Magnetic Suspension Technology at NASA Langley in September, 1990 [27]. The final design described here incorporates many of the same features, but is much more linear with coil position. This was accomplished through modification of the flux distribution.

A schematic of the typical Lorentz Actuator, along with the terminology used, is shown in Figure 5. The current carrying coil moves in and out along the core. A strong permanent magnet in the shell maintains a constant magnetic flux in the cylindrical air gap across the pole faces, irrespective of the current in the coil (within design limits). The Lorentz force generated, therefore, can be linearly varied with coil current [28].

The requirements for the laboratory prototype were fixed at a total stroke of two inches and enough force capability to isolate a mass of 75 lbs. connected by an umbilical (air dashpot) to a source generating very low frequency vibrations. Force linearity with position and with current were also required. Moreover, in view of the ultimate goal of deployment in space, such a device had to be compact and lightweight. Low power consumption and low heat generation during operation were also important.

A computer program was written to implement a simple design algorithm for a Lorentz Actuator. The steps of this algorithm are presented in Figure 6.

Using a permanent magnet material with a very high maximum energy product of 35 MGOe (mega-Gauss-Oersted) [29] resulted in a design that required

a ring magnet of 3.20 in. outer diameter. The magnet manufacturer, however, could make such a magnet in one piece only if its outer diameter were less than 2 in.; making a ring magnet with a 3.20 in. outer diameter would have required the costly assembly of multiple segments, with an escalation of costs.

The possibility of designing a Lorentz Actuator satisfying all the requirements, with the outer diameter of the magnet being additionally constrained to less than 2 in., was therefore explored. The significant parameter in this context is the gap ratio, defined as the ratio of the shell-to-core air gap to the pole-face-to-core air gap. Conventional designs use ratios of 5:1 or higher in order to minimize leakage of magnetic flux from the shell to the core. Figures produced by the design program suggested that the design requirements could be met, along with the additional constraint, if the rule of thumb of using a gap ratio of 5:1 or more were drastically violated. Apparently, flux leakage, which the computer program did not take into account, would result in the failure of such a design. It was then hypothesized that this would not necessarily be the case if the core of the actuator were saturated during normal operation. The permeability of a saturated ferromagnetic material approaches that of air, and so most of the leakage that would have occurred, with such a low gap ratio (less than 2:1) and an unsaturated core, would be prevented.

A good way of verifying this hypothesis, without actually building such an actuator, is the use of finite element analysis. A commercially available magnetic finite element analysis package, MAGGIE, with a nonlinear modeling capability, was chosen. It also allowed us to take leakage and fringing into account, and different materials and geometries could be "tested" with relative ease.

A number of designs incorporating various features, were analyzed using the finite element analysis package. The finite element model was generated so as to achieve as much accuracy as possible, within hardware limitations. The mesh consists predominantly of quad elements. Infinite air elements, used earlier, were found to cause severe restrictions on mesh fineness. A mesh with only about 100 elements could be used. An air thickness of an inch on three sides of the axisymmetric model was specified instead. This was determined to be as accurate as having infinite air elements on all three sides for a model of this size, while a relatively fine mesh with about 400 elements could be used without encountering core memory limitations. Moreover, the finest mesh allowed by the configuration of our 386-based personal computer was used for the analysis.

Position linearity was improved, relative to the intermediate design, by increasing the length of the magnet, imparting a lip to it by reducing the shell outer diameter, and reducing the core diameter. The gap ratio resulting from the last change mentioned above is still only 1.47:1 — much smaller than a typically specified value of 5:1. The use of such an unconventionally low gap ratio enabled the design of a compact and lightweight actuator. Use of a large ratio would also have required a large diameter magnet that could not be made in one piece, thus increasing costs. The decrease in flux, and therefore force, caused by the increase in the length of the magnet was compensated, to some extent, by a reduction in the inner diameter of the magnet and a doubling of the pole piece thickness. Figure 7 shows the design. The overall length of the actuator is 4 in., while the outer diameter is only 1.95 in..

The salient features of the final design of the compact Lorentz Actuator are described below:

- Long Stroke — The requirement of two inches of total stroke is satisfied.
- Position Linearity — Over the whole two inches of stroke, the actuator exhibits a high degree of linearity. For a constant coil current, this means that the actuator force is the same irrespective of the axial position of the coil, within the stroke bounds. Figures 8 and 9 depict this relationship for positive and negative coil currents respectively. Note that flux leakage has been reduced to almost zero over the shell-to-core gap to achieve this. The maximum flux density across the shell-to-core gap is only about 7% of the maximum flux density across the pole-face gap.
- Current Linearity — This requires that the average flux density in the effective air gap remain constant with variations in the coil current between the upper and the lower limits. This is indeed the case, resulting in force vs. current linearity, Figure 10.
- Force — A maximum force of 1.25 lbs is produced by this actuator, which is sufficient for our needs. This peak force requires a coil current of 2.5 A.
- Weight — At 2.28 lb., this actuator is only a tenth of a pound heavier than the previous design.
- Current Density — A value of 1000 A/sq. in. in continuous use ensures cool operation. For peak loads, a fivefold increase in current density is possible.
- Materials — The magnet is made of neodymium iron boron, which has a very high maximum energy density product of 35 MGOe. Selection of such a material helped make the design compact. The high permeability circuit material is a 48% nickel-iron alloy that saturates at 15 kG. The B-H curve for this material, provided by the manufacturer, was input to MAGGIE as a table of a large number of points on the curve. This was necessary because a nonlinear material characteristic was being modeled.

The design specifications of the Lorentz Actuator are detailed in Table 2. This actuator was built and tested in our laboratory. Figure 11 compares the measured magnetic flux density in the radial direction along the shell-to-core and pole-face-to-core gaps with the values predicted by finite element analysis, for no current in the coil. The measured peak value is lower, but is spread over a wider axial distance. There is good agreement, especially over most of the shell-to-core gap, where near-zero values of flux density are crucial to achieve force versus position linearity. The actual actuator force is plotted against position for a number of values of coil current in Figure 12. The measured values of force are greater, in each case, than the predicted values since most of the small amount of leakage flux across the shell-to-core gap was neglected in calculating the predicted forces. Moreover, since the coil does see slightly greater total flux as it moves into the actuator, because of the small amounts of leakage, the forces measured increase somewhat with such motion. However, for low values of current and for coil positions that do not place it very near the closed end of the actuator, the actual forces deviate by less than 10% from the predicted values.

5. CONCLUSION

The rig designed to demonstrate vibration isolation to microgravity levels in one—dimension has been built and assembled. Measurements of the background acceleration levels have also been made, and the quietest period for operation has been determined. A compact, long stroke Lorentz actuator has also been designed, built, and tested. Its performance has been shown to match that predicted by finite element analysis very well. Microgravity isolation experiments will be conducted in the very near future.

6. REFERENCES

1. Feuerbacher, B., "Introduction," Chapter 1, Materials Sciences in Space, Ed. B. Feuerbacher, et al., Springer-Verlag, Berlin, 1986.
2. Hamacher, H., "Simulation of Weightlessness," Chapter 3, Materials Sciences in Space, Ed. B. Feuerbacher, et al., Springer-Verlag, Berlin, 1986.
3. Teledyne Brown Engineering, "Low Acceleration Characterization of Space Station Environment," Report No. SP858-MSFC-2928, Oct. 1985.
4. Chase, T.L., "Report on Micro-g Measurements for Space Shuttle Experiments," NASA Lewis Research Center, Dec. 1985.
5. Teledyne Brown Engineering, Abstracts, Workshop on Measurement and Characterization of the Acceleration Environment on Board the Space Station. Guntersville, Alabama, Aug. 11-14, 1986.
6. Hamacher, H., R. Jilg and U. Merbold, "Analysis of Microgravity Measurements Performed During D1," 6th European Symposium on "Materials Sciences under Microgravity Conditions." Bordeaux, Dec. 2-5, 1986.
7. Booz, Allen & Hamilton, "Overview of Space Station Microgravity Requirements," report presented to Dr. J.-D. Bartoe, Chief Scientist, Office of Space Station, July 14, 1989.
8. McDonnell Douglas Corporation "Space Station Definition and Preliminary Design," WP-02, DR-02, Book 22, Section 8 (Loads and Structural Dynamics), Dec. 1985.
9. Ramachandran, N., and C.A. Winter, "The Effects of g-Jitter and Surface Tension Induced Convection on Float Zones," 28th Aerospace Sciences Meeting, AIAA, Reno, Nevada, Jan. 8-11, 1990.
10. Armentrout, R.W., "Two-Body Dynamic simulation of Space Station Exercise Treadmill Including Startup Transient Effects," Memo No. A96-J749-STN-M-RWA-900006, Jan. 10, 1990.
11. Owen, R.G., and D.I. Jones, "Columbus Applications Study (WP. 1.1)," Technical Note No. BTN-001, University College of North Wales, School of Electronic Engineering Science, Bangor, Gwynedd, Sep. 1988.
12. Naumann, R.J. and D.D. Elleman, "Containerless Processing Technology," Chapter 12, Materials Sciences in Space, Ed. B. Feuerbacher, et al., Springer-Verlag, Berlin, 1986.
13. Hendricks, C.D., "Levitation, Coating, and Transport of Particulate Materials," Materials Processing in the Reduced Gravity Environment of Space, Ed. G.E. Rindone, et al., vol. 9, pp. 59, Elsevier Science Publishing Co., Amsterdam, 1982.
14. Rhim, W.-K., M. Collender, M.T. Hyson, W.T. Sims and D.D. Elleman, "Development of Electrostatic Positioner for Space Materials, Processing," Rev. Sci. Instrum., vol. 56, no. 2, p. 307, 1985.

15. Frost, R.T. and C.W. Chang, "Theory and Applications of Electromagnetic Levitation," Materials Processing in the Reduced Gravity Environment of Space, Ed. G.E. Rindone, et al., vol. 9, pp. 71, Elsevier Science Publishing Co., Amsterdam, 1983.
16. Grodsinsky, C.M. and G.V. Brown, "Nonintrusive Inertial Vibration Isolation Technology for Microgravity Space Experiments," submitted for publication to Journal of Spacecraft and Rockets, AIAA, Jan. 1990.
17. Allaire, P.E., M.A. Scott and B.B. Banerjee, "Magnetic Actuators for Microgravity Space Isolation," Workshop on Vibration Isolation Technology for Microgravity Science Experiments," NASA Lewis, Cleveland, Ohio, Sep. 28-29, 1988.
18. Banerjee, B.B., "Analysis and Design of Magnetic Thrust Bearings," M.S. Thesis, Univ. of Virginia, Charlottesville, May 1988.
19. Allaire, P.E., A. Mikula, B.B. Banerjee, D.W. Lewis and J. Imlach, "Design and Test of a Magnetic Thrust Bearing," Journal of the Franklin Institute, vol. 326, no. 6, pp. 831-847, 1989.
20. Allaire, P.E., J. Imlach, J.P. McDonald, R.R. Humphris, D.W. Lewis, B.B. Banerjee, B.J. Blair, J. Claydon and R.D. Flack, "Design, Construction and Test of Magnetic Bearings in an Industrial Canned Motor Pump," Proc. of the Sixth International Pump Users Symposium, Texas A&M Univ., College Station, Nov. 1988.
21. Havenhill, D.D. and K.D. Kral, "Payload Isolation Using Magnetic Suspension," AAS 85-014, Annual AAS Guidance and Control Conference, Keystone, Colorado, Feb. 2-6, 1985.
22. Allen, T.S., D.D. Havenhill and K.D. Kral, "FEAMIS: A Magnetically Suspended Isolation System for Space-Based Materials Processing," AAS 86-017, Annual AAS Guidance and Control Conference, Keystone, Colorado, Feb. 1-5, 1986.
23. Hamilton, B.J., J.H. Andrus and D.R. Carter, "Pointing Mount with Active Vibration Isolation for Large Payloads," AAS 87-033, Annual AAS Guidance and Control Conference, Keystone, Colorado, Jan. 31 - Feb. 4, 1987.
24. Jones, D.I., A.R. Owens, R.G. Owen and G. Roberts, "Microgravity Isolation Mount: Design Report," Technical Note No. BTN-009, University College of North Wales, School of Electronic Engineering Science, Bangor, Gwynedd, Sep. 1989.
25. Sutliff, T., "Vibration Isolation: Airpot (Dashpot) Damping Evaluation," PIR No. 89-9, NASA, Lewis, Cleveland, Ohio, 1989.
26. Hampton, R.D. and C.R. Knospe, "Extended H₂ Synthesis for Multiple-Degree-of-Freedom Controllers," International Symposium on Magnetic Suspension Technology, NASA CP-3152, 1992.

27. Banerjee, B.B., P.E. Allaire and C.R. Knospe, "Vibration Isolation of Science Experiments in Space – Design of a Laboratory Test Setup," Workshop on Aerospace Applications of Magnetic Suspension Technology, NASA CP–10066 Part 2, Paper 26, March 1991.
28. Carlson, A.B., D.G. Gisser and F.K. Manasse, "Magnetics and Electromechanics," Chapter 17, Electrical Engineering: Concepts and Applications, Addison–Wesley Publishing Company, Reading Massachusetts, 1989.
29. McCaig, M. and A.G. Clegg, Permanent Magnets in Theory and Practice, John Wiley & Sons, New York, 1987.

Table 1: Typical Disturbance Environment on a Spacecraft

| <u>QUASI-STEADY ACCELERATIONS</u> | | |
|-----------------------------------|----------------|-----------------------------|
| 1e-7 g | (0 to 1e-3) Hz | Aerodynamic Drag |
| 1e-8 g | (0 to 1e-3) Hz | Light Pressure |
| 1e-7 g | (0 to 1e-3) Hz | Gravity Gradient |
| <u>PERIODIC ACCELERATIONS</u> | | |
| 1e-2 g | 9 Hz | Thruster Fire (Orbital) |
| 1e-3 g | (5 to 20) Hz | Crew Motion |
| 1e-4 g | 17 Hz | Ku Band Antenna |
| <u>NON-PERIODIC ACCELERATIONS</u> | | |
| 1e-4 g | 1 Hz | Thruster Fire (Attitudinal) |
| 1e-4 g | 1 Hz | Crew Push-Off |

Table 2: Design Specifications for the Lorentz Actuator

| <u>LORENTZ ACTUATOR : FINAL DESIGN</u> | |
|--|--------------|
| Total length | ▪ 3.87 in |
| Magnet outer diameter | ▪ 1.95 in |
| Magnet inner diameter | ▪ 1.25 in |
| Magnet length | ▪ 2.77 in |
| Shell outer diameter | ▪ 1.68 in |
| Pole-piece thickness | ▪ 0.80 in |
| Core diameter | ▪ 0.75 in |
| Air gap | ▪ 0.17 in |
| Shell-to-core gap | ▪ 0.25 in |
| Gap ratio | ▪ 1.47 : 1 |
| Coil length | ▪ 4.00 in |
| Coil wire diameter | ▪ 26.67 mils |
| Number of turns | ▪ 600 turns |
| Number of layers | ▪ 4 layers |
| Maximum coil current | ▪ 2.5 A |
| Air gap flux density | ▪ 0.145 T |
| Max. force generated | ▪ 1.25 lbf |
| Actuator wt. (no coil) | ▪ 2.28 lbf |

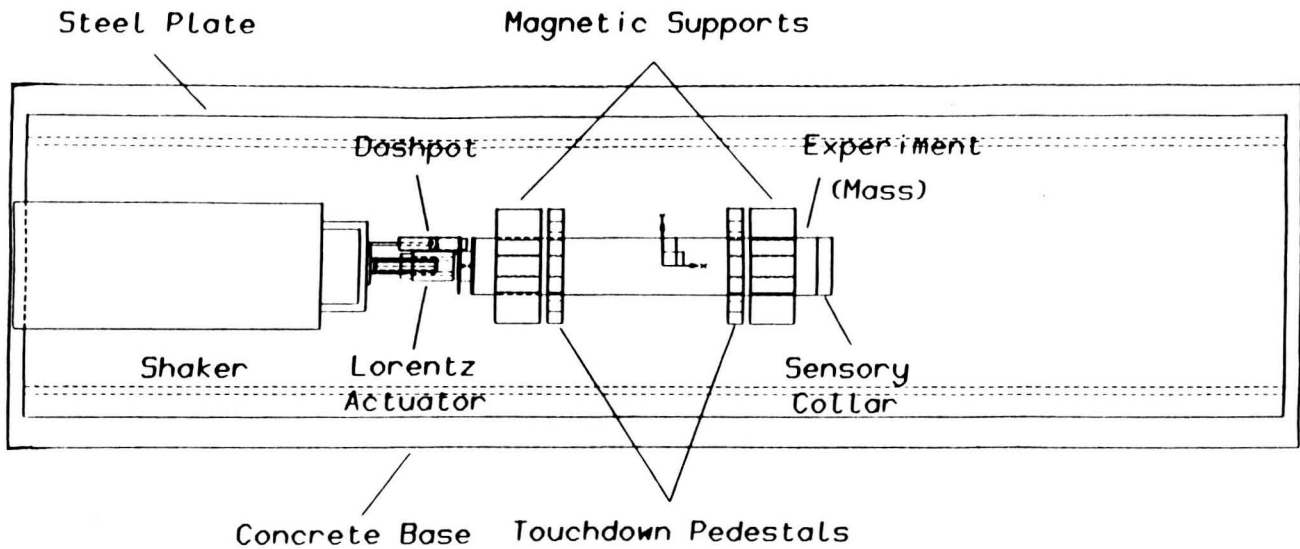


Fig. 1: Design Drawing of the Experiment Rig

ORIGINAL PAGE
BLACK AND WHITE PHOTOGRAPH

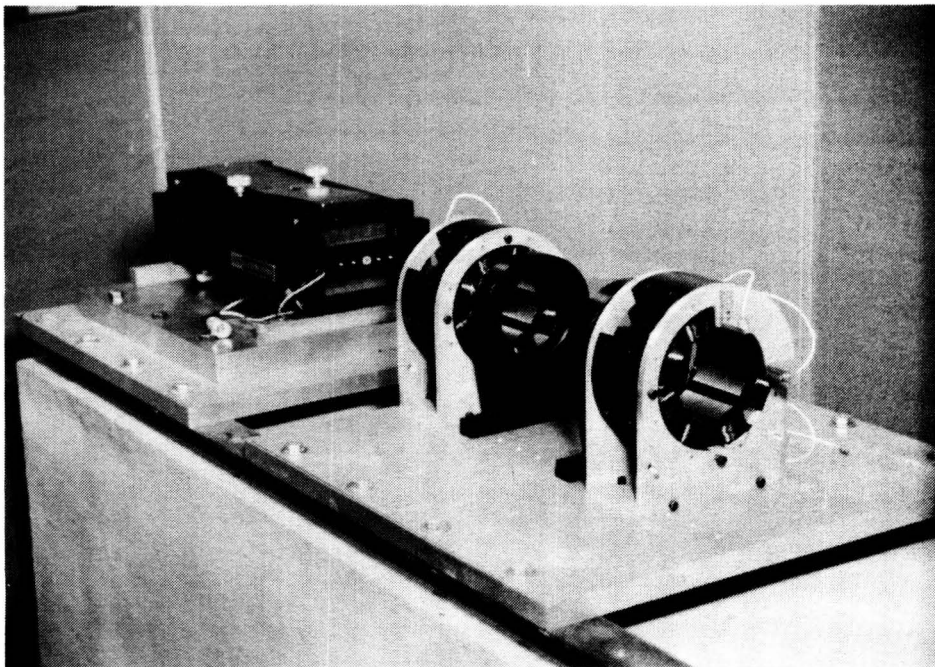


Fig. 2: The Experiment Rig Partially Assembled

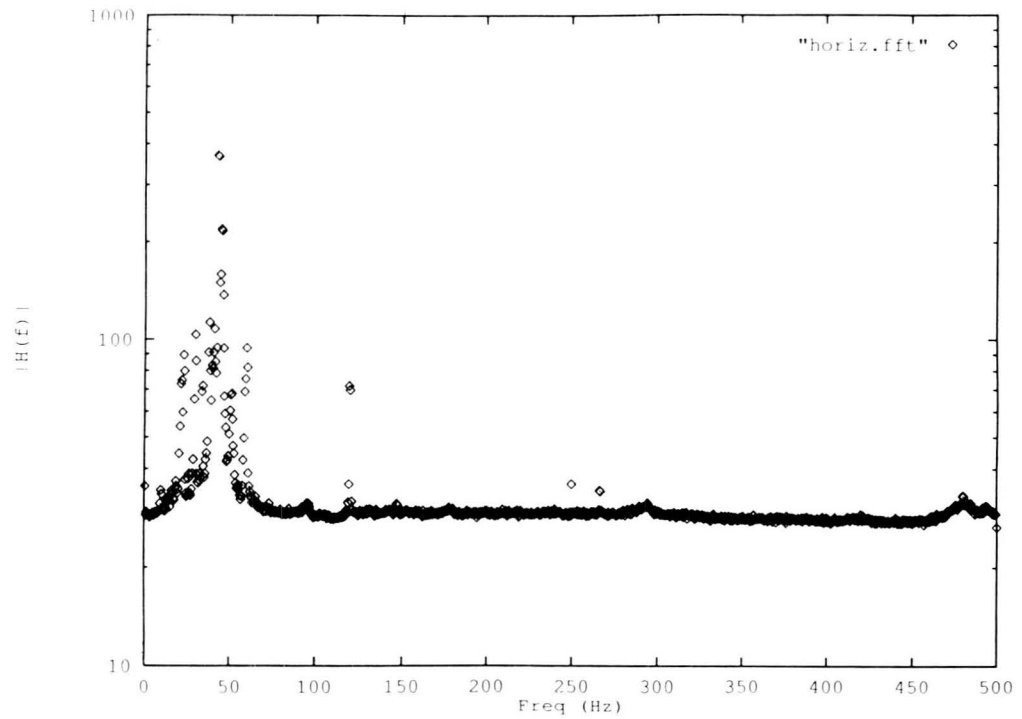


Fig. 3: Background Vibration in the Laboratory -- Horizontal

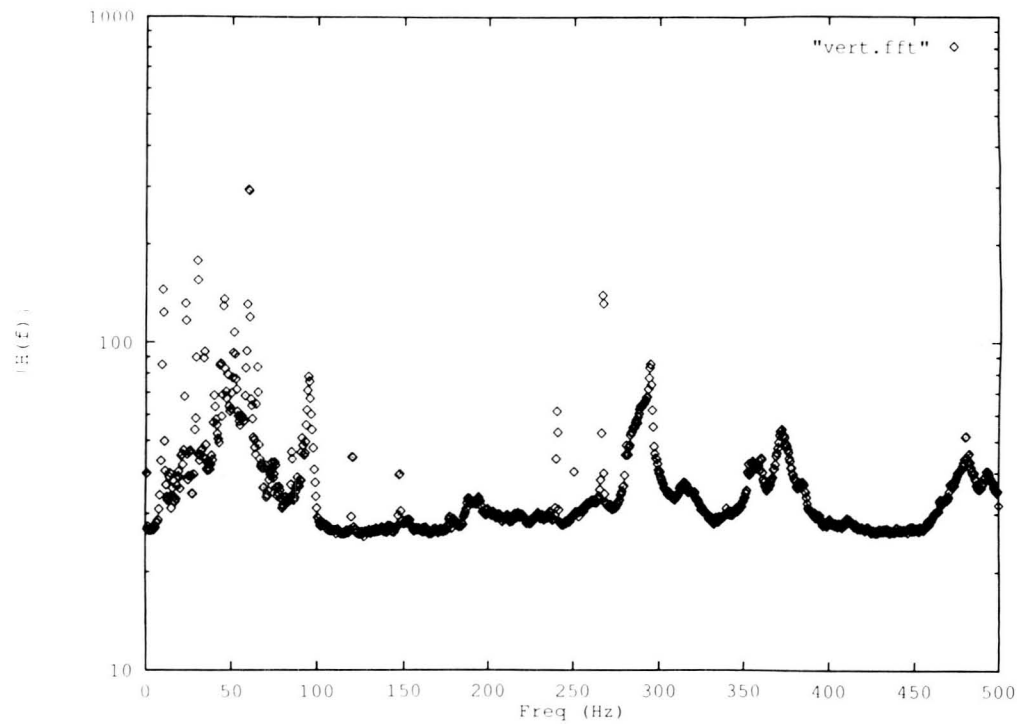


Fig. 4: Background Vibration in the Laboratory -- Vertical

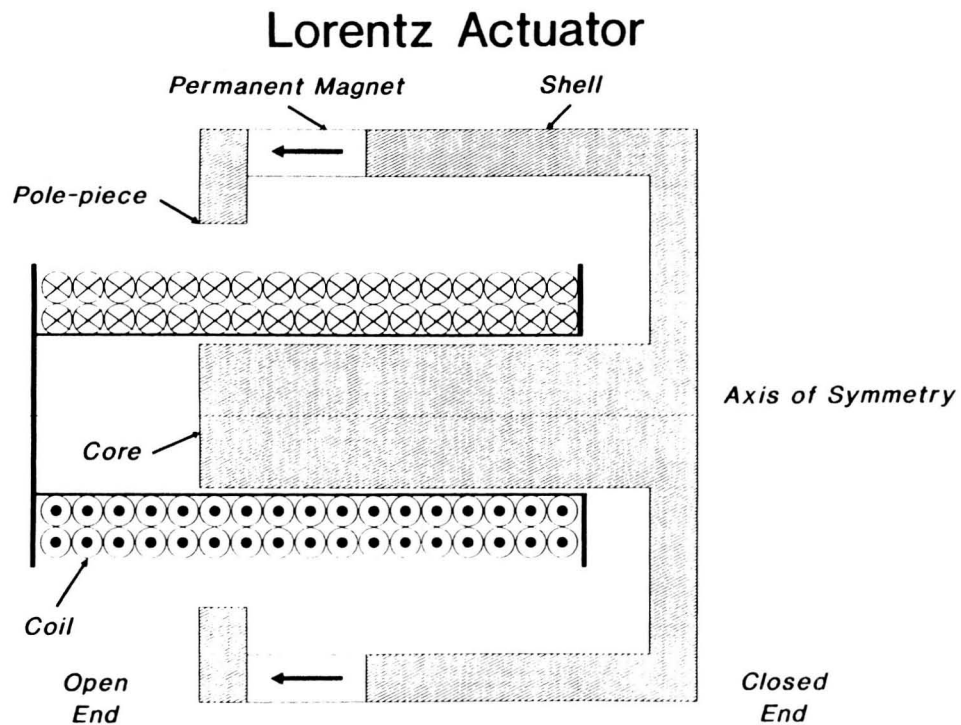


Fig. 5: Schematic of a Lorentz Actuator

LORENTZ ACTUATOR : DESIGN EQUATIONS

1. Assume permanent magnet operating point for maximum energy product : $(-H_1, B_1)$.
2. Compute magnet flux, $f_m = B_1 \cdot A_m$.
3. Compute circuit flux, $f_c = H_1 \cdot L_m / R$, where R is the circuit reluctance.
4. Compare f_m and f_c .
5. Adjust operating point until $f_m = f_c = f$, the actual operating point. (When saturated, $f = \text{saturation flux in saturated segment of circuit.}$)
6. Calculate air gap flux density, $B_g = f / A_g$.
7. Compute force capability, $F = i \cdot l \cdot B_g$, where i is the actuator current and l is the total length of coil wire in the air gap.
8. Change actuator geometry or circuit / magnet material until desired force level is achieved.

Fig. 6: A Simple Algorithm for Designing a Lorentz Actuator



Fig. 7: The Compact, Long-Stroke Lorentz Actuator

Compact Lorentz Actuator - Force Coil Currents Positive (as Shown)

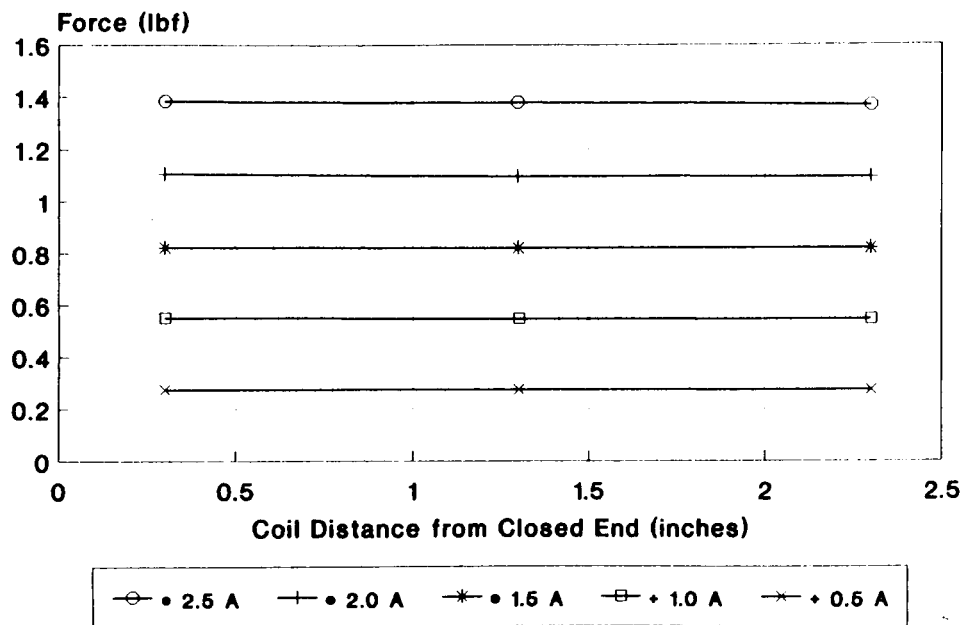


Fig. 8: Force vs. Position (for Positive Coil Currents)

Compact Lorentz Actuator - Force Coil Currents Negative (as Shown)

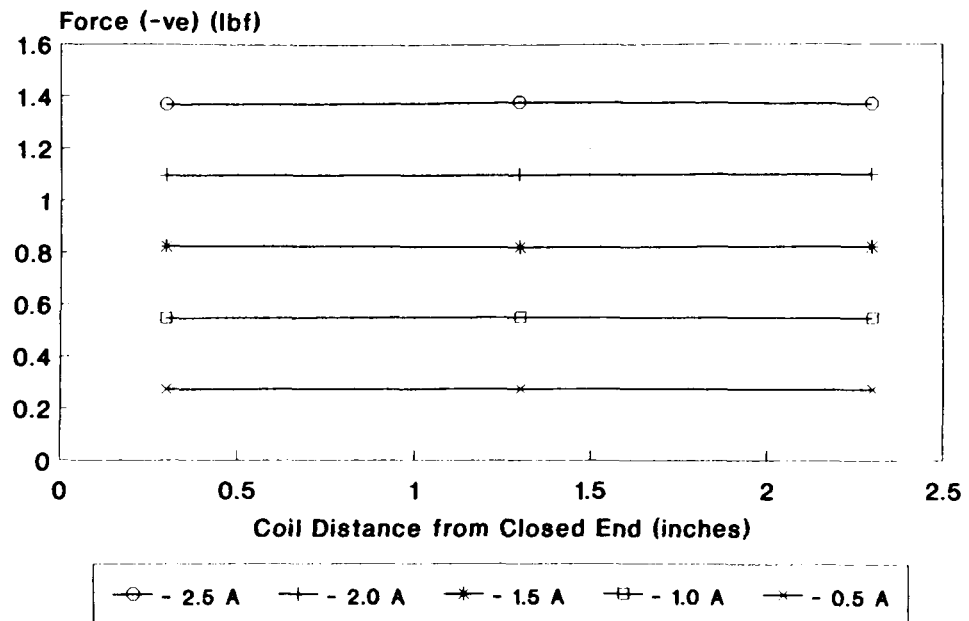


Fig. 9: Force vs. Position (for Negative Coil Currents)

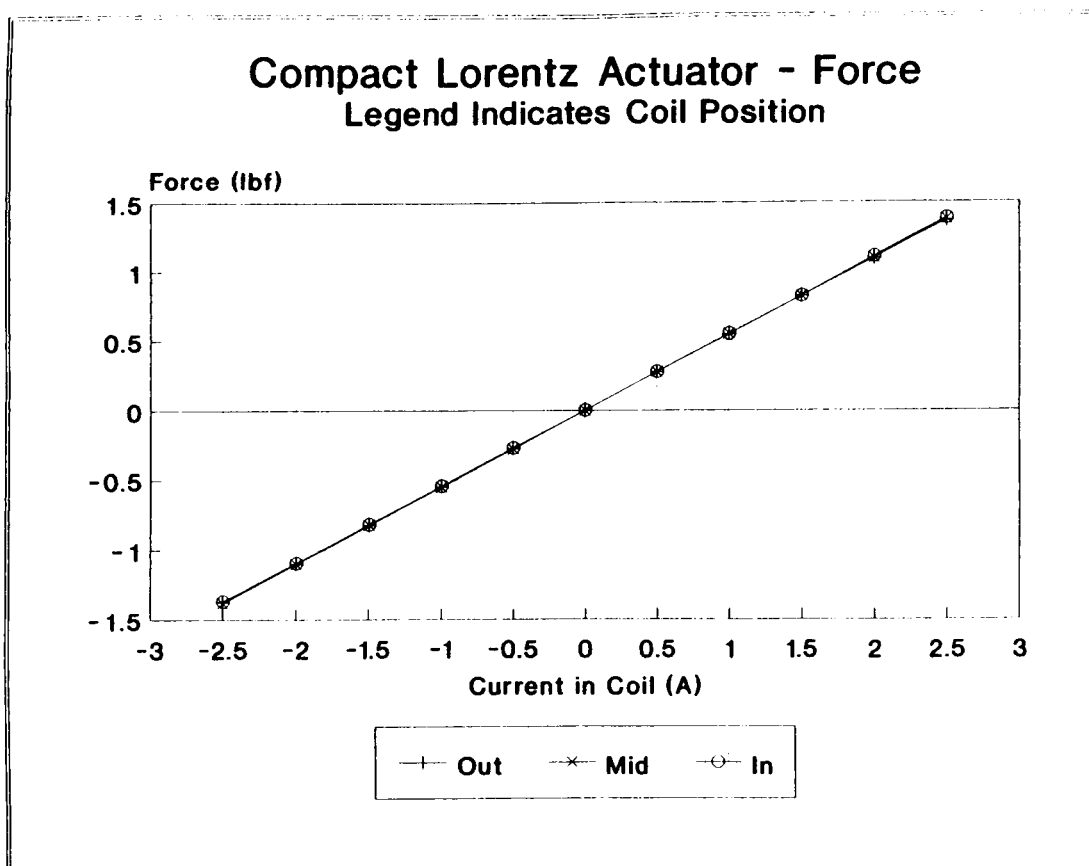


Fig. 10: Force vs. Current (for Three Different Coil Positions)

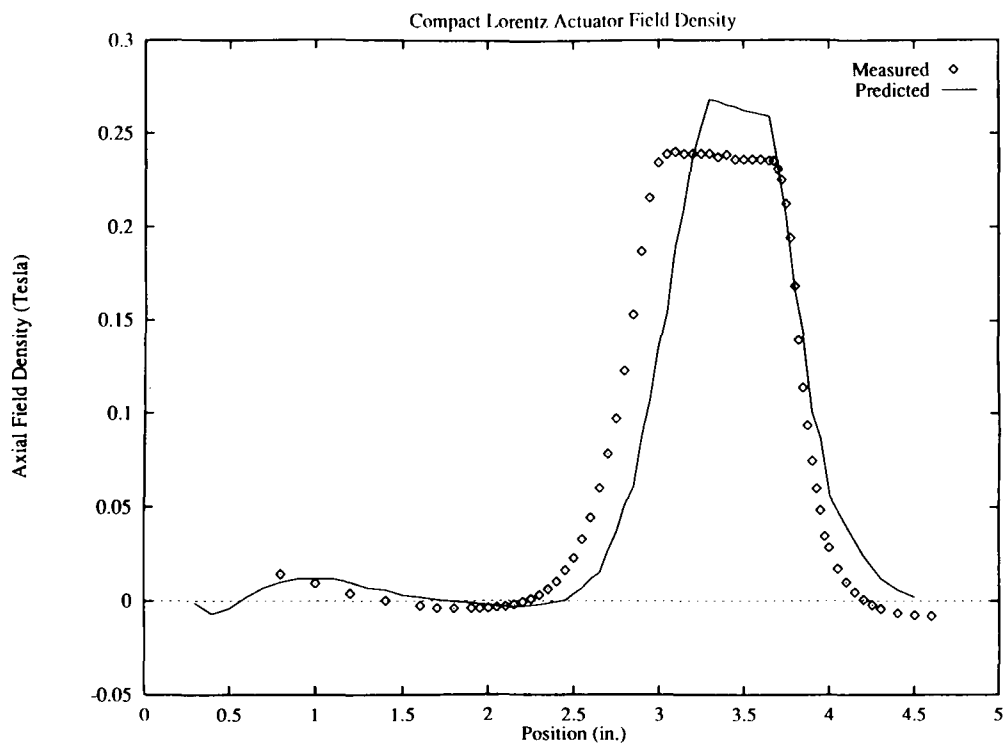


Fig. 11: Comparison of Actual Flux Density with Predicted Values (for No Current in the Coil)

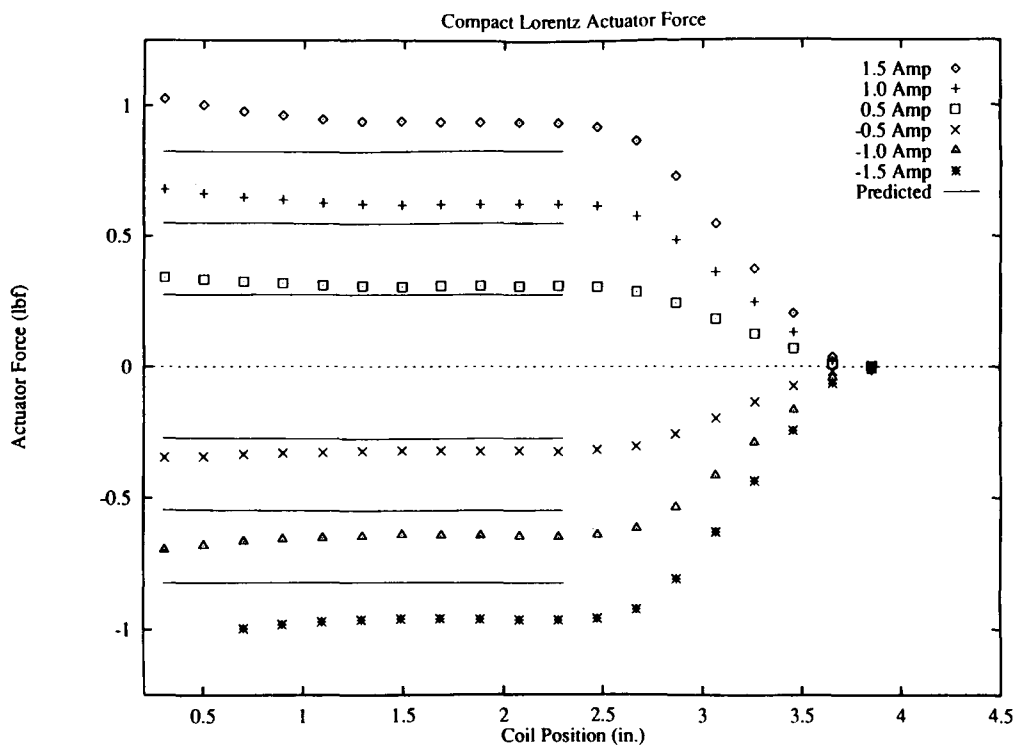


Fig. 12: Comparison of Actual Force vs. Position Characteristics with Analytical Predictions

VIBRATION DAMPING OF ELASTIC WAVES IN ELECTRICALLY CONDUCTING
MEDIA SUBJECTED TO HIGH MAGNETIC FIELDS

T. G. Horwath

TG&C Associates, Inc.
One Cessna Lane
Falmouth, Virginia 22405

21 August 1991

Abstract:

The propagation of vibrational energy in bulk, torsional, and flexural modes, in electrically conducting media can undergo strong attenuation if subjected to high magnetic fields in certain spatial arrangements. The reasons for this are induced Eddy currents which are generated by the volume elements of the media moving transversally to the magnetic field at acoustic velocities. In magnetic fields achievable with superconductors, the non-conservative (dissipative) forces are comparable to the elastic and inertial forces for most metals. Strong dissipation of vibrational energy in the form of heat takes place as a result. A simplified theory is presented based on engineering representations of electrodynamics, attenuation values for representative metals are calculated, and problems encountered in formulating a generalized theory based on electrodynamics of moving media are discussed. General applications as well as applications specific to maglev are discussed.

Introduction:

The interconnection of elastic and electromagnetic phenomena in media capable of supporting both, have with a few exceptions been only curiosities so far. Few applications have been developed so far, mainly because of the relative minuteness of the effects. The special cases of acoustic propagation and vibration in the presence of steady state magnetic fields, magneto-acoustics, however, did receive some attention and have been investigated on a few occasions.

In 1968, LILLEY and CARMICHAEL¹ at the University of Western Ontario, Canada, conducted laboratory experiments with standing elastic waves in a metal bar subjected to a magnetic field. The

investigators reported slight damping effects which depended on the magnitude as well as the gradient of the field.

Later, in 1985, LEE² at the Stanford University Department of Mechanical Engineering analyzed electromagnetic damping together with thermoelastic damping of structures. Strong dependence on structural and geometrical configurations was found, as one would expect.

The major shortcoming in exploiting magneto-acoustic phenomena for practical applications was due to the limit of magnetic field strength which could be produced by practical means. This was exacerbated by the fact that the effects have a second order dependence on field strength, as will be shown later. There is always the possibility, of course, of using conventional (low temperature) superconducting technology to generate the required fields. The complexity of the cryogenic support systems and the cost of such systems could be justified only in the rarest of circumstances.

Recent advances in the technology of high temperature superconductors, will render magneto-acoustic effects much more relevant in the future. This was first recognized by HORWATH³ in a paper presented to the 119th meeting of the Acoustical Society in May 1990. Magnetic fields of several Tesla and possibly tens of Tesla will soon be achievable with such high temperature superconducting materials at a low cryogenic overhead. Such materials have the further advantage of much higher critical fields and currents. Their only limitation at present is relatively low current densities.

In the high magnetic fields achievable with superconductors the non-conservative or dissipative forces in electrically conducting elastic media will become comparable to the elastic and inertial forces. As a result of this it will be possible to achieve significant direct dissipation of acoustic energy in metals, for instance, for both bulk waves and flexural waves. This will provide means for damping on a scale difficult to achieve before, and thus open new regimes for applications.

First order estimates of the damping effects will be presented in the following. The attenuation lengths of longitudinal waves in bulk materials subjected to high magnetic fields will be calculated. This will be followed by a similar determination of the transversal impedance component in electrically conducting plates, which are subjected to high magnetic fields. Only very simple special cases will be discussed, aimed mainly at introducing the concept.

Propagation of Longitudinal Waves in Bulk Material:

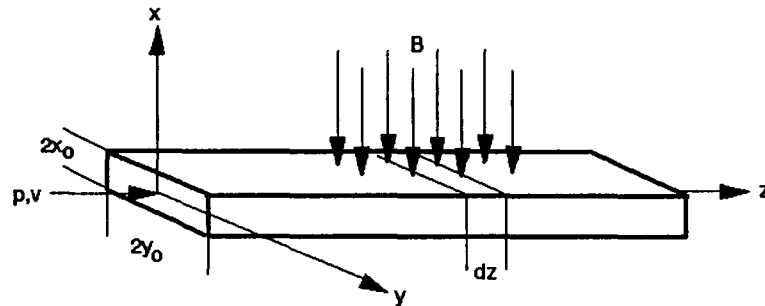


Figure 1

Figure 1 depicts a section of an electrically conducting slab, which is penetrated by a homogeneous magnetic field B , at normal incidence. A pressure disturbance, periodic or aperiodic, is applied at one end and propagates along the z -axis, through the magnetic field region, causing motion of the slab material at acoustic velocities. This produces a voltage in the y -direction in the volume element $4x_0 y_0 dz$

$$E = -d\Phi/dt = -2y_0 Bv \quad (1)$$

which in turn gives rise to a current in the same volume.

$$I = E/R = -2\sigma x_0 Bvdz \quad (2)$$

It is tacitly assumed here, for simplicity, that the current path is closed through the fringe regions outside the magnetic field with essentially zero resistance. The current flowing in this volume element of the slab experiences a Lorentz Force, which is counteracting the driving disturbance.

$$dF = 2IBy_0 = -4\sigma x_0 y_0 vB^2 dz \quad (3)$$

From this the pressure is obtained as

$$dp = dF/dA = dF/4x_0 y_0 = -\sigma v B^2 dz \quad (4)$$

For elastic wave propagation in bulk material the pressure is related to the velocity by

$$v = p/(\delta E)^{1/2} \quad (5)$$

where δ is the density and E the bulk modulus of the material. Using this relationship the differential equation is obtained from equation (4)

$$dp/p = -\sigma B^2 dz/\delta c \quad (6)$$

The attenuation length thus follows as

$$z_{a.b} = (\delta E)^{1/2} / \sigma B^2 \quad (7)$$

The attenuation is a function of the usual material parameters, such as density, sound velocity, and electrical conductivity, as expected, and has an inverse square dependence on the magnetic field.

Table 1 below presents the attenuation length calculated by the above methodology for different metals subjected to a magnetic field of 10 Tesla.

ATTENUATION LENGTH FOR BULK WAVES
IN VARIOUS METALS

(Magnetic Field = 10 Tesla)

| Material | Electrical Conductivity [$\text{Ohm}^{-1} \text{m}^{-1}$] | Density [kgm^3] | Bulk Modulus [Nm^{-2}] | Attenuation Length [m] |
|----------|---|-------------------------------|---|------------------------------|
| Aluminum | 3.77×10^7 | 2690 | 7.18×10^{10} | 3.68×10^{-3} |
| Copper | 5.85×10^7 | 8930 | 1.23×10^{11} | 5.67×10^{-3} |
| Steel | 6.21×10^6 | 7650 | 2.12×10^{11} | 6.48×10^{-2} |

Table 1

Propagation of Torsional (Shear) Waves:

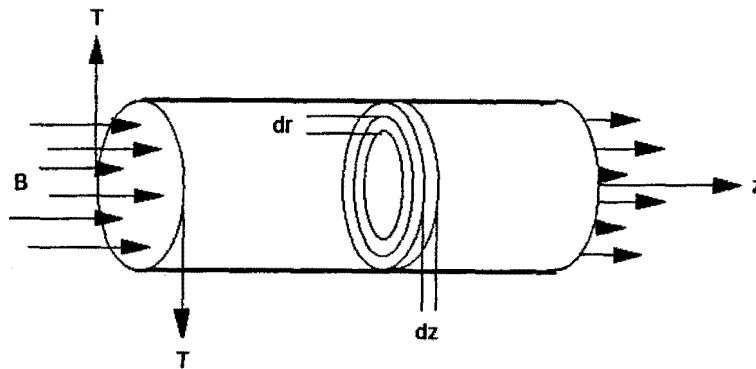


Figure 2

The calculations proceed in a similar fashion as in the above case. Figure 2 shows a section of an electrically conducting rod which is penetrated by an axial magnetic field B. A torque disturbance is applied to the rod at one end and propagates along

the longitudinal axis, producing a radial voltage in the annular volume element of the rod section $2\pi r dr dz$

$$E = -d\Phi/dt = -Br\omega dr \quad (8)$$

The current in this volume element is

$$I = E/R = -2\pi\omega B dz \quad (9)$$

The Lorentz force acting on this current element generates a counter torque, which per unit cross sectional area is

$$dT = -\sigma\omega B^2 dz \quad (10)$$

For torsional waves propagation this torque per unit area is related to the angular velocity by

$$\omega = T/(\delta G)^{1/2} \quad (11)$$

where G is the shear modulus of the material. Using this relationship together with equation (10) the differential equation follows

$$dT/T = -\sigma B^2 dz/(\delta G)^{1/2} \quad (12)$$

which yields the attenuation length for torsional waves

$$z_{\text{att}} = (\delta G)^{1/2} / \sigma B^2 \quad (13)$$

Again, as expected, the attenuation is a function of the same material parameters as above, and is inversely proportional to the square of the magnetic field.

Table 2 lists attenuation lengths for torsional waves in different metals in a field of 10 Tesla.

ATTENUATION LENGTH FOR TORSIONAL WAVES IN VARIOUS METALS

(Magnetic Field = 10 Tesla)

| Material | Electrical Conductivity [$\text{Ohm}^{-1} \text{m}^{-1}$] | Density [kgm^3] | Shear Modulus [Nm^{-2}] | Attenuation Length [m] |
|----------|---|-------------------------------|--|------------------------------|
| Aluminum | 3.77×10^7 | 2690 | 2.69×10^{10} | 2.25×10^{-3} |
| Copper | 5.85×10^7 | 8930 | 4.55×10^{10} | 3.44×10^{-3} |
| Steel | 6.21×10^6 | 7650 | 7.95×10^{11} | 3.97×10^{-2} |

Table 2

Transversal Damping Impedance in Plates:

Flexural waves are more difficult to treat in this context because of their highly dispersive nature, which precludes the use of a simple relationship between pressure and velocity. A somewhat different approach is taken therefore, calculating a damping impedance rather than an attenuation length.

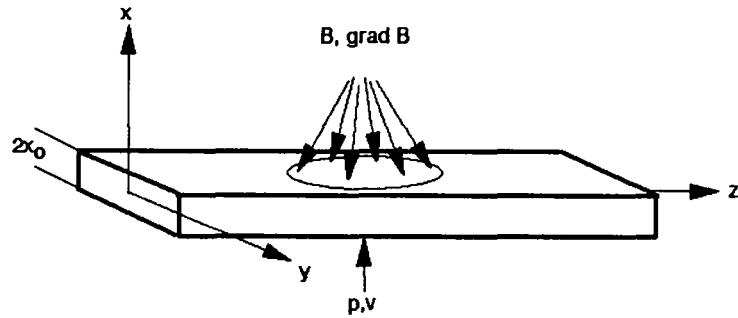


Figure 3

Figure 3 depicts a section of an electrically conducting plate is now subjected to an inhomogeneous magnetic field B , with a strong gradient $\text{grad } B$. Both field and gradient are perpendicular to the plate. It is further assumed that the field region is contained within a circle of the radius R_a . A pressure disturbance is applied from the opposite side of the plate, causing the plate material to move in the direction of the field gradient, with an acoustic velocity typical for a flexural vibration mode. Circular currents are induced in annular elements of the material with the volume $4\pi r x \cdot dr$ as a result of the changing magnetic flux caused by this motion.

The voltage induced is obtained from Faraday's Law of Induction as

$$E = -d\Phi/dt = - \iint dB/dx \, dx/dt \, dA \quad (14)$$

or

$$E = \iint v_x \, \text{grad}_x B \, dA \quad (15)$$

The current element is obtained from Ohm's Law as

$$dI = E\sigma x_0 dr/\pi r \quad (16)$$

performing the integration in (15) and substituting the result into this the current element becomes

$$dI = \sigma r x_0 dr v_x \text{grad}_x B \quad (17)$$

which allows determination of the Lorentz force element

$$dF = 2\pi r dI B_y z \quad (18)$$

and by substituting (17) into (18) and integrating, the total Lorentz force acting on the circular region is obtained as

$$F = \int 2\sigma \pi x_0 r^2 v_x B_y z \text{grad}_x B dr \quad (19)$$

which becomes

$$F = 2/3 \sigma \pi x_0 R^3 v_x B_y z \text{grad}_x B \quad (20)$$

Finally, considering that the pressure $p = F/A$, and the transversal damping impedance $z_t = p/v$, the latter becomes

$$z_t = 2/3 \sigma x_0 R^3 B_y z \text{grad}_x B \quad (21)$$

This transversal damping impedance is again a function of electrical conductivity, thickness of the plate, radius of the field region, and is proportional to the product of the magnetic field and its gradient.

Table 3 below presents the transversal damping impedances for the same materials. Assumed is a thickness of the plate of one centimeter, an active area of one square meter, and a magnetic field of 10 Tesla with a gradient of 10 Tesla per meter. For these conditions the damping impedances for metals are very high.

TRANSVERSAL IMPEDANCE FOR VARIOUS METALS

(Area = 1m^2 , Thickness = 10^{-2}m ,
Field = 10 T, Gradient = 10Tm^{-1})

| Material | Electrical Conductivity [$\text{Ohm}^{-1}\text{m}^{-1}$] | Transversal Impedance [Nm^{-3}sec] |
|----------|--|--|
| Aluminum | 3.77×10^7 | 7.09×10^6 |
| Copper | 5.85×10^7 | 1.10×10^7 |
| Steel | 6.21×10^6 | 1.17×10^6 |

Table 3

Attempts to Formulate a Generalized Theory:

The above considerations were based on very elementary electromagnetic theory, and furthermore made use of engineering representations applied to very simple, special cases. It would be desirable to have a more rigorous and generalized theory, describing all possible interactions between electromagnetic fields and sound fields in electrically conducting media. In the attempt to construct such a theory it became immediately apparent, however, that it will be very complicated at best, if not entirely impossible to develop. The reasons for this are the following:

(1) The theory would have to be based on the Electrodynamics of Moving Media, or Relativistic Electrodynamics. The Maxwell

Equations, which are the cornerstone of most electrodynamic phenomena, do not apply in this case. They have no provision for moving media, and are hence not compatible with the description of the Lorentz Force, which is, the result of a moving conductor. Relativistic Electrodynamics have much more complicated formulations than the Maxwell Equations.

(2) Electrodynamics, relativistic or not, in general deals with time variant, non-stationary phenomena, and therefore by necessity is represented in time domain. Acoustic and elastic phenomena, on the other hand, because of their stationary nature are better described in the spectral domain. This lack of very basic compatibility is another shortcoming.

For the above reasons it is believed that investigations of even slightly more complicated geometries than discussed above will have to resort to numerical methods, based on engineering formulations of electromagnetic principles. Such approaches are useful and effective, but in the view of the author do not provide the same degree of insight in a general sense, and are also not as elegant from a physicists point of view.

General Applications:

Very interesting application possibilities will become practical when high magnetic fields generated with high temperature superconductors become routinely available. A few of such possibilities are outlined in the following:

(1) Vibration Isolation: The most obvious is, of course, vibration isolation. Because of the short attenuation length in metals, it will be possible to dissipate energy directly in vibration mounts such as springs. This will minimize both transmitted vibrations to the foundation, as well as the buildup of vibrational amplitudes at the source. The vibrational energy will, of course, be dissipated as heat in the regions subjected to the magnetic field, and provisions for heat removal will be required.

(2) Selective Mode Damping: In the most general case, the dissipation of acoustic energy will be anisotropic, depending on the relative orientations of the magnetic and acoustic vector variables. This characteristic can be exploited for the selective damping of vibration and propagation modes, and also for the suppression or enhancement of mode conversions.

(3) Anechoic Structures: The impedance figures for plates indicate that it may be possible to match the characteristic impedance of water. Under such conditions, plates and other structures submerged in water may be rendered anechoic.

(4) Suppressed Radiation: The same is true for vibrating plates radiating acoustic energy. It would be possible to change the impedance of such plates either locally, or globally, to suppress

selected radiating modes, or possibly even vibration in its entirety.

(5) Structural Hardening: Finally, it is foreseen that the response of plates to impinging transient pressure waves, such as shock waves, for example, could be altered significantly, providing much greater stiffness and resistance to such phenomena.

Specific Applications to Magnetic Suspension:

The utilization of the phenomena discussed to various magnetic suspension applications can result in considerable synergies particularly when very high magnetic fields are involved. Substantial damping forces can be obtained for various magnetic suspension applications if design configurations are chosen which enhance the discussed effects.

One increasingly important system concept based on magnetic suspension is the magnetically levitated train, or maglev. Maglevs are subjected to vibrations induced by irregularities of the tracks, by fluctuations of the magnetic propulsion and levitation forces, and by various transient aerodynamic phenomena such as wind gusts, entry and exit of tunnels, and other passing maglev trains. The vibrations induced by these various sources will have to be attenuated in the interest of ride quality. Attenuation has to be accomplished mainly by the suspension, may it be the primary suspension (levitation), the secondary, or a combination of the two. Electromagnetic vibration damping is a natural choice for maglevs because of the high magnetic fields used for levitation.

The values for damping impedances of plates presented in Table 2 are comparable to the stiffnesses of electrodynamic (EDS) maglev suspensions. This type of maglev system also utilizes superconducting magnets for primary levitation. The magnetic fields are of sufficient magnitude to allow the construction of simple and efficient electrodynamic vibration isolators using the same superconducting magnets which provide the primary levitation.

Conclusions:

It is envisioned that this area of magneto-acoustic interactions will play an important role in vibration damping in the future, leading to many interesting and important applications, including the ones outlined above. Practical means for generating the necessary magnetic fields are being developed at a rapid pace, since the discovery of high temperature superconducting materials. The fields of acoustics and structural vibrations will undoubtedly benefit from these developments, which are driven by a vast commercial potential encompassing all fields of electrical technologies.

References:

- (1) Lilley, F. E. and Carmichael, C. M.
Can J Earth Sciences Vol.5, Pt.1 p 825-9 (1968)
- (2) Lee, U.
AIAA Journal Vol.23, p 1783-90 (1985)
- (3) Horwath, T. G. Paper No. JJ-4 presented at the
119-th Meeting of the Acoustical Society of America (1990)

Coarse-Fine Residual Gravity Cancellation System with Magnetic Levitation

S.E. Salcudean

*Department of Electrical Engineering, University of British Columbia
2356 Main Mall, Vancouver, B.C., Canada, V6T 1W5*

H. Davis, C.T. Chen, D.E. Goertz

*Department of Physics, University of British Columbia
6224 Agricultural Road, Vancouver, B.C., Canada, V6T 1Z1*

B.V. Tryggvason

*Canadian Astronaut Program, Canadian Space Agency
Rockliffe Base, Ottawa, Ont., Canada, K1A 1A1*

Abstract

Aircraft flights along parabolic trajectories have been proposed and executed in order to achieve low-cost, near free-fall conditions of moderate duration (*e.g.* NASA KC-135 flights). This paper describes a six degrees-of-freedom experiment isolation system designed to cancel out residual accelerations due to mechanical vibrations and errors in aircraft trajectory. The isolation system consists of a fine-motion magnetic levitator whose stator is transported by a conventional coarse-motion stage. The levitator uses wide-gap voice-coil actuators and has the dual purpose of isolating the experiment platform from aircraft vibrations and actively cancelling residual accelerations through feedback control. The coarse-motion stage tracks the levitated platform in order to keep the levitator's coils centered within their matching magnetic gaps. Aspects of system design, an analysis of the proposed control strategy and simulation results are presented. Feasibility experiments are also discussed.

I. Introduction

A number of scientific experiments require zero-gravity conditions. As an alternative to outer-space experiments and drop-towers, aircraft flights along parabolic trajectories have been proposed and executed in order to achieve low-cost, near free-fall conditions of moderate duration. Due to the deviation of the aircraft flight trajectory from a perfect parabola and due to mechanical vibrations, equipment that is solidly attached to the aircraft is still subject to small, unwanted, forces. At low frequencies, these forces are due to deviations in aircraft trajectory, while at high frequencies, these forces are due mainly to mechanical vibrations.

In order to deal with the problem of residual forces, large motion isolation mounts (LMIMs) have been proposed in joint studies between the Engineering Physics Department at the University of British Columbia (UBC) and the Canadian Astronaut Program [1, 2, 3]. The proposed approaches would allow low-friction, 3 DOF motion of an experimental setup (on an $x - y$ gantry with additional z motion) within a specified, encaged volume within the aircraft. Low-friction motion of the experimental platform with respect to the aircraft frame can be achieved by using air or magnetic bearings along each degree of freedom, thus isolating the experimental platform from the body of the aircraft. Such a large motion isolation mount would enable a closer approximation to free-fall (indeed, limited only by friction, vibrations and drag) than what can be obtained when the experimental platform is solidly connected to the aircraft.

Because an object free-floating in the aircraft could exceed its travel limit in a very short period of time which depends on the aircraft acceleration history and the release conditions, a number of experiments have been performed on a one-dimensional (z -axis) LMIM in the KC-135 to determine the time of free-fall before the limit of travel is exceeded [1, 2, 3]. The system has also been modelled to give statistical results with reasonable accuracy. From the instant of release at the start of the zero- g parabola, a 5 second free-float period can be obtained for approximately 50% of the attempts. The range of free-float times is from 1 second to 13 seconds. With optimum release conditions the free-float period can be extended to about 8 seconds with 50% assurance.

Motion isolation reduced accelerations transmitted from the aircraft to the object to under 5 mg during the free-fall period and much of that value was due to instrumentation noise. Active gravity cancellation has also been proposed and can be achieved by using linear motors to actuate one or several degrees of freedom [3].

In this paper, it is proposed that the platform carrying the zero-gravity experiment be completely isolated from the aircraft frame, by making use of active magnetic levitation. The approach is similar to the one proposed in [4, 5] for the design and control of a magnetically levitated (maglev) robot wrist for fine compliant motion. Although active magnetic levitation of the experiment platform would reduce high frequency disturbances due to aircraft frame vibrations, it would provide too little motion range to allow for the larger, low frequency deviations from free-fall due to aircraft trajectory errors. Therefore, this paper proposes a coarse-fine residual gravity cancellation system using magnetic levitation for small, high frequency motion isolation, combined with a coarse positioning system for low frequency motion isolation.

Coarse-fine motion systems have been proposed, analyzed and used before for increasing speed and dexterity in manufacturing tasks [6, 7, 8, 5]. In [5], a coarse-fine redundant manipulator using a maglev wrist was proposed. The work presented in this paper differs from what was previously reported in several ways. First, the specific problem of active zero-g control through acceleration feedback is considered and analyzed. Second, 6 DOF coarse-fine motion coordination schemes are proposed, analysed and simulated with realistic assumptions on the performance of the coarse and fine motion stages. Finally, 6 DOF tracking of a levitated platform by a coarse-motion stage is experimentally demonstrated for the first time.

This paper is organized as follows: In Section II, the new coarse-fine vibration isolation system for micro-gravity experiments is proposed and some overall design ideas are presented. In Section III, the coarse-fine motion system is modelled. Control and coordination algorithms are also proposed and analysed. These involve acceleration feedback and the use of coarse and fine sensors for tracking of the free-falling experiment platform. In Section IV, motion simulation results are presented under realistic design assumptions and using measured acceleration data from NASA KC-135 parabolic flights. In Section V, the experimental setup used to demonstrate the feasibility of the proposed system is described and the experiments performed to date are summarized. Both simulations and experiments demonstrate that a coarse-fine motion isolation system with magnetic levitation is feasible.

II. Coarse-Fine Isolation Mount Design

There are several possible approaches to isolating the experiment platform from the aircraft carrying it. The simplest solution is just to allow the platform to float inside the aircraft, while tracking it with a coarse motion stage and latching it at the end of the free-fall parabola or whenever necessary. However, there are several good reasons to consider an active vibration isolation system. These include the ability to cancel disturbances on the experiment platform, such as pulling forces by data collection and power wires, inadvertent touching of the experiment by an operator or motion caused by reaction forces due to the experiment itself. Also, as shown

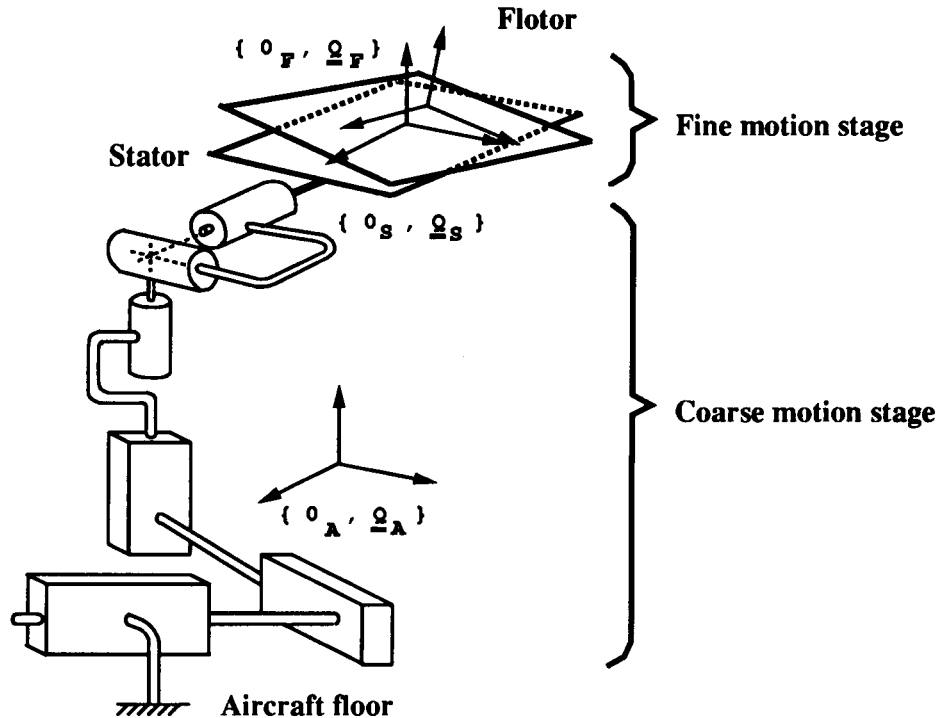


Figure 1: Overview of the proposed coarse-fine vibration isolation system.

in [1, 2, 3], the duration of free-fall of a package inside an aircraft executing a parabolic flight is strongly dependent on how it is released. An active isolation system would allow a controlled zero acceleration release at a desired instant and at a specific location in the airplane. Finally, an active large motion isolation system would allow the exertion of small centering forces on the experiment platform, in effect trading acceleration levels for experiment duration. This ability would gain in importance if the aircraft acceleration levels on parabolic flights could be decreased through better sensing and control.

Active vibration isolation solutions that involve direct mechanical linkages and that would also allow some controlled exertion of forces would be difficult to design and implement, simply because the actuator exerting the force would also transmit unwanted vibrations. Thus, some active levitation method is desirable because it would allow low cutoff frequency low-pass filtering of the actuation forces. Such active levitation methods could involve magnetic-bearing type of actuators with iron in the magnetic gap or voice-coil type of actuators (or Lorentz actuators) with conductors in the magnetic gap, the latter having several advantages, some of which are the need for just a single actuator for bi-directional motion along each degree of freedom, the linearity of applied force with command current, the better force characteristic with large magnetic gaps and the simplicity of design.

The vibration isolation system proposed in this paper would use large-gap voice-coil actuators. The system overview is given in Figure 1. The concept follows closely [4, 5]. A coarse motion stage, attached to the aircraft body, can impart fast, controlled, 3-DOF (or more) motion to the *stator* of a levitator. For simplicity, the coarse-motion stage shown in Figure 1 is a cartesian

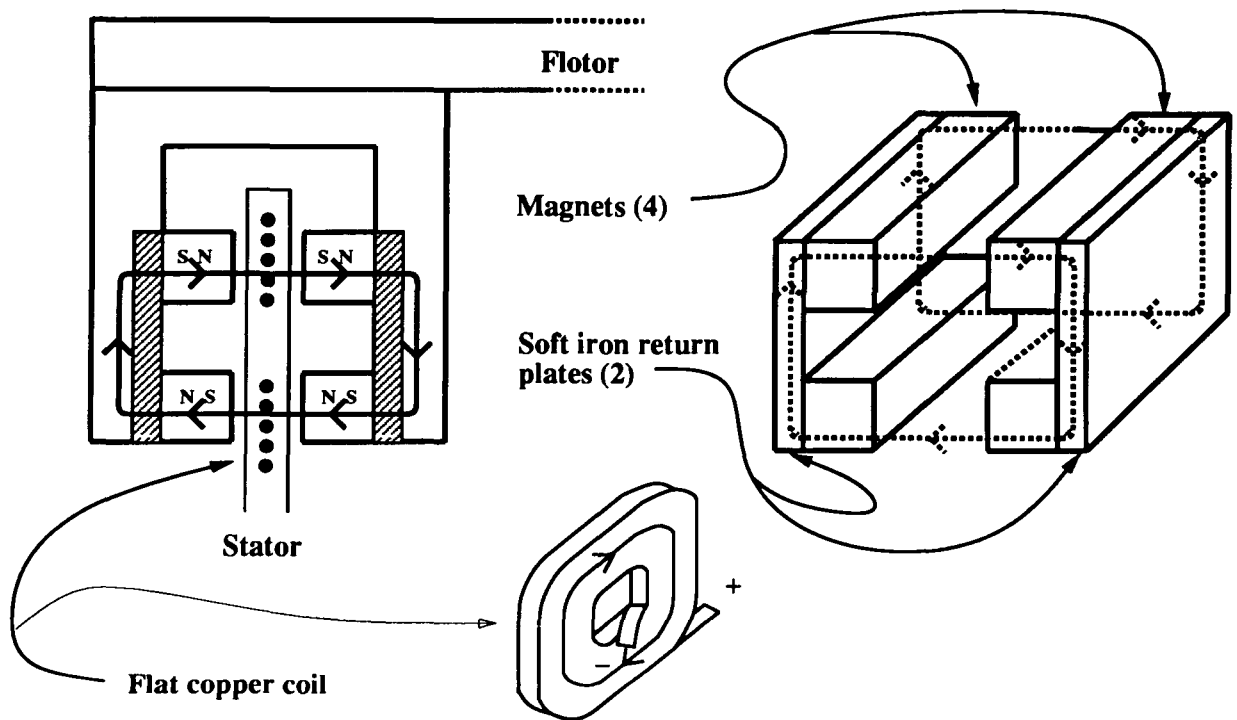


Figure 2: The schematic of the magnetic actuator used for the levitator.

robot of the gantry type equipped with a spherical wrist, but there is considerable freedom in choosing its structure.

In keeping with the terminology proposed in [5], the levitated experiment platform will be referred to as the *flotor*. The levitator's flotor is actuated by at least six moving coil or "voice coil" actuators, shown in Figure 2.

Each actuator has a magnetic assembly, attached to the flotor and a matching coil, attached to the stator. Each coil fits within the gap of the magnetic circuit created by its matching magnetic assembly, allowing only a limited motion range or *workspace* (of the order of $\pm 20 - 30\text{mm}$) of the flotor with respect to the flotor. Although the flotor is not physically attached to the stator (except, perhaps, for wires carrying signals and power) controlled Lorentz forces can be imparted to the platform by controlling the currents through the coils attached to the stator. Six linearly independent wrench vectors (6-vectors with three force and three torque components) can be generated with almost any location and orientation of the actuators. Indeed, with a suitably chosen geometry, 6 DOF motion along six degrees of freedom can be achieved without excessive coil currents [5].

With the best of current technology, it would be very difficult, if not impossible, for the levitator's voice coil motors to produce enough force to support the entire weight of the flotor under normal gravity conditions. Thus, a latch mechanism is necessary to fix the flotor under normal (or higher than normal) gravitational accelerations.

The position and orientation of the flotor with respect to the stator can be obtained by an optical sensor similar to the ones presented in [9, 4, 5] and others. An example is given in Figure 3.

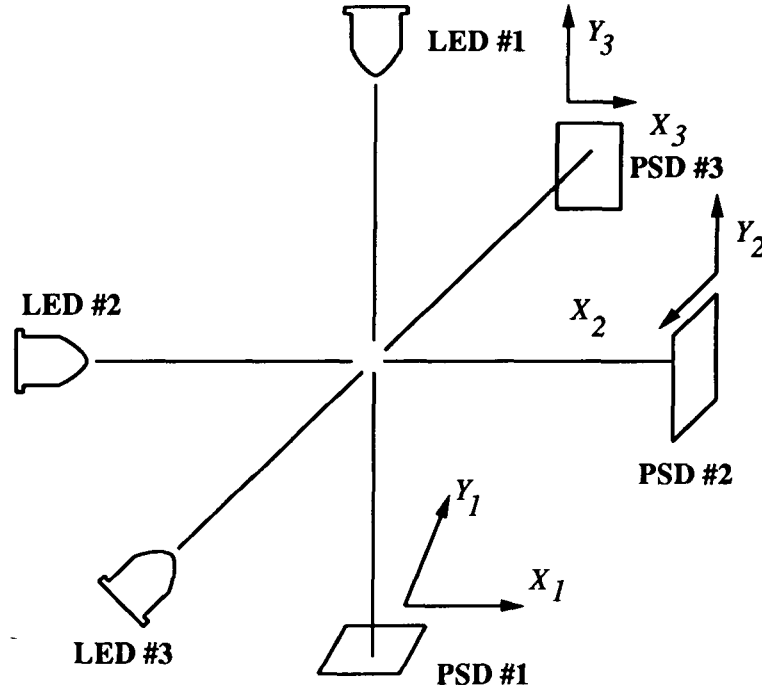


Figure 3: Optical sensing system for the levitator.

Three narrow beam light-emitting diodes are attached to the platform. They project intersecting, orthogonal beams of light on the surfaces of three orthogonal, two-dimensional, lateral-effect position sensing diodes (PSDs) [10] attached to the stator. A simple kinematic calculation (intersection of three spheres) can be used to generate the position and orientation of the flotor with respect to the stator by using the three sets of two-dimensional light spot coordinates sensed by the PSDs. The position sensing system described in Figure 3 has a limited range of motion that can be enlarged by using commercially available PSD cameras.

The performance of the coarse-fine isolation system will depend on the flight characteristics of the KC-135 aircraft. The aircraft translational acceleration levels axes are primarily stochastic during the free-fall part of the flight parabola which lasts somewhat less than 20 seconds. Typical acceleration levels are presented in [11], where it is shown that acceleration peaks perpendicular to the aircraft floor can exceed 50 mg for brief instants and can have an RMS value of 20 mg. Acceleration in the plane of the aircraft floor have much lower peak amplitudes. Thus, the coarse tracker will be expected to generate accelerations of up to 50 mg to follow the flotor in free-fall. The distance which the coarse tracker must travel is limited by the internal space in the KC-135 aircraft and is typically less than 1.5 m in the vertical direction when allowance is made for a real experimental package and installation facilities.

III. Modelling and Control

The following coordinate systems are defined and shown in Figure 4:

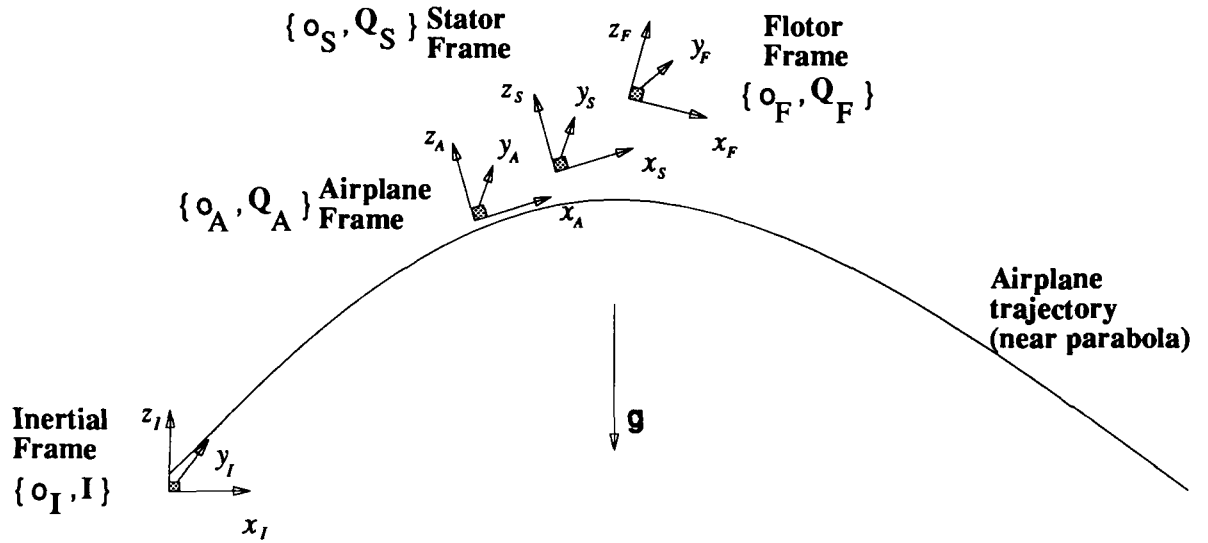


Figure 4: The coordinate systems describing the motion isolation system.

- $\{o_A, \mathbf{Q}_A\}$, attached to the aircraft frame at the nominal center of the coarse motion stage workspace.
- $\{o_S, \mathbf{Q}_S\}$, attached to the levitator's stator.
- $\{o_F, \mathbf{Q}_F\}$, attached to the flotor's center of mass and aligned about its principal axes of symmetry. When the flotor is in its nominal position, the flotor and stator coordinate systems coincide.
- an inertial system $\{o_I, \mathbf{I}\}$, whose origin coincides with o_A at the start of the free-fall parabola. The identity matrix \mathbf{I} is chosen as illustrated in Figure 4, with the z -axis being aligned with the gravitational force, and the initial aircraft velocity lying in the yz -plane. ($\mathbf{g} = [00 - 9.81]^T$).

All vectors and matrices expressed in the inertial system will be shown in bold letters.

We assume that the flotor (and the experimental platform it carries) can be accurately modelled by a rigid body having mass m and inertia matrix \mathbf{J} with respect to its center of mass in the inertial coordinate system. In flotor coordinates, the flotor's inertia matrix becomes $\mathbf{J} = \mathbf{Q}_F^T \mathbf{J} \mathbf{Q}_F$. Let \mathbf{a} and $a = \mathbf{Q}_F^T \mathbf{a}$, $\boldsymbol{\omega}$ and $\omega = \mathbf{Q}_F^T \boldsymbol{\omega}$ denote the flotor's acceleration and angular velocity in inertial and, respectively, flotor coordinates, let \mathbf{f} denote the force acting on the flotor, and let $\boldsymbol{\tau}$ denote the torque acting at the flotor's center of mass.

It is well known that the flotor's rotational motion is described by the following differential equations:

$$\frac{d}{dt} \mathbf{Q}_F = \boldsymbol{\omega} \times \mathbf{Q}_F \quad ; \quad \frac{d}{dt} (\mathbf{J} \boldsymbol{\omega}) = \boldsymbol{\tau} \quad (1)$$

where, for any vector $\mathbf{v} = [v_1 \ v_2 \ v_3]^T$

$$\mathbf{v} \times = \begin{bmatrix} 0 & -v_3 & v_2 \\ -v_3 & 0 & -v_1 \\ -v_2 & v_1 & 0 \end{bmatrix} . \quad (2)$$

In flotor frame, the equations of motion of the flotor are simply Newton's law and Euler's equation:

$$ma = mg + f + f_d \quad ; \quad J\dot{\omega} + \omega \times J\omega = \tau + \tau_d \quad , \quad (3)$$

where $\omega = \mathbf{Q}_F \omega$, $\mathbf{f} = \mathbf{Q}_F f$, $\mathbf{g} = \mathbf{Q}_F g$, $\boldsymbol{\tau} = \mathbf{Q}_F \tau$, and $\mathbf{f}_d = \mathbf{Q}_F f_d$ and $\boldsymbol{\tau} = \mathbf{Q}_F \tau_d$ are disturbance forces and torques (from eddy-current coupling between flotor and stator, flow of air, dragging power wires, etc).

The coarse-motion stage should have at least three, but preferably six, degrees of freedom. It is assumed that the coarse-motion has a closed-loop controller that servoes the stator's position and orientation with respect to the aircraft frame, *i.e.*, that the coordinates ${}^A r_{AS}$ of $o_S - o_A$ in \mathbf{Q}_A frame ($o_S - o_A = \mathbf{Q}_A {}^A r_{AS}$) and $\mathbf{Q}_S^{-1} \mathbf{Q}_A = \mathbf{Q}_S^T \mathbf{Q}_A$ are available and controllable. A reasonable assumption on the behaviour of the the stator position under feedback control is that of a second order system with limits on velocity and acceleration:

$${}^A \ddot{r}_{AS} + 2\zeta\omega_0 {}^A \dot{r}_{AS} + \omega_0^2 {}^A r_{AS} = \omega_0^2 {}^A r_{AS_d} \quad (4)$$

$$\| {}^A \ddot{r}_{AS} \| < a_{max} \quad (5)$$

$$\| {}^A \dot{r}_{AS} \| < v_{max} \quad (6)$$

where ω_0 determines the cutoff frequency at which the stator can no longer track the command input ${}^A r_{AS_d}$ and the damping coefficient ζ determines the overshoot of the response. In the above equations, the characteristic frequency, damping ratio and acceleration and velocity bounds are the same for each axis, but these can be selected to match a particular coarse-motion stage, once it will be selected. In case the coarse-motion stage has more than 3 DOF, similar assumptions can be made on the stator orientation servo by using some appropriate orientation parametrization.

It will be assumed that the disturbance forces exerted on the stator in reaction to forces applied by the levitator, as well as the effects of the aircraft motion, have negligible effects on the coarse-stage motion. If this is not the case, a detailed stability analysis of the coupled motion of the coarse and fine systems should be done along the lines of the work presented in [8]. During the free-fall part of the flight, the acceleration levels do not exceed 50 mg [11], so even with a heavy experiment platform (300 lb or so), the forces required to completely stop the platform motion are quite small.

Because of the limited motion range of the flotor with respect to the stator, the flotor will quickly exceed its motion range, even with small deviations of the aircraft trajectory from an ideal parabola. Therefore, during the free-fall part of the aircraft flight, the commanded stator position should coincide with the flotor position, *i.e.*, ${}^A r_{AS_d} = {}^A r_{AF}$, where $o_F - o_A = \mathbf{Q}_A {}^A r_{AF}$. The

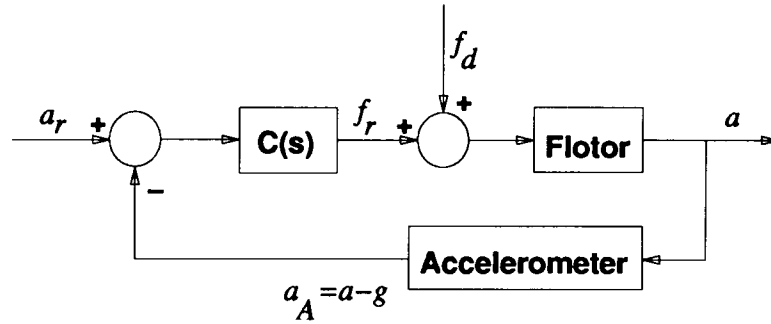


Figure 5: Control loop for the flotor acceleration feedback.

coordinates r_{AF} can be obtained from the combined measurement of the stator with respect to the aircraft (through the conventional sensors of the coarse-motion stage) and that of the flotor with respect to the stator (through the levitator's optical sensor).

III.a. Flotor Acceleration Feedback

It will be assumed that accelerometers are used to measure the acceleration \mathbf{a} of o_F with respect to an inertial frame. Since accelerometers are attached to the flotor, the flotor frame coordinates \mathbf{a} of the flotor acceleration are available.

Once the flotor can be released, the resultant f of its actuators' action is some compensated function of the acceleration error, as shown in Figure 5. In terms of Laplace transforms,

$$\hat{f}(s) = \hat{c}(s)(\hat{a}_r(s) - \hat{a}(s)). \quad (7)$$

where $\hat{c}(s)$, $\hat{a}(s)$ and $\hat{a}_r(s)$ are the Laplace transforms of the feedback compensator, the flotor acceleration and the required acceleration, respectively. Due to the simplicity of the flotor dynamics (single rigid mass) in Figure 5, *any* proper, stable, real-rational transfer function can be obtained from the desired acceleration a_r to the actual acceleration a of the flotor (of course, there will be limits on achievable performance due to plant uncertainty, actuator saturation, etc.). Choosing a first order stable transfer function leads to a compensator $\hat{c}(s)$ that is simply an integrator, *i.e.* *velocity* feedback:

$$\hat{f}(s) = k \frac{1}{s} (\hat{a}_r(s) - \hat{a}(s)), \quad (8)$$

which leads to

$$\hat{a}(s) = \frac{\frac{k}{m}}{s + \frac{k}{m}} \hat{a}_r(s) + \frac{s}{s + \frac{k}{m}} g + \frac{\frac{1}{m}s}{s + \frac{k}{m}} \hat{f}_d(s). \quad (9)$$

Usually, a is measured by a proof-mass accelerometer providing a signal $a_A = a - g$ (thus zero in free fall). In terms of this signal, the above equation becomes

$$\hat{a}_A(s) = \frac{\frac{k}{m}}{s + \frac{k}{m}} [\hat{a}_r(s) - g] + \frac{\frac{1}{m}s}{s + \frac{k}{m}} \hat{f}_d(s). \quad (10)$$

Clearly, for reasonably high gain k , the acceleration of the flotor and platform *does indeed track the desired acceleration* a_r and *rejects the disturbance force* f_d . Usually, $a_r = g$, leading to $\hat{a}_A(s) \rightarrow 0$, although, as it will be seen later, this may not always be the best approach.

The angular acceleration of the flotor can be controlled in a similar way, *i.e.*, by using angular velocity feedback. The flotor angular acceleration can be regulated to zero by the control law $\tau = -k_\omega J\omega$, with some positive gain k_ω . Indeed, consider the Lyapunov function $V = \frac{1}{2}\omega^T J\omega$. Along the trajectories described by the Euler equation in (3) (with $\tau_d = 0$), we have that

$$\dot{V} = \frac{1}{2}[\omega^T(\tau - \omega \times J\omega) + (\tau - \omega \times J\omega)^T\omega] = \omega^T\tau = -k_\omega\omega^T J\omega < 0. \quad (11)$$

Thus the signal $\delta = -\omega \times J\omega$ is bounded and decreases to zero. By taking the Laplace transform of Euler's equation and letting $a_\omega = \dot{\omega}$, we obtain that

$$\hat{a}_\omega(s) = \frac{s}{s + k_\omega} J^{-1} \hat{\delta}(s), \quad (12)$$

so the angular acceleration of the flotor should be kept small at low frequencies.

Before moving on, a comment on the nature of the disturbances acting on the flotor (or experimental platform) and on means of rejecting them is in order. On one hand, disturbance forces can be both unknown and very difficult to measure, *e.g.* forces due to an experiment operator touching the flotor. The only hope of attenuating these disturbances is through accelerometer feedback. On the other hand, some unpredictable disturbances can be easily measured, *e.g.* the forces and torques applied to the flotor by an umbilical carrying signals and power. These disturbances can be rejected to a large extent through *feed-forward through the flotor's actuating coils*, while accelerometer feedback is still in effect.

Umbilical disturbances can be measured by means of standard strain-gauge force-torque sensors or through other, more sophisticated, techniques. Even magnetic levitation can be used, with the same proof-mass principle used in some accelerometers. For example, the umbilical can be attached to the flotor through an intermediate levitated proof-mass (*i.e.*, another flotor), whose position and orientation is servoed to that of the experimental platform. By monitoring the forces needed to keep the proof-mass in place (*e.g.*, by monitoring the coil currents of Lorentz actuators, if the proof-mass uses Lorentz levitation), one obtains the forces and torques exerted by the umbilical.

III.b. Acceleration Feedback with Centering Motion

Although, ideally, the desired flotor acceleration a_r is zero, in practice, even the coarse motion platform will "run out of space" because of errors in the aircraft trajectory. Instead of letting the platform reach its motion limit (with associated high acceleration due to hard mechanical contact), it may be instead desirable to provide low-level "drift" accelerations that tend to bring the flotor to the nominal center of the coarse motion platform. We will assume that this nominal center coincides with the aircraft reference frame origin o_A . There are a couple of ways in which a centering drift motion can be obtained. First, one can modify the control action (8) by

adding a proportional derivative term in the flotor offset $r_{FA} = \mathbf{Q}_F^T(o_A - o_F)$ with respect to the aircraft frame:

$$\hat{f}(s) = k \frac{1}{s} [\hat{a}_r(s) - \hat{a}(s)] + k_p \hat{r}_{FA} + k_v s \hat{r}_{FA}, \quad (13)$$

where k_p and k_v are positive and small. The coordinates r_{FA} of $o_A - o_F$ in flotor frame are obtained from the coarse-stage and levitator's sensors.

With $k = 0$ in the above (to see what the effect of this centering force is), applying this PD controller to Newton's equation in (3) (expressed in inertial coordinates) leads to

$$m \frac{d^2}{dt^2}(o_F - o_I) = m\mathbf{g} + \mathbf{Q}_F(k_p r_{FA} + k_v \dot{r}_{FA}) + \mathbf{f}_d. \quad (14)$$

Therefore, in inertial coordinates, the equation of motion of the flotor coordinate system origin with respect to the aircraft frame becomes

$$\frac{d^2}{dt^2}(o_F - o_A) + \frac{k_v}{m} \frac{d}{dt}(o_F - o_A) + \frac{k_p}{m}(o_F - o_A) = \frac{k_v}{m} \boldsymbol{\omega} \times (o_F - o_A) + \frac{1}{m} \mathbf{f}_d, \quad (15)$$

where we made use of the fact that

$$\frac{d}{dt}(o_F - o_A) = \boldsymbol{\omega} \times \mathbf{Q}_F r_{FA} + \mathbf{Q}_F \dot{r}_{FA} = \boldsymbol{\omega} \times (o_F - o_A) + \mathbf{Q}_F \dot{r}_{FA} \quad (16)$$

and

$$\frac{d^2}{dt^2}(o_A - o_I) = \mathbf{g} \quad (17)$$

(note that errors in aircraft trajectories are included in \mathbf{f}_d).

The angular acceleration $\boldsymbol{\omega}$ of the levitator's flotor should be small, even without angular acceleration servoing, because the aircraft rotates relatively slowly during the parabolic flight.

Therefore, the error $o_F - o_A$ of equation (15) should be small. In addition, due to the orthogonality of $\boldsymbol{\omega} \times (o_A - o_F)$ to the centering force $\frac{k_p}{m}(o_F - o_A)$ acting on the flotor, it should be possible to use a Lyapunov argument to show that, in the absence of disturbance forces \mathbf{f}_d and assuming that $\boldsymbol{\omega}$ is bounded, $o_F - o_A$ converges to zero.

Therefore, by using *only local* information (*i.e.*, no inertial reference) the flotor can be made to track the aircraft center. Note that, in order to insure low accelerations, the constants k_p and k_v should be made as small as possible.

As a second way to achieve a centering force on the flotor, note that the desired acceleration a_r of (8) can be set according to a PD law similar to (13), *i.e.*,

$$\hat{a}_r(s) = k_p r_{FA} + k_v s r_{FA}. \quad (18)$$

If the acceleration controller works well, a should track $a_r - g$ closely (see equation (10)), so, in effect, (13) will be quite well approximated. Of course, for such an approach to work, the

acceleration gain of (8) should lead to a substantially faster time constant than the time constants associated with (18).

It is also possible to make the gains k_p and k_v depend on how close the platform is to the aircraft walls - the larger $o_F - o_A$, the larger k_p and k_v . In particular, a moderately large workspace without drift can be implemented by setting these gains to zero within a certain radius $\|o_F - o_A\| < r$.

A corrective term for drift in the orientation of the platform can also be devised. In particular, if the coarse-motion stage is only a 3-DOF system, as the airplane goes through a parabola, the levitator's stator will change orientation with it. Therefore, in spite of being free to move in translation, *the flotor orientation must track that of the stator*. Tracking could be achieved by using a control scheme based on the vector part of the Euler quaternion, as done in [5]. The rotation matrix $Q_{AF} = \mathbf{Q}_A^T \mathbf{Q}_F$ of the flotor with respect to the aircraft is represented by the Euler quaternion $[\beta_0 \beta^T]^T$ as

$$Q_{AF} = \exp(\phi \mathbf{s} \times) = I + 2\beta_0 \beta \times + 2(\beta \times)^2, \quad (19)$$

where $\mathbf{p} = [\beta_0 \beta^T]^T = [\cos(\phi/2) \sin(\phi/2) s^T]^T$, and s and ϕ are the normalized axis ($\|s\| = 1$) and, respectively, the angle of the rotation matrix Q_{AF} . This parametrization has several advantages, the most important one being the explicit representation of the axis of rotation.

It can be shown [12] that after linearization (approximate or by exact cancellation of the dynamics, as in computed torque control), for rotation angles less than 180 degrees, the flotor's rotational dynamics is given by

$$\ddot{\beta} = \frac{1}{2} J^{-1} \tau \quad (20)$$

Similarly to (13), a PD term can be added to the flotor torque in such a way as to bring the orientation of the flotor towards some central orientation aligned with the aircraft:

$$\tau = -\tilde{k}_p \beta - \tilde{k}_v \dot{\beta}, \quad (21)$$

where the orientation vector β that corresponds to $\beta_0 \geq 0$ can be obtained from (19) and is given by

$$\beta \times = \frac{1}{2(1 + \text{tr} Q_{AF})^{\frac{1}{2}}} (Q_{AF} - Q_{AF}^T), \quad (22)$$

where $\text{tr} Q_{AF}$ denotes the trace of Q_{AF} .

It is clear that, when the platform acceleration is not measured, there can be no acceleration error correction for the platform. This is probably no serious drawback, because the platform is in near free-fall condition (except for some interaction with the coarse motion stage through eddy current damping and very little air drag). The coarse-motion stage can still be used to track the platform and the moving coil actuators can still be used to center the flotor. However, some of the control over the acceleration levels exercised on the flotor is lost.

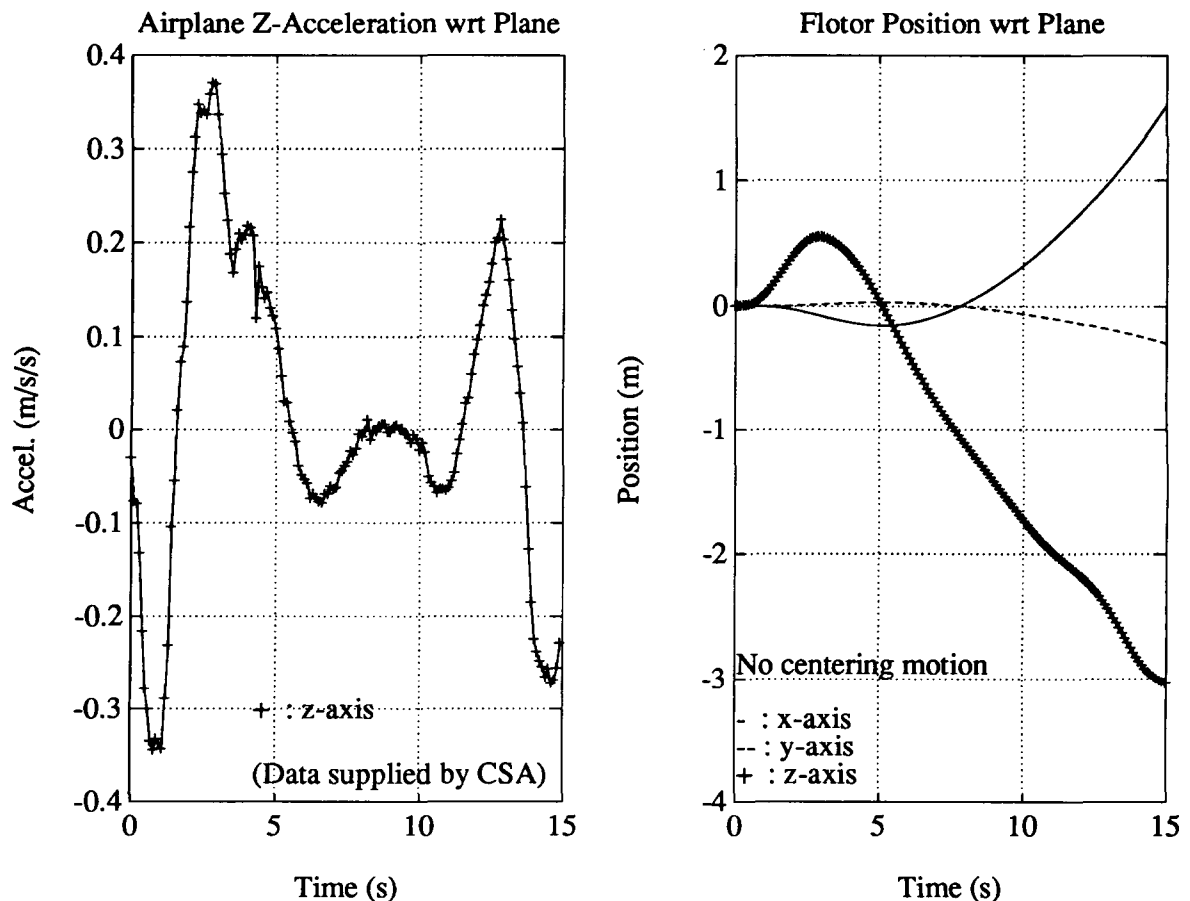


Figure 6: The position of the platform with respect to the airplane with a given disturbance in the z-axis of the airplane.

IV. Simulation Setup and Results

The motion of the system described in Section I, with the control laws described in Section II, was simulated using the software packages PRO-MATLABTM and SIMULABTM, by The MathWorks. The complete simulation was performed by describing the equations of motion of every component of the system *i.e.*, the flotor dynamics, the stator dynamics, and the aircraft kinematics, in the inertial coordinate system $\{o_I, \mathbf{I}\}$. The control algorithms presented in Section II were applied in local coordinates as described, *i.e.*, the flotor control algorithms were expressed in flotor coordinates, the coarse-motion stage dynamics were expressed in aircraft coordinates and the aircraft kinematics were expressed in inertial coordinates.

Acceleration data obtained on NASA KC-135 parabolic flights [11] were used to drive the aircraft kinematics. Although there was no measured data available on the orientation of the KC-135 during flight, the initial aircraft orientation at the start of the parabola and the final orientation at the end of free-fall are fairly well known. These show that the aircraft undergoes a change in pitch angle of about -60 degrees and is rolling to the right roughly 20 degrees during the free-fall

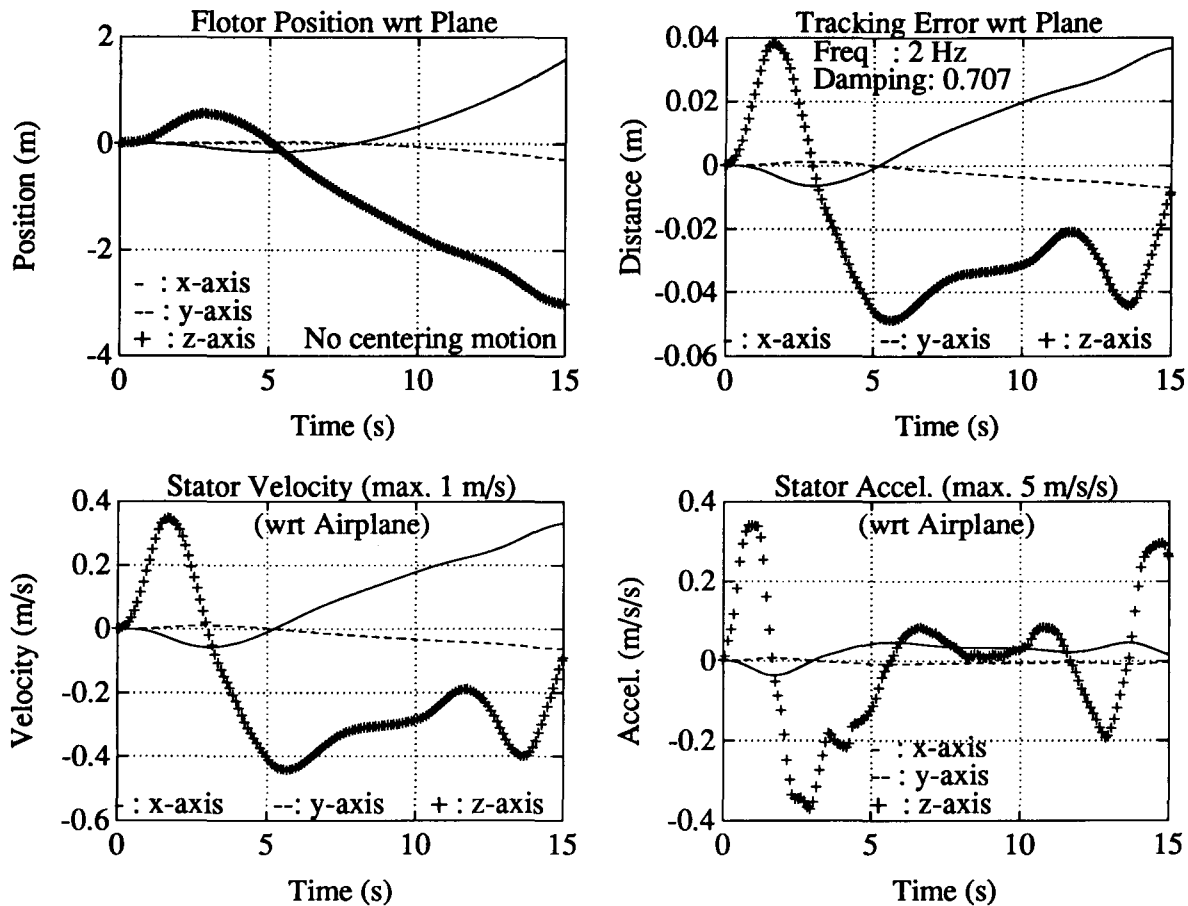


Figure 7: Flotor-stator tracking errors and stator velocity and acceleration.

parabola. In all the simulations performed, it was assumed that this rotation occurs at a constant angular rate, about the fixed Euler eigenaxis of rotation between the initial and final orientations.

Some typical results are displayed in Figures 6, 7, 8 and 9. Unless otherwise specified, airplane coordinates are used.

Figure 6 shows the acceleration data and the flotor position. Figure 7 shows the tracking errors in x , y , z . As expected, the coarse-motion stage tracking error along the z -axis is substantially larger than for the x and y axis. With fairly stringent performance limitations on the coarse motion stage (2 Hz bandwidth, 5 m/s/s max. acceleration, 1 m/s max. velocity), typical tracking errors are about ± 10 mm in the y -axis, ± 30 mm in the x -axis and ± 40 mm in the z axis. These errors are reduced drastically as the bandwidth of the tracking platform is increased. It is fairly simple to design a wide-gap levitator that matches these workspace requirements. For example, the stator could be shaped as a rectangular shell with flat coils (as shown in Figure 2) embedded in its walls. The matching flotor would have a large face available for an experiment platform, and would have a substantial travel in the z axis, while maintaining relatively small magnetic gaps for the actuators. The optical sensor shown in Figure 3 could be employed with minor

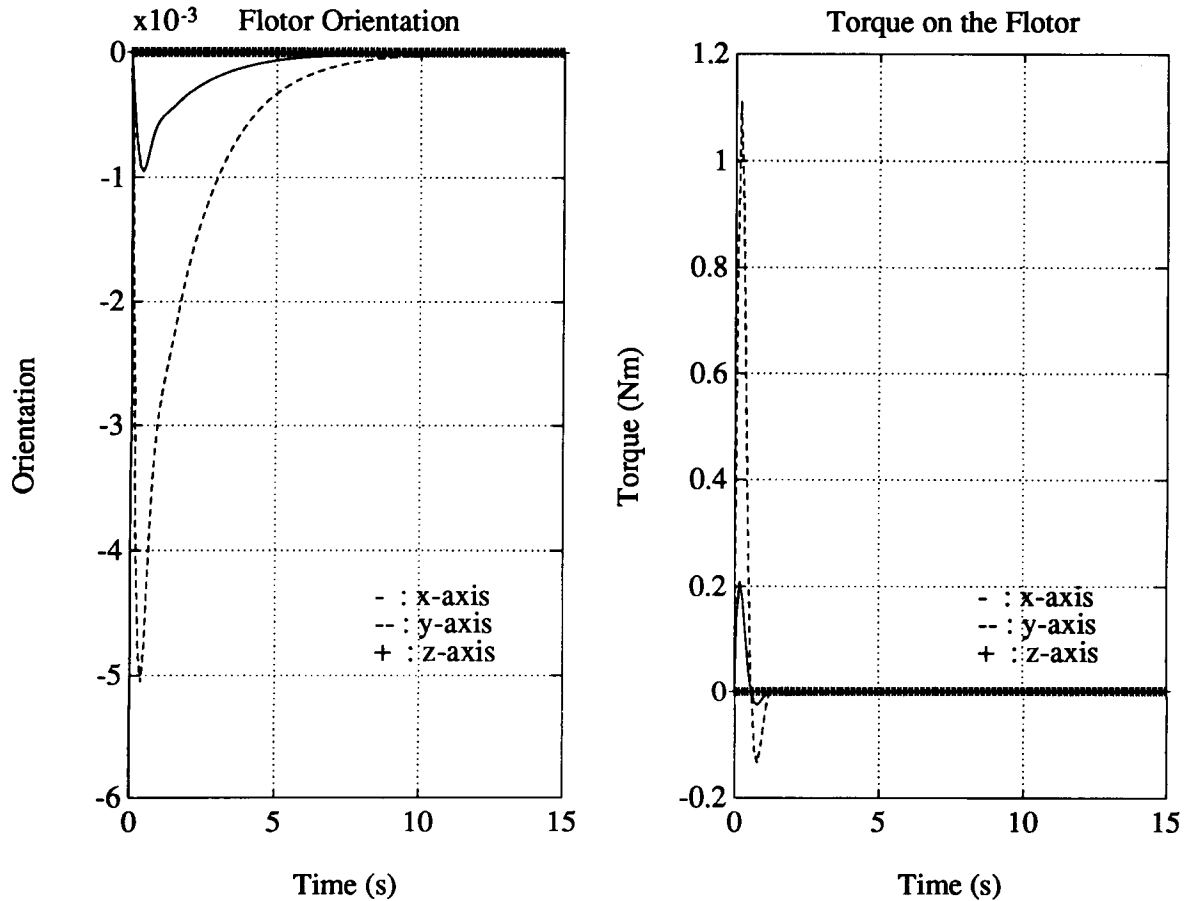


Figure 8: Orientation error components and torque applied to the flotor.

modifications for the large z -axis travel.

Figure 8 shows the rotation tracking performance (the vector part β of the Euler quaternion, as defined for equation (19), is displayed) and the torques applied to the flotor. It can be seen that the orientation errors are small and that the torques required to rotate the flotor are small (the flotor is modelled as a 300 lb cube).

Figure 9 shows the trade-off between acceleration quality and free-fall duration. Simulation results with two sets of centering gains in equation (18) are displayed. It can be seen that as these gains are increased, the flotor moves less with respect to the aircraft. At the same time, the acceleration levels on the flotor increase, as expected. If the required acceleration level for a given experiment is known, one can modify the centering acceleration of equation (18) in order to optimize experiment duration. Another possible use for centering forces is the avoidance of "crashes" into the aircraft walls.

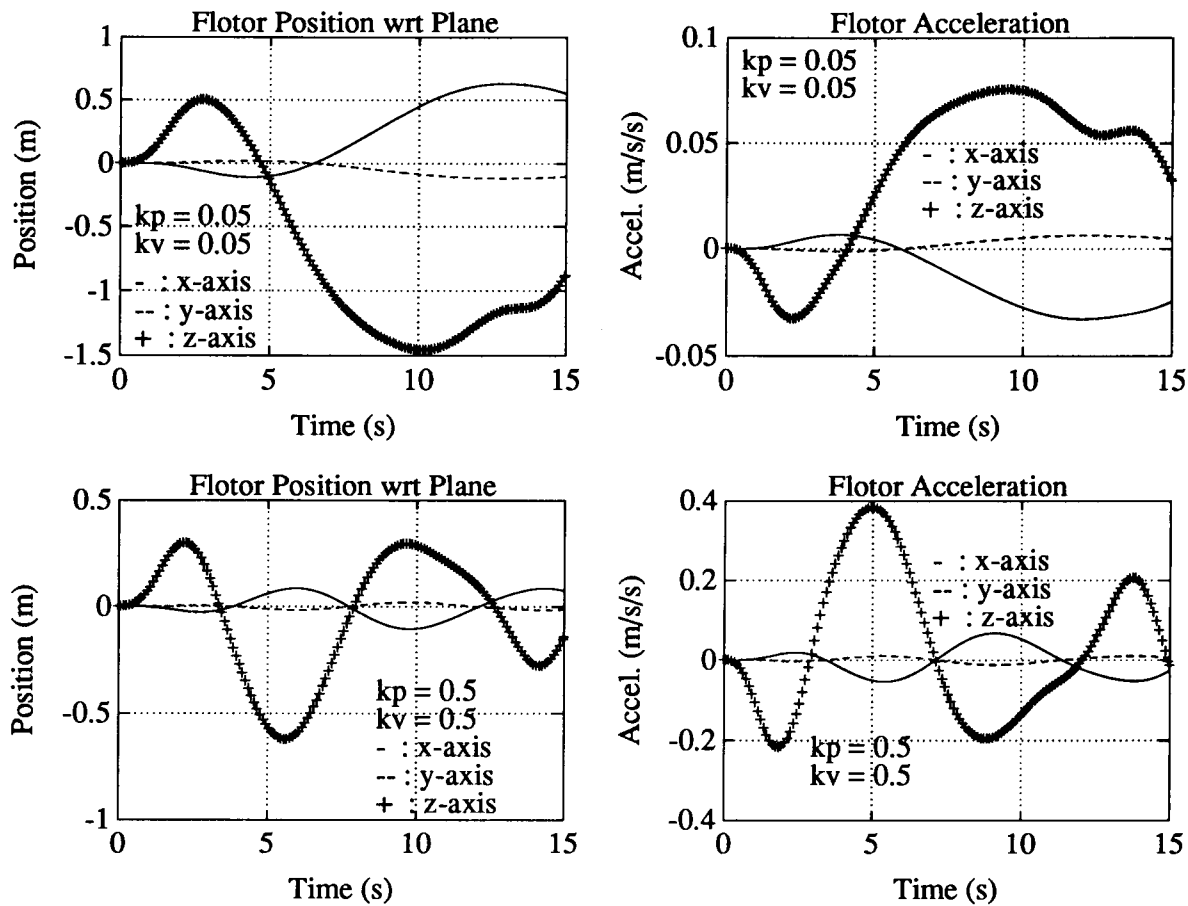


Figure 9: Effects of centering control on position and acceleration.

V. Experimental Setup and Results

To demonstrate the feasibility of the coarse-fine motion isolation system described in Section I and the validity of the control and coarse-fine motion coordination schemes presented in Section II, the authors used a Unimation PUMA 500 robot equipped with a magnetically levitated fine-motion robot wrist, developed and built in the Electrical Engineering Department at UBC. The UBC maglev wrist uses the same design principles applied to the "Magic" wrist described in [4, 5] and outlined in Section I of this paper. The weight of its flotor is 0.640 kilograms, its motion range is ± 4.5 mm and ± 7 degrees from the nominal center. Each of the wrist's voice-coil actuators produces roughly 2 N/A force per unit current and the power consumption required to "fly" the flotor without any additional payload is less than 7 Watts.

The real-time system employed for the coordinated control of the PUMA robot and the levitator's flotor is illustrated in Figure 10. An IBM PC-AT compatible computer hosts a Spectrum Inc. digital signal processing (DSP) board using a Texas Instruments Inc. TMS320 DSP chip, as well as analog input and output boards linked through a fast, private bus. The PC

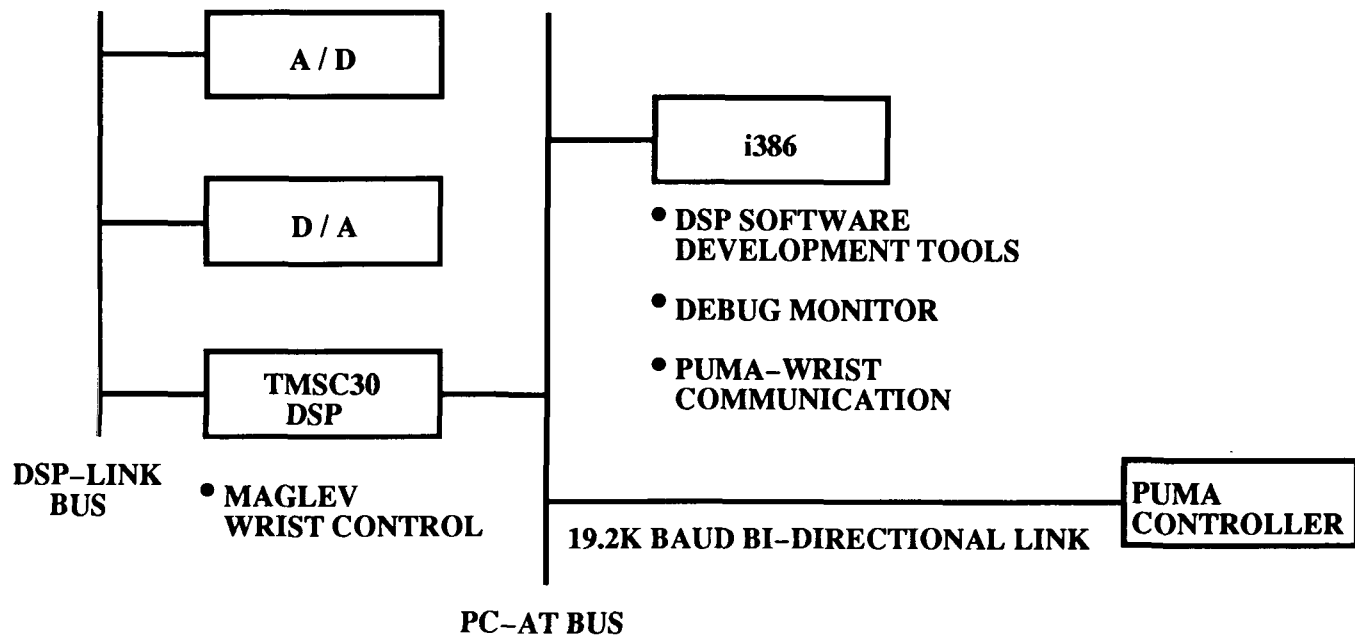


Figure 10: The block diagram of the PUMA-Wrist real-time controller.

is connected through a 19.2 Kbaud serial link to the PUMA robot controller.

The floating point DSP board controls the levitator's flotor, computes the stator's position and orientation from position and Euler angles information obtained from the robot through the serial link, and calculates the updated robot set points (δx , δy , δz , roll, pitch, yaw) as a function of flotor position. The kinematic calculations required to determine the flotor position with respect to the stator are exactly as described in [5]. The flotor controls are updated every 1.5 milliseconds, with the DSP board running at about 1 Mflop.

The PC is used for DSP software development and for the serial port communications between the wrist controller and the robot controller.

A program written in VAL II handles the serial communications on the PUMA controller side, while the robot is in INTERNAL ALTER mode, effectively making it a slave to the wrist's flotor motion. The coordination data between the robot and the wrist could only be transmitted every 56 milliseconds. This could be improved substantially if the PUMA controller could be modified. In particular, a Jacobian-based velocity tracking algorithm that does not require the on-line solution of the inverse kinematics problem could be implemented.

Coordinated motion of the flotor and the robot was demonstrated by the authors, with the robot following the wrist's flotor position and orientation. Translational tracking with locked orientation was also demonstrated.

Accelerometers were mounted on the flotor, but problems with drift and noise have so far prevented successful implementation of acceleration feedback.

VI. Conclusion

The authors proposed a coarse-fine large-motion isolation system for residual gravity cancellation on parabolic flights. The system would use wide gap magnetic levitation for vibration isolation and acceleration servoing of an experimental platform. The proposed isolation mount was modelled and control algorithms for acceleration servoing and centering motion were presented. The model and the control algorithms were simulated and an experimental coarse-fine system using a PUMA robot and maglev wrist was put together in order to demonstrate the system's feasibility.

The proposed gravity cancellation system has several advantages, among which are (i) the ability of reducing the dynamic coupling between the aircraft and experimental platform to just eddy current coupling, (ii) the ability of using maglev forces to obtain good initial release of the experiment platform, (iii) the ability of trading off experiment duration versus quality of the free-fall.

The simulation results and experimental results presented seem to indicate that such a coarse-fine approach to vibration isolation is feasible. In particular, the ability of a coarse-motion stage to track a levitated platform was demonstrated through both simulations and experiments. The only requirement left to demonstrate that the coarse-fine motion isolation system will work as proposed is the successful application of acceleration feedback. That work is now in progress.

Acknowledgements

The authors wish to thank David Fletcher for machining the maglev wrist used in their experiments, Dr. Dale Cherchas for providing space and experimentation time in his lab, and Nelson Ho for general help and for writing the symbolic debug monitor for the DSP. The support of NSERC and the Canadian Space Agency is gratefully acknowledged.

References

- [1] A. Adler and J. Bernaldez. Motion isolation mount for microgravity. Technical report, Dept. of Physics, University of British Columbia, December 1989. Engineering Physics Project No. 8918.
- [2] H. Davis. Report on the proposed modifications to the 1-d large motion isolation mount for flight tests on the NASA KC-135 aircraft. Technical report, Engineering Physics, University of British Columbia, October 1990. (prepared for NRC under contract 31016-0-6022/01-SW).

- [3] H. Davis. Report on the first flights of the large motion isolation mount on the NASA KC-135 Aircraft, June 5-9, 1990. Technical report, Engineering Physics, University of British Columbia, September 15 1990. (prepared for NRC under contract 31016-0-6022/01-SW).
- [4] R.L. Hollis. Magnetically levitated fine motion robot wrist with programmable compliance, October 1989. U.S. Patent number 4,874,998.
- [5] R.L. Hollis, S. Salcudean, and P.A. Allan. A Six Degree-of-Freedom Magnetically Levitated Variable Compliance Fine Motion Wrist: Design, Modelling and Control. *IEEE Transactions on Robotics and Automation*, 7(3):320-332, June 1991.
- [6] R. H. Taylor, R. L. Hollis, and M. A. Lavin. Precise manipulation with endpoint sensing. *IBM J. Res. Develop.*, 2(4):363-376, July 1985.
- [7] Andre Sharon and David Hardt. Enhancement of robot accuracy using endpoint feedback and a macro-micro manipulator system. In *American Control Conference proceedings*, pages 1836-1842, San Diego, California, June 6-8 1984.
- [8] S. Salcudean and C. An. On the control of redundant coarse-fine manipulators. In *Proceedings of the IEEE International Conference on Robotics and Automation*, pages 1843-1840, Scottsdale, Arizona, May 14-18 1989.
- [9] A.E. Brennemann, R.L. Hollis, and R.H. Taylor. General position and orientation sensor for fine motions and forces. *IBM Technical Disclosure Bulletin*, 26(9):4457-4462, February 1984.
- [10] United Detector Technology. Silicon photodetectors catalog. 12525 Chandron Ave., Hawthorne, CA 90250.
- [11] B. V. Tryggvason. Acceleration Levels on the KC-135. Technical report, Canadian Space Agency, October 1990. Report CSA-CAP.008.
- [12] S. Salcudean. On the control of magnetically levitated robot wrists. In *Proceedings of the 27th IEEE Conference on Decision and Control*, pages 186-191, Austin, Texas, December 1988.

ATTENDEES

Alcorn Charles W. Alcorn
Phone: 804-683-3720
Old Dominion University
Dept. of Mechanical Engineering
Norfolk VA 23529-0247

Allan A. P. Allan
Phone: 804-924-6233
University of Virginia
Department of Mech. and Aero. Engrg.
Charlottesville VA 22903

Banerjee Bibhuti Banerjee
Phone: 804-924-6233
University of Virginia
ROMAC Labs, Mech & Aero Engrg.
Thornton Hall, McCormick Road
Charlottesville VA 22903

Batterson James G. Batterson
Phone: 804-864-4059
NASA Langley Research Center
Mail Stop 161
Hampton VA 23665-5225

Bichsel J. Bichsel
Phone: 1-256-51-19
Eidgenossische Technische Hochschule
Institut für Elektrotechnische
Entwicklungen, ETH Zentrum/ETZ F
CH-8092 Zurich
SWITZERLAND

Boehm Josef Boehm
Phone: 061-745 5000
University of Salford
Physics Department, The Crescent
Salford M5 4WT
UNITED KINGDOM

Allaire Paul E. Allaire
Phone: 804-924-3292
University of Virginia
Mechanical Engineering Department
Thornton Hall McCormick Road
Charlottesville VA 22903

Anderson Willard W. Anderson
Phone: 804-864-1718
NASA Langley Research Center
Mail Stop 479
Hampton VA 23665-5225

Barrett Lloyd Barrett
Phone: (804) 924-6210
Univ. of Virginia
Dept. of Mech. and Aero.
Engrg.
Charlottesville VA 22903

Bernhardt Helmut Bernhardt
Phone:

Nebenstrasse 2B
D-W-6330
Wetzlar 22
GERMANY

Boden K. Boden
Phone: 02461-614604
Kernforschungsanlage Julich GmbH
Abteilung IGV
Postfach 1913
D-5170 Julich
GERMANY

Bondarenko Herman A. Bondarenko
Phone: 06452-4-38-46
The Sumy Frunze Machine Building
Science and Production Amalgamation
G. Kursky Avenue
Sumy 244609
U.S.S.R.

Briggs B. M. Briggs
Phone: 206-657-3735
Boeing Aerospace and Electronics
P. O. Box 3999
M/S 3C-PC
Seattle WA 98124

Britton Thomas C. Britton
Phone: 804-864-6619
Lockheed Engr. & Sciences Co.
NASA Langley Research Center
Mail Stop 161
Hampton VA 23665-5225

Castleman Bruce W. Castleman
Phone: 813-539-5708
Honeywell Inc.
Mail Station 350-1
13350 U.S. Highway 19 South
Clearwater FL 34624-7290

Cope David B. Cope
Phone: 617-890-3200
Foster-Miller Inc.
350 Second Avenue
Building 1
Waltham MA 02154-1196

Davis Harold Davis
Phone: 604-822-2961
The University of British Columbia
Department of Physics
6224 Agricultural Road
Vancouver, B.C. V6T 1Z1
CANADA

Derrickson G. Stephan Derrickson
Phone: 719-633-8333
The Spectranetics Corp.
96 Talamine Court
Colorado Springs CO 80907

Britcher Colin P. Britcher
Phone: 804-683-3720
Old Dominion University
Dept. of Mech. Engg.
Norfolk VA 23529-0247

Burrows Clifford R. Burrows
Phone: 0225 826935
University of Bath
School of Mechanical Engineering
Claverton Down
Bath BA2 7AY
ENGLAND

Chu Wei-Kan Chu
Phone: 713-743-8250
Texas Center for Superconductivity
University of Houston
4800 Calhoun
Houston TX 77004-5506

Daniels Taumi S. Daniels
Phone: 804-864-4659
NASA Langley Research Center
Mail Stop 238
Hampton VA 23665-5225

de Rochemont L. P. de Rochemont
Phone: 617-926-1167
Radiation Monitoring Devices, Inc.
44 Hunt Street
Watertown MA 02172

Dhar Debasish Dhar
Phone: 804-924-3291
University of Virginia
ROMAC Labs, Mech & Aero Egnrg
Thornton Hall, McCormick Road
Charlottesville VA 22903

Doederlein Ted A. Doederlein
Phone: 805-275-5483
Phillips Laboratory
OLAC PL/STSS
Edwards CA 93523-5000

Downer James R. Downer
Phone: 617-661-0540, X203
SatCon Technology Corporation
12 Emily Street
Cambridge MA 02142

Dress David Dress
Phone: 804-864-5126
NASA Langley Research Center
Mail Stop 287
Hampton VA 23665-5225

Dutton Jeffrey L. Dutton
Phone: 804-688-3807
Newport News Shipbuilding
4101 Washington Avenue
Dept. E55
Newport News VA 23607

Eisenhaure David B. Eisenhaure
Phone: 617-661-0540
SatCon Technology Corporation
12 Emily Street
Cambridge MA 02139-4507

Fenn Ralph Fenn
Phone: 617-661-0540
SatCon Technology Corporation
12 Emily Street
Cambridge MA 02139

Forbes David A. Forbes
Phone: 804-688-7954
Newport News Shipbuilding
4101 Washington Avenue
Dept. E55
Newport News VA 23607

Foucault Jean-Pierre Foucault
Phone: 14-65-71-160
ONERA
29 Avenue De La Division Leclerc
Chatillon 92320
FRANCE

Gaffney Monique Gaffney
Phone: 617-661-0540
SatCon Technology Corporation
12 Emily Street
Cambridge MA 02139

Garbutt Keith S. Garbutt
Phone: 703 595000, X3384
University of Southampton
Department of Aeronautics
Southampton, Hants S09 5NH
UNITED KINGDOM

Gavrilov Victor P. Gavrilov
Phone: 06452-2-55-80
Severodonetsk Manuf. Assoc. "AZOT"
5, Chimikov
Severodonetsk 349940
U.S.S.R.

Ghofrani Mehran Ghofrani
Phone: 804-683-3720
Old Dominion University
Dept. of Mechanical Engineering
Norfolk VA 23529-0247

Girault J. P. Girault
Phone: 32-21-71-71
Societe Europeenne de Propulsion
Div. Propulsion a Liquides et Espace
B. P. 802
F-27207 Vernon
FRANCE

Goodyer Michael J. Goodyer
Phone: 703-592374
The University of Southampton
Dept. of Aero. and Astro.
Hampshire SO5 5NH
ENGLAND

Halbach Klaus Halbach
Phone: 415-486-5868
UC Lawrence Berkeley Lab
MS 2-400
Berkeley CA 94720

Hawkey Timothy Hawkey
Phone: 617-661-0540
SatCon Technology Corp.
12 Emily Street
Cambridge MA 02139

Hibner David H. Hibner
Phone: 203-565-2238
Pratt & Whitney
400 Main Street
MS 163-09
East Hartford CT 06108

Holmberg Neil Holmberg
Phone: 804-864-6970
NASA Langley Research Center
Mail Stop 457
Hampton VA 23665-5225

Givan Garry Givan
Phone: 513-255-1286
US Air Force
WL/POSL
Wright Patterson AFB OH 45433-6563

Groom Nelson J. Groom
Phone: 804-864-6613
NASA Langley Research Center
Mail Stop 161
Hampton VA 23665-5225

Hampton Roy D. Hampton
Phone: 804-924-3767
University of Virginia
ROMAC Labs, Mech & Aero Engrg
Thornton Hall, McCormick Road
Charlottesville VA 22903

He Jianliang He
Phone: 708-972-2558
Argonne National Laboratory
9700 S. Cass Avenue
Bldg. 362
Argonne IL 60439

Hollis R. L. Hollis
Phone: 914-945-1653
IBM
T. J. Watson Research Center
P. O. Box 218
Yorktown Heights NY 10598

Horwath T. G. Horwath
Phone: 703-371-3531
TG&C Associates
1 Cessna Lane
Falmouth VA 22405

Howard John D. Howard
Phone: 609-921-2792
VSE International
127 McCosh Circle
Princeton NJ 08540

Ishikawa Hideyuki Ishikawa
Phone: 313-454-1500
American Koyo Corp.
47771 Halyard
Plymouth MI 48170

Jensen Carol Jensen
Phone: 818-302-9705
Southern California Edison
P. O. Box 800/Room 455G01
2244 Walnut Grove Avenue
Rosemead CA 91770

Joffe Benjamin Joffe
Phone: 818-354-6444
Jet Propulsion Laboratory
4800 Oak Grove Drive
MS 251
Pasadena CA 91109-8099

Johnson Dexter Johnson
Phone: 216-433-6046
NASA Lewis Research Center
21000 Brookpark Road
Mail Stop 23-3
Cleveland OH 44135

Jones Brian R. Jones
Phone: 415-423-3058
Lawrence Livermore Nat. Laboratory
P. O. Box 808
Livermore CA 94550

Jordan Thomas L. Jordan
Phone: 804-864-4713
NASA Langley Research Center
MS 238
Hampton VA 23665-5225

Joshi Prakash B. Joshi
Phone: 508-689-0003
Physical Sciences, Inc.
20 New England Business Center
Andover MA 01810

Joshi Suresh M. Joshi
Phone: 804-864-6608
NASA Langley Research Center
Mail Stop 230
Hampton VA 23665-5225

Judd Michael Judd
Phone: 617-981-7734
MIT Lincoln Laboratory
P.O. Box 73
77 Massachusetts Avenue
Lexington MA 02173

Juengst Carl D. Juengst
Phone: 206-773-8602
Boeing Aerospace
P. O. Box 34113
Mail Stop 82-24
Seattle WA 98124-1113

Kaplan Nicholas Kaplan
Phone: 301-628-3481
AAI Corporation
5401 Linton Road
Sykesville MD 21784

Keckler Claude R. Keckler
Phone: 804-864-1716
NASA Langley Research Center
Mail Stop 479
Hampton VA 23665-5225

Keesee John Keesee
Phone:
Magnetic Bearings, Inc.
609 Rock Road
Radford VA 24141

Kelliher Warren C. Kelliher
Phone: 804-864-4172
NASA Langley Research Center
Mail Stop 416A
Hampton VA 23665-5225

Kilgore Allen Kilgore
Phone: 804-864-5033
Vigyan, Inc.
30 Research Dr.
Hampton VA 23666

Kilgore Robert A. Kilgore
Phone: 804-864-5020
NASA Langley Research Center
Mail Stop 274
Hampton VA 23665-5225

Kipp Ronald W. Kipp
Phone: 215-824-4887
Kingsbury, Inc.
10385 Drummond Road
Philadelphia PA 19154

Kneschke Tristan Kneschke
Phone: 215-542-0700
LTK Engineering Services
Two Valley Square, Suite 300
512 Township Lane Road
Blue Bell PA 19422

Knight Josiah D. Knight
Phone: 919-660-5337
Duke University
Dept. of Mech. Engrg & Matrl Science
Durham NC 27706

Knolle Ernst G. Knolle
Phone: 415-871-9816
Knolle Magnettrans
2691 Sean Court
San Francisco CA 94080

Knospe Carl Knospe
Phone: 804-982-2603
University of Virginia
Dept. of Mech. & Aero. Engrg
Thornton Hall, McCormick Road
Charlottesville VA 22903

Kroeger John C. Kroeger
Phone: 602-561-3175
Honeywell Satellite Systems
P. O. Box 52199
Phoenix AZ 85072-2199

Kuzin Alexander V. Kuzin
Phone: 095-297-6511 (fax)
Moscow Aviation-Tech. Institute
Subfaculty "Microprocessor Systems,
Electronics, and Electrical Engg."
Petrovka, 27, Moscow, K31 103737
U.S.S.R.

Larsonneur Rene Larsonneur

Phone: 01-2562539

Mechatronics Group

Robotics Institute

ETH Zurich

Zurich CH-8092

SWITZERLAND

Lewis Pete Lewis

Phone: 804-864-7238

NASA Langley Res. Cen.

MS 440

Hampton VA 23665-5225

Meeks Crawford R. Meeks

Phone: 818-886-0250

AVCON

19151 Parthenia Street

Suite G

Northridge CA 91324

Melzer Eckhard B. Melzer

Phone: 551-709-2142

German Aerospace Research Establishment

Central Division Windtunnels

W-3400

Gottingen

GERMANY

Motter Mark Motter

Phone: 804-864-6978

NASA Langley Research Center

Mail Stop 442

Hampton VA 23665-5225

Nelik Lev Nelik

Phone: 908-859-7019

Ingersoll-Rand Company

Advanced Tech. Research and Dev.

942 Memorial Parkway

Phillipsburg NJ 08865

Lashley Christopher M. Lashley

Phone: 301-982-2093

Fare, Inc.

4716 Pontiac St. Suite 304

College Park MD 20740

McMichael Chase K. McMichael

Phone: 713-743-8262

Texas Center for Superconductivity

University of Houston

4800 Calhoun

Houston TX 77204-5506

Meier R. H. Meier

Phone: 614-392-8382

Cooper Industries

105 North Sandusky Street

Mount Vernon OH 43050

Morris Michelle L. Morris

Phone: 804-864-4179

NASA Langley Research Center

MS 416A

Hampton VA 23665-5225

Muto Masai Muto

Phone: 3-5276-6785

Railway Technical Research Inst.

Hiei-Kudan-Kita Bldg. 5F,

4-1-3, Kudan-Kita

Tokyo 102

JAPAN

Neumeyer Charles L. Neumeyer

Phone: 212-839-1643

Ebasco Services, Inc.

2 World Trade Center

New York NY 10048

Nguyen Tiep Nguyen
Phone: 704-547-4371
Univ. of North Carolina - Charlotte
Precision Engineering - ARC
Charlotte NC 28223

Oman Henry Oman
Phone: 206-878-4458
Boeing Aerospace and Electronics
19221 Normandy Park Dr., S. W.
Seattle WA 98166

Owen Andrew K. Owen
Phone: 415-321-5630
Complere Inc.
P. O. Box 1697
Palo Alto CA 94302

Paden Prof. Brad Paden
Phone: (805) 893-8165
Univ of CA
Dept. of Mech. Engg
Santa Barbara CA 93106-5070

Pang Da-Chen Pang
Phone: 301-405-5327
University of Maryland
Department of Mech. Engg.
College Park MD 20742

Pelrine Dr. Ronald E. Pelrine
Phone: 415-859-3360
SRI International
333 Ravenswood Avenue
EL137
Menlo Park CA 94025

Petukhova Irina A. Petukhova
Phone: 06452-9-6193
Severodonetsk Manuf. Assoc. "AZOT"
5, Chimikov,
Severodonetsk 349940
U.S.S.R.

Poovey Tony Poovey
Phone: 704-547-4371
Univ. of North Carolina-Charlotte
Precision Engineering - ARC
Charlotte NC 28223

Price Douglas B. Price
Phone: 804-864-6605
NASA Langley Research Center
Mail Stop 161
Hampton VA 23665-5225

Putman Thomas H. Putman
Phone: 412-256-1169
Westinghouse Electric Corp.
1310 Beulah Road
Science and Technology Center
Pittsburgh PA 15235

Queen M. A. Queen
Phone: 704-547-4371
University of North Carolina
Precision Engineering - ARC
Charlotte NC 28223

Raffi Rhonda C. Raffi
Phone: 617-661-0541
SatCon Technology Corporation
12 Emily Street
Cambridge MA 02139-4507

Rao Dantam K. Rao
Phone: 518-785-2489
Mechanical Technology, Inc.
968 Albany Shaker Road
Latham NY 12110

Reid John B. Reid
Phone: (415) 568-1500
United Magnet Tech.
1824 Woodsdale Dr.
Concord CA 94521

Richey Albert E. Richey
Phone: 518-456-5456
Intermagnetics General Corp.
P.O. Box 566
Guilderland NY 12084

Ritter Jim Ritter
Phone:
NASA Langley Res. Ctr.
MS 904
Hampton VA 23665-5225

Rock Col. J. C. Rock
Phone:
Dept. of the Air Force
6410 McKeon
San Antonio TX 78218

Roland J. P. Roland
Phone: 1-34-92-27-48
Aerospatiale
Route de Verneuil 78
Etablissement des Mureaux, BP96
78133 Les-Mureaux
FRANCE

Rosado Lewis Rosado
Phone: 513-255-6519
US Air Force
WL/POSL
Wright Patterson AFB OH 45433-6563

Rothwarf Frederick Rothwarf
Phone: 703-758-0247
ATE, Ltd.
11722 Indian Ridge Road
Reston VA 22091

Salcudean S. E. Salcudean
Phone: 604-822-3243
University of British Columbia
Department of Electrical Engineering
2356 Main Mall
Vancouver, B. C. V6T-1W5
CANADA

Sanders Clark Sanders
Phone: 704-547-4371
Univ. of North Carolina at Charlotte
Precision Engineering - ARC
Charlotte NC 28223

Schott Timothy D. Schott
Phone: 804-864-4715
NASA Langley Research Center
Mail Stop 238
Hampton VA 23665-5225

Scott Michael A. Scott
Phone: 804-864-4347
NASA Langley Research Center
MS 230
Hampton VA 23665-5225

Scurlock Ralph G. Scurlock
Phone: 703-592-046
The University of Southampton
Institute of Cryogenics
Hampshire SO9 5NH
ENGLAND

Shmilovich Alex M. Shmilovich
Phone: 301-309-0230
Maglev Technology, Inc.
14160 Saddle River Dr.
Gaithersburg MD 20878

Stephens Stuart Stephens
Phone: 612-544-2721
Fluidyne Engg.
5900 Olson Mem. Hwy
Minneapolis MN 55422

Takahata Ryoichi Takahata
Phone: 0729-77-4094
Koyo Seiko Co., Ltd.
Research & Development Center
24-1 Kokubuhiganjyo-cho
Kashiwara, Osaka 582
JAPAN

Tcheng Ping Tcheng
Phone:
NASA Langley Res. Cent.
MS 238
Hampton VA 23665-5225

Thevenot Wayne Thevenot
Phone: 202-737-9300
Maglev USA
1455 Pennsylvania Ave.
Washington DC 20024

Shewfelt Kurt Shewfelt
Phone:
Allied Signal Aerosp.
2525 W. 190th St.
Dept. 35, MS T53
Torrance, CA 90509

Siegwart Roland Y. Siegwart
Phone: 01 256 35 64
Institute of Robotics
Mechatronics Group
ETH Zurich
Zurich CH-8092
SWITZERLAND

Studer Phillip A. Studer
Phone: 301-593-7241
Magnetic Concepts
10313 Ridgemoor Drive
Silver Spring MD 20901

Tanaka Hisashi Tanaka
Phone: 81-425-73-7205
Railway Technical Research Institute
2-8-38 Hikari-cho
Kokubunji-shi
Tokyo
JAPAN

Terentiev Alexander N. Terentiev
Phone:
Institute of Chemical Physics
U.S.S.R. Academy of Sciences
117977 Moscow
U.S.S.R.

Tozoni Oleg Tozoni
Phone: 301-309-0230
Maglev Technology, Inc.
14160 Saddle River Dr.
Gaithersburg MD 20878

Trumper David L. Trumper
Phone: 704-547-4324
Univ. of North Carolina at Charlotte
Precision Engineering - ARC
Room 222
Charlotte NC 28223

Unman Prof. Daniel J. Inman
Phone: (716) 636-2593
Univ. of Buffalo
Dept. of Mech and
Aerosp. Engg.
Buffalo NY 14260

Vij Kewal K. Vij
Phone: 403-250-4792
NOVA Husky Research Corp.
2928 - 16th Street N.E.
Calgary, Alberta T2E 7K7
CANADA

Whitestone Robert C. Whitestone
Phone: 301-267-3458
David Taylor Research Center
Code 2712
Annapolis MD 21402

Yeh Ting-Jen Yeh
Phone:
MIT
77 Massachusetts Avenue
Room 35-332
Cambridge MA 02139
617-253-2108

Zhao Hong-Bin Zhao
Phone: 861-2561144-2594
Tsinghua University
Dept. of Engg Phys.
Beijing 100084
CHINA

Tryggvason Bjarni Tryggvason
Phone: 613-993-4106
Canadian Space Agency
P. O. Box 7014
Station V
Vanier Ontario KIL 8E2
CANADA

Vaidya Subhash R. Vaidya
Phone: 215-758-7355
Gardner Cryogenics
2136 City Line Road
Bethlehem PA 18017

Wassermann Johann Wassermann
Phone: VIENNA-58801-5478
Technical University of Vienna
Wiedner-Hauptstrasse 8-10
Vienna A-1040
AUSTRIA

Won Dr. Dong-Yeon Won
Phone: 042-820-2000
Korea Atomic Energy
Research Institute
P. O. Box 7
Daejun, 305-353
KOREA

Youcef-Toumi Kamal Youcef-Toumi
Phone: 617-253-2216
Massachusetts Institute of Tech.
77 Massachusetts Avenue
Room 35-233
Cambridge MA 02139

Zydron Millard Zydron
Phone: 804-688-8693
Newport News Shipb
E52 B600
4101 Washington Ave.
Newport News VA 23607

Total Number of Attendees 132

| REPORT DOCUMENTATION PAGE | | | Form Approved OMB No. 0704-0188 | |
|---|---|---|------------------------------------|--|
| Public reporting burden for this collection of information is estimated to average 1 hour per response, including the time for reviewing instructions, searching existing data sources, gathering and maintaining the data needed, and completing and reviewing the collection of information. Send comments regarding this burden estimate or any other aspect of this collection of information, including suggestions for reducing this burden, to Washington Headquarters Services, Directorate for Information Operations and Reports, 1215 Jefferson Davis Highway, Suite 1204, Arlington, VA 22202-4302, and to the Office of Management and Budget, Paperwork Reduction Project (0704-0188), Washington, DC 20503. | | | | |
| 1. AGENCY USE ONLY (Leave blank) | 2. REPORT DATE May 1992 | 3. REPORT TYPE AND DATES COVERED Conference Publication | | |
| 4. TITLE AND SUBTITLE International Symposium on Magnetic Suspension Technology | | 5. FUNDING NUMBERS 590-14-11-02 | | |
| 6. AUTHOR(S) Nelson J. Groom and Colin P. Britcher, Editors | | | | |
| 7. PERFORMING ORGANIZATION NAME(S) AND ADDRESS(ES) NASA Langley Research Center Hampton, VA 23665-5225 | | 8. PERFORMING ORGANIZATION REPORT NUMBER L-17092 | | |
| 9. SPONSORING/MONITORING AGENCY NAME(S) AND ADDRESS(ES) National Aeronautics and Space Administration Washington, DC 20546-0001 | | 10. SPONSORING/MONITORING AGENCY REPORT NUMBER NASA CP-3152, Part 1 | | |
| 11. SUPPLEMENTARY NOTES Nelson J. Groom: Langley Research Center, Hampton, VA; Colin P. Britcher: Old Dominion University Research Foundation, Norfolk, VA. | | | | |
| 12a. DISTRIBUTION/AVAILABILITY STATEMENT Unclassified-Unlimited Subject Category 18 | | 12b. DISTRIBUTION CODE | | |
| 13. ABSTRACT (Maximum 200 words) In order to examine the state of technology of all areas of magnetic suspension and to review related recent developments in sensors and controls approaches, superconducting magnet technology, and design/implementation practices, a five-day International Symposium on Magnetic Suspension Technology was held at the Langley Research Center in Hampton, Virginia, on August 19-23, 1991. The symposium included 17 technical sessions in which 55 papers were presented. The technical sessions covered the areas of bearings, sensors and controls, microgravity and vibration isolation, superconductivity, manufacturing applications, wind tunnel magnetic suspension systems, magnetically levitated trains (MAGLEV), space applications, and large gap magnetic suspension systems. A list of attendees appears at the end of the document. | | | | |
| 14. SUBJECT TERMS Magnetic bearings; Magnetic suspension; Large gap magnetic suspension; Small gap magnetic suspension; Sensors, Superconducting magnetic suspension systems; Control systems | | 15. NUMBER OF PAGES 513 | | |
| | | 16. PRICE CODE A22 | | |
| 17. SECURITY CLASSIFICATION OF REPORT Unclassified | 18. SECURITY CLASSIFICATION OF THIS PAGE Unclassified | 19. SECURITY CLASSIFICATION OF ABSTRACT Unclassified | 20. LIMITATION OF ABSTRACT | |